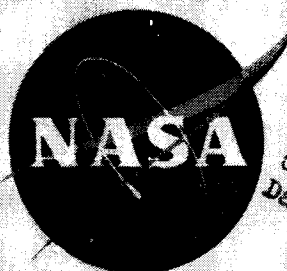


Copy

110



B. MILWITZKY

X65-80541

Declassified by authority of NASA
Classification Change Notices No. 167
Dated **

**NASA - INDUSTRY
APOLLO
TECHNICAL CONFERENCE**

**WASHINGTON, D.C.
July 18, 19, 20, 1961**

A COMPILATION OF THE PAPERS PRESENTED

**PART I
July 18, 19**

**NATIONAL AERONAUTICS AND SPACE ADMINISTRATION
WASHINGTON**

115011

CONFIDENTIAL

NASA-INDUSTRY APOLLO TECHNICAL CONFERENCE

July 18, 19, and 20, 1961

A Compilation of the Papers Presented

Part I

July 18 and 19, 1961

Washington, D.C.

CONFIDENTIAL

DECLASSIFIED

INTRODUCTION

This document is Part I of a compilation of papers presented at an NASA-Industry Apollo Technical Conference held at the Interdepartmental Auditorium, Washington, D.C., July 18, 19, and 20, 1961. These papers were presented by staff members from NASA Centers and personnel of the NASA Apollo Study Contractors. These contractors were General Dynamics/Astronautics, General Electric (Missile Systems Vehicle Division), and The Martin Company.

DECLASSIFIED

TABLE OF CONTENTS

INTRODUCTION	vii
------------------------	-----

TECHNICAL PAPERS PRESENTED

July 18, 1961

I. SPACE VEHICLE DESIGN

Session Chairman: Charles J. Donlan - Langley Research Center

1. APOLLO SPACECRAFT DESIGN . . . by Robert O. Piland, Caldwell C. Johnson, Jr., and Owen E. Maynard - NASA Space Task Group . .	1
2. SUMMARY OF THE AERODYNAMIC CHARACTERISTICS OF A VARIETY OF LOW-LIFT-DRAG-RATIO REENTRY VEHICLES . . . by Emanuel Boxer, Robert W. Rainey, and David E. Fetterman, Jr. - Langley Research Center	17
3. LAUNCH-VEHICLE DESIGN FEATURES . . . by George P. Pedigo - George C. Marshall Space Flight Center	31
4. LAUNCH-VEHICLE PERFORMANCE CHARACTERISTICS . . . by Otha C. Jean - George C. Marshall Space Flight Center	45
5. LAUNCH-VEHICLE DYNAMICS . . . by Harry L. Runyan, Jr., and A. Gerald Rainey - Langley Research Center	55

II. MISSION PROFILES

6. CONSIDERATIONS OF SPACE RENDEZVOUS . . . by John C. Houbolt - Langley Research Center	73
7. LUNAR LANDING CONSIDERATIONS . . . by Maxime A. Faget - NASA Space Task Group	89
8. LUNAR TRAJECTORY ANALYSIS . . . by William J. Praguski, Donald H. Novak, and A. Lawrence Guess - The Martin Company	99
9. ABORT CONSIDERATIONS . . . by Robert V. Battey - General Dynamics/Astronautics	113

03:15:30

III. NAVIGATION, GUIDANCE, AND CONTROL

Session Chairman: Robert G. Chilton - NASA Space Task Group

10. A GUIDANCE AND CONTROL CONCEPT FOR LUNAR MISSIONS
. . . by A. F. Bowen - General Dynamics/Astronautics 125
11. A STUDY OF A SYSTEM FOR MIDCOURSE NAVIGATION
. . . by Stanley F. Schmidt, John D. McLean, and Gerald L. Smith - Ames Research Center 133
12. GUIDANCE AND CONTROL DURING DIRECT DESCENT PARABOLIC REENTRY
. . . by Edwin C. Foudriat - Langley Research Center -
and Rodney C. Wingrove - Ames Research Center 147
13. DYNAMIC STABILITY AND CONTROL PROBLEMS OF PILOTED REENTRY
FROM LUNAR MISSIONS . . . by Martin T. Moul, Albert A. Schy,
and James L. Williams - Langley Research Center 169
14. INFLUENCE OF SUSTAINED ACCELERATIONS ON CERTAIN PILOT-
PERFORMANCE CAPABILITIES . . . by Brent Y. Creer and
Joseph G. Douvillier, Jr. - Ames Research Center 187
15. SOME PHYSIOLOGICAL FACTORS AFFECTING THE PILOT UNDER HIGH
SUSTAINED ACCELERATION . . . by Harald A. Smedal, Terence A.
Rogers, and Thomas D. Duane - Ames Research Center 201

July 19

IV. SPACE ENVIRONMENT

Session Chairman: Alfred J. Eggers - Ames Research Center

16. IMPACT RESISTANCE OF SPACE VEHICLE STRUCTURES . . . by
James L. Summers and C. Robert Nysmith - Ames Research
Center 213
17. SPACE RADIATION HAZARD . . . by Trutz Foelsche and John E.
Duberg - Langley Research Center 233
18. RADIATION-DESIGN ANALYSES FOR LUNAR MISSIONS . . . by
Jacob Abel - General Electric - MSVD 249

V. ENTRY HEATING AND THERMAL PROTECTION

19. CONVECTIVE HEATING OF BASIC SHAPES FOR LUNAR-MISSION VEHICLES
. . . by P. Calvin Stainback, Robert A. Jones, and Frank S.
Coe III - Langley Research Center 261

iv
CONFIDENTIAL

20. MEASUREMENTS OF THE THERMAL RADIATION FROM SHOCK LAYERS OF BLUNT BODIES FLYING AT VELOCITIES UP TO 44,000 FEET PER SECOND . . . by Thomas N. Canning, William A. Page, Harry E. Bailey, and Joseph M. Burge - Ames Research Center	279
21. EFFECT OF VEHICLE CONFIGURATION ON COMBINED HEATING LOADS WITH SPECIAL REFERENCE TO RADIATIVE HEATING . . . by Alvin Seiff, Glen Goodwin, and Bradford H. Wick - Ames Research Center	289
22. PROPERTIES OF MATERIALS FOR COMBINED CONVECTIVE AND RADIATIVE HEATING . . . by W. Winovich, B. H. Wick, J. H. Lundell, and R. M. Wakefield - Ames Research Center	309
23. AN EVALUATION OF THERMAL PROTECTION FOR APOLLO . . . by William A. Brooks, Jr., Kenneth L. Wadlin, Robert T. Swann, and Roger W. Peters - Langley Research Center	321
24. CHARACTERISTICS OF SMALL CONTROL ROCKETS . . . by James F. Connors and William T. Latto, Jr. - Lewis Research Center	337

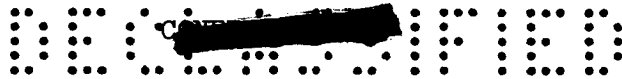
VI. ONBOARD SYSTEMS

Session Chairman: Robert O. Piland - NASA Space Task Group

25. ONBOARD PROPULSION SYSTEM FOR LUNAR MISSIONS . . . by Neil E. Munch and George R. Arthur - General Electric - MSVD	351
26. ENVIRONMENTAL-CONTROL SYSTEM FOR LUNAR MISSIONS . . . by Fred Parker - General Electric - MSVD	369
27. TRACKING AND COMMUNICATIONS SYSTEM FOR A LUNAR MISSION . . . by Ray E. Thompson - General Dynamics/Astronautics	385
28. ELECTRIC POWER SUPPLY SYSTEM FOR APOLLO . . . by E. W. Colehower, G. O. Allen, and S. H. Scales - The Martin Company	395
29. EARTH-LANDING-SYSTEM DESIGN ANALYSIS . . . by R. C. Chandler and R. L. Lohman - The Martin Company	405
30. AERODYNAMIC CHARACTERISTICS OF PARAWINGS . . . by Donald E. Hewes, Robert T. Taylor, and Delwin R. Croom - Langley Research Center	423

DECLASSIFIED

**I.
SPACE
VEHICLE
DESIGN**



APOLLO SPACECRAFT DESIGN

By Robert O. Piland, Caldwell C. Johnson, Jr.,
and Owen E. Maynard

NASA Space Task Group

INTRODUCTION

The Apollo studies conducted in the past year have consisted of both research and design nature. The results of four spacecraft design studies are discussed in this paper. Consideration is given to systems general arrangements, the various modules which make up the spacecraft, and spacecraft weights.


TECHNICAL GUIDELINES

Before considering the spacecraft designs it would be well to review the guidelines on which the studies were based. It is pertinent to note that all of the studies which are discussed in the subsequent papers were conducted within the general framework of these guidelines.

The first several guidelines deal with the missions and space vehicle:

1. Capable of manned lunar reconnaissance with lunar mission module
2. Capable of corollary earth orbital missions with lunar mission module and with space laboratory
3. Compatible with Saturn launch vehicle (weight not to exceed 15,000 lb for complete lunar spacecraft)
4. Capable of 14-day flight time

The first guideline states that the spacecraft shall be capable of manned lunar reconnaissance with a lunar mission module. At the time the guidelines were formulated the lunar landing mission was not a firm Apollo mission as it is now. A subsequent paper by Maxime A. Faget will deal with lunar landing considerations. The second guideline states that the spacecraft shall be capable of corollary earth orbital missions with the lunar mission module and with a space laboratory. The spacecraft shall be compatible with the Saturn launch vehicle and its weight shall not exceed 15,000 pounds for the entire spacecraft. The



CONFIDENTIAL

15,000 pounds refers to the escape-velocity payload of the Saturn C-2. A basic result of the study is that the spacecraft cannot be built within this limitation and a launch vehicle of greater capability than that of the C-2 will be required for circumlunar and lunar orbital missions. Such a launch vehicle, the C-3, is now underway. The last of this series of guidelines states that the spacecraft be capable of 14-day flight.

The next series of guidelines consider return, reentry, and landing:

1. Capable of safe recovery from aborts
2. Capable of ground and water landing (also capable of avoiding local hazards)
3. Designed for 72-hour postlanding survival period
4. Capable of small-area landing
5. Auxiliary propulsion required for maneuver in space

The spacecraft shall be capable of safe recovery from aborts. The spacecraft shall be capable of either ground or water landings and also be capable of avoiding local hazards. The spacecraft shall be designed for a 72-hour postlanding survival period. The spacecraft shall be capable of a preselected small-area landing on return from normal missions. Auxiliary onboard propulsion is required for maneuver in space.

The next guidelines deal with the crew and their environment:

1. Designed for "shirt-sleeve" environment
2. Designed for three-man crew
3. Provisions for radiation protection

The spacecraft shall be designed for a "shirt-sleeve" environment and for a three-man crew, and there shall be provision for radiation protection.

The last two guidelines which deal with command and communications are

1. Primary command of mission to be onboard
2. Communications and tracking required

Primary command of the mission shall be onboard. Communications with and tracking of the spacecraft are required except possibly when the spacecraft is blanketed by the moon.

CONFIDENTIAL

The systems designs discussed are based on the guidelines as stated. They will require additional scrutiny in the light of the now firm lunar landing mission and new launch-vehicle capability.

SYSTEMS DESIGNS

General Arrangement

The general arrangements of the systems are based, with varying modifications, on a modular concept. The object of this concept is twofold: to allow jettisoning of expended or no longer necessary stores or subsystems prior to reentry, so that the penalty of protecting these parts during reentry and landing will not be incurred; to meet special mission requirements by modifying only single modules, thereby keeping certain modules constant throughout the project. At the beginning of the study it was envisaged that three basic modules might be used, which for a lunar mission would consist of the following: a command module to house the crew during launch and reentry and to provide mission control; a propulsion module for abort, for course corrections, and for entry and exit from lunar orbit; and a mission module containing life support and possibly equipment for lunar reconnaissance.

The general arrangements of systems resulting from four separate design studies are presented in figures 1 and 2. Each system incorporates the modular concept; however, the arrangements vary widely. All four systems are shown mounted on the Saturn S-IV stage, which is the second stage of the C-1 or the third stage of both the C-2 and the C-3. The S-IV stage is 220 inches in diameter.

Design I (fig. 1) employs a blunt symmetrical command module with a habitable mission module mounted forward of the command module with a connecting tunnel. Several crew positions are illustrated. A propulsion module consisting of four H_2O_2 engines providing 6,000 pounds of thrust each and their associated tankage and systems is proposed. The complete system is encased in a fairing. The launch abort system consists of eight solid rockets mounted on the fairing as indicated. The total length of the spacecraft is 425.5 inches. The total weight of the spacecraft with the H_2O_2 propulsion system giving a velocity capability of 6,600 fps is 16,900 pounds.

Design II (fig. 1) features a tower-type launch abort system employing a single solid rocket. The command module which is a blunt symmetrical shape is rearward of this solid rocket. Several crew positions are illustrated. A propulsion module employing two 15,000-pound-thrust engines and using storable propellants is shown. A service

037120000000

module containing stores and systems jettisonable prior to reentry is incorporated with the propulsion module and is used in lieu of a habitable mission module. Note that this is the only design with only a single habitable module. The length of the system is approximately 500 inches. The total weight of this system with the storable propulsion system which also provides a velocity capability of 6,600 fps is 25,100 pounds.

Design III (fig. 2) also features a tower-type launch abort system. A command module employing a M-1 type of configuration, a habitable mission module connected by a hatch, a 15,000-pound-thrust H_2O_2 engine, and associated systems complete the spacecraft. The overall length of the system is 615 inches. The total weight of this system with the H_2O_2 propulsion system and a velocity capability of 6,600 fps is 21,170 pounds.

Design IV (fig. 2) employs a tower-type escape system and a command module using the M-1 configuration mounted blunt-end forward and immersed in the habitable mission module. The propulsion module incorporates two 15,000-pound-thrust H_2O_2 engines and tanks as shown. Note that although the command modules are mounted differently in designs III and IV, the crew is in an optimum position for launch accelerations in both cases. The overall length of the system is 622.5 inches and the total weight with the H_2O_2 system and a velocity capability of 6,600 fps is 18,200 pounds.

There are several major differences in the designs described. These differences include the use of pusher-type launch abort systems as opposed to the tower-type system, the use of one habitable module as opposed to two, different reentry configurations, and the use of storable or cryogenic propulsion systems.

Launch Abort System

The launch abort system provides abort capability for emergency separation from the launch vehicle while on the pad or during atmospheric flight. In order to separate the spacecraft rapidly from the launch vehicle in the presence of high drag, relatively high thrust is required. This requirement for high thrust must be tempered by allowable crew tolerance to acceleration when the drag is low. The launch abort system of design I (fig. 1) provides a statically stable abort configuration, a relatively clean overall configuration, and the ability to jettison the eight rockets singly or in pairs as the density decreases and less thrust is required for abort. Less desirable features of this approach include the necessity of aborting the mission module and fairing as well as the command module. This leads to a relatively complex sequencing

[REDACTED]

and separation operation to get the command module clear of the rest of the system and in a position for landing system deployment.

The tower system employed by the other three designs (figs. 1 and 2) allows abort of only the command module and a subsequent relatively simple sequence for separation of the tower. The tower designs, however, pay the penalty of having a "dirty" aerodynamic configuration with the resulting possibilities of unsteady flow and considerable noise generation.

Manned Mission Module Considerations

One consideration affecting the choice of single or dual habitable modules is weight, a basic reason for modularity. The ability to jettison the mission module prior to reentry affords a weight saving for the dual module arrangement. A comparison of the dual and single modules is illustrated in figure 3. The dual arrangement consists of a mission module and a command module. The weight of the dual arrangement is to be compared with that of the larger single command module on the right taken from design II. The characteristics of the two approaches are summarized in the chart. The volume of the mission module is 215 cubic feet and that of the smaller command module is 215 cubic feet, giving a total of 430 cubic feet. This is the same volume as that of the single module; therefore, this comparison is based on equal volumes. The structural and heat-protection weight for the two arrangements is shown on the lower line. The two modules weigh 3,572 pounds as compared to 4,122 pounds for the single module arrangement. The unit weights assumed are based primarily on loading and heating requirements. As expected, the dual arrangement is lighter with a calculated weight saving of 500 pounds.

For a given volume the space utilization characteristics of the single module will be greater in the case of the single module than in the dual arrangement. Space is lost in the additional corners of the dual arrangement. Consequently, less volume would be required for the single module than for the dual modules, resulting in a reduction of the estimated 500-pound weight penalty calculated in the "equal-volume" comparison. The length-to-diameter ratio of the dual modules is inherently greater than that of the single module and will result in a less-compact arrangement and greater moments on the launch vehicle.

The mechanical features of the dual module arrangement are more complex than those of the single module because of the requirement for connecting hatches. The location of the crew in a single module makes it easier to adapt to an emergency situation. A minimum of movement to reach duty stations with no requirements for the closing of hatches offers a significant safety feature.

SECRET

03171: [REDACTED] 031

Both approaches offer a high degree of flexibility. The mission module can be enlarged as required for particular missions. A mission module can be added to the single module if space is required for a particular mission. The smaller module is inherently limited, however, to being able to return a maximum crew of three to earth and has a minimum of allowable space for unforeseen requirements within the command module. The larger command module could, if required, return to earth a crew of six. Equipped with a mission module, the capability of the large command module is further enhanced. In summary, therefore, it may be stated that for the lunar mission the dual manned module arrangement appears to offer a weight advantage of up to 500 pounds. The single module, however, appears to have many design and operational features which make it the more desirable approach. More important, the use of the large reentry module offers the more flexible approach, especially in view of the contingencies that may arise in the course of a project of this scope and time scale. A parallel development of a space-laboratory module which could be used with the large single module for earth orbital missions would appear reasonable.

Internal-Space Requirements

The previous illustrative comparison of the single and dual module arrangements points up the question of the absolute volume requirements for the system. A summary of the volumes of the command and mission modules for the four designs is presented in the following table:

Spacecraft design	Volume, cu ft		
	Command module	Mission module	Total
I	165	126	291
II	430		430
III	350	380	730
IV	340	1,300	1,640

The first design appears to be of a minimum volume. Designs III and IV appear more than adequate in total volumes. Figure 4 presents the internal arrangement for design II which incorporates all living quarters in the single module. This blunt symmetric shape has a total volume of 430 cubic feet and a diameter of 160 inches. For launch, reentry, and other periods of stress of the mission, the crew members

[REDACTED]

DECLASSIFIED


7

are seated three abreast as indicated in the top and side views. The middle seat is retractable and allows access to other duty stations during less stressful periods of the mission. Sleeping and sanitation quarters are located behind the control positions. A work station is located on the opposite side of the module. Privacy is provided by the simple expedient of lightweight walls or curtains. An air lock is provided for exit into space, to other vehicles, or to the moon surface. The internal space is the equivalent of a room 10 feet in diameter and 6 feet in height. It may be concluded therefore that a volume of approximately 400 cubic feet is adequate to conduct the operational and normal living functions for the mission.

Reentry Configurations

A large number of configurations received consideration during the design study. A small number of these are shown in two views in figure 5. The first and second configurations on the top row consisting of lenticular and winged shapes offer the capability of a horizontal landing in a relatively conventional manner on a prepared surface. It was found that these configurations generally weighed several thousand pounds more than the compacts, and that the high hypersonic lift-drag capability of the winged configuration was not required for range purposes. More important, however, is the inability of these configurations to cope with any but prepared landing surfaces. The nature of the project makes it imperative that the selected configuration and landing system be suitable for landing over a relatively broad range of landscapes and water conditions. These configurations cannot fulfill this very necessary requirement without extensive weight and complexity penalties. The third configuration was a slender, symmetric shape which offered very high-heat-protection weights and was a poor shape for space utilization. The fourth configuration offered only advantages in particular areas. The four configurations in the lower part of the figure were given more detailed attention and are incorporated into the systems arrangements previously shown in figures 1 and 2. The two on the left represent variations on the blunt symmetrical body, and the two on the right have features similar to the M-1 configuration. More detailed characteristics of the configurations are shown in figures 6 and 7.

The configuration of the command module of design I (fig. 6) is 113.2 inches in diameter and is used with a manned mission module. The crew sits three abreast and the accelerations during both launch and reentry are in the eyeballs-in or desirable direction for tolerance to accelerations which might be encountered under emergency conditions. Control in the atmosphere is obtained by use of a flap and roll jets. The weight of this configuration whose volume is 165 cubic feet is estimated to be 5,118 pounds.






The configuration of the command module of design II (fig. 6) is similar except that it is considerably longer, has a diameter of 160 inches, and assumes that the crew will remain in this command module throughout the mission. The acceleration directions are similar. No flaps are shown on this configuration. The control technique assumes an offset center of gravity which causes the module to trim at some fixed angle of attack corresponding to a required maximum lift-drag ratio. The command module may be rolled through the use of roll jets allowing control of the direction of the lift vector. Modulated roll rates effectively reduce the lift-drag ratio. The weight and volume resulting from this study are 8,500 pounds and 430 cubic feet.

The configuration of the command module of design III (fig. 7) is a variation of the M-1 shape, with a length and span of 150 inches. During launch the accelerations are from the rear, or eyeballs-in position. During reentry the direction of acceleration varies as indicated by the two arrows as the module is pitched between the angle of attack corresponding to the maximum lift coefficient and that corresponding to the maximum lift-drag ratio. This is the range of angles of attack over which this reentry configuration is intended to operate. It should be mentioned that whereas the accelerations are from a less favorable direction, the magnitude of the accelerations for the particular technique used is within allowable tolerances. This design employs two flaps for lateral control and a single large flap for pitch control with a total flap area of 28 square feet. Its weight is estimated as 6,954 pounds for a volume of 350 cubic feet. This spacecraft design configuration assumes a habitable mission module, although a moderate increase in volume would provide the capability to conduct the mission without the mission module.

The configuration of the command module of design IV (fig. 7) is closer in detail to the basic M-1 configuration, being modified only by rounding the base. The length and span of this configuration are 136 and 150 inches, respectively. The crew's positions are in the opposite direction of those of design III. This position allows the accelerations to be taken in the eyeballs-in direction during reentry in a manner similar to the blunt shapes. The launch accelerations are also taken in this manner by mounting the module blunt-end first, immersed in the habitable mission module. Four flaps are employed for lateral and pitch control as shown. The total flap area is 28 square feet. The estimated weight of this configuration is 5,637 pounds for a volume of 340 cubic feet. The lighter weight of design IV results to some extent from a larger number of systems located in the mission module.

The design studies therefore have resulted in a preference for the relatively compact configurations as opposed to the configurations having high lift-drag ratios. Within the range of compact configurations, two particular types seem to be preferred: the blunt, symmetrical



CONFIDENTIAL

shape and the asymmetric M-1 type of configuration. General geometric considerations for configuration selection include the relative usefulness of a given volume for a particular shape. The blunt shapes probably have some small advantage in this regard. The symmetrical configuration also offers advantages for carrying structural loads, for ease of fabrication, and in the aerodynamic loads imposed on the launch vehicle during boost.

The directions of the acceleration vectors imposed on the crew were described previously for the several designs. The blunt shape lends itself towards placing the crew in a position where they have the greatest tolerances to acceleration for both launch and reentry. The asymmetric configuration through particular mounting arrangements such as shown in design IV can also achieve this feature.

The aerodynamics of configurations are discussed in a subsequent paper by Emanuel Boxer, Robert W. Rainey, and David E. Fetterman, Jr. The configurations discussed in detail herein have lift-drag ratios of less than 1. Guidance and control accuracies from incomplete studies indicate that lift-drag ratios of the order of 0.5 are sufficient to meet guideline requirements. Higher lift-drag ratios naturally could provide more flexibility. The control techniques range from the use of no control surfaces to the use of a full set of four controls. The use of offset center of gravity combined with roll jets proposed for the blunt configuration is an attempt to do away with the need for aerodynamic flaps and their resulting heating and mechanical problems. Further study will be required to completely confirm the ability to achieve this goal. The M-1 configuration could also possibly employ such a scheme.

The effects of heating on the configuration are also discussed in more detail in a subsequent paper by Alvin Seiff, Glen Goodwin, and Bradford H. Wick. The weight of heat-protection systems to take care of the convective heating will be less for the symmetrical blunt body. The effects of nonequilibrium radiation are not fully defined, but present estimates indicate that the protection required for this type of heating is not a significant part of the total.

In conclusion, the symmetrical blunt shape would appear to offer simpler design features and would lend itself to crew protection from high accelerations, although particular design arrangements might minimize this consideration for normal missions. The basic aerodynamic characteristics of lift-drag ratio and controllability appear similar for the configurations. Convective-heating considerations would favor the blunt body; however, the less well understood phenomena of nonequilibrium radiation could have effects on the heat-protection systems of undefined magnitude.

CONFIDENTIAL

03112 [REDACTED] 30

Onboard-Propulsion Consideration

The propulsion module provides the impulse to be used in space for a particular mission such as lunar orbit, or it may be used for abort or emergency return. The particular mission requirement can cause the weight of the onboard-propulsion module to vary greatly and consequently greatly affect the total weight of the spacecraft. These effects are summarized in table I. Assume that the weight of the spacecraft less the weight of the propulsion module is 11,000 pounds. The estimated spread in weights from the studies is from 8,500 to 11,000 pounds. This is the weight of the command module just described plus the weight of the mission or service module. The missions under consideration are shown on the left and include earth orbit and circumlunar and lunar orbit. The functions of the onboard propulsion are as follows: (1) retrograde and maneuvers for the earth orbit mission, (2) course corrections and abort for the circumlunar mission, and (3) course corrections and entry and exit from lunar orbit for the lunar orbital mission. With reference to the initial guideline, which gave a weight limit of 15,000 pounds, it can be seen that the C-2 launch vehicle could place the spacecraft to escape velocities only if the abort capability were limited. The lunar-orbit spacecraft weights, assuming a 6,600 fps requirement, are 21,170 and 25,100 pounds, respectively. Therefore, it is concluded that the C-2 does not have the capability for general lunar missions. It is to be noted also that the spacecraft weights for the different Apollo missions can vary as much as 100 percent for the variety of missions considered due to the different propulsion requirements.

SYSTEMS WEIGHTS

These spacecraft weights, as discussed previously, were based on a basic command and mission module weight of 11,000 pounds. This weight represents the maximum of the weights estimated in the studies which varied from 8,500 to 11,000 pounds. Table II gives the spread in weights by the various systems and spacecraft.

The difference in maximum and minimum structure and heat-protection weights results primarily from size considerations. Factors of 100 percent for various systems are not uncommon reflecting such considerations as overall size of system, redundancy, and particular design. The propulsion variation for the system reflects the difference between the use of H_2O_2 propulsion systems as opposed to a storable system and the fact that the minimum propulsion system is accelerating 8,500 pounds as opposed to 11,000 pounds for the maximum system. In conclusion, the lightest weight system estimate having lunar orbit capability and employing H_2O_2 may weigh in the order of 16,900 pounds,

[REDACTED]

DECLASSIFIED

11

whereas more conservative and larger systems employing storable propellants would weigh up to 25,100 pounds.

CONCLUSIONS

1. The modular approach is desirable, although for the lunar mission a single manned module is preferable, accepting a modest weight penalty.
2. Compact configurations such as the blunt symmetrical shape with lift-drag ratios less than 1 and their lower weight and less sensitivity to emergency conditions appear desirable.
3. The C-2 launch vehicle is capable of injecting the spacecraft to escape velocities for only the circumlunar mission and then only if the abort requirements are relaxed.
4. The total Apollo spacecraft weight may vary from 13,000 to 25,000 pounds for its various intended missions.

03:17:20:0000

TABLE I.- PROPULSION-MODULE CHARACTERISTICS

[Spacecraft less propulsion module = 11,000 lb]

Mission	ΔV , fps	Spacecraft total weight, lb	
		H ₂ O ₂	Storables
Earth orbit: Retrograde and maneuvers	1,300	12,845	13,200
Circumlunar: Course corrections	600	12,050	12,258
Abort, immediate return	5,600	19,600	22,640
Lunar orbit: Course corrections and enter-exit orbit	6,600	21,170	25,100

TABLE II.- SPACECRAFT-WEIGHT ESTIMATES

	Weight, lb	
	Minimum	Maximum
Structure, heat protection, and adapter	4,000	5,500
Landing-recovery system	450	800
Attitude-control system	350	660
Guidance and navigation	270	830
Communication system	170	430
Electrical-power supply	620	1,430
Environmental control	700	1,700
Crew systems	980	1,400
Instrumentation	220	650
Propulsion (6,600 fps)	8,400	14,100
Spacecraft	16,900	25,100

GENERAL ARRANGEMENT

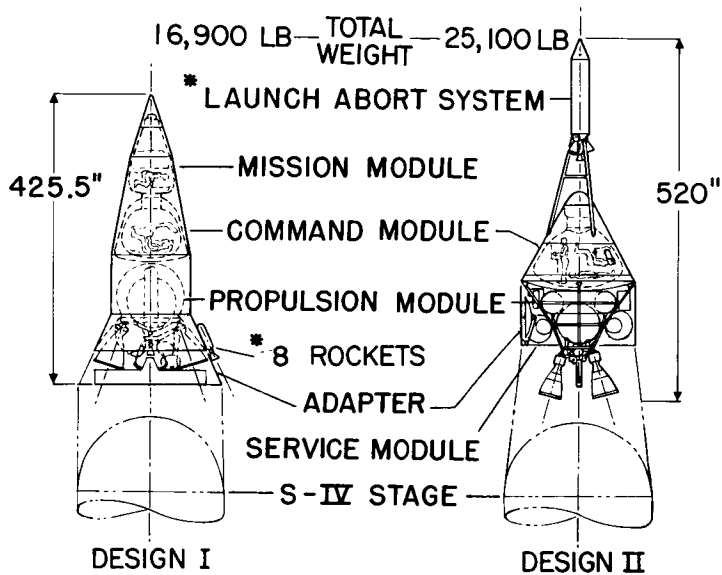


Figure 1

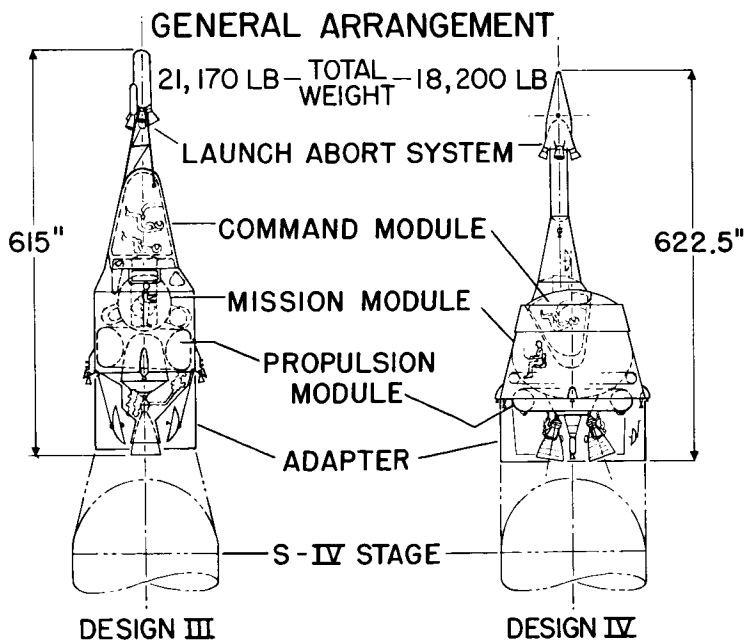


Figure 2

037123 [REDACTED]

COMPARISON OF DUAL AND SINGLE MANNED MODULES FROM DESIGN II

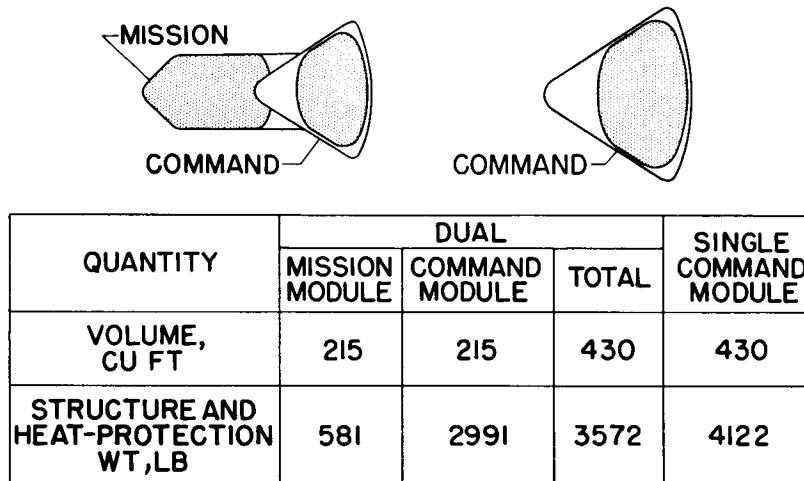


Figure 3

INTERNAL ARRANGEMENT DESIGN-II

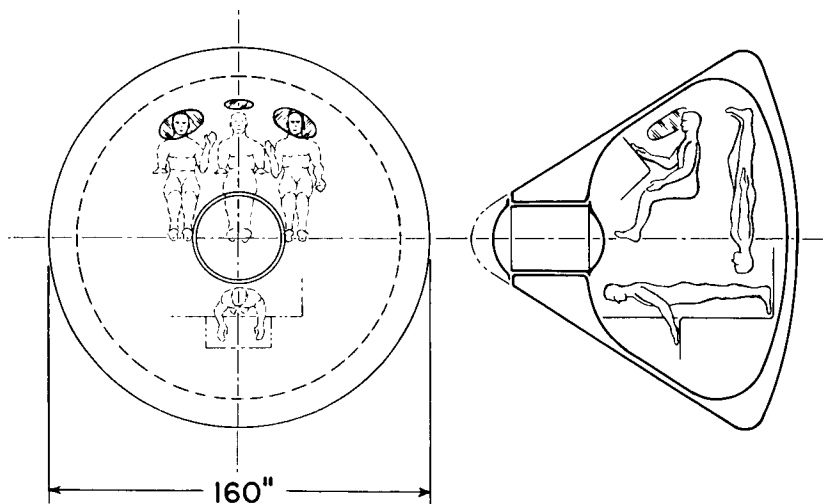


Figure 4

[REDACTED]

TYPICAL REENTRY CONFIGURATIONS CONSIDERED

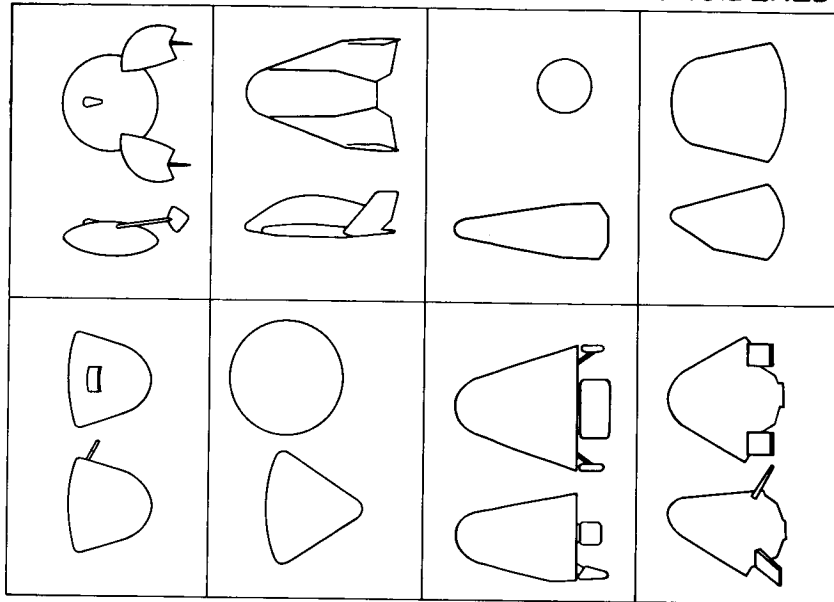


Figure 5

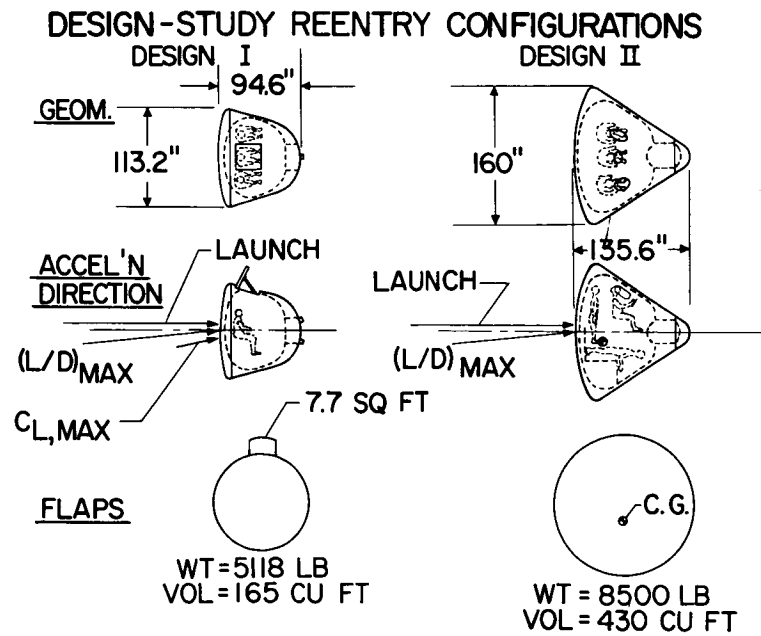


Figure 6

031712Z010000

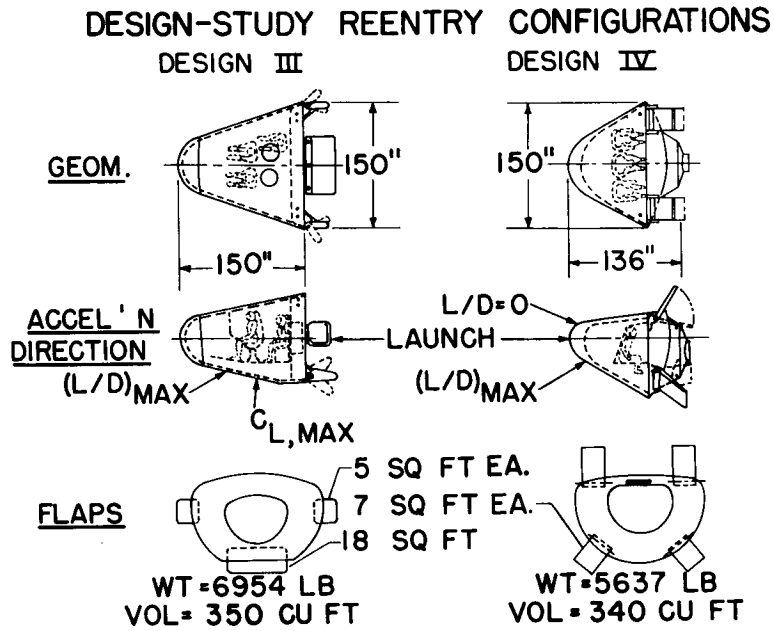


Figure 7

SUMMARY OF THE AERODYNAMIC CHARACTERISTICS OF A VARIETY OF LOW-LIFT-DRAG-RATIO REENTRY VEHICLES

By Emanuel Boxer, Robert W. Rainey,
and David E. Fetterman, Jr.

Langley Research Center

INTRODUCTION

NASA studies of planetary entry (refs. 1 and 2) have indicated that the full benefits derived from utilizing lift - namely, increased entry corridor width, the considerable reduction of decelerating forces, and the ability to maneuver to a preselected touchdown site - can be obtained only at the expense of increased weight.

For the Apollo mission where the all-up weight is a major constraint, it appears as though a design maximum lift-drag ratio on the order of $1/2$ is an acceptable compromise between the desire for minimum structural weight and vehicle maneuverability. The Lunar Mission Reentry Vehicle therefore will be a blunt compact wingless capsule. It must be stable and controllable through an angle-of-attack range that includes zero lift to that for a maximum lift-drag ratio on the order of $1/2$. Although some aerodynamic studies have been made upon blunt bodies at hypersonic speeds in the past, they were limited to a few specific configurations so that the results were not applicable to a variety of body types (refs. 3 to 8). Furthermore, little experimental data were available dealing with the effects of control deflection upon the stability and maneuverability of such bodies. (See ref. 9.) In order to supply this information the NASA Ames and Langley Research Centers initiated extensive test programs on a wide variety of blunt body shapes capable of producing trimmed lift-drag ratios on the order of $1/2$ through the use of simple flap-type controls. In this paper the pertinent hypersonic results obtained from these investigations are summarized and problem areas are indicated.

SYMBOLS

C_D drag coefficient

C_L lift coefficient



037122-1000

C_m	pitching-moment coefficient
C_p	pressure coefficient
d	maximum body diameter
L/D	lift-drag ratio
M_∞	free-stream Mach number
q	dynamic pressure
r	edge radius
R_d	Reynolds number based upon body diameter
α	angle of attack
δ_a	roll-control deflection
δ_e	pitch-control deflection
δ_r	yaw-control deflection
ΔC_l	incremental rolling-moment coefficient
ΔC_m	incremental pitching-moment coefficient
ΔC_n	incremental yawing-moment coefficient
ΔC_N	incremental normal-force coefficient
W	weight
A	area

Subscripts:

TRIM	trimmed condition
MAX	maximum



CONFIGURATIONS

Most of the configurations shown in figures 1 and 2 were subjected to a weight and balance analysis to determine a realistic center-of-gravity location about which aerodynamic moments were referenced. The first three configurations shown are, or are derived from, forward-facing blunt cones and are designed to operate in the low angle-of-attack range. The conical shape was selected partially because of the inherent stability of such bodies. The M-1 which is a blunt flat-top half-cone configuration has been reported in NASA publications (e.g., ref. 4). It exhibited satisfactory lateral and directional characteristics and, with a slight modification to the nose shape, satisfactory longitudinal stability at higher angles of attack. The flat-face cone is an unsymmetrical truncated-cone body which utilizes a blunt flat nose to provide a pitching-moment input to trim at near maximum lift-drag ratio. An interesting method of trim altitude control suggested is to vary the nose angle during flight. The calculated effectiveness of this method over a range of shape variables is included in reference 10. The blunt cone designated L-8 was selected for investigation for reasons of stability since calculations indicated that the center of pressure is invariant with Mach number. In addition, the launch-vehicle-spacecraft aerodynamic and mating problems are minimized.

The next two configurations, the L-1 and L-4, are designed for moderate angle-of-attack attitudes during reentry and utilize flat surfaces to generate lift. The L-1 shape was derived from an extensive study of conical lifting bodies reported in reference 6. It is a flat-bottom half-cone with a canted flat nose to provide bluntness and a pitching-moment input that requires small flap deflection to trim at maximum lift-drag ratio. Because the conical portion is essentially shielded from the flow at higher angles of attack, triangular flat sides were incorporated to provide directional stability. The L-4 was designed to investigate the aerodynamic characteristics of a square-cross-section body which should provide more efficient utilization of the enclosed volume.

The remaining shapes are highly blunt bodies designed for entry at high angles of attack with reference to a line parallel to the heat-shield face. The L-2C has a spherical face of large radius, rounded shoulders, and a shielded symmetrical truncated-cone afterbody. The L-3A shape has a modified delta planform with rounded edges and a shielded afterbody. It was included in the program because previous investigations on delta wings indicated that such a shape has the minimum overall convective heating rate during a high-angle-of-attack lifting reentry. The L-7 is a lenticular design with elliptical cross section which deploys horizontal- and vertical-tail surfaces at supersonic speeds to enable it to make a horizontal landing. During the

031715781930

high-heating portion of the reentry an offset center-of-gravity position is used to trim at a fixed high angle of attack.

Except for the M-1 and the flat-face cone, detail drawings of all configurations and extensive experimental data obtained at Mach numbers up to 10 are included in reference 11.

The L-3A and L-4 exhibited serious static stability and control problems which could be overcome by redesign should there be any, as yet unproven, advantage in utilizing such shapes. The flat-face cone suffers from a lack of experimental data upon which to assess its merits. The L-7 has associated with it a serious weight penalty to provide for the horizontal landing capability. Therefore only the results of test on the M-1, L-1, L-8, and L-2C are discussed because they include at least one model of each type which can meet the aerodynamic requirements of the Apollo mission.

TRIMMED CHARACTERISTICS

It has been found that the four vehicles can be trimmed from $L/D = 0$ to $(L/D)_{MAX}$ between 0.5 and 0.62 as shown in figure 3. All curves are based upon experimental data except those for M-1 which are from Newtonian calculations. These data are representative of results obtained from tests in the Mach number range from 3 to 10. Included in this figure are the values of the trimmed angles of attack at approximately $C_L = 0$ and maximum L/D for all vehicles. It is seen that for all vehicles except L-8 the required angle-of-attack range is between 35° and 45° which is a stringent requirement insofar as longitudinal stability at all trim conditions is concerned. However, by small adjustments in the centers of gravity all of these vehicles have been made statically stable throughout their trim α range with their location in close proximity to that determined from a weight-and-balance study.

Two of these vehicles utilize the high drag portion of the polar and therefore have lower values of W/C_{DA} (of the order of 45 at $L/D < 0.4$); consequently, for a given L/D , the convective heat loads for these vehicles would be expected to be comparatively lower. However, the variations in aerodynamic resultant-force coefficient for the high-drag-type vehicles are small and these two vehicles would have a small penalty in g-alleviation.

The variation of trimmed lift coefficient as a fraction of the maximum lift coefficient is shown in figure 4 as a function of the lift-drag ratio. At high angles of attack all configurations tested to the

031715781930

point where the maximum trimmed lift coefficient was obtained, in addition to those shown in figure 4, correlated very well with respect to flat-plate impact theory up to about L/D on the order of 0.4. Thus the simple flat-plate theory may be used to prescribe the lift, drag, and L/D variation for any compact body at high angles of attack in trajectory studies. From 0.4 to maximum lift-drag ratio, the blunt-cone predictions appear to follow the data in the region where nose drag effects influence the lift-drag ratio and specific shape begins to affect the correlation.

BASIC CONFIGURATION PREDICTIONS

The ability to predict the longitudinal characteristics of these configurations is shown in figures 5 and 6. Since body-alone data were not available for the M-1 configuration, the data shown include inputs from trailing-edge flaps at zero deflection. The experimental data are representative of the speed range between Mach numbers of 6 and 10.

For the axisymmetric configurations (L-8 and L-2C) and the M-1 configuration, simple theory, for the most part, gives very good predictions of the static force and moment characteristics. The lift-drag ratio for L-8, however, is overpredicted. This is due primarily to the neglect of skin friction and base drag on this relatively low-drag shape.

The characteristics of the L-1 configuration are affected to a very large extent by both the strong bow shock produced by the inclined flat-nose section and the windward surface discontinuities (nose break and leading edges). As a result the various surface components experience pressure variations which are not accounted for in the theory and the force characteristics are not predicted very well as seen from the overprediction of both C_L and L/D and the angle of attack for $(L/D)_{MAX}$. In view of these induced pressure variations, the apparent good agreement in pitching moment, especially at the lower angles of attack, is somewhat fortuitous.

Since Newtonian theory does not account for pressure relief near the edges, the theory considerably overpredicted the drag for both L-1 and L-2C at the extreme angles of attack; however, because of the low lift in this angle-of-attack range good predictions of both C_L and L/D are obtained.

Similar results apply to the predictability of the lateral and directional stability derivatives for these configurations; namely,

DECLASSIFIED

0311230 1730

that good predictions (within 10 to 15 percent) can be obtained for bodies which do not employ windward flat sides.

Effect of Edge-Radius Variation

The L-2C edge radius was specified somewhat arbitrarily without a detailed heat-transfer or structural analysis. The edge radius could be changed subject to the type of heat-protection material used on the edge and provided that the aerodynamic characteristics would be acceptable. The results of a brief study of edge-radius variation on this configuration at $M = 6.7$ are presented in figure 7. The edge radius was varied from 0 for a sharp edge to a value $1/2$ the body diameter which is, of course, a hemisphere. The center-of-gravity location was held constant at 20 percent of the body diameter aft of the face and offset 2 percent of the body diameter to provide trim at $\alpha < 90^\circ$. As can be seen, good agreement between predicted and experimental values of C_L and L/D was obtained. The effect of edge-radius variation upon pitching moment was adequately predicted; however, because of the low slope and the small values of C_m the computed values of trim α are in poor agreement with the measured values. From these results the conclusion may be made that a fairly wide range of edge radius (up to 15 percent of the face diameter) may be utilized and still maintain the desired L/D of $1/2$ (or higher) with static longitudinal stability. Similar results and conclusions have been obtained on bodies where the afterbody was tangent to the edge.

Cross Coupling

With these short blunt body shapes the choice of location of controls is, in some cases, somewhat limited. The age-old problem exists of placing the controls so that they will have sufficient effectiveness to do the job, preferably without cross-coupling inputs. Two methods of alleviation of cross coupling on the reentry vehicles are presented in figure 8. For the L-1 vehicle type when the unswept elevons were differentially deflected for roll control, the difference in axial force of each elevon resulted in a severe adverse yaw due to roll control. This existed throughout the range of α and is shown here for $\alpha = 40^\circ$ only. It was calculated that this adverse yaw could be essentially removed with little reduction in roll control by sweeping the elevon hinge lines so that the planes of the elevon resultant forces act through the vehicle center of gravity. This method of alleviation of roll-control-on-yaw cross coupling has been substantiated by experimental results. The effect of roll-control deflection on pitching moment is negligible.

DECLASSIFIED

23

For the M-1, as anticipated, there was considerable pitch due to yaw control when the combined pitch-yaw control was located in the lower quadrant of the body. Shown here is a typical example at $\alpha = 0^\circ$. For the M-1, estimates indicated that the relocation of the flap to the side of the body increased the available yaw control and reduced the pitch cross coupling because the plane of the flap force is essentially in the horizontal body plane. Again the theoretical estimates of the cross coupling and the corrective action have been substantiated by experiment. Of course, an additional flap for pitch control must be added on the bottom of the M-1. For either of the flap schemes on the M-1, there was no yaw-control-on-roll cross coupling.

CONTROL EFFECTIVENESS

The controls investigated are basically simple flaps and fall into three categories with similar performance in each group. There are those following a flat-body surface such as on the L-1, upper surface of M-1, and the L-4; those following a conical surface such as on the L-8 and lower surface of the M-1; and shoulder or edge flaps as on the L-2 and L-3. As can be seen in figures 9 and 10, where comparisons are available, there is little effect of Mach number variation on control effectiveness at hypersonic speed. The large difference between data at Mach numbers 6 and 6.7 obtained in two different facilities is attributed to a Reynolds-number-separation phenomenon since the body-alone data agree very well.

The ability to predict the pitching-moment increment on the L-1 for small deflections is reasonably good. Where applicable, shock theory gives better predictions of the incremental normal force and pitching moment if calculated for the measured surface Mach number. For large flap deflections and at low angles of attack where the surface flow is supersonic, the pitching moment is overpredicted but the normal-force increment agrees with that predicted. At angles of attack greater than 30° , the subsonic flow on the surface is influenced by the deflected flap so that the large normal-force increment is underpredicted by 100 percent but the pitching moment does not show as large a discrepancy. It is evident that the flap produces a large load carry-over on the body which has a small moment arm with respect to the center of gravity. When the surface velocity is subsonic, the incremental pitching moment and normal force can be predicted more closely for large flap deflections by assuming a parabolic distribution of pressure coefficient from the Newtonian value at the leading edge of the flat surface to the stagnation value behind a normal shock at the body-flap juncture with the result as indicated.

03171020 1950

For conical-type bodies such as L-8, Newtonian theory underpredicts the incremental pitching moment at angle of attack because of the higher dynamic pressure which exists in the region of the flap due to body cross flows washing away the low energy air near the control. Dynamic pressure corrections estimated from previously measured stagnation pressure in the region of the flap on the M-1 show better agreement with the data at moderate angles of attack.

Reasonably good agreement exists between prediction and experimental data for the shoulder or edge flap on the L-2 at the higher Reynolds number. However because of the small moments generated by the body and the low slope of the moment curve, the trim attitude is difficult to predict with any precision.

CONCLUDING REMARKS

The vehicles involved will produce the desired lift-drag ratio, and it is possible to compute with confidence some of the basic body characteristics; however, such was not possible for the body types where the surface slopes change rapidly and edge relief or carryover effects are evident. The type and location of the controls must be selected with care to avoid cross-coupling problems. At present, in the computation of control effectiveness, it is seldom possible to theoretically account for the local conditions and flow phenomena in the vicinity of deflected controls, and reliance upon experiment is mandatory.

A great deal of experimental data, sufficient for preliminary design purposes, has been obtained on a wide variety of these blunt bodies with various aerodynamic control schemes at speeds up to Mach number 10; however, the experimental studies must be extended into the higher Mach number and temperature regimes in order to assess real-gas effects upon stability and control.

03171020 1950

DECLASSIFIED

25

REFERENCES

1. Chapman, Dean R.: An Approximate Analytical Method for Studying Entry Into Planetary Atmospheres. NASA TR R-11, 1958. (Supersedes NACA TN 4276.)
2. Grant, Frederick C.: Analysis of Low-Acceleration Lifting Entry From Escape Speed. NASA TN D-249, 1960.
3. Eggers, Alfred J., Jr., and Wong, Thomas J.: Re-Entry and Recovery of Near-Earth Satellites, With Particular Attention to a Manned Vehicle. NASA MEMO 10-2-58A, 1958.
4. Sarabia, Michael F.: Aerodynamic Characteristics of a Blunt Half-Cone Entry Configuration at Mach Numbers From 3 to 6. NASA TM X-393, 1960.
5. Armstrong, William O.: Effect of Various Forebody Modifications on the Static Longitudinal Stability and Control Characteristics of a Reentry Capsule at a Mach Number of 9.6. NASA TM X-469, 1961.
6. Armstrong, William O.: Hypersonic Aerodynamic Characteristics of Several Series of Lifting Bodies Applicable to Reentry Vehicle Design. NASA TM X-536, 1961.
7. Penland, Jim A., and Armstrong, William O.: Static Longitudinal Aerodynamic Characteristics of Several Wing and Blunt-Body Shapes Applicable for Use as Reentry Configurations at a Mach Number of 6.8 and Angles of Attack up to 90°. NASA TM X-65, 1959.
8. Intrieri, Peter F.: Effects of Transverse Center-of-Gravity Displacement, Afterbody Geometry, and Front-Face Curvature on the Aerodynamic Characteristics of Mercury-Type Models at a Mach Number of 5.5. NASA TM X-569, 1961.
9. Sammonds, Robert I., and Dicky, Robert R.: The Trim Effectiveness of Several Types of Aerodynamic Flap Controls on a Mercury Type Capsule. (Prospective NASA paper.)
10. Davy, William C., and Seiff, Alvin: A Study of the Stability and Performance of Some Unsymmetrical Truncated Conical Configurations for Lifting Re-Entry. NASA TM X-504, 1961.
11. Rainey, Robert W., Compiler: Summary of Aerodynamic Characteristics of Low-Lift-Drag-Ratio Reentry Vehicles From Subsonic to Hypersonic Speeds. NASA TM X-588. (Prospective NASA paper.)

0317120 1971

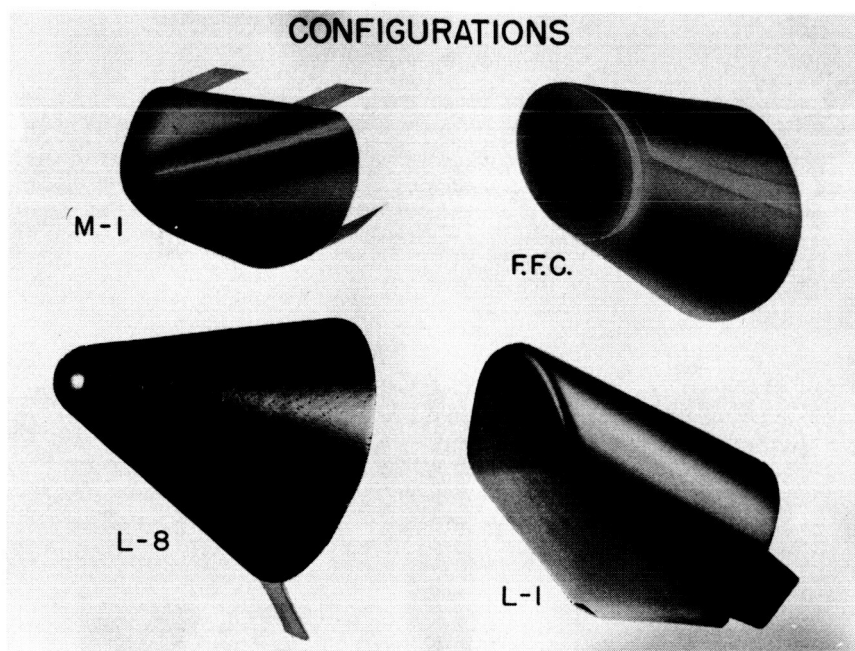


Figure 1

L-61-2248

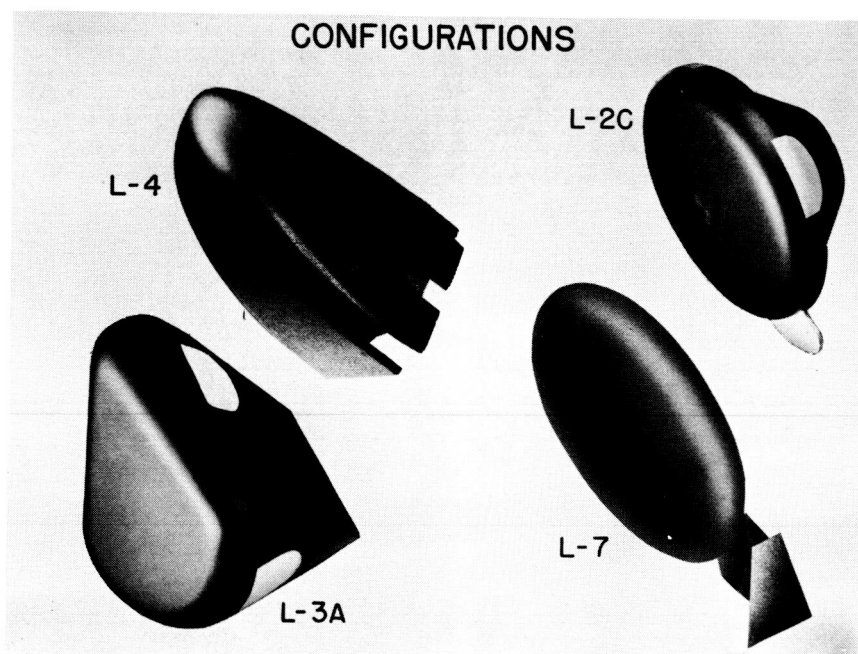


Figure 2

L-61-2249

[REDACTED]

HYPERSONIC TRIMMED CHARACTERISTICS

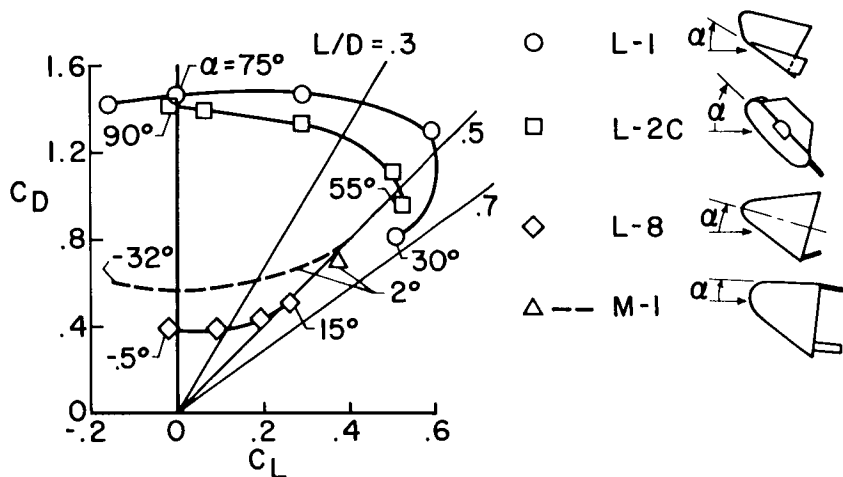


Figure 3

TRIM LIFT VARIATION AS A FUNCTION OF $(L/D)_{TRIM}$

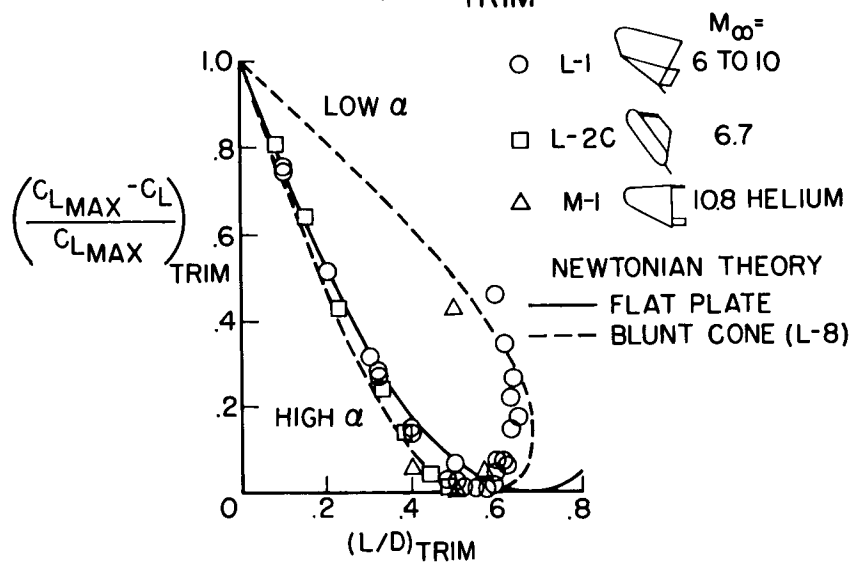


Figure 4

BASIC-BODY HYPERSONIC CHARACTERISTICS

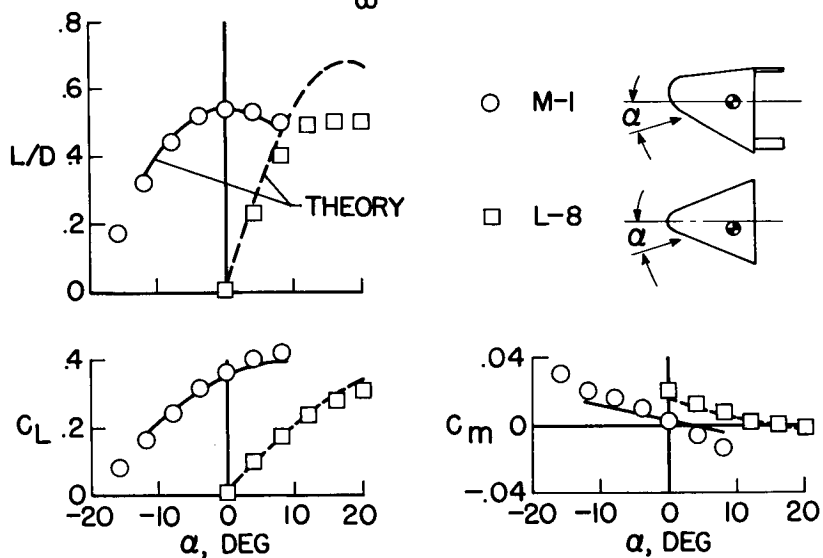
 $M_\infty = 6 \text{ TO } 10$ 

Figure 5

BASIC-BODY HYPERSONIC CHARACTERISTICS

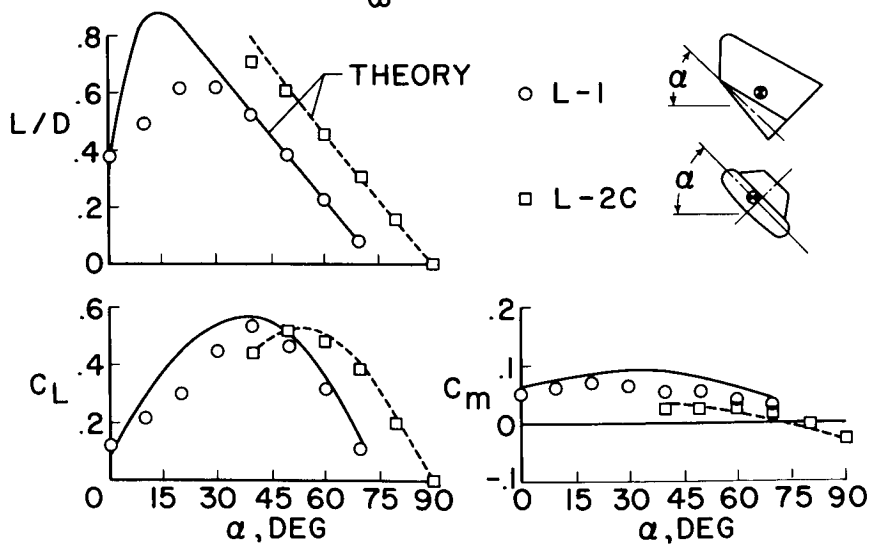
 $M_\infty = 6 \text{ TO } 10$ 

Figure 6

EFFECTS OF EDGE-RADIUS VARIATION AT HYPERSONIC SPEEDS

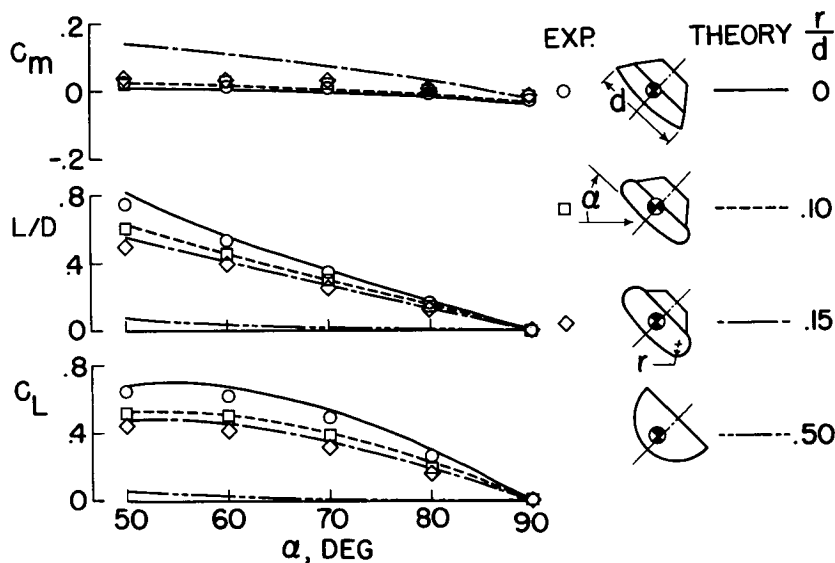


Figure 7

CONTROL CROSS COUPLING AT HYPERSONIC SPEEDS

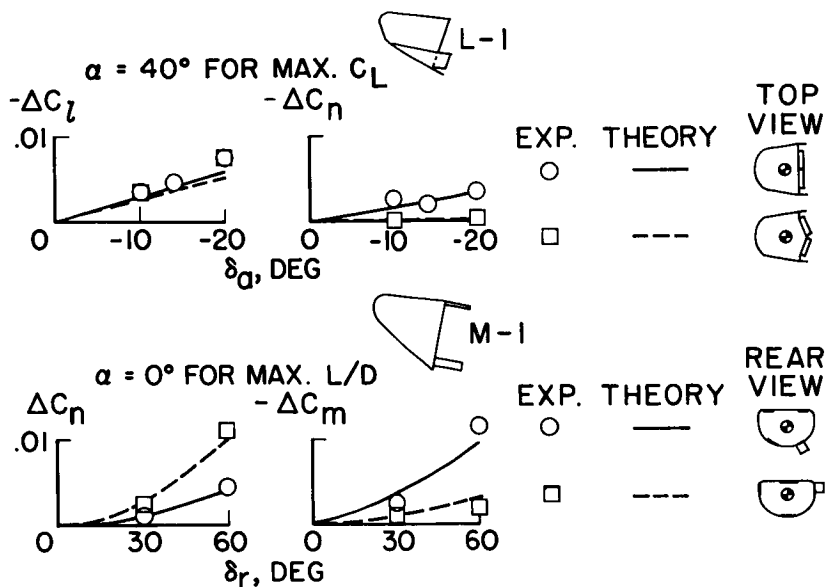


Figure 8

0371224 [REDACTED]

LONGITUDINAL-CONTROL EFFECTIVENESS

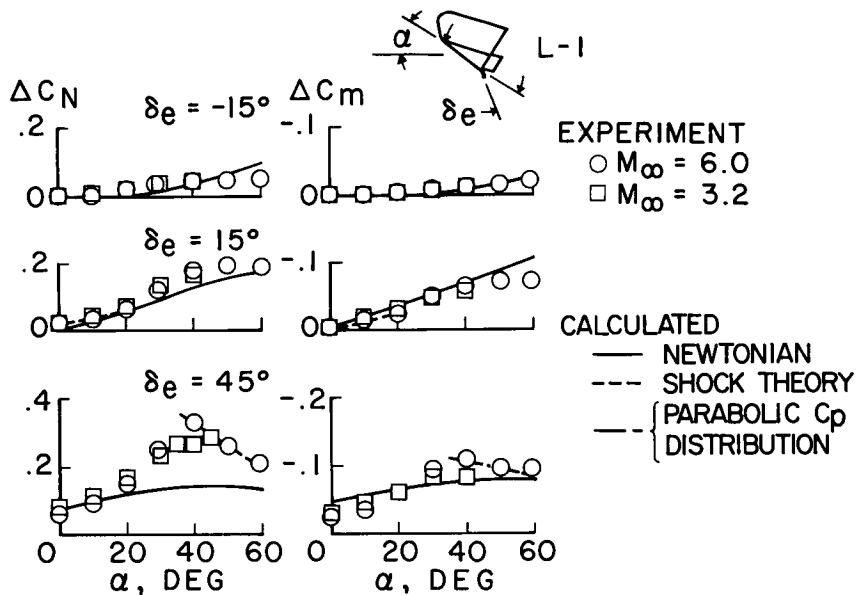


Figure 9

LONGITUDINAL CONTROL EFFECTIVENESS

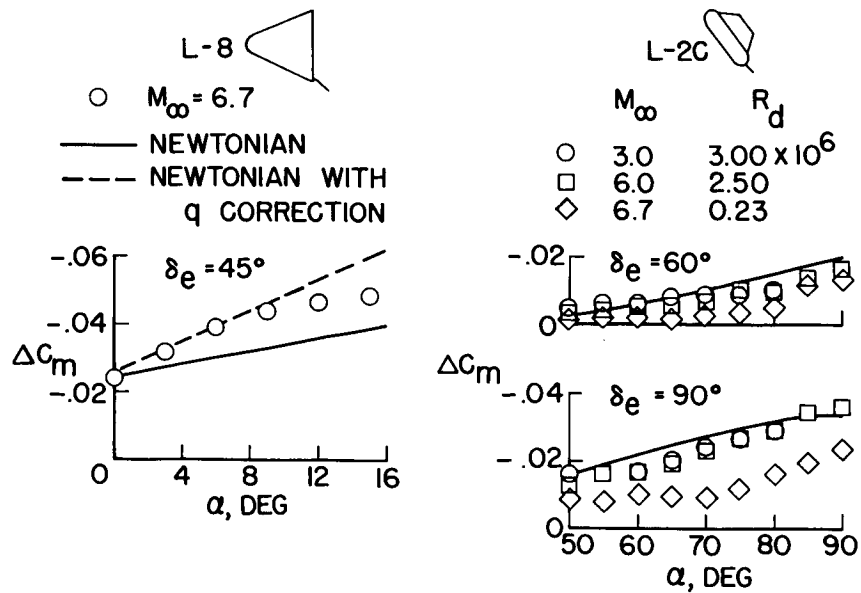


Figure 10

LAUNCH-VEHICLE DESIGN FEATURES

By George P. Pedigo

George C. Marshall Space Flight Center

The Saturn C-1 research and development program includes ten launch vehicles. Tables I and II present a schedule of the major events in this program. The first four vehicles (SA-1 to SA-4), indicated as block I in table I, will be devoted to flight-testing only the first stage, called the S-I.

Block II, as indicated in table II, will start the first flight testing of the launch vehicle in which a live second stage will be used. These tests will give data on the S-I stage, as well as on the live second stage, called the S-IV, and the C-1 instrument unit of the launch vehicle in the expected configuration to be used for Apollo.

There are presently two launch complexes (identified as VLF 34 and 37) under construction at Cape Canaveral, Florida, with a total of three launch pads. VLF-34 has one launch pad and VLF-37 has two launch pads. These complexes will permit up to ten launchings per year. Any future increase in launch rates will require additional facilities.

Although the mission of the ten vehicles listed in tables I and II is the development of the launch-vehicle system, the opportunity exists to flight test some early models of the proposed Apollo research and development spacecraft beginning with SA-7. A discussion of this configuration of the Saturn C-1 will therefore be made at this time. Figure 1 shows the space-vehicle configuration, which is divided into two sections: the spacecraft at the forward end and the launch vehicle comprising the rear portion. At the forward end of the launch vehicle, behind the spacecraft, is a section 58 inches long and 154 inches in diameter. This section contains the guidance, control, measuring, and other equipment in service of the launch vehicle. This equipment is contained in a thermally controlled pressure-sealed compartment. Figure 2 depicts the presently planned instrument unit. It is designed so that complete component racks (as well as individual components) can be exchanged without disassembly of the vehicle. The skin of the section takes the structural loads during flight and allows for convenient mounting for antennas, umbilical connections, and other apparatus.

The second stage of the basic C-1 Saturn (designated the S-IV stage) is being developed and produced by the Douglas Aircraft Company. This stage has a diameter of 220 inches and has a profile view as shown in figure 3. Some stage data are also shown in this figure.



03:41:00:00:00:00

The S-I stage shown in figure 4 is comprised of nine tanks, eight of which are 70 inches in diameter clustered around one central tank which is 105 inches in diameter. Four outside tanks and the center tank carry liquid oxygen (lox) and take the entire stage longitudinal and bending loads experienced in flight. The remaining four outer tanks contain fuel and are not utilized as a load-carrying structure except for their own weight and loads imposed by air flow. The exterior tail configuration of this stage is shown in figure 5. Note that a short stub fin is located between each major fin. These stub fins, together with the large fins, support the vehicle on the launcher.

One important area of possible interest to the developer of the spacecraft is the vehicle dynamics. This discussion does not include dynamics of control, which is discussed by Otha C. Jean in a subsequent paper. The one area of vehicle dynamics that will be mentioned, since it is important in design of the control system, is the vehicle bending characteristics. Table III presents in summary the bending characteristics at some of the critical flight times. The data presented were arrived at analytically. Extraneous bending characteristics were expected since the vehicle structure is complex and equipped with several thrust elements. Both scaled and full-scale dynamic tests are being conducted. Small-scale tests are under way at the Langley Research Center. Harry L. Runyan, Jr., and A. Gerald Rainey have included some results of these tests in a subsequent paper. A test facility has been built at Marshall Space Flight Center capable of dynamically testing a full-scale Saturn C-1 launch vehicle. Preliminary results indicate that several intermediate bending frequencies do occur. Further testing is required to define fully the characteristics and to assess the consequences. Methods are under study which may be employed to attenuate the S-I stage tank action if conditions so dictate.

Another area that would likely be of interest to the developer of the spacecraft is the sound and vibration environment induced by the launch vehicle. The data presented in figure 6 are a plot of predicted sound-pressure level against frequency. These data together with those shown in figure 6 of the launch-vehicle induced vibration data were arrived at by extrapolating test measurements analytically to the base of the spacecraft. The maximum sound pressure as shown in the curve is that expected to be transmitted through the atmospheric and structural medium. The value of 143 decibels given at the bottom of figure 6 as total sound-pressure level (SPL) is representative of a total single-frequency level. The degree to which the Apollo equipment and crew will experience this environment together with that induced by air flow will depend largely on the design of the spacecraft. In figure 7, the dashed portion of the curves is indicated in double-amplitude displacements rather than in g units.

Inasmuch as the theme of this conference is manned space flight, it seems in order that some comment be offered regarding what is being done in the Saturn C-1 program to make the launch vehicle eligible for carrying man. Throughout the research and development program, the highest possible probability of mission success is being sought through all available means. Some of the primary considerations are design adequacy, component and systems qualification test programs, and reliability programs.

Design adequacy embodies primarily the basic overall launch-vehicle design. One such consideration is the selection of structural safety factors, which should be considered a compromise between necessary safety for manned launch vehicles and payload capability. For example, factors of safety for the primary structure are 1.1 to yield strength and 1.4 to ultimate strength.

Design assumptions are conservative in such areas as aerodynamics, dynamics of control, and other flight conditions. For example, the design maximum bending moment is 45×10^6 inch-pounds as compared with the 32×10^6 inch-pounds that Saturn C-1 Apollo is expected to experience. This margin of safety will allow greater attitude divergence and consequently more time for escape. It is pointed out that if spacecraft configurations with higher aerodynamic lift than that previously shown in figure 1 are introduced, this margin of safety will be rapidly reduced. Figure 8 is offered as a quantitative estimate of the expected loading conditions that would be experienced in flight with a 2σ wind loading. Assumptions as to the angle of attack α that is expected under these conditions are conservative in that a 3° margin of safety is used. (Dynamic pressure q is 4.994 psi and engine gimbal angle β is -0.47° .) Note that in addition to the bending-moment plot, shear and longitudinal loading diagrams are included.

Another specific design feature which results in improved flight conditions is the addition of fins on the first stage. This addition, by increasing aerodynamic stability, reduces the stresses of larger motions of the control engines and, in the event of control failure, reduces the attitude divergence rate; and thus more time is allowed for failure sensing and escape.

It should be pointed out that, should one of the S-I engines fail, seven-engine operation is within the design capability of the control system as well as the structure. Although weight requirements for some payloads may be such that seven engines are not capable of providing a complete mission, the engine-out capability still will give more assurance that abort can be accomplished.

[REDACTED]

[REDACTED]

[REDACTED]

[REDACTED]

[REDACTED]

DECLASSIFIED

35

In the area of reliability there is a continued effort specifically devoted to study of systems for improvement of reliability by constant design review, systems simplification, and redundancy.

Another area in which study is beginning is assessment of phenomena, which may be measured, that will be indicative of the development of a catastrophic event. Such diagnostic presentation to the spacecraft is certainly necessary if the highest probability of crew survival is to be realized. Early participation of those responsible for the spacecraft in this important area is highly desirable.

Before this discussion is concluded, mention should be made of some of the advanced launch-vehicle programs that are being studied that will have an important future role in manned space flight. Two of these programs are the Saturn C-3 and Nova. The Saturn C-3 is under study concerning stage size, diameter, and other design criteria. Figure 10 depicts a typical configuration based on lower stages of 320-inch diameter. The Nova is in the very early conceptual design phase and no design features will be offered at this time. A brief statement on the Saturn C-3 and Nova capabilities is included in the next paper by Mr. Otha C. Jean of the Marshall Space Flight Center.

TABLE I.- SATURN C-1 SCHEDULE - BLOCK I

	SA-1	SA-2	SA-3	SA-4
Saturn serial number	Oct. 1961	Mar. 1962	Oct. 1962	Mar. 1963
Launching date	Aug. 1961	Jan. 1962	Aug. 1962	Jan. 1963
Prepare for launch	Aug. 1961	Jan. 1962	July 1962	Dec. 1962
Shipping date	May 1961	Oct. 1961	Mar. 1962	Sept. 1962
Final checkout	Mar. 1961	Sept. 1961	Mar. 1962	Aug. 1962
S-I static test	Jan. 1961	Aug. 1961	Feb. 1962	Jan. 1962
Checkout	May 1960	Dec. 1960	Sept. 1961	Feb. 1962
Start assembly	-----	-----	-----	-----
S-IV stage delivery date . .	VLF 34	VLF 34	VLF 34	VLF 34
Launch complex				

TABLE II.- SATURN C-1 SCHEDULE - BLOCK II

Saturn serial number	SA-5	SA-6	SA-7	SA-8	SA-9	SA-10
Launching date	June 1963	Aug. 1963	Oct. 1963	Dec. 1963	Feb. 1964	Apr. 1964
Prepare for launch	Apr. 1963	June 1963	Aug. 1963	Oct. 1963	Dec. 1963	Feb. 1964
Shipping date	Apr. 1963	May 1963	July 1963	Sept. 1963	Nov. 1963	Jan. 1964
Final checkout	Jan. 1963	Mar. 1963	Apr. 1963	Aug. 1963	Oct. 1963	Dec. 1963
S-I static test	Nov. 1962	Jan. 1963	Mar. 1963	None	None	None
Checkout	Oct. 1962	Dec. 1962	Feb. 1963	July 1963	Sept. 1963	Nov. 1963
Start assembly	May 1962	July 1962	Sept. 1962	Feb. 1963	Apr. 1963	July 1963
S-IV stage delivery date	Mar. 1963	May 1963	July 1963	Sept. 1963	Nov. 1963	Jan. 1964
Launch complex	VLF 37B	VLF 37A	VLF 37B	VLF 34	Optional	Optional

0371220000

TABLE III.- BENDING FREQUENCIES FOR SATURN C-1 APOLLO VEHICLE

Vehicle status	Frequency, cps		
	1st mode	2nd mode	3rd mode
Filled on launcher	0.302	1.69	3.29
Lift-off, 1st stage	1.76	4.35	6.73
Maximum q, 1st stage	2.09	5.10	7.91

APOLLO SATURN C-1 SPACE VEHICLE CONFIGURATION

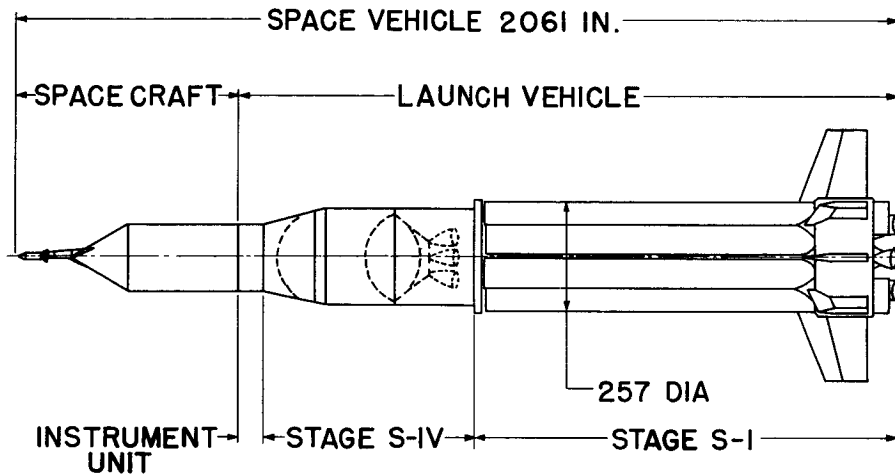
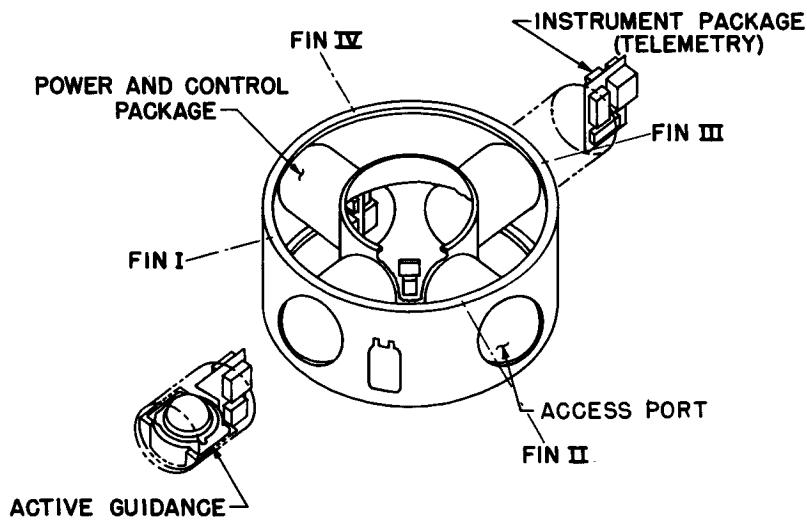


Figure 1

INSTRUMENT UNIT



VIEW LOOKING AFT FROM STA 1517.596

Figure 2

037120 [REDACTED]

SATURN C-I, S-IV STAGE

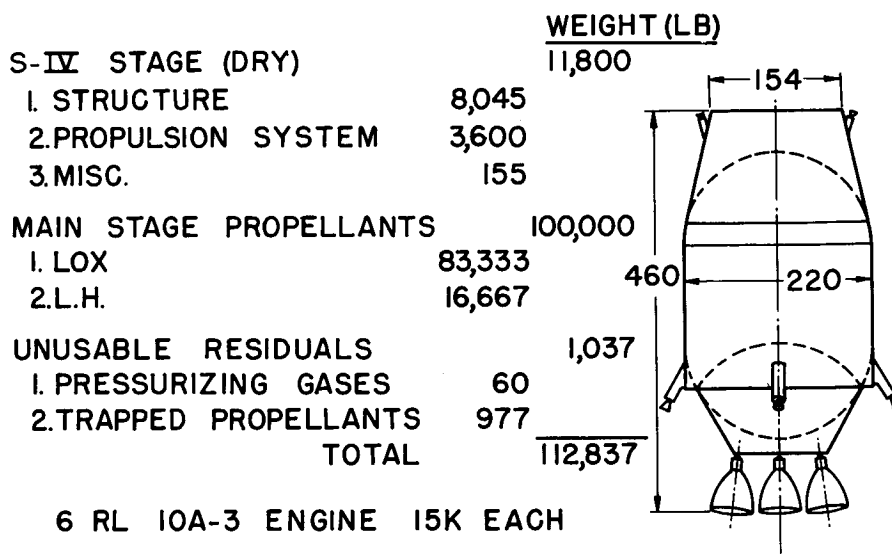


Figure 3

SATURN C-I, S-I STAGE

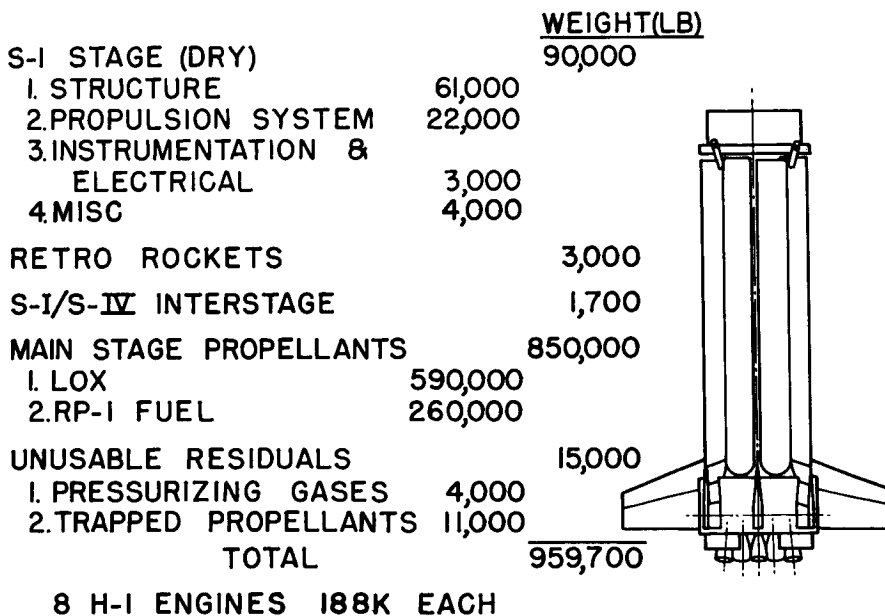
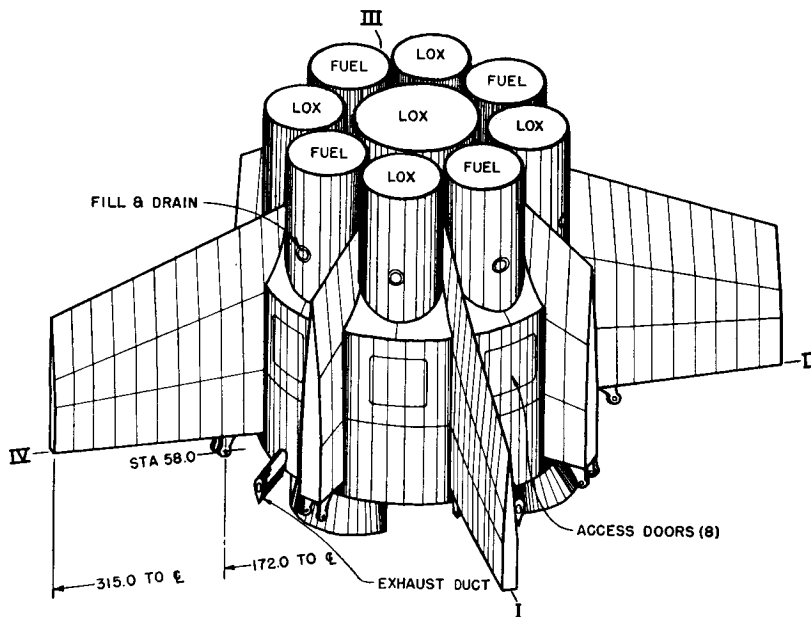


Figure 4

[REDACTED]



TAIL CONFIGURATION

Figure 5

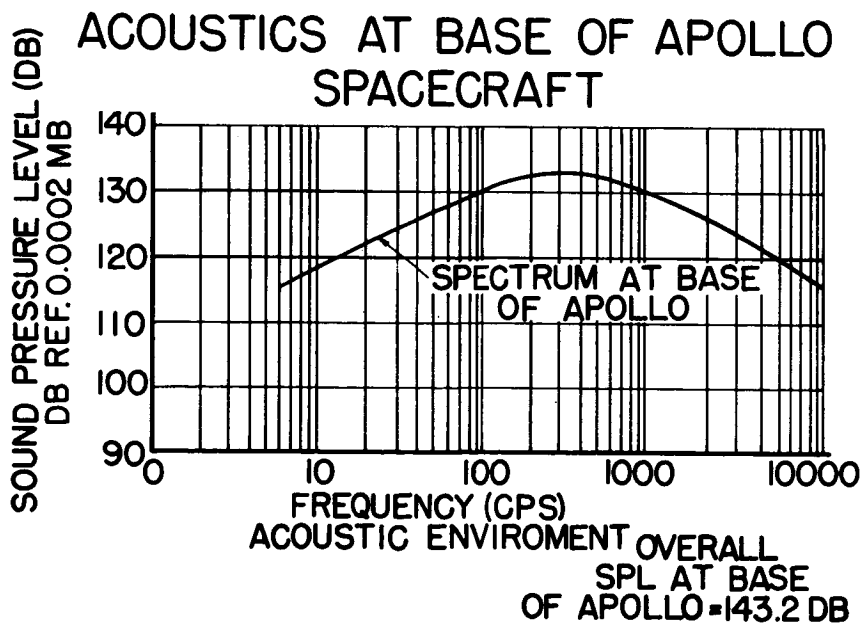


Figure 6

037120 1030

VIBRATION AT BASE OF APOLLO SPACECRAFT

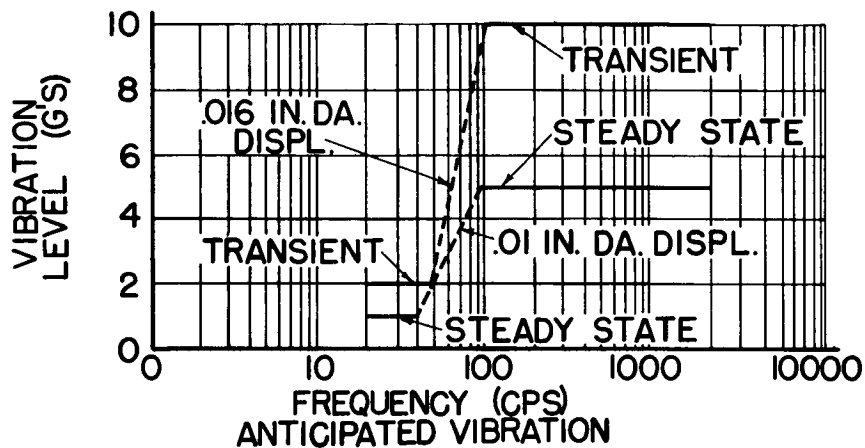


Figure 7

SATURN C-1 APOLLO

SHEAR AND BENDING MOMENT VS VEHICLE STATION - 8 ENGINE OPERATION

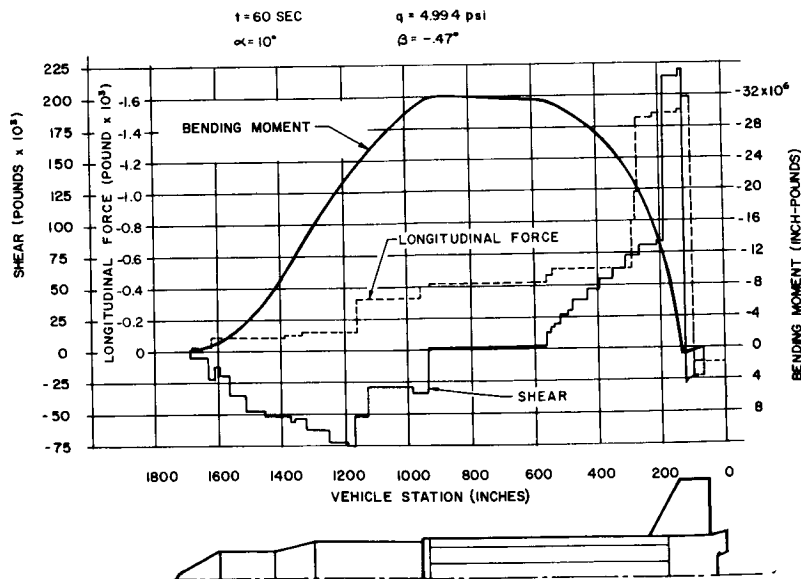
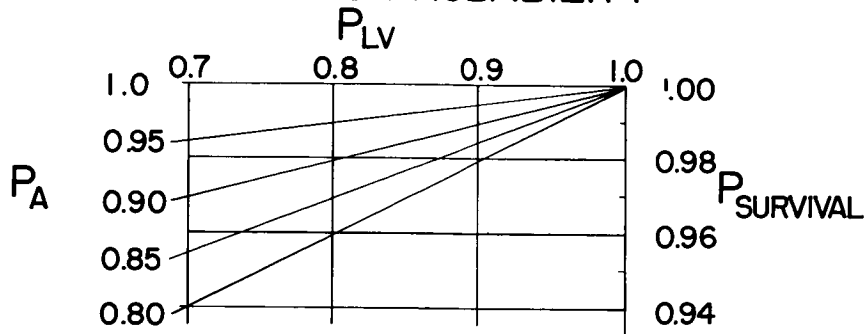


Figure 8

LAUNCH PHASE SURVIVAL PROBABILITY



$$P_{LV} = P_{\text{LAUNCH VEHICLE MISSION}}$$

$$P_A = P_{\text{APOLLO ABORT SUCCESS}}$$

$$P_{SURVIVAL} = P_{LV} + (1 - P_{LV})P_A$$

Figure 9

SATURN C-3 VEHICLE

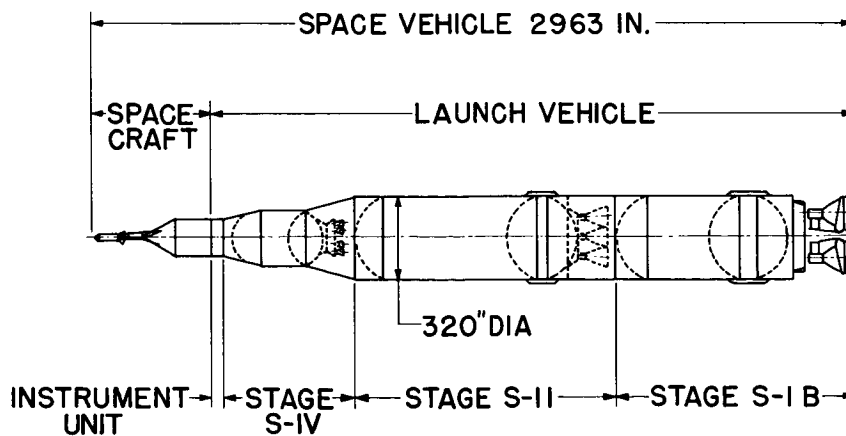


Figure 10

DECLASSIFIED

45

LAUNCH-VEHICLE PERFORMANCE CHARACTERISTICS

By Otha C. Jean

George C. Marshall Space Flight Center

This presentation will deal with the performance capabilities of the Saturn C-1 and C-3 vehicles. The first part of the presentation will cover the C-1 which is to be used for the orbital Apollo and possible reentry test shots.

The C-1 vehicle as described by George P. Pedigo in the previous paper is a two-stage vehicle using lox-RP1 as propellants in the base-ment stage and high-energy propellants in stage two or the S-IV stage. Table I gives a weight and engine performance summary of the Saturn C-1 vehicle. The listed weights refer to the 100-nautical-mile orbital conditions.

The total configuration weighs 1,104,600 pounds at first motion. The S-I stage is powered by a cluster of eight 188,000-pound thrust engines. Four of these engines are fixed mounted and four are gimbal mounted to provide control during the ascending phase. The specific impulse of this stage is 255 seconds. The propellant tanks are sized to load 850,000 pounds of usable propellants, but 5,100 pounds are kept in reserve in the event of mixture-ratio shifts. After $2\frac{1}{2}$ minutes of flight, the S-I stage depletes its propellants and cuts off with a cut-off weight of 259,700 pounds.

The S-IV stage separates at this point and continues flight. At separation, the S-IV stage plus the payload weighs 139,850 pounds. The stage is powered by six Pratt & Whitney engines, each rated at 15,000 pounds in vacuum. All six engines swivel for control. The specific impulse of the system is 420 seconds. The tanks of the stage have been sized for 100,000 pounds of liquid oxygen and hydrogen. After reaching the 100-nautical-mile orbital conditions (velocity and path angle), the S-IV stage cuts off with a weight of 40,700 pounds. Of course, all of this weight is not available for the designer in sizing his spacecraft. The S-IV stage itself weighs 11,700 pounds; 500 pounds of propellants are reserved for mixture-ratio shifts; 832 pounds of propellants are trapped in fuel lines, tanks, and engines; and 518 pounds are reserved for flight performance errors. This totals to 13,550 pounds to be subtracted from the cutoff weight. This leaves an effective or useful payload of 27,150 pounds. The effective payload is defined to contain the guidance and control equipment of the vehicle. There are small differences between the weights just quoted and those quoted in

0371228 1034

the previous paper by George P. Pedigo which are the current design data.

The typical trajectory shaping schemes in establishing ascending trajectories will now be discussed. Two typical trajectories are shown in figure 1, a 300- and 100-nautical-mile mission. After 10 seconds of vertical rise, a small angle of attack is introduced to initiate gravity turning. Except for this initial angle of attack, the first-stage trajectory is flown under a zero-lift program. This leaves the complete swivel freedom of the engines available for control purposes. The S-IV stage trajectory is shaped by the variational calculus theory method. This method selects the optimum thrust direction for the missile to follow in order to have a minimum burning time between two fixed points (first-stage cutoff and desired orbital condition). Since the S-IV stage ignites in rather thin atmosphere, large angles of attack from a structural viewpoint are permissible. In figure 1 it is interesting to note that rather large angles of attack are encountered during the S-IV burning. This is due to the low thrust-to-weight ratio of this stage, which is 0.6g at ignition. The optimum program in the 100-nautical-mile case encounters angles of attack up to 16° magnitude and in the 300-nautical-mile case, 17° near cutoff of the terminal stage.

Figure 2 shows the velocity-vector magnitude and direction for each of the two previous orbital trajectories. The left ordinate gives the path angle measured against the local vertical in degrees and the right ordinate gives the velocity magnitude in feet per second. These are plotted as a function of flight time. The velocity vector and direction during first stage are depicted in earth-fixed coordinates and a transformation is made at stage-one cutoff to a space-fixed system. The assumed launch azimuth is due east. The top curve of each set is the 100-nautical-mile mission case. If a malfunction should occur while the spacecraft is following either of these trajectories, the conditions shown in figure 2 would be the initial conditions for abort. It is interesting to note that for the 300-nautical-mile case, the path-angle-velocity combination is similar to ICBM type conditions, and the reentry deceleration would be excessive if abort should occur.

This leads to an important trajectory restraint and that is the allowable altitude-velocity-path-angle combination which is allowed for safe abort or the so-called famous abort corridor. The abort corridor would determine the upper limit for orbital altitudes.

Another important flight mechanical condition for the spacecraft designer is the dynamic pressure to be expected during first-stage flight. Shown in figure 3 is dynamic pressure plotted against flight time for the two missions. The two top curves are for eight engines

DECLASSIFIED

47

operating in first stage. Dynamic pressures up to 800 lb/sq ft would be experienced for the 100-nautical-mile case. In the case of only seven engines operating in first stage, the peak dynamic pressure would be about 600 lb/sq ft.

At this point it should be mentioned that the Saturn C-1 has been designed for engine-out capability from launch. The loss of an engine during first stage introduces two major problems. First, the performance capability of the vehicle is reduced as will be shown in a subsequent figure, and, second, the controllability of the missile is reduced. The controllability of the vehicle is reduced in two ways. First, the thrust vector of each engine does not pass through the center of gravity (CG) and the loss of an engine creates an unbalance of moments about the CG and the remaining engines swivel to restore this balance. Second, if the engine that failed is a control engine, the control torque available to compensate for winds is reduced.

The stability characteristics of the vehicle are shown in figure 4. The center-of-pressure data (CP/D), center-of-gravity data (CG/D), and lift-coefficient data (C_{Z_α}) are given over first-stage flight time. The trajectory is the 100-nautical-mile case. The missile is stable up to 75 seconds of flight. The high-wind region and maximum dynamic pressure (Max q) occurs prior to this time while the vehicle is stable. The importance of this stability margin is emphasized in figure 5. In this figure the aerodynamic restoring coefficient C_1 and control force coefficient C_2 over first-stage flight is presented. The aerodynamic restoring coefficient is given by the formula

$$C_1 = \frac{N(CG - CP)}{\Theta}$$

where N represents the lift force, $CG - CP$ represents the aerodynamic lever arm, and Θ represents the moment of inertia. The control force coefficient is given by the formula

$$C_2 = \frac{F(CG)}{2\Theta}$$

where F represents the force, CG represents the distance from the swivel point to the center of gravity, and Θ represents the moment of inertia. The factor 2 enters into this formula since only one-half of the total thrust is capable of swiveling. The importance of the positive value of C_1 is that if a malfunction requires shutdown of the eight engines, the vehicle will not immediately tumble. The ratio of the coefficients gives a true representation of the controllability of the Saturn C-1 vehicle. The swivel-angle requirement to compensate for

0371301030

48

wind torque and other malfunctions is the ratio C_1/C_2 times the angle of attack resulting from these disturbances. For winds in the order of 250 feet per second at maximum dynamic pressure, the angle of attack would be near 7° and the engines would be required to swivel near 6° to compensate for these disturbances.

Conclusions can be made from figures 4 and 5 that for symmetric or nonlifting payloads (as shown in fig. 4) the fin size may be too large. For the Apollo type missions, the eight stubs used for vehicle support and holddown on the pad may be sufficient aerodynamic surfaces for stability. Since the four fins are detachable, the decision of flying with fins is optional.

Figure 6 presents the performance capability of the C-1 for different orbital altitudes. Two pieces of information are offered, the cut-off weight in orbit and the useful payload. The mode of ascent is continuous, burning until the orbital conditions are satisfied. The payloads for both eight- and seven-engine boost trajectories are given. For the 100-nautical-mile orbital case, the payload is 27,150 pounds in the eight-engine case and drops to 19,500 pounds at the 300-nautical-mile altitude level. For the seven-engine case the payload is about 3,000 pounds less for each altitude - about 24,000 pounds of capability at the 100-nautical-mile level and 16,000 pounds at the 300-nautical-mile level.

For the larger orbital altitude, the payload capability may not be sufficient to meet the actual weight of the Apollo. Shown in figure 7 is a method of achieving larger orbital altitudes with more payload than can be brought up directly. This is the classical Hohmann transfer method of first going into a low circular orbit and adding an impulse to initiate transfer and then coasting to the apogee of the transfer ellipse and at that point adding an additional velocity increment in order to have circular velocity. About 5,000 pounds of weight is gained at the 300-nautical-mile altitude by use of the Hohmann transfer.

A word of caution should be given at this point - the Hohmann transfer requires at least one restart of the S-IV engines and an attitude control system for control during the transfer phase. Neither of these features are being planned for the research and development S-IV stage. Possibly the attitude control system on the payload could be used for control and the auxiliary propulsion system for abort could be used to circularize at the apogee of the transfer ellipse.

At present, the Marshall Space Flight Center is in the preliminary phase of sizing a C-3 vehicle. The C-3 will be a three-stage vehicle with the basement stage utilizing lox-RP1 for propellants and the two upper stages carrying high-energy propellants. Table II presents a

DECLASSIFIED

49

preliminary weight and engine performance summary of a C-3 vehicle as it is presently planned.

The total vehicle weighs 2,400,000 pounds at lift-off and is powered by two F-1 engines each having 1,500,000 pounds of thrust. The specific impulse is 260 seconds. The tank capacity of this configuration is 1,500,000 pounds.

The S-II stage at lift-off weighs 786,500 pounds. The thrust is provided by four J-2 engines each with a thrust rating of 200,000 pounds. The specific impulse is 422 seconds. For this mission 550,000 pounds of propellants are used in the S-II stage.

The third stage, a modified S-IV stage, lifts off with a weight of 190,000 pounds. The thrust is 90,000 pounds and specific impulse is 420 seconds. Orbital velocity would be reached after 58,200 pounds of propellants have been burned. The cutoff weight is 131,780 pounds.

Figure 8 gives the payload capability of this vehicle for different orbital altitudes up to escape. A parking orbit is assumed at the 100-nautical-mile altitude. The higher orbital altitudes are achieved by Hohmann transfer from this reference orbit. The escape weight for this configuration is near 60,000 pounds, of which 18,500 is dry S-IV weight, trapped propellants, flight performance reserve, and guidance and control equipment. This leaves a net payload at escape of about 40,000 pounds. The circular payload would be about 110,000 pounds.

If the C-3 is to be used for the man on the moon and return mission, a number of vehicles would need to be mated together in orbit since approximately 400,000 pounds of circular weight is necessary to land on the moon and return a 12,500-pound spacecraft.

Considerations to do the above mission directly have led to the Nova configuration. The circular capability of the Nova is to be of the order of 400,000 pounds, which means the Nova could perform the same lunar mission directly and this would eliminate the rendezvous maneuvers.

037122A1030

50

TABLE I

WEIGHT AND PERFORMANCE DATA		
	S-I	S-IV
Lift-off Weight (lb)	1,104,600	139,850
Thrust (lb)	8 x 188K (SL)	6 x 15K (VAC)
Specific Impulse (sec)	255 (SL)	420 (VAC)
Propellants (lb)	844,900	99,144
Cutoff Weight (lb)	259,700	40,700*
S-IV Dry Weight (lb)		11,700
Mixture-Ratio Reserve (lb)		500
Trapped Propellants (lb)		832
Flight Performance Reserve (lb)		<u>518</u>
		13,550
Effective Payload		<u>27,150</u>
		40,700

*100 nm Orbit

TABLE II

WEIGHT DATA OF 3 STAGE SATURN C-3 (100 nm Mission)			
	S-I B	S- II	S-IV
Lift-off Weight (lb)	2,400,000	786,500	190,000
Thrust (lb)	3,000,000 (SL)	800,000 (VAC)	90,000 (VAC)
Specific Impulse (sec)	260 (SL)	422 (VAC)	420 (VAC)
Propellants (lb)	1,500,000	550,000	58,200
Cutoff Weight (lb)	907,200	236,500	131,780
Separated S-IV (lb)		18,510	

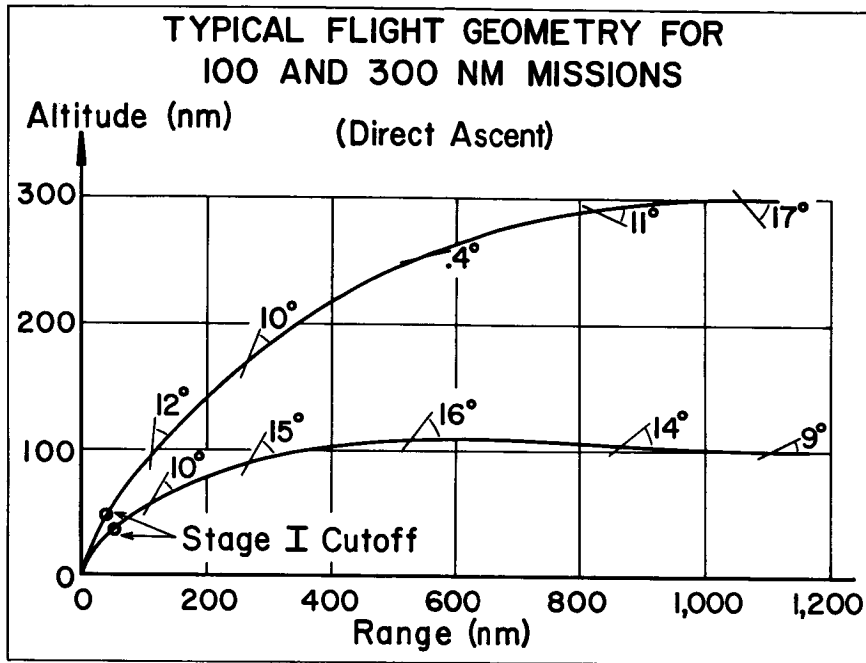


Figure 1

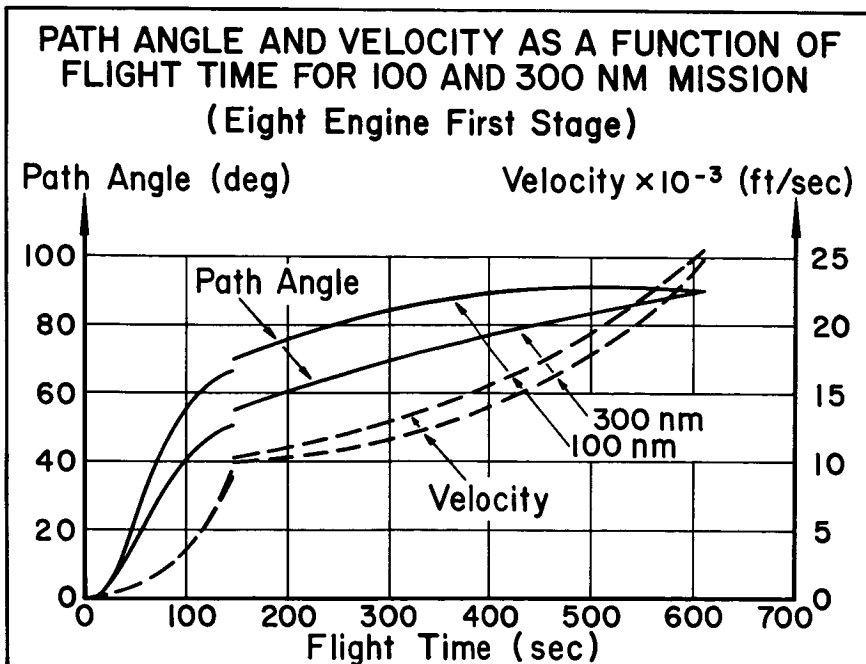


Figure 2

031712001030

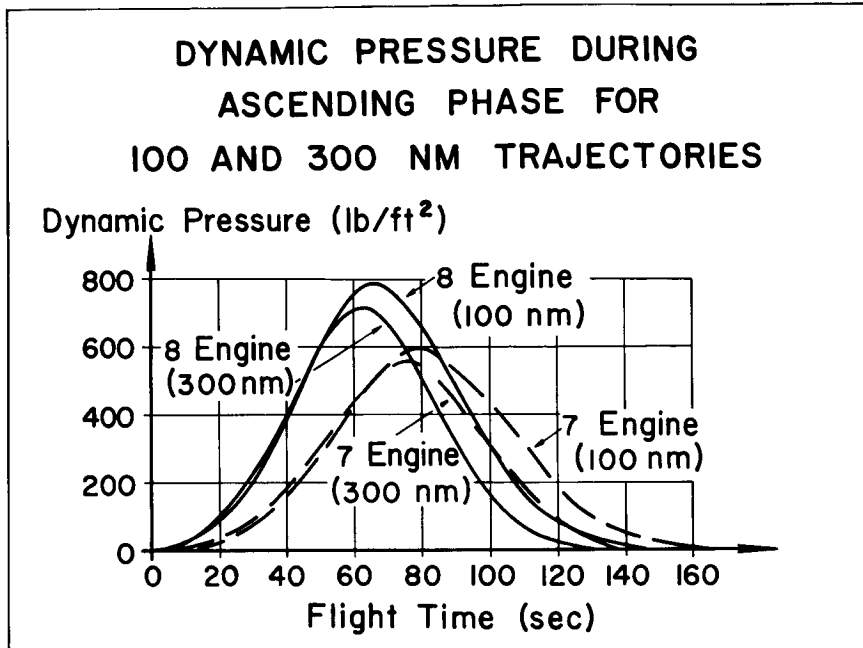


Figure 3

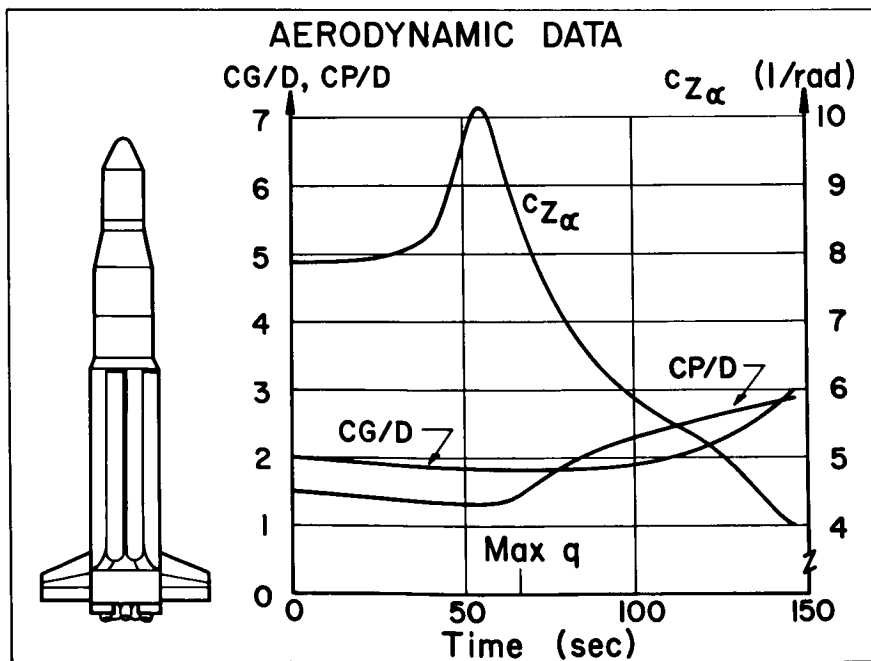


Figure 4

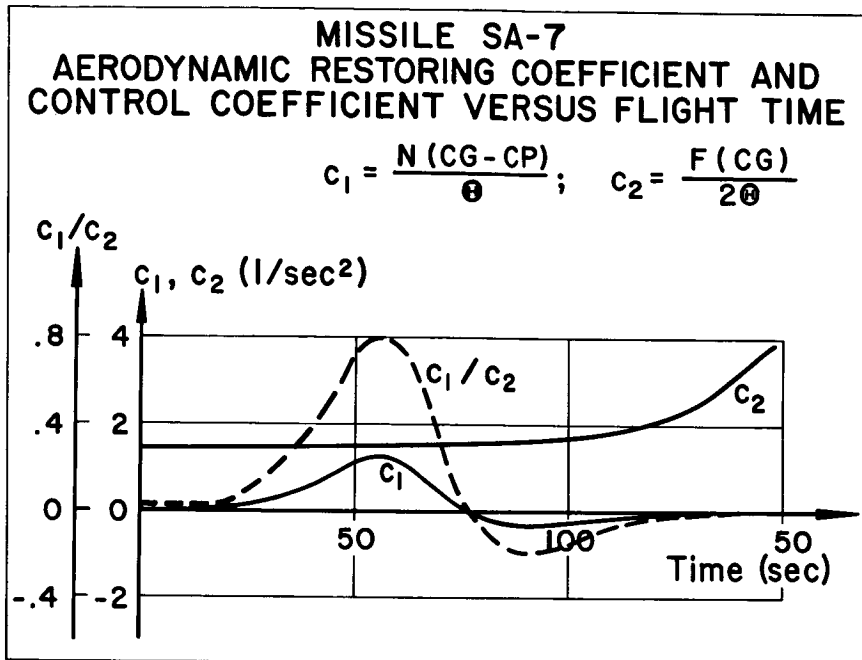


Figure 5

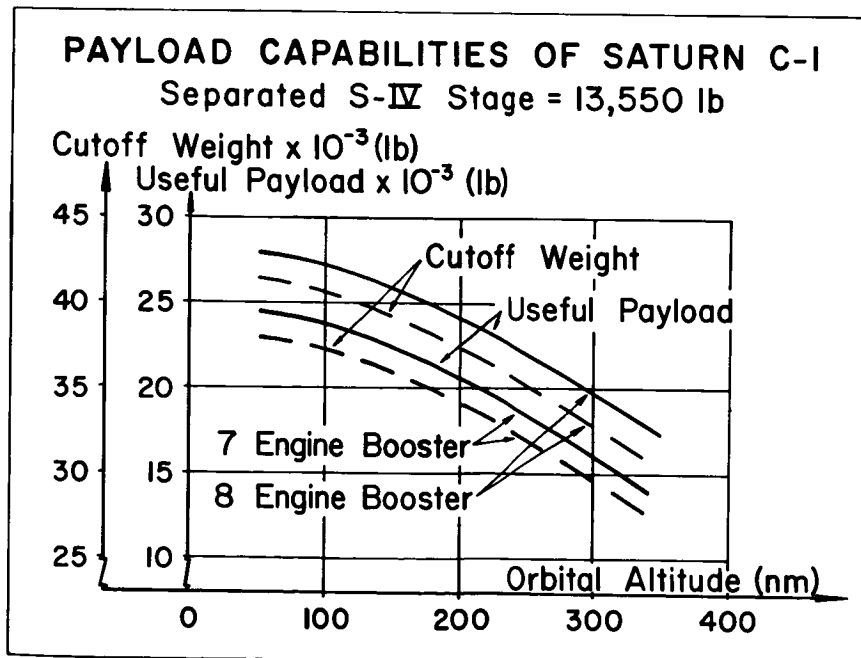


Figure 6

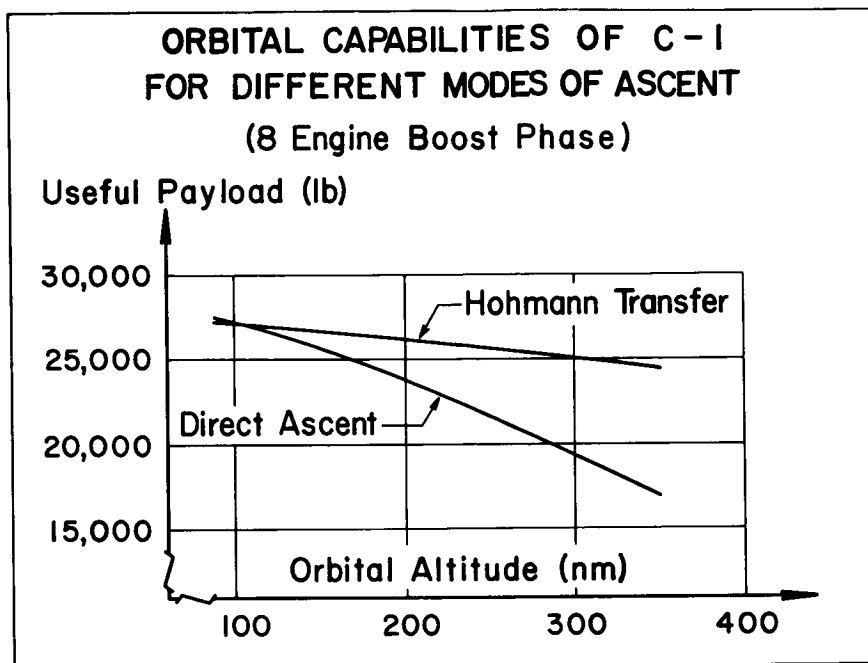


Figure 7

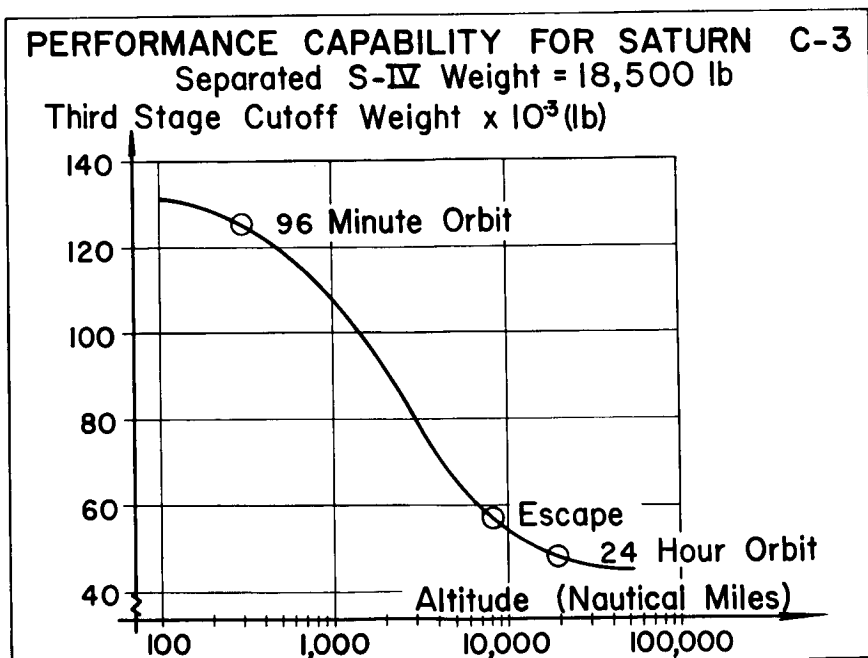


Figure 8

LAUNCH-VEHICLE DYNAMICS

By Harry L. Runyan, Jr., and A. Gerald Rainey

Langley Research Center

INTRODUCTION

The idea that a launch vehicle is a space truck on which any spacecraft, within performance capabilities, can be carried without giving due consideration to problems of structural dynamics can lead and has led to serious consequences. A launch vehicle with a new spacecraft is in essence a new system. The purpose of this discussion is to present several of the more important factors affecting launch-vehicle dynamics both with regard to system inputs and dynamic behavior.

SYMBOLS

5

C	damping
C_{cr}	critical damping
$\Delta C_{p,rms}$	root mean square of incremental pressure coefficient
f_{exp}	experimental frequency, cps
f_{cal}	calculated frequency, cps
M_b	bending moment, in-lb
M_{∞}	free-stream Mach number
q	dynamic pressure, lb/sq ft

DISCUSSION

In figure 1 are listed some of the more important loading inputs plotted against time of flight; namely, lift-off, transonic effects, and maximum dynamic pressure. The dark areas represent the times of maximum loading for the particular source. Indicated are such load

031712000000

sources as fuel slosh, acoustics, buffet, panel flutter, and winds. The main point of this figure is to illustrate that most of the loads occur between the vertical lines which indicate the transonic and maximum dynamic-pressure conditions. Most of the loads are shown to reach a maximum value at about the same time during the flight. Briefly discussed are some details concerning ground wind loads, acoustics, buffet, and winds, as well as the vibration modes, which in effect comprise the transfer function for buffet, fuel slosh, and wind loads of Saturn.

One of the basic ingredients in the design of a control system and in loads estimation is an accurate knowledge of the launch-vehicle vibration characteristics. Both the vibration mode shapes and the frequencies must be known to ensure that no coupling will exist between the control-system sensors and the structural modes. The Saturn is the launch vehicle for the Apollo program; therefore, an accurate knowledge of the vibration characteristics is needed as early as possible. A 1/5-scale dynamic model of the Saturn has been constructed for investigation at the Langley Research Center. Figure 2 illustrates the model installed in the test tower. (The man shown indicates in general the size of the model.) The model is suspended by an unusual and simple system which provides very little restraint from the support system and thus approximates a free-free system such as occurs in flight. The comparatively large model scale (1/5) was chosen to permit accurate simulation of joints, fittings, and skin gages, which were considered especially important for the cluster configuration, since motion of tanks within the cluster relative to each other is possible. This model program can also provide immediate modal and frequency data for the Saturn program, demonstrate the feasibility of obtaining accurate vibration data from scaled models, and provide a test bed to evaluate future changes in the vehicle, along with future payloads.

Free-free vibration tests of the model have been made, and data have been obtained with the model ballasted with water to simulate the weight at the point of maximum dynamic pressure in the launch trajectory. Figure 3 shows the acceleration response of a point on the nose of the vehicle for various driving frequencies. The frequencies have been scaled to correspond to full-scale frequencies. The driving force was provided by two electromagnetic shakers, located at the top and bottom of the model. The large number of peaks that appear indicate a number of resonant frequencies. For comparison purposes, the arrows have been placed on the abscissa to show natural frequencies calculated by simple beam theory, which assumes an equivalent stiffness for the clustered-tank portion of the launch vehicle. Notice that the calculated frequencies agree fairly well with some of the measured peaks. It is apparent, also, that several frequencies appear experimentally which were not predicted analytically. These results indicate additional vibration modes or effects in the model not accounted for by the simple analysis. The predominant characteristic of these higher modes (and their frequencies are still low enough to be of concern in

DECLASSIFIED

57

control-system design) is the large amount of relative motion between the various tanks in the booster cluster. This phenomenon is illustrated by the measured mode shapes which correspond to the two lowest frequencies of the model.

The measured mode shape corresponding to the first resonant peak is shown in figure 4. The deflection of the center line is plotted, normalized to unit deflection at the nose of the launch vehicle. The calculated first mode is also plotted (as a dashed line) and indicates good agreement with the experiment. The behavior of the cluster is shown in the cross-section A-A. The arrows indicate the relative motion of each tank. Note that all tanks move together, with about the same amplitude. The overall behavior observed for this mode is that of bending as a beam, predictable by the usual methods of vibration analysis.

The behavior is considerably different when the experimental vibration mode corresponding to the second resonant frequency is examined (fig. 5). The center-line deflection, plotted in the center, now shows only one node point, in contrast to three node points expected from beam behavior. The predicted mode shape, obtained by the beam analogy, is sketched as a dashed line to show this deviation. Again, the arrows are used to indicate the relative motion of individual tanks (section A-A). If the center tank moves in one direction, the tanks on the sides move directly opposite. The tanks in line with the motion of the center body tend to remain still, while the remaining four tanks actually have a component of motion out of the plane of the exciting force. However, these tanks still tend to move opposite to the center tank. The mode of one of these tanks on the sides has been superimposed on the center-line mode, in the middle sketch, to show the relative amplitude of the tank motion. Note that the tank motion is relatively larger than the center-line motion. Because of the rather complicated motion of this mode, it has been termed a "cluster" mode, rather than a second-beam bending mode as it would be in the conventional case. The other resonant peaks shown on the frequency response curve have equally complicated modal patterns, containing not only relative motion of tanks within the cluster but also local distortions and shell-type responses.

Vibration tests on the model are continuing to order to better define and understand the vibration characteristics of the Saturn and for extension to future clustered configurations. A full-scale vibration test is being conducted at Marshall Space Flight Center, and correlation of model and full-scale test results is planned in order to demonstrate the feasibility and accuracy of model test results. More refined analyses of vibration characteristics will also be attempted in order to develop and prove the analytical techniques.

CONFIDENTIAL

It is anticipated that the model will be kept up-to-date so that later configurations including, for instance, a dynamically scaled Apollo spacecraft, may be tested.

The next subject to be discussed concerns the loads caused by the ground winds on the launch vehicle while supported on the launch stand. The loads resulting from steady winds manifest themselves in two ways. First, there exists a drag load and, consequently, a steady bending moment in the direction of the winds. The second loading manifests itself in an oscillation, principally in the direction normal to the wind. Data obtained on a dynamic model of Saturn (fig. 6) tested in the Langley transonic dynamics tunnel are shown in figure 7.

In this investigation, the response of a dynamically and elastically scaled 1/13-scale model of the Saturn SA-1 vehicle was measured at simulated ground winds up to 80 feet per second and at full-scale Reynolds numbers. The model results shown have been scaled up to the full-size Saturn. For the data presented, the model airstream orientation was such that one of the eight barrels along the launch vehicle was directly in line with the wind.

In figure 7 the steady-drag bending moment measured at the base tie-down location (station 121.75) is presented; also presented, for comparison, is the maximum oscillatory bending moment in the lateral (perpendicular to the wind) direction, which was the largest oscillatory bending moment measured. At low velocities the oscillatory bending moment generally exceeds the steady-drag bending moment. At higher velocities the steady-drag moment becomes several times the oscillatory moment and approaches the static overturn moment for the unfueled vehicle resting unclamped on the launch arms. Thus, for the Saturn SA-1 the critical load from ground winds is the steady-drag load rather than the oscillatory response lateral to the winds, which has been the critical load for some other launch vehicles.

The variation with wind velocity of the maximum oscillatory base bending moments in the drag direction has also been obtained. As is typical of such cylindrical structures, the oscillatory response in the lateral direction was much greater than in the drag direction. Of general interest is the unexpected peak in the response at velocities of about 30 feet per second, which are not typical of supercritical Reynolds number responses. Adding roughness or spoilers to the nose of the model increased the peak response at this velocity. Other data indicate that the peak tends to disappear if the plain model is rotated 22.5° to orient the valley between two barrels to a position aligned with the wind direction. Therefore, it may be that this peak response is a function of the details of the flow around the eight barrels of the launch vehicle which present a noncylindrical shape to the airstream. It seems unlikely that this peak response at low wind velocities will

CONFIDENTIAL

DECLASSIFIED

59

present a problem to the Saturn SA-1 since, as is shown in figure 7, the steady-drag moment at higher wind velocities is much greater than this peak oscillatory moment.

The next subject to be considered is the noise environment of the vehicle, both at launch and during flight. The two main sources of noise for the Saturn launched Apollo vehicle will be the rocket engines and the aerodynamic boundary layer. In figure 8 the estimated noise levels outside the manned region of a two-stage Apollo vehicle are shown as a function of time. The noise levels from the rocket engines and from the aerodynamic boundary layer are indicated by the cross-hatched area and single-hatched areas, respectively. The rocket-engine noise levels are based on measured data obtained for Saturn static firings and Atlas launching tests. The highest rocket-engine noise levels are indicated during the static firing and lift-off because of flow impingement and ground reflections. After the vehicle leaves the ground, there is a decrease in the rocket-engine noise levels because of beneficial effects of the vehicle forward velocity. The aerodynamic noise levels increase as the dynamic pressure increases, the noise pressures being approximately proportional to the dynamic pressure. The aerodynamic noise levels shown are based on estimated dynamic pressures for the Apollo spacecraft. The extent of the cross-hatched areas is based on wind-tunnel studies and flight data for aircraft and for Project Mercury spacecraft; the lower limit applies to clean aerodynamic surfaces ($0.006q$), whereas the upper limit is for regions of separated flow ($0.02q$).

It should be noted that the estimated noise levels are for a region of the vehicle where the manned compartment might be located. For regions of the vehicle near the rocket-engine nozzles, noise levels approximately 15 db higher than those on the nose would be expected during static firing and lift-off. The aerodynamic noise levels estimated are believed to be of about the same order of magnitude for other regions of the vehicle; however, there would probably be differences in the spectral content of the noise (i.e., the peak of the spectrum would shift toward lower frequencies for regions farther aft).

Buffeting of launch vehicles is a relatively new problem which has received considerable attention in the past year. This buffeting has been suspected as a cause for several vehicle failures, either directly through structural failures or indirectly because of failure of equipment subjected to the severe environment produced by buffeting flows.

Buffeting occurs on a wide variety of aerodynamic shapes. Some of the configurations which are representative of those used in various NASA research programs are shown in figure 9. The so-called "hammerhead"

shapes which are used as payload fairings on several vehicles are very susceptible to buffeting flows at transonic speeds. The cone-cylinder-flare configurations used on several warhead reentry vehicles are also subject to buffeting. And, of course, the configurations with escape towers, such as Mercury and some Apollo configurations, also have their buffeting problems. These and other shapes are under intensive investigation.

The three different types of shapes produce at least three different types of buffeting flow, which are illustrated schematically in figure 10. The first type of flow is very similar to the familiar transonic buffeting of thick airfoils. At Mach numbers just below 1.0 the flow expands to supersonic speed over the thicker portion of the nose and is terminated by a normal shock, which in general separates the boundary layer in an unstable manner and produces large pressure fluctuations near the shock location. The second type of flow illustrated is associated with the separation caused by the high pressure, produced by the flare, propagating forward through the boundary layer. This type of flow can persist to low supersonic Mach numbers and is often intermittently asymmetrical even at zero angle of attack. The third type of flow resembles wake buffet in that it is similar to the flow phenomena of an airplane having its horizontal tail in or near the wake of the wing. Various types of protuberances on the forward part of the launch vehicle can produce a wake which passes back over the body of the vehicle and causes the shocks to fluctuate with large pressure fluctuations. This type of buffeting also persists to low supersonic speeds and can be a serious problem at the time of maximum dynamic pressure as well as near Mach number 1. Of course, this is just one particular listing of types of buffeting flows. Some configurations experience combinations of all these types and others as well.

An example of specific results obtained at Ames Research Center for one model is shown in figure 11. The root-mean-square values of pressure coefficient are shown plotted against pressure cell location for a cone-cylinder combination similar to the Centaur launch vehicle. Results are shown for three subsonic Mach numbers. Of particular note is the highly localized characteristic of this type of buffet at each Mach number which occurs at or near the intersection of the cone and cylinder. However, this pressure peak shifts back with increasing Mach number, so that even though it is of a highly localized nature, strengthening of the structure may be required over a considerable length of the vehicle. Similar results have been obtained on essentially every configuration being flown in the space program as well as on a number of planned configurations.

In order to obtain an indication of the buffet characteristics of Apollo spacecraft during launch, a model of one of the Apollo design

DECLASSIFIED

61

configurations has been tested in the Langley 8-foot tunnel. In figure 12 the fluctuating pressures in the form of a root-mean-square pressure coefficient are plotted at the various locations on the spacecraft and second stage. The pressure fluctuations on the nose are small for both configurations, but the presence of the tower causes very high pressure fluctuations over the downstream portions. This highest value just behind the shoulder of the spacecraft is about 23 percent of free-stream dynamic pressure on the basis of root-mean-square values. This effect would correspond to fluctuating peak pressures of nearly 430 pounds per square foot for a nominal Saturn launch trajectory.

This large effect of the escape tower differs from results obtained on the Mercury configuration, which indicated generally high levels (16 percent of q) either with or without the tower. It is evident that more basic research will be required to obtain a full understanding of these phenomena. The limited amount of information obtained with this model indicates that a buffet problem can exist for Apollo. During the development of the vehicle, careful consideration should be given to the configuration modifications that might alleviate the problem, and detailed studies appear necessary to ensure that the structure, equipment, and occupants can perform under the buffeting environment.

As a final item in this buffet problem, the Ames Research Center recently found that for certain nose shapes (principally the hammerhead) the aerodynamic buffet forces are phased in such a manner that a condition of negative damping can occur in a vibration mode. This result means, simply, that a single-degree-of-freedom flutter is possible. At the Langley Research Center, a flexible model has been tested and the damping in the first elastic mode is shown in figure 13. The damping ratio is plotted against Mach number for two configurations. One represents a clean configuration and the damping (structural plus aerodynamic) is shown to be above the structural damping which is indicated by the dashed line. Thus, this configuration has positive damping and is stable. The second configuration, shown at the lower part of the figure, has a region of negative aerodynamic damping as shown by the region where it is below the structural-damping line. Thus, it is apparent that elastic models of proposed configurations should be tested to determine the possibility of negative aerodynamic damping.

The largest single source of loads on a launch vehicle during the atmospheric portion of the flight is due to the wind velocities normal to the launch-vehicle flight path. This problem of wind loads may be resolved into two parts. The first deals with the proper selection of the wind velocities to be used in the basic design, i.e., a design criterion. The second, of an operational nature, involves the requirement of a knowledge of the winds shortly before a firing so that a decision can

be made with regard to the probability of success. As regards the design wind loads, the present practice utilizes an envelope of winds such that the winds over the altitude range of interest will not be exceeded for a certain percentage of time, which are referred to as 1, 2, or 3σ Sissenwine winds. These curves are essentially a series of straight lines and hence do not contain information concerning the details of the wind velocities. As a means of partially accounting for this neglected loading source, it is common practice to superimpose on the loading determined from the steady winds the loading determined from flying through a single 1 - cosine wind gust (which is tuned to excite the fundamental structural mode). The actual winds, of course, have a large number of wind variations which, coupled with low aerodynamic and structural damping, could excite the lower structural modes. An example of the finer grain structure of the winds is shown by the solid line in figure 14, where the altitude is plotted against wind velocity. Unfortunately, the large quantity of information needed to provide more precise wind criteria is lacking. A rather concentrated effort is being made, however, to determine the fine-grain structure of winds. At Langley Research Center, a smoke-trail technique has been developed for obtaining more precise measurements of the winds. This technique utilizes either the natural exhaust of a solid-propellant rocket or an artificially generated smoke trail. Photographs are taken of the trail from two positions which are about ten miles from the launch site. From these photographs, then, the fine-grain detail of the wind velocities may be determined. The winds shown in figure 14 were obtained by the smoke-trail procedure, as well as by a simulated balloon sounding.

The simulated balloon sounding was obtained by reading and averaging the smoke-trail wind in the same manner that is used to obtain a balloon sounding, the usual averaging distance being about 2,000 feet. Large discrepancies between the two soundings are noted, particularly at 17,000 feet.

On a digital computer, a Scout launch vehicle was "flown" through these two winds, the results of which are shown in figure 15. Shown is an envelope of the bending moment plotted against altitude for the smoke trail and simulated balloon inputs. Note, in particular, the large difference in loading at an altitude of about 17,000 feet. Most of this difference can be ascribed to dynamic effects of flying through this detailed wind velocity as given by the smoke trail. In the insert is shown the actual bending-moment trace and again the large dynamic effect is noted. Thus, it is apparent that more detailed and realistic wind profiles are needed for proper design.

With regard to providing information for operational purposes, the smoke-trail procedure requires too much time for data reduction.

DECLASSIFIED

63

However, the U.S. Air Force has under development a so-called "super pressure balloon" which, when used with a much more accurate radar system, could provide this operational information.

CONCLUDING REMARKS

This discussion has pointed up a number of structural dynamic areas that will require detailed investigation when the final configuration is selected. In particular, the vibration characteristics of the Apollo on the Saturn launch vehicle should be determined, perhaps by a dynamic model, and a very thorough buffet investigation will have to be made. Of course, research efforts to advance the state of the art must proceed hand in hand with these more specific items to provide a reliable basis for design procedures and prediction of loads associated with launch-vehicle dynamics.

031712301030

64



LOADING CONDITIONS DURING FLIGHT

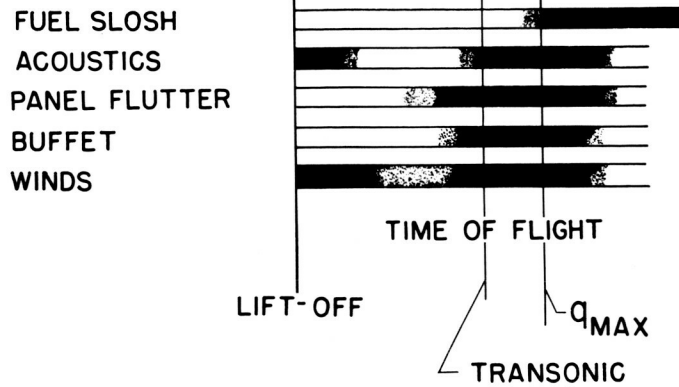


Figure 1

SATURN VIBRATION MODEL

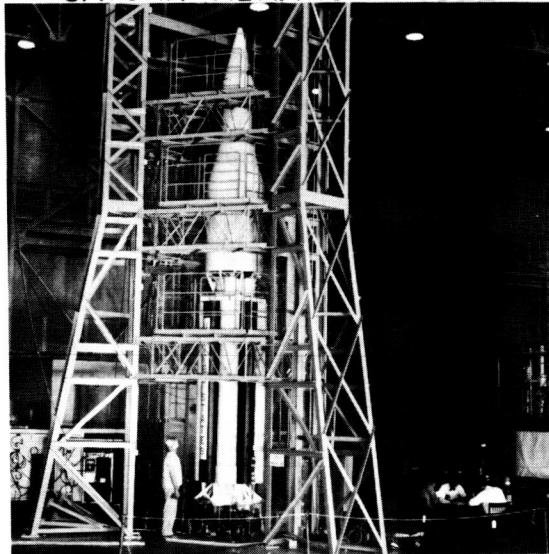


Figure 2

L-61-3024

CONFIDENTIAL

FREQUENCY RESPONSE OF SATURN MODEL

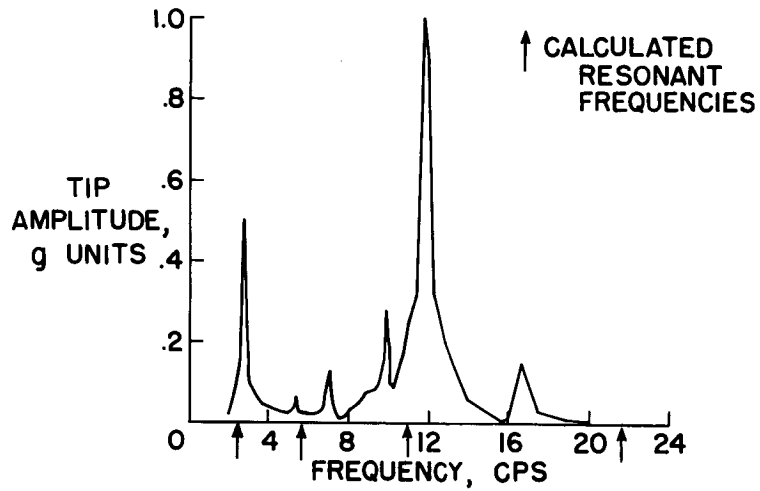


Figure 3

FIRST VIBRATION MODE

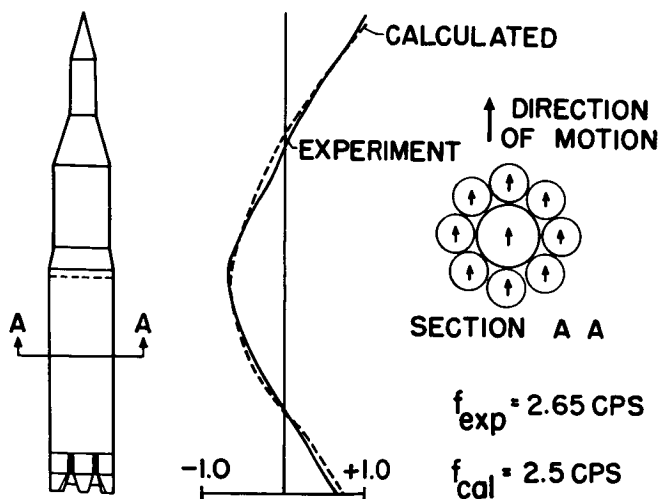


Figure 4

SECOND VIBRATION MODE

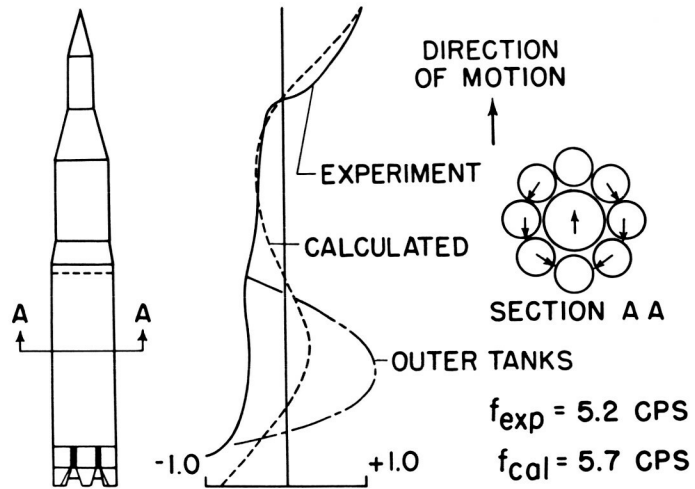


Figure 5

GROUND-WIND-LOADS MODEL

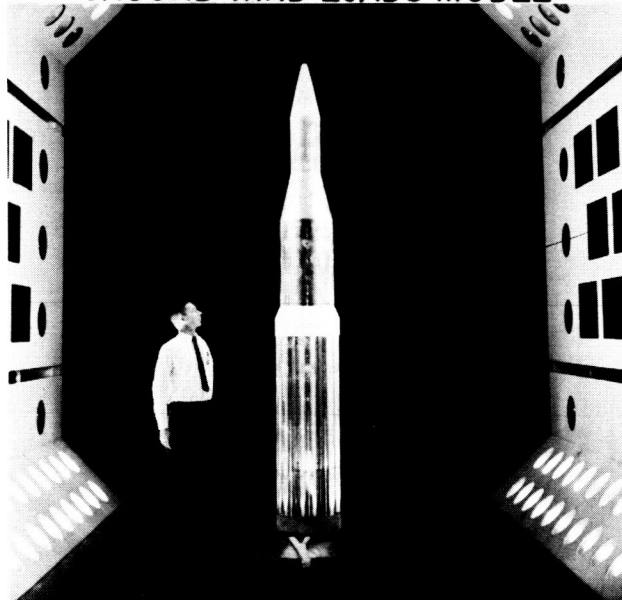


Figure 6

L-61-1628

SATURN GROUND-WIND INDUCED LOADS

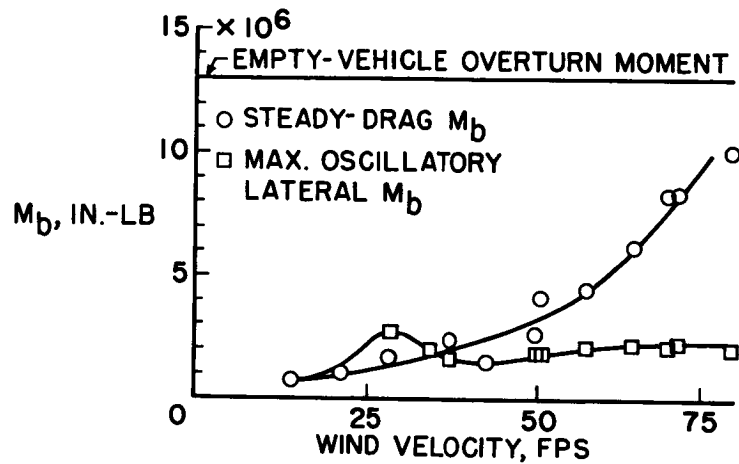


Figure 7

ESTIMATED EXTERNAL ACOUSTIC ENVIRONMENT OF MANNED SPACECRAFT

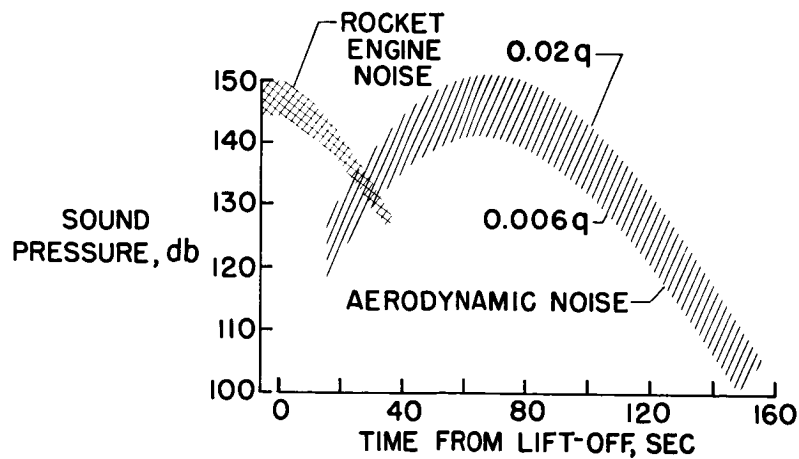


Figure 8

031712001030

SOME CONFIGURATIONS STUDIED IN NASA BUFFET PROGRAM

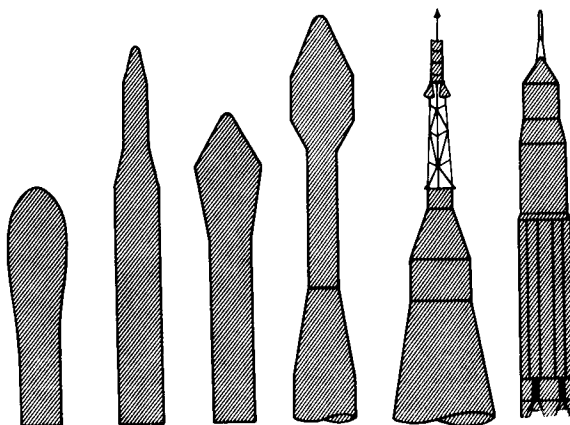
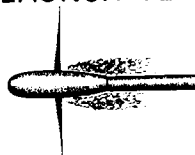


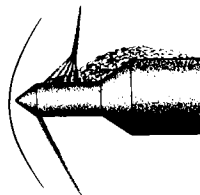
Figure 9

TYPES OF BUFFET FLOWS ON LAUNCH VEHICLES

I SHOCK-BOUNDARY
LAYER INTERACTIONS



II UPSTREAM PRESSURE PROPAGATION



III WAKE BUFFET

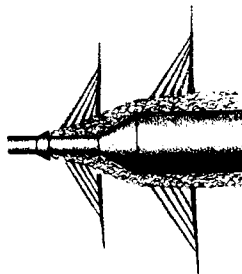


Figure 10

CONFIDENTIAL

BUFFET PRESSURE DISTRIBUTION ON CONE CYLINDER

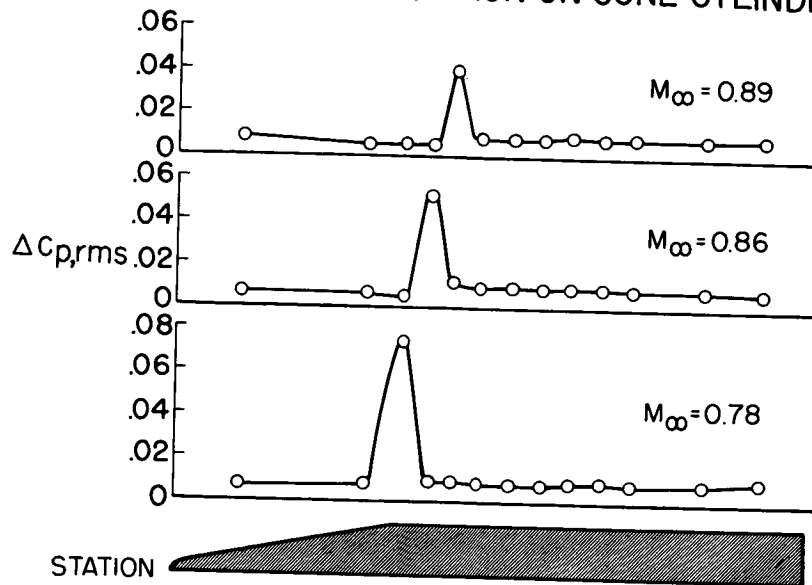


Figure 11

EFFECT OF ESCAPE TOWER ON BUFFET LOADS

$M_\infty = 0.95$; $\alpha = 0^\circ$

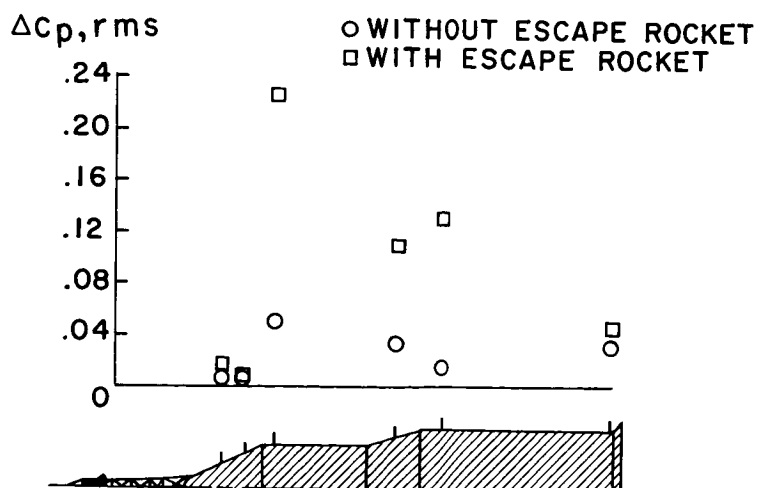


Figure 12

EFFECT OF NOSE SHAPE ON AERODYNAMIC DAMPING OF FIRST ELASTIC MODE

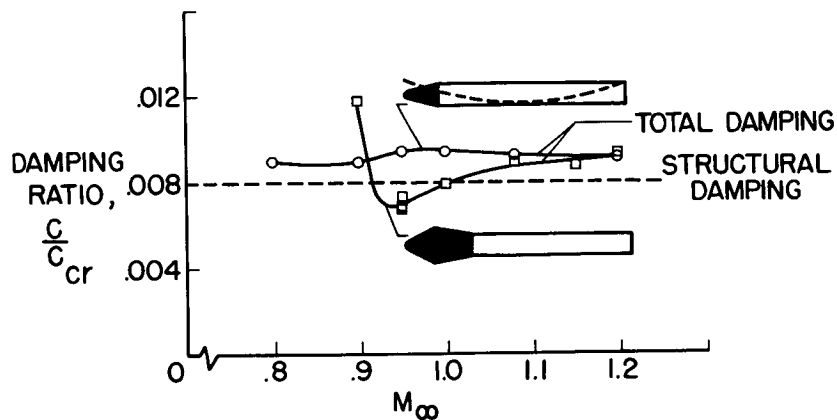


Figure 13

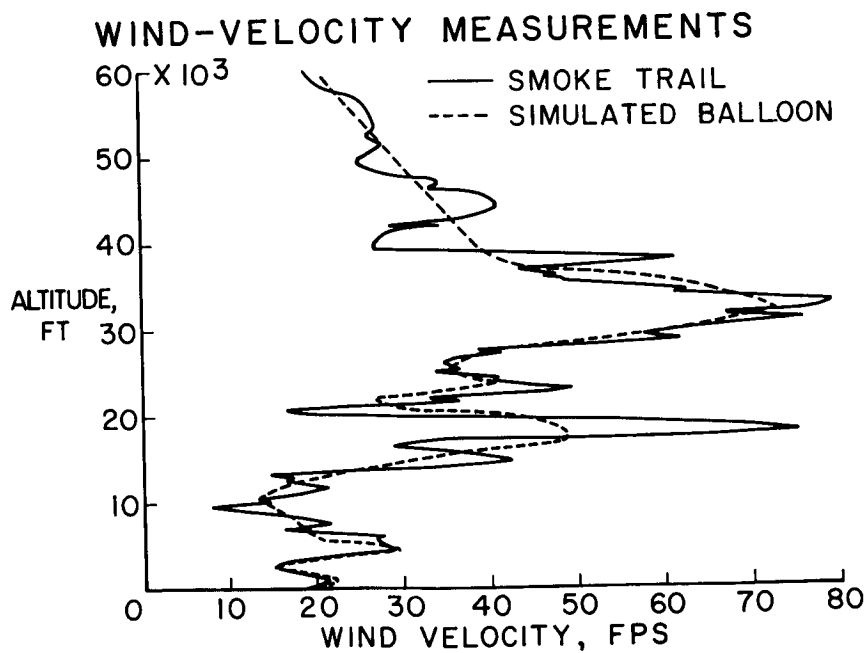


Figure 14

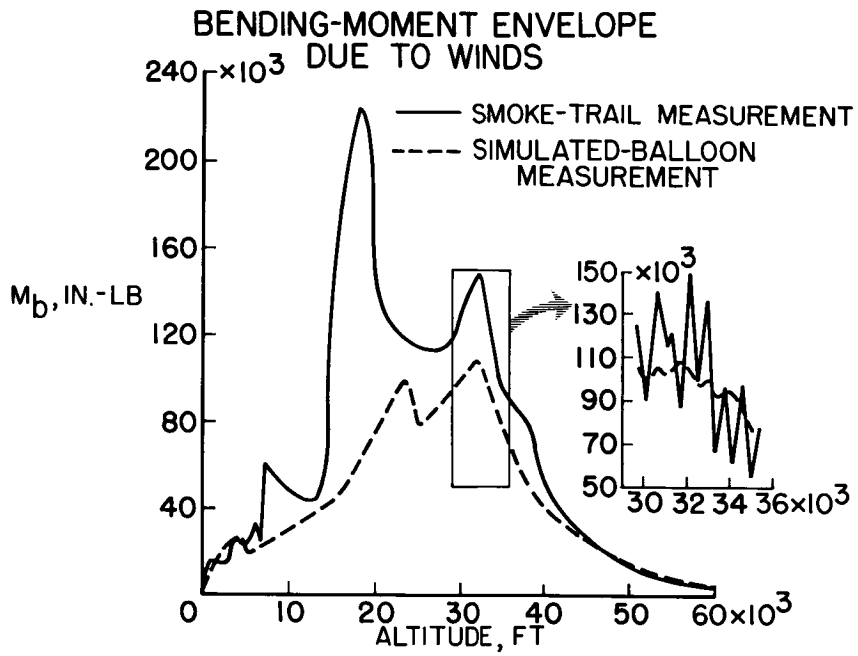


Figure 15

DECLASSIFIED

II.
MISSION
PROFILES

CONSIDERATIONS OF SPACE RENDEZVOUS

By John C. Houbolt

Langley Research Center

INTRODUCTION

This paper discusses some of the basic results that have been found in studies of the problem of rendezvous in space, involving for example the ascent of a satellite or space ferry so as to make a soft contact with another satellite or space station in orbit. Rendezvous is considered of interest before this group because of its contemplated use in some of the Apollo missions.

The main intent of this discussion is to highlight some of the basic advances that have been made in the understanding of rendezvous. Emphasis is given to launch timing, trajectories, guidance, basic rendezvous schemes, and the role of a pilot in rendezvous missions, and attempts will be made to dispel certain misconceptions that have arisen with regard to some of these aspects. Attention is directed to reference 1, which discusses some of the points in much greater detail and gives a list of 60 references dealing with recent rendezvous studies.

PHASES OF RENDEZVOUS

Figure 1 depicts the commonly adopted phases that are involved in an earth-orbit rendezvous; namely, the ascent or injection phase which places the ferry near the target, the controlled terminal or closing phase which starts, say, 50 miles away from the target and usually involves only a fraction of an orbit revolution, and the docking phase wherein latches, lines, and air locks are attached. Some comments will be made about each of these phases.

Launch and Ascent

Injection techniques.— There are at least five basic injection techniques as illustrated in figure 2: an in-plane scheme in which the ferry is launched essentially in the orbital plane of the target, a parking-orbit technique which uses a suborbit to make up for angular position deficiencies between the ferry and the target, an adjacency scheme which requires an orbital-plane correction at the node point,

CONFIDENTIAL

a two-impulse method which involves an intercept trajectory with a second impulse at ferry apogee (the rendezvous point) to make speed and direction coincident, and, finally, the general scheme which involves a Keplerian transfer of the ferry to intercept the target on either the outgoing or return leg and an impulse at this intercept to make speed and direction coincident. The first four techniques are really subcases of this fifth general scheme. Studies have shown that all five schemes are capable of once-a-day rendezvous operations and that some offer the possibility of rendezvous on from three to four successive orbital passes of the target; advantages and disadvantages differ, of course, with each scheme.

Direct ascent "launch windows".- Launch time intervals that are associated with direct ascent rendezvous are illustrated in figure 3. On the left is shown a planar projection of several paths to rendezvous. At the end of booster burnout the ferry is injected with a velocity V_L and a flight-path angle γ_L . If the target is at the position A_L , rendezvous can occur at A_R via a Hohmann type transfer or minimum energy path. If the target is at B_L , rendezvous can be made on the outgoing leg at B_R ; whereas if the target is at C_L , rendezvous will occur on the incoming leg at C_R . At each of the intercept points a finite velocity increment ΔV_R must of course be applied to make the rendezvous soft.

The maximum spread between the positions B_L and C_L is determined by vehicle performance capabilities; that is, the largest value that can be obtained from the vehicle for the sum $V_L + \Delta V_R$. On the right in figure 3 are shown results for two different values of this sum. For a total velocity of 27,000 fps, launch can be made when the target is from 6.1° ahead to 7.4° behind the ferry, a spread or "launch window" of 13.5° . For a 300-mile orbit, an orbital arc of 4° corresponds to about 1 minute of orbit time; thus, the launch window is 13.5 divided by 4 or about $3\frac{1}{2}$ minutes of time. A total velocity of 30,000 fps is seen to increase the launch window to 61.8° or about 15 minutes of time suitable for launch.

Circumstances of large holddown intervals.- Suppose holddown times go beyond the launch window capabilities discussed in the preceding section. Recourse is then simply to abandon the direct-ascent approach and make use of a scheme that is based on the two basic ideas embodied in figures 4 and 5. In figure 4 the heavy curve represents the intersection of earth surface with the orbital plane of a target which was launched in an essentially east-west direction. For this case the launch site is found to be very close to the orbital plane for four successive orbital passes of the target, or to put it another way, the

launch site is near the orbital plane for a time interval of as much as $4\frac{1}{2}$ hours; this nearness condition is desired so that rendezvous ascents can be made without excessive fuel penalties. With this factor in mind, the procedure would be to launch the ferry at any time that it is ready during this $4\frac{1}{2}$ -hour period so as to intercept a point in the orbital path of the target, with no regard being given to where the target is (in other words, the launch window is in this manner increased for times up to several hours). Instead of injecting the ferry at full orbital velocity, however, an incremental velocity ΔV is held back at apogee, which thus causes the ferry to go into a chasing orbit, depicted by the inner orbit on the right of figure 5. Because of the shorter orbit period, angular position is made up on each revolution. After the angular position has been made up, the velocity increment not previously used is then added; there is therefore essentially no fuel penalty over that required by a direct ascent rendezvous. As an illustration, consider the curves on the left of figure 5, which apply to the case of a 300-mile circular target orbit. For an angular position error of about 11° , which corresponds to a launch time miss of 2.8 min., the results indicate that a holdback velocity of about 250 fps will make up this angular deficiency in one revolution, or that 22° will be made up in two revolutions, and so forth. From the scale on the right, Δr is also determined to make sure that the ferry doesn't dip back toward the earth too much; for the example treated, Δr is 170 miles, giving a minimum altitude of 130 miles, which should be satisfactory. Hence, by employing launchings of the due east type and through use of chasing orbits, the launch window has been increased up to several hours. It should be mentioned that parking or suborbits can be employed in a similar manner, with a little better make up in time.

Terminal Guidance

Basic terminal phase schemes.- Essentially there are two basic schemes for performing the terminal phase of rendezvous, one based on proportional navigation or fire-control viewpoint, the other on orbital mechanics. (See fig. 6.) Orbit path is shown on the left, and the relative motion of the ferry as seen from the station is shown on the right.

In the proportional navigation scheme the rate of rotation of the velocity vector is controlled in proportion to the angular rate of the line of sight. With reference to rendezvous studies, it is perhaps more appropriate to call this a constant bearing navigation scheme, since generally conditions are sought where the line of sight remains stationary in space; an inertially fixed set of axes is implied in this scheme.

[REDACTED]

The orbital-mechanics scheme is based essentially on the homogeneous equations of motion in a reference frame fixed to the target. These equations are solved to determine the proper course to rendezvous; impulsive corrections are given to put the ferry on a collision course, and a final impulse is given at intercept to match velocities.

Both systems require onboard sensors, such as radar or optical devices (or a man), to measure range, range rate, and angular rate of the line of sight. Either piloted or automatic control may be used, and thrusting (or braking) may be variable or of the on-off type.

Braking logic.- Figure 7 depicts the braking logic that may be used in the proportional navigation case. The principal idea is first to null the angular rate of the line of sight, which thus puts the ferry on a collision course to the target. A one-directional braking maneuver along the line of sight can then be used; a braking schedule often used is based on the simple one-dimensional acceleration law

$$a = \frac{\dot{R}^2}{2R}$$

For path 1, the angular rate of the line of sight has been nulled; a drift at constant \dot{R} is then allowed until conditions satisfying the chosen acceleration law are met; at this point the rocket motors are turned on, resulting in a parabolic phase-plane path to end up simultaneously with $R = \dot{R} = 0$ at rendezvous. In path 2 (on-off control), after initial nulling of the angular rate of the line of sight, drift is allowed until an "on" line is reached; thrusting then occurs till the "off" line is reached. Action is repeated in this sequential fashion until rendezvous is completed.

For path 3, most of the range rate, as well as the angular rate of the line of sight, is nulled simultaneously in the initial maneuver. This procedure is the most efficient as regards fuel, but the time to rendezvous is lengthened considerably, because of the very low \dot{R} . In path 4 range rate is increased in the initial maneuver; this procedure shortens the time to rendezvous but at the expense of some fuel.

The paths depicted are basic for either manned or automatic operation.

PILOT'S PERFORMANCE

As a check on the ability of either a manned or an automatic system to control the terminal phase of rendezvous, a number of analytical and

simulator studies have been made. In general, it was found that either system could be used quite successfully. A quick review will be given here of some of the piloted studies. Figure 8 is a picture of one of the cockpit setups employed, showing the instrument display and controls.

Figure 9 presents fuel-consumption results as obtained in a number of different test runs conducted by different people including airplane pilots, engineers, and even secretaries. The actual amount of fuel used, presented in terms of incremental velocity (100 fps requires a fuel consumption of roughly 1 percent of ferry mass), is plotted against the actual ΔV required; the ΔV_R corresponds to the ideal initial maneuver wherein both the \dot{R} and normal velocity ΔV_N (which is the velocity due to angular rate of the line of sight) are nulled simultaneously. The range of ΔV used in repeat runs and by various pilots is shown by short horizontal ticks. The circled points indicate the fuel that would be used if ΔV_N is first canceled, and then \dot{R} . The average value used, as shown by the longer horizontal ticks, indicates that in the more severe cases pilots have a natural tendency to cancel out some of the range rate as well as ΔV_N in the initial maneuver. In general, it is seen that the average fuel consumption is only about 1 percent greater than that actually required, so that a very good performance capability of a manned operator is indicated.

Simplified terminal phase schemes.- Studies have also been made to see to what extent the electronic equipment, sensors, and such devices could be simplified or even eliminated. The following typify some of the results obtained in terminal phase simulation by use of visual techniques. The studies were made in an inflatable planetarium (fig. 10) by the setup depicted schematically in figure 11. In this scheme the basic idea is that angular rate of the line of sight can be determined by visually noting the motion of the target relative to the star background. Thus, only range and range rate need be supplied by instruments. On the left is shown the pilot's seat, the star projector, and the collimated beam and mirror setup which produces the target light; note that this signal is a flashing light so that it may be easily distinguished from the stars. The rotating mirror is driven by the analog equipment which simulates the relative motion of the ferry and the target. On the right is depicted the motion of the target as seen by the pilot. In operation the pilot simply rolls the spacecraft so that the relative motion appears either horizontal or vertical to him; he then fires a transverse rocket until the motion stops. He has thus nulled all the angular rate of the line of sight and is on a collision course. Then, by use of the R and \dot{R} instruments he brakes to rendezvous as before.

A typical simulation for a very severe test case is shown in figure 12. The "drunkard's walk" pattern simply shows that during braking some angular motion reappears because of residual misalignments, but despite the severity of the case, final rendezvous was accomplished with relative ease.

In passing it is remarked that a scheme has also been advanced for eliminating the R and \dot{R} instruments. All that is necessary is a stop watch and a telescope containing a grid for indicating angular displacement of the target. By measuring the time necessary to traverse several angular segments, the pilot can deduce R and \dot{R} by simple geometric considerations, and thus have the necessary information to go into a braking schedule.

Docking and Discerning Objects in Space

The docking problems of rendezvous are perhaps the least well understood. A number of mechanical schemes and gadgets have been advanced and some studies of contact dynamics have been made. The general feeling is that docking presents no major obstacle, but perhaps the most pertinent comment that can be made about docking at this time is that a flight experiment is needed to help define what the problems really are.

Apart from the kinematics and dynamics of docking, a problem of discerning objects in space may also be present. A question that is often raised is whether a person in space can see objects near him. That is, depending on the placement of the person himself, the object, or various objects, the sun and nearby planets, can he discern the object, tell whether it is between himself and another object, tell whether it is coming toward him or going away, etc.? These questions are of course of vital concern in rendezvous operations, especially if visual techniques are employed.

For the purpose of gaining some insight into these questions, some visual studies were made of different objects with various finishes; the lighting condition simulated was that of an object in an assumed black void of space with sun lighting from the rear of the observer. Figure 13 shows some of the results; figure 13(a) applies to spheres of equal size but with various finishes; figures 13(b) and 13(c) to cylindrical cans simulating booster casings in space, and figure 13(d) shows an unlighted ordinary light bulb, a golf ball, and a Christmas tree ornament. In general, objects with painted or rough surfaces stand out well and, as expected, the polished objects were least distinguishable.

~~CONFIDENTIAL~~

Thus, with properly painted patterns, objects in space should be quite discernible. For nighttime rendezvous, where visual techniques are intended, colored flashing lights such as are carried on airplanes and boats, and flashing spotlights should be quite sufficient to determine motion and attitude of a target for rendezvous.

CONCLUDING REMARK

Probably the most important conclusions to be made are that rendezvous appears technically feasible and that both manned control and automatic control are practical. A further point that must be made with respect to the merit of rendezvous is that by orbital assembly of units, rendezvous offers a very flexible and versatile means for performing space missions, or for making possible missions which could not otherwise be made.

REFERENCE

1. Houbolt, Jonn C.: Problems and Potentialities of Space Rendezvous. Presented at the International Symposium on Space Flight and Re-Entry Trajectories, organized by the International Academy of Astronautics of the International Astronautical Federation, Louveciennes, France, June 19-21, 1961.

PHASES OF RENDEZVOUS

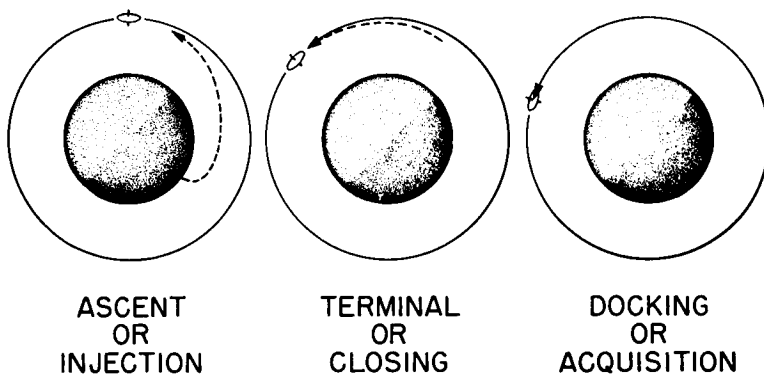


Figure 1

RENDEZVOUS ASCENT TECHNIQUES

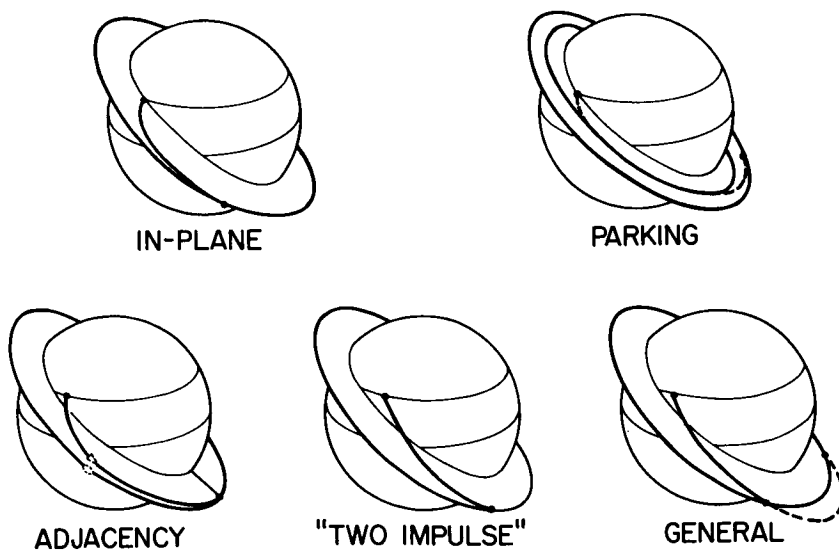


Figure 2

~~CONFIDENTIAL~~

ASCENT PATHS AND "WINDOWS" OF RENDEZVOUS

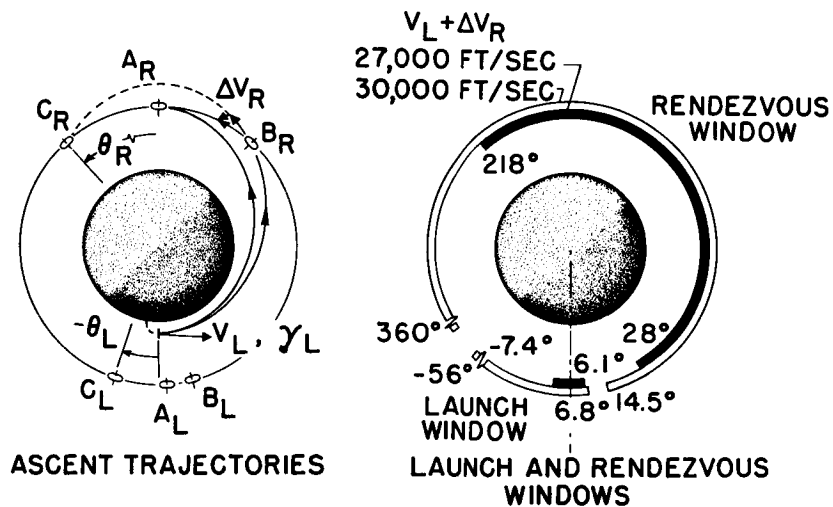


Figure 3

ACCEPTABLE LAUNCH DURATION (300 MILE ORBIT)

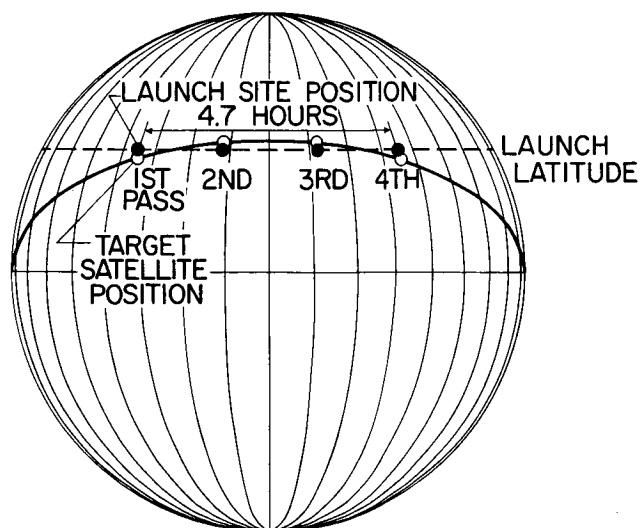


Figure 4

CORRECTIONS FOR POSITION MISMATCH SPECIFIC EXAMPLE

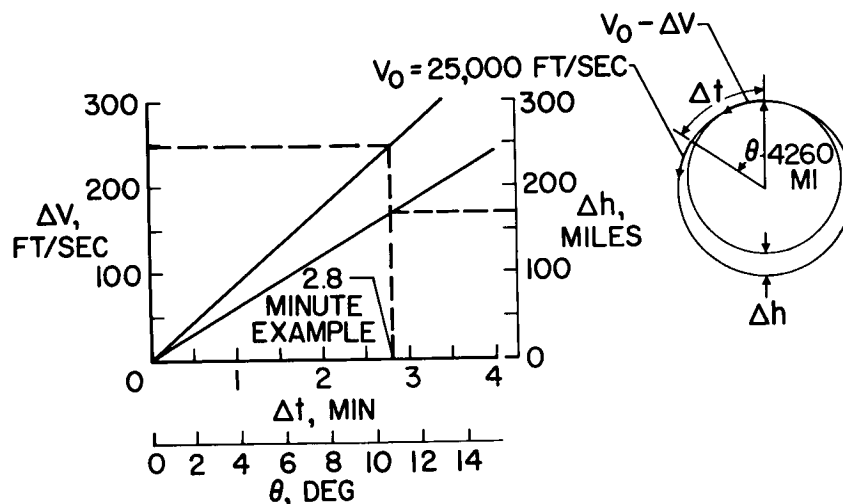
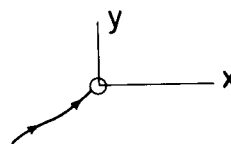
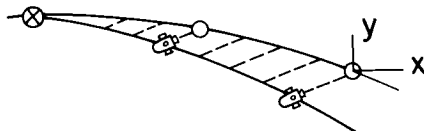


Figure 5

BASIC TERMINAL PHASE SCHEMES

I PROPORTIONAL NAVIGATION



II ORBITAL MECHANICS

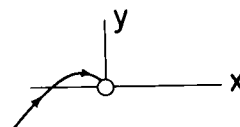
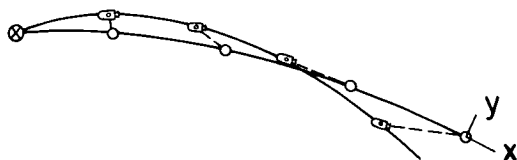
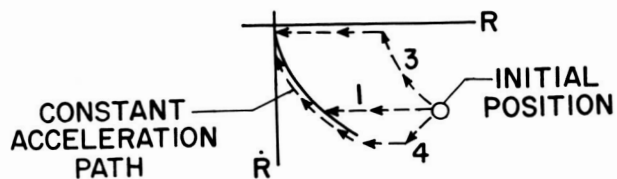


Figure 6

PHASE PLANE PATHS

I VARIABLE THRUST CONTROL



II ON-OFF THRUST CONTROL

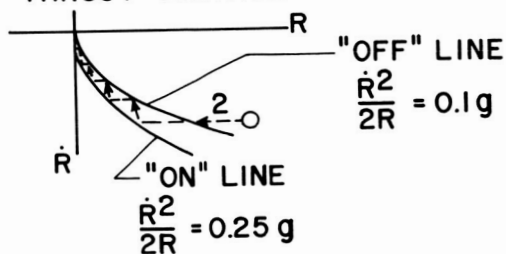


Figure 7

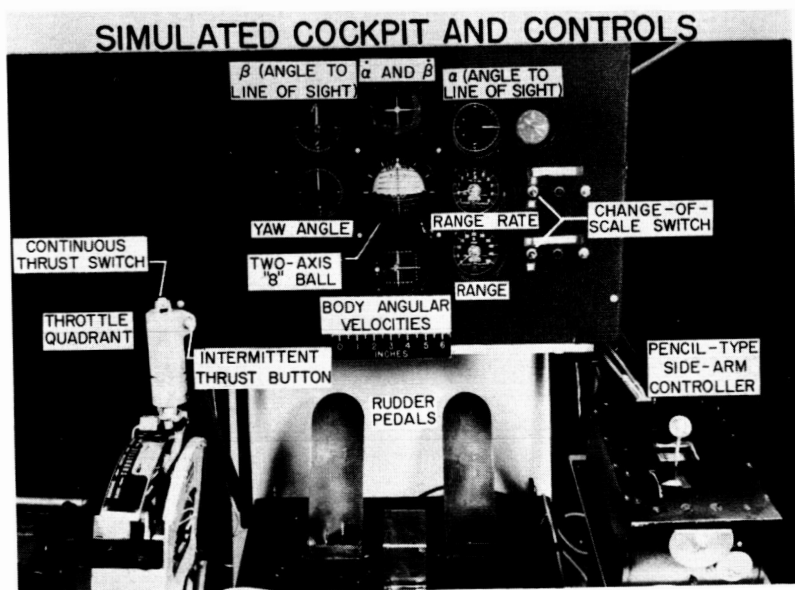


Figure 8

L-60-4266.2

03171239.0000

PILOTS PERFORMANCE DURING TERMINAL PHASE

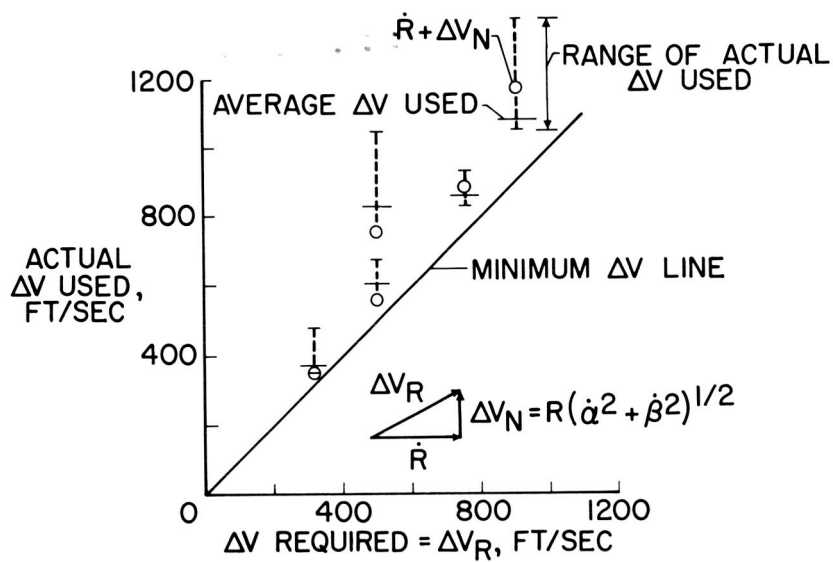


Figure 9



Figure 10

L-61-3399

VISUAL TERMINAL PHASE SIMULATION

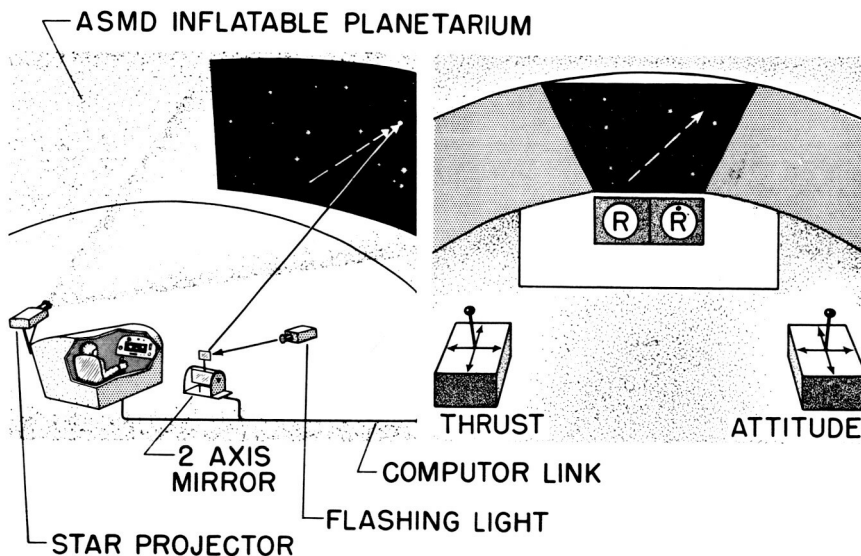


Figure 11

TARGET PATH IN SIMULATED RUN

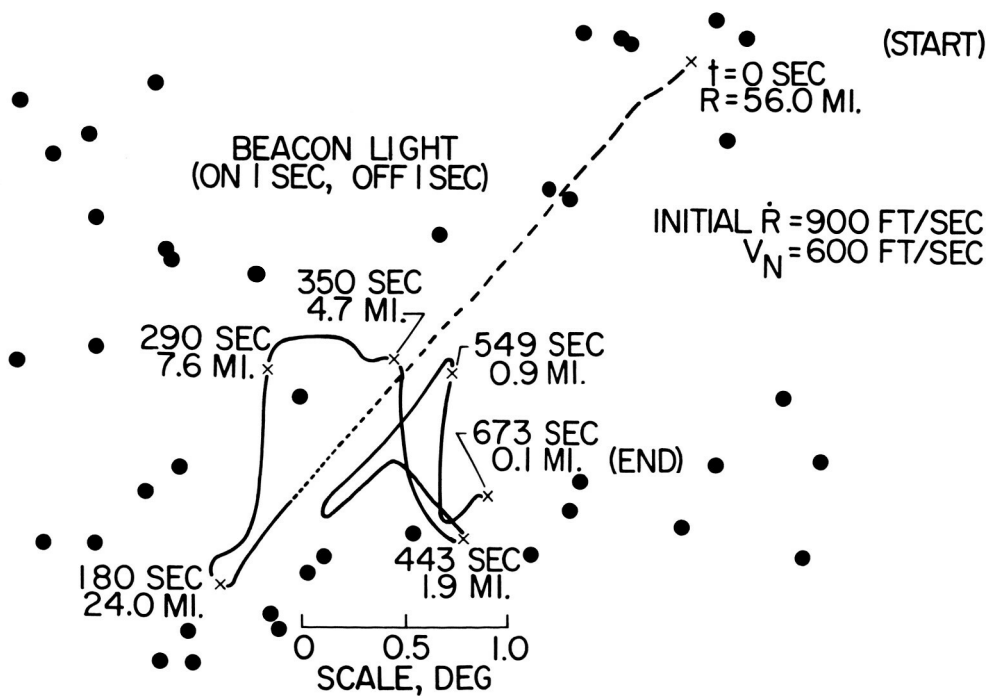


Figure 12

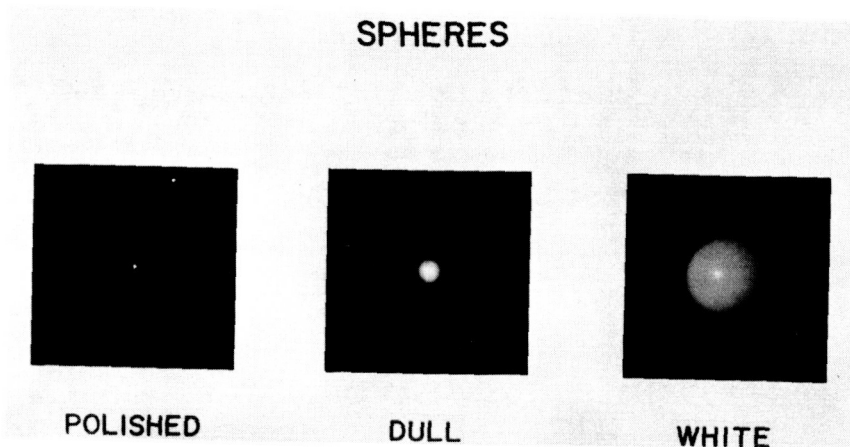


Figure 13(a)

L-61-2245

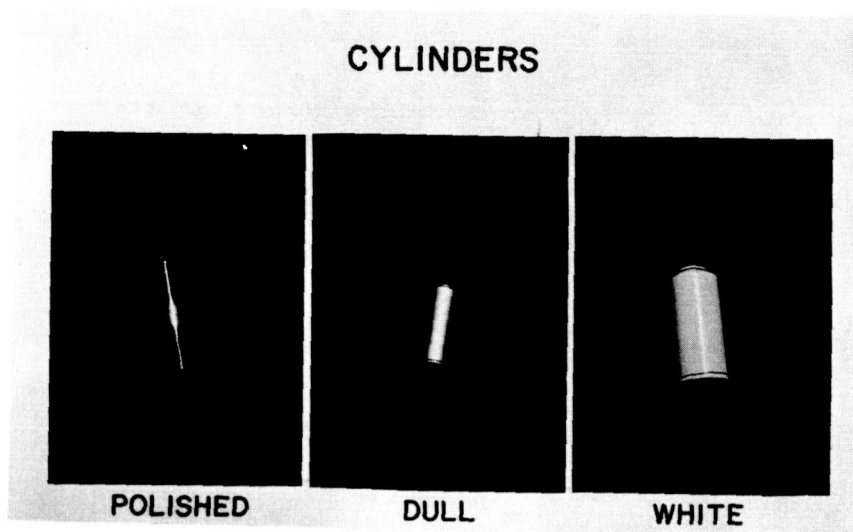


Figure 13(b)

L-61-2246

~~SECRET~~ RELEASED 87

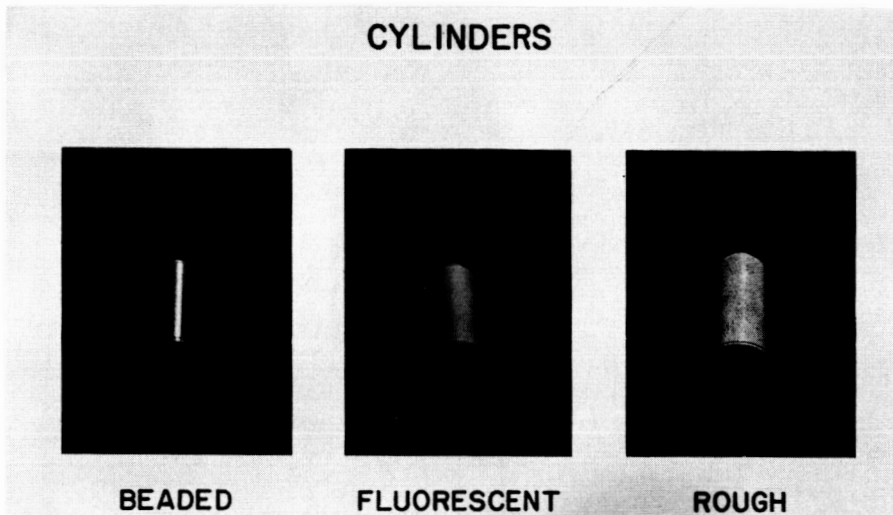


Figure 13(c)

L-61-2247

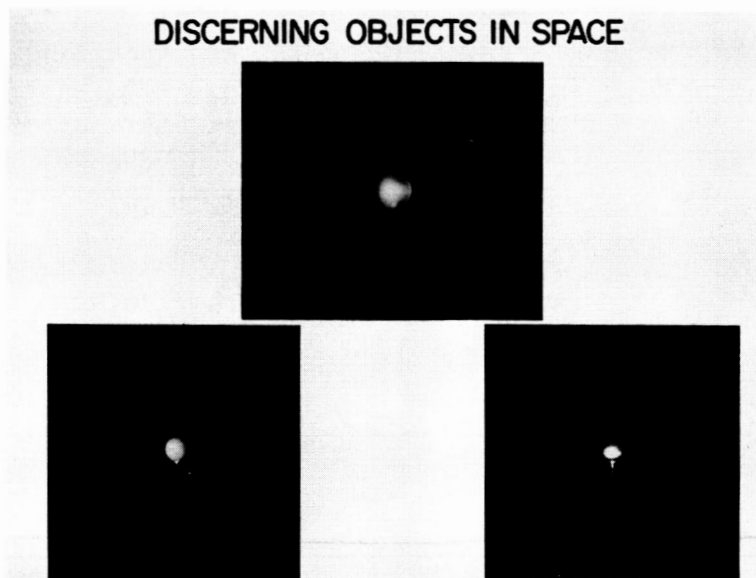


Figure 13(d)

L-61-2243

~~SECRET~~

LUNAR LANDING CONSIDERATIONS

By Maxime A. Faget

NASA Space Task Group

The design mission for Project Apollo is now set as a lunar landing. This paper will be a discussion of the considerations and problems associated with landing a manned spacecraft on the moon, staying there a short period, and then returning from the lunar surface. It is not intended to set forth in a detailed manner how this can be done. As a matter of fact, there are a number of problem areas needing more analysis, experimental work, and just plain facts before some details of the landing can be decided upon or properly argued about. However, there are other aspects of the operation that seem suitable for serious consideration. It is hoped that a discussion of these and the associated problems will help focus attention on areas of work that need immediate effort in order to clarify the situation.

The general considerations and problem areas associated with landing men on the moon which will be discussed are as follows:

- (1) How should the approach and landing be made?
- (2) What abort capabilities are required in the event the mission must be terminated?
- (3) How long should the crew stay on the moon?
- (4) What are the return maneuver considerations?
- (5) What significant environmental factors must be considered?
- (6) How can the crew best be used and what factors are associated with this desire to use the crew?

Figure 1 will be used to provide a means for discussing the landing and return maneuvers and the possible abort situations.

If it were desired to provide complete protection against propulsion system failure during both the landing and return maneuvers, an additional redundant propulsion system having sufficient energy to provide the approximate 9,000 feet per second needed for either of these maneuvers would have to be carried unused throughout the mission. This would more than double the payload requirement for the launch vehicle and for this reason is considered impractical. An alternate scheme is

90 13171209.1 ~~SECRET~~

to place extreme emphasis on reliability, at the sacrifice of performance in the return propulsion system. In this case, high performance in the landing propulsion system may still be emphasized since the return propulsion system provides protection against failure.

In examining the maneuvers in the vicinity of the moon, keep in mind the use of the return propulsion system for emergencies during landing and that the landing site will undoubtedly be located on the side visible to the earth in order to provide communications during the period on the moon. The approach to the moon will be along hyperbolic paths as shown in figure 1. The approach path can either lead directly to the moon's surface or to a maneuver into a low orbit around the moon. The direct approach which appears attractive for unmanned flights is not recommended because of the following reasons:

(a) To abort from a failure would require more energy than would be needed for a normal return; thus, an oversize return propulsion system would be required.

(b) The direct approach to the lunar surface would require variable thrust engines so zero velocity and zero altitude can be achieved simultaneously.

(c) The requisite precision in timing and control would minimize the effectiveness of the crew in monitoring the maneuver.

(d) This approach limits the choice of landing area.

On the other hand, the orbital approach will be similar to previously completed lunar-orbital missions.

Landing from an orbit will, therefore, be discussed in some detail. It would seem best to carry out this maneuver in a number of steps. The first step would be one of obtaining the proper orbit. The next is descending from orbit to a standstill a short distance above the moon's surface, and the final step is making a hovering descent to touchdown. The transfer maneuvers from hyperbolic velocity to the initial orbit must be done on the backside of the moon as shown. Unless it is desired to land approximately 180° from this point, it would seem best to first enter into a circular orbit and then if a low perigee over the landing point is desired, a second transfer maneuver may be made. From an energy standpoint there seems to be little to be gained by making the initial orbit less than 100 miles above the lunar surface; at the same time, it appears that such an orbital altitude is within the guidance system capability.

The descent from the 100-mile circular orbit can be carried out either directly or by first transferring to an orbit with perigee close

~~SECRET~~

to the surface in the vicinity of the chosen landing area. How many orbits should be used, and how low should be the final pass over the landing area, may be determined only after the completion of detailed mission analysis. It might be mentioned, however, that with only $3\frac{1}{2}$ -percent penalty in characteristic velocity, the descent from the initial 100-mile circular orbit can be made with the landing area in line-of-sight during the complete maneuver. This would make it reasonable to consider landing during the first or second pass if it becomes desirable to reduce the mission time and if suitable electronic beacons have been previously located in the landing area.

If it is desired to make a direct return abort during the landing maneuver, the landing area should be to the right of the limit line shown in figure 1, otherwise the energy requirements may exceed the return propulsion system capability.

Figure 2 shows a typical descent maneuver from a low perigee orbit (100,000 ft) and with a propulsion system burning hydrogen and oxygen at an initial ratio of thrust to earth weight of 0.2. Shown in the figure are altitude and vertical-velocity time histories. The optimum maneuver was determined by the calculus of variations and is similar to backing down an optimum launch maneuver. The preferred maneuver differs from the optimum one in that it is shaped to achieve the final altitude of approximately 100 feet with no residual vertical velocity 10 seconds prior to cut-off. This eliminates the need for thrust level control (throttling) and provides a maneuver which can be more easily followed and monitored by the crew. This departure from the optimum maneuver would result in the use of $1\frac{1}{2}$ percent more fuel.

The period of time on the moon will be dependent on a number of yet undefined problems and requirements. Operationally, it appears desirable to have the capabilities to remain for a period in excess of 24 hours in order to avoid imposing restrictions on return transit time and trajectory, since this would allow for a full rotation of the earth.

For return from the lunar surface the maneuver can be direct or by way of a parking orbit. The parking orbit route has the advantage of duplicating a return maneuver which will have been made in previous Apollo flights. The direct return maneuver, on the other hand, eliminates the hazard of one maneuver at a time when there is no emergency propulsion. From a performance standpoint, the parking orbit is favored for low-thrust propulsion systems. From a navigation and guidance standpoint, there would seem to be little reason to prefer one method or the other. In either case, an inertial system tuned to the moon's gravity field would be needed for the landing maneuver as well as the return. However, it seems reasonable to expect the same inertial system


used for other phases of the mission could be easily provided with this capability.

Figure 3 simply shows the expected general arrangement of components when the Apollo vehicle is provided with lunar landing capability. The landing propulsion system is attached behind the launch propulsion system which is, in turn, attached to the command module. With this basic arrangement, a number of various landing configurations suggest themselves.

Three of the more interesting hovering and landing configurations are shown in figure 4. The hovering and landing phase will start possibly 100 to 200 feet above the moon's surface at termination of the deceleration and descent from orbit. Since the engines used for these maneuvers will be of a thrust level that greatly exceeds the terminal maneuver requirements, it seems desirable to provide a separate propulsion unit for this. The hovering and landing propulsion will also require thrust level control which will not previously be required. An extended period of hovering is not too costly because of the low gravity level on the moon. For instance, each hovering period of 1 minute would require a weight increase of $3\frac{1}{2}$ to 4 percent if a storable system were employed. Hovering periods on the order of 1 minute would seem adequate from helicopter experience for providing some choice of touchdown points and for reasonable rates of descent.

The particular arrangements in figure 4 are essentially self-explanatory. The configuration in the upper part of this figure shows the spacecraft landing in about the same attitude that it is in at termination of the deceleration maneuver. This configuration also has the advantage of a short landing gear. The configuration on the left shows the case for turning the spacecraft up prior to landing. This configuration has the advantage that the hovering and landing engine may be started prior to the termination of the deceleration maneuver. It also provides a vertical launch attitude. The configuration on the right shows the case where staging has taken place prior to the hovering and descent maneuver. In this case, the part of the launch propulsion system may be employed for hovering and a system could be eliminated.

Up until this point, the landing has been discussed from the standpoint of maneuver control and performance. Right up to the actual contact with the moon surface, a fairly positive analysis can be made. In going beyond this point, a great deal of uncertainty is involved because of insufficient factual information. This situation must improve. It is planned to obtain data from unmanned lunar missions such as Surveyor. The significant environmental factors for the lunar landing and the period on the moon are as follows:



- (1) Surface characteristics
- (2) Surface temperature
- (3) Light (sunshine or earthlight)

The surface characteristics are important from the standpoint of landing gear design and from the standpoint of the effect of the jet on loose surface materials, such as dust and rocks. These could damage the spacecraft or interfere with vision and radar. Experimental programs duplicating full-scale conditions are needed in this area.

The surface temperature of the moon is shown in figure 5. It is plotted as an angular variation from the position where the sun would be directly overhead toward sunset and night. The temperature varies from 250° F to -250° F with a very sharp gradient at dusk. The temperature is significant only from the standpoint of conduction of heat to things in contact with the surface and for radiation to areas facing the surface. Although it is possible to plan the mission to cater to a desired surface temperature, it would appear that spacecraft, pressure suits, and other equipment can, if necessary, be designed to meet the extremes of this environment.

The mission may also be considered from the standpoint of lighting. Both the sun and the earth are sources of light. The earthlight on the moon is two orders of magnitude brighter than is moonshine on the earth. For a full earth with nominal cloud cover, the light from the earth amounts to 1.6 lumens per square foot. This is equal to the light obtained from a 100-watt bulb at 9 feet. There may be some advantage in operating in earthlight as opposed to sunshine since it will be less difficult to fill in the shaded areas with supplemental light.

Some human factors aspects considered are:

- (1) Use of crew
- (2) Visual consideration
- (3) Displays
- (4) Sitting position desired

It is felt that proper planning of the systems and operations to utilize the capabilities of the crew will greatly enhance the probability of success. The hovering and landing should be in direct control of the crew in order to be able to choose and maneuver the spacecraft to the most desirable touchdown point. It is possible that the crew could be

used to conduct other maneuvers (ref. 1). In any event all maneuvers should be planned with crew supervision in mind.

The spacecraft should afford good direct vision capability for the hovering and landing maneuver. Since the vehicle will be going propulsion-end first during the deceleration from orbit it will be difficult to provide direct vision ahead and it may be necessary to rely on a closed-circuit television system.

The effectiveness of the crew will be largely dependent upon the proper display of useful information. The X-15 pilots, for instance, rely heavily on their display throughout the approach and landing. The display must include altitude and sink rate. Lateral and longitudinal drift rates during hovering are also desired. Suitable displays for monitoring maneuvers into and out of orbit such as those described in reference 1 must also be included. Such display requirements, however, seem compatible with those of other mission phases.

Experience with VTOL aircraft and with helicopters strongly indicate that a properly oriented seated position is desirable. The horizontal landing configuration naturally affords this position. The other configurations could be arranged to temporarily place one crew member in this position for the landing maneuver.

In summary, it would appear that it is reasonable to plan the lunar landing mission up to the point of actual contact with the moon's surface. Details of the landing gear arrangement and definition of the effect of the lunar environment on the operation and equipment while on the surface of the moon must await more factual data, simulation experiments, and analysis.

REFERENCE

1. Queijo, Manuel J., and Riley, Donald R.: A Fixed-Base-Simulator Study of the Ability of a Pilot To Establish Close Orbits Around the Moon. NASA TN D-917, 1961.

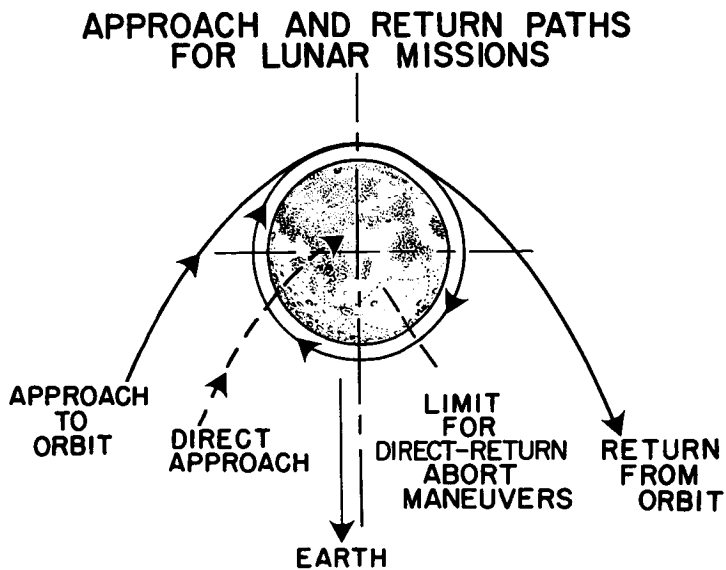


Figure 1

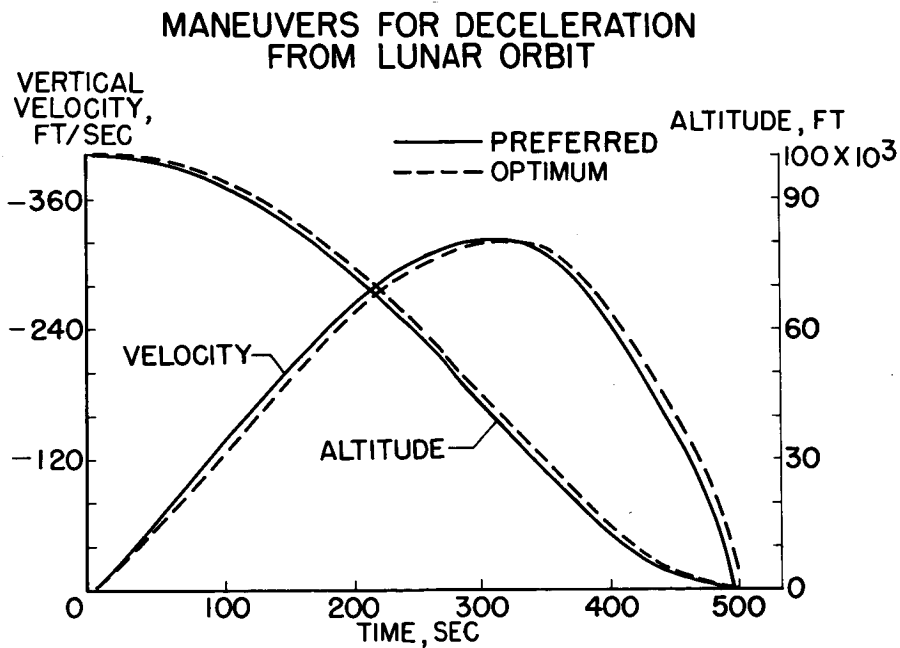


Figure 2

CONFIGURATION FOR APOLLO LANDING MISSION

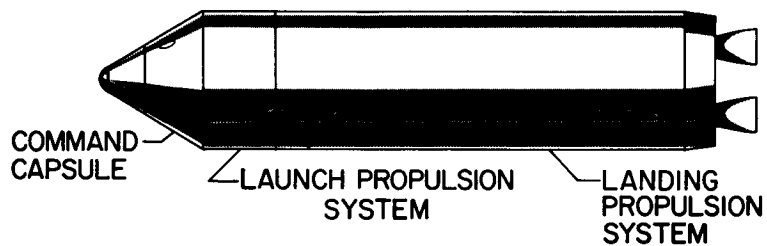


Figure 3

POSSIBLE HOVERING AND LANDING CONFIGURATIONS

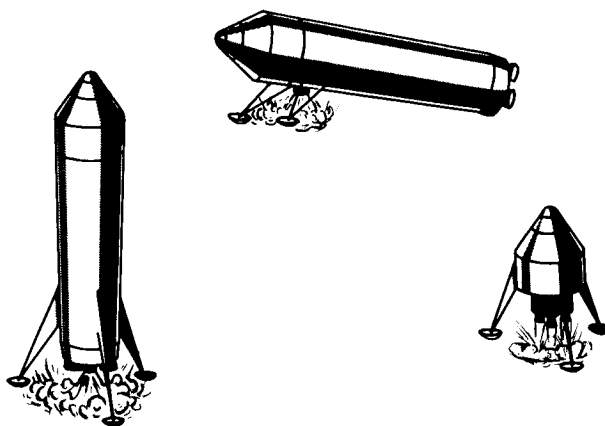


Figure 4

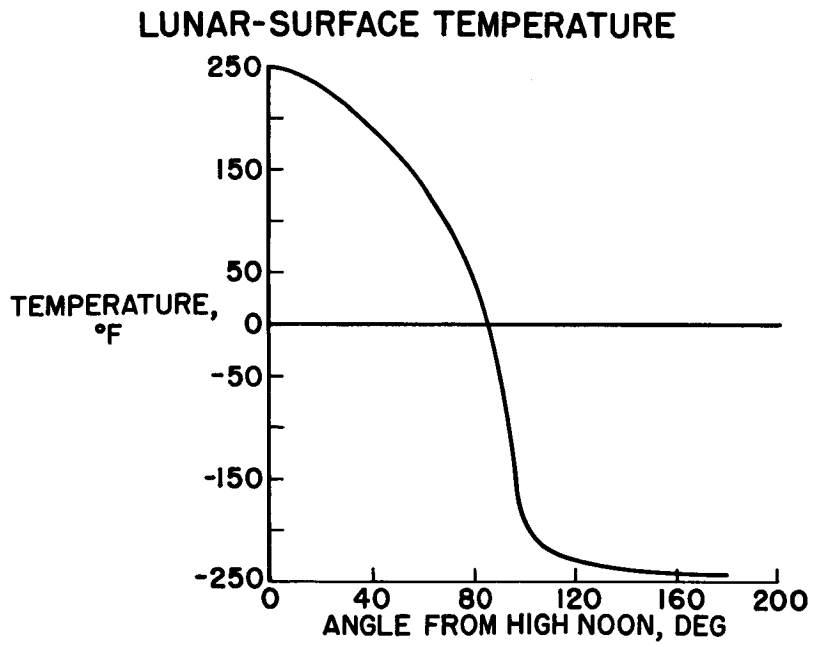


Figure 5

REF ID: A55159

LUNAR TRAJECTORY ANALYSIS

By William J. Praglusk, Donald H. Novak,
and A. Lawrence Guess

The Martin Company

SUMMARY

This paper defines the basic problem in synthesizing circumlunar trajectories. It also presents a brief discussion of the problem and describes how the cataloging of an entire subgroup of circumlunar trajectories, satisfying typical injection and reentry conditions, has permitted a systematic and complete study to be made of the interplay of many parameters influencing Apollo missions. Flexibility of operational concept costs little because of the extreme sensitivity of the trajectories. This sensitivity also makes accurate midcourse navigation and steering vital.

SYMBOLS

i_{VTE}	inclination of transearth vehicle trajectory plane with respect to moon's orbital plane
i_{VTL}	inclination of translunar vehicle trajectory plane with respect to moon's orbital plane
Φ	angle defining moon lead angle at injection
Ψ	angle defining in-plane injection position
θ_0	angle defining in-plane return vacuum perigee position
h_0	injection altitude
γ_0	injection flight-path angle
R_M	distance from earth center to moon center
i_{EQTL}	inclination of translunar plane with respect to equator
i_{EQTE}	inclination of transearth plane with respect to equator

DEFINITION OF PROBLEM

When one undertakes to synthesize a trajectory for a manned lunar mission, the following factors play important roles in the trajectory selection process:

- (1) Launch-site location
- (2) Allowable launch azimuths
- (3) Injection altitude and flight-path angle
- (4) Day of the lunar month
- (5) Desired moon miss distance
- (6) Flight time
- (7) Return-base location
- (8) Desired direction of approach to return base

The purpose of this paper is to report a systematic study of the rather complicated interplay of all of these parameters. The data presented are based upon completely ballistic circumlunar trajectories because

(1) Such trajectories are the most difficult since they are the most sensitive to initial conditions.

(2) Early Apollo flights will be circumlunar.

(3) In later flights, the translunar portion of flights to lunar orbits or even to lunar landings probably should be flown as the outgoing legs of appropriate circumlunar trajectories in order to guarantee a "free return" in the event of a mission engine failure. This return is free only in the sense that large corrective velocities will not be required. The usual corrections of the midcourse type will be necessary.

All trajectories are based on injection at an altitude of 760,000 feet with a flight-path angle γ of 30° and on a return to earth with a vacuum perigee of 150,000 feet. These values were chosen as typical of what launch vehicles could give on ascent and of what would be required on return to hit a tolerable aerodynamic reentry corridor.

Figures 1 and 2 indicate the geometry and terminology of the problem.

DISCUSSION

The problem is restricted to the class of trajectories defined previously; and for given angles of inclination of the outgoing and return trajectory planes relative to the moon's orbital plane, the total time of flight from injection to perigee is uniquely related to the pericynthion altitude. Two such curves of total flight time as a function of pericynthion altitude are shown in figure 3. These curves represent the extreme cases of zero-inclination (or in-plane) trajectories - one for direct and the other for retrograde return. All other inclination combinations (for either direct or retrograde return) lie in between. This relationship between time of flight and pericynthion altitude for given outgoing and return inclinations is important, as will be seen in the following discussion of factors influencing the choice of these values.

It is possible to choose a trajectory which will include any pre-selected earth landing site in its return plane. Such a procedure obviates the need for any lateral maneuvering during atmospheric reentry to guide the spacecraft to this site. The right combination of moon lead angle, injection position, and velocity in any outgoing plane needs only to be found in order to achieve any desired inclination of the return plane relative to the moon's orbital plane. The exceptional cases of zero inclination to the moon's orbital plane are excluded. Once the space planes (giving the inclinations) out and back have been chosen, the discrete times at which the landing site will rotate into the return plane can be identified. Then, the corresponding curve of the family represented in figure 3 will give the pericynthion altitudes commensurate with each of these discrete times.

The direction of approach to the landing site is important from the standpoints of ground tracking and recovery operations. Although it is true that any return inclination relative to the moon plane can be achieved and that this allows all points on earth to be reached with no lateral maneuvering, in general it is not possible to approach all landing sites from any arbitrary direction. The geometry of this problem is shown in figure 4. The moon's orbital plane is inclined to the earth's equatorial plane at an angle which slowly varies between about 18.5° and 28.5° . Therefore, if the spacecraft should be at pericynthion when the moon is sufficiently far from either of its nodes, then the lowest return inclination relative to the equator that the vehicle can achieve is roughly equal to the moon's declination at pericynthion. If the landing-site latitude should be less (nearer the

equator) than the moon's pericynthion declination, then the landing-approach direction will be limited at this time of the month. The least favorable situation occurs when the moon plane is inclined at the maximum value of 28.5° to the equator, because the moon at maximum northerly and southerly declinations would permit minimum return inclinations of only 28.5° . If unrestricted operation on any day of the lunar month is desired, the landing site should be chosen above 28.5° north latitude or below 28.5° south latitude.

The moon's position and the moon's orbital inclination to the equator together with the approach direction specify the in-plane reentry longitudinal maneuver requirements. If, for example, a single site is chosen at Edwards Air Force Base, California and the return trajectory is restricted to an inclination of 35° from the southwest along the Pacific Missile Range, the required range from the reentry point to the landing site will vary from 3,300 to 10,000 nautical miles during the lunar month, the assumption being made that the moon's orbital inclination is 28.5° .

On the other hand, if the return base were on the equator and no return inclination restriction existed, then the reentry range requirement would vary from 0 to 2,000 nautical miles during the month. The 2,000-mile range would correspond to a polar return from the moon at maximum declination at pericynthion.

The unique specification of the translunar trajectory requires that the spacecraft arrive at the injection point with a prescribed velocity and precisely at the correct time. Therefore, for a launch of a specified launch vehicle from Cape Canaveral, it is not possible, in general, to find a launch time that would allow a direct powered ascent to injection to be flown. It is necessary, therefore, to launch into an appropriate parking orbit as the Cape rotates into the desired orbital plane. Then, from this parking orbit, another powered phase could accomplish the simultaneous matching of the prescribed velocity and position at the correct time.

Range safety, tracking facilities, and abort-recovery considerations for the launch site, when taken together, limit the allowable launch azimuth to a definite sector. Orbits within this sector will have different inclinations relative to the moon plane, depending upon the time of the month. Taking advantage of the inclinations available results in a very effective way of obtaining a large launch-time tolerance with payload penalties on the order of only 1 percent. This tolerance has been evaluated as a function of day of the lunar month for the case where injection into the translunar orbit is made from the ascending portion of the parking orbit. The launch-azimuth variation at Cape Canaveral is from 70° to 110° from true north. This

spread corresponds to a trajectory-inclination variation from 28.5° to 34.2° with respect to the equator. Figure 5 shows that this variation gives nearly a 5-hour tolerance throughout the month. It is clear that, if the launch-azimuth variation is not symmetrical about 90° , the launch-time tolerance becomes dependent upon the day of the month. If the injection point into the translunar orbit is made on the descending portion of the parking orbit, the total launch-time tolerance obtainable is exactly the same as that shown in figure 5, except that the launch-azimuth variations from 70° to 90° and 90° to 110° are reversed from those shown.

For a launch-azimuth variation of 90° to 110° , a reasonably large tolerance could be obtained by injecting into the translunar orbit on the ascending part of the parking orbit for moon positions between the descending node (maximum south) and the ascending node, and by injecting on the descending part of the parking orbit when the moon is between the ascending node (maximum north) and the descending node. The azimuth sector from 90° to 110° is superior to the sector from 70° to 90° from the standpoint of existing tracking facilities.

Since the technique illustrated employs a variable translunar orbit plane inclination, its use may mean a variable pericynthion altitude with delay time on the ground. The variation will depend upon the details of the situation but can be on the order of 50 nautical miles per hour delay time.

This variation in pericynthion altitude with hold time on the ground can be eliminated by fixing the translunar trajectory and by utilizing other techniques to obtain a launch-time tolerance. The most flexible of these schemes involves trajectories coplanar with the moon plane. Even with this restriction, the cost of launch-time tolerances comparable to those shown in figure 5 exceeds 10 percent of the spacecraft weight. In addition to this penalty, this technique suffers a loss of mission flexibility and of return-base positional freedom.

TYPICAL RESULTS

The points just discussed will be illustrated for the particular case of a 35° inclination to the equatorial plane at injection for all translunar trajectories and all days of the lunar month. The injection point was reached after coasting along a parking orbit which originates at Cape Canaveral. Since the inclination of the parking orbit is greater than the inclination of the moon's orbital plane to the equatorial plane (28.5°), there is a choice, any day of the lunar month, whether to inject onto the translunar trajectory from either the ascending or descending portion of the parking orbit. The transearth

~~SECRET~~

trajectory can approach the return vacuum perigee from any direction. Figures 6 and 7 show the return-trajectory vacuum perigee as approached from either the north or south in a direct direction so that the trajectory is inclined 35° to the equatorial plane. Figure 6 represents an injection into the translunar orbit from the descending portion of the parking orbit, and figure 7 represents an injection from the ascending portion. Data are presented at pericynthion altitudes of 300, 500, 1,000, and 1,500 nautical miles for moon pericynthion positions at the ascending or descending nodes. Moon positions at the maximum northerly and maximum southerly declinations are shown for the pericynthion altitude of 500 nautical miles, and the results shown are typical of the data from all altitudes.

The definite relationship between the pericynthion altitude and the transearth-trajectory vacuum perigee position can be seen in figures 6 and 7. A comparison of the 500-nautical-mile data in these figures shows an important distinction between northward and southward injections. If the transearth trajectory is to return from the southwest toward the northeast to a single return base, the northward injection trajectories required during the lunar month can be flown to approximately the same pericynthion altitude. If, for example, the return base is Edwards Air Force Base, California, the required pericynthion altitude is approximately 250 nautical miles (or alternatively 2,100 nautical miles). The actual pericynthion altitude as a function of the day of the lunar month is shown in figure 8. If a southward injection is used for the same example, the required pericynthion altitude will vary from approximately 600 nautical miles when the moon is at its most southerly declination to approximately 1,300 nautical miles for the most northerly declination when the spacecraft reaches pericynthion. The opposite characteristic would occur if, for example, the return base were in Australia and the transearth-trajectory vacuum perigee were approached from the northwest. In this case, the southward injection would require trajectories with a pericynthion altitude of approximately 100 nautical miles throughout the lunar month, whereas the northward injection trajectories would require pericynthion altitudes varying between approximately 300 and 1,000 nautical miles.

The illustrations given in figures 6 and 7 have fixed both the translunar orbit plane inclination at injection and the transearth orbit plane inclination at perigee at 35° to the equatorial plane. Therefore, the discrete vacuum perigee positions shown correspond to the single points from the time-of-flight curves of figure 3 at the given altitudes. If the outgoing inclination remains fixed at 35° (with injection toward the north) but the return inclination is allowed to vary, the loci of return perigee positions, corresponding to cuts at given altitudes across the flight-time curves, appear as the curves shown in figure 9. Data are presented for the moon positioned at the

REF ID: A537185

descending node for pericyynthion altitudes of 300 and 1,000 nautical miles and for the moon at its most southerly declination for a pericyynthion altitude of 1,000 nautical miles. As can be seen, there is a wide variation in the longitude of the transearth-trajectory vacuum perigee as the inclination of the return trajectory is changed from direct to retrograde from either the north or south. This variation in the longitude does not change appreciably with day of the lunar month but does increase appreciably with pericynthion altitude. It is simply a manifestation of the flight-time characteristics shown in figure 3.

The relationships illustrated have been between the transearth-trajectory vacuum perigee position and the pericynthion altitude, day of the lunar month, and inclination of the transearth trajectory at perigee to the equatorial plane. The last parameter to be considered is the inclination of the translunar orbit plane at the injection point. An example of its effect is shown in figure 9 for a pericynthion altitude of 300 nautical miles and a pericynthion moon position at its most northerly declination. The translunar-orbit-plane inclination is fixed at 30° and 40° and the transearth-orbit-plane inclination is varied. The variation of the loci of the transearth-trajectory vacuum perigee points with translunar-orbit-plane inclination is not as regular as the trends shown in the previous examples. The trend of eastward or westward shift in the return-trajectory vacuum perigee position depends upon the pericynthion altitude as well as the inclination of the transearth-trajectory plane. Since the effect of translunar-orbit-plane inclination is not as important as the other trends presented, it will not be covered in any more detail at this time.

If all the computations required to carry out the trajectory cataloging program necessary to this study were done by numerical integration, the amount of machine running time would have been prodigious. The computation actually involved a process of piecing together Keplerian (or two-body) orbits valid within appropriate volumes of influence surrounding each gravitating body (the earth and the moon). Since the explicit form of these solutions is known, there was no need for numerical integration, and use of these solutions effected a great saving of machine time. Of course, the approximation involved in the mathematical model raises a question concerning the accuracy of the results. Although it is true that the inexact trajectories deviated considerably from the exact ones far away from either of the large bodies, the focusing effect of these force centers made the trajectories coincide closely in the immediate vicinity of the earth and the moon. Since it was in these close-in regions that the problem constraints were imposed, the approximate injection conditions agreed accurately with the exact values, and the sensitivities were virtually the same. In fact, these results have been used to "ball-park" the

031712201130
106. [REDACTED]

initial conditions for any given case with sufficient accuracy that only a very few iterations were required to "home in" on the integrated trajectory.

[REDACTED]

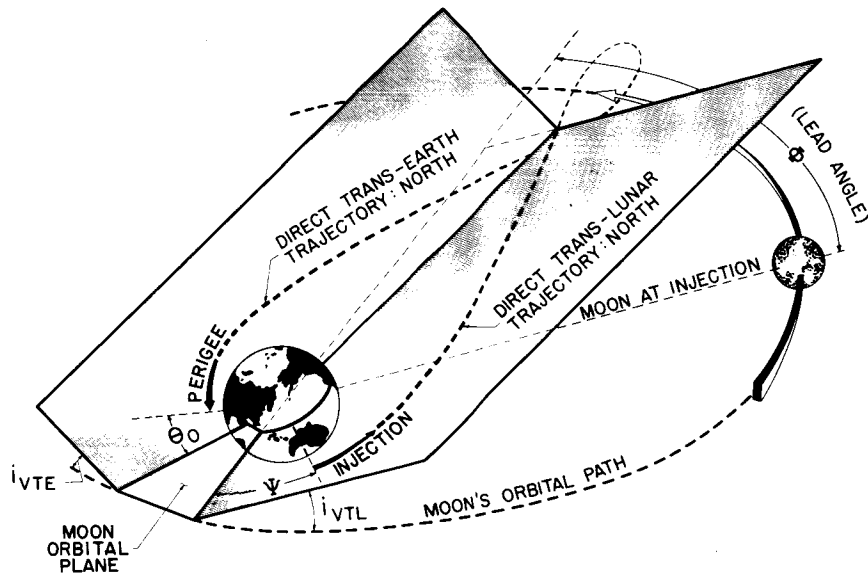


Figure 1

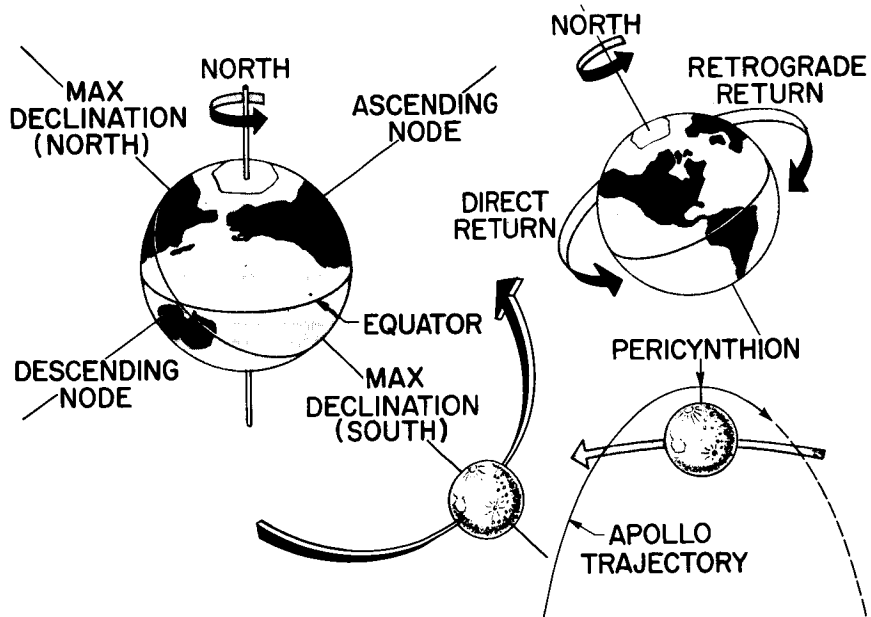


Figure 2

03171250

MAXIMUM AND MINIMUM FLIGHT TIMES VS PERICYNTHION ALTITUDE

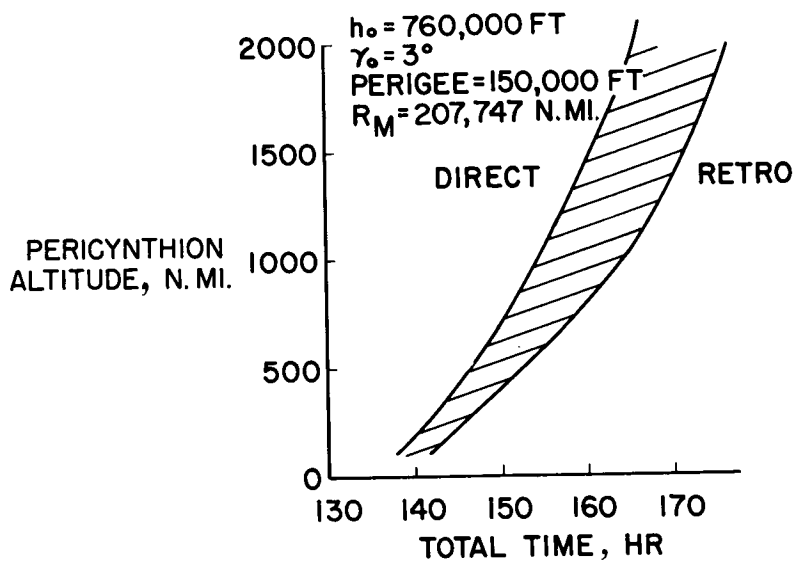


Figure 3

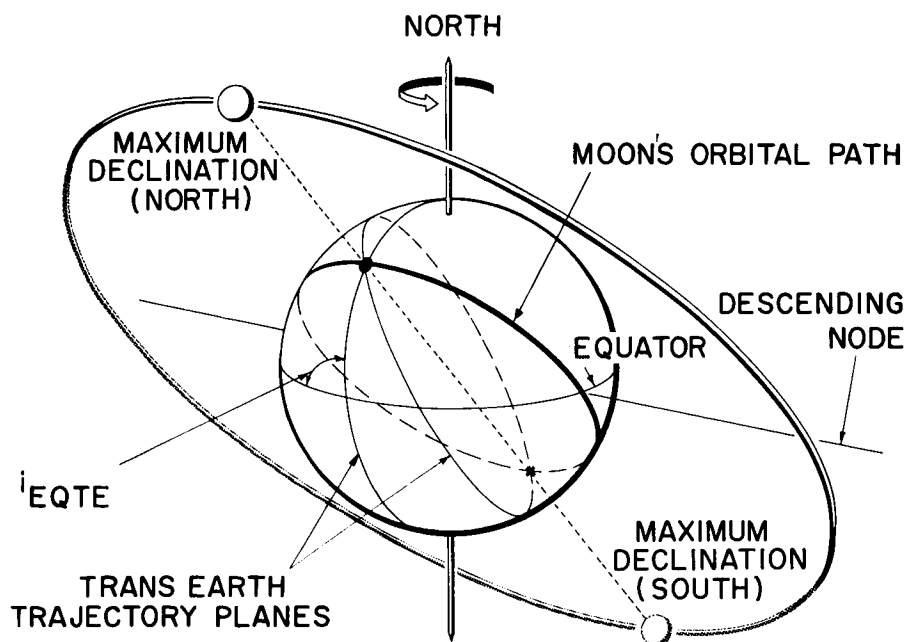


Figure 4

03171250

LAUNCH TIME TOLERANCE VS MOON POSITION AT PERICYNTHION

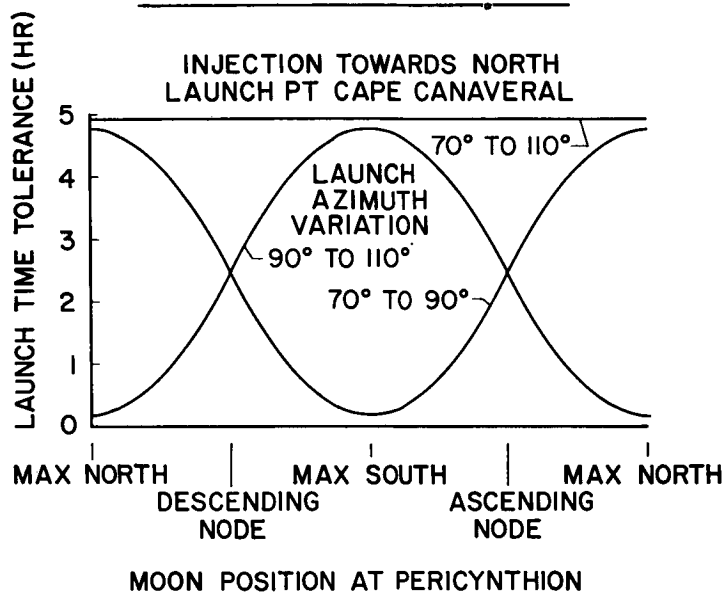


Figure 5

VACUUM PERIGEE LOCATION FOR SEVERAL PERICYNTHION ALTITUDES

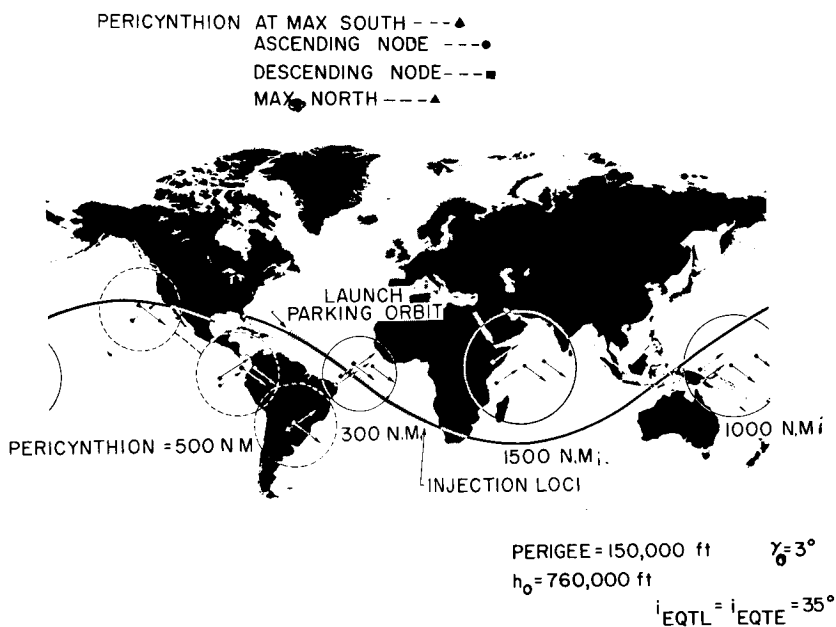


Figure 6

VACUUM PERIGEE LOCATION FOR SEVERAL PERICYNTHION ALTITUDES

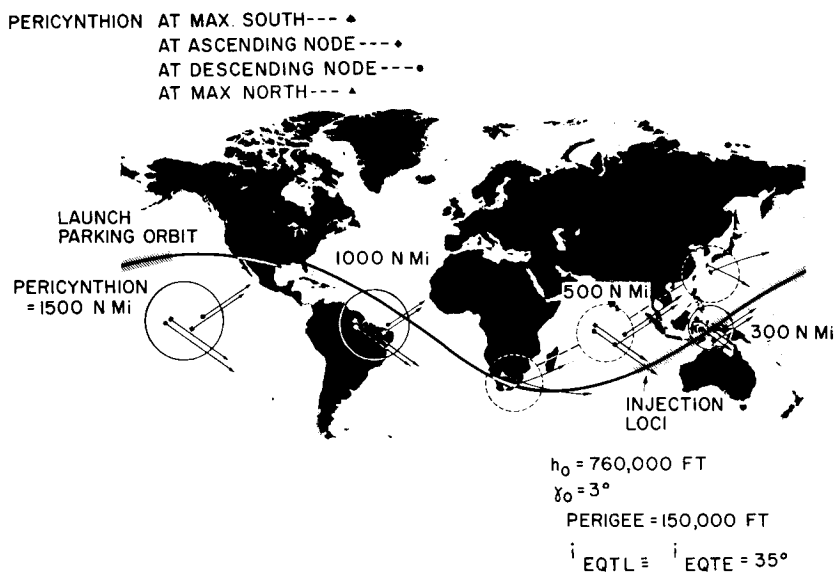


Figure 7

DAY OF LUNAR MONTH VS PERICYNTHION ALTITUDE FOR DIRECT RETURN TO EDWARDS AFB

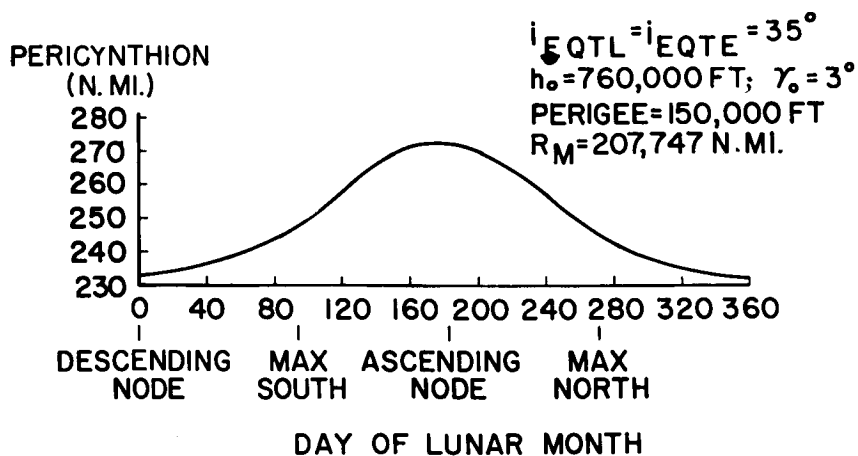


Figure 8

LOCII OF VACUUM PERIGEEES FOR TWO PERICYNTHIONS AND MOON POSITIONS

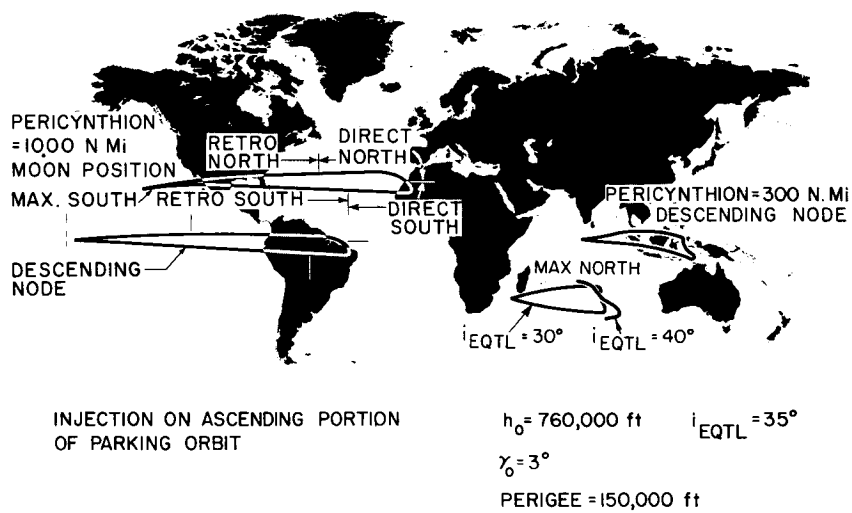


Figure 9

ABORT CONSIDERATIONS

By Robert V. Battey

General Dynamics/Astronautics

INTRODUCTION

One of the guidelines in the design of the Apollo vehicle is that the vehicle must be capable of returning the crew safely to earth after an abort at any time during the launch trajectory. There are three areas of concern for any abort maneuver: separating from the launch vehicle, reentering safely, and controlling the landing range. The propulsion systems proposed to fulfill the requirements of these areas of concern include:

- (1) An escape tower with two thrust levels and an attitude control system for separating the spacecraft from the launch vehicle in the atmosphere
- (2) A small solid propellant rocket, in addition to the launch vehicle retrorockets, for separating the Apollo vehicle from the launch vehicle above the atmosphere
- (3) Two 15,000-pound thrust engines with enough propellants for an ideal velocity of at least 4,000 feet per second for reentry and landing range control.

Figure 1 shows the launch-trajectory profile used for determining the abort requirements. This launch trajectory used a parking orbit at an altitude of 100 nautical miles. The use of a parking orbit not only permits the size of the launch window to be increased, but also allows the same trajectory profile to be flown for any hold time, thereby greatly simplifying the task of predicting reentry conditions and selecting landing areas.

The study was divided in accordance with several phases of the launch trajectory: aborts in the atmosphere, vacuum aborts before the parking orbit, immediate return aborts at supercircular orbital velocities, and nonimmediate return aborts for the remainder of the launch trajectory. The important aspects of an abort in each of these areas are discussed in detail.

~~CONFIDENTIAL~~




ATMOSPHERIC ABORTS

The atmospheric portion of the trajectory is shown as figure 2. The most difficult task for aborts which might occur in the atmosphere will be getting away from the launch vehicle. Since the launch vehicle has relatively less drag than the escape vehicle, merely separating from the launch vehicle will not be sufficient. The escape vehicle must be able either to outrun the launch vehicle or to get off to one side and let the launch vehicle go by. The escape tower proposed in this study would provide enough impulse to keep it ahead of a tumbling launch vehicle, as well as an attitude control system which would enable the escape vehicle to get out of the way of the launch vehicle. Other important functions of an attitude control system would be to prevent the escape vehicle from tumbling and to eliminate high normal accelerations during the abort maneuver.

Figure 3 shows the axial acceleration as a function of time of application which would result for an off-the-pad abort, for an abort at maximum drag, and for an abort in the upper fringe of the atmosphere. The first thrust level was 100,000 pounds for 2 seconds and the second thrust level was 50,000 pounds for the next 3 seconds with an escape vehicle for which separation weight was 7,100 pounds, including a 2,700-pound escape rocket.

The thrust levels are bounded by conflicting requirements. The first thrust level must be high enough for rapid separation from the launch vehicle for an abort at maximum drag while the accelerations are kept as low as practical for off-the-pad and high-altitude aborts. The second thrust level should be set high enough to sustain separation relative to the launch vehicle and to prevent the deceleration due to drag from becoming excessive when the escape rocket burns out. If only one thrust level were used, the deceleration at burnout could be more than 12g. The reduced thrust of a second thrust level would reduce the velocity required for a given separation distance and consequently would greatly reduce the deceleration after escape rocket burnout. There are several other advantages to using a reduced second thrust level; namely, the duration of high acceleration loads is reduced, the separation distance is greatly increased for a given total impulse, and more time is available for maneuvering to avoid being hit by the launch vehicle.

Figure 4 shows the separation distance produced by this configuration for an abort at maximum drag. The altitude is plotted as a function of range for the envelope of possible launch-vehicle travel and the path of the escape vehicle. The envelope of possible launch-vehicle trajectories was obtained by simulating the trajectories of a launch



vehicle perpendicular to the velocity vector and then alined with the velocity vector. For the first approximation, it was assumed that the launch vehicle would be somewhere along the constant time line connecting these two trajectories.

The escape vehicle was pitched down at a rate of 6° per second for the first 2 seconds after abort to avoid the path of the launch vehicle, and then was allowed to return to zero angle of attack during the next 3 seconds. This pitching maneuver would keep the escape vehicle ahead of a tumbling launch vehicle. For example, 40 seconds after abort the escape vehicle would be at the point indicated in figure 4 and the launch vehicle would be somewhere along the 40-second line, approximately 2,000 feet behind the spacecraft.

VACUUM ABORTS BEFORE THE PARKING ORBIT

Figure 5 shows the portion of the flight between the atmosphere and the parking orbit. This part is the easiest for a successful abort because no propulsion is required to produce a satisfactory reentry. There is a possibility that an abort during this phase would result in excessive accelerations during reentry; however, the accelerations can be limited to $10g$ by using the lifting capability of the reentry vehicle, shaping the launch trajectory, or using the onboard propulsion system.

The onboard propulsion system can also be used to reduce the number of landing areas necessary during this portion of the launch trajectory. With an impulse of 4,000 feet per second available, there are two unique landing areas which could support an abort at any time up to the parking orbit. One would be 1,100 nautical miles and the other would be 2,700 nautical miles from Cape Canaveral. Figure 6 shows how these landing sites could be reached from an abort at any time during this portion of the launch trajectory. The center line assumes no impulse was used. The top line shows the landing range if the entire impulse of 4,000 feet per second were used to accelerate the vehicle. The bottom line shows the landing range if all of the onboard propellants were expended as retrothrust to slow the vehicle down. An abort just after the escape tower has been jettisoned would require a small posigrade impulse to achieve the landing area 1,100 nautical miles from the Cape. Aborts at later times would require less and less posigrade impulse to reach this landing area until an abort at 280 seconds, at which time no impulse would be required. After this time, increasing amounts of retrograde impulse would be required to land at the landing area 1,100 nautical miles from the Cape until approximately 350 seconds from launch. Beyond this time there would not be enough retrograde impulse available to produce a landing at that site. From then on, a posigrade impulse would be required to reach the landing site 2,700 nautical miles from the Cape and so on.

03171204

IMMEDIATE RETURN ABORTS

Figure 7 indicates the immediate return portion of the launch trajectory. For an abort during or after the parking orbit, an impulse must be applied at some angle to the velocity vector to depress the perigee altitude into the atmosphere to prevent the vehicle from skipping back out. Figure 8 illustrates how much impulse would be required to produce a satisfactory reentry. The reentry flight-path angle is plotted as a function of the reentry velocity which would result for a given impulse from an abort after the parking orbit. If the flight-path angle at 400,000 feet is below the 10g line, the reentry acceleration would be excessive. If, on the other hand, the flight-path angle is above the overshoot boundary, the vehicle would skip out of the atmosphere.

The solid lines in this figure form a family of reentry conditions which would result from an abort just at engine restart to leave the parking orbit if increasing amounts of retrograde impulse were applied at several angles of retrofire; namely, 0° , 20° , 40° , and 60° . For example, 4,000 pounds of retropropellants expended at an angle of 40° down from the local horizontal would result in a reentry angle of about -8.5° and a reentry velocity of a little over 23,000 feet per second. These conditions would result in an acceleration of more than 10g during reentry if the maximum L/D of the reentry vehicle was 0.5.

The dashed line is the locus of the steepest reentry angle which could be produced with a retrograde impulse of 4,000 feet per second. For the configuration studied, 1 pound of propellants would produce a change of velocity of approximately 1 foot per second so these two parameters are practically synonymous. Notice that 4,000 pounds of propellants could not be expended at the most efficient angle without producing accelerations of more than 10g during reentry until about 50 seconds after leaving the parking orbit.

At about 120 seconds after leaving the parking orbit, the centrifugal force is enough greater than the gravitational attraction that all 4,000 pounds could be expended at the optimum retroangle and the vehicle would still skip back out of the atmosphere. From this time on, the configurations studied followed a nonimmediate return-type abort trajectory. That is, the escape vehicle would coast out to an apogee before reentering.

The landing area control capability for aborts during the immediate return portion of the launch trajectory varies greatly from the practically infinite range control while in the parking orbit to the range control capability of the reentry vehicle alone for aborts at the point where

all available onboard propellants are required to prevent skip out. The latter defines the landing area location.


Figure 9 shows the proposed abort landing areas as well as other significant aspects of the launch trajectories used for this study. The flight paths shown represent the four launch azimuths that the launch vehicle would use for a 4-hour launch "window." These azimuths assume a 15-minute launch attempt followed by a 1-hour hold for refilling the lox tank, another 15-minute launch attempt, and so on. The landing areas for aborts prior to the parking orbit are as shown in this figure. The landing area for the last point in the launch trajectory from which an immediate return could be accomplished would result in a landing in Africa for the two northerly launch azimuths, unless the maximum aerodynamic range capability of a reentry vehicle is used. The recommended landing area for nonimmediate return aborts is just south of Hawaii. The impulse required to achieve a satisfactory reentry for a landing in this area is shown in figure 10.

NONIMMEDIATE RETURN ABORTS

Nonimmediate return aborts are illustrated in figure 11. Impulse is shown as a function of the velocity at the time of abort in figure 10. For example, at a velocity of 32,000 feet per second, the vehicle is not going fast enough to reach Hawaii. Therefore, a positive ΔV of 2,800 feet per second would have to be applied to power the spacecraft into the ellipse which would provide a 6° reentry angle near the Hawaiian landing area. An abort at higher velocities would require less and less forward impulse until an abort near 34,000 feet per second would require just enough impulse to correct the reentry conditions. Aborts at higher velocities would require increasing amounts of retrograde impulse until injection into the lunar orbit, where a velocity of 2,700 feet per second would be required.

The time to return to earth for this nonimmediate return abort ellipse is dependent on the launch azimuth. A launch azimuth of 77° would require about 9.8 hours, whereas an azimuth of 108° would require only 6.7 hours.

After injection into the lunar transfer ellipse, the impulse required to reach the Hawaiian landing area would be less than it was at the point of injection. However, the time required to return to the landing site begins to get quite large. For example, an abort at 50,000 miles altitude (6.72 hours after injection) would require about 50 hours to return to Hawaii as compared with a minimum return time of approximately 35 hours.



03:13:28.55

This large time penalty suggests that the abort guidance system be given several landing areas for nonimmediate return aborts such that the guidance system would select the best landing area and the corresponding impulse needed to get to that area.

One area of concern for nonimmediate return abort trajectories is the radiation dose that the crew would receive from passage through the Van Allen belts. The maximum dose rates which could result with the vehicle studied were integrated and found to be under the maximum allowable dose limit.

CONCLUDING REMARK

The preceding discussion points up the need for an abort guidance system in the Apollo spacecraft to determine the landing site to be used for any abort and the impulse required for a safe reentry to land at that site. However, the need for an emergency return might preclude landing in one of the predetermined areas. In such an event, the crew should have the option of overriding the guidance system and manually controlling the return trajectory.



[REDACTED]

CLASSIFIED 119

LAUNCH PROFILE

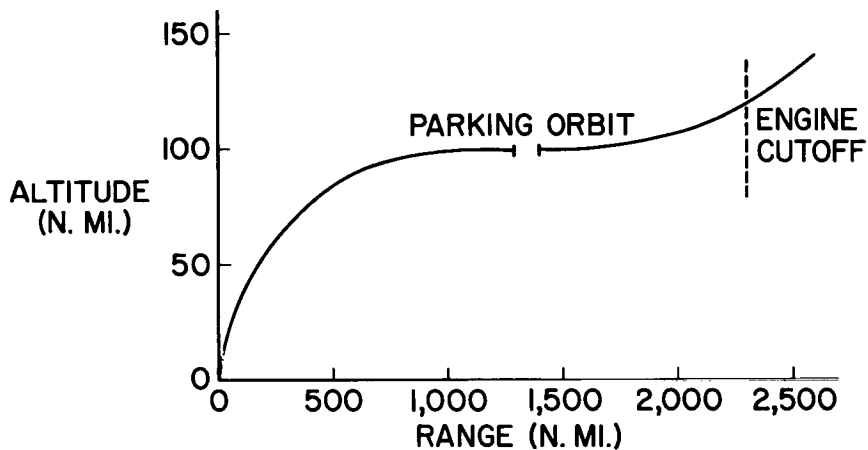


Figure 1

ATMOSPHERIC ABORTS

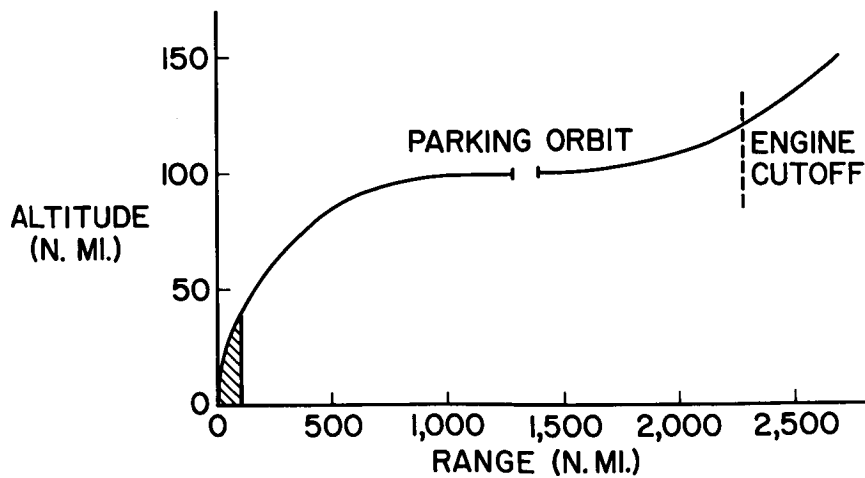


Figure 2

[REDACTED]

AXIAL ACCELERATION PROFILE

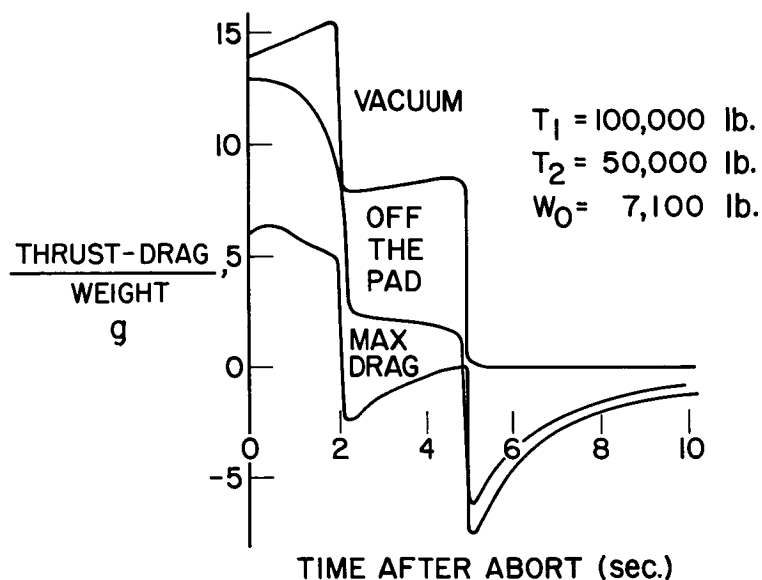


Figure 3

SEPARATION DISTANCE

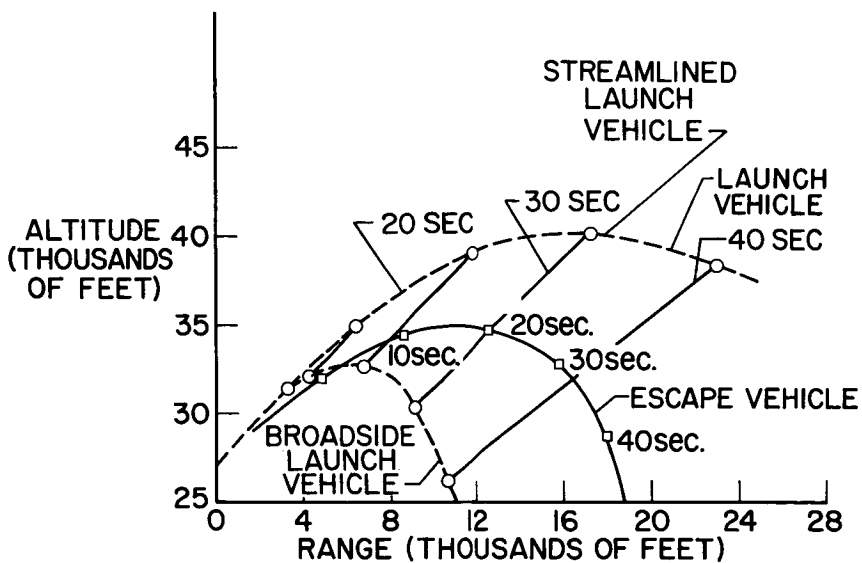


Figure 4

SUB ORBITAL VACUUM ABORTS

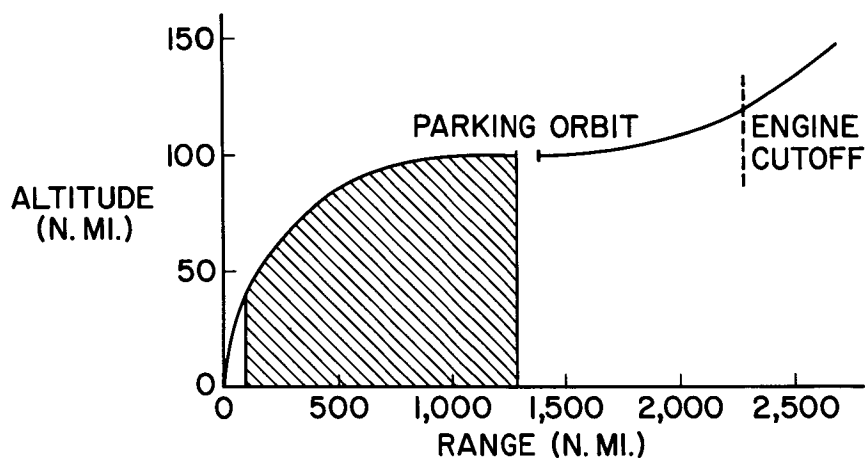


Figure 5

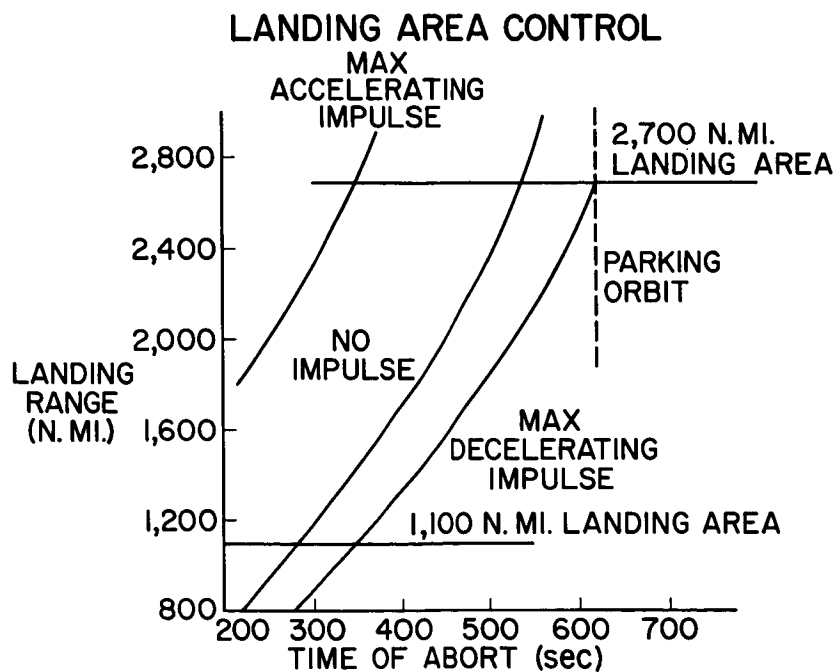


Figure 6

0371220555

SUPER ORBITAL IMMEDIATE RETURN

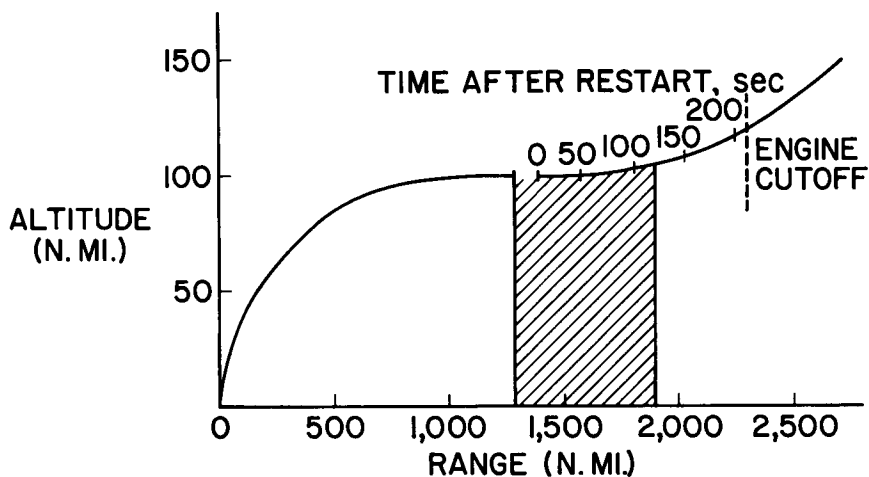


Figure 7

RE-ENTRY CONTROL

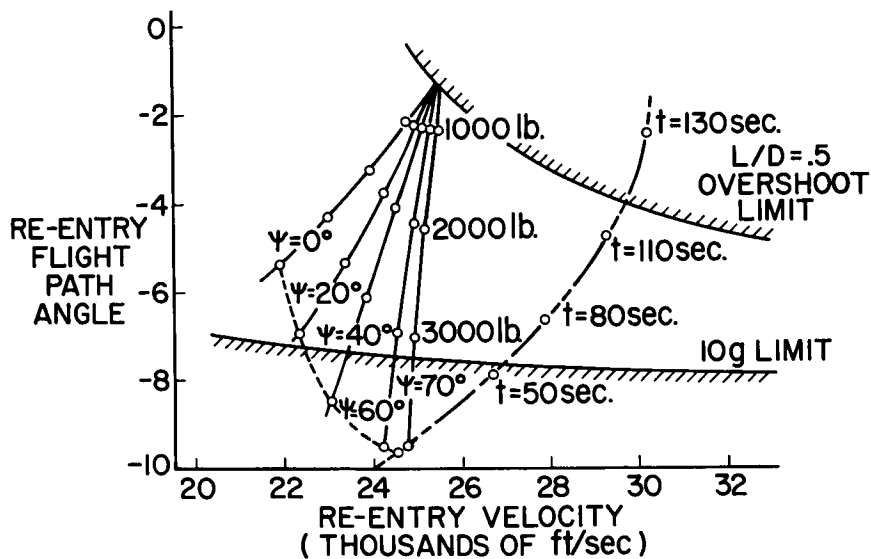


Figure 8

ABORT LANDING AREAS

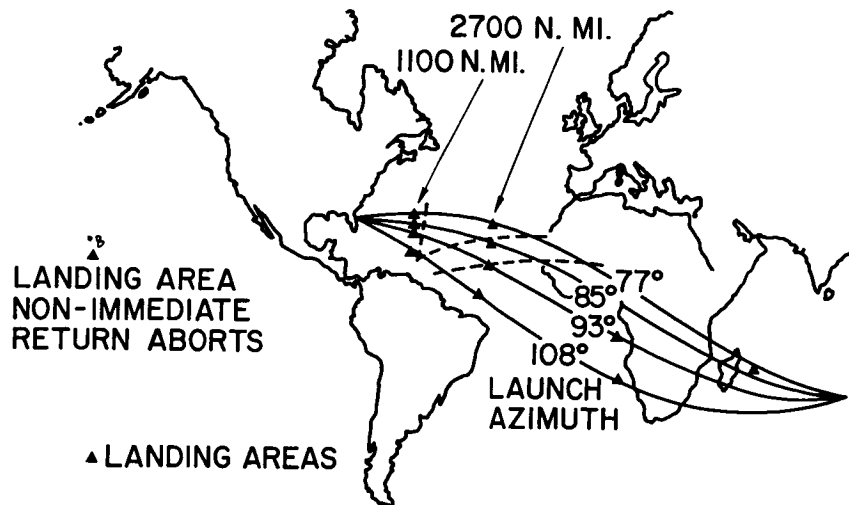


Figure 9

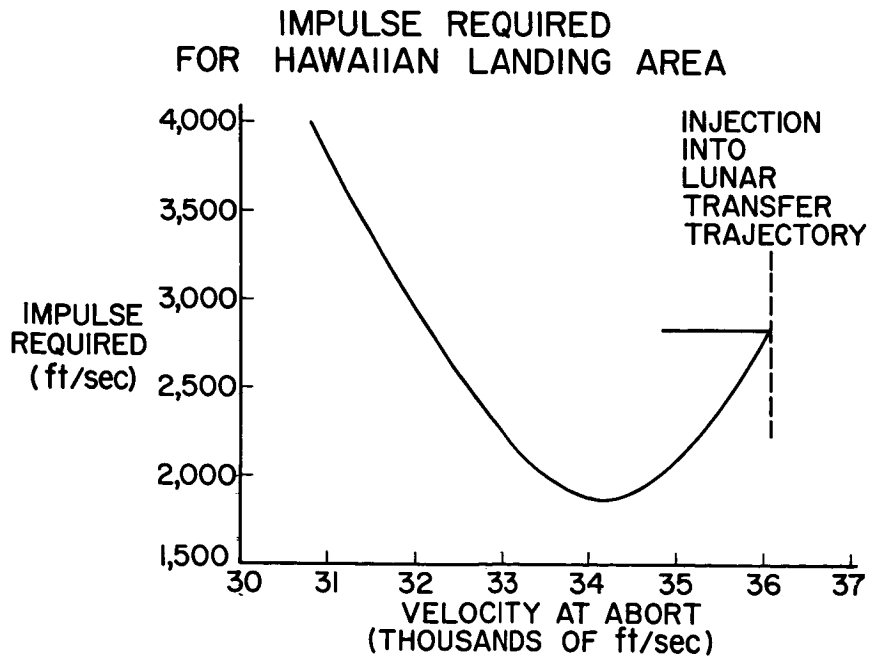


Figure 10

SUPER ORBITAL NON-IMMEDIATE RETURN

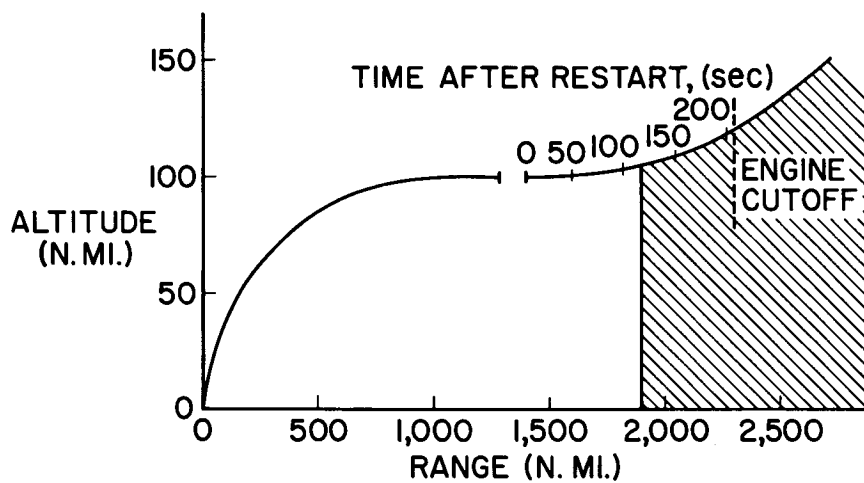


Figure 11

DECLASSIFIED

**III.
NAVIGATION,
GUIDANCE,
AND CONTROL**

A GUIDANCE AND CONTROL CONCEPT FOR LUNAR MISSIONS

By A. F. Bowen

General Dynamics/Astronautics

One of the Apollo design requirements is for onboard command of the vehicle, which implies the ability to perform the mission without the use of intelligence transmitted to the vehicle. This requirement does not preclude the use of information from earth-based tracking and computation, when available, but it does regulate the manner in which it is used.

In order to provide onboard command capabilities, the major guidance functions listed as follows must be performed by the spacecraft system:

Injection guidance or monitoring

Abort guidance

Navigation measurements

Trajectory determination


Calculation of required corrections

Inertial guidance during velocity corrections

Inertial guidance during reentry

The launch guidance can be performed by an inertial guidance system located either in the launch vehicle or in the spacecraft. In considering the possibility of abort due to a guidance failure, it proves advantageous to perform the guidance function in the launch vehicle and to monitor the trajectory with the spacecraft system. If an abort due to launch vehicle guidance is necessary, the spacecraft system is intact for abort guidance.

For abort during the launch phase, several recovery areas are required, and the guidance system must select one on the basis of position at the time of abort. Aborts inside the atmosphere, using the abort tower, can be performed without closed-loop guidance. Aborts occurring after the abort tower has been jettisoned require guidance for adjusting the trajectory to hit a suitable reentry corridor and also during reentry.



0371220 [REDACTED]

In order to obtain information for establishing the trajectory of the spacecraft, navigation measurements with respect to the earth and moon are required. The following measurement methods are applicable:

1. An automatic center tracker can be used to determine the direction to the center of the disk by scanning the limb and thereby establish a line of position for the vehicle. For making measurements of this type against the moon, the use of reflected solar radiation is most advantageous. Because of the low temperature of the dark side, the self-radiation of the moon is not adequate for highly accurate tracking of the lunar disk. The earth, however, can readily be tracked by means of its natural radiation. Because of the blanketing effect of the earth's atmosphere, the diurnal variation in the radiation temperature of the earth is small.

2. An automatic edge tracker can be used to measure the direction to points on the limb. If the location of the point on the limb is unknown, such a measurement defines a cylindrical surface on which the vehicle is located at the time of the observation. It should be noted that a measurement of this type conveys less information than one obtained with the center tracker.

3. Optical instruments can be used to measure the direction to points on the surface or limb. Each measurement on a known point establishes a line of position, while each measurement on an unknown point on the limb defines a cylindrical surface, as with the automatic edge tracker.

4. Optical instruments of the sextant type can be used to measure the subtended angle between the limb and selected stars. Each such measurement defines a conical surface on which the spacecraft is located at the time of the observation.

5. Navigation data can also be obtained by observing the times at which known stars are occulted by the earth or moon. Each occultation defines a cylindrical surface on which the vehicle is located. The occultation of a star by the moon may be observed by noting the time of disappearance of the star behind the moon. Because of refraction in the earth's atmosphere, a different method must be used to obtain useful information from the occultation of a star by the earth. One suitable method is to detect the shift in apparent direction to the star as the line of sight dips into the atmosphere.

6. Stadimetric ranging on the earth or moon disk provides useful range data at ranges out to several times the radius of the observed body. The measurement can be made with the automatic center tracker or with a sextant.

[REDACTED]

7. A radar altimeter provides more accurate altitude data than can be obtained by stadimetric ranging. Ranges out to a few thousand miles can be obtained with practical equipment.

In order to make use of the navigation measurements, trajectory determination calculations must be performed. Each measurement, or set of measurements, need not determine the position of the spacecraft. Rather, a series of partial fixes taken over a period of time can be used to determine the trajectory of the spacecraft. Statistical methods are necessary to reduce the significance of random errors in the measurements. At General Dynamics/Astronautics a recursive method is being developed for performing a least-squares fit to all available trajectory data. A slightly different technique is discussed in some detail in a subsequent paper by Stanley F. Schmidt, John D. McLean, and Gerald L. Smith.

For the calculation of required velocity corrections, two methods apply. In the first method, a stored reference trajectory is employed, and the velocity corrections keep the spacecraft near the reference trajectory. The required corrections are calculated from linear perturbation equations. In the second method, a general four-body trajectory simulation is carried onboard for calculation of trajectories. By iterating with the four-body simulation, a trajectory which meets the desired end-point conditions can be found and the required velocity correction can be established. In comparing the two methods in detail, the orbit-determination problem should also be considered if the same method of generating trajectory data is used for these computations. The four-body simulation provides far more flexibility with regard to dispersions on launch time and injection conditions, abort trajectories, lunar departure time, times for making observations and corrections, and so forth. If the reference trajectory method is employed, several trajectories must be stored to allow for such factors. If the advantage of the reference trajectory method in reducing computations is to be fully utilized, then a large quantity of information for each reference trajectory must be stored.

During thrust application for velocity correction, the thrust acceleration must be measured by an inertial system. For midcourse corrections, a very simple guidance system could be used because the magnitude of each correction is small and low acceleration is used. For maneuvers with the spacecraft main engines, such as entering a lunar orbit, closed-loop inertial guidance is desirable.

For reentry, the NASA requirements are for landing in a 10-mile-square prepared area. In view of the limitations imposed by radio blackout and vehicle maneuvering capabilities, inertial guidance seems to provide the only practical means for achieving this objective. If the initial conditions provided by the midcourse guidance system at the

start of reentry are sufficiently precise, the landing in a 10-mile-square area can be achieved with presently available inertial instruments.

Figure 1 shows the block diagram of a system to perform the guidance and control functions for a lunar orbit mission. The gyrostabilized instrument platform serves as a mounting base for three linear accelerometers and two trackers. One tracker is a combination star and planet tracker operating in the visible spectrum, and the other is an infrared horizon scanner. Both trackers are automatic in that they track the center of the planet body and are separately gimballed relative to the platform. Precision angle pickoffs are used to read out tracker angles relative to the platform. The visible spectrum tracker is used for periodic alinement of the platform by star tracking and for navigation sightings on the earth and the moon. The infrared tracker is used for obtaining a position fix just prior to reentry into the earth's atmosphere, and can also be used near the moon against the fully illuminated lunar disk. The accuracies of the instruments on the platform are given in the following table:

Planet tracker, min	1/3 to 1
Infrared horizon scanner, min	6
Platform alinement (star tracker), min	1/6
Gyro drift rates:	
Fixed drift uncertainty, deg/hr	0.05
Mass unbalance uncertainty, deg/hr/g	0.1
Anisoelastic coefficient, deg/hr/g ²	0.02
Accelerometer errors:	
Bias uncertainty, g	0.0001
Scale factor uncertainty, g/g	0.0001

The estimated 1σ accuracy in measurement of each of the angles defining the direction to the center of the earth or moon with the visible spectrum tracker is 1/3 to 1 minute, depending on the range. The subtended angle can be measured to the same accuracy. Near the earth and moon, the accuracy is degraded by terrain and cloud errors, oblateness, and so forth. The infrared tracker is used very near the earth and is assumed to have an accuracy of 6 minutes. The accuracy of alinement of the platform with respect to the stars is 10 seconds, 1σ. The accuracies given for the inertial components are typical of today's state of the art and are adequate for the lunar mission. The reentry phase of the flight establishes the required accuracy of the inertial components.

The radar altimeter provides altitude measurements to an accuracy of 0.1 percent at altitudes of 2,000 nautical miles or less from the earth and the moon. The power required to obtain this range capability is modest, amounting to about 200 watts.

A hand-held sextant provides a backup method for making navigation measurements on the earth and moon. This instrument is similar to a marine sextant and can be used to measure angles between the limb of the earth or moon and selected stars and to measure the subtended angles of the earth and moon. The accuracy obtainable is comparable to that of the automatic tracker, 1/3 to 1 minute.

Computations are performed on a central digital computer. A combination general purpose and digital differential analyzer computer is used. Typical operating times are as follows:

Add or subtract, μ sec	10
Multiply, μ sec	80
Divide, μ sec	296

The estimated computer memory requirement is 10,000 words of permanent storage for programs and constants and 1,450 words of temporary storage. These figures include the four-body simulation and provision for pre-launch checkout, star catalog, servicing the instrument platform, attitude control, sequencing, displays, and so forth. The word length is 24 bits. Special attention to the reliability of the computer is necessary. In addition to highly reliable components and design, some form of redundancy in the computer is required.

The autopilot controls vehicle attitude and angular rates in accordance with commands from the computer or the crew control panel. Gimballed main engines and on-off rockets provide the control torques during space flight. On-off rockets are also used for control of the abort tower-vehicle combination during in-atmosphere aborts. Aerodynamic control flaps are used during reentry. Analog control loops are used, with rate gyros providing the damping. A simple sun tracker provides attitude feedback for orienting the vehicle with respect to the sun for illuminating solar-cell panels and controlling temperature.

A strapped-down inertial system provides a capability for return to earth in the event of failure of the inertial platform. This unit contains three precision pulse-rebalanced rate-integrating gyros and three pendulum accelerometers, and functions as a simple strapped-down guidance system.

Integration of the crew into the guidance and control subsystem is provided at several levels. Primary emphasis is given to the decision-making functions of the crew and provisions are made for detailed

operations to be performed at the option of the crew. For assistance in making decisions, adequate displays are provided. The periscope is useful in manually controlling the vehicle and may be used for referencing the strapped-down inertial system and for diverse other purposes.

For the lunar landing mission, a multiple-beam Doppler radar for measuring velocity relative to the lunar surface may be required, and a radar beacon on the moon will be desirable.

The following table gives the weight and power requirements for the system:

	Weight, lb	Power, watts
Instrument platform	70	100
Platform electronics	18	170
Computer	80	200
Autopilot electronics	40	50
Radar altimeter	30	200
Backup inertial reference	20	50
Sextant	5	0
Sun tracker	2	12
	<hr/> 265	<hr/> 782

Average power drain: 532 watts


Total weight is 265 pounds and total power is 782 watts peak and 532 watts average. These figures do not include the on-off rockets, actuators, guidance and control displays, and communications.

The accuracy of this system in performing a lunar orbit mission has been analyzed through use of a digital simulation. Figure 2 shows the accuracy at several points along the trajectory. The numbers given in the figure are the standard deviations. The transfer time for this trajectory is $3\frac{1}{2}$ days each way, and the outbound trajectory approaches within 67 nautical miles of the moon. The accuracy at injection into the outbound trajectory is based on the capability of the Centaur guidance system. At a point 145,000 nautical miles from earth, the standard deviation in each component of the required velocity correction is less than $4\frac{1}{2}$ ft/sec. At a point 17,000 nautical miles from the moon, the standard deviation in each component is less than 3 ft/sec. At the approach pericynthion point where injection into the lunar orbit occurs, the components of position and velocity are known to better than 1 nautical mile and 2 ft/sec. At the start of reentry into the earth's atmosphere, position is known to an accuracy of 6 nautical miles horizontally and 0.1 nautical mile in altitude. Velocity is known to



7 ft/sec in magnitude and 0.02° in direction. The flight-path angle with respect to the local vertical is within an acceptable corridor about 2° wide and is controlled to about 0.1° . In order to assure landing within the 10-mile-square prepared area, radio assistance is required after the radio blackout portion of reentry is over. A TACAN system to provide position up-dating for the inertial system, starting 150 nautical miles from the landing area, is discussed in a paper by Ray E. Thompson.

In summary, this guidance and control concept provides a capability for performing lunar missions through the use of onboard equipment. Data from ground-based equipment may be used during the mid-course phase at the option of the crew. The use of a TACAN system to improve the guidance accuracy at the earth landing site has numerous precedents in aircraft systems, and does not detract from the onboard command feature of the system.



GUIDANCE & CONTROL SYSTEM

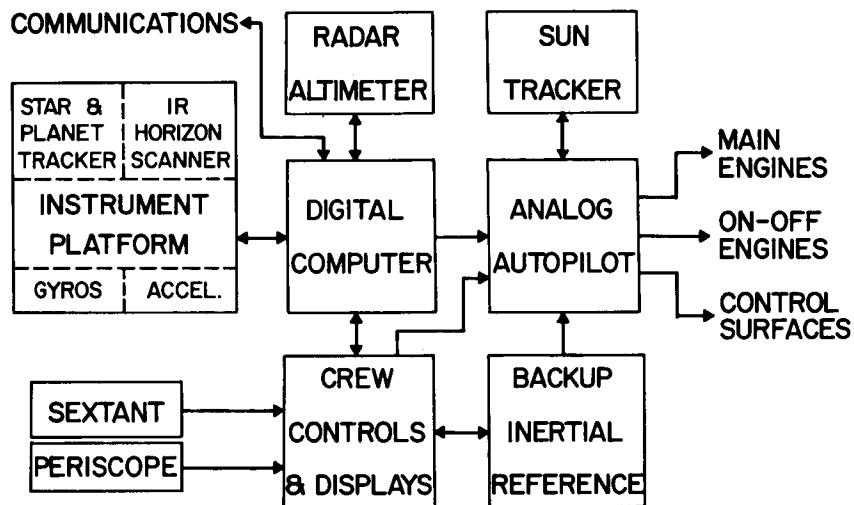


Figure 1

SYSTEM NAVIGATION ACCURACY

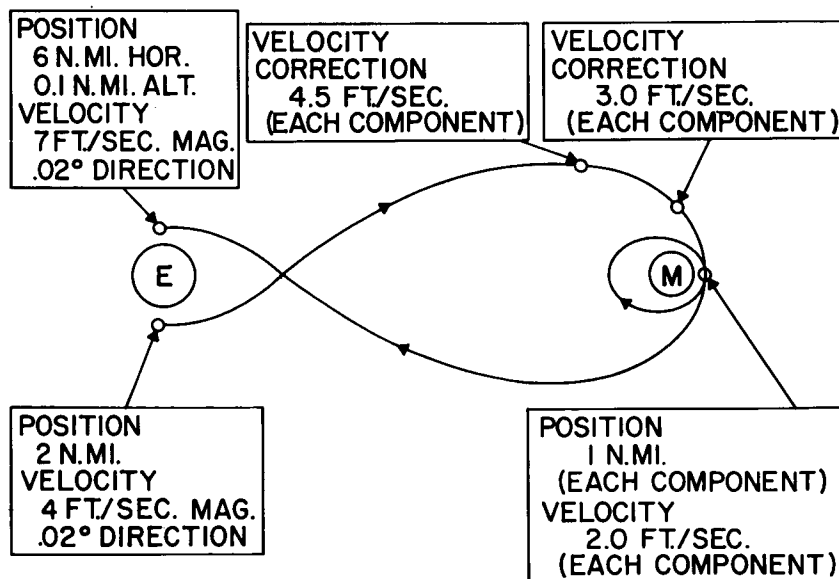


Figure 2

A STUDY OF A SYSTEM FOR MIDCOURSE NAVIGATION

By Stanley F. Schmidt, John D. McLean,
and Gerald L. Smith

Ames Research Center

INTRODUCTION

A study of midcourse guidance for Apollo missions has been underway for about a year at the Ames Research Center. This study has culminated in a digital simulation of a system and the results to date have been encouraging. It is the purpose of this paper to describe in the following order: the midcourse navigation system requirements considered desirable, a description of the system studied, and the results obtained from the simulation. A discussion of the mathematics involved have been omitted since, although of extreme importance, they are too complex to be described herein.

It is pertinent first to discuss briefly the various guidance phases of the mission studied. Figure 1 illustrates an artist's sketch of the familiar figure eight circumlunar trajectory. Phase I includes boost from the launch pad to final injection into the lunar trajectory. During Phase II or the midcourse phase of the trajectory, beginning at injection, the vehicle is essentially in free fall except for short periods of accelerated flight when velocity corrections are made. These corrections are required because of the extreme sensitivity of such trajectories to small injection errors; for example, a 1-foot-per-second velocity error at injection can result in several thousand miles miss at perigee. The midcourse phase is considered completed upon entry into the earth's atmosphere, and terminal guidance (Phase III) proceeds from this point to landing.


Before proceeding further it is appropriate to identify the specific operations or functions demanded of a midcourse navigation system. First, it is necessary to determine the best estimate of the position and velocity (that is, the state) of the spacecraft by means of a smoothing scheme applied to data obtained from imperfect sensors (optical instruments are assumed in this case). This is referred to as trajectory determination. Then knowing the present state, end-point conditions must be predicted; that is, for example, what will be the estimated perilune or perigee as the case may be if no corrective action is taken. As will be elaborated upon later, a reference trajectory passing through the desired perilune and perigee is a necessary feature of the system studied. Next, a guidance law must be formulated and used to calculate the magnitude and direction of the corrective action

necessary to change the estimated end-point conditions to correspond to those of the reference trajectory. Finally, the indicated control action is implemented by applying corrective velocity in the appropriate direction by means of a small rocket motor.

MIDCOURSE NAVIGATION SYSTEM REQUIREMENTS AND DESCRIPTION

The requirements for the midcourse navigation system in addition to its basic function of guiding to a predetermined perilune and perigee may be divided into three basic requirements. First, the system should allow the pilot to have command of the mission. This imposes a requirement for onboard tracking, display and control, and computation. Second, ground tracking information and computation should be usable but not necessarily required. By this requirement it is meant that the system should be able to accept and properly include all sources of information useful for the onboard trajectory determination and guidance calculations. The third requirement concerns abort as it relates to the midcourse phase, particularly the portion of the flight out to the moon. This requirement would appear to be broadly divisible into two parts by the time required to return to earth which, of course, is related to the seriousness of the emergency. The first part of the abort requirement, referred to as the shortest time of return, is predicated on the need to return safely to earth only and guides to the closest reentry corridor (such an emergency might arise due to the emergence of a solar flare). The second part allows some relaxation in the time allowed to return to earth and requires the abort mode to guide towards one of several alternative landing locations.

A description of the concept of the system is illustrated by the block diagram in figure 2. The primary sources of data necessary for the determination of the position and velocity of the spacecraft are indicated as optical tracking and the onboard inertial platform and associated accelerometers. The platform and accelerometers would have multiple functions other than monitoring the midcourse corrections. For example, in conjunction with the use of the computer to make some elementary calculations, it would provide the pilot with an estimate of injection conditions for use as initial conditions for the midcourse navigation system. The optical tracking measurements would be made manually by the pilot and also evaluated before insertion into the computer by means of a keyboard. As indicated in figure 2, these data would be transmitted to the ground computation center through telemetering or if necessary by the voice communication link. Periodically ground-based data, which include both onboard and earth tracking information, would be transmitted back to the pilot for evaluation and comparison with his onboard calculations. The pilot also is considered to have discretionary control over energizing the attitude and velocity



control subsystems. These subsystems would possibly have an automatic mode to relieve the pilot of manual control except in times of emergencies.

Some of the features of the proposed midcourse navigation system are enumerated in the following discussion.

The display to the pilot should include:

- (1) An estimate of the trajectory, that is, the current position and velocity vector.
- (2) The indicated miss at periapsis if no velocity correction is made.
- (3) The velocity correction required to reduce the indicated miss to zero.
- (4) The root-mean-square (rms) prediction error.
- (5) Statistics of the difference in the observed and computed angles.
- (6) Information on the two emergency abort situations previously discussed.
- (7) Monitoring of the subsystems.

Quantities (1) to (5) are discrete quantities calculated by the digital computer and would normally be updated at the time of the observations and included on the pilot's display panel. If the pilot decides he wants this information in between observations, this is accomplished by commanding the computer to update the display. In the event that the pilot decides a correction is required, he activates the computer to calculate the required velocity correction in magnitude and direction at some selected time in the future. He then either orients the vehicle through the manual control system or monitors an automatic orientation and initiates the velocity correction at the appropriate time.

The control includes the:

- (1) Activation of the subsystems.
- (2) Activation and operation of the computer for including observation points.
- (3) Manual keyboard computer inputs.

These displays and controls plus training in their use will provide the pilot sufficient information and control for command of his mission. Further studies of methods of display and details of mode selection and controls are necessary before the system can proceed to the design stage.

Figure 3 illustrates a more detailed block diagram of the trajectory determination portion of the midcourse navigation system. As noted previously, optical instrumentation is the primary source of information in this scheme. The smoothing operation shown to the right of the summation symbol is performed by the digital computer to obtain the optimal estimate of the position and velocity vector during the flight. The operation of the system is best understood by considering the sequence of events for one observation as follows:

First, the observation of a celestial body is made and its angles with respect to a chosen axes system and time are recorded and directed to both the Ground Computation Center and the digital computer.

Second, the computer integrates the equations of motion from the time of the last observation to the time of the next observation and calculates what the observed angles should be, the difference between the observed and computed angles, and their statistical rms deviations.

Third, the pilot compares these last two pieces of information and if the angular difference is greater than about 3 times the rms value, it is likely that a mistake in the observation has been made and corrective steps are taken to repeat the measurement and to check with Ground Computation Center. If the difference is less, the pilot activates the computer to include the data point. The manner in which the computer includes the data point is to:

(1) Compute the optimum weighting function for the particular type measurement made.

(2) Multiply the difference angles by the weighting function and modify the estimate of the trajectory at the observed time by the result. This trajectory determination scheme is a specialized application of a general theory on linear filtering developed by Kalman (ref. 1).

At periodic intervals, perhaps every 6 to 12 hours, the estimated trajectory is obtained from the Ground Computation Center, compared with onboard data by the pilot, and after sufficient cross-checking is inserted into the computer to update the trajectory calculations. This could be accomplished by voice communication and the manual keyboard rather than telemetering and automatic read-in. However, further study of this procedure is necessary. The onboard estimate is, therefore, as good as the ground estimate of the position and velocity of

the spacecraft at these times. Since the ground estimate includes both ground tracking and onboard data, these data represent the best estimate available.

The next subject for consideration is midcourse guidance calculations which are shown in figure 4. Essentially the problem is: Given the estimated trajectory, that is, the position and velocity vector, to predict the periapsis and devise a means of computing the velocity corrections necessary to obtain the desired periapsis. For this study, a fixed time of arrival navigation system has been used to meet this requirement. In essence, the vehicle is guided to arrive at a particular time at the perilune and perigee of a known predetermined reference trajectory. The fixed time of arrival feature is not absolutely essential and further study is necessary to determine the advantages of a more flexible system. Now by using linearized equations of motion around the reference trajectory, the computations are considerably simplified. Therefore, linear prediction matrices have been used to transfer the deviation from the reference trajectory at the present time to future time. Relatively simple calculations can be made of:

- (1) The predicted miss.
- (2) The velocity correction required to reduce the predicted miss to zero.
- (3) The rms error in prediction.

The application of linear prediction methods has some problems if large launch time variations are required in that the nonlinear effects of large deviations from a single reference trajectory would cause sizeable errors in the prediction. To have a large launch window, this system requires a number of onboard stored reference trajectories. The pilot would then choose from this list a member which closely fits his measured injection conditions. Further studies to determine the number of reference trajectories required or of other means of circumventing this problem are required.

SYSTEM EVALUATION RESULTS AND DISCUSSION

In order to evaluate the midcourse phase of this navigation system, a relatively complex simulation was made. Before presenting some results, it is necessary to note the objectives and to understand the assumptions under which the simulation was conducted. One such objective was to determine if the mission could be accomplished by the use of onboard optical measurements only. As will be shown this objective

was achieved but the results to be presented are not considered as good as they would be if ground tracking data were included. Shown in figure 5 are some pertinent assumptions relative to the study made for a $6\frac{1}{2}$ -day circumlunar trajectory. An onboard optical device was assumed to measure the subtended angle and the right ascension and declination of the center line of the earth or the moon every 6 minutes during observation periods. The procedure for taking measurements was to begin observing only the earth starting one-half hour after injection for a period of 3.9 hours and again prior to entry. The moon only was observed for a period of 12.1 hours when near the moon. During the remaining portion of the flight the earth was observed and then the moon with a half-hour period of no observations interposed. This sequence resulted in a total of 844 observations for the $6\frac{1}{2}$ -day flight. Noted also in figure 5 are the times selected in advance for the six velocity corrections to be made. The first correction was made $1/2$ day from injection and was followed by two other corrections on the outbound trajectory and three on the inbound trajectory of the flight. The last velocity correction was made about 2 hours from entry. At least 15 minutes was allowed between observations and velocity corrections in order to allow time for vehicle orientation.

The assumed errors for what is referred to as the standard case are as follows: First, the standard deviation of the errors in seconds of arc in each of the observed angles was assumed to be

$$\sigma = \sqrt{100 + (0.001\theta)^2}$$

where θ is the subtended half-angle. For infinite distances this error has an rms value of 10 seconds of arc and for 100 miles altitude from the earth, it is about 290 seconds. This error formula gives conservative results according to some instrumentation studies made recently. Second, the standard deviation of injection errors was 1 kilometer and 1 meter per second in each of three geocentric Cartesian inertial position coordinates. Third, the statistical errors in making the necessary velocity correction were 0.7 degree in direction and 0.1 meter per second in magnitude. Fourth, the error in measuring the velocity correction was taken as 0.01 meter per second in each of the three coordinates.

The final measure of any guidance scheme for a manned space vehicle is, of course, its ability to position the vehicle in space so that a safe entry can be made. Presuming this can be achieved by the reference trajectory, then a measure of the guidance effectiveness is the variations between the actual and the reference trajectory. Figure 6 illustrates the manner in which this variation can be envisioned. The

dotted line indicates the reference trajectory. For any point in time on the reference trajectory, there is a known probability that the actual trajectory will lie within a given range r and a given velocity V from the reference. Similarly, if one actual trajectory is chosen, as is shown by the solid line, then there will be a known probability that the estimated trajectory will lie within a given range \tilde{r} and a given velocity \tilde{V} from the actual trajectory. The rms values of these deviations have been calculated for the entire trajectory and will be presented for the time of reference perigee. It is well known also that a successful entry can be made if the vacuum perigee height is within a given band; therefore, the rms value of the variation in vacuum perigee between the actual and reference trajectories has been computed.

Table I summarizes the rms perigee data obtained from the simulation studies. These results are the same as would be obtained by averaging, in an rms sense, the results of many trajectories from the ensemble having the same statistical errors, sequence of observations, and velocity corrections times. In the first row are listed results for the standard case referred to previously. Note that the rms variation in perigee height is only 0.30 nautical mile indicating a highly satisfactory entry survival potential for the spacecraft and its occupants. The next two numbers of 6.2 nautical miles and 36 feet per second for the rms range and velocity, respectively, are given at vacuum perigee but are of the same order of magnitude at atmospheric entry conditions. Since the spacecraft is reentering at near parabolic velocity, it is apparent that the entry flight-path-angle variation is less than 0.001 of a radian and the error in range can easily be eliminated during terminal guidance. A second set of data, those of the error in knowledge of position and velocity, are given at the time of reference perigee as 4.2 nautical miles and 22 feet per second, respectively. These latter quantities influence the terminal guidance system and unfortunately time was not available to calculate the miss on landing caused by these errors for a perfect terminal guidance system.

The total corrective velocity required in making the six corrections for the $6\frac{1}{2}$ -day flight for the standard case has an rms value of 30 feet per second. The magnitude of this quantity is a figure of merit related to the amount of onboard fuel necessary for midcourse corrections.

The effects of various parametric changes from the standard trajectory are shown in the next 4 rows in table I. For example, if one could make and measure the velocity corrections perfectly, then the perigee errors are reduced, but there is not a significant reduction in total corrective velocity. Increasing the errors in observations by a factor of 5 increases all the terminal errors by a factor of 2 to 4 but again does not substantially increase the total corrective velocity.

As might be expected, since we have a very good trajectory determination system onboard the vehicle, an increase in injection errors by a factor of 5 increases the total velocity required by about the same factor of 5 but has no effect on terminal errors. If the trajectory could be determined perfectly and injection errors were not sufficiently large to greatly modify the approximate linear relationships, then the total velocity required is directly proportional to injection errors. The variance in the test condition from the standard for the last row is due to the sequence of observations being made regularly at 2-hour intervals for a total of 77 observations. A comparison of the data in the third and fifth rows shows that a good measurement system allows the liberty of taking less observations to achieve the same perigee error. Even though the total number of observations was decreased from 844 for the standard case to 77, it can be seen that the total velocity required did not increase appreciably. It should be noted that in each case cited in the table, the spacecraft should return well within the reentry corridor requirements for a spacecraft with $L/D = 1/2$.

Table II shows the rms perilune data. The behavior is so similar to perigee it is left to the reader to make the various accuracy comparisons.

The corrective velocities shown are determined to a great extent by the hypothetical set of injection errors assumed. Thus before great confidence can be attached to these numbers the magnitude and direction of the injection errors must be known more precisely.

CONCLUSIONS

The simulation results may be summarized in the following two statements: (1) the performance of the midcourse guidance system studied is well within the accuracy requirements needed for the return to an established reentry corridor, and (2) the corrective velocity associated with this performance is small.

The important features of the proposed system are: (1) because of the manner in which it operates, this system gives the optimal estimate of the position and velocity of the spacecraft at all times with a minimum storage capacity in the computer and is also adaptable for use in guiding during abort, and (2) guidance and navigation can be successfully accomplished without reliance on tracking information transmitted from the earth. The implications of this latter conclusion are that: (a) an integrated ground-control onboard system would minimize potential errors and secure a measure of redundancy by the duplication of

DECLASSIFIED

141

calculations, and (b) the complete onboard system provides an additional emergency mode to that of the pilot following instructions from the ground-control center.

REFERENCE

1. Kalman, R. E.: A New Approach to Linear Filtering and Predictions Problems. Jour. Basic Eng., Mar. 1960, pp. 35-44.

TABLE I.- RESULTS AT PERIGEE - RMS VALUES

Condition	Miss			Uncertainty		Applied total ΔV , ft./sec
	$(R_{REF} - R_{ACT})$, naut. mi.	r, naut. mi	V, ft./sec	\tilde{r} naut. mi.	\tilde{V} , ft./sec	
Standard trajectory	0.30	6.2	36	4.2	22	30
Perfect velocity corrections	.05	3.0	17	2.5	13	28
(Observation error) $\times 5$.65	18.0	98	15.0	77	38
(Injection error) $\times 5$.30	6.2	39	4.2	22	138
77 observations	.59	15.0	78	8.1	43	33

TABLE II.- RESULTS AT PERILJUNE - RMS VALUES

Condition	Miss			Uncertainty		ΔV outboard used, ft/sec
	$(R_{REF} - R_{ACT})$, naut. mi.	r , naut. mi.	V , ft/sec	\tilde{r} , naut. mi.	\tilde{V} , ft/sec	
Standard trajectory	0.90	2.6	3.8	0.42	0.25	27
Perfect velocity corrections	.39	2.0	3.4	.39	.22	27
(Observation error) $\times 5$	1.86	7.3	10.0	1.90	1.06	31
(Injection error) $\times 5$.92	2.7	13.5	.43	.25	136
77 observations	1.23	4.6	7.2	1.57	.87	29

03712201030

144

CIRCUMLUNAR MISSION

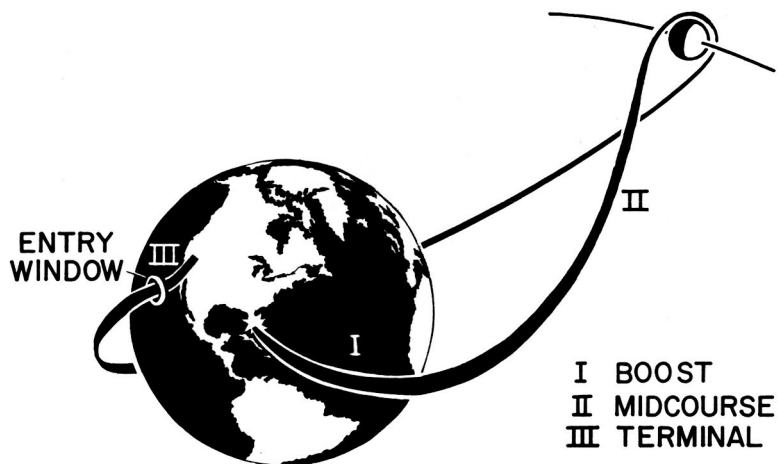


Figure 1

BLOCK DIAGRAM OF THE PROPOSED SYSTEM

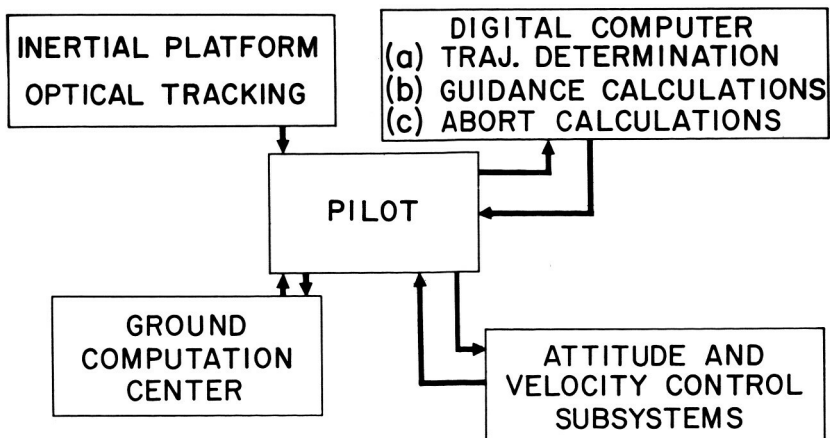


Figure 2

TRAJECTORY DETERMINATION

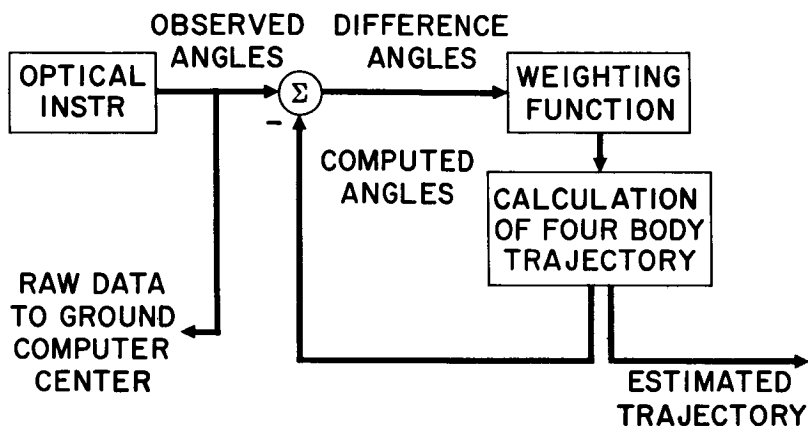


Figure 3

MIDCOURSE GUIDANCE CALCULATIONS

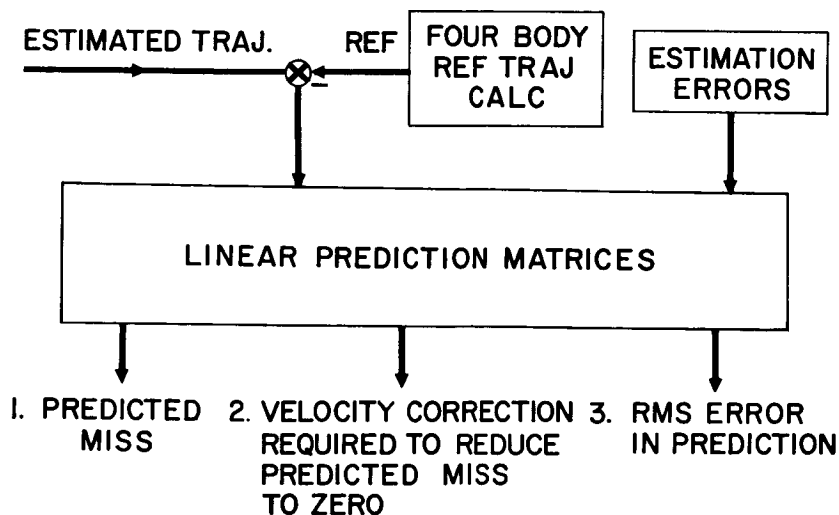


Figure 4

PROCEDURE FOR MEASUREMENT AND CORRECTION

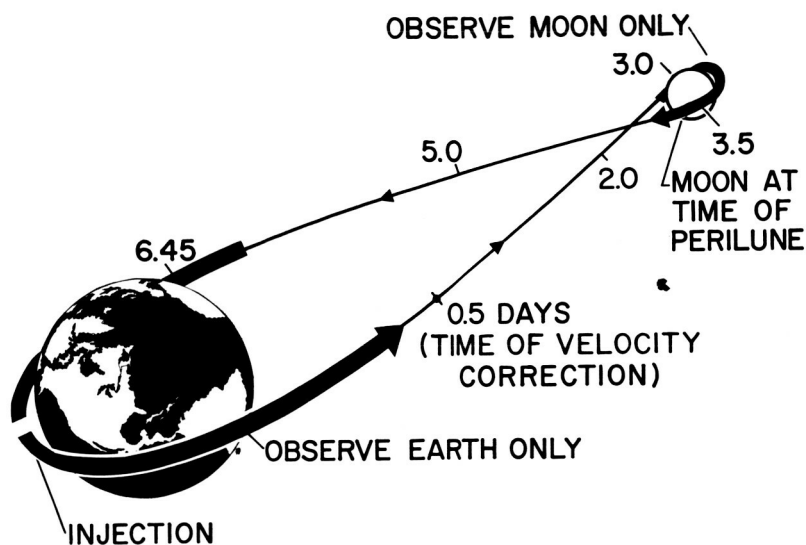


Figure 5

ERRORS AT TIME OF REFERENCE PERIGEE

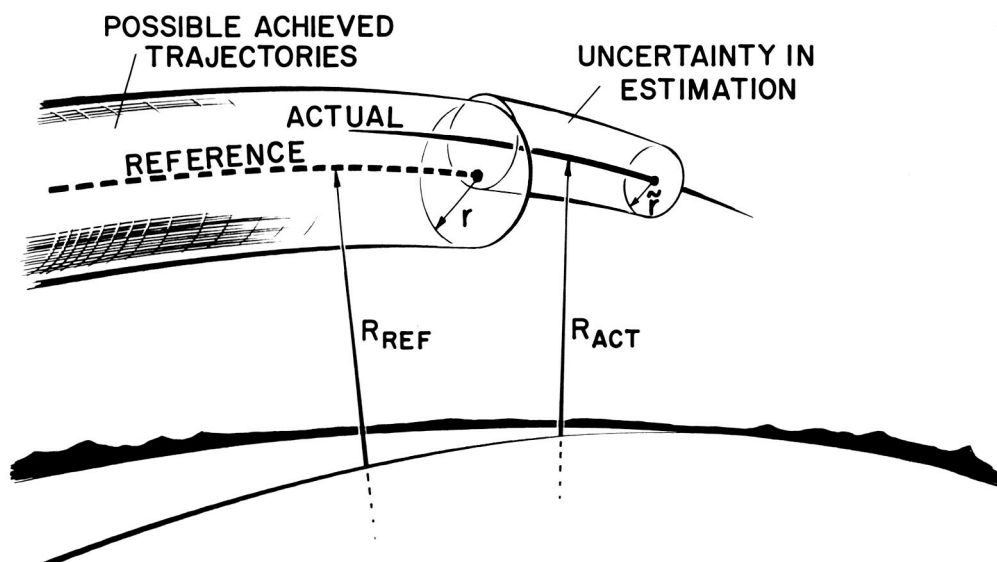


Figure 6

GUIDANCE AND CONTROL DURING DIRECT DESCENT PARABOLIC REENTRY

By Edwin C. Foudriat
Langley Research Center

and Rodney C. Wingrove
Ames Research Center

INTRODUCTION

The conclusion of a successful lunar or outer space mission will require the reentry from a near parabolic orbit to a prescribed landing point on the earth's surface. In order to accomplish this a navigation guidance and control system will be required for the Apollo spacecraft.

From the beginning of the space age intensive study has been conducted on the reentry procedures, range capability, and heating of reentry vehicles (refs. 1 to 3). Reference 4 contains an excellent bibliography of the recent work in the area related to the reentry capability from escape speeds. The area of energy management, that is, the procedure by which the reentry capability is used to attain a desired landing point, has also been studied intensively for orbital reentry conditions (refs. 5 to 11). With the advent of the lunar and outer space missions, recent studies have been reported on reentry energy management from parabolic reentry conditions (refs. 11 to 14).

In addition to these studies, additional programs have been initiated by the NASA. The purpose of this paper is to review the earlier studies, indicate information obtained from recent programs, and indicate the areas where future work may be profitable in extending the range capabilities for parabolic reentries.

Four studies are reported on in this paper. The first of these is a piloted simulator study, where the pilot's intelligence and learning capability are used to provide the guidance logic and control commands. Most of the information provided to the pilot may be derived from an inertial reference navigation system. The second program is an automatic control study using a reference trajectory procedure. Here, the control feedbacks are developed for the successful operation of the system and the range capability illustrated. The last two systems discussed in this paper include the use of prediction to obtain control of range. The first of these employs a linear predictor which combines stored trajectories and influence coefficients to determine the final range error (ref. 11). The second uses a rapid-time analog computer to extrapolate the range capability from the present conditions. The pilot

is provided this information in order to control the vehicle to its desired destination (ref. 12).

To date, direct-descent reentries have been used in most of the studies; that is, the vehicle does not skip out of the atmosphere. Although for extreme extensions of range skip out is required, a large range for direct-descent trajectories is available if proper procedures to avoid skip out are employed. These procedures will be discussed and the range available indicated.

DEFINITION OF RANGE CAPABILITY FOR DIRECT-DESCENT TRAJECTORY

The direct-descent trajectory is defined as one for which a vehicle upon entering the earth's atmosphere does not exit or skip out. The restrictions upon the range of such trajectories can best be classified with the help of figure 1. The vehicle trajectory must be controlled outside the atmosphere so that it penetrates at an entry angle steep enough to decelerate but shallow enough to avoid the limit of human tolerance. Once in the atmosphere the minimum range is restricted by the ability of the human occupant to tolerate sustained high-level deceleration. For this paper this limit has been arbitrarily set at 10g in order that the work by the various guidance investigators can be compared. However, a detailed discussion of the actual tolerance requirements is presented in the paper by Brent Y. Creer and Joseph G. Douvillier, Jr. The maximum range is limited by a trajectory which reaches the edge of the usable atmosphere, or about 300,000 feet. These two trajectories then define the down-range capability for the direct-descent reentry. In addition to down-range control it will generally be necessary to change the vehicle's great-circle course. This is designated as cross- or lateral-range capability. Thus, the range capability of any system is the combination of the down and cross ranges available and is a factor of major importance in judging the energy management system.

In order to obtain additional range, it is possible to employ skip-out procedures. Here the maximum range is limited only by the requirement to avoid the Van Allen regions of high-intensity radiation. It should be noted that extreme ranges are available if controlled skip out is used. However, very little study has been reported on guidance and control schemes which employ skip procedures. It is indicated in reference 4 that the sensitivity of such maneuvers to the velocity and flight path can be extremely large under certain conditions. In addition, by storage of small amounts of energy, a parking orbit (ref. 14) is possible which permits an infinite range to be obtained.

DECLASSIFIED

149

PILOT SIMULATOR STUDIES

The first NASA program to be discussed consisted of a piloted study conducted on a fixed-base simulator. The study was conducted to determine the ability of the pilot to fly a reentry-type vehicle, to determine the requirements for instrument display, and to obtain procedures which would permit him to use his intelligence and learning abilities to pilot the vehicle to the desired destination.

The instrument display used for this study is shown in figure 2. The control instrument used to display vehicle attitudes and body rates is the three-axis "8" ball. This instrument displays yaw, pitch, and roll (the Euler angles) and the body angular rates. The lift forces on the vehicle are indicated by the angle-of-attack and sideslip meters to the left of the "8" ball. The vehicle is capable of trimming from 0° to 40° angle of attack and $\pm 20^{\circ}$ in sideslip. This angle-of-attack range corresponded to a lift-drag ratio of 0 to 0.58. The vehicle's velocity, altitude, and range to go (distance to the target) are indicated in the column of instruments to the right of the "8" ball. The altitude rate was found to be extremely useful and is indicated on the dial below the "8" ball. An ILS type of instrument which shows down- and cross-range-to-go errors (directly above the "8" ball) is used by the pilot to obtain the desired direction of bank angle and is required for precision maneuvering near the target site. The instrument at the bottom is a memory oscilloscope used in the manner of an x-y plotter. Altitude was plotted on the vertical scale with range to go plotted on the horizontal scale. In addition to plotting the vehicle's past history a reference trajectory curve is traced on the face of the instrument. The pilot is thus able to correlate the past history of the flight with respect to the target and the reference to which he is to fly.

The pilot was provided with a two-axis pencil-type controller and rudder pedals. In addition, trim wheels operated by the left hand were available for pilot control. The damping was provided by auxiliary feedback controls with a minimum damping ratio of at least $\delta = 0.2$. Roll control was provided by proportional reaction control with a maximum acceleration of 5° per second squared and a feedback time constant of 1 second.

The piloting procedure will be described with the aid of figure 3 which shows the vertical and horizontal profile of a short- and a long-range pilot-controlled mission. In both missions the initial phase of the reentry was the same. For the short-range case the pilot remained at approximately the pullout altitude until he reached the reference trajectory. By remaining at the lower altitude the pilot was able to reduce the velocity more rapidly. As the reference was reached the

pilot started the descent to the target. Actually, in the case shown in figure 3 the pilot overshot the reference and had to dive more steeply to reach the target.

For the long-range mission the pilot did not remain at the lower altitude but started a pullup which he terminated at about 250,000 feet. The proper pullup procedure is very necessary in order to obtain long ranges and must be done with some care in order to avoid skip out. The procedure was to start the pullup at a velocity between 30,000 and 32,000 ft/sec. For the pullup a rate of climb of 800 ft/sec was established. At an altitude of 230,000 feet the pilot rolled the vehicle over and used all the lift in the negative direction in order to avoid skip out. When done properly this reduced the rate of climb to zero between 250,000 and 260,000 feet with a velocity between 25,000 and 27,000 ft/sec. At this condition the pilot could be considered at the edge of the atmosphere with near superorbital velocity and with the capability of extremely long range. This has been termed the coasting phase as indicated in figure 3. As can be seen from the figure the pilot initiated the rate of descent when he reached the reference trajectory.

The pilot had no trouble correcting the cross range. When lift was not used vertically the pilot rolled the vehicle to 90° to reduce the cross range. For these runs the roll was initiated at the end of the initial pullout as indicated by the cross-range-error reduction. The remainder was eliminated during the coasting and reference trajectory phases.

It should be indicated that the pilot procedure was to fly a reference trajectory which is similar to the automatic control procedure to be discussed. During the initial portion of the reentry, however, the pilot did not use the error between the present position and the reference trajectory to direct his control inputs. Instead he used a procedure which when properly executed placed him in a position where he was able to attain the reference trajectory once the initial or superorbital phase was completed. This point has an important bearing on the use of reference trajectory for control as will be indicated subsequently.

Figure 4 shows the range capability of a skilled pilot for three entry angles which include the steeper two-thirds of the reentry corridor. The shaded area indicates the maneuver range for all entry angles studied. The ranges between 2,200 and 3,500 miles are obtained when the pullup maneuver is made so that a velocity of approximately 25,000 ft/sec is reached at the initial point of the coasting phase. As indicated in figure 4, a range extension of 1,500 miles is obtained when the pullup maneuver is made so that initial coasting phase velocities of 27,000 ft/sec are obtained. There is no reason why further

down-range extensions should not be possible since for some reentry conditions higher velocities at the beginning of the coasting phase are possible. In addition, further range extension is available by increasing the altitude during the coasting phase as indicated in reference 4.

The results of the pilot studies also indicate that lateral range is a function of initial entry angle γ_0 . Figure 4 indicates that the lateral range available for entries at $\gamma_0 = -6.5^\circ$ is 500 miles greater than that at $\gamma_0 = -5.5^\circ$ and about 300 miles greater than that at $\gamma_0 = -7.5^\circ$. This increase is due to the fact that the $\gamma_0 = -6.5^\circ$ entry is closer to the ballistic entry and therefore less lift is needed either to keep the vehicle from skipping out or to prevent diving too deep in the atmosphere. This means that during the initial (supercircular) portion more lift is available to obtain larger lateral velocities. Thus, it may be desirable from a control and range-available standpoint to attempt to control the vehicle so that its initial reentry is nearly a ballistic trajectory.

Pilot opinion of the learning, the work load, and the timing required to make successful reentries following this procedure were obtained from this study. The research pilots who participated in the study stated that considerable time was required to attain proficiency in the simulator, basically because they were unfamiliar with the mechanics of reentry. Once this learning period was completed so that the pilots understood the reasoning for the steps in the procedure they found the task only moderately difficult. With sufficient damping the vehicle work loads were considered reasonable, and although good timing was necessary, the experienced pilots felt that with an understanding of each phase, sufficient time was available for anticipating the next control inputs.

STUDY OF THE REFERENCE TRAJECTORY CONTROL PROCEDURE

A second study has been conducted by the NASA to determine the usefulness of controlling parabolic reentry by an automatic control system in which stored reference trajectories are used. Such systems have been studied extensively for circular reentries (refs. 5 to 8 and 14). The technique is explained with the help of figure 5. A nominal trajectory (one in which the vehicle enters with the specified conditions and position) is selected and stored in the control system. During the actual flight the measured conditions are compared with those of the reference trajectory and the errors obtained. These errors are passed through constant-gain weighting factors K and the sum of the weighted errors is used to specify the lift-drag ratio L/D to be used to force the actual vehicle conditions to conform to those

of the reference trajectory. For the system studied the feedbacks found to be most effective were altitude rate \dot{h} , deceleration A , and range R as an outer loop control. For the study these were programed as a function of velocity. Also shown in figure 5 is a switch in the range control loop which provides for closing the range loop at the appropriate velocity. The reason for this switch will be discussed subsequently.

A simplified analysis of feedback control during reentry was conceived to study various feedback conditions using only those variables that strongly effect reentry motion. Reference 13 has presented a method of setting up the approximate reentry motion equations in block diagram form. The Chapman equation (ref. 15) used in this study allows important feedback quantities for range control to be recognized and its relative ease of mechanization on an analog computer allows a straightforward method in the investigation of reentry control.

The study reported in reference 13 has shown the control range to be a third-order control system. As for any other third-order control system, it was found that two inner-loop control terms were desirable. Damping the trajectory is especially important for those velocities greater than satellite velocity, where the vehicle can either skip back out of the atmosphere or exceed a given deceleration limit.

The fixed-trajectory control studies of reference 13 have been extended here to show the characteristic of feedback control in damping the trajectory above satellite velocity. Also, the manner in which range feedback must be used is demonstrated, and the maximum down and cross ranges available are indicated.

Figure 6 shows the typical entrance-angle limits for a body with $L/D = 0.5$ entering the atmosphere at 400,000 feet at a velocity 40 per cent above satellite speed. The overshoot limit is determined by the entrance angle at which the vehicle will just stay within the atmosphere when full negative lift is used. The undershoot limit, which is a function of the maximum deceleration, is determined by the entrance angle at which the vehicle will just reach the given g -value with full positive lift. The scale of this figure is adjusted so that the corridor width corresponding to given entrance-angle limits is a linear extrapolation. The entrance-angle limits for various control laws are shown with respect to the available limits of the vehicle. By controlling L/D as a function of altitude rate of change or deceleration rate of change, all but the upper 1° of the available corridor width can be used.

Although the altitude rate of change would have to be measured from an inertial reference during reentry, the deceleration measurement could be obtained from an accelerometer strapped to the vehicle in such

a position that it will not couple with the short-period dynamics. The other control law is control to a trajectory in which deceleration varies as a function of velocity. Although this system used almost all the capability available to the vehicle for high design maximum decelerations, when the design maximum deceleration is low (below 6g) the vehicle will tend to skip out of the atmosphere after the initial dive to maximum deceleration. It was found that combining the two concepts shown in figure 6 would use almost all the corridor width available to the vehicle over the complete deceleration range.

The control of range about the design trajectory is next considered with the following control equation:

$$\frac{L}{D} \begin{vmatrix} .5 \\ -.5 \end{vmatrix} = K_1 \dot{h} + K_2 [A - A(\bar{u})] + K_3 [R - R(\bar{u})]$$

where \bar{u} is nondimensional velocity. The term $K_1 \dot{h} + K_2 [A - A(\bar{u})]$ is for inner-loop control and the term $K_3 [R - R(\bar{u})]$ is for range control. The inner-loop terms are a combination of those already shown to keep the controlled trajectory within limits during the supercircular portion of the trajectory.

Figure 7 shows the maximum range values that can be obtained for range control starting both above and below satellite velocity. As seen in the figure, a high value of range control gain K_3 will allow very little range control above satellite velocity, but with low feedback gain some range control is available. Just below satellite velocity, full range control can be added because the vehicle cannot usually skip back out of the atmosphere.

Two important points are indicated in figure 7. The first point is that it is more important during the supercircular portion to control the vehicle in order to avoid skip out than to control the error in range from the fixed reference. This point, which was indicated in the piloted procedure, is forcefully illustrated in figure 7. The second point is that when proper range control is used the reference trajectory approach gives good range control within a down-range capability of 2,000 miles.

The maximum cross range that could be used during the supercircular entry was determined by flying the vehicle at a trim L/D condition of 0.5, letting the roll angle command the L/D value that was used for control in the previous section. The command roll angle becomes

$$\text{Command roll angle} = \cos^{-1} \frac{\text{Command } L/D}{\text{Trim } L/D = 0.5}$$

The cross range was computed by using the method of reference 16 and letting the roll angle control side force to only one side of the trajectory during the full reentry.

Figure 8 shows the cross range available for this control scheme. As presented, about twice the cross range is available if lateral range control is started at parabolic velocity than if range control is started at satellite velocity since the vehicle has no tendency to skip out when lateral force is used.

Actually the reference trajectory and piloted procedure described in the previous section have a great deal of similarity. In the Chapman equation of reference 15 acceleration is comparable to altitude in the standard equations. Thus, whereas the pilots controlled the supercircular portion using altitude and altitude rate with velocity as an index, the automatic feedback control system used acceleration and altitude rate. Suborbitally both used reference trajectories based upon range.

LINEAR PREDICTION

In addition to the more simplified guidance approaches just described, prediction of critical reentry quantities has been used to improve or augment the control logic of the reference trajectory approach.

The linear prediction technique has been studied for entries with two degrees of freedom from circular orbit (ref. 10). This work has been extended to include some of the problems of reentry from parabolic orbits. Figure 9 shows a block diagram of the linear prediction scheme and how the method works. First, the similarity between it and the reference trajectory technique is quite evident. The stored trajectory variables are compared with the present flight conditions and the errors are obtained. However, instead of using constant weighting functions a set of influence coefficients calculated by the adjoint technique (ref. 10) is used to predict the effect of these present errors on the end conditions. This predicted final value in range is then used to control the lift-drag ratio of the vehicle. Thus, where the reference trajectory technique forces the vehicle to fly to a single trajectory, the prediction technique selects one of many trajectories which terminate at the desired destination.

The use of the linear prediction technique is illustrated in figure 10 where the errors in the vehicle variables and the predicted range error are plotted as a function of time for a circular reentry control. The figure indicates that the initial altitude is above the reference trajectory, the initial velocity and flight path are correct,

and the vehicle's range error ϵ_R is about 280 miles beyond the target. Therefore, the vehicle is trimmed to a minimum lift until the predicted error goes to zero. At this point the velocity and flight path have large but canceling errors - the velocity is 1,600 ft/sec faster than the reference velocity but the flight path is about 0.4° steeper. When zero range error was predicted the vehicle returned to the nominal lift condition and no further control inputs were required.

The use of prediction has been extended to supercircular reentries. The first control problem is to keep the vehicle from overdeceleration. Figure 11 illustrates the ability of the system to predict the peak decelerations from a nominal 7.6g reentry trajectory. Over the range of interest from 5g to 10g the prediction error was less than 0.2g for the cases studied. In addition, the predictor shows improved accuracy as the time when this acceleration will be obtained is decreased.

It should be pointed out that the prediction of range superorbitally will suffer from a problem similar to that for the reference trajectory; that is, the control of range in the superorbital portion will cause the vehicle to skip out. Studies are being conducted to determine how the superorbital control may be accomplished to avoid skip out.

REPETITIVE PREDICTION BY FAST-TIME COMPUTATION

In addition to the use of linear prediction, a more sophisticated prediction system, the use of a high-speed repetitive computer has been used to aid the pilot in the reentry energy management problem. Although the basic concepts of this procedure have been summarized in references 12 and 13, a brief description of the prediction method of end-point guidance and control is presented here.

The aerodynamic range capability of the vehicle is predicted from existing conditions along the flight path by solving equations of motion for constant trim conditions (assumed to give maximum maneuver). In this study three constant trim conditions were used:

- (1) $(L/D)_{\max} = 0.5$ and bank angle zero ($\phi = 0^\circ$) for maximum range
- (2) $(L/D)_{\max} = 0$ and $\phi = 0^\circ$ for minimum range
- (3) $(L/D)_{\max} = 0.5$ and $\phi = 45^\circ$ for maximum cross range

This area of aerodynamic range is solved repetitively, as fast as possible, for changing flight conditions by an airborne computer. The

assumed maximum maneuver capability is thus known continuously as the vehicle conditions vary.

The prediction method of endpoint guidance and control was simulated using an electronic analog computer, fixed cockpit, and pilot to close the guidance loop. The guidance display used in this simulation is shown in figure 12. The "footprint" or range envelope is a transparent overlay on the face of a 5-inch oscilloscope. The destination is a moving dot on the scope presented in relation to the predicted maximum range capabilities of the vehicle. The oscilloscope display appears to the pilot as though he were looking at the nondimensionalized maneuver capability of the vehicle. The desirable procedure is for the pilot to control so that the destination is in the center of the maneuver capability; that is, the pilot should fly the destination dot to the center of the scope. Then the pilot has maximum maneuver capability about the target site to take care of unpredicted errors (wind, drifts, etc.). For the conditions shown in figure 12 the procedure would be for the pilot to establish a bank angle of about 40° with an L/D of 0.5 and thus overcorrect to force the destination toward the center of the display.

In the simulation two restrictions were placed upon the vehicle trajectory, a maximum deceleration limit of $10g$ and a maximum skip altitude of 300,000 feet. The repetitive prediction was capable of predicting these boundary values which were displayed to the pilot as bars on the scope. For reentries at the shallow entry angles the upper bar would appear near the lower boundary of the scope indicating to the pilot to use negative lift to remain in the atmosphere. At the steep entry angles the lower bar would appear at the top of the scope indicating that maximum positive lift was required in order to avoid severe decelerations.

The pilots considered this system entirely satisfactory. The pilot's function needed here was to close the control loop between the bank and trim indicators and navigation display. Pilots had no difficulty coping with emergency or abort reentry conditions far removed from parabolic entry conditions. This ability of the guidance system to predict range, deceleration, and skip-out limits for any entry condition makes it an almost universal control method.

A point of interest should be made about the equations used by this repetitive prediction technique. The procedure investigated by the NASA was conducted by using the Chapman approximate equation (ref. 15) for the solution in the fast-time computer. Other than the simplification of the computation one factor involving the change from geometric to effective density altitude is clearly pointed out by use of the approximate equations. First, the use of density altitude provides a compensation for nonstandard atmosphere conditions. In addition, the instability

in the inertial reference system affects the control procedure less if density altitude is used. Actually, this procedure is applicable to all systems and it is felt that the use of density altitude will be advantageous.

As indicated previously, the range capability is probably a major factor in assessing the quality of a reentry guidance system. Figure 13 shows a summary of the down-range capability for the repetitive prediction, the reference trajectory, and the pilot-controlled systems. (The linear prediction procedure is left off because range data have not been obtained on the reentry from parabolic orbits.) In the control of minimum range the use of the prediction system indicates a definite superiority. This is due to the fact that the predictor gives the lift-drag ratio at which to trim the vehicle in order to reach peak deceleration, and the pilot can easily control the dive into the atmosphere to obtain and hold this value, thereby obtaining shorter ranges.

For the maximum range the piloted system shows a definite superiority in obtaining ranges in excess of those obtained so far by the other systems. This is due to the fact that the automatic system was forced to fly a trajectory not designed to obtain optimum long ranges and the predictor system was confined to the prediction of maximum range by a procedure in which L/D is fixed. However, a varied L/D program, similar to that developed in the piloted procedure where high coasting phase velocities are obtained, is required for maximum range when skip out is not permitted.

Although the research to date has indicated that the pilot is capable of using his experience and judgment in order to obtain longer ranges than are obtained by the other systems, this conclusion should be tempered in light of possible future developments. First, there is no reason theoretically why the reference and prediction schemes cannot take advantage of similar procedures. Additional study will be required to assess the system complexities which may result from their use. In addition, none of the systems has approached the ranges predicted in reference 4. Therefore, further study will be required on all systems including the piloted technique in order that a more nearly optimum percent of the total range capability may be obtained. Finally, the use of skip-out procedures needs to be studied in order that comparison with direct-descent procedures may be obtained in those areas where their range capabilities overlap and in order to increase the reentry range capabilities beyond those of direct-descent trajectories.

CONCLUSIONS

The following conclusions have been obtained from the NASA reentry studies conducted to date on reentry guidance and energy management procedures:

037130A 1030

1. The procedures studied have not provided nearly the optimum direct-descent range that is available. Further study will be necessary in order to assess the additional complexities required in each system in order to obtain a more nearly optimum range.

2. The repetitive prediction technique provides for excellent control of the initial peak decelerations and a more nearly universal reentry procedure, in that abort conditions are easily handled.

3. The piloted study has indicated that the human operator with experience and a good display of flight information can capably perform the reentry guidance maneuvers required.

4. The reference-trajectory and linear-prediction control techniques appear applicable to the problem and will require more study to assess their true value.

5. Procedures for skip out should be investigated so that a comparison with direct-descent procedures is possible and in order to provide a system when extreme down-range control is required.

037130A 1030

DECLASSIFIED

159

REFERENCES

1. Chapman, Dean R.: An Analysis of Corridor and Guidance Requirements for Supercircular Entry Into Planetary Atmospheres. NASA TR R-55, 1960.
2. Lees, Lester, Hartwig, Frederic H., and Cohen, Clarence B.: Use of Aerodynamic Lift During Entry Into the Earth's Atmosphere. ARS Jour., vol. 29, no. 9, Sept. 1959, pp. 633-641.
3. Grant, Frederick C.: Modulated Entry. NASA TN D-452, 1960.
4. Becker, J. V., Baradell, D. L., and Pritchard, E. B.: Aerodynamics of Trajectory Control for Reentry at Escape Speed. Presented at International Academy of Astronautics Symposium (Paris), June 21, 1961. (To be presented in Astronautica Acta.)
5. Cheatham, Donald C., Young, John W., and Eggleston, John M.: The Variation and Control of Range Traveled in the Atmosphere by a High-Drag Variable-Lift Entry Vehicle. NASA TN D-230, 1960.
6. Assadourian, Arthur, and Cheatham, Donald C.: Longitudinal Range Control During the Atmospheric Phase of a Manned Satellite Reentry. NASA TN D-253, 1960.
7. Young, John W.: A Method for Longitudinal and Lateral Range Control for a High-Drag Low-Lift Vehicle Entering the Atmosphere of a Rotating Earth. NASA TN D-954. (Prospective NASA paper.)
8. Eggleston, John M., and Young, John W.: Trajectory Control for Vehicles Entering the Earth's Atmosphere at Small Flight-Path Angles. NASA MEMO 1-19-59L, 1959.
9. Creer, Brent Y., Heinle, Donovan R., and Wingrove, Rodney C.: Study of Stability and Control Characteristics of Atmospheric-Entry Type Aircraft Through Use of Piloted Flight Simulators. Paper No. 59-129, Inst. Aero. Sci., Oct. 5-7, 1959.
10. Foudriat, Edwin C.: Study of the Use of a Terminal Controller Technique for Reentry Guidance of a Capsule-Type Vehicle. NASA TN D-828, 1961.
11. Lowry, James H., Jr., and Buehrle, Clayton D.: Guidance and Control of Point Return Vehicles. Proc. Nat. Specialists Meeting on Guidance of Aerospace Vehicles (Boston, Mass.), Inst. Aero. Sci., May 1960, pp. 28-33.

03171304 1030

160

12. Wingrove, Rodney C., and Coate, Robert E.: Piloted Simulator Tests of a Guidance System Which Can Continuously Predict Landing Point of a Low L/D Vehicle During Atmosphere Re-Entry. NASA TN D-787, 1961.
13. Wingrove, Rodney C., and Coate, Robert E.: Piloted Simulation Studies of Re-Entry Guidance and Control at Parabolic Velocities. Presented at joint national meeting of IAS-ARS (Los Angeles, Calif.), June 1961.
14. White, J. A., Foudriat, E. C., and Young, J. W.: Guidance of a Space Vehicle to a Desired Point on the Earth's Surface. Preprint No. (61-41), American Astronautical Soc., Jan. 1961.
15. Chapman, Dean R.: An Approximate Analytical Method for Studying Entry Into Planetary Atmospheres. NASA TR R-11, 1959.
16. Slye, Robert E.: An Analytical Method for Studying the Lateral Motion of Atmosphere Entry Vehicles. NASA TN D-325, 1960.

DIRECT-DESCENT BOUNDARY AREAS

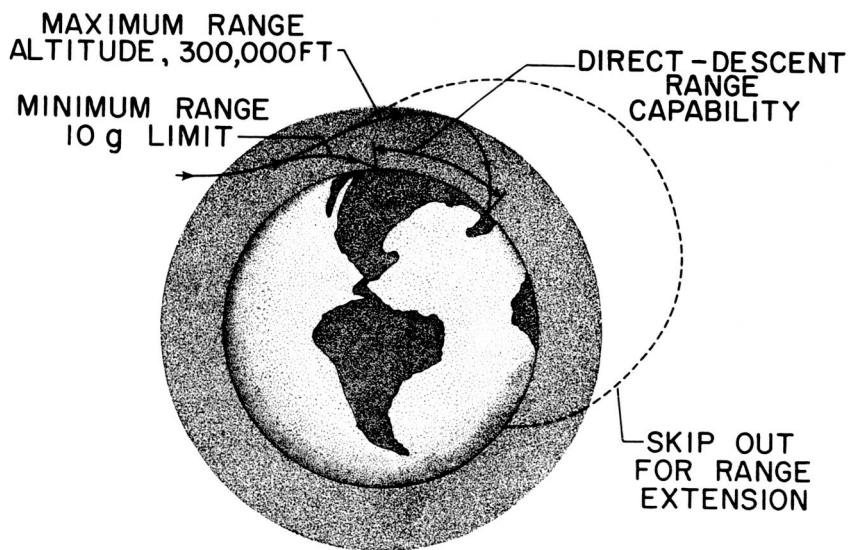


Figure 1

INSTRUMENT PANEL USED IN PILOTED GUIDANCE SYSTEM

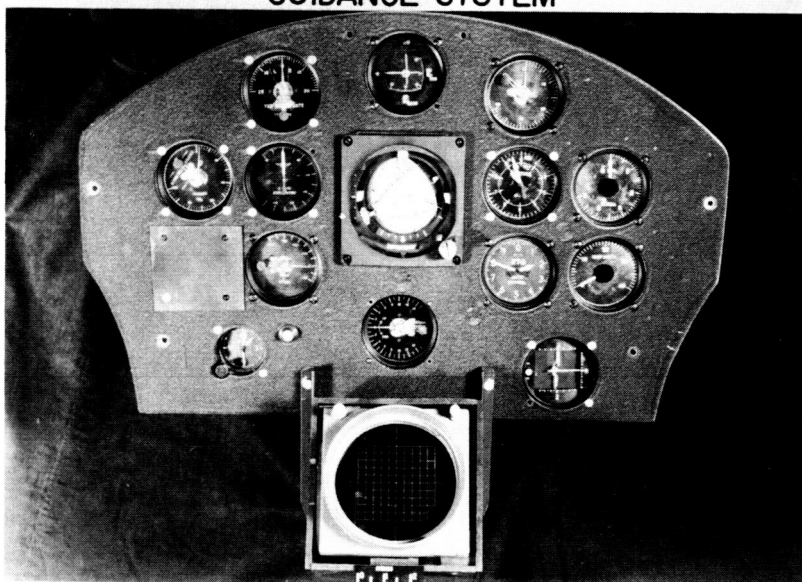


Figure 2

L-61-4422

031712201930

PILOT-CONTROLLED REENTRIES

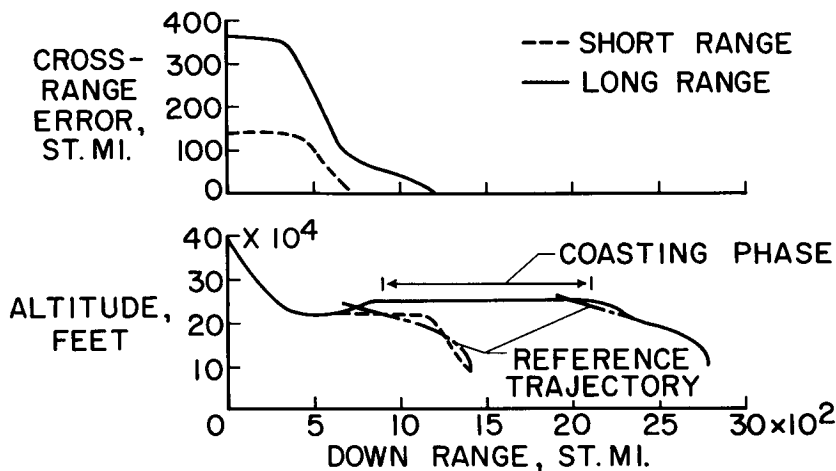


Figure 3

PILOT-CONTROLLED RANGE CAPABILITY

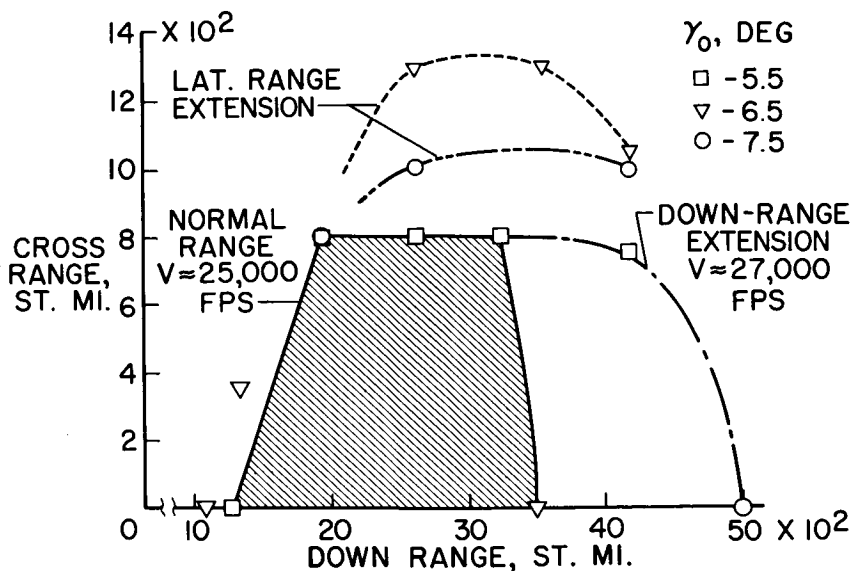


Figure 4

CONFIDENTIAL

REFERENCE TRAJECTORY DOWN-RANGE CONTROL SYSTEM

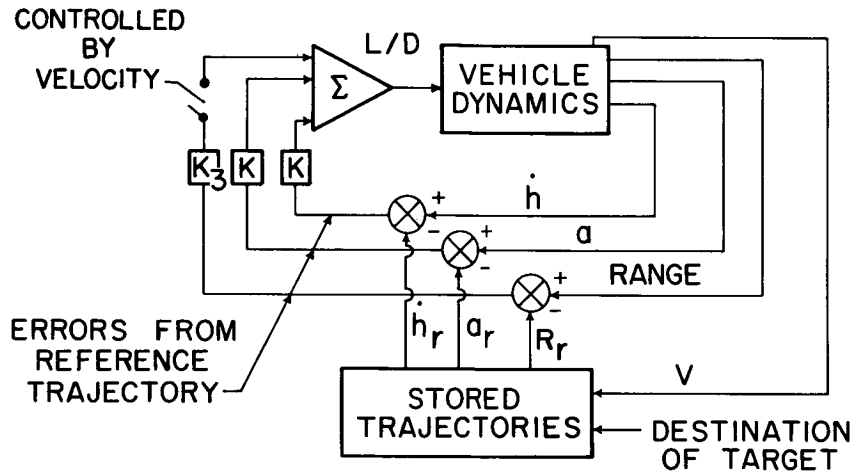


Figure 5

CORRIDOR WIDTH FOR TRAJECTORY DAMPING

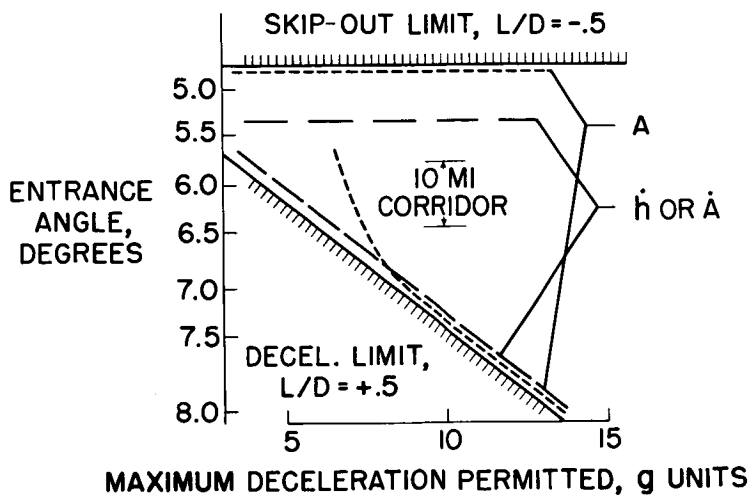


Figure 6

03710 [REDACTED]

DOWN-RANGE CAPABILITY FOR CONTROL TO A FIXED TRAJECTORY

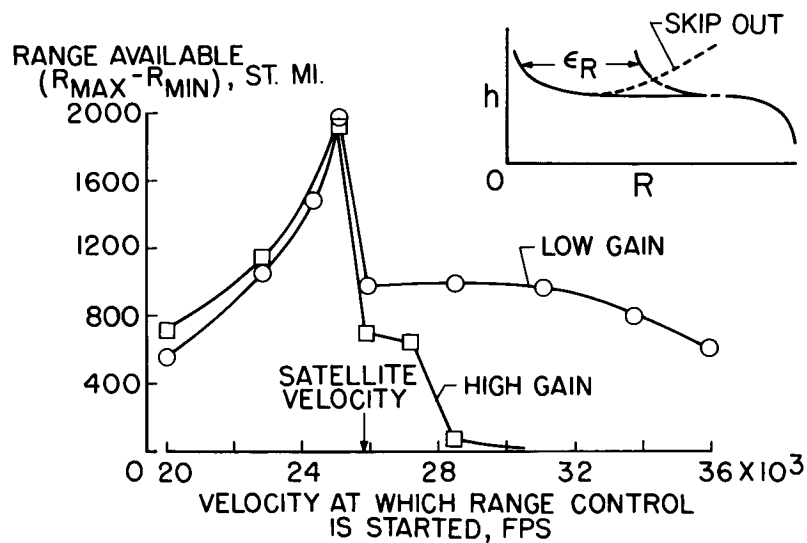


Figure 7

LATERAL RANGE CAPABILITY FOR TRAJECTORY CONTROL

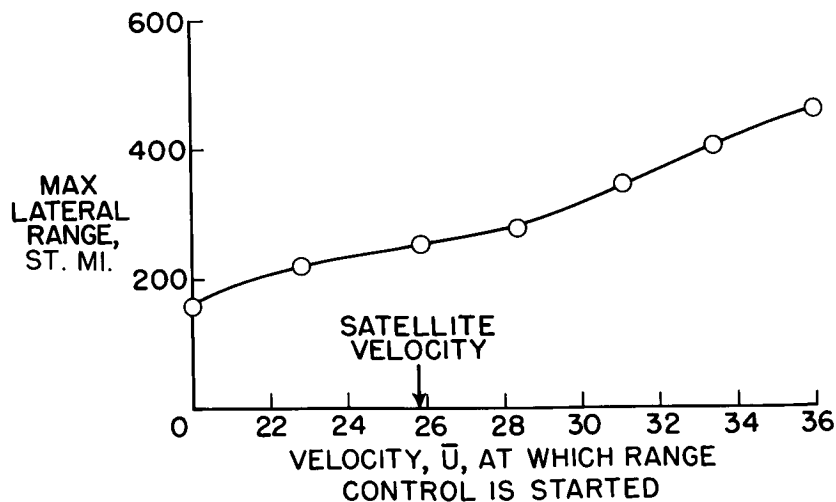


Figure 8

[REDACTED]

BLOCK DIAGRAM OF LINEAR PREDICTOR CONTROL SYSTEM

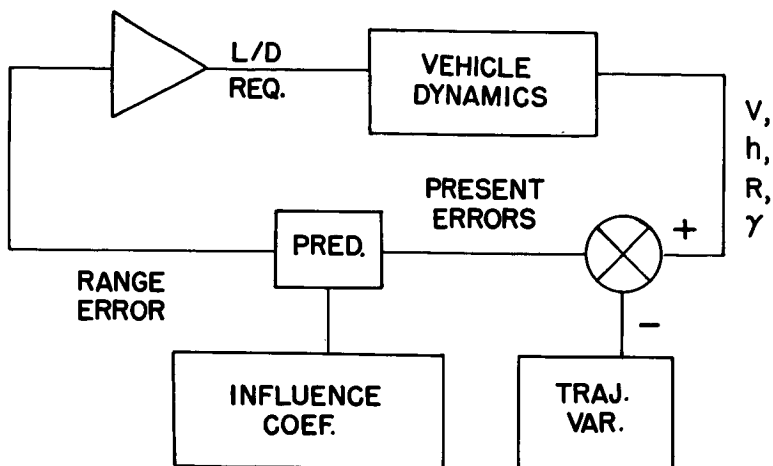


Figure 9

EXAMPLE OF LINEAR PREDICTION OF RANGE ERRORS IN TRAJECTORY VARIABLES

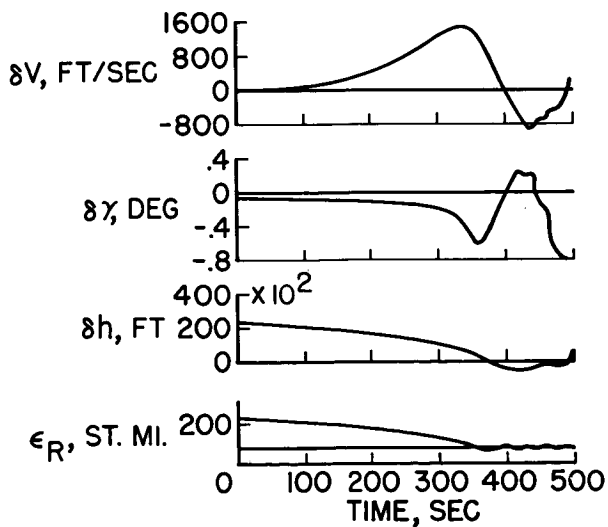


Figure 10

03712 [REDACTED]

PREDICTOR DECELERATION ACCURACY

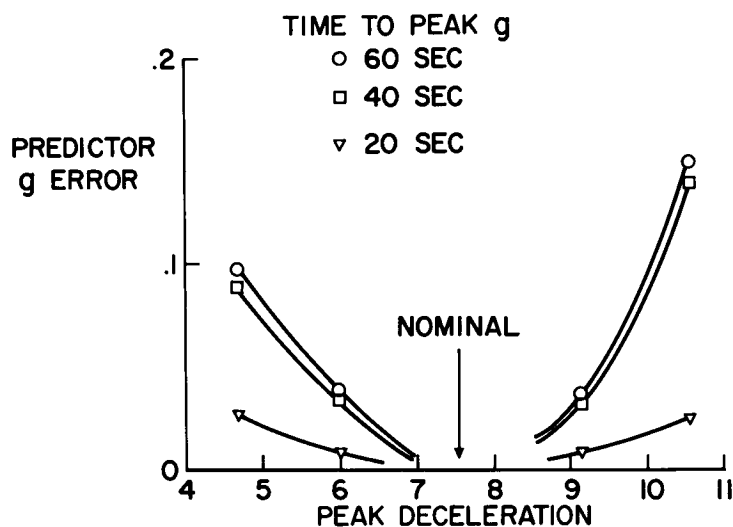


Figure 11

GUIDANCE DISPLAY

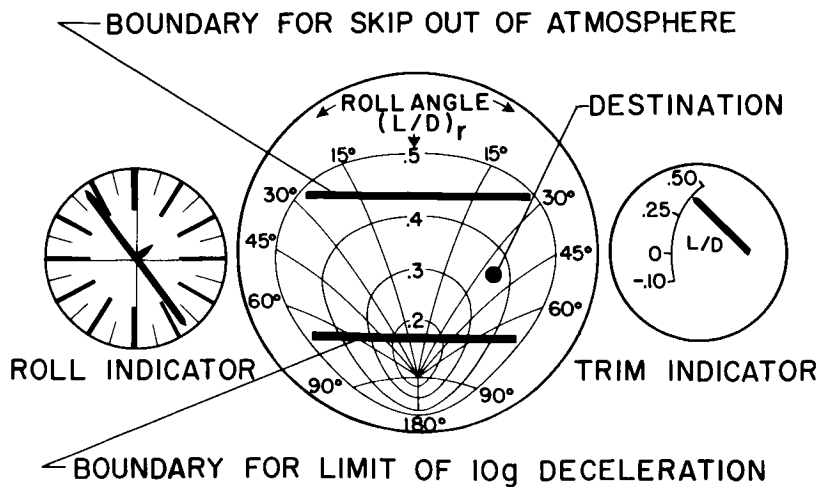


Figure 12

[REDACTED]

COMPARISON OF RANGE CAPABILITY FOR GUIDANCE SYSTEMS STUDIED

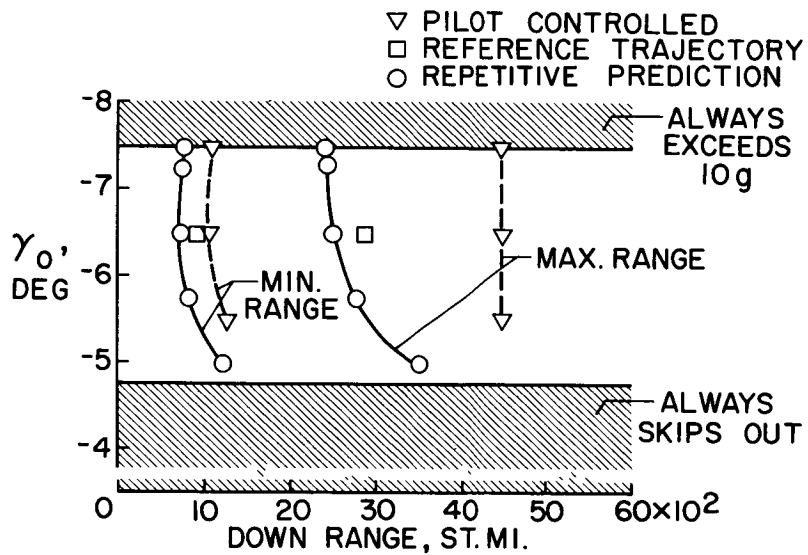


Figure 13

DECLASSIFIED

169

DYNAMIC STABILITY AND CONTROL PROBLEMS OF
PILOTED REENTRY FROM LUNAR MISSIONS

By Martin T. Moul, Albert A. Schy,
and James L. Williams

Langley Research Center

INTRODUCTION

In this paper some results are presented of a preliminary analog simulation study of dynamic stability and control problems during piloted reentry from lunar flight. One of the main purposes of the study was to investigate the ability of a human pilot to make a safe reentry in case of failures in the automatic damping equipment. Figure 1 presents a typical reentry trajectory at parabolic speed, which will be used to illustrate some of the basic control problems involved in making a safe reentry. This type of reentry has received considerable attention in trajectory studies of this problem and was chosen as the standard reentry task used to familiarize the pilots with the problem.

In the pull-out, the pilot held maximum lift until level flight was reached, in order to minimize the peak decelerations and heating rates occurring at this point. (Note that the heavy arrows indicate the required direction and relative magnitude of lift at various points on the trajectory.) During a steep pull-out the pilot will be subjected to a combination of high decelerations, rapidly varying dynamic conditions, and high natural frequencies which can lead to serious control problems. For shallow reentry angles, on the other hand, the critical problem is to avoid skipping out of the atmosphere. The steepest reentry angle considered was determined by limiting the maximum deceleration to 8g. The shallowest reentry angle was limited by the condition that available aerodynamic lift must be able to cancel the skipping tendency caused by the supercircular velocity.

After the pull-out, the pilot must make a transition maneuver to reverse the direction of vertical lift in order to maintain level flight as required in the slowdown portion of the standard trajectory. The two types of transition maneuvers considered in this paper are the roll-only maneuver, in which maximum trim angle of attack is maintained and vertical lift is controlled by bank angle, and the roll-pitch maneuver, in which the pilot rolls 180° and modulates angle of attack. After the transition maneuver, the pilot's two main problems are to learn to control the flight path accurately in the presence of the

13

03:15:20:12:30

varying centrifugal force and to control the tendency to increasing oscillations in damper-out conditions, which results from decreasing dynamic pressure. After passing through circular speed the lift is again upward, and the trajectory eventually ends in a final glide which was not considered in this investigation.

After the subject pilots had familiarized themselves with the basic control problems of the reentry, simulated range-variation maneuvers were introduced for the study of damper-out conditions. In the range-increase type of maneuver, the pilot entered at the steepest reentry angle and was commanded to pull up to an altitude above the pull-out altitude and level off. For range decrease, the vehicle entered at the shallowest angle and was commanded to pull down and level off. In addition, heading commands were sometimes included. These maneuvers are similar to those discussed in the previous paper on the pilot-controlled guidance system by Edwin C. Foudriat and Rodney C. Wingrove.

PILOT STATION AND DISPLAY

Figures 2 and 3 show pilot station and instrument display. In front of the pilot is the instrument display, while to his left is an X-Y plotter on which the vehicle trajectory was generated. This is a two-axis side-arm controller for pitch and roll control. Foot pedals were used for yaw control.

The details of the display are shown in figure 3. Initially the pilot uses the "8 ball" and α -meter to establish his proper roll and pitch attitude for reentry. He monitors his pull-out trajectory on the X-Y plotter. As level flight is approached, he observes h on this meter. As h goes to zero, he performs a 180° roll using the 8 ball and continues to hold constant altitude by varying angle of attack. For the task of climbing or diving to a designated altitude, this meter was used to display a quickened altitude error. Altitude error and rate were combined and used as a zero-reader instrument by the pilot to make accurate altitude changes.

While the display presented is by no means optimum, it was felt to be reasonably good. The two-axis hand stick and rudder pedals were reasonably satisfactory, but somewhat sloppy for attempting to damp high-frequency oscillations. The nonoptimum nature of controls and display should tend to make the results presented more conservative.

CONFIGURATIONS AND ANALOG PROGRAM

Figure 4 shows the vehicles considered in this investigation. These are rather simple examples of the two types of reentry bodies generally considered for the Apollo mission. The L-2C is a blunt-face, high-drag vehicle and the L-8 is a lifting cone. Each vehicle was designed with some vertical center-of-gravity offset to aid in pitch trim. The figure shows the maximum and minimum trim angles of attack, with the controls deflected appropriately. Both vehicles could be trimmed from $L/D = 0$ to $L/D = 0.5$. The L-2C used a small center-of-gravity offset and both upper and lower pitch flaps. For the L-8 a large center-of-gravity offset was assumed, so that it was self-trimmed at $L/D = 0.5$. A single lower flap was used to trim to $L/D = 0$. The rear view shows the pitch and yaw flaps in deflected position.

For roll control both vehicles were equipped with proportional reaction rockets. Above an altitude of 300,000 feet, proportional rockets were also included for pitch and yaw control. Full stick deflection produced accelerations from reaction rockets of $400/\text{sec}^2$ in roll and $40/\text{sec}^2$ in pitch and yaw. Constant gain automatic dampers about all three axes were included for altitudes less than 300,000 feet.

With the use of the roll-only maneuver, the L-8 vehicle has the capability of making entries with no aerodynamic controls as a result of its self-trimming feature, and some of these results will be presented.

The aerodynamic characteristics of the vehicles were determined from wind-tunnel tests and reported in a previous paper by Emanuel Boxer, Robert W. Rainey, and David E. Fetterman, Jr. The nonlinear aerodynamics considered for this investigation and programed on the analog computer were pitching moment as a function of angle of attack and pitch control deflection, chord force as a function of angle of attack, and $C_{n\beta}$ and $C_{l\beta}$ as functions of angle of attack.

In the analog set-up the chief aims were to obtain accurate trajectories and a good simulation of vehicle dynamics both with and without dampers. The axes system chosen were body axes for the moment equations and local horizontal axes for the force equations. Considerable attention was given to the problem of analog scaling and to the selection of high-response nonlinear equipment, multipliers and resolvers, by our analog computing personnel. As a result, good simulation of both vehicle dynamics and trajectory were obtained.

03171530:030

RESULTS

All Dampers In

Figure 5 shows trajectory results, as recorded on the X-Y plotter for the two extreme reentry angles, with all dampers in. Altitude is plotted in thousands of feet and range in nautical miles. Two cases shown are constant L/D reentries followed by level flight, which were used in pilot familiarization. The other two are a pull-up from a steep reentry and a pull-down from a shallow reentry into level flight, which were the typical range variation maneuvers used in most of the damper-out reentries. Brief consideration was also given to two more extreme altitude maneuvers, in which the pilot pulled down from a shallow reentry and leveled off at maximum g or pulled up to a very high altitude from a steep reentry. The pilot was also given a heading task to either hold 0° or to make a designated turn.

After a brief training period to become familiar with the vehicle control characteristics and the required maneuvers, the subjects were able to make all these reentries with complete consistency and with the accuracy shown here. Although not shown, similar results were obtained with the L-2C.

Effect of Damper Failure

Some results pertaining to emergency conditions in which damper failures were considered are discussed. For these reentries the task was to control the trajectory to a commanded altitude and heading angle. In the event of trouble in controlling motions, the pilots neglected the trajectory tasks and concentrated on making safe reentries. In controlling the vehicle the pilot attempted to damp large oscillations with his pitch and yaw controls. Table I summarizes these results.

The first column shows the damper condition and the second column, the rating. The damper-out conditions are listed in the order of increasing difficulty, and results are included for both vehicles using roll-only and roll-pitch maneuvers. In figure 6 trajectory results for four of the damper conditions are presented.

With all dampers in, both vehicles are rated satisfactory. With the yaw or roll damper out, the subject was able to keep the lateral oscillations small with a minimum of attention. He still did a good job of flight-path control. With the pitch damper out or roll and yaw out, the subject had to devote more time to controlling the dynamic

variables. However, a reasonably good job was done of controlling the trajectory, as seen in figure 6(a) for the pitch damper out. For the remaining conditions, successively more time and effort had to be devoted to controlling dynamics and this result can be seen in figure 6(b). Even though the last five cases shown in table I carry the same rating, an extreme degradation of control capability exists between the top and bottom conditions. The pitch-damper-out condition is not very far removed from the acceptable category, whereas considerable practice and training were required in order to make successful reentries with all dampers out. With all dampers out, proper techniques of making control motions in a smooth and gradual manner to minimize disturbances and of using pitch and yaw controls to damp oscillatory motions were important for keeping the vehicles under control. It was also generally noted that the use of roll-only maneuvers with the all-dampers-out condition result in better controlled reentries.

In this investigation no consideration was given to the condition of dampers failing during the run. From X-15 simulator studies, such failures sometime resulted in dangerous situations and consideration should be given to such conditions in future investigations.

Vehicle Dynamics

Before leaving the discussion of damper-out controllability, one significant qualitative difference between the lateral characteristics of the L-2C and L-8 should be mentioned. This difference is attributable to the very large difference in the dihedral effect $C_{l\beta}$ of the vehicles: -0.086 for L-8 and -0.006 for L-2C. Figure 7 shows that the L-8 vehicle, because of its relatively large dihedral, presented a much more difficult roll-control problem than the L-2C. In this maneuver the pilot was performing a steep reentry with no aerodynamic damping. He attempted to maintain a 180° bank angle for a while, followed by 0° . Note the irregular and larger ϕ and p variations and more frequent roll-jet operation for the L-8 even though the β magnitudes are almost identical. In fact, only one β is shown, for convenience.

The larger dihedral of the L-8 is partly caused by the larger center-of-gravity offset assumed, but a more important factor is the larger side-force coefficient $C_{Y\beta}$ which acts through the center-of-gravity offset to provide the large $C_{l\beta}$ dihedral effect. By simple Newtonian-flow theory, it can be seen that the L-2C, because it flies blunt-face forward, develops very small forces normal to its axis of

031713201230

symmetry, whereas the L-8 can develop large off-axial forces. Figure 8 shows the effect of this difference in configurations on the off-axial accelerations imposed on the pilot. (Note that the time scale on this figure starts when the rolling motion is initiated.) Presented in this figure are the normal, lateral, and longitudinal accelerations, beginning at the time of the first roll maneuver. The L-2C has no off-axial accelerations, whereas the L-8 has an appreciable normal acceleration, and a lateral-acceleration oscillation. This level of lateral acceleration would not appear to present any difficulty with a well designed body-restraint system.

There are two reasons why the lateral accelerations are not larger in this reentry. The first is that the runs shown are rather well-controlled examples for the damper-out condition, as can be seen by the small sideslip angle developed. The second reason is that the pilot's standard damper-out task for a steep reentry was to climb 25,000 feet immediately after pull-out. This caused the dynamic pressure to drop just as the oscillations built up. Figure 9 shows the sort of accelerations that might result if both these factors were less favorable.

In this case the pilot performed a maneuver which represented an attempt at extreme shortening of range. He entered at a shallow flight-path angle, but maneuvered to pull down and level out at 150,000 feet with maximum g. Also, the maneuver was not as well controlled as the others shown. The motions shown are angle of attack, sideslip, normal, and lateral accelerations, all of which became oscillatory at high dynamic pressures. The large lateral accelerations in this run (a maximum of 1.4g) would certainly represent a serious problem. This problem needs to be investigated more closely using a human centrifuge to determine if such effects are significant enough to influence the choice of a configuration.

Another problem related to the dynamic characteristics of the vehicles was encountered with the L-2C. With this vehicle, a divergence in angle of attack sometimes occurred when a roll maneuver was initiated at very low dynamic pressure. Figure 10 shows a reentry at a shallow reentry angle (-5.25°), in which the subject performed a 180° roll at an altitude of 300,000 feet, in order to pull down to a lower altitude. Time histories are presented of dynamic pressure, bank angle, and angle of attack. In performing the roll at low q, large transient motions in angle of attack and sideslip occur, as the vehicle rolls about its principal body axis. Eventually the effect of the vehicle's static stability comes into play and returns the vehicle towards its trim condition, which was 30° . A large overshoot of the trim value occurred, and the vehicle reached an angle of attack at which it is statically unstable. The result is a divergence in angle of attack and loss of control. Solutions to this problem are: (1) perform rolls

for low dynamic pressure at 0° angle of attack, (2) restrict rolling to higher \bar{q} , (3) include sufficient damping to avoid such an overshoot, or (4) design the vehicle to have stable pitching-moment curve to a higher angle of attack.

Roll-Control Only Reentries

The L-8 vehicle, as mentioned earlier, is self-trimming at $L/D = 0.5$ and hence has the capability of reentering by using a roll maneuver and roll reaction controls only, that is, with no aerodynamic controls whatever. The L-2C with some modification could be controlled in this manner also. With three-axis damping the L-8 vehicle was flown in this manner with no difficulty, these results having been included in the all-dampers-in case of table I. In addition, entries were made in this mode in which no automatic damping was provided in either pitch or yaw.

Figure 11 presents such results for a shallow reentry. The pilot was given both an altitude and heading task. He did a good job of accomplishing the altitude task and had almost accomplished his heading task when the run was terminated. Although the pilot did a reasonable job of flight-path control, he rated this condition acceptable for emergency use only because of the undamped lateral oscillation, which can be seen in the β and p motions, and pilot effort required to control bank angle, which can be seen in the irregular ϕ and pilot input motions.

With all dampers out, reentries could also be safely made, as shown in table I.

Effect of Aerodynamic Damping

There is considerable controversy whether it is necessary to obtain data on rotary derivatives (such as C_{mq} , damping in pitch, and C_{nr} , damping in yaw) for accurate simulation of reentry-vehicle dynamic characteristics. The general opinion seems to be that they can have no importance at these speeds. In this simulation, values obtained from limited wind-tunnel studies were used. For the L-8, for example, stable values of C_{nr} and C_{mq} equal to -0.7 were obtained. To see whether rotary derivatives of this magnitude could have any significant dynamic effects, a number of L-8 damper-out reentries were run with the algebraic sign of these quantities reversed.

In figure 12, results are shown for a steep reentry. With the unstable damping values, the motions are much more divergent and the



pilot soon lost control of the vehicle. These preliminary results indicate that rotary derivatives can still be important in the marginal damper-out conditions, even at these extreme speeds.

CONCLUSIONS

Although a good dynamic simulation was obtained for this investigation, the limitations of a fixed base simulation are recognized, and during the course of Apollo development, more extensive simulator programs will be required employing angular motion simulators and human centrifuges to further investigate problems of the types considered herein. It is hoped that the results of the present study will have a significant input into those studies by better defining the range of capabilities of a human pilot with regard to the basic control and guidance tasks and also in emergency conditions.

The following conclusions are indicated by the results of this preliminary investigation:

1. With all dampers in, both the L-2C and L-8 can be controlled through reentry, with altitude and heading tasks being accomplished with precision.
2. Both vehicles with all dampers out could be controlled to some degree and were rated satisfactory for emergency operation.
3. The existence of excessive dihedral effect makes the precise control of bank angle a difficult task for conditions of dampers out, as shown by the example of the L-8.
4. In damper-failure conditions, lifting-cone vehicles may encounter appreciable oscillatory accelerations. The effects of such accelerations require investigation in a human-centrifuge program.
5. The performance of rolling maneuvers at low dynamic pressures with vehicles having unstable pitching-moment curves at high angles of attack may result in a divergence and loss of control, as shown by the L-2C example.
6. Required reentry maneuvers can be satisfactorily performed without any aerodynamic controls by using vertical center-of-gravity offset to trim at required lift-drag ratio and roll reaction controls to make rolling maneuvers.

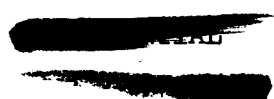


TABLE I

EFFECT OF DAMPER CONDITIONS
ON CONTROLLABILITY

DAMPER CONDITION	CONTROLLABILITY
ALL IN	SATISFACTORY
YAW OUT	ACCEPTABLE
ROLL OUT	ACCEPTABLE
PITCH OUT ROLL AND YAW OUT PITCH AND YAW OUT PITCH AND ROLL OUT ALL OUT	ACCEPTABLE FOR EMERGENCY OPERATION

CONFIDENTIAL

STANDARD REENTRY TRAJECTORY

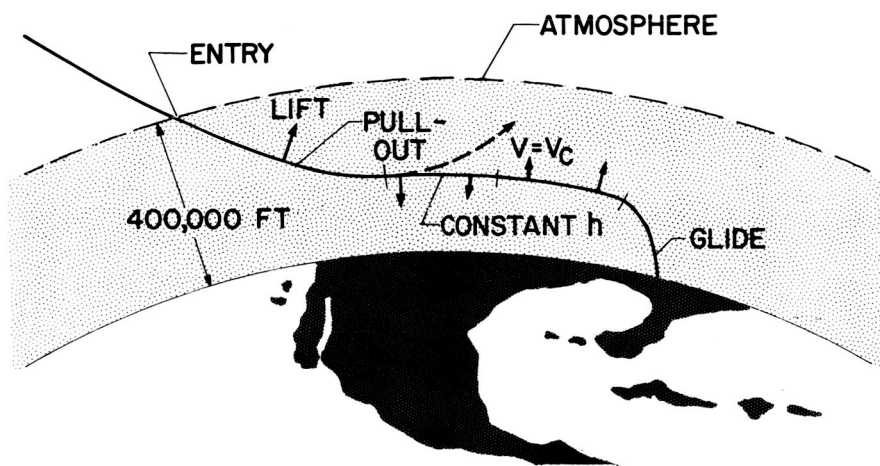
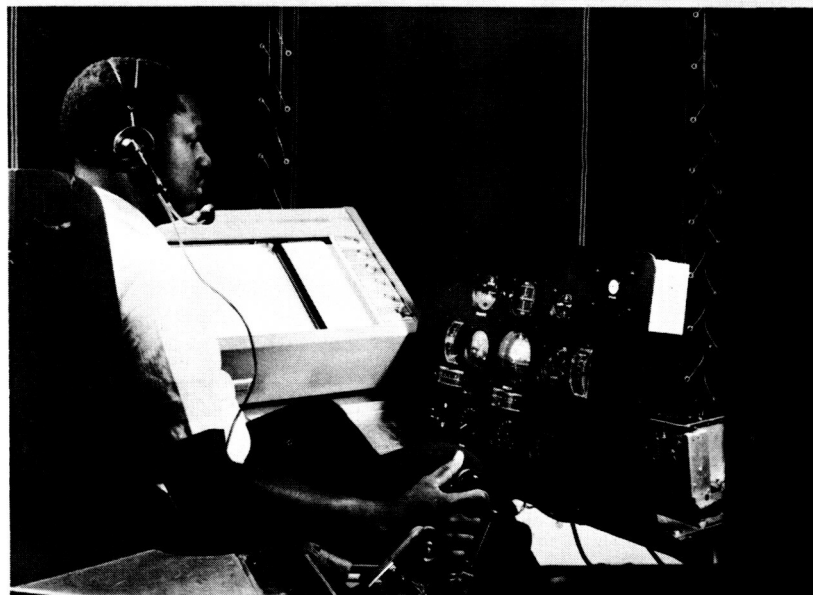


Figure 1

SIMULATED COCKPIT



L-61-4183

Figure 2

CONFIDENTIAL

DECLASSIFIED

INSTRUMENT PANEL

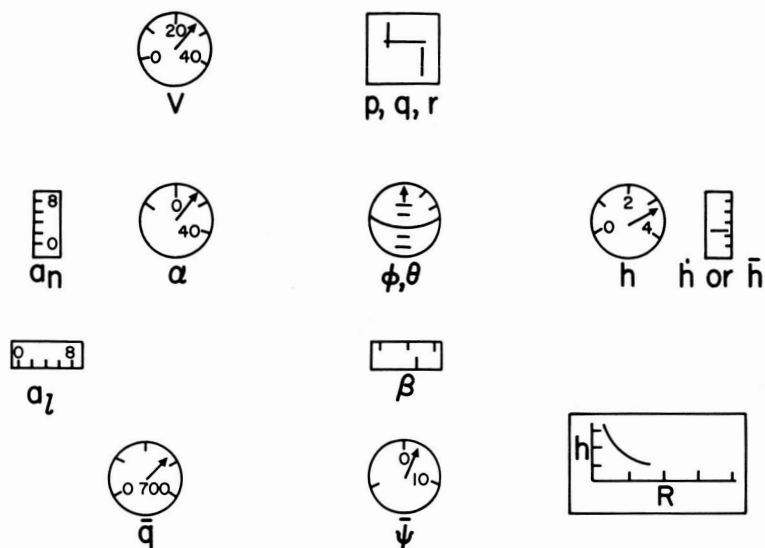


Figure 3

REENTRY VEHICLE CONFIGURATIONS

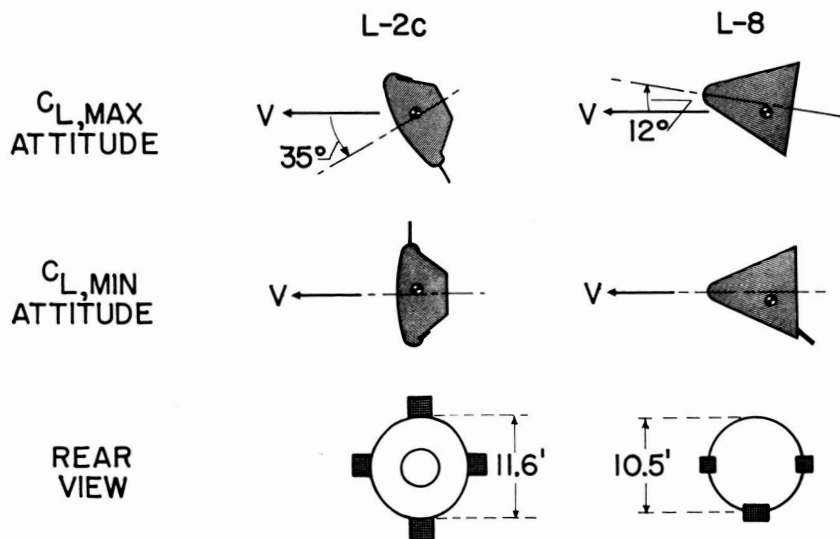


Figure 4

031712341930

TRAJECTORY RESULTS WITH AUTOMATIC DAMPING CONFIGURATION L-8

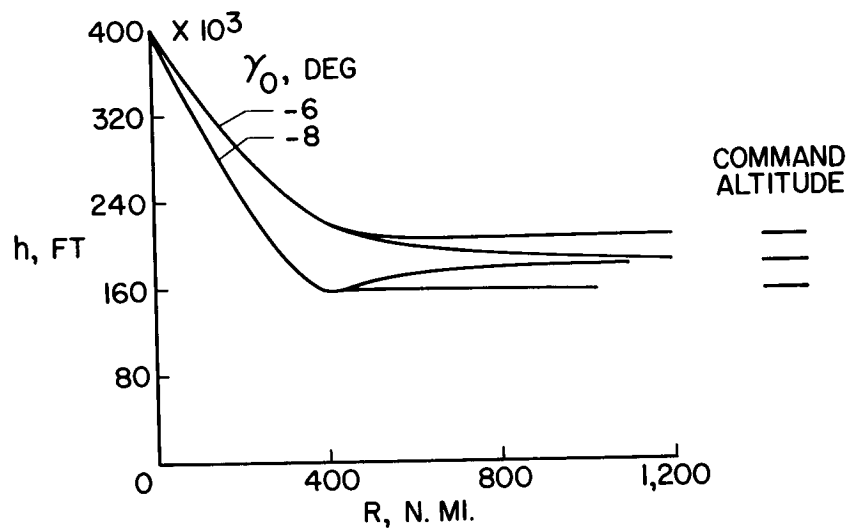


Figure 5

EFFECT OF DAMPER CONDITION ON TRAJECTORY CONFIGURATION L-2C

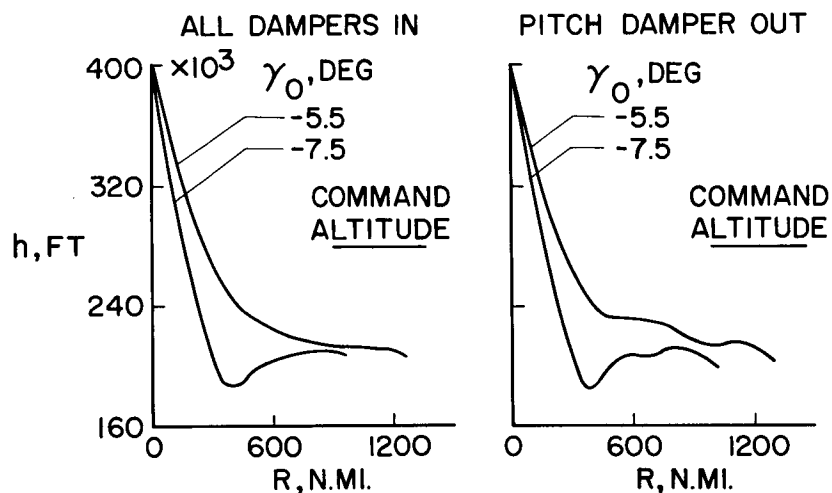


Figure 6(a)

EFFECT OF DAMPER CONDITION ON TRAJECTORY

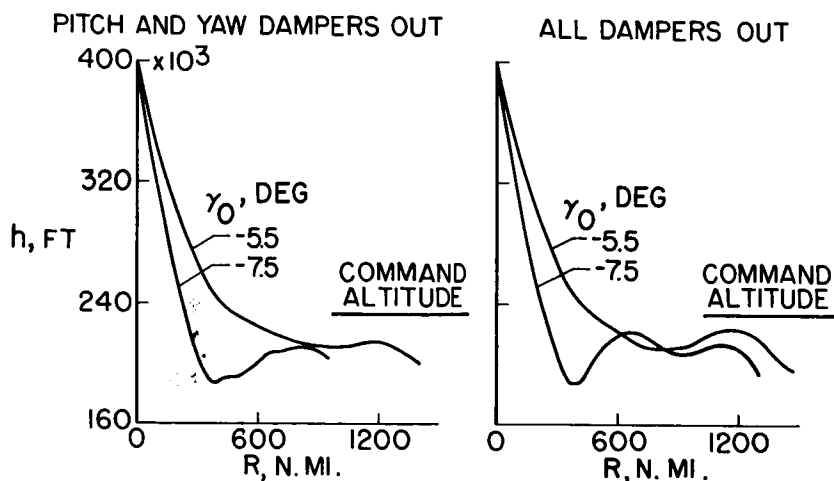


Figure 6(b)

The figure consists of four vertically stacked plots sharing a common x-axis labeled "TIME, SEC" ranging from 0 to 250. The top plot shows ϕ , DEG, with a y-axis from 0 to 200. It features two curves: a solid line labeled "L-2C" and a dashed line labeled "L-8". Both curves start at 0, rise to a peak of approximately 200 degrees around 20 seconds, and then gradually decay towards 0. The L-8 curve shows more initial oscillations. The second plot shows β , DEG, with a y-axis from -5 to 5. It displays high-frequency oscillations centered around 0, with the amplitude decreasing over time. The third plot shows ρ , DEG/SEC, with a y-axis from -20 to 20. It shows oscillations that start with a large amplitude (up to 20) and decay towards 0. The fourth plot shows a, p , DEG/SEC², with a y-axis from 0 to 0 (implying a range around 0). It shows small-amplitude oscillations centered around 0.

EFFECT OF DIHEDRAL ON ACCELERATION COMPLEMENTS

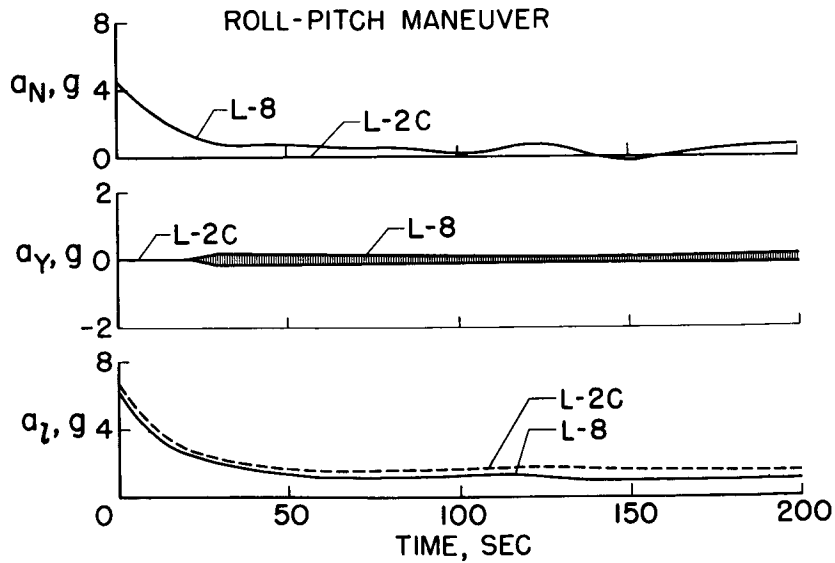


Figure 8

L-8 REENTRY WITH LARGE LATERAL ACCELERATIONS

$\gamma_0 = -6^\circ$; ALL DAMPERS OUT

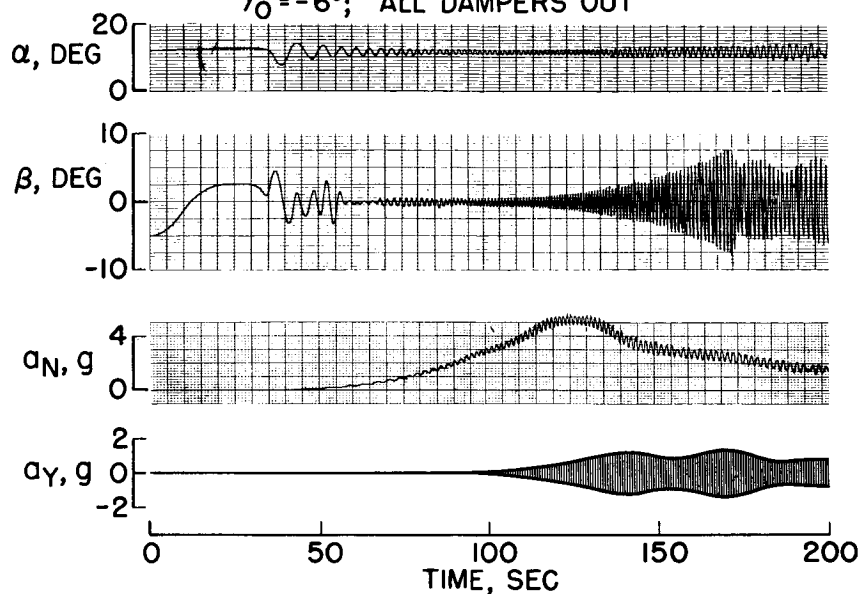


Figure 9

PITCH DIVERGENCE OCCURING IN ROLL MANEUVER AT LOW DYNAMIC PRESSURE

CONFIGURATION L-2C; $\gamma_0 = -5.25^\circ$

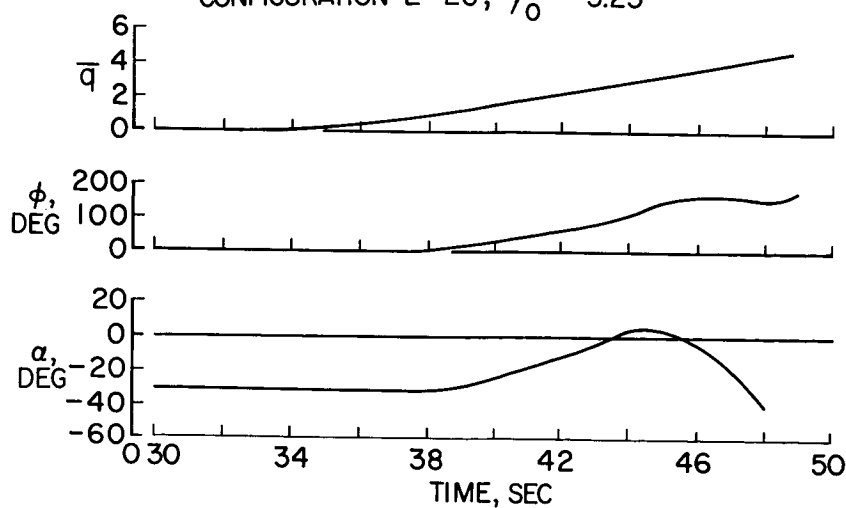


Figure 10

0371020000

REENTRY OF L-8 USING ROLL-CONTROL ONLY $\gamma_0 = 6^\circ$; ROLL DAMPER ONLY

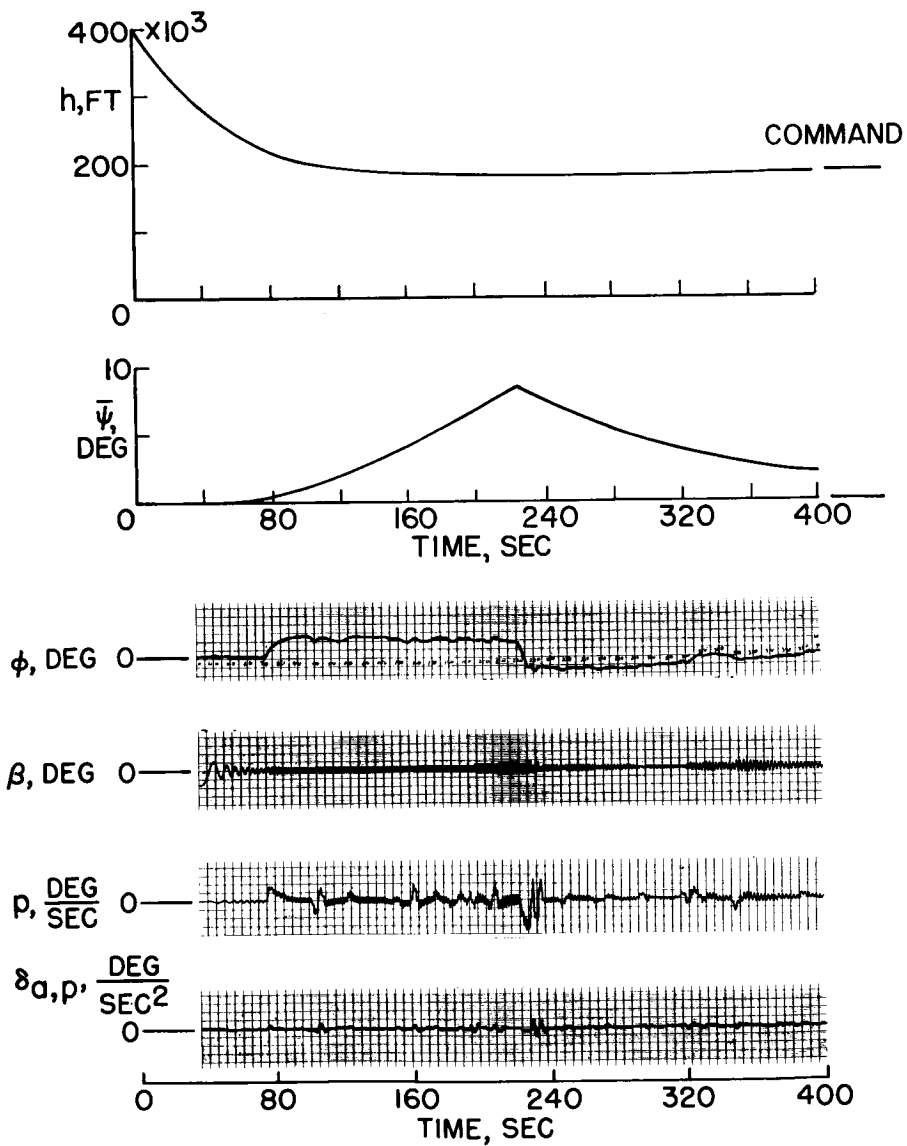


Figure 11

EFFECT OF AERODYNAMIC DAMPING ON CONTROLLABILITY
CONFIGURATION L-8; ALL DAMPERS OUT; $\gamma_0 = -8^\circ$

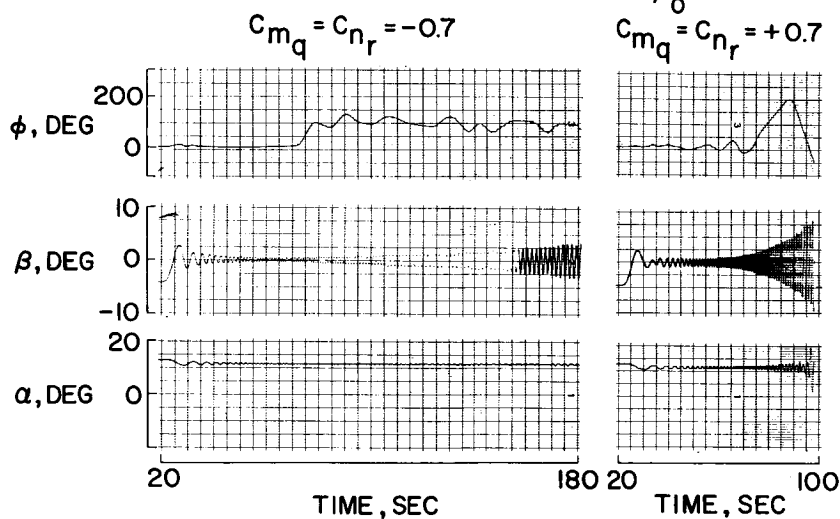


Figure 12

INFLUENCE OF SUSTAINED ACCELERATIONS ON CERTAIN
PILOT-PERFORMANCE CAPABILITIES

By Brent Y. Creer and Joseph G. Douvillier, Jr.

Ames Research Center

INTRODUCTION

In accordance with the established Apollo guidelines, it is desired to use the pilot as a primary element in the control of the Apollo vehicle. If it is assumed that the pilot will be used to control the Apollo vehicle in the atmosphere entry maneuver, certain fundamental questions must be answered relative to the influence of acceleration forces on the pilot. Among those questions are (1) How should the pilot be positioned in the vehicle in order to best withstand the applied g load; (2) What are the maximum periods of time a pilot can tolerate various selected levels of acceleration force while performing his control function; (3) What are the maximum rates-of-onset of the acceleration force to which the pilot should be subjected. It would be desirable to evaluate the precise Apollo piloting tasks in the precise Apollo acceleration stress environment. However, the Apollo vehicle is not defined clearly enough for such an evaluation.

There remains at least two alternate ways to proceed. One method which might be used is to place the test pilot in the desired acceleration-force environments and continue the test until the pilot fails physically and the required limit point is defined. A second approach would be to place the pilot in the desired acceleration-force environment and require the pilot to perform an arbitrary task which might not match the Apollo piloting task exactly, but which would be sufficiently difficult to increase the pilot's sensitivity to acceleration as measured by a sudden fall off in task performance and which could be used to weigh the answers to the posed questions. If the selected task were sufficiently difficult, a degradation in pilot performance would occur well before any physical endpoints were encountered.

The National Aeronautics and Space Administration has a general program to study the effects of acceleration on the pilot of a space vehicle. As part of this research program, a rather extensive investigation of the effects of acceleration on pilot performance and pilot physiology was conducted on the Johnsville human centrifuge by the Ames Research Center. This program was very general and was not directed at any specific vehicle. However, certain results from this general program have been selected, and will be used in the manner just discussed,

in an attempt to answer the subject questions, which are pertinent to the Apollo project. That is, the approach used in this study was to provide the subject test pilots with a very difficult control task, which, although probably not representative of the actual Apollo vehicle piloting tasks, certainly produced the desired effects of causing a measurable deterioration in pilot performance well before a physical tolerance limit was reached.

In this paper, the vernacular of the test pilot has been used to describe the direction of the applied acceleration force. The terms "eyeballs in" (EBI), "eyeballs out" (EBO), and "eyeballs down" (EBD) correspond to acceleration fields A_X , $-A_X$, and A_N , respectively, where A_X , $-A_X$, and A_N refer to the direction of acceleration forces measured in the conventional airplane body-axis coordinate system.

APPARATUS

The Aviation Medical Acceleration Laboratory Centrifuge, Naval Air Development Center, Johnsville, Pa., was used in this research program to investigate the pilot control problems associated with the atmosphere reentry of space vehicles. For a fairly detailed description of the centrifuge, see references 1 and 2.

It is self-evident that the ability of the pilot to perform while immersed in high-sustained-acceleration-force fields and his tolerance-to-acceleration limits are critically dependent upon the quality of the pilot's restraint system. In order to insure the maximum in pilot performance, a development program was initiated to provide an integrated mobile pilot restraint system. An earlier pilot restraint system, developed by the Ames Research Center and described in reference 3, utilized a moulded couch arrangement similar to the Mercury system but with what is regarded as an improved anterior restraint system to provide support for the eyeballs-out (EBO) g-field direction. The present system relies heavily on the experience gained in using the previously described restraint system.

The presently evolved pilot restraint system was designed with the following two general points in mind. In essence, the restraint system must not only provide maximum protection to the pilot, but must also reduce to a minimum any deterioration in the pilot's ability to perform. The specific design specifications were as follows:

- (1) The system should provide adequate restraint over a wide g-range for EBO, EBI, and EBD accelerations and any combination thereof.

(2) The system should be compatible with the required respiration and cardiovascular measurements being contemplated.

(3) A given restraint unit should fit a wide range of sizes of pilots.

(4) The system should allow the pilot to be quickly connected to, or disconnected from, the main support system.

(5) Release from the support system should be manually actuated by the pilot.

(6) The restraint system should allow adequate movement for all piloting functions.

(7) The ease of ingress and egress from the vehicle should be a prime consideration in the design of the restraint system.

(8) The weight and bulk of the restraint system should be held to a minimum.

The pilot's restraint system was composed of two major items, namely, the pilot's restraint suit and the restraint-suit support structure. The restraint suit which could be donned and worn as a piece of personal gear is shown in detail in figure 1.

The restraint suit featured a helmet which consisted of a rigid facepiece and a backpiece which were hinged on each other. A transparent lens and a latched door were suitably located in the helmet frontpiece. The purpose of the door was to allow the pilot to expel debris in the event of vomiting. A high level of pilot comfort during eyeballs-out accelerations was provided by a facial insert which fit into the frontpiece of the helmet and which was contoured to each individual pilot's face. A padded plate supported the back of the pilot's head during the EBI accelerations. An airtight space was provided around the pilot's mouth and nose so that a controlled breathing mixture could be given the pilot (as in a conventional airplane oxygen system).

Protection against eyeballs-in accelerations was provided by a series of shell-like supports which fit over the pilot's back and legs, labeled in the figure as back frame, thigh supports, and back-frame cover. A desirable feature of this system was that a given suit would fit a wide range of pilot sizes. This was accomplished by a set of bladders, placed between the back support and the pilot. Upon inflation, the bladders conform closely to the shape of the individual pilot. A fabric bib, pelvic strap, and modified g-suit provided protection against eyeballs-out and eyeballs-down accelerations. The upper thighs

03:15:30.1334
[REDACTED]

were restrained by a broad cover which was zippered over the front of the upper leg. Knee restraint was accomplished by a metal cap contoured to the approximate shape of the front of the bended knee, with the metal knee cap secured by an appropriate arrangement of straps.

The hand and arm were restrained by a cuff which was laced and zippered over the pilot's forearm. The cuff embodied the "Chinese magic chain principle"; that is, the tension of the cuff around the forearm increased with an increase in the applied load. The cuff was attached to a pendulum which acted to counterbalance the mass of the pilot's arm during EBO acceleration.

Foot restraint was accomplished by securing the feet into a set of toe pedal devices. These toe pedals were attached to the restraint-system support structure.

With the pilot dressed in the suit as shown in figure 2, he could walk to the centrifuge gondola and be quickly connected to the support structure. This quick connection was accomplished by a series of tapered pins which were anchored to the restraint suit and helmet (see fig. 2) and which were inserted and locked in corresponding receptacles located in the support structure.

It appears that some of the basic concepts incorporated in the Ames restraint system would also be useful in the design of a restraint system for an orbital or space vehicle. It has the capability of quick donning and rapid attachment to or release by the pilot from the basic support, which is highly desirable for use in any type of vehicle. However, since movement about in a shirt-sleeve environment would be a desirable requirement in a flight vehicle, further simple modifications are necessary to facilitate the pilot's donning the fabricated torso and limb anterior restraints unassisted. The primary purpose of this support and restraint system has been to permit simulator studies of flight vehicle control under varying conditions of acceleration stress. For this, its primary function, it has performed well.

There are two main areas in which this current restraint system is untested, namely, impact accelerations and lateral transverse forces, either sustained or impact. It is probable that the present restraint, with certain modifications to the bladder system, will adequately protect the pilot against impact acceleration forces. A more complete description of the Ames restraint system is given in reference 4.

For all the pilot performance data presented in this paper, the pilot controls consisted of a finger-operated two-axis sidearm controller and toe pedals. A description of the finger-operated sidearm controller and of the toe-pedal controls is given in reference 5.

[REDACTED]

TEST CONDITIONS

The pilot flew the centrifuge as a closed-loop system; that is, for acceleration fields greater than $1g$, the centrifuge was driven in response to the pilot control inputs in such a way that the impressed linear accelerations varied in the same manner as the linear accelerations computed from the aircraft equations of motion. A detailed description of the closed-loop centrifuge operation is given in reference 6. The test setup was arranged so that the total g-field impressed on the pilot consisted of two separate components; to a specified constant (biased) g-field was added the computed perturbations in normal and side accelerations which resulted from the vehicle maneuvering about a given trim condition. The perturbations in side and normal accelerations were generally not greater than $\pm 0.5g$. In this experiment, the aircraft equations of motion described five degrees of freedom with the vehicle forward velocity assumed to be constant.

Prior to any high-g data runs, the subject pilots were conditioned to the effects of sustained accelerations and familiarized with the piloting tasks and riding the centrifuge. For the most part, the pilots were not exposed to acceleration levels over $6g$ during this familiarization period.

Prior to any centrifuge run, the subject pilots were given a fairly detailed briefing. The pilots were instructed to perform the piloting task continuously from the beginning of the run, through the complete acceleration-profile time history, up to the termination of the run. The subject pilots were instructed to terminate the run any time that they felt there was a marked deterioration in their ability to fly the vehicle. The pilots were also instructed to terminate the run at any time they felt that a real physiological problem existed, when physical discomfort reached a level that it precluded retaining effective control over the vehicle, or when anything of an untoward nature occurred. Specific medical instructions to the pilots were to terminate the run whenever there was a marked sudden loss of vision, whenever there was marked disorientation or vertigo, or if there was a sudden onset of pain in the chest. The project medical doctor monitored a certain pilot's physiological recordings and terminated the run at his discretion. The project engineer monitored the tracings of pilot task performance and terminated the run if the task performance deteriorated markedly.

A qualitative measure of pilot performance was obtained for these runs by having the pilot give a numerical rating on the controllability of the simulated vehicle, using a pilot-opinion-rating schedule similar to that presented in reference 7. In order to obtain a quantitative measure of the pilot's performance, a tracking task was utilized.

The pilot control task consisted of having the pilot fly a simulated entry vehicle and track a randomly driven target. A cathode-ray tube in the instrument panel was used to display the tracking task. The centrifuge runs began at the 6g level and, in general, progressed at 2g increments up to the maximum g level the pilot's physiological or psychological condition permitted.

DISCUSSION

Figure 3 shows a typical time history of a pilot-performance centrifuge run. As can be seen from the figure, the run was divided into three major segments. In that segment noted as "preacceleration" the pilot was required to fly the simulated vehicle and track the randomly driven target for 1 minute in order to establish a baseline on his tracking performance. The pilot continued to track the target during the onset of acceleration, while immersed in the g-field, and during the postacceleration period which extended 30 seconds after the decline of the acceleration. For nearly all runs, the rate of onset of acceleration was constant at 0.25g per second. The rate of decline of acceleration was fairly rapid and followed an exponential curve. It should be noted that the tolerance time was measured over that interval wherein the acceleration was within about 10 percent of the desired value.

A measure of the pilot's ability to track is shown in the second trace in figure 3. The pilot tracking score is presented on a qualitative scale, since the conclusions to be drawn from the performance data are of a relative nature.

About the only strong point which comes through from the tracking trace is the fairly marked deterioration in pilot tracking ability during and immediately after the onset of acceleration. This was most marked for the eyeballs-out runs; however, it did show up to a lesser extent in the eyeballs-in runs. This deterioration in tracking is apparently due, for the most part, to pilot vertigo, the vertigo sensations being caused by the angular rotations of the centrifuge gondola as the centrifuge was brought up to the desired operating speed. In figure 4, where the effect of g magnitude on pilot-tracking performance is shown, the pilot-tracking performance is measured during the latter portion of the run, after these vertigo effects have subsided.

The data in figure 4 have been presented from the viewpoint of shedding some light on the question of how should the pilot be positioned in the vehicle. The results obtained from an earlier centrifuge investigation (ref. 5) are shown in the figure by the crosshatched regions, and the results obtained from the present investigation are

shown by the plotted data points. The crosshatched regions cover data obtained for the EBI, EBO, and EBD accelerations for well-damped and lightly damped vehicle motions. The well-damped case corresponds to a fairly easy control task and the lightly damped case corresponds to a fairly difficult control task. The conclusions drawn from reference 5 were that, to a first approximation, the pilot tracking score was independent of the direction of the applied acceleration investigated. The pilot tracking score deteriorated markedly at accelerations greater than $4g$ for a lightly damped dynamic situation. Finally, it appeared the the more difficult control task greatly magnifies any deficiencies in the pilot's performance. For the present investigation the simulated vehicle motions were well damped and the general trend of the plotted data points should be compared with the upper crosshatched curve (fig. 4). There is a fairly marked difference in the baseline tracking score between the two sets of data. This difference in baseline tracking is attributed primarily to the fact that in the present study the pilots were required to track the target in pitch and azimuth, whereas in the original study the pilot was required to track the target in pitch only.

The general trend of data obtained in the present study would tend to confirm the results of reference 5. When flying this well-damped vehicle, there was a moderate drop in tracking performance with increases in the magnitude of the g -field for the EBO and EBI g -field directions. At $14g$ EBI, the pilot could momentarily control the vehicle quite effectively; however, his tracking performance was considerably lower than that in the earth's $1g$ field. The tentative interpretation of the pilot tracking capabilities was that, with the given vehicle dynamics, the pilot could adequately control the aircraft while immersed in an EBI acceleration field of $14g$. Although only a preliminary amount of data has been worked up at this time, it appears that at least up to the $10g$ level there is little or no difference in performance between pilots operating in an eyeballs-out or an eyeballs-in g -field direction.

The second worthwhile point shown in figure 4 is that there was a marked deterioration in the measured pilot performance for g levels above 7 for the eyeballs-down g -field direction. At the $7g$ level, the subject's ability to see was greatly reduced, and at the 8 and $9g$ levels, the subjects were on the verge of unconsciousness. One of the major objectives of this program was to determine the maximum acceleration level beyond which the pilot could not do an effective job of manually controlling the vehicle. The abrupt falling off of pilot performance when immersed in a 7 to $8g$ eyeballs-down acceleration-force field is a good demonstration of this point.

Figure 5 presents the pilot-performance boundaries established by the Ames investigation. The term "pilot-performance boundaries" is

used since these curves are based on the longest time the subject pilots could manually fly the vehicle in a given g-field with no marked deterioration in their performance. However, these boundaries essentially define the longest periods of time a test pilot, preconditioned to the effects of acceleration and suitably restrained, would voluntarily endure a given sustained g level and perform any kind of a control task. The pilot's posture upon which these boundaries are based is shown in the figure. The normal seated position was used for eyeballs-in and eyeballs-out runs. For the eyeballs-down runs, the pilot's lower legs were elevated in order to minimize the pain and reduce the hydrostatic pressure in the pilot's feet. An anti-g garment was worn by the test pilot subjects during the eyeballs-down runs.

The pilot can perform longer with the acceleration forces applied in an eyeballs-in or eyeballs-out direction, as compared with the eyeballs-down direction, substantiating a well-established conclusion. The limit boundaries would also indicate that for a given acceleration force the pilot can perform longer in an eyeballs-in g-field than if the force is applied in an eyeballs-out direction. From the Ames tests it was documented that the pilot's respiratory efficiency was higher in the eyeballs-out g-field as compared with that in the eyeballs-in g-field direction. However, an overriding point was that the pilot's visual problems were greater for the eyeballs-out g-field direction. In the eyeballs-out runs, watering of the pilot's eyes could obscure the pilot's vision to the extent he could no longer see the disturbed target clearly. The fact that the eyeballs-out boundary lies below the eyeballs-in boundary seems to be a direct consequence of this visual problem. These points are discussed in detail in the following paper by Harald A. Smedal, Terence A. Rogers, and Thomas D. Duane.

It appears that a pilot could not manually control the vehicle for any extended period of time at acceleration levels in excess of 7 to 8g eyeballs down. The cut-off boundary for the eyeballs-out or eyeballs-in g-field direction was not determined. It appeared from this investigation that a well-trained pilot could still do a fair job of tracking the target between the 12 and 14g level for the eyeballs-in g-field direction. However, from figure 4, it is seen that his tracking performance at 14g was substantially lower than that of his baseline tracking performance in the earth's 1g field. Medical opinion was that it would be inadvisable to expose a pilot to g levels greater than 14 if the given pilot restraint system is used.

In figure 6, the acceleration levels and period of time these acceleration levels must be sustained during entry into the earth's atmosphere beginning at parabolic velocities are compared with the pilot performance limit boundaries. These curves are drawn for initial entry angles γ_1 ranging from -5.6° to -8.8° for a vehicle with

$L/D = 0.5$. It should be noted that these curves do not represent a time history. Perhaps the best way to explain these curves is to give an example. Given $\gamma_1 = -8.1^\circ$, the vehicle will sustain an acceleration force equal to or greater than $10g$ for 0.35 minute. In comparing these curves with the pilot-performance boundaries, it would appear that the pilot could, if properly positioned, perform and tolerate the acceleration levels expected during an atmosphere entry with the initial entry angle of -8.1° . With an entry angle of -8.8° there may be some question as to whether the pilot could physically tolerate the expected acceleration levels. The applicability of these tolerance boundaries to the case wherein the pilot is in a weightless condition for an extended period of time immediately prior to encountering a high sustained acceleration force is, of course, unknown at this time.

In figure 7 data are presented showing the effect of rate of onset of acceleration on pilot performance. Rate-of-onset values of $0.1g$, $0.25g$, $0.75g$, and $2g$ per second were investigated. The acceleration profiles to which the test pilot subjects were exposed are shown in the lower left of figure 7. The baseline tracking ability of the pilot was measured by having the pilot track the randomly driven target for 1 minute in a $2g$ force field. This was followed by the onset of the acceleration force up to an acceleration level of 5 or $8g$. Pilot vertigo, caused by the angular motions of the gondola as the centrifuge was brought up to the desired operating speed, was minimized by initiating the acceleration ramp from the $2g$ level. The tracking data were measured during the interval from the beginning of the ramp to the end of the ramp. The data presented were gathered for both the eyeballs-out and eyeballs-in g-field directions.

The trend of the data is quite consistent and shows a fairly rapid decline in the pilot's ability to track for acceleration onset rates greater than $0.75g$ per second. It might be noted that for a vehicle with $L/D = 0.5$ the maximum acceleration onset rate encountered during a $10g$ entry is approximately $1/2g$ per second. The extent to which these data were influenced by pilot vertigo caused by the angular motion of the centrifuge gondola is unknown. In the opinion of the test pilot subjects, the vertigo effects on the pilot's ability to track were nominal for this phase of the investigation.

CONCLUDING REMARK

This paper should be regarded as an interim report on the influence of accelerations on the pilot's ability to perform, and a considerable amount of acceleration research work is still required before an adequate store of information exists on which to base the Apollo vehicle design.

STAT

REFERENCES

1. Crosbie, Richard J.: Cam Designing for the Human Centrifuge. MA-5512, Aviation Medical Acceleration Lab., U.S. Naval Air Dev. Center (Johnsville, Pa.), Nov. 18, 1955.
2. Brooks, Charles E.: Data Sensing and Recording Techniques Established for the Human Centrifuge. MA-5306, Aviation Medical Acceleration Lab., U.S. Naval Air Dev. Center (Johnsville, Pa.), 1954.
3. Smedal, Harald A., Stinnett, Glen W., and Innis, Robert C.: A Restraint System Enabling Pilot Control Under Moderately High Acceleration in a Varied Acceleration Field. NASA TN D-91, 1960.
4. Alexander, George: NASA Develops High-Mobility Space Suit. Aviation Week and Space Technology, vol. 75, no. 1, July 3, 1961, pp. 57-59.
5. Creer, Brent Y., Smedal, Harald A., and Wingrove, Rodney C.: Centrifuge Study of Pilot Tolerance to Acceleration and the Effects of Acceleration on Pilot Performance. NASA TN D-337, 1960.
6. Woodling, C. H., and Clark, Carl C.: Studies of Pilot Control During Launching and Reentry of Space Vehicles, Utilizing the Human Centrifuge. Rep. No. 59-39, Inst. Aero. Sci., Jan. 1959.
7. Cooper, George E.: Understanding and Interpreting Pilot Opinion. Aero. Eng. Rev., vol. 16, no. 3, Mar. 1957, pp. 47-51, 56.

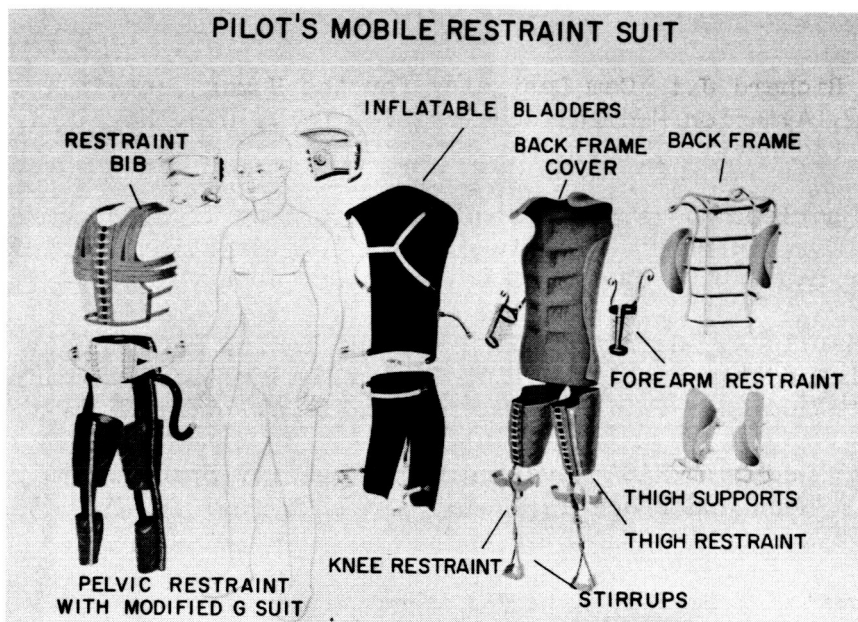


Figure 1

PILOT'S MOBILE RESTRAINT SUIT

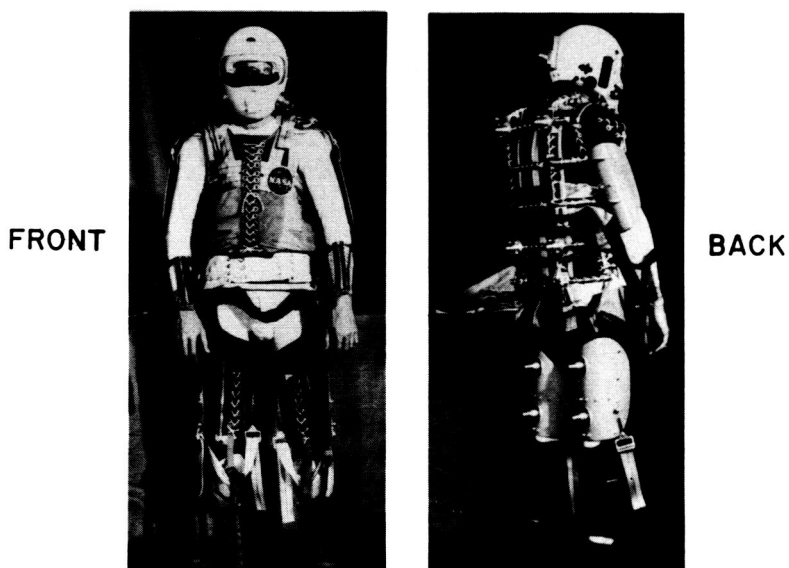


Figure 2

TOLERANCE AND PERFORMANCE RUN

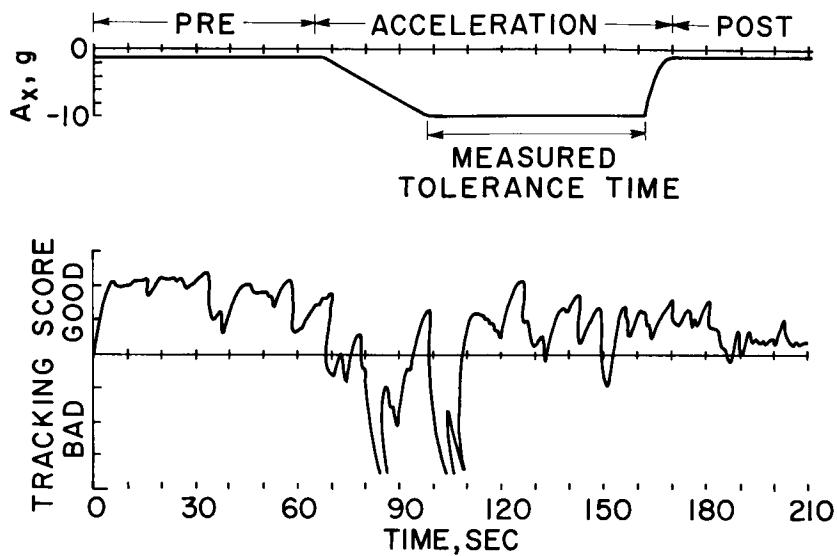


Figure 3

EFFECT OF ACCELERATION ON PILOT PERFORMANCE

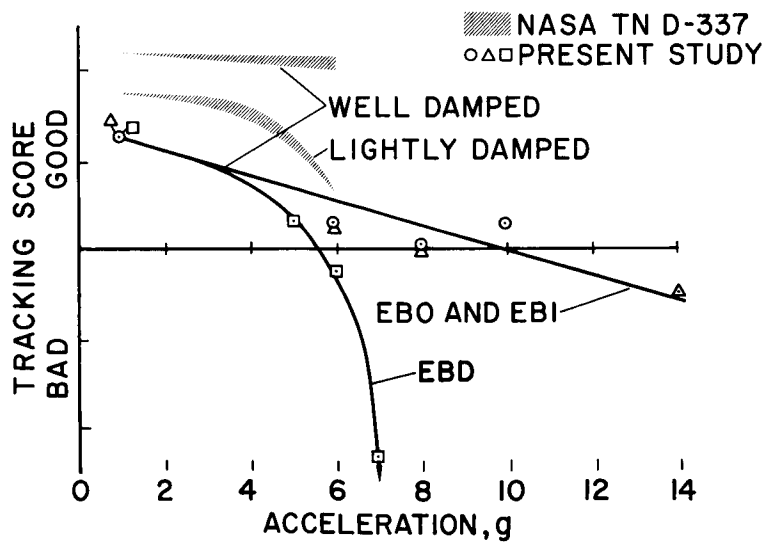


Figure 4

PILOT PERFORMANCE BOUNDARIES

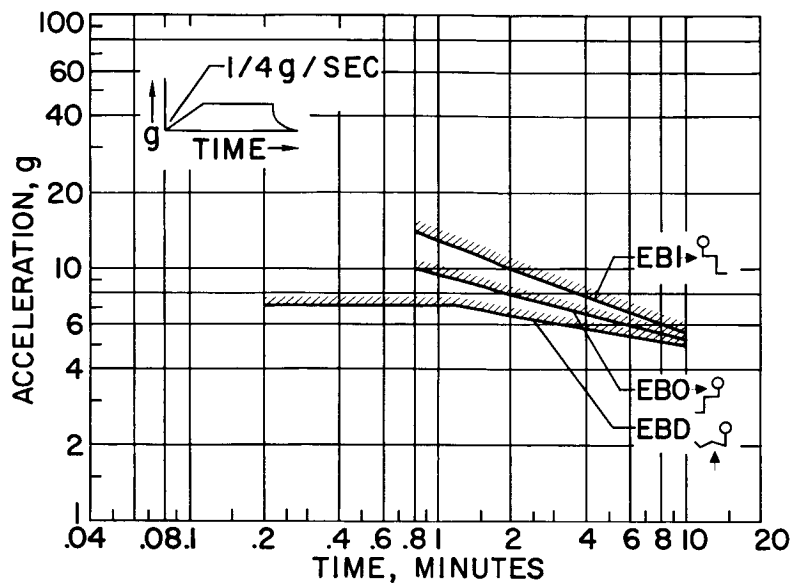


Figure 5

COMPARISON OF PILOT PERFORMANCE LIMITS WITH ACCELERATIONS DURING ENTRY

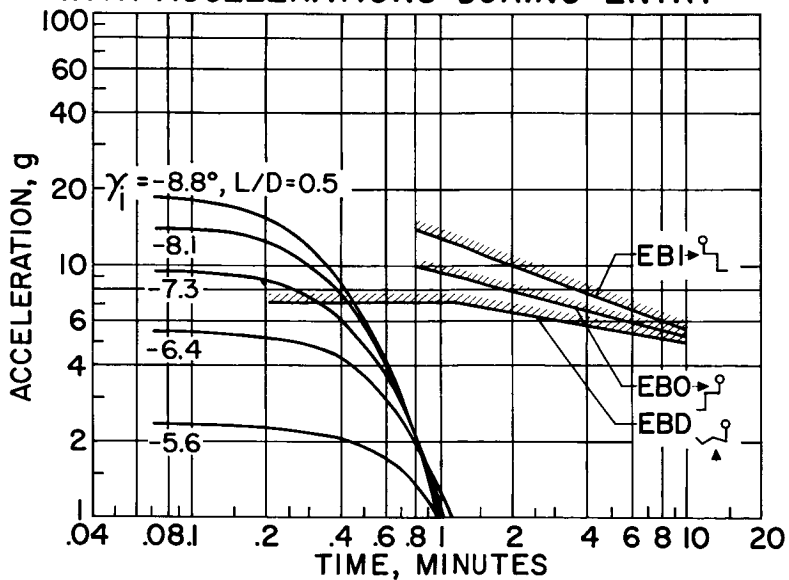


Figure 6

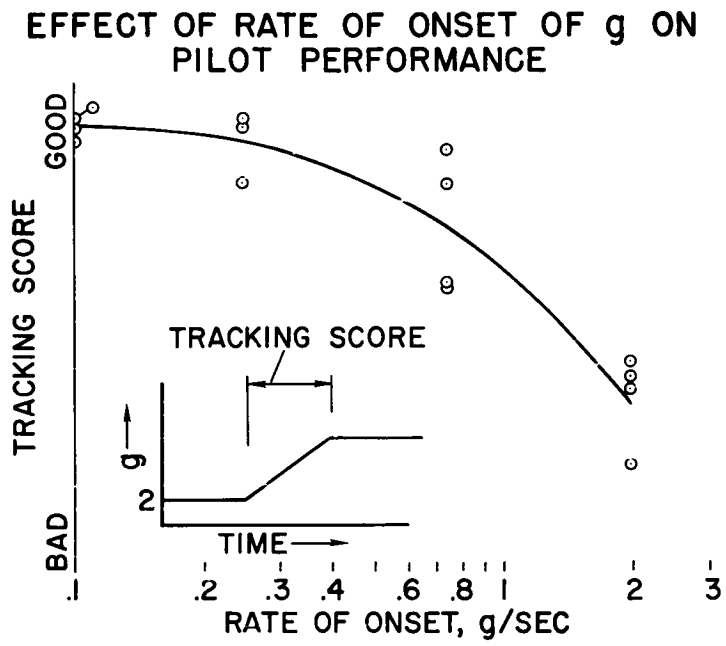


Figure 7

DECLASSIFIED

201

SOME PHYSIOLOGICAL FACTORS AFFECTING THE PILOT
UNDER HIGH SUSTAINED ACCELERATION

By Harald A. Smedal, Terence A. Rogers,
and Thomas D. Duane

Ames Research Center

INTRODUCTION

A study of the effects of acceleration on pilot performance conducted by the Ames Research Center has produced interesting corollary information about the effects of acceleration stress on the normal physiological functions of the pilot. It would be clearly unrealistic to attempt an evaluation of tolerance levels from performance data alone; it is also necessary to measure directly the physiological changes which cause the decline in psychomotor performance.

15

The acceleration stresses imposed upon the pilot during reentry will vary with the lift-drag ratio of the vehicle and with the pilot's orientation relative to the direction of motion of the vehicle. In the studies which have been submitted for the Apollo missions, both forward and rearward facing positions are proposed for the crew. It has also been made clear that the g-vectors will not be purely of the eyeballs-in, eyeballs-out, or eyeballs-down type (EBI, EBO, or EBD) but will be combinations of these applied accelerations. Experiments were planned, therefore, to yield both subjective and objective information about the physiological functions which are most apt to be the limiting factors in the pilot's tolerance to the accelerations likely to be encountered in orbital or lunar flight missions.

The purpose of this report is to present a brief summary of the physiological data obtained and to discuss the results in the light of the requirements for the Apollo missions. Preliminary reports have already been published as part of this continuing study. (See refs. 1 to 6.)

METHODS

The subjects in this study are qualified test pilots. Some of them had had previous centrifuge experience and all could be considered

~~CONFIDENTIAL~~

expert in their tracking skills and in their subjective evaluation of the overall problem. Their motivation was uniformly excellent, and in the tolerance tests, some subjects were highly competitive. It is appreciated that this is a select population, but nevertheless, one similar to that which will make up the Apollo crew members. With the exception of the visual tests, the physiological monitoring system was designed to operate concurrently with the tracking task and not to interfere with this performance assay. For obvious reasons, the visual tests had to be conducted during specially designed runs with the centrifuge under open-loop operation. The physiological tests were as follows:

a. Visual

- (1) Placido disc reflection on the cornea for distortion
- (2) Accommodation ability of the eye
- (3) Visual fields (subjective)
- (4) Visual acuity (objective and subjective)

b. Respiratory

- (1) Vital capacity
- (2) Tidal and minute volumes
- (3) Inspiratory pressure
- (4) Oxygen uptake
- (5) Carbon dioxide concentration in expired air
- (6) Nitrogen concentration in expired air
- (7) Functional residual capacity

c. Cardiovascular

- (1) Electrocardiogram and vector cardiogram
- (2) Blood pressure (systolic and diastolic)
- (3) Arterial pulse wave at eye level (ear pulse)

The monitoring instruments used in these studies are described in detail in reference 7. Continuous records of several quantities were obtained on an 8-channel recorder during each run.

~~CONFIDENTIAL~~

RESULTS AND DISCUSSION

It has been observed that when acceleration forces are applied at right angles to the spinal axis of the body (i.e., eyeballs-in or eyeballs-out acceleration), there is a decrement in visual acuity, depending on the magnitude and duration of the g-stress. This decrease in vision is a blurring, rather than the grayout experienced with eyeballs-down acceleration, and it has been attributed to (a) changes in curvature of the cornea, (b) changes in the position of the crystalline lens, and (c) tilting of the rods and cones in the retina; all three possibilities are the result of physical deformation of the eye.

It would be expected that the well-supported crystalline lens and the rods and cones are less susceptible to mechanical displacement than the cornea. Vision is particularly sensitive to corneal deformation because the cornea and the aqueous humor of the anterior chamber of the eye account for more than 75 percent of the refraction. Therefore, an experiment was designed in which the reflection of a placido disc on the cornea was photographed continuously under acceleration. This technique is described in reference 8.

The setup in the gondola of the centrifuge at Johnsville, Pa., is illustrated in figure 1. A movie camera was mounted behind the center of the placido disc so that the photograph was taken through the orifice in the center. Figure 2 shows a placido disc reflection on the cornea at 1g. A great many films were obtained of the corneas of four test pilots at 4g, 6g, and 8g EBO and EBI. Careful examination of the films revealed no distortion of the placido disc reflection due to corneal deformation, although at accelerations of more than 6g EBO, intermittent watering occurred which resulted in marked distortion of the placido disc reflections. These distortions are illustrated in figures 3 and 4. This watering, of course, leads to blurred vision for the pilot.

Another experiment was devised to evaluate the ability of the eye to accommodate under acceleration. A phoropter, a device used by an oculist to examine the eye and shown in figure 5, was modified so that a series of lenses could be rotated in front of the eye of the pilot. The normal eye can accommodate to give a clear image when lenses of a wide range of power are placed in front of it. This phoropter was modified so that the pilot could rotate spherical lenses in front of his eyes varying in power from 0 to 1.50 diopters. The pilot was then asked to read a properly lighted Snellen chart with appropriately sized letters at a distance of 1 meter. This test was carried out at 1g, 4g, 6g, and 8g EBO and EBI. The pilots' reports indicated that there was no decrement in their accommodation ability under acceleration; therefore, it is concluded that this capability is unaffected by accelerations of the aforementioned order of magnitude.

A recent experience on the centrifuge at Johnsville demonstrated a possible overall distortion of the entire eyeball. A nearsighted person with -4 diopters of myopia was given an 8g EBI exposure. The lines on the oscilloscope which were blurred at 1g became sharper in their outline. This would lead one to believe that the entire globe of the eye had been deformed. This time the deformity is advantageous, bringing the image to focus on the retina.

When accelerations of 8g, 10g, 12g, and 14g are encountered in both the EBO and EBI directions, the circulation of the blood to the eye is altered and the pilot experiences symptoms of grayout or blackout and a narrowing of the visual field. These symptoms are highly characteristic of EBD acceleration in excess of 4g or 5g. Figure 6 attempts to present graphically the overall visual problem under various acceleration stresses.

The investigations reported in references 3 and 4 have shown that there are some interesting respiratory changes when either EBI or EBO accelerations are applied to the pilot. In the study reported in reference 3, the pilots observed that ventilation of the lungs was easier during EBO than during EBI accelerations. These subjective impressions were borne out by the evidence of some simple pneumograph studies. In order to confirm these impressions, a closed-circuit breathing system was designed to measure under acceleration ventilatory excursions, oxygen uptake, and carbon dioxide and nitrogen output on a breath-by-breath basis. Figure 7 shows that in EBO acceleration there is only a minor decrement of vital capacity up to 6g, whereas during EBI acceleration, the vital capacity is decreased to a very small volume. Figure 8 shows that the minute volumes were fairly well maintained up to 8g EBI, although the actual ventilation of the alveoli in the lungs must decrease as the tidal volume approaches the volume of the dead space of the airway. With EBO acceleration, the minute volume actually increases.

Data obtained very recently at higher levels of EBI acceleration (10g, 12g, and 14g) demonstrate clearly that the tidal volume is reduced to very little more than the pulmonary dead space. Therefore, at 10g or more, alveolar ventilation is seriously diminished and the pilot is probably suffering from "acceleration hypoxia." One subject reported symptoms similar to environmental hypoxia when subjected to an 8g EBI run with a slow rate of onset (0.1 g/sec). Figure 9 shows actual time histories of 6g EBI and EBO compared with 1g EBI in the same subject. This figure also illustrates the character of the respiratory excursions.

Under EBI acceleration each subject must establish a pattern of voluntary respiration and when this is disrupted by coughing (which is very apt to occur during EBI acceleration), the subject is greatly distressed and forced to terminate the run. If extremely forced ventilatory excursions are attempted (as in measuring vital capacity, for

example), coughing follows invariably. It is for this reason that the plot of vital capacity against g is not extended beyond $6g$.

The carbon dioxide levels in the expired air fell to about 1 percent during EBI acceleration. At the termination of the acceleration the CO_2 level rises quickly to about 6 percent. This is further evidence of reduced alveolar ventilation; only the dead-space air is being exchanged.

It was found that by adding an EBD component to the EBI vector, such as a combination of $6g$ EBI and $3g$ EBD, ventilation of the lungs was often subjectively as well as objectively enhanced but at the expense of a cardiovascular deterioration as evidenced by symptoms of loss of vision. One subject showed a 40-percent increase in his minute volume ventilation during $6g$ EBI plus $3g$ EBD as compared with $6g$ EBI alone.

From a survey of the data as a whole an impression that the small and thin-chested individuals perform somewhat better in their respiratory efforts under EBI acceleration than do the heavily built individuals has been gained.

The blood pressures of the pilots were measured by the Ames automatic blood-pressure device. With both EBI and EBO accelerations, the pilots' blood pressures (both systolic and diastolic) measured at heart level increased invariably. The pulse-wave excursions were measured by a photocell device attached to the ear. These measurements showed little changes except at high accelerations when there was a decrease in amplitude. This decrement is synchronous with the visual deterioration at high accelerations and reflects the decline in blood pressure at the eye level which probably causes the visual symptoms. During EBD acceleration, the systolic blood pressure at heart level showed little change but the diastolic blood pressure increased considerably. There was also a pronounced increase in the heart rate. The ear pulse, as would be expected, was markedly diminished.

The heart-rate responses to EBI and EBO acceleration stresses fell into three seemingly random categories. In some runs, the pilots' heart rates showed a great increase, which is the response one would expect. In other runs however (on the same individual), there was a pronounced slowing of the heart rate. In still other runs, the heart rate varied with the respiratory cycle.

Premature cardiac contractions were observed frequently during EBI and EBD accelerations but rarely with EBO acceleration.

031713201030

206

. . CONCLUDING REMARKS

In summary, the major limiting physiological factors which influence a pilot's tolerance to acceleration appear to be grouped about three body systems - visual, respiratory, and cardiovascular.

The loss of vision may be due to watering or to the lack of proper blood supply to the eye, depending on the acceleration vector, but it appears to be the most universal limiting factor, regardless of how the acceleration is applied to the body. This loss of vision is closely related to the effect that acceleration has on the respiratory and cardiovascular systems of the body.

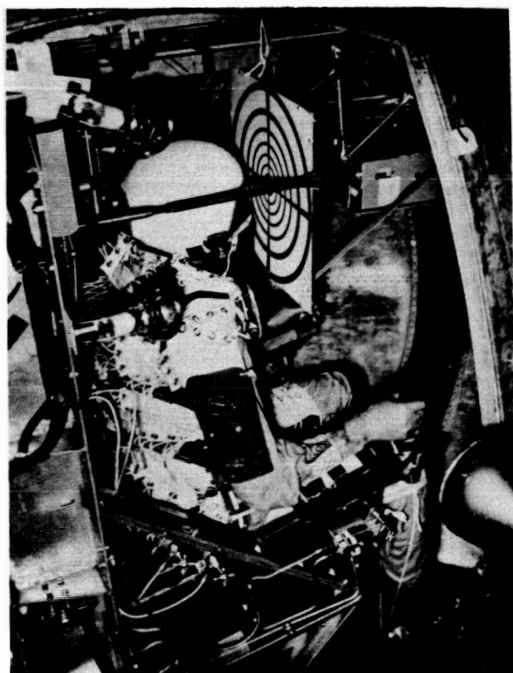
The respiratory system is greatly embarrassed by accelerations applied not only at right angles to the spinal axis but also along the spinal axis of the body. However, this embarrassment is of greatest importance in EBI acceleration and of least importance in EBO acceleration. In EBD acceleration there is an intermediate respiratory problem.

The most important effect that these accelerations have on the cardiovascular system is the limitations they exact on the fluid dynamics of this system. Cardiac irregularities caused by these accelerations are perhaps also of importance.

REFERENCES

1. Smedal, Harald A., Stinnett, Glen W., and Innis, Robert C.: A Restraint System Enabling Pilot Control Under Moderately High Acceleration in a Varied Acceleration Field. NASA TN D-91, 1960.
2. Creer, Brent Y., Smedal, Harald W., and Wingrove, Rodney C.: Centrifuge Study of Pilot Tolerance to Acceleration and the Effects of Acceleration on Pilot Performance. NASA TN D-337, 1960.
3. Smedal, Harald A., Creer, Brent Y., and Wingrove, Rodney C.: Physiological Effects of Acceleration Observed During a Centrifuge Study of Pilot Performance. NASA TN D-345, 1960.
4. Rogers, Terence A., and Smedal, Harald A.: The Ventilatory Advantage of Backward Transverse Acceleration. Presented at the Aerospace Medical Assoc. meeting (Chicago, Ill.), Apr. 1961.
5. Vykukal, Hubert C., Gallant, Richard P., and Stinnett, Glen W.: Description and Performance of an Interchangeable, Mobile Pilot-Restraint System, Designed for Use in High Sustained Acceleration Force Fields. Presented at the Aerospace Medical Assoc. meeting (Chicago, Ill.), Apr. 1961.
6. Smedal, Harald A., Vykukal, Hubert C., Gallant, Richard P., and Stinnett, Glen W.: Crew Physical Support and Restraint in Advanced Manned Flight Systems. Presented at IAS-ARS Joint Meeting (Los Angeles, Calif.), June 1961.
7. Holden, George R., Smith, Joseph R., Jr., and Smedal, Harald A.: Physiological Instrumentation Systems for Monitoring Pilot Response to Stress at Zero and High G. Presented at the Aerospace Medical Assoc. meeting (Chicago, Ill.), Apr. 1961.
8. Morgan, Willard D., and Lester, Henry M.: The Leica Manual. Third ed., Morgan & Lester, Publs. (New York), 1940, pp. 435-456.

CONFIDENTIAL



PLACIDO DISC
INSTALLATION
ON CENTRIFUGE

Figure 1

PLACIDO DISC REFLECTION ON CORNEA, 1g

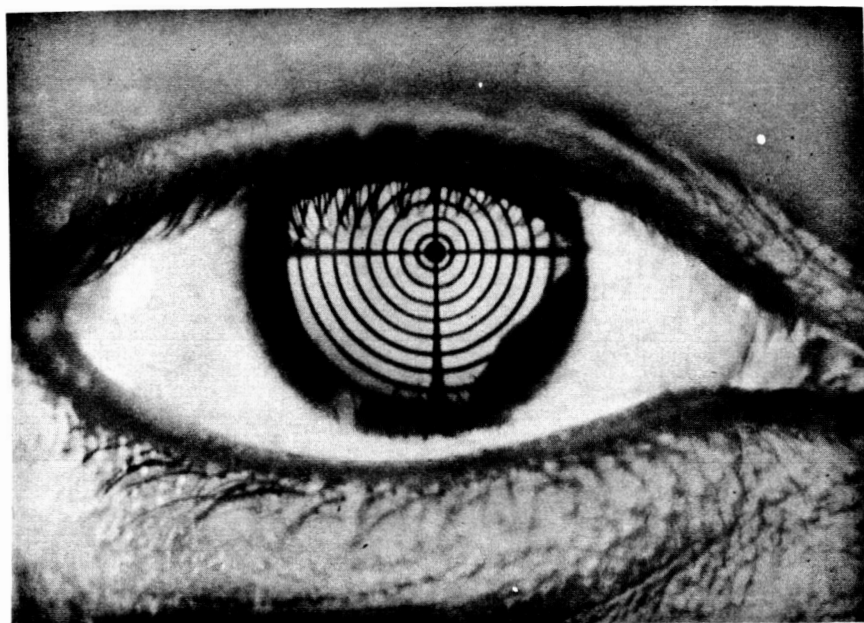


Figure 2

CONFIDENTIAL

DECLASSIFIED

209

PLACIDO DISC REFLECTION ON CORNEA, 6g
EBO

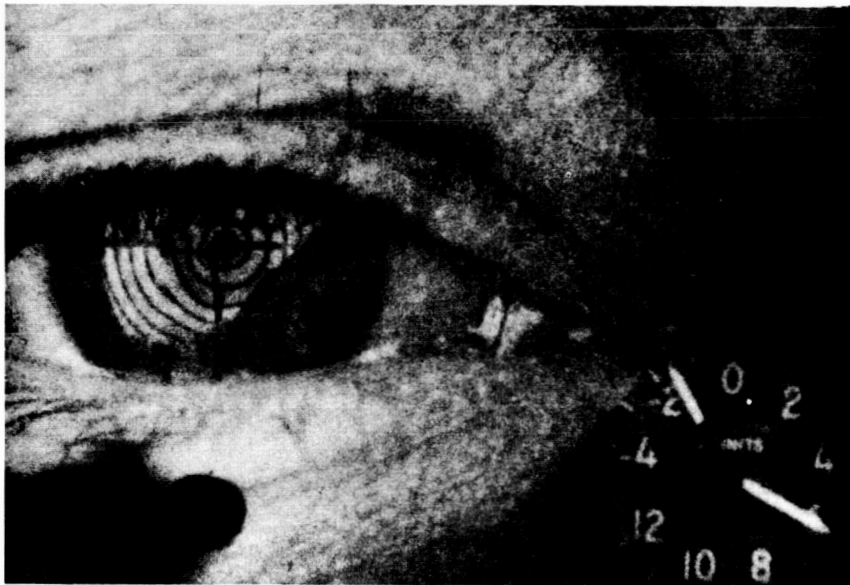


Figure 3

PLACIDO DISC REFLECTION ON CORNEA, 8g
EBO



Figure 4

DECLASSIFIED

0371230 1430

PHOROPTER INSTALLATION ON CENTRIFUGE

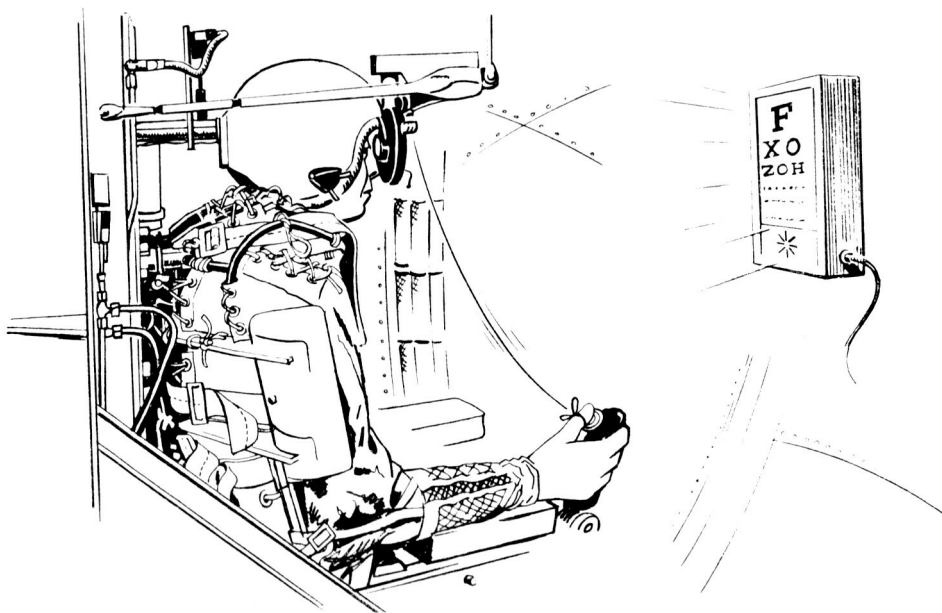


Figure 5

VISUAL CAPABILITY UNDER SUSTAINED ACCELERATION

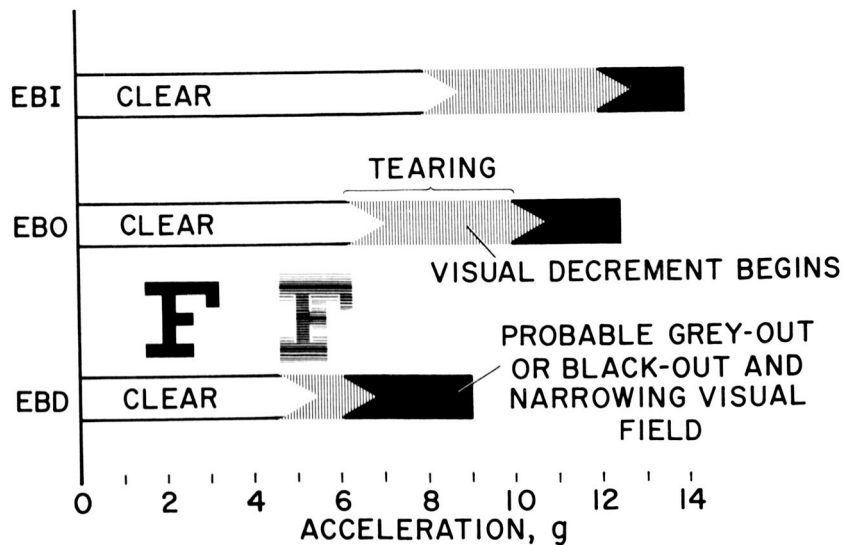


Figure 6

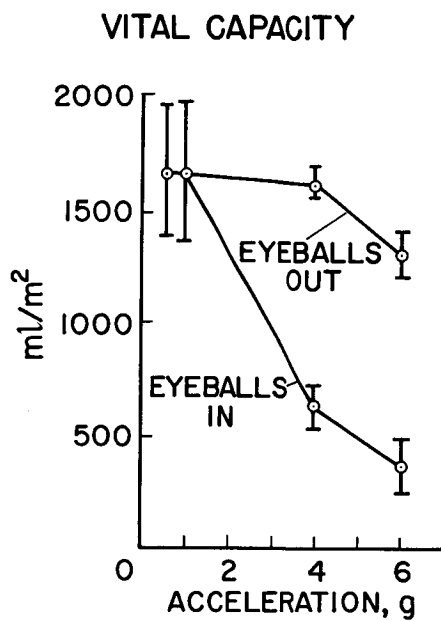


Figure 7

VENTILATION VOLUME PER MINUTE

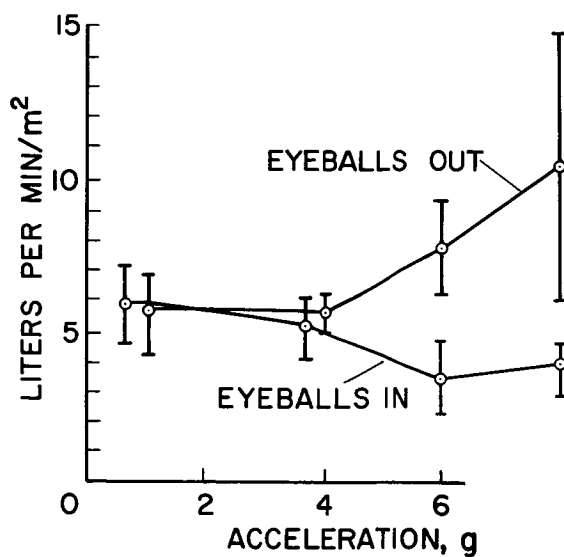


Figure 8

03:71220 1970

RESPIRATION ABILITY WITH DIFFERENT ACCELERATION VECTORS

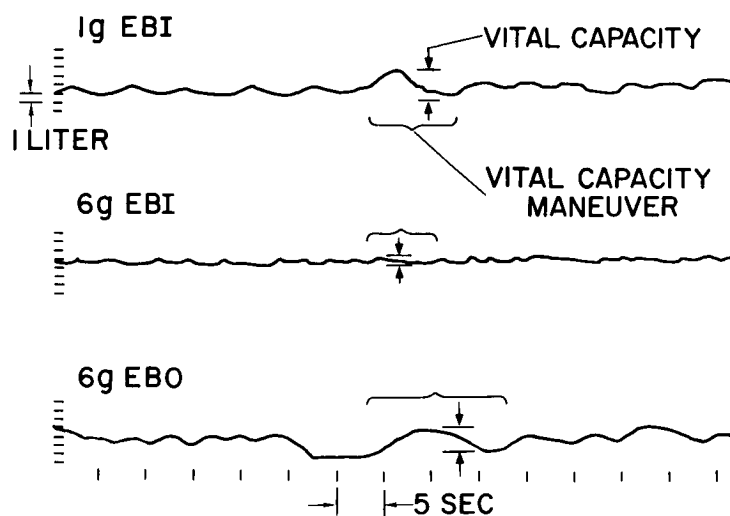


Figure 9

DECLASSIFIED

**IV.
SPACE
ENVIRONMENT**

IMPACT RESISTANCE OF SPACE VEHICLE STRUCTURES

By James L. Summers and C. Robert Nysmith

Ames Research Center

The problem of designing the shell of a space vehicle to be resistant to meteoroid damage is complicated by the lack of complete answers to two basic questions. First, what is the impact process that covers penetration and cratering at meteoric speeds, and second, just how much hazardous debris is there in space? In the discussion of the impact process, only simple composite structures will be considered, that is, structures that are composed of two spaced plates, the intermediate space either being empty or filled with some light material and the outer plate, which is the meteor bumper, being made of materials of various density. The experimental data to be presented were obtained by using small glass spheres as projectiles because glass will shatter at impact just as a stony meteoroid would be expected to do. These spheres were shot from powder and light-gas guns at velocities ranging to 23,000 feet per second. The spheres were mounted in sabots, which protected them from damage from both the driving gas and friction in the gun barrel. The sabots separated in flight and allowed an undamaged pellet of known size, shape, and mass to strike the targets. The models were photographed and timed in flight in order to obtain the impact velocity. For many cases, high-speed motion pictures were taken of the actual impact.

Before the penetration data are presented, it is of importance to recall some results of impact in semi-infinite targets. It was shown by Charters and Summers (refs. 1 and 2) that impact can be classified in several categories as a function, primarily, of impact velocity. Of course, where various materials are involved, material characteristics play a part too. Penetration relations obtained in one region of impact were not applicable to other regions. As indicated subsequently, impact in composite targets also falls into various categories and again, is a function of the velocity. As a result, relations obtained at low speeds governing the perforation of such structures are no longer applicable at high speeds, say 20,000 feet per second, and could be expected to be of no value at all at meteoric speeds. That this is the case is illustrated in figure 1. Shown are individual movie frames of a 1/8-inch-diameter glass sphere impacting a structure composed of two sheets of 2024-T3 aluminum, spaced at 1 inch. The movie was taken at 1.35×10^6 frames per second. Upon impact, both the projectile and the portion of target material removed from the first sheet are shattered into a thin shell of fine fragments. This shell is hemispherical in appearance as it approaches the second sheet and is traveling at

03171230 1970

about 60 percent of the impact velocity for this case. Upon striking the rear sheet a burst of light is produced and material is sent back to the rear of the first sheet, some of it passing out of the hole. It should be noted that the ambient pressure during the impact tests was sufficiently low so that there was no deceleration of the hemispherical shell.

Figure 2 shows a photograph of a typical front sheet after impact at 20,000 feet per second. Figure 3 is a photograph of the corresponding rear sheet. Note that a substantially large area is more or less uniformly damaged. Figure 4 is a photograph of a typical rear plate after initial impact of about 11,000 feet per second. Note that, although there is an overall scattering of craters, the major damage is confined to a small central region, in contrast to the relatively large area shown in figure 3. In order to see why the damage is different, compare figure 5 with figure 1(c). The retouched black line in figure 5 is the front plate and the initial impact velocity for this case was about 10,000 feet per second. Note that the projectile and the target material punched out of the front sheet form a tight cluster of relatively large chunks as contrasted to the shell of fine fragments shown in figure 1(c).

All of the data are presented in the form of log-log plots. This type of presentation has the advantage that trends are quickly observed.

Plotted in figure 6 is the total metal thickness t divided by sphere diameter d , of a structure made of two sheets of 2024-T3 aluminum alloy, as a function of the velocity that is just required to damage the second sheet to the point where it will no longer hold a pressure difference of 1 atmosphere. This critical velocity is called the ballistic limit of the structure. This plot then is somewhat comparable to a plot of the variation of penetration with velocity for impact into a very thick target. At low speeds, it is apparent that target thickness varies as the first power of the velocity just as does penetration in thick 2024-T3 aluminum targets as reported by Collins and Kinard (ref. 3). However, with increasing velocity, a transition region is reached where the character of impact changes from the low-speed type to the high-speed type previously described. At velocities greater than 20,000 feet per second, thickness varies as the $2/3$ power of the velocity. Penetration in thick 2024-T3 aluminum targets at velocities greater than 20,000 feet per second also varies as the $2/3$ power, on the basis of recent results from the Ames Research Center (unpublished).

It might also be reasoned that sheet spacing may have different effects at high and low speeds. That this is the case is shown in figure 7 where the ratio of sheet spacing to sphere diameter is again plotted as a function of the target ballistic limit. At low speeds,

03171230 1970

spacing does not strongly affect the ballistic limit. The results obtained by Funkhouser (ref. 4) indicate that spacings greater than about 2 inches have little effect on improving the performance of a meteor bumper. This conclusion means that the curve defined by the circles would rise vertically from the uppermost symbol. At higher speeds, spacing is much more effective and varies as the square of the velocity. If the hypothesis is made that the shock compression caused by impact at meteoric speeds results in vaporization at the meteor bumper, it can be reasoned that spacing will vary as the first power of velocity and thereby be even more effective in reducing the meteoroid hazard.

From the data just presented it was apparent that structures expected to be resistant to meteoroid impact should be studied at the very highest velocities attainable if meaningful results are desired. Consequently, the several structures shown in table I were impacted at a velocity of 20,000 feet per second. It was anticipated that the structures would simply be compared with each other to assess relative performance. The result was, however, that all structures shown have essentially the same ballistic limit and they all have the same weight per unit area. Comparison of the first two structures listed indicates that changing the front and rear sheet weight distribution from a 50-50 ratio to a 25-75 ratio results in no change in the performance of the structure. Going to the extreme of a 1-mil bumper, however, resulted in a great loss of performance. Therefore, changes in the weight distribution probably should not be carried much beyond that shown. Comparison of the four structures, all having the same rear sheet with the front sheets of various materials but with the thickness adjusted so that all have the same weight, indicates that, for a given mass per unit area of the meteor bumper, the bumper material is not important, at least within the limits of this investigation. The difference in strength of the two brass sheets has no effect either. It should be pointed out, however, that no really high-strength material was tested as a meteor bumper.

A meteor bumper (not shown on this table) made of window glass was also tested simply to show the effect of brittleness. The glass was covered on the back side with masking tape but a small clear area was left for the projectile to strike. The glass plate was in one piece after impact but was completely cracked into tiny fragments as a result of the strong shock wave produced. Without the masking tape to hold the pieces together, the entire 6-inch-square plate would have been destroyed. Therefore, if a brittle material is required for the outer surface of a space vehicle, perhaps as an ablative surface for reentry, then a bonded, unbrittle backup would also be required.

A number of fillers were also tested at impact speeds of 20,000 feet per second. The fillers were placed between two sheets of

031712001430

0.050-inch-thick 2024-T3 aluminum alloy spaced at 1 inch. Without fillers, such a target has a ballistic limit of about 9,500 feet per second. For the three fillers tested, the ballistic limits of the structures were raised to well above the impact velocity, certainly above 25,000 feet per second and possibly above 30,000 feet per second as estimated from the damage to the rear sheet. The best filler was the lightest and was polyurethane as shown in figure 8. Shown are photographs of the filler with both metal plates removed. The rear sheet of aluminum for this target was only slightly dented. The lost filler material was probably partly vaporized and shredded and was discharged out of the hole in the front sheet. Note the radial lines on the back of the filler. These lines are actually razor-sharp slices in the filler extending for several inches and are caused by the spray from the front sheet and also the back-splash from the face of the rear sheet. The cells in this filler are generally interconnected, that is, it is like a sponge and, when put under water, the air can be squeezed out. Therefore, under vacuum conditions, no gas would be trapped in the filler. Figure 9 shows a polystyrene filler after impact. It was the least impact-resistant of the fillers but also the densest. This apparent paradox can be explained as follows. The cells in this filler contain carbon dioxide which very readily transmits the impact shock wave into the filler and destroys a large portion of it. The rear sheet was substantially bulged out but not perforated or spalled. It appears, then, that a filler for a space structure should contain no trapped gases. Shown in figure 10 is a glass-wool filler after impact. It is slightly more dense than the polyurethane filler first shown but is slightly less effective. Perhaps the resilience of the lightweight polyurethane filler added to its performance.

So far only impact normal to the target surface has been discussed. It has been suggested many times that most of the meteoroid impacts will be on oblique surfaces and, therefore, this hazard would be materially reduced. Shown in figure 11 are individual movie frames showing an 1/8-inch-diameter glass sphere striking a target at an angle of 45° . The entire image was optically rotated when the film was made so that the sphere is rising as it passes along. The third sheet shown is a "witness sheet." It helps to show the extent of the damage to the second sheet. After impact, a complex spray develops. Note that material is spalled off normal to the back of the front sheet and note also that there is a cluster, characteristic of the cluster described earlier for the low-speed impact case, traveling along the trajectory of the pellet. (See fig. 11(c).) The spall traveling normal to the sheets strikes the rear sheet first and perforates it. A short time later, the cluster arrives at the rear sheet and just perforates it. It has been observed that, for oblique impact at low speeds, the rear sheet is punctured along the line of the trajectory but not elsewhere even though some fragments are spalled off normal to the front sheet. A

second shot at a target similar to this target but at a somewhat higher velocity resulted in perforation by the spall moving normal to the target but not by the cluster. It would seem likely, then, that oblique impact at meteoric speeds would result in damage to the rear sheet primarily from, if not completely from, the spall moving normal to the surface. This is another case where low-speed impact data could lead to erroneous conclusions regarding meteoric impact. As far as the quantitative effects of obliquity on impact damage, it can be stated that inclining this target 45° approximately doubled its ballistic limit.

Shown in figure 12 are three structures. Each will be evaluated on the basis of hull weight required for a given probability of meteoroid puncture. The metal used is 2024-T3 aluminum alloy. For the double-sheet structures, the weights are increased by 25 percent to account for the weight of the supporting structure between the sheets.

An analysis of the amount of space debris based on both astronomical measurements and satellite measurements, has been made in reference 5. From this analysis, two distributions for meteoroid mass with number were evolved and are described as pessimistic (or conservative) and optimistic (or nonconservative) distributions of meteoric material. The distributions are shown in figure 13 and are based on the usual assumption that number times mass is a constant. The distributions shown differ by two orders of magnitude. The pessimistic (or conservative) distribution will be used in the calculations. Much of the meteoric material is described as light cometary material, probably much less than 10 percent being solid bodies. Only the solid stone meteoroid will be considered. This choice is also conservative. The question arises, what about the iron-nickel meteoroid of much higher density? First, the iron-nickel meteoroid is only a small fraction of the solids, possibly only a few percent. Secondly, it has been regarded by many, based on the examination of recovered iron-nickel meteorites, that because of their great mechanical strength, meteoroids no smaller than about 5 pounds will be found in space. Obviously, it would be impossible to protect against a 5-pound or larger chunk of iron traveling at meteoric speed, at least for the Apollo mission.

In this evaluation of the hazard, only normal impact on the full projected area of the vehicle will be considered. Assumed in the calculations is a vehicle with a volume of 850 cubic feet, comparable to that of a mission module, with a projected area (that is, the exposed area) of 150 square feet. A flight time of 14 days is assumed. Assumed also is the average meteoroid velocity, 98,000 feet per second. Finally, for the evaluation of the performance of the single-sheet structure, the penetration equation given in reference 2 will be used with an additional factor of two to account for the back-spall of plates at high impact speeds as well as for the extra penetration in thin plates

031712000000

as reported in reference 6. The performance of the multiple-sheet structures will be evaluated from the data presented. By combining these calculations with the conservative stony meteoroid distribution, one can compute the relative performance of the vehicle with the three types of shells. The summarized results of these calculations are shown in figure 14. Plotted is the weight of the shell as a function of the probability of penetration. It is immediately obvious that, with the conservative assumptions made, a shell made of a single plate would be prohibitively heavy. It can also be seen that, if a probability of puncture of 10 percent is assumed, that is, one puncture in ten 14-day missions, a shell weighing 1,000 pounds could be made by employing a double sheet with a filler type of construction. The two lower curves were arbitrarily ended when the total metal thickness became 0.1 inch. This shell could be a structure having a 0.025-inch outer sheet and a 0.075-inch inner sheet which is capable of containing a pressure of 1 atmosphere with a substantial margin of safety. This structure with the filler is by no means an optimum structure. Additional research will undoubtedly reveal other composite structures capable of even more efficient performance.

In the calculation of these weights, normal impact was assumed over the entire projected area of the vehicle. However, it is apparent from earlier remarks that impact at oblique angles is much less damaging than normal impact. Therefore, if a spacecraft could be designed to present much of its surface at oblique angles to the oncoming meteoroids, which are primarily in the plane of the ecliptic, the hazard could be reduced substantially. However, the possibility that the vehicle might encounter an unknown meteor stream with a resulting increase in the hazard was not taken into account in these calculations. The decrease in the hazard due to oblique impact and the increase in the hazard due to meteor streams are assumed to be compensating.

It is stated that, in spite of the fact that a difference has been shown between low- and high-speed impact, velocities are still not sufficiently high to give reliable quantitative data pertaining to impact at meteoric speeds. It is felt, however, that the analysis presented gives a conservative picture of the meteoroid hazard to the Apollo vehicle because, first, the extrapolation of impact results to meteoric speeds overestimates the damage and, second, the choice of the combination of the stony meteoroid with the pessimistic distribution overestimates the danger of the meteoric debris.

Future impact research will be directed toward testing composite structures employing materials and types of construction more typical of the Apollo vehicle.

DECLASSIFIED

219

REFERENCES

1. Charters, A. C.: High-Speed Impact. Scientific American, vol. 203, no. 4, Oct. 1960, pp. 128-140.
2. Summers, James L.: Investigation of High-Speed Impact: Regions of Impact and Impact at Oblique Angles. NASA TN D-94, 1959.
3. Collins, Rufus D., Jr., and Kinard, William H.: The Dependency of Penetration on the Momentum Per Unit Area of the Impacting Projectile and the Resistance of Materials to Penetration. NASA TN D-238, 1960.
4. Funkhouser, John O.: A Preliminary Investigation of the Effect of Bumpers as a Means of Reducing Projectile Penetration. NASA TN D-802, 1961.
5. Nysmith, C. Robert, and Summers, James L.: Preliminary Investigation of Impact on Multiple-Sheet Structures and an Evaluation of the Meteoroid Hazard to Space Vehicles. NASA TN D-1039, 1961. (NASA Prospective Paper.)
6. Kinard, William H., Lambert, C. H., Jr., Schryer, David R., and Casey, Francis W., Jr.: Effect of Target Thickness on Cratering and Penetration of Projectiles Impacting at Velocities to 13,000 Feet Per Second. NASA MEMO 10-18-58L, 1958.

031712341930

TABLE I

**DOUBLE SHEET STRUCTURES HAVING
BALLISTIC LIMIT $\approx 20,000$ FT/SEC**

SPACING = 1"

d = .125"

ALL STRUCTURES
HAVE SAME WEIGHT PER UNIT AREA

FRONT SHEET		REAR SHEET	
MATERIAL	THICKNESS	MATERIAL	THICKNESS
2024 - T3	.062"	2024 - T3	.062"
2024 - T3	.031"	2024 - T3	.093"
HARD BRASS	.010"	2024 - T3	.093"
SOFT BRASS	.010"	2024 - T3	.093"
ACRYLIC	.075"	2024 - T3	.093"

DECLASSIFIED

221

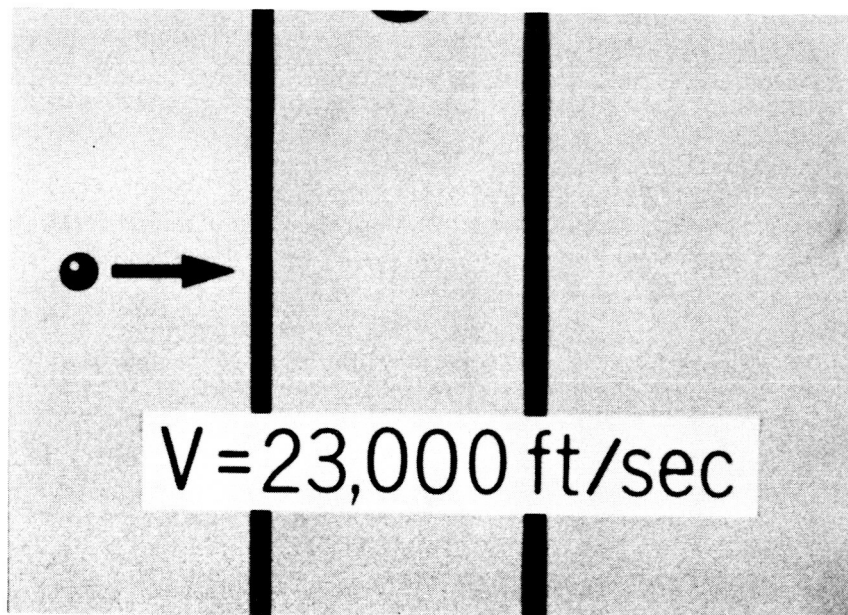


Figure 1(a)

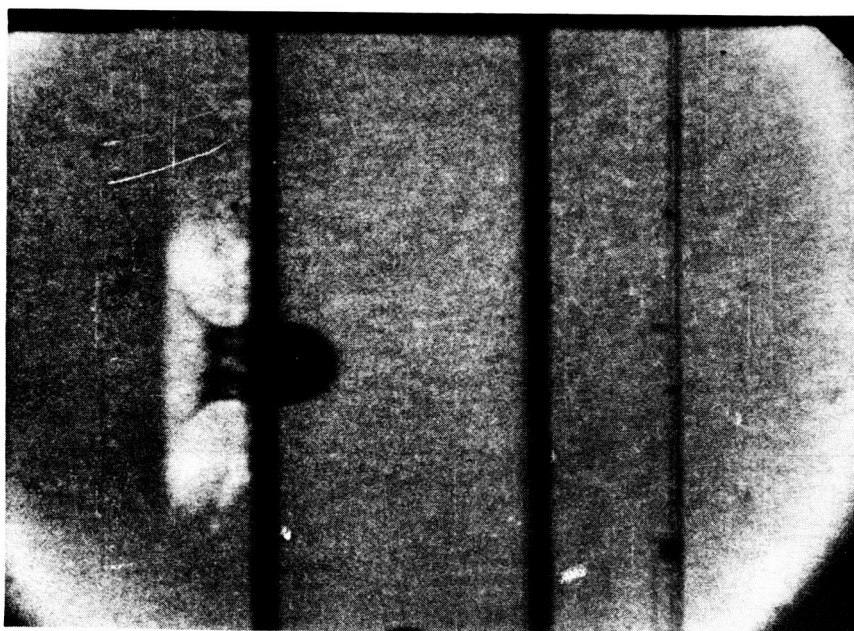


Figure 1(b)

DECLASSIFIED

03713201030

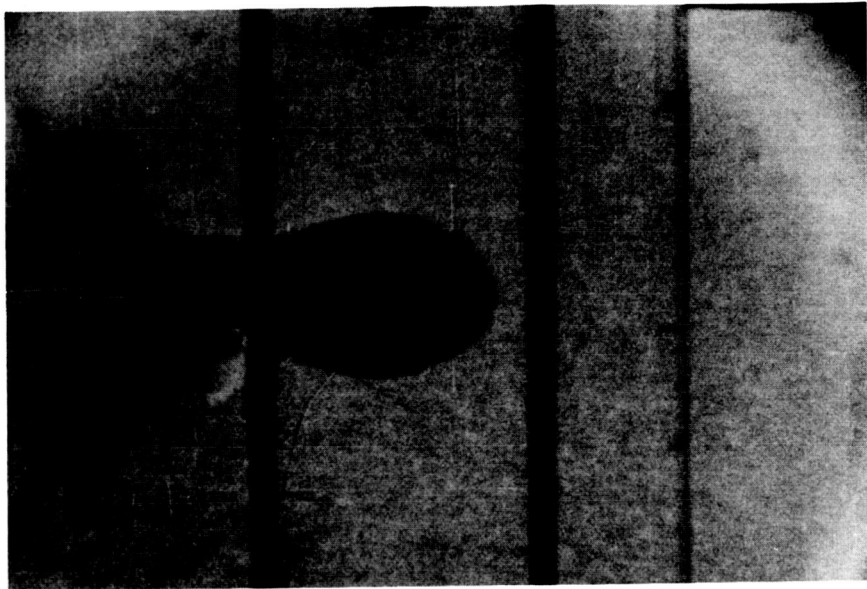


Figure 1(c)

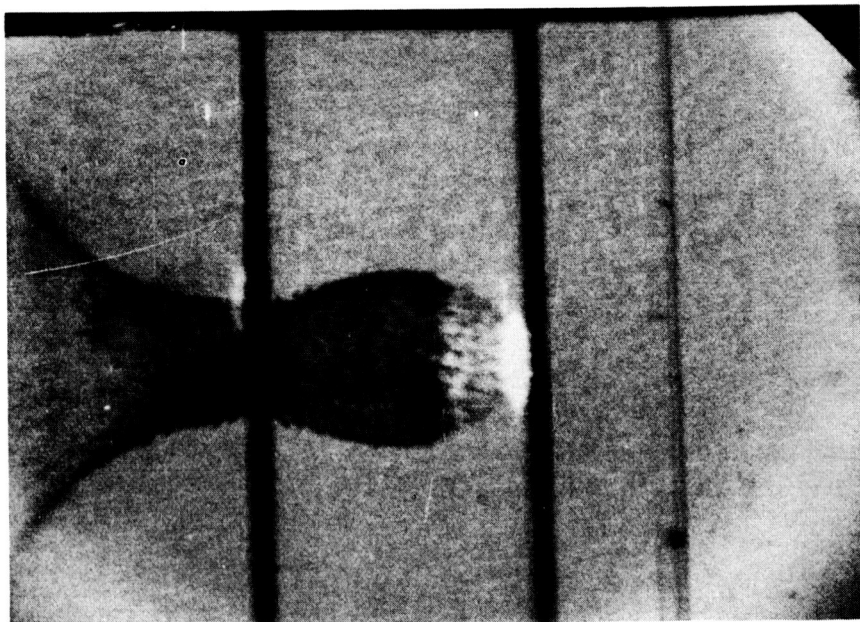


Figure 1(d)

CONFIDENTIAL

DECLASSIFIED

223

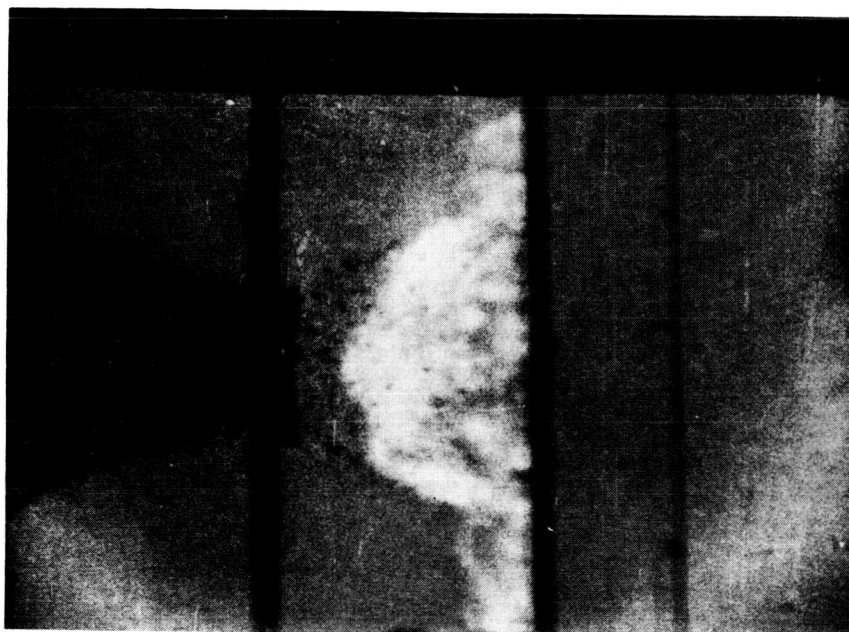


Figure 1(e)



Figure 1(f)

[REDACTED]

031712201030

FRONT SHEET FOR IMPACT VELOCITY
OF 20,000 FT/SEC

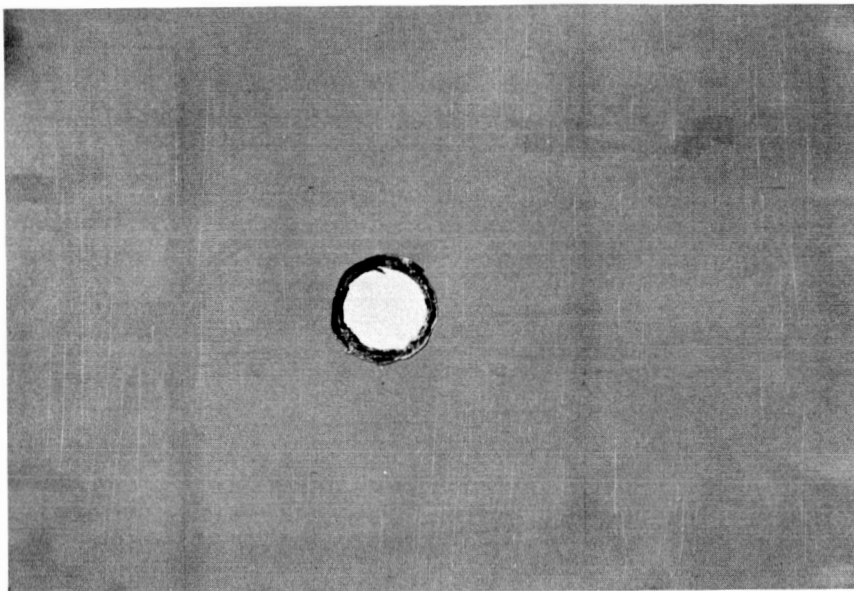


Figure 2

REAR SHEET FOR IMPACT VELOCITY
OF 20,000 FT / SEC

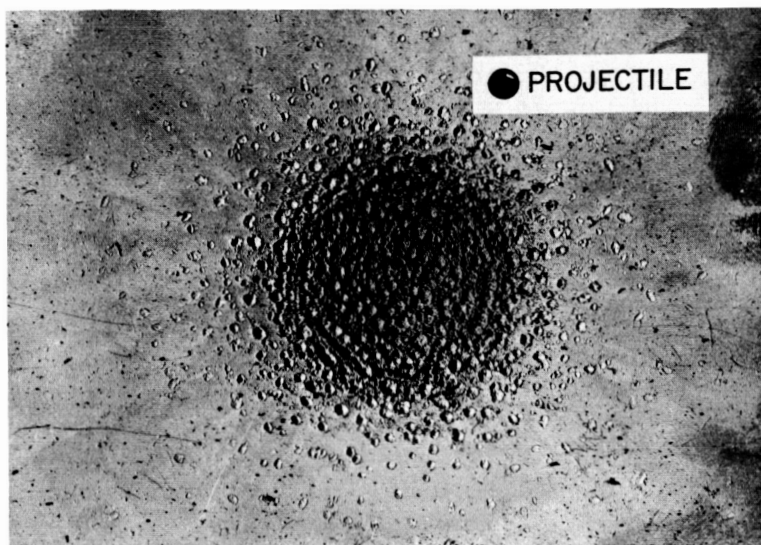


Figure 3

A-27963.1

DECLASSIFIED

225

REAR SHEET FOR IMPACT VELOCITY
OF 11,000 FT / SEC

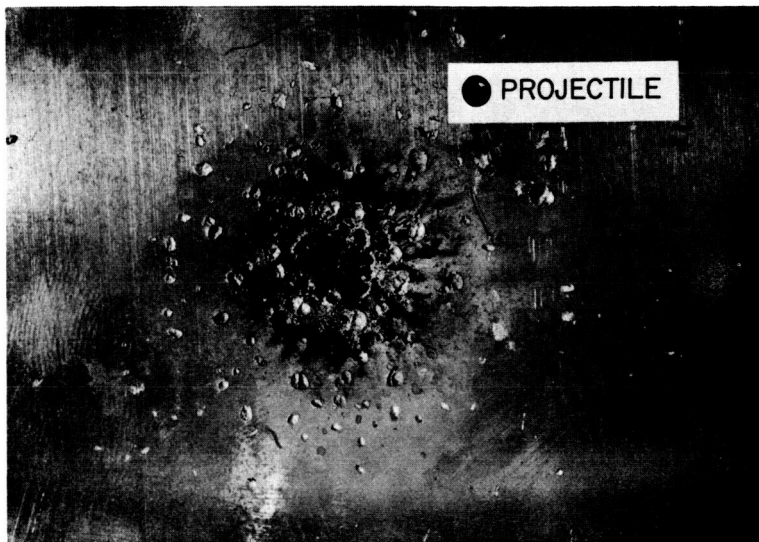


Figure 4

A-27964.1

FRAGMENTED CLUSTER AFTER IMPACT
AT 10,000 FT/SEC



Figure 5

DECLASSIFIED

03171300 1930

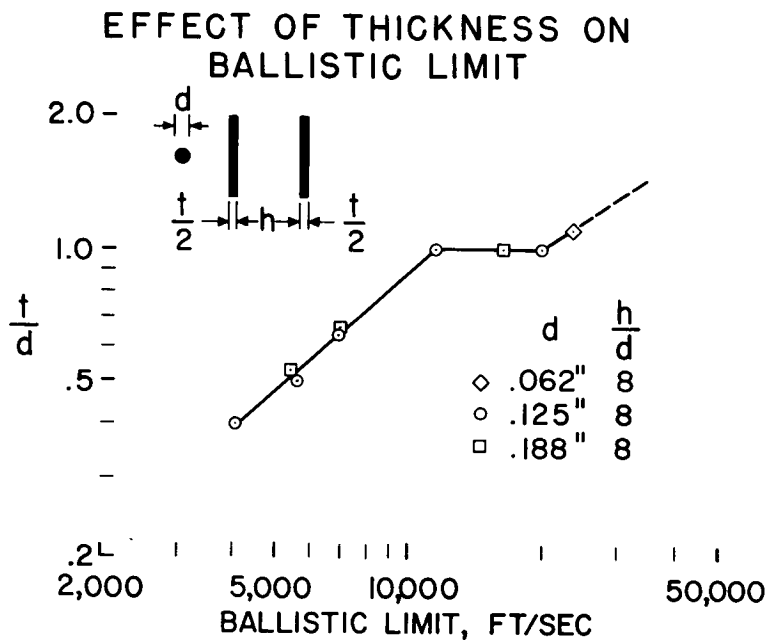


Figure 6

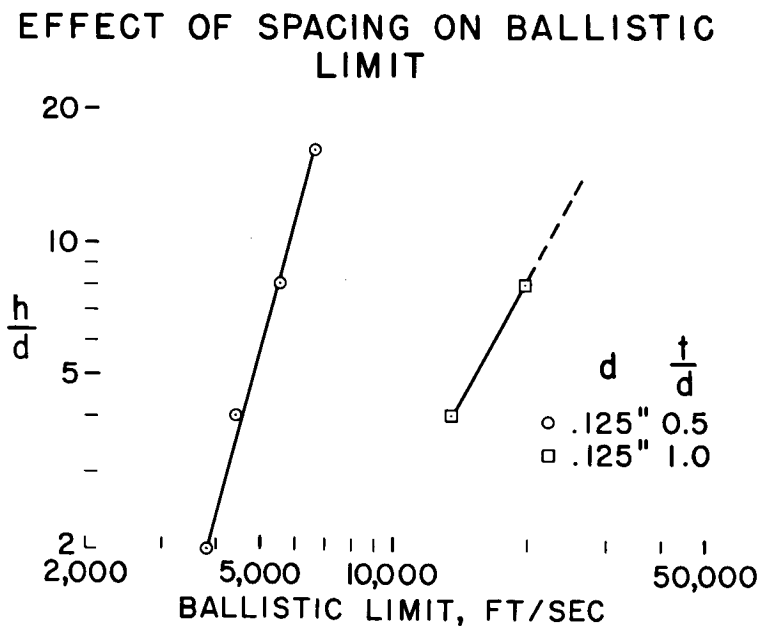


Figure 7

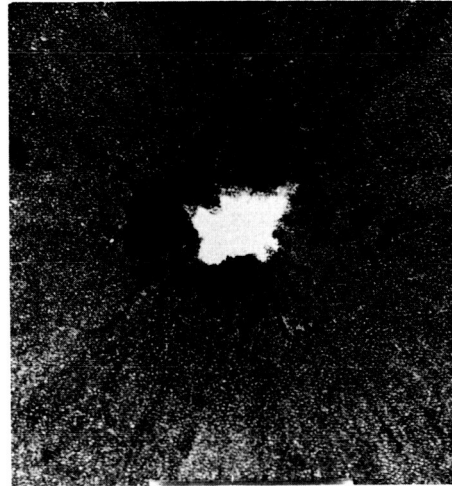
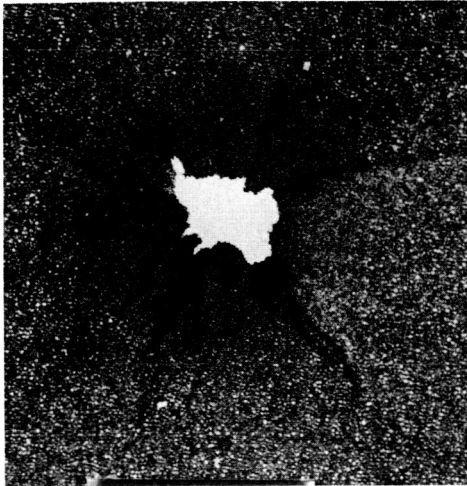
DECLASSIFIED

227

**1-INCH THICK POLYURETHANE FILLER
DENSITY: 1.5 LB/CU FT**

FRONT

REAR



A-27966.1

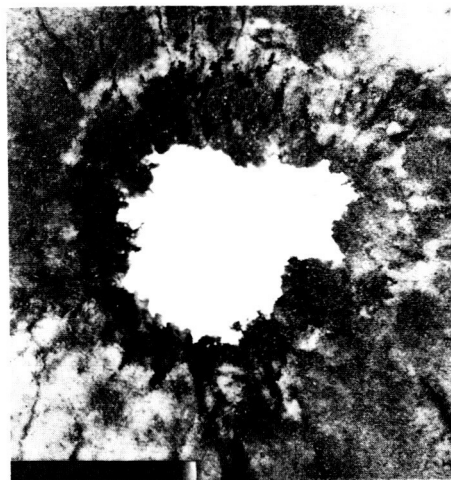
A-27967.1

Figure 8

**1-INCH THICK POLYSTYRENE FILLER
DENSITY: 4 LB/CU FT**

FRONT

REAR



A-27968.1

A-27969.1

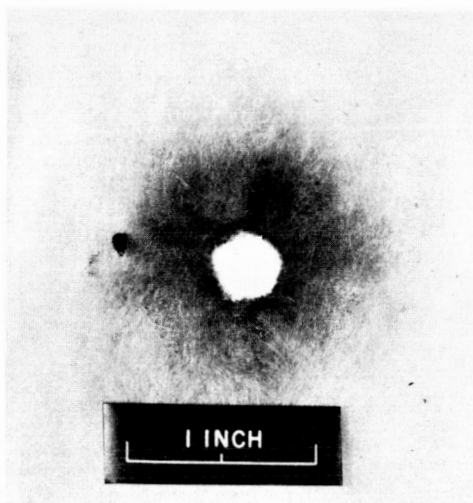
Figure 9

CONFIDENTIAL

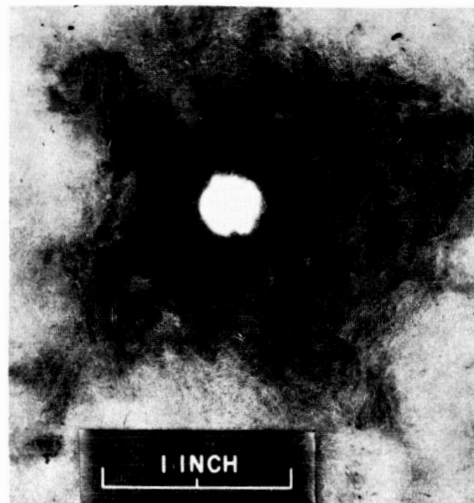
1-INCH THICK GLASS WOOL FILLER
DENSITY: 2 LB / CU FT

FRONT

REAR



A-27970.1



A-27971.1

Figure 10

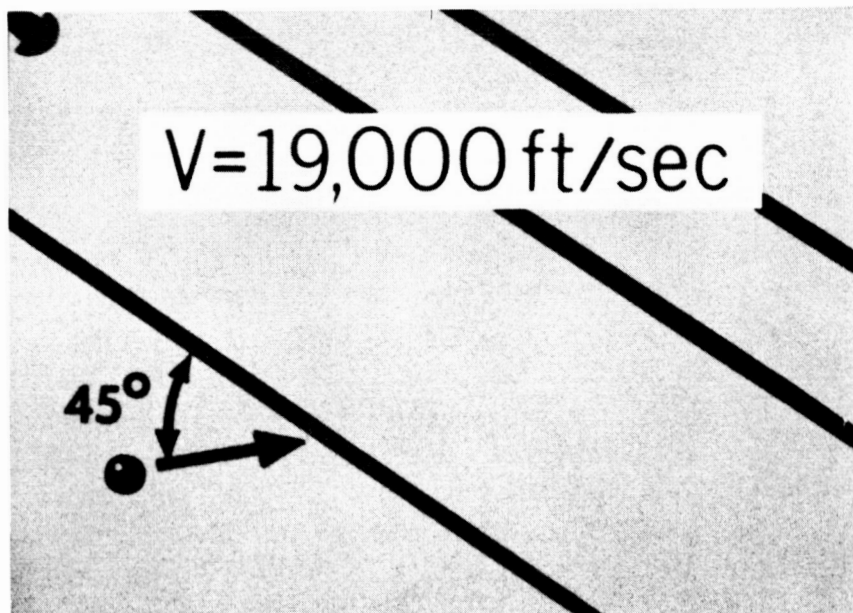


Figure 11(a)

CONFIDENTIAL

DECLASSIFIED

229



Figure 11(b)

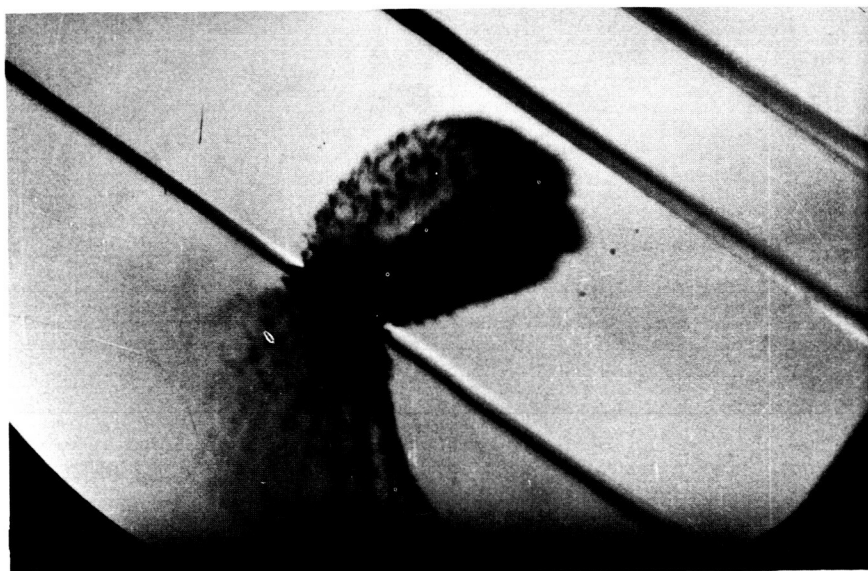


Figure 11(c)

CONFIDENTIAL

0371020 1430



Figure 11(d)

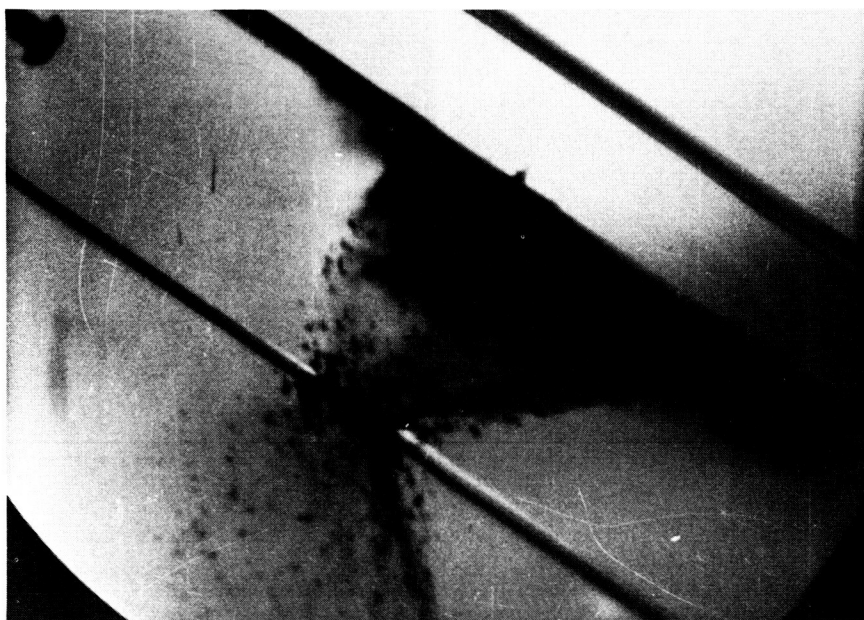


Figure 11(e)

~~CONFIDENTIAL~~

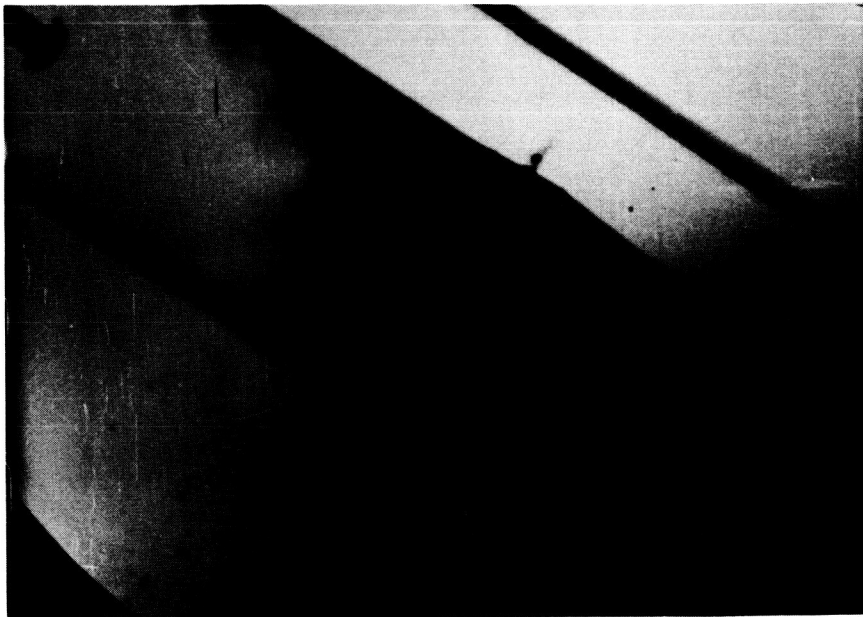


Figure 11(f)

SHELL CONSTRUCTION

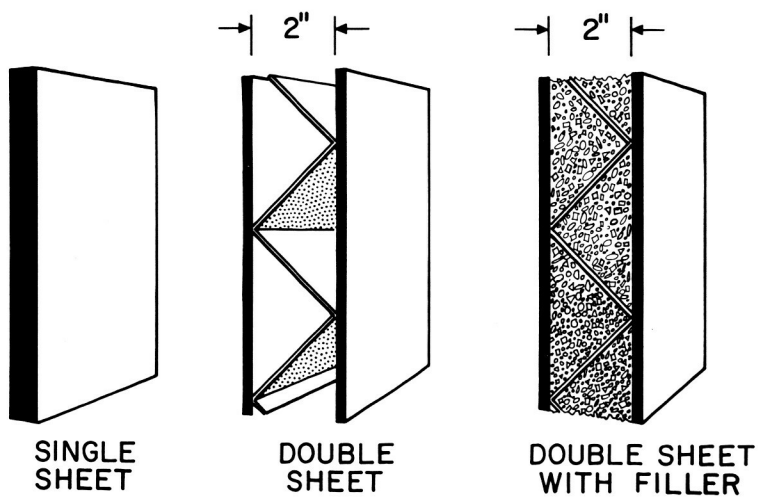


Figure 12

03:13:00 1991

METEOROID MASS-NUMBER DISTRIBUTION

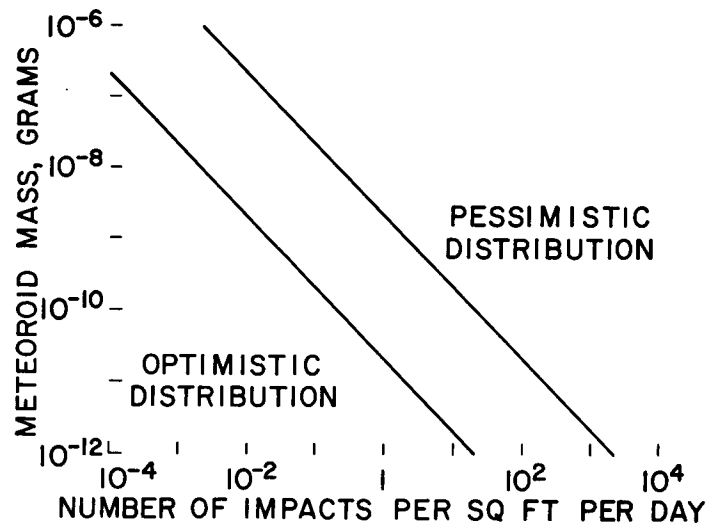


Figure 13

ESTIMATED SHELL WEIGHT VS PENETRATION PROBABILITY

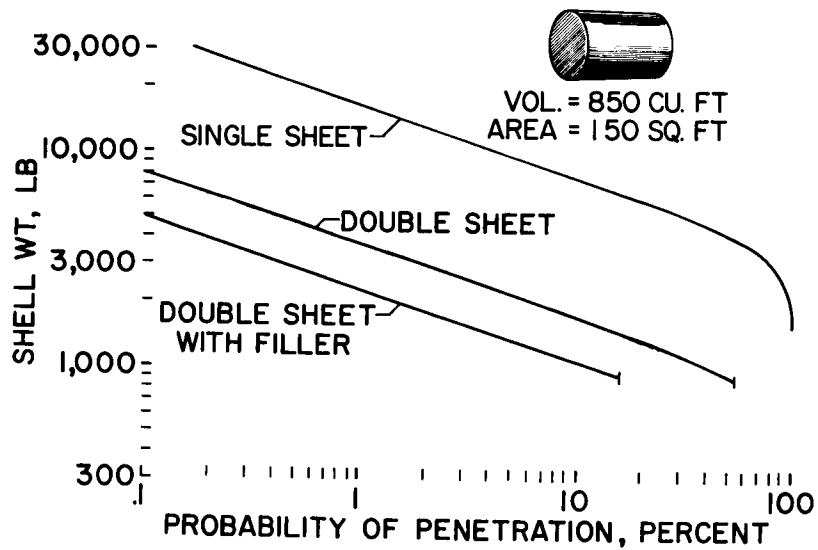


Figure 14

SPACE RADIATION HAZARD

By Trutz Foelsche and John E. Duberg

Langley Research Center

INTRODUCTION

It is the intent of this presentation to summarize in a gross way the kinds of radiation problems which exist for manned space vehicles and to indicate the levels of anticipated dose rates or doses behind various amounts of shielding. The survey is limited mainly to studies made under contract to the National Aeronautics and Space Administration or the Army Ballistic Missile Agency or made within NASA itself. These studies have indicated that consideration must be given to radiation associated with the protons and electrons trapped within the Van Allen radiation belts, the background radiation of the primary galactic cosmic rays, and the solar proton streams ejected by energetic solar flares. These sources are not equally intense nor uniformly distributed in space and, in the case of the solar proton streams, not always present so that their relative significance in vehicle design depends on the trajectory and mode of operation of the space vehicle.

It might be well to define some terms which will be used in this paper and in the next paper by Jacob Abel:

One roentgen r is defined as the amount of X-radiation that produces 2.1×10^9 pairs of ions per cubic centimeter of standard air. It corresponds to an energy absorption of about 83.7 ergs per gram of air.

One roentgen equivalent physical rep is defined and used here as the unit of absorbed dose or absorbed energy per gram of material. The unit 1 rep is 93 ergs per gram and corresponds to the energy absorbed in 1 gram of soft tissue or water when this material is exposed to 1 r of X-radiation. It is essentially the same as the more modern unit 1 rad which equals 100 ergs per gram.

There are other sources of ionizing radiation besides X-rays and these radiations can be biologically more or less damaging for the same absorbed physical dose; a dose in roentgen equivalent man rem is defined as the dose in rep increased by an appropriate multiplication factor, the radio biological effectiveness RBE . For penetrating protons of an energy greater than 15 Mev the RBE is about 1.5 or smaller. The average lethal dose is 450 rem and the average dose for radiation sickness is 150 rem .

RADIATION BELTS

The original measurements of Van Allen (ref. 1) have established the existence of radiation belts surrounding the earth and consisting of energetic charged particles trapped by the earth's magnetic field. Figure 1 gives in polar coordinates the relative intensity distribution by Geiger counter rates of protons and electrons, at distances ranging to 50,000 kilometers from the center of the earth and at angular distances above and below the magnetic equator. These results were reduced by Van Allen (refs. 2 and 3) from data obtained aboard Pioneer IV, after a period of major solar activity, and from Pioneer III and Explorer IV (1958 Epsilon). The results indicate two regions of maximum intensity, a near-earth region at a distance of about 10,000 kilometers from the earth's center and a more remote region at about 25,000 kilometers. The inner maximum has been identified with an energetic proton flux and the remote maximum with an energetic electron flux.

Later almost comparable experiments aboard Explorer VI (1959 Delta) carried out by Arnoldy, Hoffman, and Winckler (ref. 4), during a period of relatively quiet solar activity, indicated a stable inner belt but a considerably shrunken outer region, especially in its extent above and below the equator. (See fig. 2.) These results further indicate that within the range of this plot, that is, 50,000 kilometers, the counting rate is down to 2 counts per second, a rate just greater than the background count for this instrumentation. Two outer region maximums were measured at about 17,000 kilometers and 23,000 kilometers. During magnetic storms that followed this quiet period further depletion of the outer zone was observed. This depletion, in turn, was followed by an increase in the intensity of the outer zone, the disappearance of the intermediate maximum, and the return to the contours indicated in figure 1.

Calculation of dose rate behind various amounts of shielding in the more intense regions of these belts requires the energy spectrum of the particles. Van Allen (ref. 3) has found that, for the inner belt at an altitude of approximately 3,000 kilometers above the magnetic equator, the flux is about 20,000 protons/cm²-sec for protons having energy greater than 40 Mev. This value could perhaps be increased by a factor of 2 to 40,000 protons/cm²-sec. The more detailed spectrum of protons above 75 Mev has been measured in low magnetic latitudes with nuclear emulsions by Freden and White (ref. 5). This spectrum was obtained at an altitude of 1,200 kilometers, the lower edge of the inner belt. When this spectrum is extrapolated to 40 Mev, it yields a count of 1,000 protons/cm²-sec, a value 1/20 of that obtained by Van Allen for the center of the belt.

CONFIDENTIAL

235

Based on the spectrum of Freden and White, detailed calculations have been made by Hermann Schaefer (ref. 6), by Keller and Schaeffer (ref. 7), and by Allen and coauthors (ref. 8) with essentially the same results. Results obtained by Schaefer for the fringe are multiplied by a factor of 20. In figure 3, the dose rate at the center of a spherical shield is plotted against shield weight in g/cm^2 of water. The lower curve is based on the work by Schaefer, and by Allen and coauthors and is in units of roentgen equivalent physical per hour. The upper curve based on the work by Keller and Schaeffer is expressed in units of roentgen equivalent man per hour. The curves differ by a factor of approximately 2 which arises mainly from assigning a relative biological effectiveness of two for protons of less than 40 Mev and to a much lesser extent from a slightly different extrapolation of the low-energy end of the spectrum of Freden and White. Dose rates of 12 rep/hr behind a shield of 2 g/cm^2 of water and 2.7 rep/hr behind 25 g/cm^2 of water are obtained.

Calculations of the increase in dose rate from fast secondary neutrons produced in nuclear collisions have been made (refs. 7 and 8) and indicate that these neutrons can add as much as 10 percent more dose behind shields of the order of thickness of 20 g/cm^2 made of carbon (C), magnesium (Mg), or aluminum (Al).

A straight flight through the inner belt at Apollo trajectory velocities would accumulate, for this range of shield weight, a total dose of 1.3 to 0.3 rep.

The contribution of the electrons in the outer belt to the dose rate inside the vehicle is indirect and is due to the X-rays produced by their deceleration on the surface of the vehicle. Electrons of even 100 Kev energy have only a range of 0.1 millimeter of Al. The radiation flux can also vary in time since the outer belt has been shown to depend in intensity and extent on solar activity. At the center of the expanded outer belt and for an electron flux of 10^{11} electrons/ cm^2 for energy E greater than 20 Kev, Van Allen has calculated an X-ray dose of 100 r/hr behind 1 g/cm^2 of Al. Behind similar amounts of aluminum, Winckler (ref. 4) has measured aboard Explorer VI dose rates of 10 r/hr during quiet periods and 30 r/hr during periods when the outer zone expanded. The radiation is essentially soft and can be reduced to the order of 5 r/hr by 1 to 2 g/cm^2 of lead (Pb) or to 1 to 2 r/hr by a structural weight of 10 g/cm^2 of Al with a thin surface coating of carbon which, by virtue of its lower atomic number, reduces the X-ray production by about one-third.

At Apollo velocities, passage through this belt would take about 1/2 hour and a total dose of 1.3 rep would be accumulated for shielding corresponding to 1 to 2 g/cm^2 of lead.

CONFIDENTIAL

CONFIDENTIAL

GALACTIC COSMIC RAYS

There is always present in space a background of the primary galactic cosmic radiation. It consists of positively charged atomic nuclei of high energy of which about 85 percent are protons, 12 percent are α particles, and the rest are heavier atoms up to tin stripped of all electrons.

Figure 4 (from ref. 9) shows a meridional cross section of the relative overall ionization at the top of the atmosphere, at a depth of about 10 g/cm² or an altitude of about 30 kilometers. Near the magnetic equator, the ionization is relatively low and not much influenced by the state of solar activity. As magnetic latitude increases, the earth's magnetic shielding decreases and the ionization rate increases by a factor of about 35 during years of solar minimum and by a factor of about 20 during years of solar maximum. The increase of ionization by a factor of almost 2 at the poles during periods of solar minimum indicates that it is the low-energy part of the primary spectrum that is increased during this period.

During solar-activity years sudden further decreases in ionization of as much as 25 to 30 percent are observed. These so-called "Forbush decreases" are associated with solar flare activity. Simultaneous observations (ref. 10) of such decreases both on earth and aboard Pioneer V (1960 Alpha) during 1960 and at 5,000,000 kilometers from the earth indicate that they are due not to distortions of the earth's magnetic field but to interplanetary magnetic clouds associated with ejected solar plasmas.

The flux of primary particles is low compared with belt fluxes and in free space during solar-activity years is 2.5 particles/cm²-sec (ref. 3). The spectra of the various particle species are well known and, considering the higher relative biological effectiveness associated with the heavier nuclei, a dose rate of 0.45 rem/week is calculated (refs. 11 and 12) for free space with no external shielding, with secondary production ignored, but with the self-shielding of the body included. Such a dose rate would not accumulate to a significant level in a flight of about 10 days. This is fortunate since shielding to reduce this overall ionization dose rate would be expensive in terms of weight, because of the high energy of the particles and the build up of secondaries (ref. 13). Shielding weights as high as 80 g/cm² of low-atomic-number material could reduce the dose only slightly and, in fact, would increase it during solar-activity years when the low energy content is reduced. This effect parallels the well-known increase in ionization which is observed in the earth's atmosphere at depths of 60 to 80 g/cm² in medium latitudes during solar-activity years.

CONFIDENTIAL

The biologically more damaging aspect of primary cosmic rays is not the overall or average ionization dosage but the damage done by a number of slow, heavy primary nuclei that come to rest in the body by normal ionization. Figure 5 (from ref. 14) shows on the left the ionization spread and "thin-down" of such a heavy primary nucleus of tin, atomic number about 50, in comparison with a track of a thorium alpha particle and two sections of the track of a nucleus of atomic number 20 at energies of 4,000 Mev and 400 Mev. In the core of the tracks there occur doses of the order of 10,000 to 20,000 roentgen. At the top of the atmosphere the number of hits/cm³ of such heavy primary nuclei is extrapolated to about 40/cm³-day during sunspot minimum and about 6/cm³-day during sunspot maximum. The number of hits to produce significant biological effect on man is as yet not clear. During the Man High II balloon flights of 1957 at an altitude of 90,000 feet and latitude greater than 55°, on the whole body of a man a total of 150,000 hits by particles of atomic number greater than 6 were estimated to have been accumulated during a period of 15 hours (ref. 15). No significant biological effects developed during subsequent weeks. Balloon observations (ref. 16) indicate that 20 g/cm² of atmosphere reduce the number of hits by a factor of 10 during solar-minimum years and a factor of 5 during maximum years.

SOLAR FLARE PROTONS

The most significant space radiations to be shielded against are the energetic protons ejected by solar flares. Each such event is an individual in its energy spectrum and life history but it is convenient for discussion to characterize roughly by the general character of their spectra those events that are significant. High-energy events are characterized by relatively low fluxes but of sufficiently high energy that their secondaries can be observed at sea level and in lower latitudes. Such events are rare. They have occurred in 1942, 1946, 1949, 1956, and 1960. They have occurred along the rising and falling slopes of a sunspot cycle and may be said to occur at the rate of 1 to 2 every 4 to 5 years. The most important of such events in the last 20 years occurred on February 23, 1956. A second class may be termed low-energy events which can exhibit, however, extremely high fluxes. The energy level of such events only permits observations directly from high-altitude balloons or indirectly by the strong absorption of galactic radio noise by the low-altitude ionized layers they produce over polar regions. These low-energy events occur more frequently than high-energy events. A third category may be termed medium-energy events which are accompanied by only a slight increase of neutron intensity at sea level and in latitudes above 45°.

03713 20 1959

Figure 6 adapted from reference 17 has been prepared to serve several purposes. During the years of solar maximum (1957, 1958, and 1959) continuous observations of solar proton events were made by observing radio absorption in the polar regions. All such events are indicated by the several types of plus signs above the lines. Plus signs enclosed by boxes represent events producing radio noise absorption in the range 0 to 4 decibels; plain plus signs, events in the range 4 to 15 decibels; and circled plus signs, events that produced more than 15 decibels absorption and which can be regarded as low- and medium-energy high-flux events. At least during years of solar maximum the conclusion can be reached that such extreme flux events occur at the rate of 2 to 4 per year. Low-intensity medium- and low-energy events can occur, as in 1957, at the rate of almost 1 per month.

A second purpose of this figure is to indicate a correlation due to Kinsey Anderson (ref. 17) which could form the basis of a technique for the prediction of the arrival at earth of solar proton streams. Periods of time during which grayish penumbral areas around sunspots existed and exceeded a critical area are indicated by solid lines; periods of time during which such areas were absent or below a critical area are indicated by the open boxes. In all except two instances no solar events occurred during periods of absence of penumbral areas and when such events occurred they were no earlier than 2 days after the occurrence of increase of penumbral areas. If a histogram of the duration of such clear periods is made, as is shown in figure 7, the mean duration of such periods is about 6 days. There is a reasonable certainty, if the 2-day delay in arrival is added, that excursions of the order of 2 to 4 days may be made with little likelihood of encountering a flare.

It is to be noted that these events tend to occur in bunches and that there are times of the year, for instance, the month of December, during which the events seem less likely to occur (fig. 6). In order to study these effects over a period of time greater than that for which radio absorption data of solar events were available, a study was made by Adamson and Davidson (ref. 18) to correlate solar events with large magnetic disturbances as measured by the magnetic index A_p . Data are available for this index for more extended periods. The dots below each line indicate the periods, during the years 1957, 1958, and 1959, when this index exceeded 80. The correlation between the events and the index is fair.

A summary from reference 18 of all magnetic disturbances of $A_p > 80$ for the solar cycle 1943 to 1953 and for the solar cycle 1954 to 1960 is given in figures 8 and 9. Based on the assumption that large magnetic disturbances indicated by $A_p > 80$ constitute solar events, hypothetical 10-day flights were flown during the years of the

solar cycle 1943 to 1953 and the solar cycle 1954 to 1960. Such hypothetical flights indicated that the tendency for events to occur in groups reduces the probability of encountering one or more flares by a factor of 0.74 with variance 0.07 in the cycle 1943 to 1953 and by a factor of 0.91 with variance 0.15 in the cycle 1954 to 1960 below the probability which would be anticipated if the events were random and uncoupled. It was also found, however, that the probability of encountering two or more flares was increased during these periods over the probability of uncoupled chance encounters by factors of 2.58 with variance 0.51 in the early solar cycle and by 1.67 with variance 0.71 in the present cycle.

Further study of the sequence of flights indicated that, during the periods February 10 to April 10 and August 10 to October 10, events occurred more frequently than uncoupled chance encounters by factors of 1.65 and 1.77 in the two cycles, respectively. During the remainder of the year encounters occurred less frequently by factors of 0.68 and 0.62.

If space flights of the order of 10 days are considered, neither the present status of prediction techniques nor the experimental study of solar-event statistics reveals that the probability of encountering a solar flare can be reduced to a negligible quantity. At the rate of 4 per year the expected number in a flight of 10 days is 1 in 9 if bunching and seasonal effect are neglected. Consideration must be given to providing an adequate amount of shielding. In order to provide this it is necessary to know the time histories of the energy spectra of the several classes of flares previously described. A summary from reference 19 of such experimentally determined spectra is included in figure 10 in which the integral flux $N(>E)$ in protons/cm²-sec-steradian is plotted against energy in Bev. The prompt and 19-hour spectrum of the February 1956 event, which is classed as a high-energy event, is shown as is the 33-hour spectrum for the May 1959 event, which is classed as a high-flux low-energy event. The spectrum for the low-energy medium-flux event of August 1958 is shown 14 hours after start. Also included for comparison is the spectrum for the inner Van Allen belt protons.

Time variations of these spectra are required to obtain the total integrated dose. Such histories can be inferred from instrumented balloon flights at high altitude, from the depth and duration of galactic radio noise absorption, and, for high-energy events, by the surge of secondary neutrons produced at sea level. Figure 11 from reference 20 shows the time history of the increment of neutron surge at sea level in multiples of normal background intensity for the February 1956 event and indicates a prompt rise which occurred shortly after the flare erupted on the sun and which continued above background intensity for about 18 hours.

037132-1111

On the basis of the available information on time variations of solar flare events, upper and lower estimates of total doses behind various amounts of shielding were computed (ref. 19). These estimates are summarized in figure 12 for the several classes of events. Dose in rep is given as a function of various spherical shield thicknesses expressed in g/cm^2 of water. Secondary radiation production is ignored. Some significant dose levels should be noted. For a biological effectiveness of one, 450 rep is the average lethal short-time total body dose; 150 rep, the short-time total body dose for radiation sickness. A short-time dose below about 100 rep produces only mild symptoms in a few cases or no effect other than minor blood changes followed by complete recovery. Vehicle wall thicknesses required by other design considerations without regard to shielding average 6 to 8 g/cm^2 . This makes relatively insignificant the more frequent low-flux low-energy events. The total dose can be reduced to about 25 rep for a single encounter with either of the two more extreme types of events by a total shield weight of 25 g/cm^2 of H_2O equivalent. If two or three encounters are considered, total shield weights of 20 to 25 g/cm^2 of H_2O equivalent will maintain the sum of the doses from the encounters at less than 100 rep.

CONCLUDING REMARKS

In summary it can be stated that, for flights of the order of 10 days, the most difficult aspect of the space radiation to be considered in spacecraft design is that of encounters with solar proton events. Shield weights adequate to reduce total doses from these events to tolerable limits are more than adequate to reduce drastically the radiation dose from Van Allen belt protons and electrons in a flight straight through the belts. The cosmic-ray background is much too energetic to be reduced by shielding but for flights of the Apollo duration would amount to less than one rem and the heavy nuclei of the cosmic rays are for the most part absorbed by the shields required for the solar protons.

DECLASSIFIED

241

REFERENCES

1. Van Allen, James A., and Frank, Louis A.: Radiation Around the Earth to a Radial Distance of 107,000 km. *Nature*, vol. 183, no. 4659, Feb. 14, 1959, pp. 430-434.
2. Van Allen, J. A.: The Geomagnetically Trapped Corpuscular Radiation. *Jour. Geophys. Res.*, vol. 64, Nov. 1959, pp. 1683-1689.
3. Van Allen, J. A., and Frank, L. A.: Radiation Measurements to 658,300 km with Pioneer IV. *Nature*, vol. 184, July 25, 1959, pp. 138-140.
4. Arnoldy, R. L., Hoffman, R. A., and Winckler, J. R.: Observations of Van Allen Radiation Regions During Geomagnetic Storms. Observations of Corpuscular Radiation With Satellites and Space Probes. IGY Satellite Rep. No. 11, *Nat. Acad. Sci.*, June 1960, pp. 89-104.
5. Freden, St. C., and White, R. St.: Protons in the Earth Magnetic Field. *Phys. Rev. (Letters to the Editor)*, July 1, 1959, pp. 9-10.
6. Schaefer, Hermann J.: Tissue Depth Doses in the High Intensity Proton Radiation Field of the Inner Van Allen Belt. Rep. No. 16 (Res. Project MR005, 13-1002), U.S. Naval School of Aviation Medicine, Nov. 10, 1959.
7. Keller, J. W., and Schaeffer, N. M.: Shielding of Manned Vehicles From Space Radiation. Paper presented at 31st Annual Meeting of Aero-Space Medical Assoc. (Miami Beach, Fla.), May 1960.
8. Allen, R. I., Dessler, A. J., Perkins, J. F., and Price, H. C.: Shielding Problems in Manned Space Vehicles. First Semi-Annual Technical Summary Report - Dec. 31, 1959 - June 30, 1960. NR-104, Lockheed Nuclear Products, July 1960.
9. Winckler, J. R.: Primary Cosmic Rays. Appendix A of NASA TN D-588, 1960.
10. Simpson, J. A., Fan, C. Y., and Meyer, P.: Preliminary Results From the Space Probe Pioneer V. Paper presented at Washington AGU Meeting, Planetary Science Program, Fifth Session, Apr. 29, 1960.
11. Schaefer, Hermann J.: Definition of a Permissible Dose for Primary Cosmic Radiation. *Jour. Aviation Medicine*, vol. 25, no. 4, Aug. 1954, pp. 392-398.

03171250 0000

12. Foelsche, T.: Energetic Particles in the Environment of the Earth (With Emphasis on Their Implications to Space Flight). (Prospective NASA Paper.)
13. Wallner, Lewis E., and Kaufman, Harold R.: Radiation Shielding For Manned Space Flight. NASA TN D-681, 1961.
14. Schaefer, Hermann J.: Exposure Hazards From Cosmic Radiation Beyond the Stratosphere and in Free Space. Jour. Aviation Medicine, vol. 23, no. 4, Aug. 1952, pp. 334-344.
15. Simons, D. G.: Man High II. AFMDC-TR-59-28 (ASTIA Doc. No. AD-216892), 1959.
16. Yagoda, Herman: Cosmic Ray Monitoring of the Manned Stratolab Balloon Flights. AFCRL-TN-60-640, Air Force Cambridge Research Labs., Sept. 1960.
17. Anderson, Kinsey A.: Preliminary Study of Prediction Aspects of Solar Cosmic Ray Events. NASA TN D-700, 1961.
18. Adamson, David, and Davidson, Robert E.: Statistics of Solar Cosmic Rays as Correlated With Geophysical Effects. (Prospective NASA Paper.)
19. Foelsche, T.: Protection Against Solar Flare Protons. Proc. American Astronautical Soc., Seventh Annual Meeting (Dallas, Texas), Jan. 1961.
20. Schaefer, Hermann J.: Radiation and Man in Space. Advances in Space Science, vol. 1, Academic Press, Inc. (New York), 1959, pp. 267-339.

AL

COUNTING RATE CONTOURS IN RADIATION ZONE

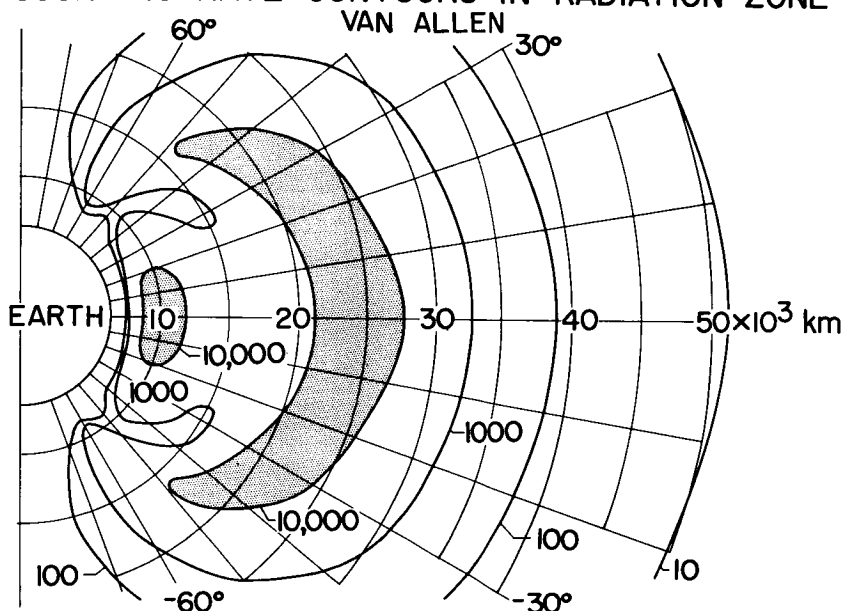
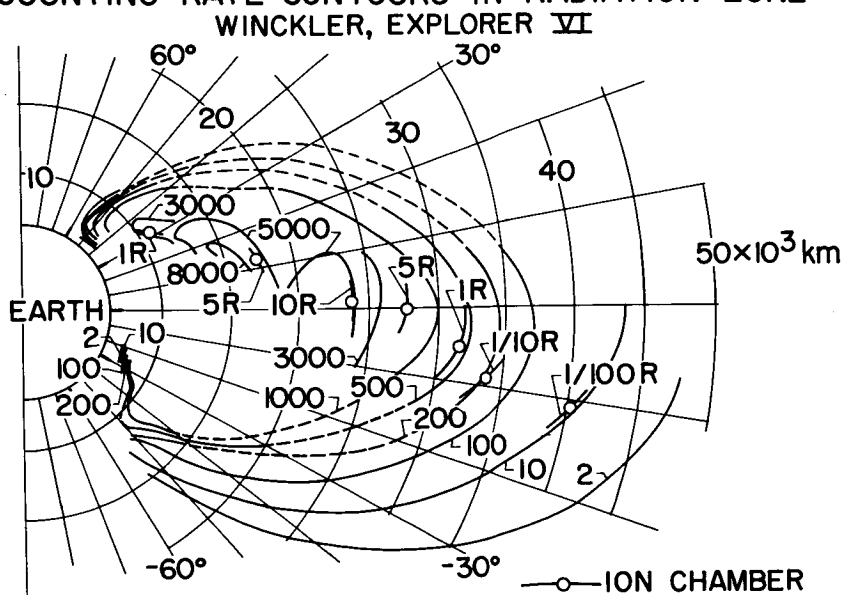


Figure 1

COUNTING RATE CONTOURS IN RADIATION ZONE



NASA

L-1638-2 DUBERG 7/18-20/61

Figure 2

0371220 1990

DOSE RATE IN CENTER OF SPHERICAL SHIELD NEGLECTING SELF-SHIELDING OF BODY

INNER BELT PROTONS

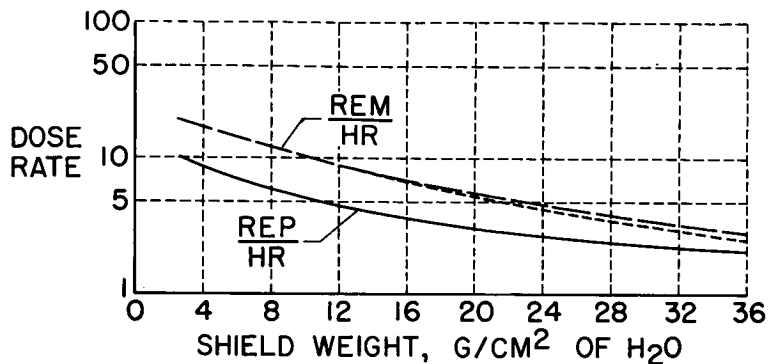


Figure 3

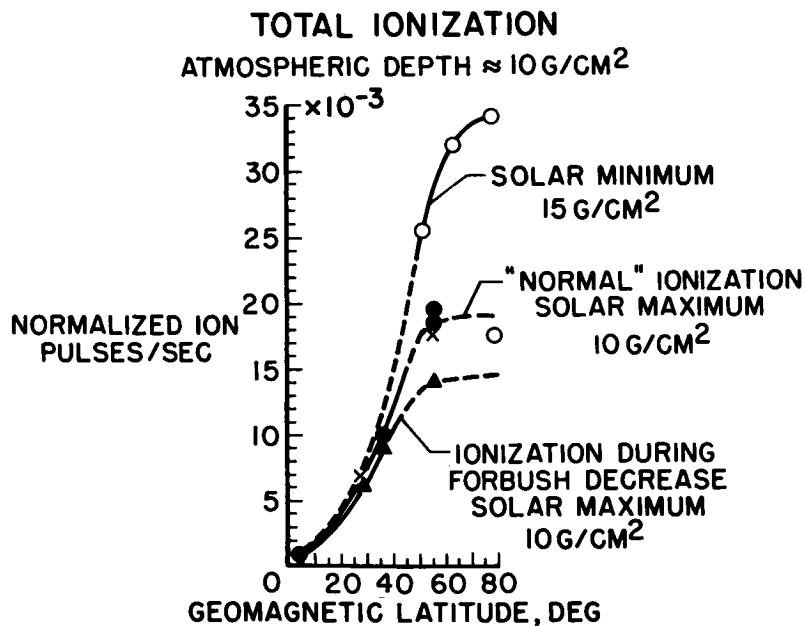


Figure 4

HEAVY NUCLEI TRACKS

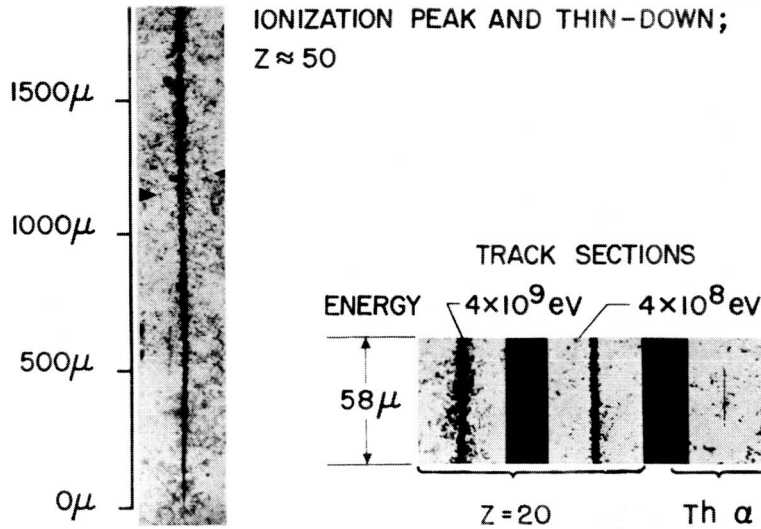


Figure 5

CORRELATION OF SOLAR EVENTS, LARGE PENUMBRA L AREAS, LARGE MAGNETIC DISTURBANCES

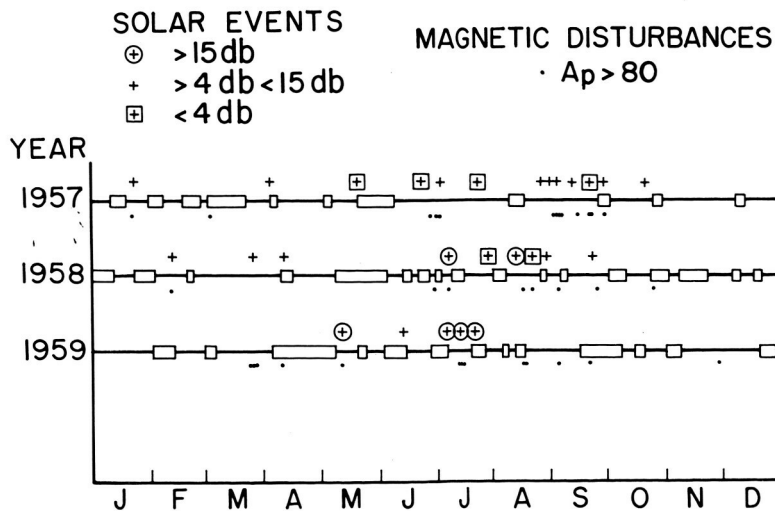


Figure 6

CONFIDENTIAL

DURATION OF PENUMBRAL ABSENCE

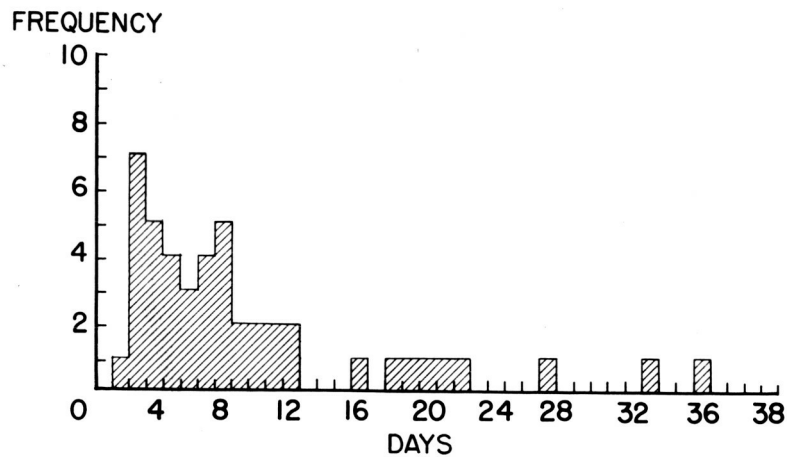


Figure 7

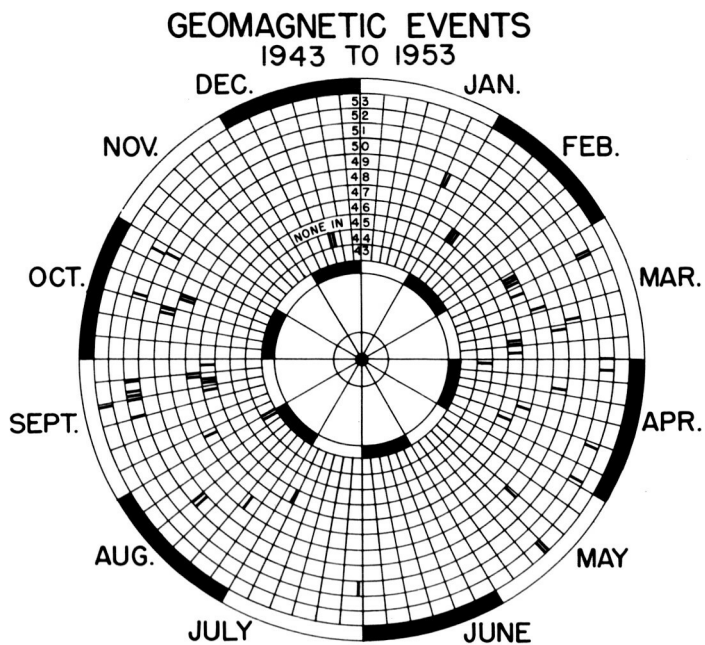


Figure 8

CONFIDENTIAL

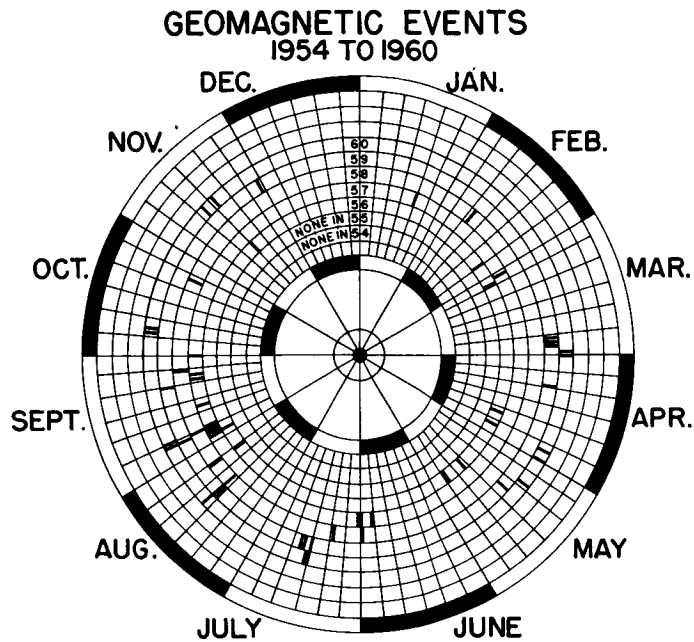


Figure 9

INTEGRAL ENERGY SPECTRA OF SOLAR PROTONS

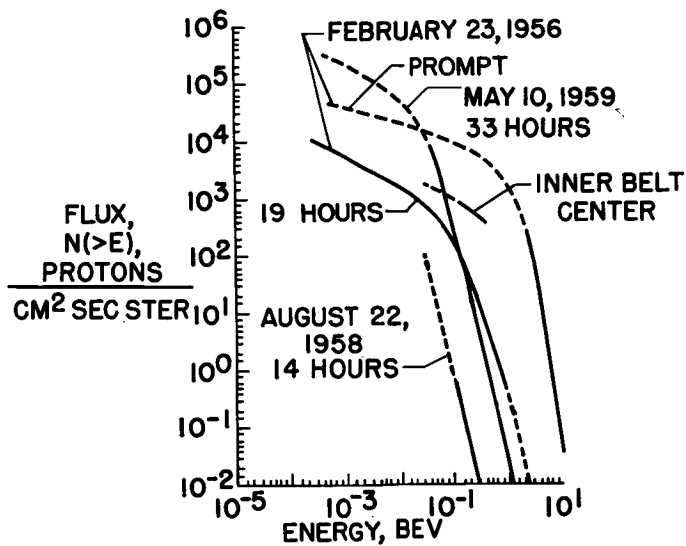


Figure 10

03713001001

NEUTRON SURGE AT SEA LEVEL DURING SOLAR FLARE OF FEBRUARY 23, 1956

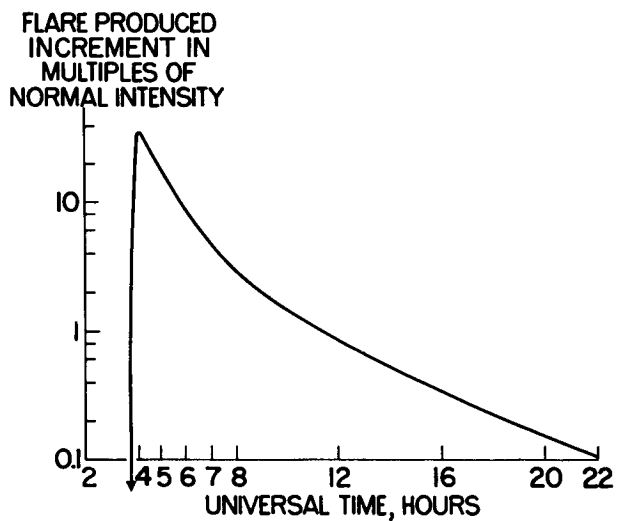


Figure 11

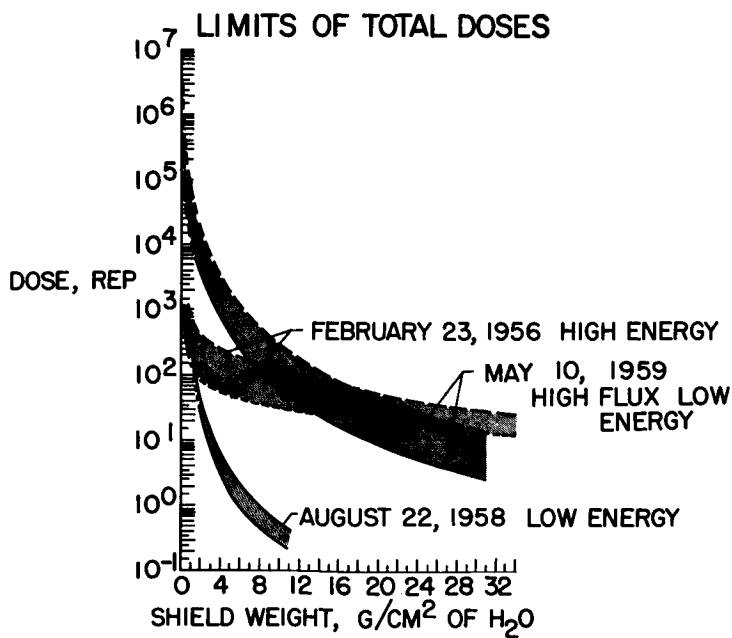


Figure 12

RADIATION-DESIGN ANALYSES FOR LUNAR MISSIONS

By Jacob Abel

General Electric - MSVD

INTRODUCTION

Present knowledge of Van Allen belt and solar flare radiations permits the analysis of many aspects of the lunar mission with regard to the radiation hazard. This paper is concerned primarily with the biological dose to which crew members will be exposed since dose levels which will be encountered are well below those which will produce detrimental effects in structural materials or electronic components. The principal areas of study which bear on this problem are: effect of Van Allen belt on trajectory selection, solar-flare-encounter probability, and vehicle-shielding characteristics.

Completion of these studies permits a determination of the probable dose function for a given spacecraft and mission. These studies yield a method of characterizing the radiation hazard on a basis similar to that upon which other spacecraft system risks are described.

The radiation hazard may be ameliorated by providing additional shielding on the spacecraft. Thus, the designer is faced with an ultimate trade-off of shielding weight penalty and mission safety. The manner in which the additional shielding is provided represents another variable at the disposal of the spacecraft designer. Shielding may be incorporated in the vehicle structure or may be applied to the person of the crew members. In addition, an equivalent weight of vehicle equipment or apparatus may with diminished effectiveness be employed as radiation shielding.

Before describing the results of these studies, a word about the maximum dose limitation is in order. The original study was conducted with a value of 25 REM (roentgen equivalent man) as a maximum emergency dose. This value was based on relatively conservative safety standards for an earth-based operation. Results are presented here relative to a maximum emergency dose of 100 REM, a value which can be expected to produce no permanent biological damage or incapacitation.




VAN ALLEN BELT

A computer program was developed which accepts initial position and velocity information and generates a solution of the trajectory equation. A model of the radiation belts is stored in memory and gives dose rate in roentgens per hour as a function of geomagnetic latitude and distance from the center of the magnetic dipole. For the type of radiation involved, an assumption of an RBE (relative biological effectiveness) of 1 will be accurate. This assumption yields the equivalence of 1 roentgen and 1 REM. Integration of the dose rate along the trajectory yields the total dose for the traverse of the trapped radiation belts.

The data employed are taken from the experiments carried in the Explorer VI (1959 Delta), Explorer IV (1958 Epsilon), and Pioneer III (1958 Theta). The value of shielding implicit in these data is about 1.0 gram per square centimeter and thereby yields a conservative estimate for the dose rates which will be encountered. Figure 1 shows a map of the belts and the trace of a lunar ascent trajectory generated from Saturn burnout data on launch from Cape Canaveral. The point marked by a triangle is the point at which a simulated emergency return is initiated, and the resultant return trajectory trace is shown also. For the family of lunar ascents which were simulated, a total dose of only 1 roentgen was encountered in each case. Figure 2 shows the integrated dose as a function of time for the outbound trajectory. It may be observed that the belt radiation is effective for a period of about 1 hour. These results taken in light of the conservative shielding estimate indicate that, for a nominal direct-ascent trajectory, the Van Allen belts do not constitute a primary hazard.

A family of emergency return trajectories were simulated from various altitudes along the outbound trajectory. The returns were initiated by inducing a velocity increment and flight-path angle change which would produce acceptable reentry conditions at an altitude of 400,000 feet.

Table I summarizes the results from a series of emergency returns showing abort altitude, return time, and integrated dose. Case I represents a return from an altitude of 345 miles with a resultant dose which is acceptably low, 11.6 roentgens. In case IIA a dose of 22 roentgens was encountered which in view of a 25 REM limit was sufficiently high to prompt an investigation to determine whether the dose could be lowered by varying the return trajectory. Alternate velocity and flight-path angle changes produced the results of cases IIB and IIC. It may be seen that a 50-percent reduction in total dose was achieved with the alternate return trajectories. It is significant to note that the reduction in total dose was achieved with a smaller



velocity increment and an increased return time; this result contradicts intuition. It may be concluded that, on an emergency return, trajectory shaping will permit minimization of the radiation dose from Van Allen belts and that immediate return does not necessarily yield a reduction in total dose due to the Van Allen belt.

SOLAR FLARE

Because of the apparent randomness of the occurrence of solar flares, the problem of encountering these streams of high energy protons is best approached on a probability basis. The probability of encountering a solar flare is naturally a function of frequency of occurrence and mission duration.

Figure 3 shows encounter probability as a function of mission duration for flare frequencies of 9 per year, 3 per year, and 1/4 per year. These frequencies correspond to an estimate of the peak rate of occurrence of three types of flares classified by energy spectra as follows:

Spectrum	Example obtained on -	Frequency per year
Low energy, high intensity	22 Aug. 1958	9
Low energy, extreme intensity	10 May 1959	3
High energy, high intensity	23 Feb. 1956	$\frac{1}{4}$

This model for the relationship between frequency of occurrence and flare type underlies the analysis of the probable dose function to be described later. The probabilities of encounter for a 1-week mission are, respectively, 16 percent, 5.8 percent, and 0.3 percent. Thus, for this mission the solar-flare hazard is of sufficiently high probability to merit further analysis.

In a previous paper by Trutz Foelsche and John E. Duberg the characteristics for the variation of dose with shielding for some solar proton events were shown. The high probability of encounter associated with these events necessitates analysis of the spacecraft from the point of view of radiation shielding. In the analysis of spacecraft structure three principal characteristics are sought:




(1) Because of the isotropic nature of the solar flare radiation, complete continuous enclosure of the crew compartment by the structural element is essential.

(2) The rapid decrease of dose with increased shielding (approximately inversely as the cube of shielding) places emphasis on the amount of mass per unit area.

(3) Where possible, low atomic number material is desired to minimize the production of secondary radiation.

Figure 4 shows a reentry vehicle with details of two areas of the structure. It may be seen that the elements shown fulfill the three requirements set forth. Complete enclosure of the crew compartment is afforded by the ablation material and substructure. The values of 2 grams per square centimeter and 5 grams per square centimeter represent appreciable contributions to the radiation protection. The ablation material, being a hydrocarbon (perhaps phenolic nylon), is characterized by a low atomic number and a high stopping power. Similarly, the aluminum substructure is a low atomic number material.

Applying a similar analysis to the total spacecraft yields a representation of the vehicle shielding. (See fig. 5.) This plot, termed the vehicle mass distribution, describes completely the shielding characteristics of the vehicle relative to a point at the mass center of the crew. On the mass distribution the radius is proportional to the shielding in grams per square centimeter and the angle is equal to the direction from the vehicle longitudinal axis. Circles are loci of constant shielding thickness, and the radius of the largest circle wholly contained within the vehicle contour gives the minimum value of allover protection. As the radius increases, larger and larger portions of the circle lie outside the contour and thereby define the so-called vulnerable solid angles. If it is desired to achieve a certain minimum value of allover shielding, supplemental shielding must be provided in the vulnerable areas. This plot then provides the basis for determining the weight penalty incurred as a function of the desired augmented shielding, a basic input to the trade-off between the weight penalty and mission safety. In this figure two concentric contours represent the reentry vehicle alone (designated R/V) and the entire space vehicle (designated S/V) configuration in assembly. For any given value of shielding, the complete spacecraft configuration affords more complete protection. Combination of the encounter probability data and the characteristics of dose and shielding of solar flares produces a probable dose distribution for a mission of specified duration. By considering the probability of encountering one, two, or three flares of the same or mixed types, the modes of encounter having probabilities in excess of 0.1 percent are exhausted. This condition produces a probability density distribution consisting of a finite number of points which leads to an integral distribution composed of a



series of steps. (See fig. 6.) This unfortunate discreteness in the integral distribution could only be eliminated by constructing a continuous relationship between flare type and frequency of occurrence which the present scarcity of data does not permit. In figure 6 the probability of exceeding a given dose for a 1-week mission is presented. Probabilities are given for three values of shielding. The value of 2 grams per square centimeter represents a lightly shielded vehicle or perhaps a man outside a vehicle in a pressure suit. The value of 7 grams per square centimeter corresponds to the effective shielding inherent in a typical spacecraft structure with little utilization of equipment. By incurring a weight penalty of 2,900 pounds, a typical vehicle may be supplemented to achieve an effective value of shielding of 20 grams per square centimeter. The decrease in risk with shielding is shown by considering the probability of exceeding 100 REM on a 7-day mission. The probability varies from 7 percent to 6 percent to virtually zero percent as the effective shielding is increased. This relationship constitutes the basis for a trade-off wherein the probability of exceeding the design dose limit, 100 REM, may be decreased by incurring a weight penalty. Thus, the probable dose determination leads to the relationship between weight penalty and mission safety and defines the "price" which must be paid to ensure a given level of reliability. This condition then characterizes the radiation hazard in a manner whereby it may be treated along with the other system risks, and wherein it may be handled as a fundamental input to the analysis of the overall system reliability.

The curves of the probability of exceeding 100 REM as a function of supplemental shielding weight (fig. 7) show the relationship for three modes of shielding augmentation. The curve on the right represents vehicle shielding wherein supplemental material is added to the structure in vulnerable areas. The center curve represents the case in which supplemental material is placed in close proximity to each crew member in the form of a garment or small enclosure. The curve on the left represents the case in which 50 percent of the supplemental shielding is developed by appropriate positioning of vehicle equipment and supplies. This curve is an estimate of what might be achieved in an optimum design. In order to reduce the probability of exceeding the design dose to less than 0.1 percent, the required supplemental shielding weight is for the three methods 1,600 pounds, 1,030 pounds, and 800 pounds. The choice of shielding mode will, of course, be affected by factors relating to crew comfort and performance, structural design, and materials selection which might override certain weight savings.

CONFIDENTIAL

CONCLUSIONS

On the basis of these analyses, the following conclusions may be made:

Van Allen belts: For a direct-ascent trajectory the Van Allen belts do not constitute a primary hazard. Consideration of emergency return points up a need for trajectory shaping on premature termination of the mission. The immediate or shortest return from an ascent trajectory does not necessarily produce the lowest integrated dose.

Solar flares: The risk of exceeding the dose limit has been established. A significantly high probability of encounter exists and this condition places emphasis on the shielding characteristics of the spacecraft under consideration. For a spacecraft with shielding of 7.0 grams per square centimeter the probability of exceeding the 100 REM dose is 6 percent. The probability may be decreased to a prescribed level of less than 1 percent by augmenting the shielding of the spacecraft with attendant weight penalties of 800 to 1,600 pounds.

The final resolution of the radiation problem requires the establishment of a dose limit and desired confidence level. It is then incumbent upon the spacecraft designer to provide sufficient shielding to attain this reliability and to trade off the attendant weight penalty with other means of improving system reliability.

CONFIDENTIAL

DECLASSIFIED

255

TABLE I

EMERGENCY RETURN TRAJECTORIES

CASE	ABORT ALT. ST. MI.	RETURN TIME HRS.	INTEGRATED DOSE ROENTGENS	VELOCITY INCREMENT FT./SEC.
I	345.5	3.2	11.63	6,000
II A	3,998.2	6.4	21.82	6,000
II B	3,998.2	23.5	8.22	2,000
II C	3,998.2	11.4	12.00	4,000
III	11,641.1	10.0	10.09	6,000

03710301301

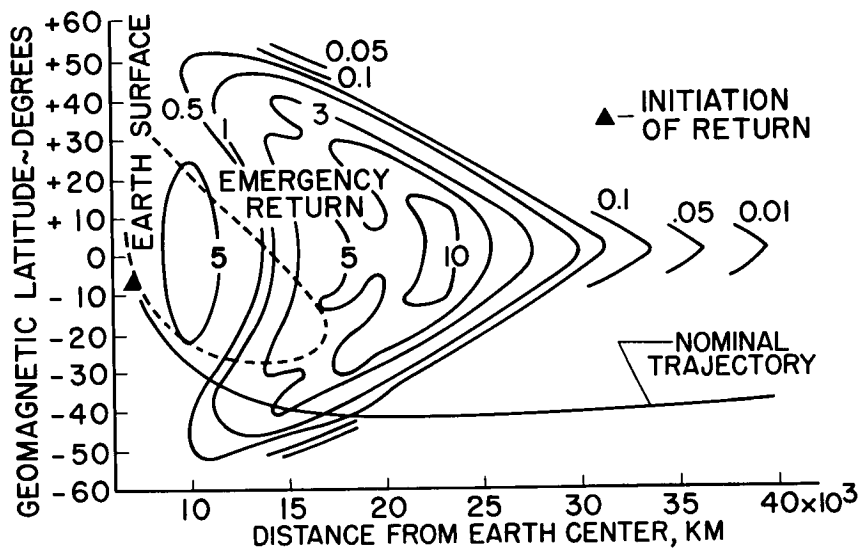
RADIATION INTENSITY CONTOURS
IN ROENTGENS/HR

Figure 1

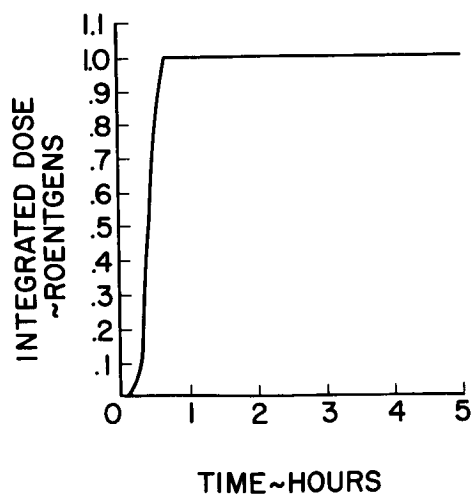
INTEGRATED DOSE VS. TIME
LUNAR ASCENT

Figure 2

REF ID: A65110

ENCOUNTER PROBABILITY vs MISSION DURATION

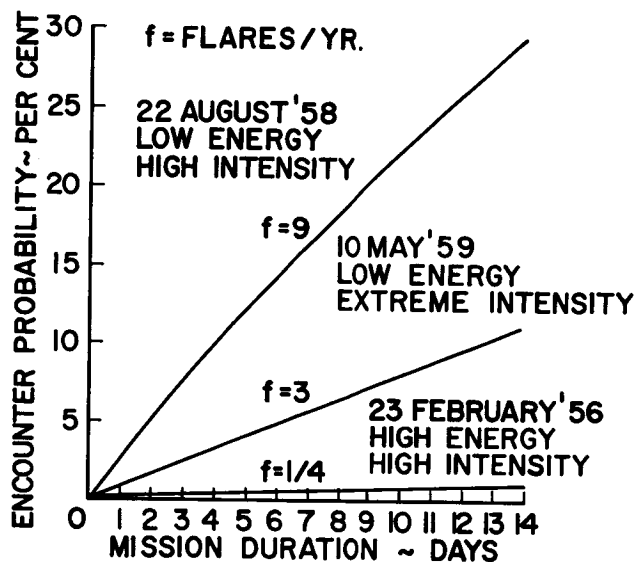


Figure 3

STRUCTURE SHIELDING ANALYSIS

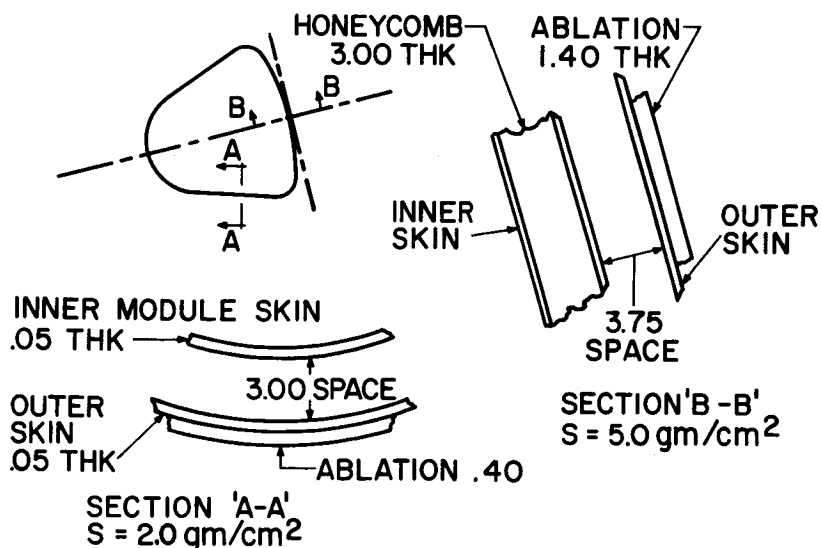
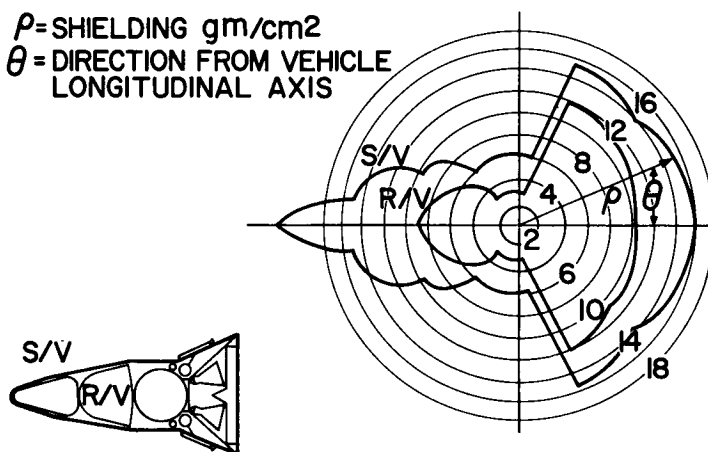


Figure 4

CONFIDENTIAL

VEHICLE MASS DISTRIBUTION

ρ = SHIELDING gm/cm²
 θ = DIRECTION FROM VEHICLE
 LONGITUDINAL AXIS



VEHICLE CROSS SECTION

Figure 5

PROBABILITY OF EXCEEDING DOSE 7 DAY MISSION

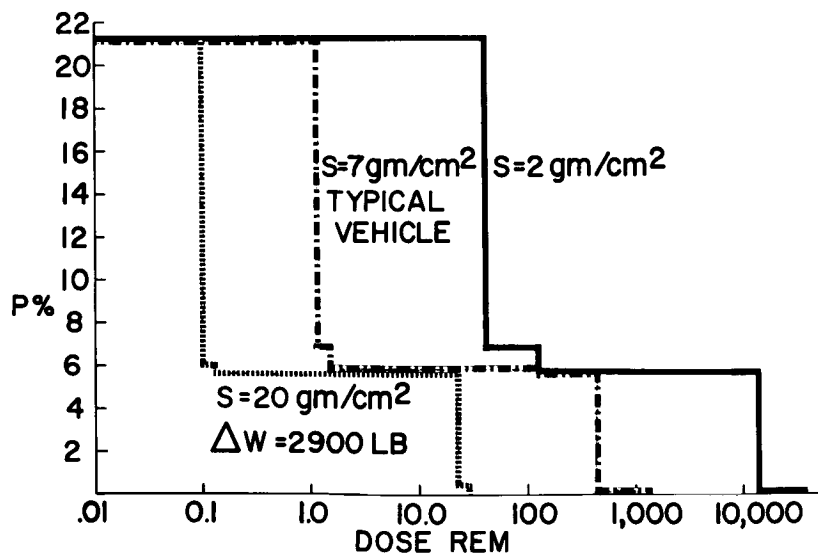


Figure 6

CONFIDENTIAL

PROBABILITY OF EXCEEDING 100 REM VS. ΔW

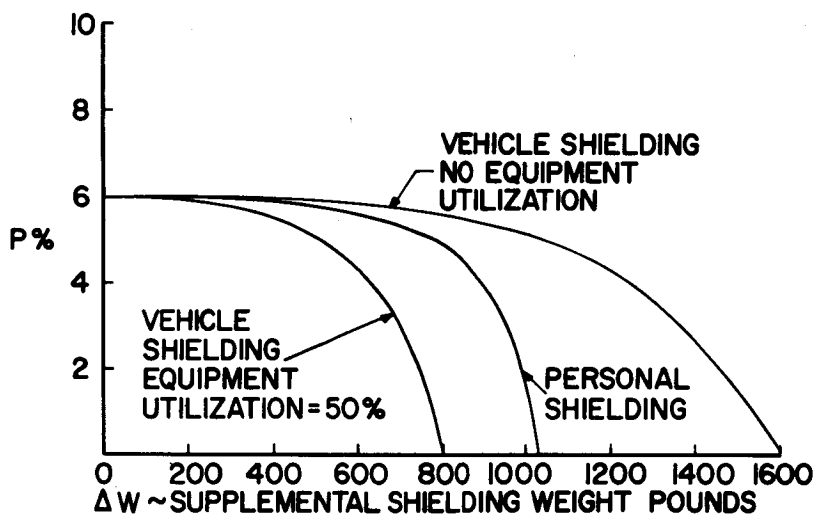


Figure 7

DECLASSIFIED

**V.
ENTRY HEATING
AND THERMAL
PROTECTION**

CONVECTIVE HEATING OF BASIC SHAPES

FOR LUNAR-MISSION VEHICLES

By P. Calvin Stainback, Robert A. Jones,
and Frank S. Coe III

Langley Research Center

INTRODUCTION

Since convective heat transfer will have a dominant influence on the heat-shield design, it is necessary to predict its distribution for vehicles considered for the Apollo mission. This paper is concerned with convective heating both to basic body shapes suitable for Apollo entry vehicles and to the control surfaces which may be required to maneuver these bodies.

General trajectory calculations for entry at parabolic velocities can be used to obtain the convective stagnation-point heat-flux variation with time and the integrated heat load for some arbitrary reference body, usually taken to be a sphere (refs. 1 and 2). Thus, the heating rate and the heat load to any point on an arbitrary vehicle can be calculated provided the distribution around the body from the stagnation point and the stagnation-point level, relative to the reference body, can be estimated.

The data were obtained in the Mach number range from 5 to 10 at values of gas enthalpy up to 500 Btu/lb. Therefore, the applicability of the data, obtained from an ideal gas, to high flight speeds where real-gas effects are encountered must be justified. For a body without transition or separation, such a justification may be obtained as follows: First, the test Mach number was sufficiently high to minimize the influence of Mach number on the results. Second, current information (ref. 3) indicates that the inviscid flow around the body during peak heating will be in equilibrium. The boundary layer, however, can be in nonequilibrium. If the boundary layer is in equilibrium, the ideal-gas distribution is approximately equal to the real-gas distribution; if nonequilibrium exists in the boundary layer, the distributions are essentially equal provided the wall is catalytic (ref. 4). A non-catalytic wall can, of course, result in a reduction in the heating level when the boundary layer is in nonequilibrium. Finally, the effect of free electrons on the heat transfer does not appear to be a serious problem in the parabolic-velocity range (ref. 5).

CONFIDENTIAL

The aforementioned application of low enthalpy test results to surfaces heated by boundary layers subject to transition, separation, reattachment, shock impingement, and so forth may not be justified. The effects of the interplay between Reynolds number and enthalpy on these boundary layer phenomena are not presently understood. The data reported herein arose from an exploratory program in which this interplay could not be investigated sufficiently. Consequently, the data for the flap configurations may not necessarily be valid for the Apollo environment but are presented as a guide to be used until data become available at the correct higher enthalpy levels.

The tunnel conditions for the data presented simulate the free-stream Reynolds number range for full-scale Apollo vehicles at altitudes between 175,000 and 230,000 feet, the range of conditions where peak heating will be experienced. The data for the basic bodies without flaps correlated in a laminar manner with a single exception which will be noted.

The data are presented in nondimensional form; therefore, the stagnation-point heating rate for the reference body can be calculated by any suitable method and the usefulness of the data depends only on the distribution being invariant with gas conditions.

SYMBOLS

d	base diameter
h	aerodynamic heat-transfer coefficient
\bar{h}	normalized heat-transfer coefficient
M_{∞}	free-stream Mach number
N_{Pr}	Prandtl number
R_d	Reynolds number based on maximum diameter
r	radius
s	surface distance
α	angle of attack
δ	flap-deflection angle

CONFIDENTIAL

ϕ angular displacement

Subscripts:

c corner
e equivalent disk
n nose
s stagnation point

HEAT-TRANSFER DISTRIBUTIONS TO BASIC BODIES

Heating distributions are presented for the basic bodies and flaps for the four configurations shown in figures 1(a) to 1(d). The distribution for the blunted half-cone, shown in figure 1(a), was not included since the data are available from reference 6. The data are presented in dimensionless form where the local heat-transfer coefficient was divided by the stagnation-point heat-transfer coefficient of the reference body, a sphere. The size of the sphere in relation to the model was such that, if the model were scaled up to equal the size of the full-scale Apollo vehicle, the scaled-up reference sphere would have a radius equal to 1 foot.

Since the models were not geometrically similar to the Apollo vehicle, the characteristic dimension used for scaling purposes was taken to be the dimension governing the stagnation-point heating rate at the design attitude of the vehicle. This dimension is noted on the model drawings in figures 1(b) to 1(d).

The local heat-transfer coefficients presented are based on a Prandtl number of 1 except for the truncated half-cone. The heat-transfer coefficients for this model were based on recovery factors estimated from local fluid properties obtained from measured pressures and the assumption of isentropic flow from stagnation conditions.

The data presented were not corrected for conduction effects. Since most of the data were obtained at very short times, the model was essentially isothermal; therefore, conduction effects were small. This was not the case for the truncated half-cone, and conduction effects in regions of high heating and high surface curvature could result in estimated conduction corrections from 30 to 50 percent of the measured convective rates. The heating to most of the body was, however, essentially unaffected by conduction effects.

CONFIDENTIAL

The conduction effects on the flap data for the models tested could be significant. These data were not corrected, however, because of the limited instrumentation available.

Blunted Cone

The first shape considered was a simple 25° blunted cone (fig. 1(b)) with a ratio of nose radius to base radius of 0.2. Figure 2 presents the normalized heat-transfer coefficient as a function of the dimensionless surface distance s/r , where r is the base radius of the model. Data are presented for the most leeward and most windward meridians at the angles of attack of 0° , 15° , and 45° . No data were taken on the spherical cap, located between the large ticks on the s/r coordinate, in order to simplify the construction of the model. However, the heat-transfer characteristics of the sphere are well known. The theoretical stagnation-point heat-transfer coefficient ratio to the sphere, calculated from reference 7, is noted in the figure for reference.

The solid and dashed curves shown in figure 2 represent Lees blunt-cone theory at zero angle of attack (ref. 8) and a swept-cylinder theory, respectively. There was good agreement between these theories and data for the test angle-of-attack range for the most windward meridian and up to 15° angle of attack for the most leeward meridian. Heat transfer to the most leeward meridian was negligible for angles of attack greater than 15° .

The heating has been predicted to the windward meridian and, if its distribution around the body can be predicted, as related to the windward meridian, the complete heat-transfer distribution on the cone will be known.

In figure 3 the heat-transfer distribution around the blunt cone is presented as a function of the angular displacement ϕ for an angle of attack of 15° . The local heat-transfer coefficient was nondimensionalized by the local coefficient at $\phi = 0^\circ$, the most windward meridian. It is to be noted that the data are independent of the heating level.

The cross-hatched region represents data taken in the s/r range from 0.4 to 2.0. The theoretical curve was calculated by using the results of reference 8 and pressures obtained from the tangent cone method. The data indicated that the distribution was fairly insensitive to s/r and was in good agreement with the theoretical curve in the range of ϕ from 0° to 180° .

CONFIDENTIAL

Truncated Half-Cone

Shown in figure 4 is the heat transfer to the truncated half-cone as a function of the distance along the body for the upper and lower surfaces of the model in the vertical plane of symmetry. The characteristic dimension assumed to control the stagnation-point heating, when the flat portion of the nose was normal to the free-stream velocity, was taken to be the inscribed circular disk illustrated in figure 1(c). The stagnation-point heating level to the disk was calculated by using the variation of the stagnation-point pressure gradient with corner radius based on unpublished correlation studies made at the Langley Research Center by Mitchel H. Bertram.

Data are presented for angles of attack of 30° and 40° , angles which bracketed the design angle of attack. Theory (ref. 8) is presented for an angle of attack of 30° , the angle of attack at which pressure data were available, and there is fair agreement between the theory and data. It should be noted that the pressure measurements available were not extensive and it can be assumed that, if more detailed measurements were available, the agreement between the theory and data would be somewhat better.

The heat-transfer distribution around the truncated half-cone as a function of the dimensionless distance from the lower center line is presented in figure 5 for 30° angle of attack. The distribution, non-dimensionalized by the lower center line heat-transfer coefficient, was relatively insensitive to its chordwise location except for the 80-percent-chord position; there was fair agreement between the data and theory. Again the pressure data were not extensive and the pressure information required for the theory (ref. 8) was obtained by fairing a curve through the pressure data for the four chordwise stations noted in the figure.

A more detailed discussion of this configuration can be found in reference 9.

Flat-Face Body of Revolution

The heat transfer to a flat-face body of revolution (fig. 1(d)) with a ratio of shoulder radius to base radius of 0.2 is presented in figure 6 as a function of the surface distance from the face center. Data and theory are presented for angles of attack of 0° and 45° . The theoretical curve for $\alpha = 0^\circ$ was calculated by use of the method and measured pressures of reference 10, and there was reasonable agreement between the data and theory. The stagnation-point level was obtained from the previously mentioned correlations by Bertram. At 45° angle of

03710281030

attack the stagnation point is located on the small-radius shoulder and the heat transfer to the body can be estimated, as indicated by figure 6. The method of reference 8 and Newtonian pressures were used to calculate the theoretical distributions and the method of reference 11 was used to estimate the stagnation-point level. For angles of attack between $\alpha = 0^\circ$ and 45° , stagnation-point pressure measurements are required in order to determine the velocity gradient and subsequent heat-transfer distribution.

The distribution on the plane of symmetry is, of course, only part of the picture for this body. Distributions are shown in figure 7 for several values of ϕ and for $\alpha = 45^\circ$, which is near the design angle of attack for such blunt-face bodies. The theoretical curves and data for $\phi = 0^\circ$ and 180° were shown in figure 6. The heating for $\phi = 45^\circ$ is represented by the square symbols and there is good agreement between the theory and data. The theoretical curve was calculated by assuming that the model in this region was a swept wing and by use of the method of reference 12 from which the distribution and level were computed.

The heat transfer for $\phi = 90^\circ$, 135° , and 180° , noted by the cross-hatched region, is essentially constant on the face of the body. The theoretical curve $\phi = 90^\circ$ (dashed curve) was obtained by referencing the theory of reference 10 to the level at the center of the front face, as obtained from the theory of reference 8. The theoretical distribution for $\phi = 90^\circ$ and 180° brackets the data for the lower front face of the body.

FLAPS

In addition to the data obtained for the basic bodies, heat-transfer measurements have been made for flaps on the blunted cone, the flat-face body of revolution, and the blunted half-cone. Heat-transfer data for the basic blunted half-cone without flaps have not been included in this discussion since most of the available information was presented in reference 6. The flap configurations investigated for the various models are presented in figure 1.

Blunted Cone

In figure 8 the heat transfer to a flap on the blunted cone is presented as a function of the flap-deflection angle δ measured from the conical surface for four angles of attack and two Reynolds numbers. The position on the flap for which data are presented is noted in figure 1(b). It should be pointed out that the length of the flap used

CONFIDENTIAL

for the test at $\delta = 65^\circ$, noted as F-1 in figure 1(b), was 75 percent of that of flap F-2 used for testing at lower values of δ .

At $\alpha = 0^\circ$ the heat transfer to the flap increased rapidly with flap-deflection angle δ but, as the angle of attack was increased, the rate decreased until at $\alpha = 45^\circ$ the heat transfer to the flap was almost invariant with δ . At $\alpha = 0^\circ$ the peak heating on the flap was about three times the stagnation-point value when $\delta = 65^\circ$. At $\alpha = 45^\circ$ the peak heating was somewhat less than the stagnation-point heating.

The influence of Reynolds number appeared to be somewhat greater at 15° angle of attack. For this angle of attack transition occurred on the cone without a flap for a Reynolds number of 1.75×10^6 , so that sensitivity to Reynolds number is probably due to the character of the boundary layer approaching the flap.

Figure 9 presents the heat-transfer distribution across and along the flap of the blunted cone. Data are presented for an angle of attack of 15° , a flap-deflection angle of 15° , and two Reynolds numbers. The higher Reynolds number causes higher heating and this was probably due to the aforementioned transition. This transition also probably explains the reverse trend with chordwise position for the two Reynolds numbers. The heat transfer to the flap in the spanwise direction was essentially constant in the range where measurements were made and the chordwise variation is not large.

Blunted Half-Cone

Heat transfer to the control surfaces of the blunted half-cone is shown in figure 10. The controls consist of four flaps, two on the upper surface and two on the lower conical surface.

The heating is presented as a function of the flap-deflection angle δ measured from the body surface for angles of attack of 0° and -14° . The shaded regions represent the range of heating for the flaps as determined from seven thermocouples located around the edge of the flaps. The heat transfer to the lower flap increased moderately with increased flap-deflection angle δ and for $\delta = 30^\circ$ and $\alpha = 0^\circ$ attained a value about 40 percent greater than that at the body stagnation point. The upper flap heating increased at a somewhat faster rate with flap-deflection angle for $\alpha = -14^\circ$, and at $\delta = 46^\circ$ reached values approximately 2.5 times the stagnation-point value for the basic body.

Flat-Face Body of Revolution

In figure 11, the heat transfer to a flap of the flat-face body of revolution is presented as a function of the flap-deflection angle δ , measured from the surface of the conical afterbody. Data are presented for three thermocouples located on the midchord of the flap and for angles of attack of 0° , 15° , 30° , and 45° .

In general, heating on the flap increased with δ and the variation with δ increased with angle of attack. This is in contrast to the heating of the blunt cone where the highest variation with flap deflection was associated with zero angle of attack. The magnitude of the heating at $\delta = 135^\circ$ varied little with angle of attack and had a value that was approximately equal to the stagnation point at $\alpha = 45^\circ$. The heat transfer to this portion of the flap was found to be almost invariant with Reynolds number when the free-stream Reynolds number varied by a factor of about 6.

The effect of the flap on body heating is shown in figure 12 where data are presented as a function of the surface distance for $\alpha = 45^\circ$ and three flap-deflection angles. The dashed curve represents the heating on the body without flaps. At $\delta = 75^\circ$ the heating on the flap and the influence of the flap on the basic-body heating were small. As δ was increased, the heating on the flap increased and attained a value that was 15 percent greater than the heat transfer to the stagnation point when $\delta = 135^\circ$. At this condition the flap increased the heating on the body, in the vicinity of the flap, until at the base of the flap it was 60 percent of the stagnation-point value.

CONCLUDING REMARKS

Estimates satisfactory for preliminary design purposes can be made for convective heating to blunted-cone bodies, half-cone modifications, and to the flat-face bodies of revolution treated in this paper. For simple bodies, only theoretical pressures were required to make heat-transfer estimates; whereas, for more complicated bodies, measured pressures were necessary. These estimates can be considered reliable in regions not influenced by separation, transition, or flap interactions.

Heat transfer to typical control surfaces was large for large flap-deflection angles. The extent to which flap heating can be minimized will be dependent on trade-off studies for the particular system approach employed.

REFERENCES

1. Chapman, Dean R.: An Analysis of the Corridor and Guidance Requirements for Supercircular Entry Into Planetary Atmospheres. NASA TR R-55, 1960.
2. Grant, Frederick C.: Simple Formulas for Stagnation-Point Convective Heat Loads in Lunar Return. NASA TN D-890, 1961.
3. Wong, Thomas J., Goodwin, Glen, and Slye, Robert E.: Motion and Heating During Atmosphere Reentry of Space Vehicles. NASA TN D-334, 1960.
4. Cohen, Nathaniel B.: Boundary-Layer Similar Solutions and Correlation Equations for Laminar Heat-Transfer Distribution in Equilibrium Air at Velocities up to 41,100 Feet Per Second. (Prospective NASA Report.)
5. Adams, Mac C.: A Look at the Heat Transfer Problem at Super Satellite Speeds. [Preprint] 1556-60, American Rocket Soc., Dec. 1960.
6. Reller, John O., Jr., and Seegmiller, H. Lee: Convective Heat Transfer to a Blunt Lifting Body. NASA TM X-378, 1960.
7. Reshotko, Eli, and Cohen, Clarence B.: Heat Transfer at the Forward Stagnation Point of Blunt Bodies. NACA TN 3513, 1955.
8. Lees, Lester: Laminar Heat Transfer Over Blunt-Nosed Bodies at Hypersonic Flight Speeds. Jet Propulsion, vol. 26, no. 4, Apr. 1956, pp. 259-269, 274.
9. Coe, Frank S., III, and Feller, William V.: Experimental Investigation of the Pressures, Heat Transfer, and Surface Flow Patterns Around a Blunt Half-Cone Lifting Reentry Body at a Mach number of 9.6. NASA TM X-589, 1961.
10. Beckwith, Ivan E., and Cohen, Nathaniel B.: Application of Similar Solutions to Calculation of Laminar Heat Transfer on Bodies With Yaw and Large Pressure Gradient in High-Speed Flow. NASA TN D-625, 1961.
11. Reshotko, Eli: Heat Transfer to a General Three-Dimensional Stagnation Point. Jet Propulsion, vol. 28, no. 1, Jan. 1958, pp. 58-60.
12. Stainback, P. Calvin: Heat-Transfer Measurements at a Mach Number of 4.95 on Two 60° Swept Delta Wings With Blunt Leading Edges and Dihedral Angles of 0° and 45°. NASA TN D-549, 1961.

BLUNTED HALF-CONE

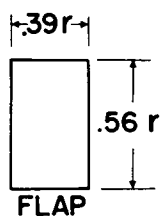
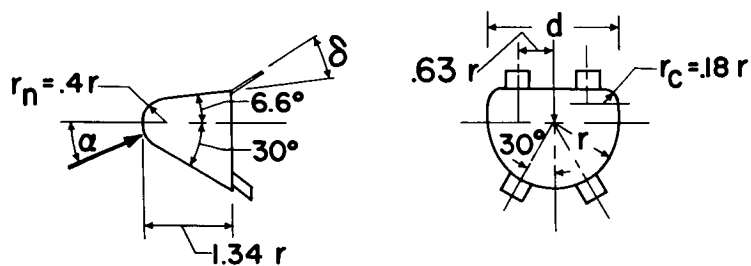


Figure 1(a)

BLUNT CONE

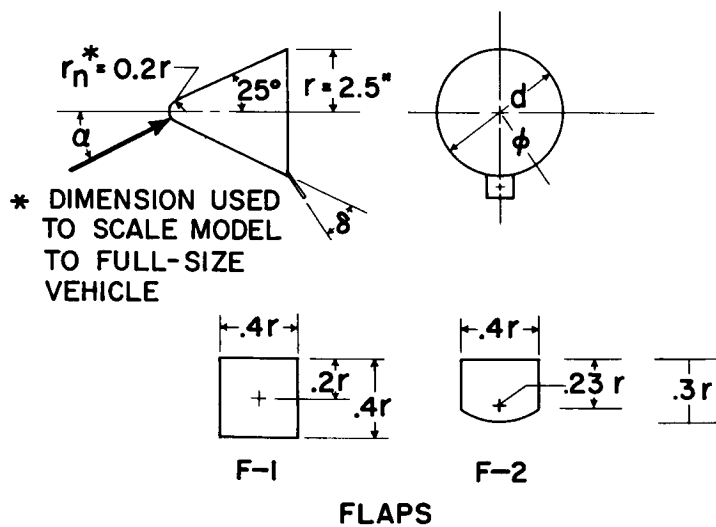
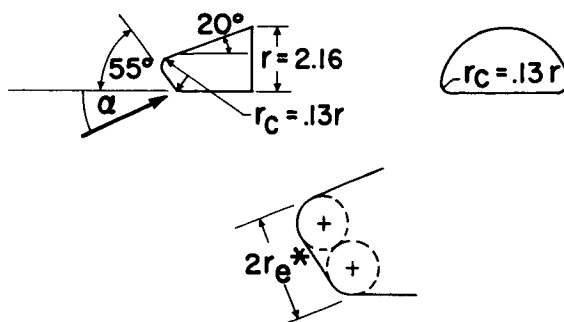


Figure 1(b)

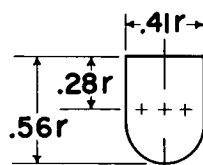
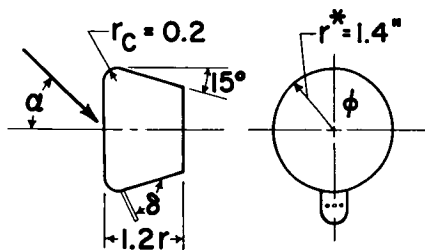
TRUNCATED HALF-CONE



* DIMENSION USED TO SCALE MODEL TO FULL-SIZE VEHICLE

Figure 1(c)

FLAT-FACE BODY OF REVOLUTION



FLAP

* DIMENSION USED TO
SCALE MODEL TO
FULL-SIZE VEHICLE

Figure 1(d)

HEAT TRANSFER TO BLUNT CONE, $M_\infty = 8$

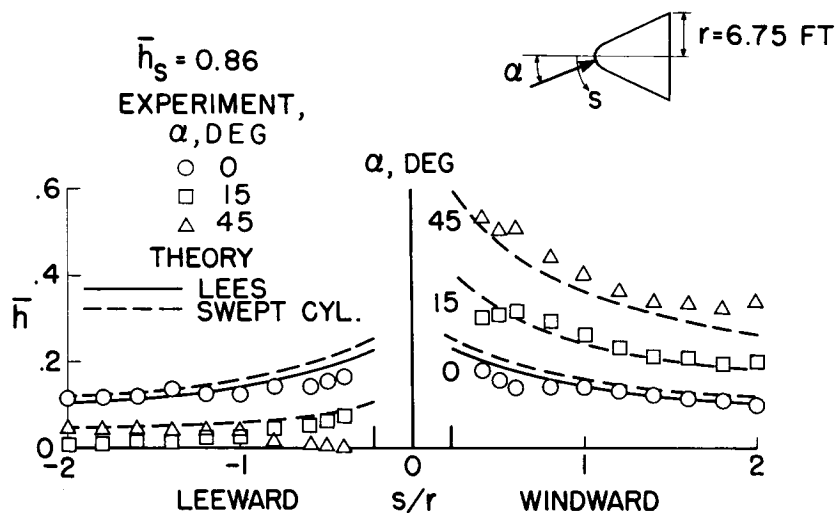


Figure 2

HEAT-TRANSFER DISTRIBUTION AROUND BLUNT CONE

$M_\infty = 8$; $\alpha = 15^\circ$

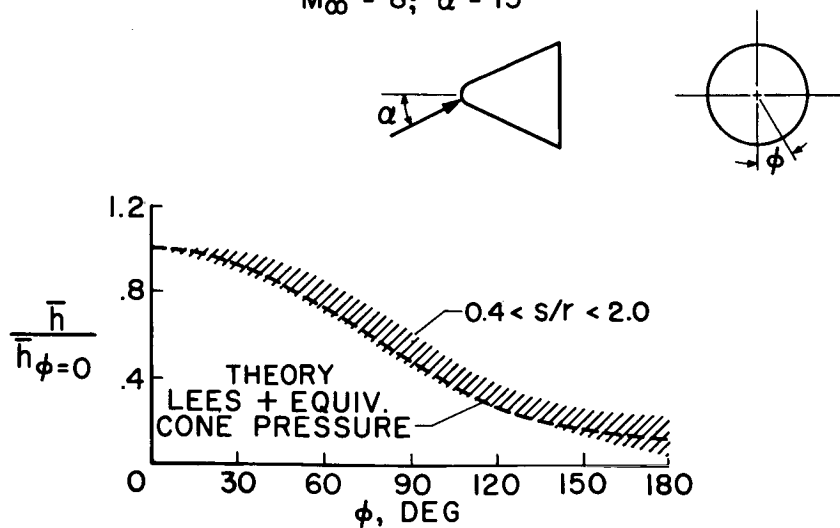


Figure 3

HEAT TRANSFER TO TRUNCATED HALF-CONE

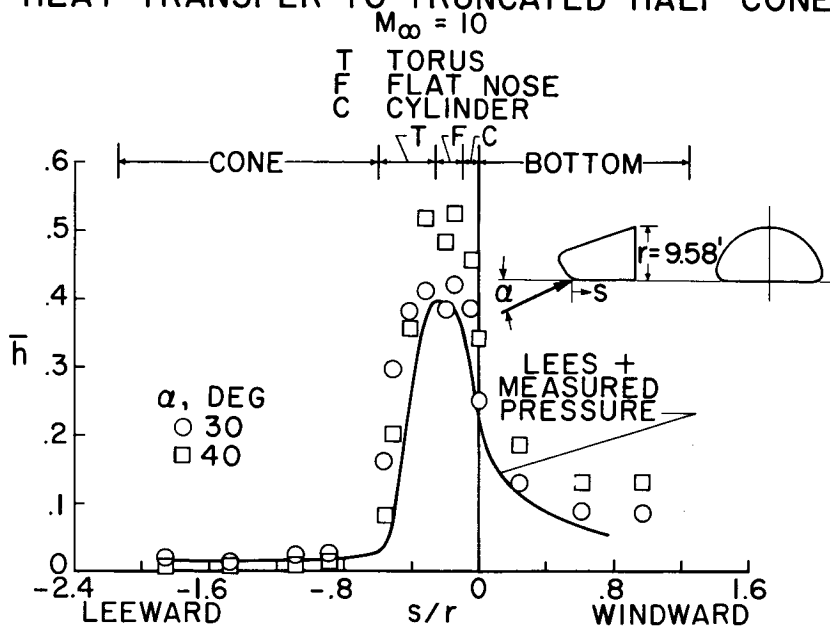


Figure 4

HEAT-TRANSFER DISTRIBUTION AROUND TRUNCATED HALF-CONE

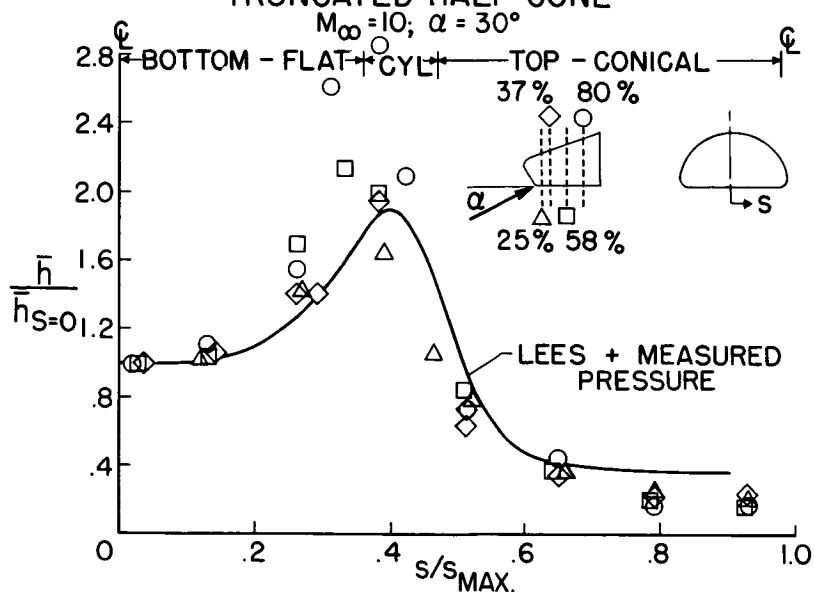


Figure 5

HEAT TRANSFER TO FLAT-FACE BODY

$$M_{\infty} = 8$$

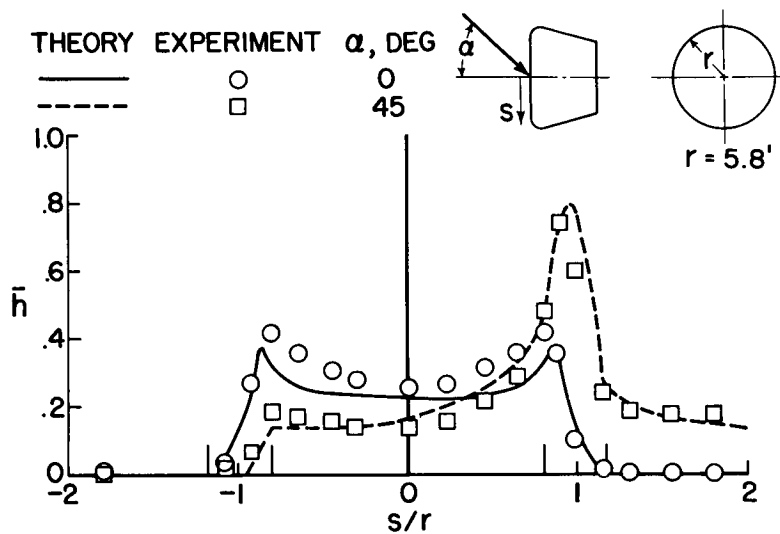


Figure 6

HEAT TRANSFER TO FLAT-FACE BODY

$$M_{\infty} = 8; \alpha = 45^\circ$$

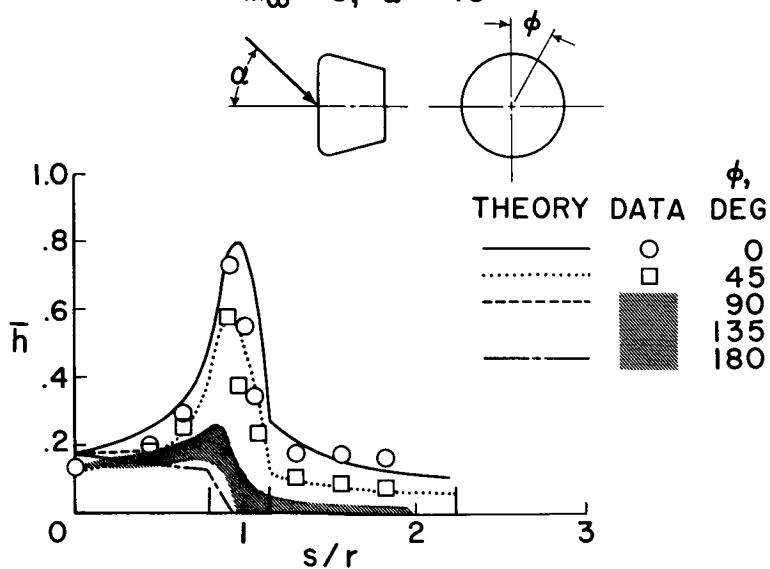


Figure 7

HEAT TRANSFER TO FLAP OF BLUNT CONE $M_\infty = 8$

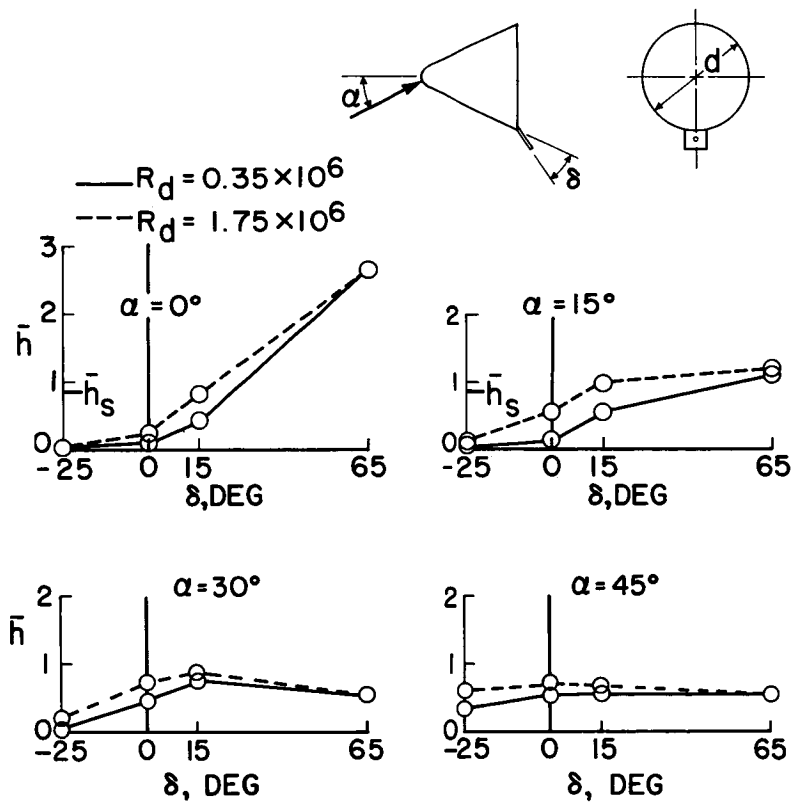


Figure 8

HEAT-TRANSFER DISTRIBUTION ON FLAP OF BLUNT CONE

$M = 8; \alpha = 15^\circ; \delta = 15^\circ$

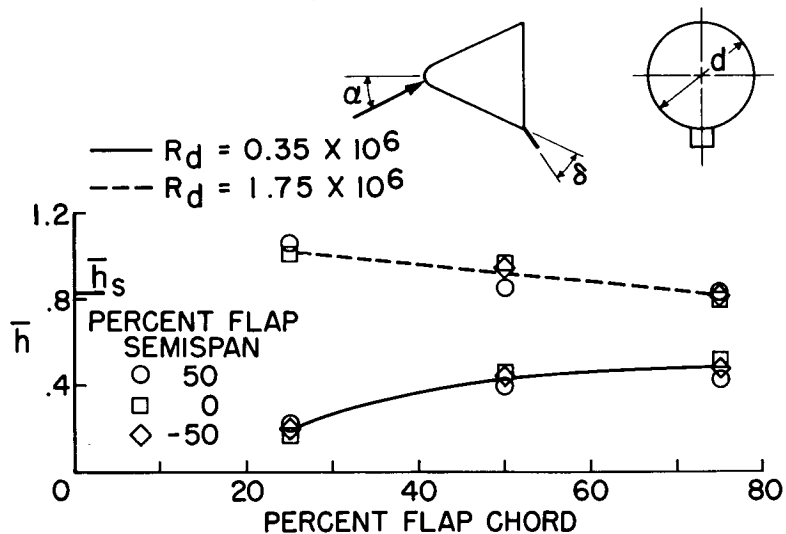


Figure 9

HEAT TRANSFER TO CONTROL SURFACES OF A BLUNTED HALF-CONE

$M_\infty = 5$

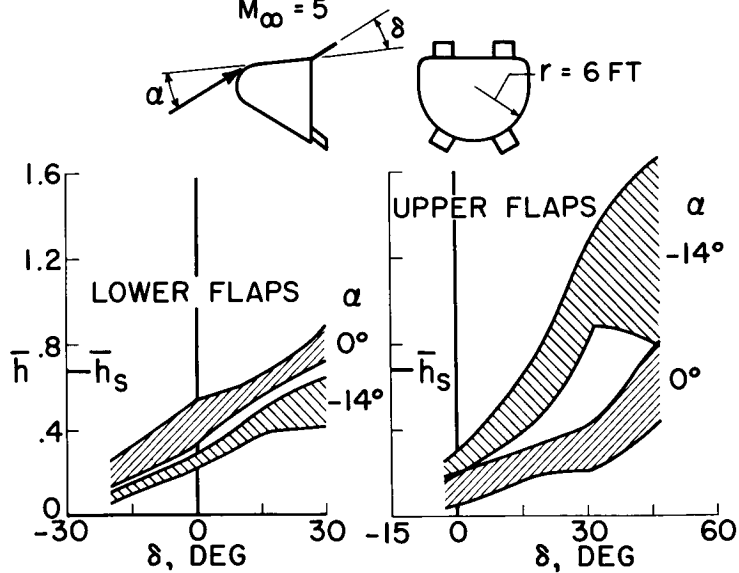


Figure 10

HEAT TRANSFER TO FLAP OF FLAT-FACE MODEL

$M_\infty = 8$

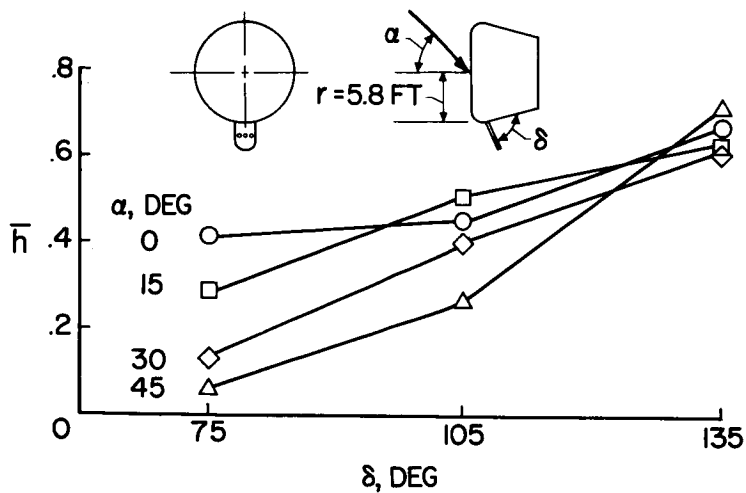


Figure 11

INFLUENCE OF FLAP ON HEATING TO FLAT-FACE MODEL

$M_\infty = 8; \alpha = 45^\circ$

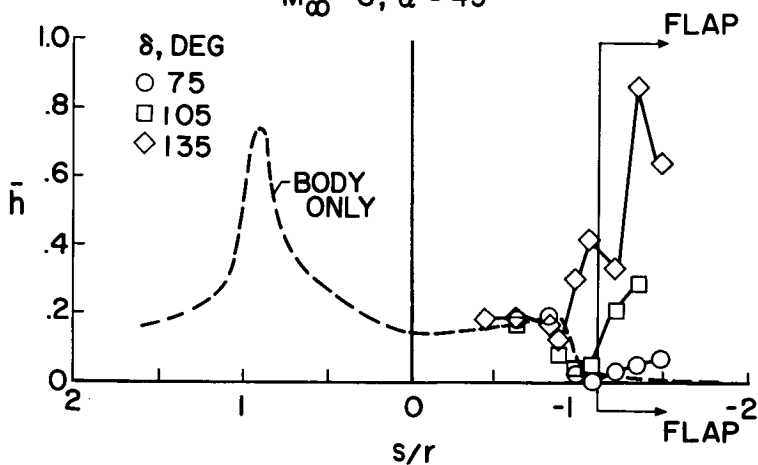


Figure 12

DECLASSIFIED

279

MEASUREMENTS OF THE THERMAL RADIATION FROM
SHOCK LAYERS OF BLUNT BODIES FLYING AT VELOCITIES
UP TO 44,000 FEET PER SECOND

By Thomas N. Canning, William A. Page,
Harry E. Bailey, and Joseph M. Burge

Ames Research Center

INTRODUCTION

During the past few years, there have been a number of efforts, both theoretical and experimental, to estimate the amount of radiative heating which will be felt by the heat shield of hypervelocity vehicles entering the earth's atmosphere (refs. 1 to 5). At orbital speeds, reentry appears to be not too greatly affected by radiation from the hot-gas cap. However, since the radiation is known to increase extremely rapidly with increasing velocity, the problem is expected to be not so simple in the case of parabolic entry. Several independent experimental investigations of radiative heating have been conducted at the Ames Research Center. Two of these investigations have been conducted in such manner that the flight parameters are simulated fairly well. The experimental information presented herein are measurements of the properties of the radiation being emitted from the shock layer about small free-flight models at velocities up to 44,000 ft/sec.

SYMBOLS

I	radiation intensity
r	nose radius
T_{EQ}	equilibrium temperature
U_{∞}	total velocity
λ	wavelength
ρ_0	sea-level standard density

03171234 1030

 ρ_2 density behind bow shock ρ_∞ free-stream density

FACILITIES AND INSTRUMENTATION

The facilities used for the investigation consist of small-caliber light-gas guns operating at muzzle velocities up to 31,000 ft/sec. The models are fired into countercurrent air streams generated by shock-tube-driven wind tunnels having stream velocities up to 14,000 ft/sec. A combined velocity of 44,000 ft/sec has been obtained.

Observations of the radiation from the shock layers of the models are made with multiplier phototubes. For measurements of the total emitted radiation, broad-band phototubes were used. For determining the spectral distribution of the radiation, phototubes were fitted with various narrow-bandwidth optical filters. Each phototube and phototube-filter combination was calibrated using calibrated light sources in the manner described in reference 5. Figure 1 shows schematically the manner in which the models were viewed by the multiplier phototubes. The insert photograph of the model in this figure is a self-illuminated photograph taken with a Kerr-cell camera having an exposure time of 50 nanoseconds (0.05 microsecond). The velocity of the model relative to the camera for this particular example was 26,000 ft/sec. Also shown in the figure is a typical oscilloscope trace of the output of a phototube. The trace records radiation from the hot-gas cap of the model followed by that of the wake.

The models were spherically nosed cylinders of 1/2-cm nose radius made of either linear high-density polyethylene or polycarbonate (trade name, Lexan). One pyrex sphere, 1/16 inch in diameter, was also tested in order to determine the effect of model material and size on the magnitude of the observed radiation.

Other instruments typically used in ballistic ranges and shock-tube-driven wind tunnels were used to establish test conditions and model velocity.

DATA REDUCTION

To reduce the experimental measurements of the power emitted by the model gas cap to a form comparable to available theory (i.e., power per unit volume), it was necessary to estimate the effective volume of

the radiating gas. These estimates were made in the same manner as is described in reference 5. Also, the effects of the spectral distribution of the radiation on the fraction of the total radiation seen by the phototube were calculated with the use of the tabulations of reference 1 in the same manner as described in reference 5.

RESULTS

Total Radiation

The results from the experiments are summarized in figure 2 as a function of velocity. The estimated total radiation per unit volume is presented in a form normalized to standard sea-level density in the stagnation point region by dividing by the density ratio (ρ_2/ρ_0) raised to the 1.7 power. The quantity ρ_2 is the density directly behind the bow shock; ρ_0 is sea-level standard density. This method of presentation was also used in reference 5 and was chosen because it normalizes the theoretical curves for different densities, from references 1 and 2, to a narrow band over the range of densities specified in figure 2. The agreement between experiment and theory appears quite satisfactory for the data points plotted with open symbols. In these tests, the computed gas-cap density (assuming the gas to be in thermodynamic and chemical equilibrium) was always greater than one-seventh of standard sea-level density. As the computed density in the gas cap was reduced below this value, progressively greater amounts of normalized radiation were observed above the values predicted by the equilibrium-radiation theory. Since it is believed that this greater radiation intensity results from failure of the air in the gas cap to achieve thermodynamic and chemical equilibrium, a simple flow model, which explains the increased radiation, will be described. This flow model has been proposed by Camm (ref. 3), and others.

In one-dimensional flow behind a strong shock wave, it may be argued that the temperature varies in a manner such as that sketched in figure 3. In an exceedingly short distance behind the wave front the translational temperature reaches a value close to that which would be achieved by a perfect gas. Subsequently the air achieves thermodynamic and chemical equilibrium, and the temperature reduces to the equilibrium value. In this transient period, collisions produce excited particles which decay to lower states and emit copious quantities of radiation apparently related to the higher-than-equilibrium temperatures existing in the gas layer. The radiation intensity therefore may reach a maximum greater than the equilibrium radiation intensity and then reduce to the lower equilibrium value as the gas flows back

from the shock front and relaxes to the equilibrium state. The situation for a lower gas density is depicted in figure 4. The relaxation process requires a longer distance to achieve completion because the number of collisions per second is reduced if the density is reduced. It can be seen, then, that greater and greater fractions of the shock layer are out of equilibrium and may radiate at greater-than-equilibrium radiation levels when the density of the shock layer is low. The counteracting variables are the thickness of the shock layer (i.e., vehicle size) and the air density. Since the chemical reaction rates during the decay of the radiation overshoot vary inversely with the density, the parameter $\rho_{\infty} r$ (where ρ_{∞} is free-stream air density and r is the vehicle nose radius) characterizes the departure from equilibrium. This nonequilibrium radiation has been observed in earlier ballistic-range tests at Ames Research Center and in many shock-tube tests by a number of experimenters.

The data of figure 2 have been replotted in figure 5 in such a manner as to use the suggested scaling factor $\rho_{\infty} r$. The overshoot ratio, which is the ratio of observed radiation to that which would be calculated using equilibrium theory, is plotted against the altitude-

size parameter $\frac{\rho_0}{\rho_{\infty} r}$ for three velocities. The test density appears

to predominate over the effect of velocity in determining the overshoot ratio. It should be noted particularly that the results of the test for the 1/16-inch-diameter pyrex sphere at 20,000 ft/sec (overshoot ratio of 20) agree reasonably well with data from the models having a radius 6.5 times larger. Direct comparison cannot be made without more detailed computations of the theoretical equilibrium radiation than were possible in the present investigation. This comparison suggests that the scaling rule may work reasonably well for these small models. The largest radiation overshoot noted during the tests was a factor of 860. The nature of the faired curves in figure 5 suggests that the overshoot ratio would be higher at densities lower than those investigated with the present facilities. If the air density is reduced to extremely low levels, however, the radiation from the gas cap must eventually be extinguished, because insufficient time would be available to produce the necessary excited particles.

One of the uncertainties of the present tests is the possibility that the ablation vapors from the plastic model surfaces might influence the radiation observed from the gas cap by interference with the thermodynamics and chemistry of the shock layer. (This possibility was mentioned in ref. 5.) The test of the pyrex sphere, mentioned earlier, was made to see whether any measurable differences could be demonstrated. For the flight conditions of the pyrex model, the mass flow of ablation vapor into the shock layer was calculated by Dean R. Chapman

of Ames Research Center to be seven parts per million of the airflow into the shock layer. This amount is 10^4 times less than the amount estimated for the plastic models. The fair agreement of the radiation observed from the pyrex model with that observed from the plastic models, shown in figure 5, suggests, however, that the ablation vapors are not influencing the observed radiation to any large extent.

Spectral Distributions

In applying the results of the total-radiation measurements made thus far, it is of great importance to know the approximate spectral distribution of the radiation and, in particular, to determine whether the theoretical estimates of the spectrum (ref. 1) are valid. A series of tests is being pursued at Ames to provide information of this type. Figure 6 shows in bar-graph form some of the first results obtained. The spectrum is from the gas cap of a plastic model flying at 32,000 ft/sec and under conditions where the shock layer should be in equilibrium. Fairly good consistency between experiment and the theory for equilibrium radiation from reference 1 is seen except for the large excess of infrared radiation. (It should be mentioned that the phototubes used for measurements of total radiation, presented earlier in this paper, cut off at about 0.65 micron, and they do not respond to infrared radiation.) A similar spectral distribution is presented in figure 7 for a higher test altitude. In this test, the radiation, estimated from the equilibrium theory, was expected to be reduced by a factor of 100. Instead it was lower by only a factor of 8. Thus the spectrum represents a condition where the nonequilibrium radiation causes an overshoot ratio of 12. It can be seen that the general shape of the spectrum is about the same for the two cases presented. The reason for the excessive infrared radiation shown by these spectra is not yet known. Two possibilities have been suggested. One is the possibility of contributions from the ablation vapors that are known to be present in the gas cap near the body surface. The other is contamination in the air stream, either carbon, salts, or excessive water vapor. The air used for these tests was by no means spectroscopically pure. It is entirely possible that some of the very large overshoot ratios observed and presented in figure 5 could result from contamination. Future tests are expected to resolve some of these questions.

One further spectrum is shown in figure 8. It is the spectrum of the model-wake radiation measured during the same test presented in figure 6. Interestingly, it shows little ultraviolet radiation and large amounts of infrared. It can be reasoned that such a result might be expected because of the very much lower temperatures in the wake. It is also felt that ablation products streaming downstream from the model might radiate strongly in the infrared region.

03:12:29 1971

CONCLUDING REMARKS

The measurements of radiation from hypervelocity models presented herein provide some guide for calculating the radiative heat loads in the stagnation region of bodies entering the atmosphere at speeds up to 44,000 ft/sec. The application of the results for extremely high-altitude flight, although correct as far as Reynolds number, Mach number, and enthalpy are concerned, must remain in some doubt because of the necessity of scaling the radiative relaxation times to the conditions existing in the shock layer of vehicles many times larger than the models used during this investigation. In addition to this problem, calculating radiative heating on areas other than the stagnation region involves considerable additional difficulty even disregarding the problems of scaling the nonequilibrium radiation effects that have been discussed.

REFERENCES

1. Meyerott, R. E., Sokoloff, J., and Nicholls, R. W.: Absorption Coefficients of Air. LMSD 288052, Lockheed Aircraft Corp., 1959.
2. Kivel, B., and Bailey, K.: Tables of Radiation From High Temperature Air. Res. Rep. 21 (Contracts AF 04(645)-18 and AF 49(638)-61), AVCO Res. Lab., Dec. 1957.
3. Camm, J. C., Kivel, B., Taylor, R. L., and Teare, J. D.: Absolute Intensity of Non-Equilibrium Radiation in Air and Stagnation Heating at High Altitudes. Res. Rep. 93 (AFBMD TR 60-184), Avco-Everett Res. Lab., Dec. 1959.
4. Kivel, Bennett: Radiation From Hot Air and Its Effect on Stagnation-Point Heating. Jour. Aerospace Sci., vol. 28, no. 2, Feb. 1961, pp. 96-102.
5. Page, William A., Canning, Thomas N., Craig, Roger A., and Stephenson, Jack D.: Measurements of Thermal Radiation of Air From the Stagnation Region of Blunt Bodies Traveling at Velocities up to 31,000 Feet Per Second. NASA TM X-508, 1961.

INSTRUMENT SET-UP

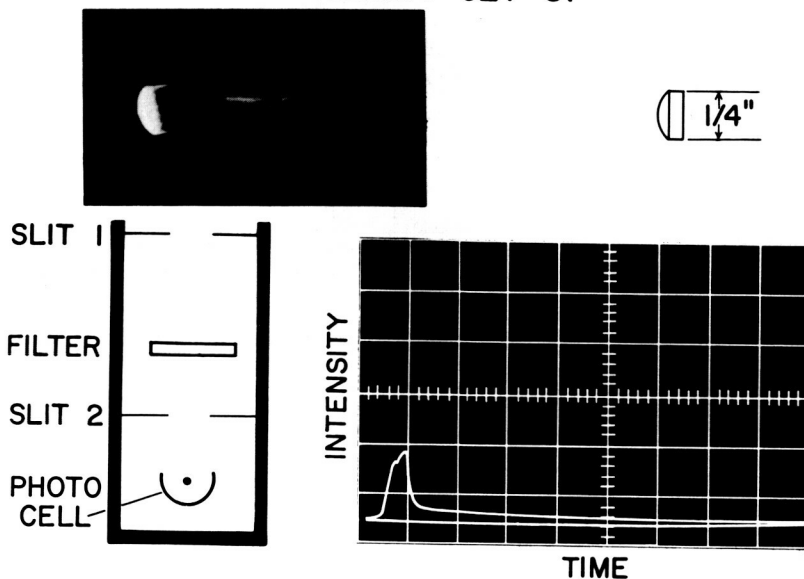


Figure 1

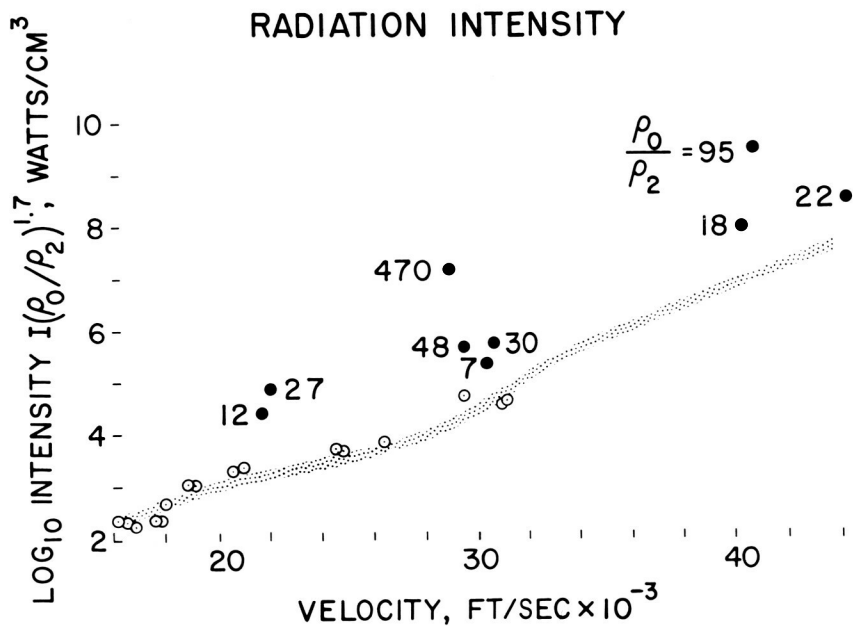


Figure 2

IDEALIZED FLOW MODEL

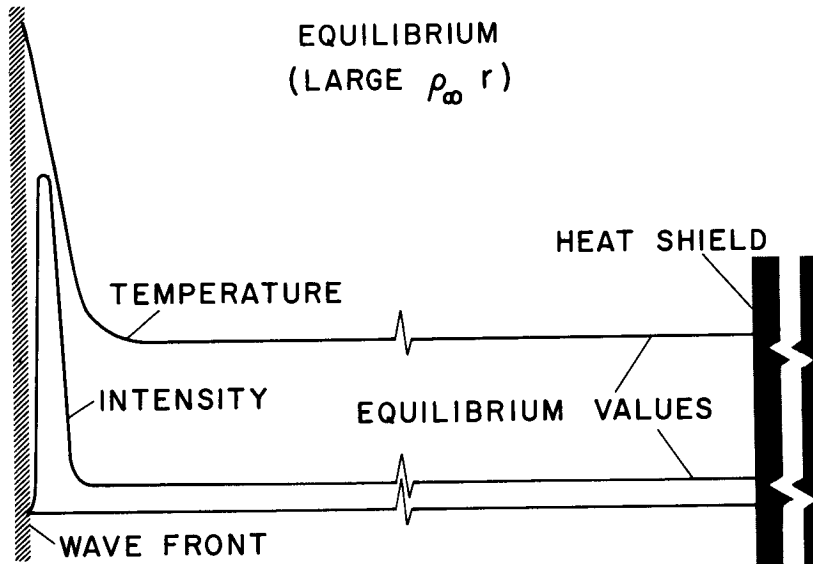
EQUILIBRIUM
(LARGE $\rho_\infty r$)

Figure 3

IDEALIZED FLOW MODEL

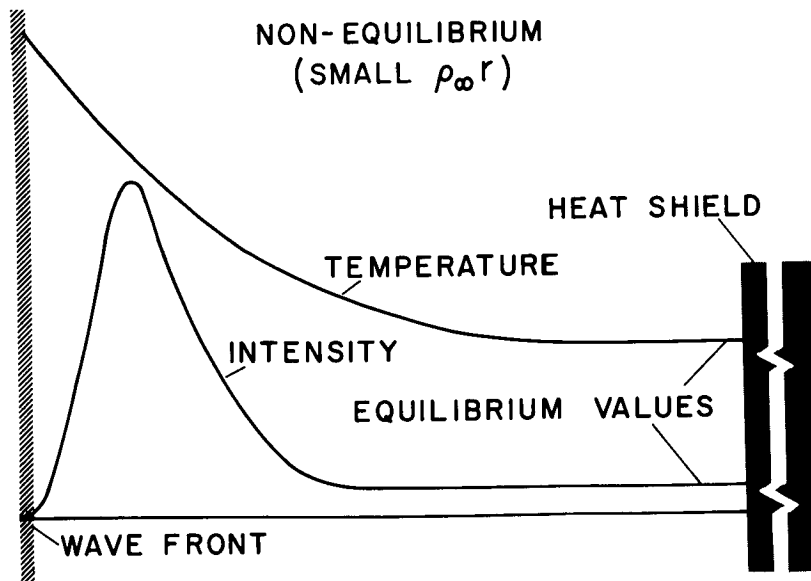
NON-EQUILIBRIUM
(SMALL $\rho_\infty r$)

Figure 4

REF ID: A55180

287

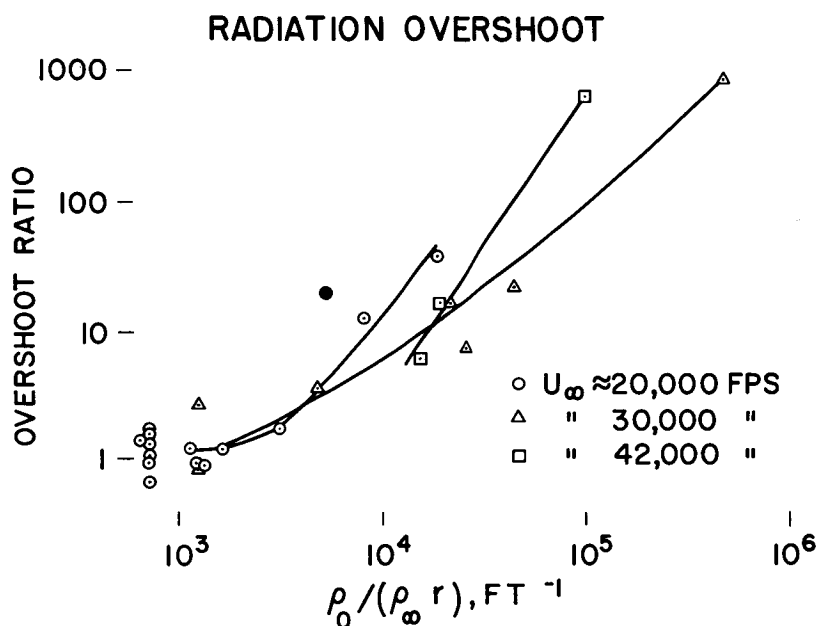


Figure 5

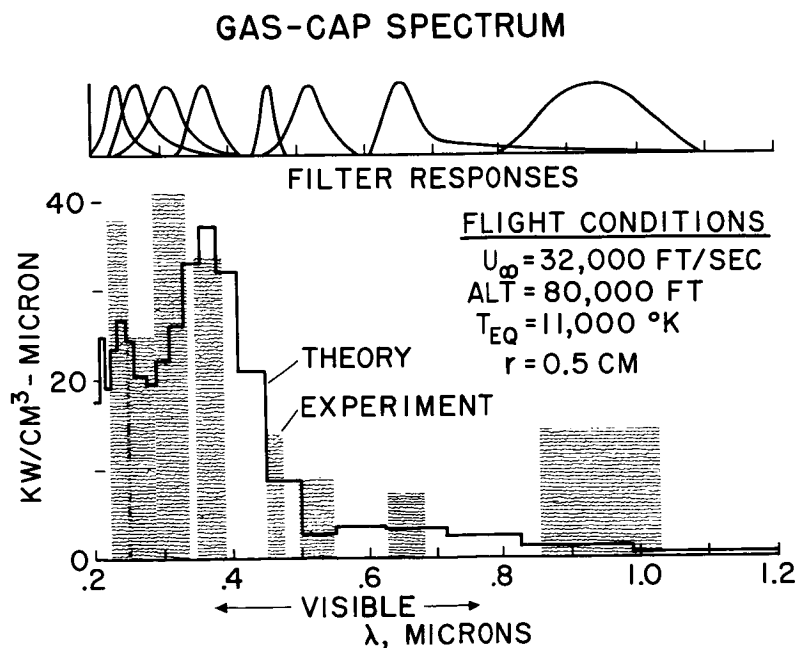


Figure 6

GAS-CAP SPECTRUM

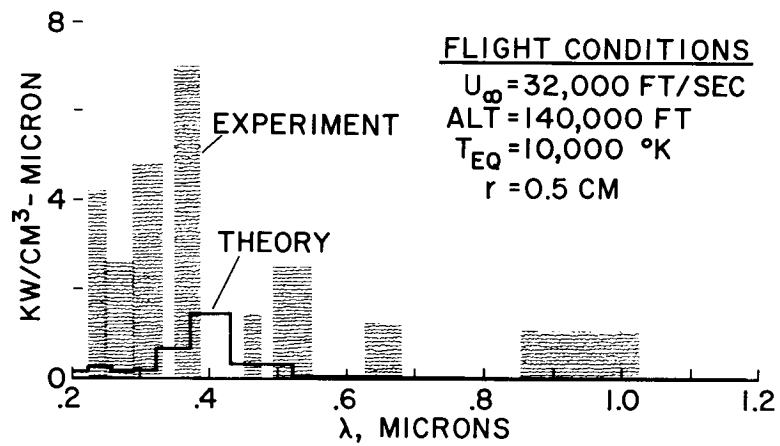


Figure 7

WAKE SPECTRUM

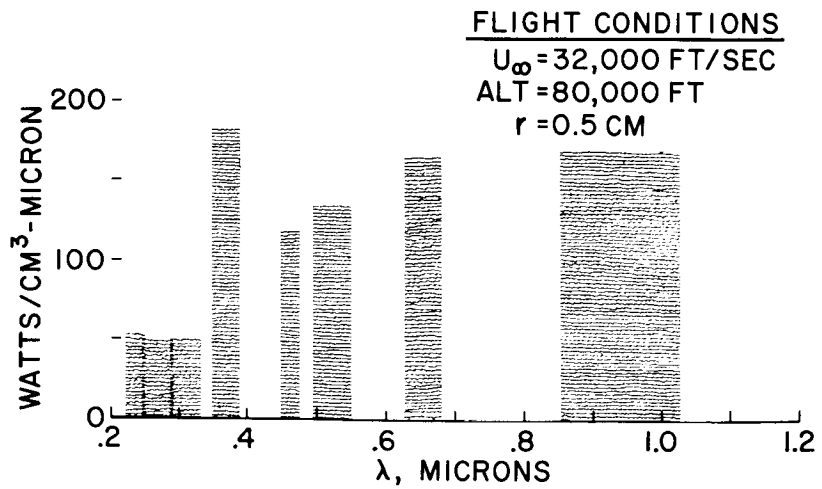


Figure 8

EFFECT OF VEHICLE CONFIGURATION ON COMBINED HEATING LOADS

WITH SPECIAL REFERENCE TO RADIATIVE HEATING

By Alvin Seiff, Glen Goodwin, and Bradford H. Wick

Ames Research Center

SUMMARY

Calculations have been made of the radiative and convective heating of vehicles entering the atmosphere on trajectories representative of the Apollo mission. The primary purpose was to assess the importance of the radiative heating (including nonequilibrium effects when present) and to determine the effects of configuration on heating. The method of procedure was to calculate the distributions of temperature and density in the real-gas flow fields and to integrate the radiant-energy distributions deduced therefrom.

Results showed that total radiative inputs were small compared with convective inputs ranging from less than 1 percent for pointed and round-nosed cones to about 20 percent for a blunt ballistic capsule on an undershoot boundary. The peak radiative heating rates, however, were comparable to (but smaller than) the peak convective rates. Radiative heating falls off more rapidly away from the stagnation point than does convective heating in the examples treated.

The significant effects of configuration were found to be as follows: Increasing the nose radius for a given weight and frontal diameter produced little effect on stagnation-point radiation due to counteracting effects on shock-wave standoff distance and $W/C_p A$. However, more area was exposed to significant levels of radiative heating on the configuration of large nose radius. The conical region of the round-nosed cone and the entire surfaces of pointed cones were found to be exposed to essentially negligible levels of radiation for this mission, because of sweepback of the bow shock wave. An interesting downstream influence of the blunt nose occurs on round-nosed cones which tends to increase radiation to the conical surface. However, for the particular conditions investigated, this phenomenon was calculated to be of no practical importance.

The radiative heating rates at high altitudes on overshoot trajectories were found to be smaller than those on the undershoot boundary, in spite of the presence of nonequilibrium radiation on overshoot. The nonequilibrium effects were large only when the equilibrium radiation levels were low.

INTRODUCTION

This paper presents the results of calculations of the aerodynamic heating of several configurations during atmospheric entry along trajectories representative of those which have been studied for the Apollo mission. The emphasis will be on radiative heat transfer for two reasons: (1) Radiative heating is relatively less well understood than convective heating. (2) On the basis of existing theory and experiment, the weight efficiency of some ablation heat shields appears to be lower for radiative heating than for convective heating. The objectives will be to obtain the magnitudes of the heating contributions due to gaseous radiation and convection for a number of entry configurations and in this way to obtain some insight into the complicated interaction between configuration and heating.

SYMBOLS

A	reference area, sq ft
C_D	drag coefficient
d	body diameter, ft
D	drag force, lb
L	lift force, lb
q	heat-transfer rate, Btu/sec-ft ²
r_b	body base radius, ft
r_n	nose radius, ft
s	surface distance from the center of the face, ft
T	air temperature, °R
U	velocity, ft/sec
W	weight, lb
Δ	shock wave standoff distance, ft

ρ air density, slugs/cu ft

θ cone half-angle, deg

Subscripts:

o sea-level atmospheric

∞ free stream

2 behind normal shock wave

ANALYSIS

General Considerations

A well-known important effect of entry-body shape on radiative heat transfer is the effect of nose radius, which fixes the volume of hot gas available to radiate to the vehicle nose. The shock-wave stand-off distance is approximately proportional to the nose radius. It can be shown that for a given flight speed and altitude, radiation intensity to the surface is proportional to nose radius. Another significant point is the effect of shock-wave sweepback in reducing radiation. A sweptback shock wave behaves like a normal shock wave at a lower speed, and, since the radiation is highly sensitive to speed, large benefits are associated with shock-wave sweepback. A less generally appreciated effect of configuration is illustrated in figure 1. This figure shows the relationship that exists between the ambient air density and the vehicle drag-loading parameter W/C_{DA} at a given flight speed, in this case 34,000 feet per second, which is near the speed for peak radiative heating. The density, given in ratio to sea-level density, increases almost linearly with increasing W/C_{DA} . This result is, of course, a trajectory influence, the vehicles of higher weight or lower drag penetrating to lower altitudes at a given speed and hence encountering higher air densities. Since it has been shown (for example, ref. 1) that the gaseous radiation increases approximately as the 1.7 power of the air density, it follows that the radiation will increase with the 1.7 power of W/C_{DA} . This result was obtained earlier by Yoshikawa, Wick, and Howe (ref. 2) from comparisons of radiative heat-transfer computations for bodies of varying W/C_{DA} on an undershoot boundary. It can be seen here to hold approximately for the overshoot boundary as well.

It is important to note that nose radius and $W/C_D A$ are not, in most practical applications such as the Apollo mission, truly independent variables. The weight and frontal area are very nearly fixed by considerations of available boost capability and required internal dimensions. Thus, $W/C_D A$ will tend to vary inversely with C_D . Vehicles of large nose radius, which are penalized by their large shock-layer volume, will tend to have large C_D and hence small $W/C_D A$. This permits them to operate at low air density, for a given speed, and hence to obtain a reduction in radiation. Thus, it is not immediately obvious what the overall effect of nose radius will be.

Nonequilibrium boundaries are shown in figure 1. For densities below these boundaries, nonequilibrium radiation can be expected. For vehicles of small nose radius, the flow times are comparatively short, and nonequilibrium effects at peak heating can be expected on the overshoot boundary for all values of $W/C_D A$ up to about 700 pounds per square foot, although these effects may be local. Large nose-radius shapes are also subject to nonequilibrium effects at peak heating on overshoot if the $W/C_D A$ is less than about 80 pounds per square foot.

A photograph taken from reference 3 of an entry configuration experiencing radiative heat transfer in a shock tunnel test at a speed of 14,000 feet per second is shown in figure 2. Radiating gas appears on the conical surface downstream of the blunt nose and on the deflected controls, as well as in the stagnation region. The radiation originating near the conical surface is a consequence of the hot core of air which has passed through the normal shock wave near the stagnation point. The hot core is predictable theoretically. From this photograph, it is evident that the radiative heating is not restricted to the stagnation-point region and that other regions of the flow field must be considered.

Detailed calculations were made of the flow fields around the configurations shown in figure 3, which vary in shape from extremely blunt to pointed. All configurations studied, however, were of the compact capsule type. The blunt-faced capsule with a ratio of face radius to cross-sectional diameter of 1 was studied for both zero lift and lifting attitudes. The 30° round-nosed cone has a ratio of nose radius to base radius of 0.4, to match that of the M-1 configuration. The pointed cones were included for a reason which will be developed later in the discussion. Although no emphasis was placed on the specific design of vehicles having these face shapes, it seems probable that the cones of larger angle would require an afterbody of some kind, such as the one shown dotted on the 50° cone, in order to contain sufficient volume. These configurations were assigned weights and frontal areas consistent with Apollo study contract data, namely weights in the neighborhood of

5,700 pounds, and diameters around 12 feet, to obtain realistic values of $W/C_p A$ for the present purposes. The values selected are shown in figure 3.

With the exception of the blunt capsule, the complete bodies of revolution shown were considered to be modified to form lifting bodies by removing the top halves. This operation on the 30° round-nosed cone would result in the M-1 shape. The virtue of this consideration for present purposes was that it permitted the study of lifting bodies from axially symmetric flow fields. The calculations made may be considered applicable to the lower halves of lifting bodies, where the most critical heating regions are found.

Trajectories were computed on an IBM 704 computer. Studies were confined to the undershoot and overshoot boundaries of the entry corridor. The trajectories were selected for maximum range in the atmosphere at fixed L/D of ± 0.5 in order to maximize convective heating. Ranges of about 6,000 miles were obtained. No skip above altitudes of 400,000 feet was permitted. Although the restriction on L/D is somewhat arbitrary for speeds below satellite speed, the number of possible trajectories is almost unlimited and the one chosen is entirely satisfactory for showing the magnitudes of radiative heating, which is important only above satellite speed. Furthermore, the trends obtained with these trajectories should be representative of what will be obtained on other trajectories. The trajectories for the blunt capsule at zero lift were, of course, ballistic trajectories.

Real-gas properties employed in the analysis were taken from reference 4. The shock-wave data were those given for real gases in reference 5. The radiation intensities for equilibrium conditions were taken from reference 6 and are supported by the data of reference 1. The nonequilibrium data of references 1 and 7 were used as a basis for estimating nonequilibrium effects. Reference was also made to the shock-tube data in references 8 and 9 for guidance on nonequilibrium radiation. The flow fields for the blunt capsule were calculated at the Ames Research Center by George E. Kaattari by use of the methods described in reference 10 and unpublished extensions thereof. The flow fields on the round-nosed and pointed cones were calculated by Alvin Seiff using an unpublished method of analysis, which is a method of successive approximations.

Results and Discussion

Two of the calculated shock-wave configurations and standoff positions are shown in figure 4 for the case of the blunt capsule in non-lifting and lifting attitudes. The shock shape and standoff distance

are drawn to scale for a speed of 33,000 feet per second at the appropriate altitudes for undershoot trajectories. Note that these altitudes differ because of the difference in $W/C_D A$ associated with the change in drag coefficient and the difference between ballistic and lifting trajectories. Note also that the shock layers are relatively thin, and that the standoff distance at the stagnation point is smaller for the lifting case than for the nonlifting case by a factor of 2.5. Also, the shock wave is swept back at nearly the local face angle throughout. Over a relatively large part of the frontal area, the effects of sweepback will tend to reduce the radiative heating, especially in the lifting case.

The temperature and density conditions in the shock layer are shown in further detail for this case in figure 5. The temperature is shown on the left in ratio to the temperature behind a normal shock wave and is plotted against surface distance from the center point of the front face for the vertical plane of symmetry. The stagnation point is near the upper corner, at s/r_n of about 0.36. Away from the stagnation point, the air temperature drops off, particularly immediately behind the shock wave. As shown on the right, the air density decreases appreciably along the body surface away from the stagnation point and contributes further to a reduction in radiative intensity.

The consequences of these variations in temperature and density are shown in figure 6. Both the zero lift and lifting cases are examined at the conditions for peak radiative heating on the undershoot boundary. A strong variation in radiative heating rate over the face is obtained in both cases. The peak heating rate is higher for the lifting case than for the nonlifting case because of its $W/C_D A$. The peak heating in the lifting case does not occur at the stagnation point, but occurs closer to the center of the face. This is a consequence of the fact that the shock layer is thicker at this location than at the stagnation point.

The convective heat transfer was also calculated at the condition for peak convective heating and is shown for comparison. The boundary layer was assumed to be laminar over the entire face, inasmuch as the local Reynolds numbers were calculated to be below 180,000 for which fully laminar flow in the presence of ablation has been previously observed in flight tests. Obviously, if turbulent flow occurs, higher convective heat-transfer rates can be expected. The peak laminar convection is 20 to 60 percent greater than the peak radiation but falls off less rapidly away from the stagnation point.

A similar representation of the characteristics of the round-nosed 30° cone is shown in figures 7 and 8. The speed and altitude combination

[REDACTED]

represented occur on the undershoot trajectory near peak heating. In this case, the spherical-arc nose extends only to s/r_n of 1.05, and the remainder is the conical section. The core of high-temperature low-density air referred to previously and observed in the shock-tunnel photograph (fig. 2) is seen to extend the full length near the body surface. Behind the shock wave, the air is relatively cooler and more dense. A peculiarity of the real-gas flow is the higher density observed on the nose away from the stagnation point than that at the stagnation point. This result is due to the nonuniform variation of the state properties of real air. It should be noted that the variation of temperature between the conical surface and the shock wave is nonlinear and decreases rapidly at first to a constant level in the outer region. The constant levels are approximately those for pointed cones. The peak radiative heating rates calculated for equilibrium from the distributions of temperature and density are given in figure 8. A peak radiative heating rate of 200 Btu/sec-ft² occurs at the stagnation point and falls off rapidly around the spherical nose. On the afterbody, very low intensities are calculated in spite of the hot core. Near the base, the radiative heating rate is less than 1 percent of the stagnation-point value. This is in seeming contradiction with the shock-tunnel photograph (fig. 2). However, it should be noted that the photograph views the hot core tangentially and thus looks along a long path of radiating air, much longer, for example, than the path through the stagnation region. Furthermore, the heat transfer at any point is governed by the thickness of the layer normal to the body surface, which is small by comparison to the tangential length. Hence, the photograph can be misleading if used as an indication of local radiative heating rates. Another possibility worth mentioning, however, and suggestive of possible further research, is the possibility of a nonequilibrium process somewhat different from the ones discussed in references 1, 7, 8, and 9. The hot-core air, excited in the stagnation region, may not have relaxed into local equilibrium as it flows around the body and thus may be radiating more intensively downstream than it would if it were in local equilibrium there. This is a nonequilibrium process typical of those associated with expansion of excited gas flows. At the present time, the importance of this phenomenon for radiative heat transfer is unknown.

The convective heating to this configuration is again larger than the equilibrium radiative heating, by a factor of 3 at the stagnation point and by a factor of 90 at the body base. The convective transfer was again computed for laminar boundary layer, by use of Lees' equation.


Although the radiative heating is apparently brought to acceptable levels on the round-nosed cone by shock-wave sweepback, two possibly objectionable characteristics have been noted; namely, the high stagnation point radiative rate, and the downstream effect of the blunt nose.

These characteristics can be avoided by use of pointed cones. The radiative heating can in this way be reduced to negligible proportions over the entire body. In figure 9, the equilibrium radiative heating level is shown plotted against cone half-angle, and lies essentially on the horizontal axis. These calculations were made for a fixed ratio of weight to frontal area of 75 pounds per square foot, and the value of $W/C_D A$ was permitted to increase with decreasing drag coefficient to a maximum value of 333 pounds per square foot for the 20° cone. In spite of this, the radiative heating continued to decrease with decreasing cone angle. Maximum radiative heating occurs on cones at the base station, and varies linearly with distance from the apex. Maximum heating rates of 3 Btu/sec-ft² were calculated for the 50° cone at a velocity of 34,000 feet per second, assuming equilibrium radiation. The 20° cone experiences a maximum of 0.09 Btu/sec-ft², slightly less radiative heating than it would experience if placed in full sunshine.

Convection, however, is increased on the pointed cones over that for the corresponding round-nosed cones. This result is due to the fact that the hot-core layer on the blunted cone is also a low Reynolds number layer, which acts to reduce the convection on the blunted cone.

In the event the choice is made of avoiding the hot-gas radiative heating problem while accepting higher convective heating, which may become a more attractive possibility at speeds slightly higher than those considered here, the question arises as to whether a pointed cone can retain its point through the period of intensive heating which occurs at velocities above satellite velocity. Below satellite velocity, the radiative heating is low enough so that no particular concern exists on its account. Calculations were made to establish the degree of point burn-off to be expected, on the basis of an assumed ablative tip material having an effective heat of ablation of 5,000 Btu per pound. The results are shown in figure 10. The smaller-angle cones, having higher $W/C_D A$, penetrated deeper in the atmosphere at a given speed and as a result suffered more burn-off of the tip. However, the final tip radii are in all cases small, less than 1/10 of the base radius. The two inset shadow photographs show plastic models which were tested in an arc-jet wind tunnel. These photographs show the change in shape of a pointed cone with ablation, and the photograph at the right shows the shape when the tip has ablated to about 0.2 of the base radius, twice as blunt as calculated for the 20° cone in flight. It is concluded that the degree of burn-off to be expected will still permit the cone to be considered essentially sharp.

A few preliminary experiments have been made with pointed cones in the Ames pilot-scale hypersonic free-flight facility (ref. 1), at a speed of 30,000 feet per second. The experimental techniques used were substantially those described in reference 1. The data obtained are



shown in figure 11, in which the total radiation emitted by the shock layer is plotted as a function of cone half-angle. Results were recorded for cones of 40° , 60° , and 75° half-angle. The 40° and 60° cones have attached bow waves, which is a necessary condition for obtaining a large reduction in radiative heating. The 75° cone was a very blunt body with a detached bow wave and should produce radiation comparable to that for a right-circular cylinder, for example.

These tests were made at an air density which had given equilibrium radiation levels on the spherical-nosed bodies, the equivalent altitude for a 12-foot base diameter body being 233,000 feet. However, analysis indicated that there was reason to suspect that nonequilibrium effects should occur at lower altitudes on cones than on bluff bodies. This analysis was based on considerations of the mean flow time of an air particle through the shock layer, which is smaller for pointed cones than for bluff bodies. In addition, the Mach number normal to the shock wave is lower for the cones by as much as a factor of 2. At lower Mach numbers, and consequent lower shock-layer temperatures, the relaxation time is longer (ref. 8). These considerations provided a basis for quantitatively estimating the nonequilibrium effects on the test cones, and the estimate made is shown in figure 11. The estimate agrees with the observed result for the 40° cone, but overestimates the observed result for the 60° cone.

Applying the same nonequilibrium criterion to the flight case gave the result that the cones in flight should be in equilibrium at peak heating on undershoot and not seriously out of equilibrium on overshoot. The conclusion made previously that the radiative heating to cones is very small remains unchanged.

It is evident from this limited study that nonequilibrium effects are dependent on configuration and that present knowledge of these effects needs to be expanded.

The preceding radiative heating information has been for equilibrium radiation on the undershoot boundaries. The radiation expected for undershoot and overshoot boundary flights will now be compared, first for the case where the radiation occurs at the equilibrium value, and then with best present estimates of the nonequilibrium effect. Figure 12 shows the calculated results in which equilibrium is assumed. Radiative heating rate is plotted against velocity, and the results show peaks for velocities around 34,000 feet per second. The results for the round-nosed cone are on the left, those for blunt capsule on the right. Notice that these are stagnation-point values only and that the higher values shown for the round-nosed cone are confined to a few square feet around the stagnation point. The equilibrium heating rates on the overshoot boundary are, in consequence of the

0317123A 1030


higher altitudes, small by comparison to those on the overshoot boundary. An opposite effect of the overshoot boundary is the longer flight time (more than 3 times as long through this speed range as that of the undershoot boundary), which increases relatively the total radiative input on overshoot.

The nonequilibrium curves are given in figure 13. The equilibrium curves, where superseded, have been shown as dashed lines and brought forward for comparison. Nonequilibrium effects on the overshoot boundary increase the heating rates substantially, but the resulting values remain below those for the undershoot boundary. Nonequilibrium effects also influence the heating on the undershoot boundary at the higher altitudes. This is true over a greater speed range for the blunt capsule than for the round-nosed cone. However, in this case and throughout the calculations of this study, where the nonequilibrium factor was large, the equilibrium radiation was small. Hence, no severe heating problem due to nonequilibrium occurred. Nonequilibrium factors up to 42 were applied in obtaining the results shown.

The heating calculations discussed in this paper are summarized in figure 14, which shows in a bar graph the total heat inputs to four configurations which are identified across the top of the figure. Afterbody convective heating is included in the case of the blunt capsule. The smallest total heat input is experienced by the blunt ballistic capsule of low $W/C_D A$, and the total heat input increases progressively to the right under the combined influence of $W/C_D A$ and shape. The radiative heating, shown by the hatched portion of the bars, progresses in reverse order, being maximum for the blunt capsule. Although it is a small fraction of the total heat input in all cases, ranging from less than 1 percent to a maximum of about 20 percent for the blunt ballistic capsule on an undershoot trajectory, this can be deceptive if the weight efficiency of the ablation heat shield is poor for radiative heating. Consideration of this aspect is, however, beyond the scope of the present study.

CONCLUDING REMARKS

From the calculated results of this investigation, some statements can be made concerning the magnitude of radiative heating of Apollo vehicles on atmospheric entry, and on certain influences of configuration. It appears that peak radiative heating rates comparable to but smaller than peak convective heating rates can be expected. When configuration bluntness is changed, compensating changes tend to occur through effects of nose radius on shock wave standoff distance and on $W/C_D A$, so that the stagnation-point radiation may actually be reduced



DECLASSIFIED

299

by increasing nose bluntness. However, the blunter nose has a large area over which the radiative heating occurs at relatively high levels and hence will tend to have the higher total radiative heat input than the small-radius nose.

The total radiative inputs for the Apollo mission will apparently be small compared to the convective. The main reason for this is that the convective heating is sustained over the entire entry while the radiative heating occurs in one brief pulse above satellite speed. Also, the radiative heating falls off more rapidly at points away from the stagnation point than does the convective heating. A look at the combined total heating, radiative plus convective, shows that the blunt ballistic capsule experienced the least total in this study. Of the lifting bodies, the lifting blunt capsule and the lifting blunt half-cone had comparable total heating. Of this total, however, the radiative contribution was five times as great for the blunt capsule as for the half cone.

Shock-wave sweepback offers a powerful approach to reducing radiative heat input. This may become of importance for flight speeds above 40,000 feet per second. Present calculations show that pointed cones experience essentially negligible radiative heating on Apollo entry trajectories. Furthermore, the points can be retained reasonably well down to satellite speed by use of available ablation materials. The convective heating of pointed cones is, however, significantly greater than that of round-nosed cones. Further studies should be made to assess the merits of pointed-cone configurations, particularly at speeds above escape speed and for missions other than the Apollo mission.

The radiative heating rates on overshoot boundaries are less than those on undershoot boundaries, in spite of the presence of nonequilibrium effects which increase the radiation by factors up to 50. For the conditions of this study, the nonequilibrium factors were large only when the equilibrium radiation was small. The total radiative heat inputs on overshoot, however, were comparable to those on undershoot, due to the longer flight times above 30,000 feet per second in the former case.

03171329.1030

300

REFERENCES

1. Page, William A., Canning, Thomas N., Craig, Roger A., and Stephenson, Jack D.: Measurements of Thermal Radiation of Air From the Stagnation Region of Blunt Bodies Traveling at Velocities up to 31,000 Feet Per Second. NASA TM X-508, 1961.
2. Yoshikawa, Kenneth K., Wick, Bradford H., and Howe, John T.: Radiative Heat Transfer During Atmospheric Entry at Parabolic Velocity. NASA TN D-1074. (Prospective Publication.)
3. Reller, John O., and Seegmiller, H. Lee: Convective Heat Transfer to a Blunt Lifting Body. NASA TM X-378, 1960.
4. Moeckel, W. E., and Weston, Kenneth C.: Composition and Thermodynamic Properties of Air in Chemical Equilibrium. NACA TN 4265, 1958.
5. Hochstim, Adolf R.: Gas Properties Behind Shocks at Hypersonic Velocities - I. Normal Shocks in Air. Rep. No. ZPh(GP)-002, CONVAIR, Jan. 30, 1957.
6. Kivel, B., and Bailey, K.: Tables of Radiation From High Temperature Air. Res. Rep. 21 (Contract AF 04(645)-18 and AF 49(638)-61), AVCO Res. Lab., Dec. 1957.
7. Canning, Thomas N., Page, William A., Bailey, Harry E., and Burge, Joseph M.: Measurements of Thermal Radiation From Shock Layers of Blunt Bodies Flying at Velocities up to 44,000 Feet Per Second. (Paper No. 20 of Present Compilation.)
8. Wray, K., Teare, J. D., Kivel, B., and Hammerling, P.: Relaxation Processes and Reaction Rates Behind Shock Fronts in Air and Component Gases. Res. Rep. 83, AVCO-Everett Res. Lab., Dec. 1959.
9. Camm, J. C., Kivel, B., Taylor, R. L., and Teare, J. D.: Absolute Intensity of Non-Equilibrium Radiation in Air and Stagnation Heating at High Altitudes. Res. Rep. 93, AVCO-Everett Res. Lab., Dec. 1959.
10. Kaattari, George E.: Predicted Shock Envelopes About Two Types of Vehicles at Large Angles of Attack. NASA TN D-860, 1961.

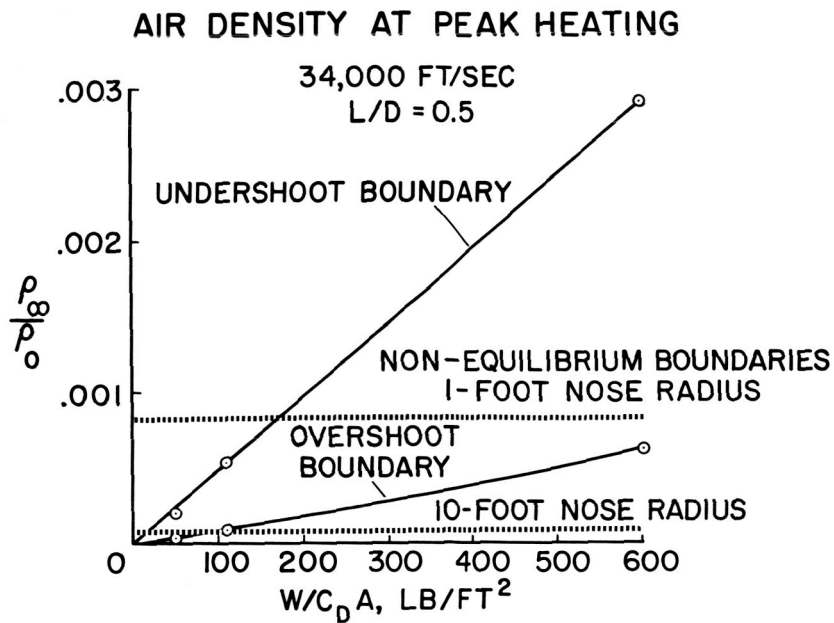


Figure 1

RADIATING GAS AROUND AN ENTRY BODY



Figure 2

CONFIGURATIONS STUDIED

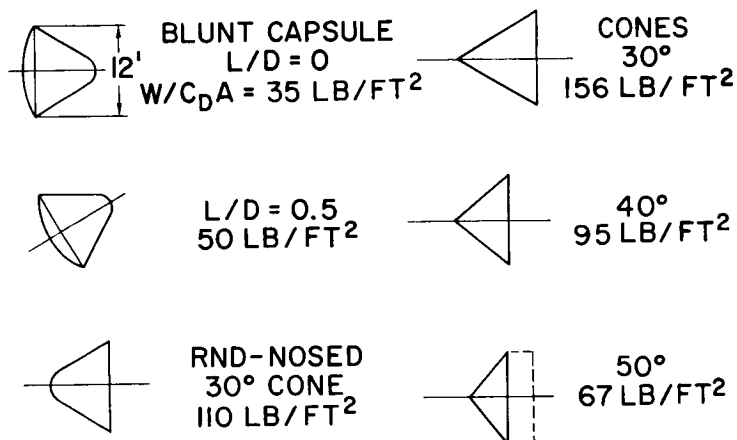


Figure 3

SHOCK WAVE GEOMETRY
FOR BLUNT CAPSULE

$$U_\infty = 33,000 \text{ FT/SEC}$$

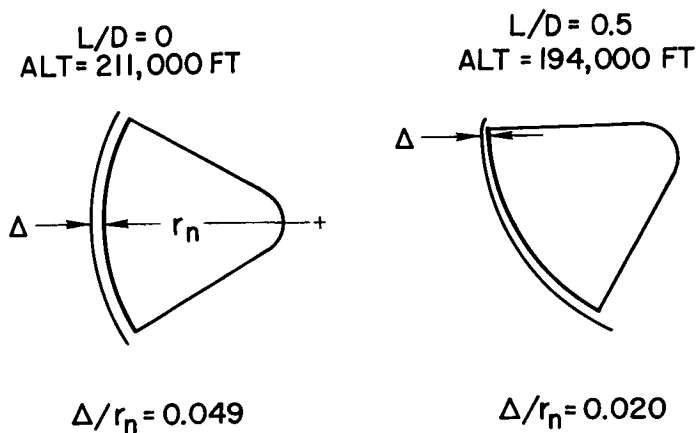


Figure 4

SHOCK-LAYER CONDITIONS, BLUNT CAPSULE, L/D=0.5

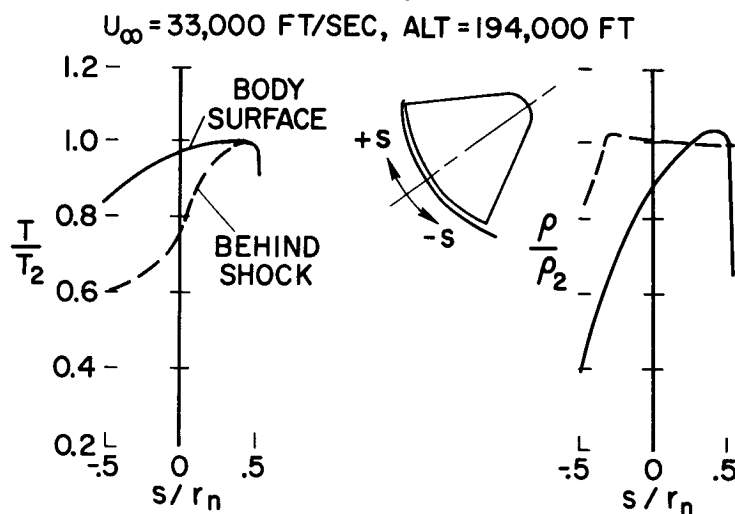


Figure 5

HEATING RATE DISTRIBUTIONS

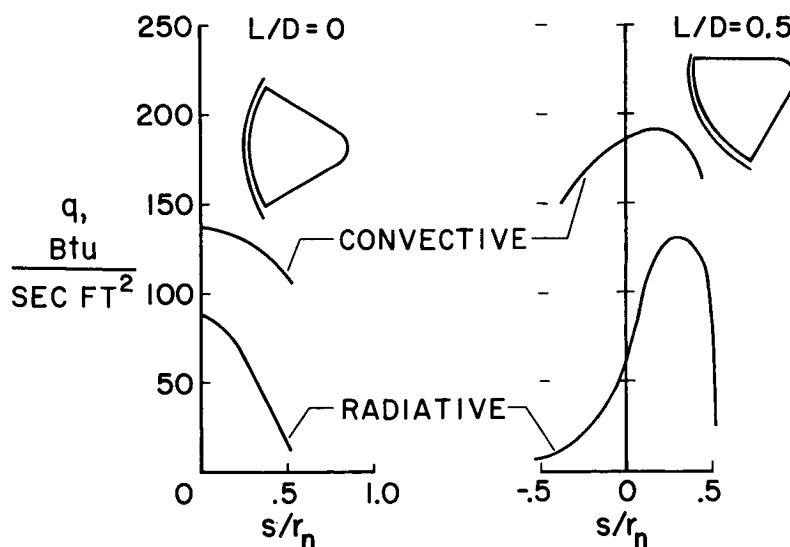


Figure 6

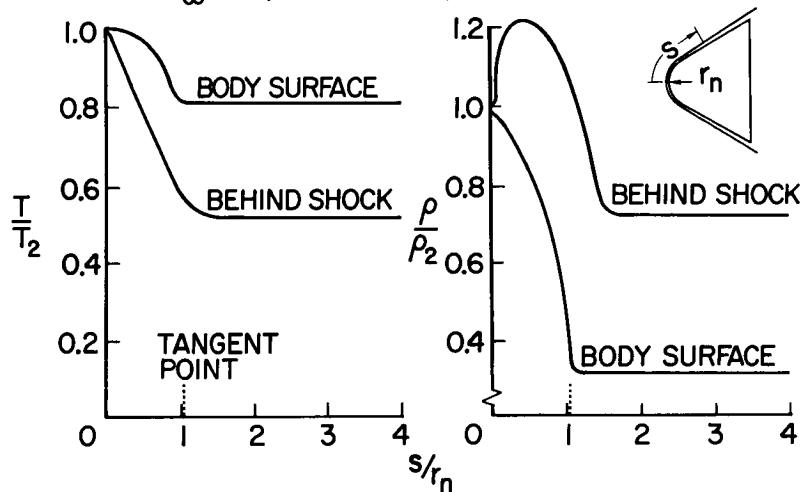
SHOCK-LAYER CONDITIONS,
ROUND-NOSED 30° CONE $U_{\infty} = 33,000$ FT/SEC, ALT=171,500 FT

Figure 7

HEATING RATE DISTRIBUTION

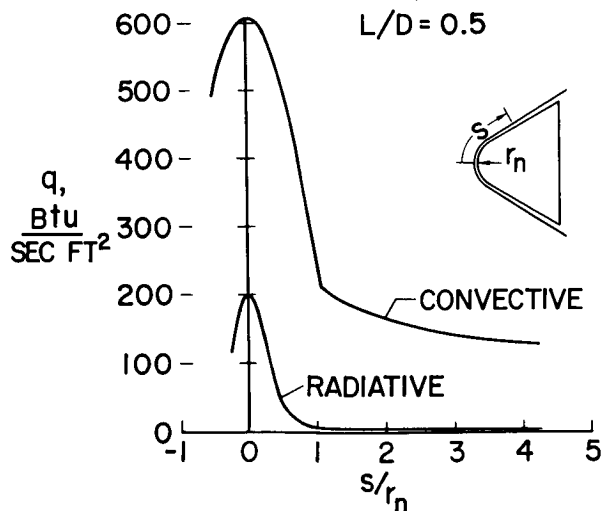
 $W/C_D A = 110$ LB/FT²
 $L/D = 0.5$ 

Figure 8

AVERAGE HEATING RATE FOR POINTED CONES, PEAK HEATING

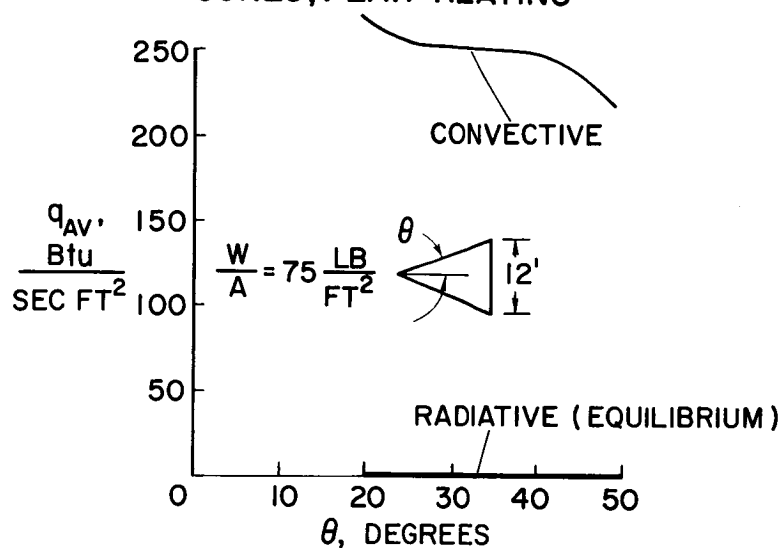


Figure 9

NOSE RADIUS AFTER FIRST HEAT PULSE

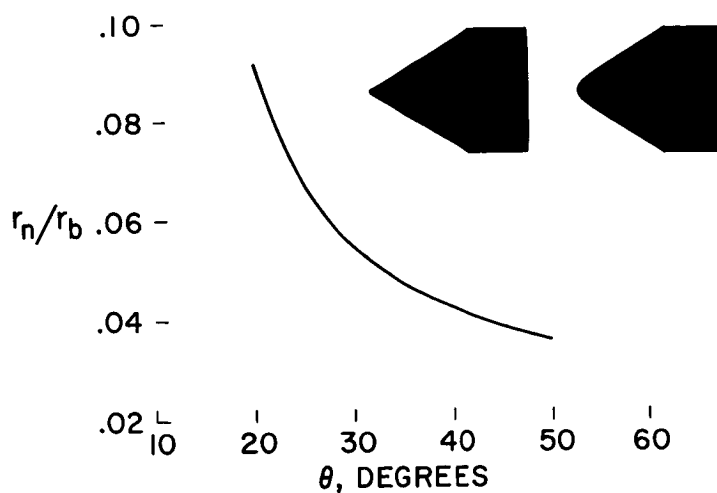


Figure 10

RADIATION DATA, POINTED CONES

$U_1 = 30,000$ FT/SEC, $\rho_1/\rho_0 = .038$, $d = .28$ IN

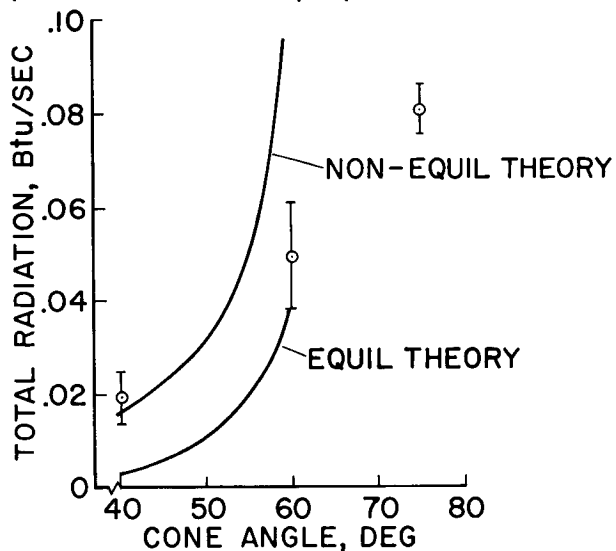


Figure 11

STAGNATION POINT RADIATIVE HEATING, $L/D = 0.5$ EQUILIBRIUM THEORY

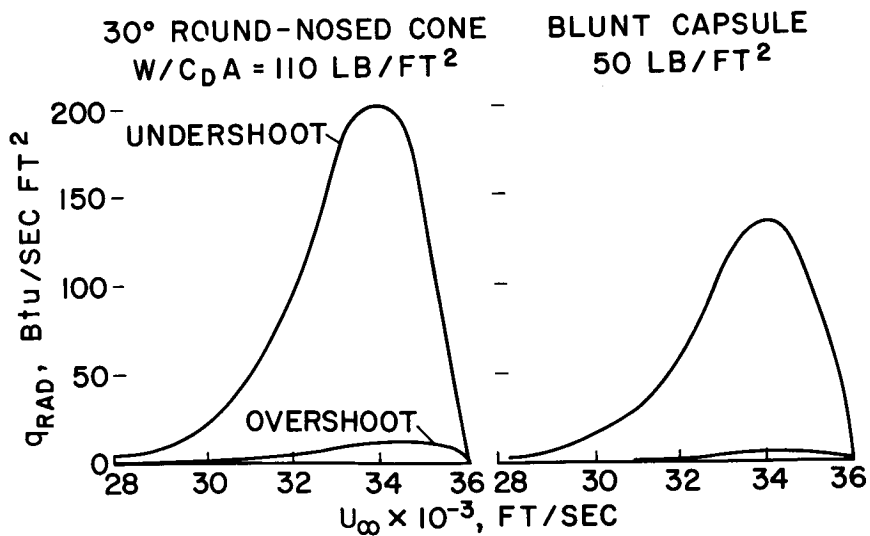


Figure 12

STAGNATION POINT RADIATIVE HEATING, $L/D=0.5$ NON-EQUILIBRIUM CORRECTIONS

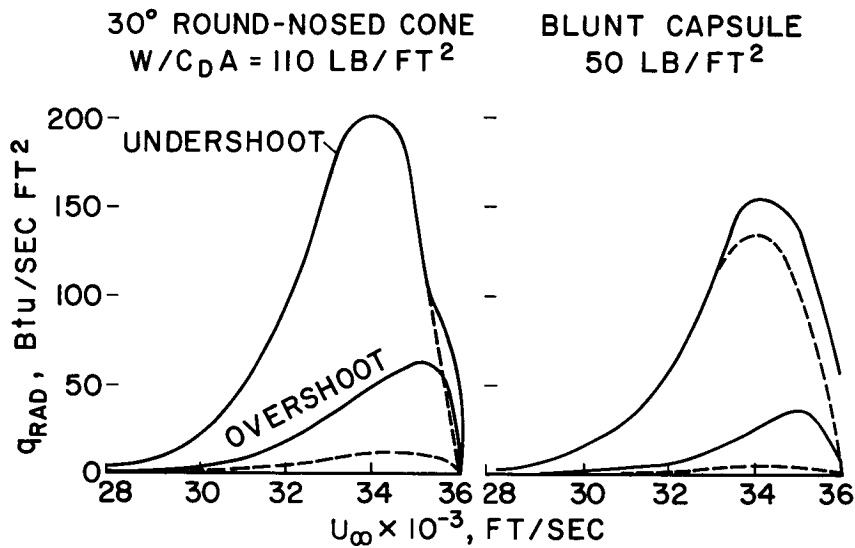


Figure 13

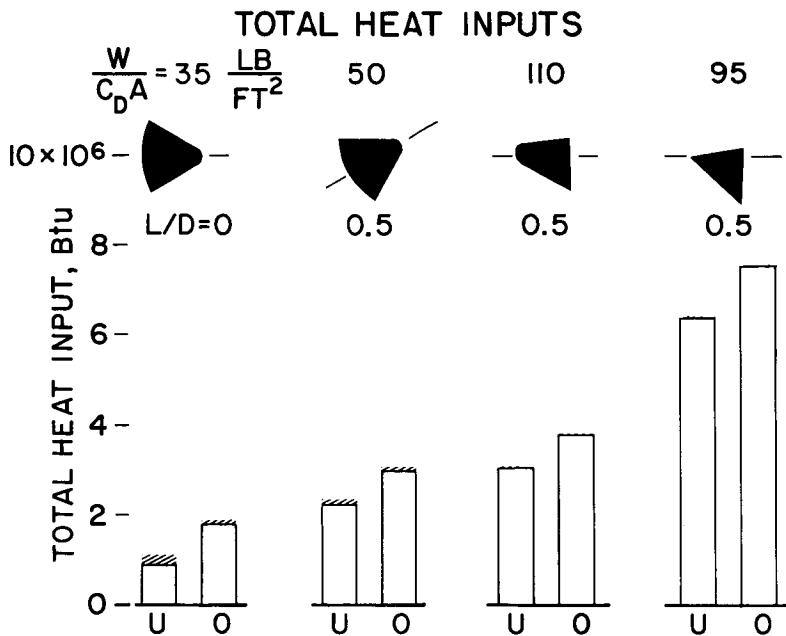


Figure 14

PROPERTIES OF MATERIALS FOR COMBINED CONVECTIVE AND RADIATIVE HEATING

By W. Winovich, B. H. Wick, J. H. Lundell,
and R. M. Wakefield

Ames Research Center

SUMMARY

Low-temperature noncharring and high-temperature charring ablating heat-shield materials have been tested under combined convective and radiative heating. An arc-heated wind tunnel operating at enthalpies up to 5,000 Btu/lb supplied the convective component, and the radiative component was obtained by focusing the output of an arc image furnace onto the model. It was found that for the noncharring material the effective heat of ablation can be substantially reduced under combined heating conditions, but the charring material exhibits an increase in the effective heat of ablation.

INTRODUCTION

The purpose of this paper is to present some recently obtained effective heats of ablation for materials subjected to combined convective and radiative fluxes. The rates of heating are representative of reentry from the Apollo mission given in the preceding paper presented by Alvin Seiff, Glen Goodwin, and Bradford H. Wick.

SYMBOLS

h	enthalpy, Btu/lb
H_a	intrinsic heat capacity, Btu/lb
H_{EFF}	effective heat of ablation, Btu/lb
\dot{m}	mass loss rate, lb/sec-ft ²
q	heating rate, Btu/sec-ft ²
T	temperature, °R

ϵ emissivity

σ Stefan-Boltzmann constant, 0.483×10^{-12} , $\frac{\text{Btu/sec}}{\text{ft}^2 \cdot \text{R}^4}$

Subscripts:

B with ablative blowing

c convective

co convective with no transpiration

EFF effective

NB no ablative blowing

r radiative

s stagnation

w wall

TEST FACILITY

Figure 1 shows the facility from which the data were obtained. The convective heating was supplied by an arc-heated wind tunnel which produced a supersonic flow at a Mach number of 3. The enthalpy for these tests was nominally 2,600 and 5,000 Btu/lb at 1 atmosphere and 1/2 atmosphere total pressure, respectively. These test conditions resulted in cold-wall convective heating rates of from 150 to 350 Btu/sec-ft² for the range indicated. The radiative heating was supplied simultaneously with an arc-imaging furnace. The radiative flux from the arc source was focused by two ellipsoidal mirrors, through filters, onto the model. The model surface temperature was measured by means of a detector mounted on the end of the nozzle. The filters were chosen to tailor the spectral distribution of the radiation to conform to that expected from shock-heated air at 18,000° R and an altitude of 180,000 feet. For the tests described here, the radiative heating flux ranged up to 500 Btu/sec-ft².

Figure 2 shows the degree of simulation attained. Relative intensity of radiant energy is shown as a function of wavelength for three cases: (1) shock-heated air at conditions representative of the Apollo mission as predicted by the emissivity values of Meyerott; (2) the

arc-image furnace output unfiltered; and (3) the arc-image furnace output with the filters (Corning Glass Co. Blue Filter No. 1-64 with a 1/4-inch layer of distilled water surrounding it). The filters cut out the unwanted radiation at the longer wavelengths and provided a reasonably close approximation to air at entry conditions.

MATERIALS AND TESTS

Limited tests have been made on a number of plastic materials of both the noncharring and charring types. Results for one of each type are presented in this paper. The noncharring, low-temperature ablator chosen was Teflon with 10-percent carbon black added to make it opaque to radiation. The charring plastic material is a 50-50 mixture of phenolic-resin and nylon.

RESULTS

The experimental results for the noncharring plastic, black Teflon, are shown in figure 3. The effective heat of ablation is plotted against the enthalpy potential across the boundary layer. The effective heat of ablation is defined as the net heating rate divided by the steady-state mass-loss rate - that is, the convective-heating rate to a nonablating surface at the same temperature as the ablating surface plus the incident radiation and less the heat reradiated from the ablating surface which was measured. The last term was negligible for the tests of black Teflon. The convection-only data are shown by open symbols; the combined heating data, by the solid symbols. The usual straight line was faired through the convection-only data. For ratios of radiative heating rates to convective heating rates of 0.4 and 0.8, the effective heats of ablation lie close to the line for convection only. When the radiative rate was 2.2 times the convective rate, however, the effective heat of ablation was reduced to about one-half of the value for convection alone.

Since the test data were obtained at enthalpies no greater than 5,000 Btu/lb, existing transpiration cooling (ablation) analyses were used to extend the results to enthalpies corresponding to those for Apollo entry, about 23,000 Btu/lb. The details of the procedure are given in an appendix. The key step in the procedure, however, is illustrated in figure 4. This figure shows the reduction in convective heating rate provided by the injection of ablated vapors into the boundary layer. The ratio of the convective heating rate with blowing to the rate with no blowing is plotted against the blowing parameter, the product of mass injection rate and enthalpy difference divided by the

convective heating rate without blowing. Again the data for convective heating alone are shown by the open symbols; the data for combined heating, by the solid symbols. The present experimental data for black Teflon lie in between the laminar and turbulent white Teflon results obtained by Savin in the Ames atmospheric entry simulator. For the present data with only convective heating, the ratio of heating rate with blowing to that without blowing is reduced to 0.4 for the highest test enthalpy, which was 5,000 Btu/lb. Note that further reductions in the convective heating can be obtained by increasing the blowing parameter - that is, by increasing the blowing rate or by increasing the enthalpy potential. At the present time the stagnation enthalpy is limited by the arc heater; therefore, the blowing rate was increased by the addition of radiative heating to the convective heating. As more radiative heating was applied, the ratio of heating with blowing to that without blowing appears to approach a lower limit. Our prediction of effective heats of ablation for the high enthalpy conditions that are shown is based on the assumption that the blowing parameter is a valid correlating parameter; hence, the reductions in convective heating are independent of the mechanism of heating.

The results of the prediction are shown in figure 5. The test data along with the predicted curves have been replotted. The enthalpy potential and velocity for peak heating for the Apollo reentry vehicle are indicated.

Consider now the effect of radiative heating on effective heat of ablation at Apollo peak heating conditions. As indicated in the previous paper by Seiff, et al, the radiative peak heating rate ranged from about one-quarter to one-half the corresponding convective values. For these conditions the effective heat of ablation is about one-half that for convective heating alone - about 2,000 Btu/lb compared with 5,000 Btu/lb.

The charring material, phenolic nylon, was treated in a similar manner as the noncharring material. Figure 6 shows the measured effective heats of ablation for phenolic nylon as a function of the enthalpy potential across the boundary layer. (Compare fig. 6 with fig. 3 for black Teflon.) For the charring plastic, the effect of the addition of radiative heating is to increase the effective heat of ablation. Because of the high surface temperature (up to 5,600° R) at which phenolic nylon ablates, the heat reradiated from the charred surface is now an important factor.

For all of the test conditions with phenolic nylon, the net radiative heating flux was away from the surface because of the high surface temperature. In the analysis of the data, the net radiative flux measured during the test was used, and the data was plotted with only input radiation as a reference to be consistent with the notation for

the Teflon experiments. These net radiative rates which were assumed to apply for all predicted conditions are given in the following table:

$\frac{q_r}{q_{co}}$	$\frac{q_r - \epsilon_w \sigma T_w^4}{q_{co}}$
0	-0.75
.6	-.45
1.2	-.35
2.2	-.08

Therefore, the effect of ablative blowing is treated differently for the charring plastic than for the noncharring plastic.

In figure 7, the ratio of the heating rate with blowing to the rate without blowing is again plotted against the blowing-rate parameter. However, the net radiative heating rates are included in the ordinate. The data for convective heating only are shown with open symbols and the data for combined heating are shown with solid symbols. Additional testing is required to define the extremely important lower portion of the correlation curve.

If the correlation curve is stopped as shown, the curves for the predicted heat of ablation appear as shown in figure 8. If the curve is extended directly to the axis, the curves for the predicted effective heat of ablation would be extended linearly to Apollo reentry conditions. For convection only, the effective heat of ablation would be about 7,000 Btu/lb; and, for a ratio of radiative to convective heating of 0.25, the effective heat of ablation would be on the order of 10,000 Btu/lb.

If, however, the correlation curve is extended in a more realistic manner, as shown in figure 9, the curves for the predicted effective heat of ablation are as shown in figure 10. The effective heat of ablation for the charring plastic, phenolic nylon, at Apollo reentry conditions is about 6,000 Btu/lb - more than twice that for the non-charring plastic, black Teflon. It should be emphasized that this extrapolation is tentative, pending confirmation with additional data in the region of higher values of the blowing-rate parameter.

APPENDIX

DETERMINATION OF HEAT BLOCKING RATIO FOR CONVECTIVE HEATING

The actual amount of heat that enters the surface to cause ablation of the material is given by a First Law analysis at the surface as:

$$\dot{m}H_a = q_c + q_r - \epsilon_w \sigma T_w^4 \dots \quad (A1)$$

The effective heat of ablation is defined by the following equation:

$$H_{EFF} = \frac{q_{co} + q_r - \epsilon_w \sigma T_w^4}{\dot{m}} \dots \quad (A2)$$

The ratio of convective heating with blowing to that without blowing of ablated vapor is obtained by combining equations (A1) and (A2):

$$\frac{q_c}{q_{co}} = \frac{H_a}{H_{EFF}} \left(1 + \frac{q_r - \epsilon_w \sigma T_w^4}{q_{co}} \right) - \left(\frac{q_r - \epsilon_w \sigma T_w^4}{q_{co}} \right) \dots \quad (A3)$$

The ratio is determined by measurements of the mass loss rate, heat input, and the reradiated heat corresponding to the wall temperature T_w . For the present series of tests, the wall temperature was below 1,500° R for the black Teflon plastic. The emissivity of this material is about 0.83; thus, the reradiated energy amounts to less than 2 Btu/sec-ft² - a value which is negligible compared with the other heat inputs. For the phenolic nylon material, however, the wall temperature was considerably higher; and it was found to vary linearly with input heating rate. The enthalpy level of these tests (2,600 to 5,000 Btu/lb) did not affect the linear relation. Temperature measurements for the phenolic nylon material are summarized in figure 11.



ENTRY HEATING SIMULATOR

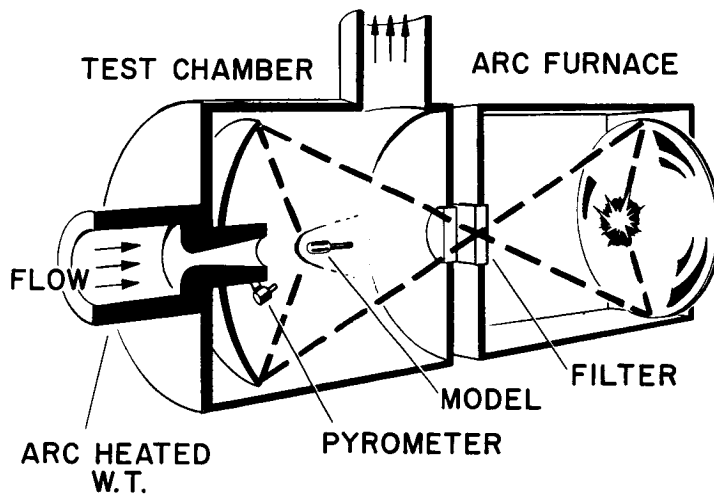


Figure 1

SPECTRAL ENERGY DISTRIBUTIONS

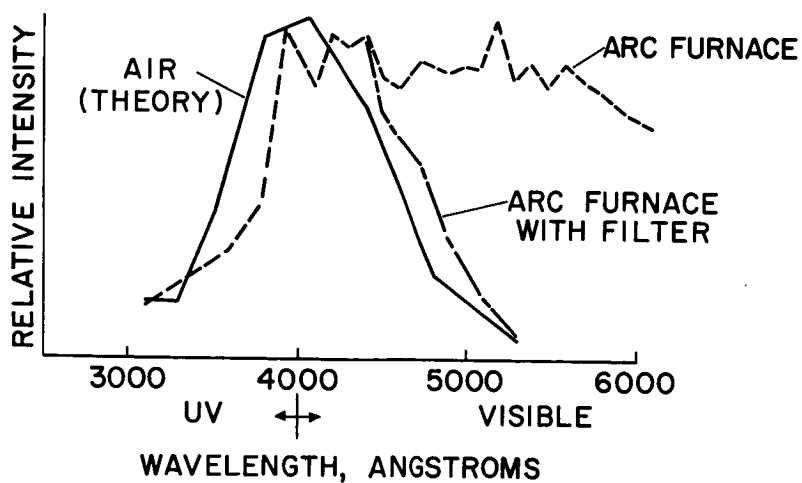


Figure 2

031712301030

HEAT OF ABLATION FOR A NON CHARRING PLASTIC (BLACK TEFLON)

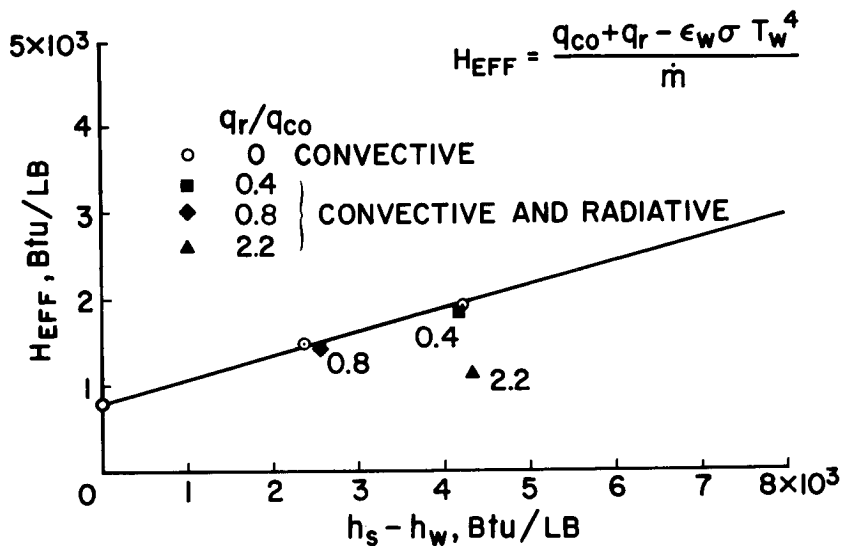


Figure 3

EFFECT OF ABLATIVE BLOWING ON CONVECTIVE HEATING FOR NON CHARRING PLASTICS

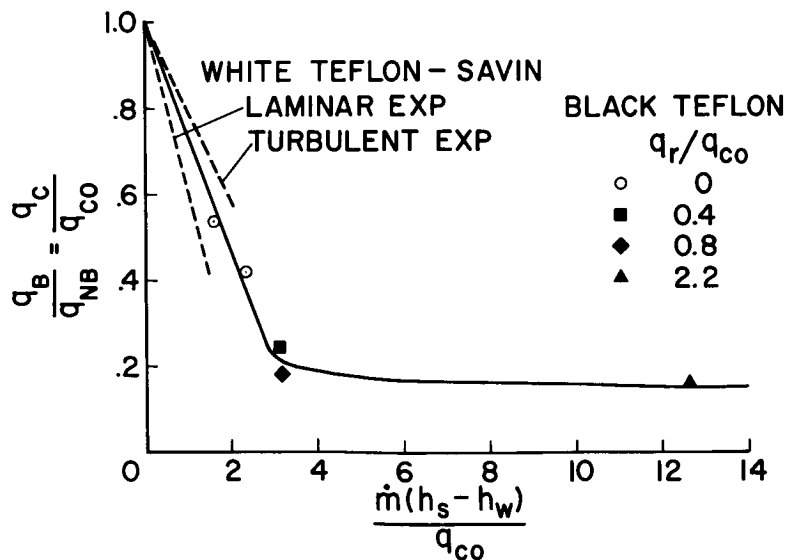


Figure 4

PREDICTED HEAT OF ABLATION FOR A NONCHARRING PLASTIC

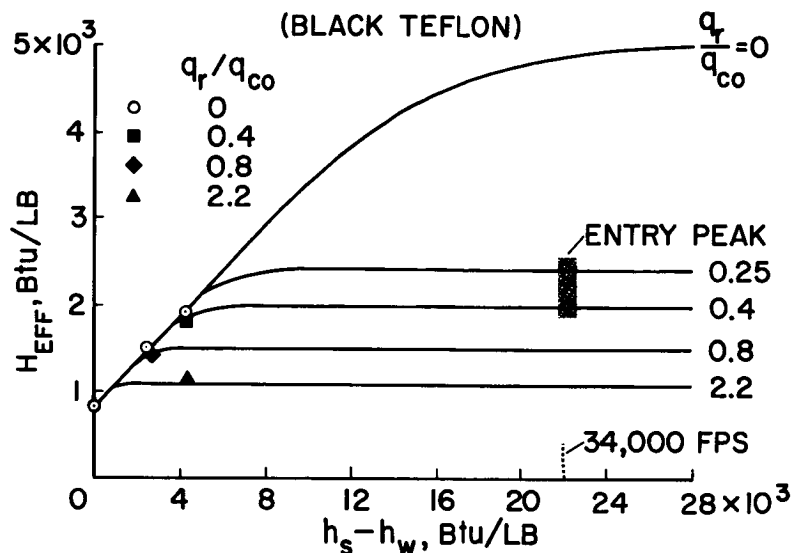


Figure 5

HEAT OF ABLATION FOR A CHARRING PLASTIC

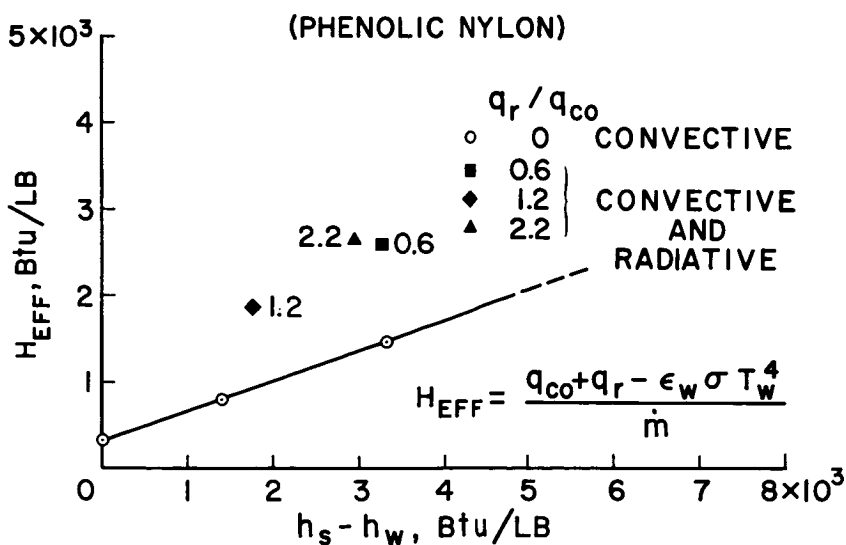


Figure 6

EFFECT OF ABLATIVE BLOWING ON NET HEATING RATE FOR A CHARRING PLASTIC (PHENOLIC NYLON)

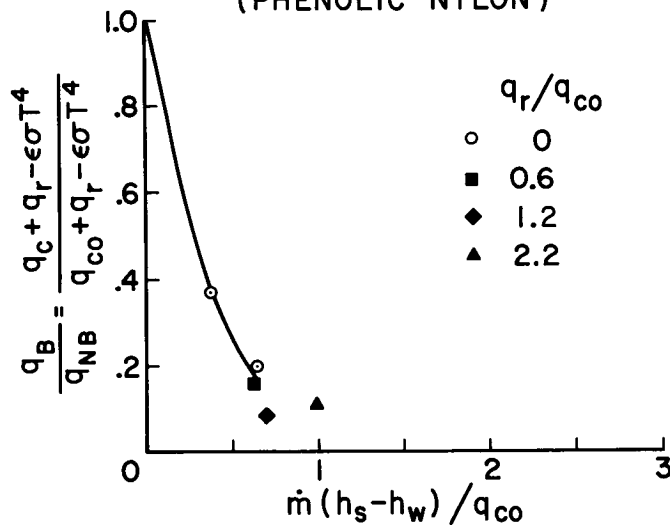


Figure 7

HEAT OF ABLATION FOR A CHARRING PLASTIC (PHENOLIC NYLON)

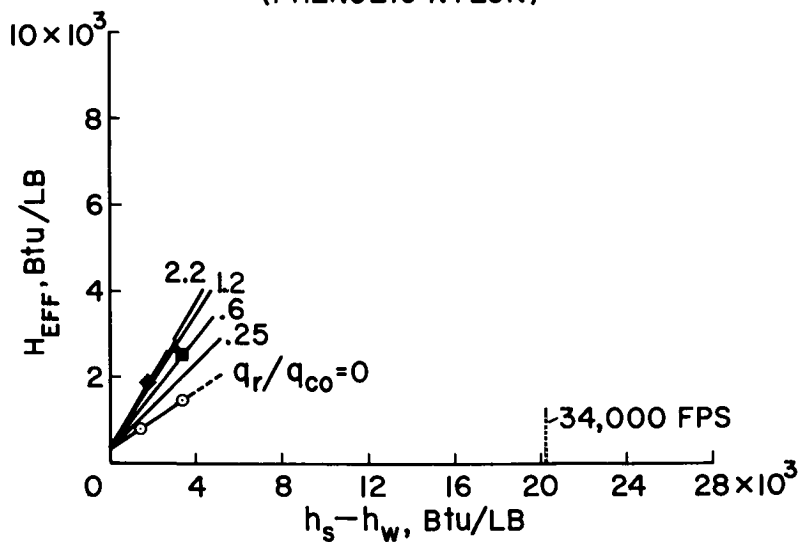


Figure 8

EFFECT OF ABLATIVE BLOWING ON NET HEATING RATE FOR A CHARRING PLASTIC (PHENOLIC NYLON)

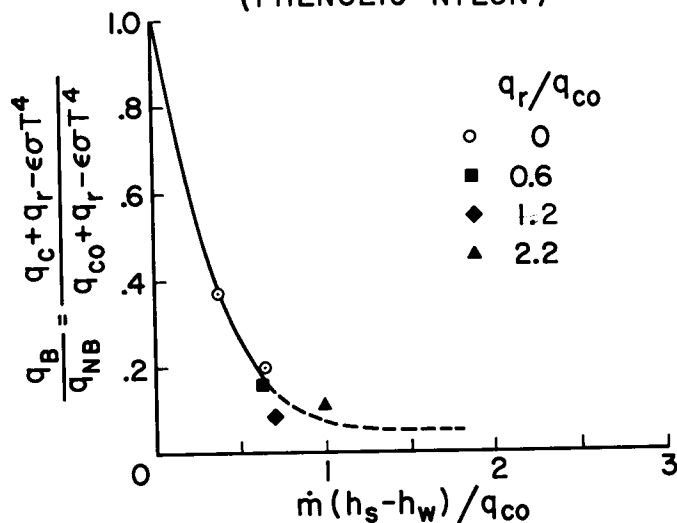


Figure 9

PREDICTED HEAT OF ABLATION FOR A CHARRING PLASTIC (PHENOLIC NYLON)

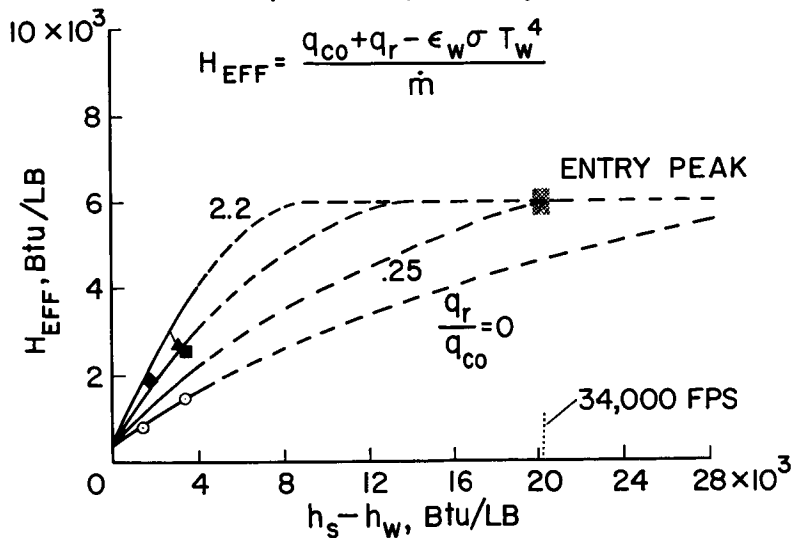


Figure 10

SURFACE TEMPERATURE FOR CHARRING PHENOLIC NYLON

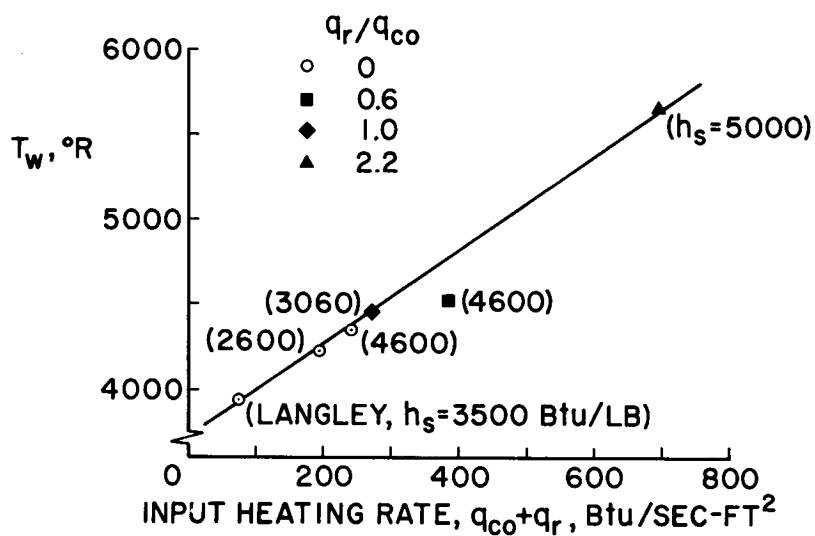


Figure 11

AN EVALUATION OF THERMAL PROTECTION FOR APOLLO

By William A. Brooks, Jr., Kenneth L. Wadlin,
Robert T. Swann, and Roger W. Peters

Langley Research Center

23

A survey of recent Apollo studies has indicated that thermal-protection weight for the reentry module may constitute 20 to 30 percent of the total reentry weight. Considerable effort should therefore be devoted to obtaining an understanding of the requirements for thermal-protection systems with the objective of developing and utilizing high performance systems which afford weight reduction. The discussion which follows is centered on the analysis of some experimental investigations and on analytical predictions of thermal-protection requirements for the Apollo spacecraft.

Figure 1 shows a typical reentry heating condition for the stagnation point of a vehicle with a small nose radius such as the M-1 configuration. The convective heating, which is characteristic of a long-range overshoot mode of operation, consists of a high, relatively short pulse followed by a low long pulse. One of the dominant features of this type of reentry is the long heating time and the resulting high convective heat input Q_C of 100,000 Btu/ft². Another distinguishing feature is the large amount of radiative heat transfer to the body from the hot gases.

The pulse indicated by the dashed curve in figure 1 is an estimated total radiative heating rate (equilibrium plus nonequilibrium radiation) which was obtained from reference 1. The nonequilibrium component of the radiative heating is several times as large as the equilibrium component. There is considerable uncertainty regarding the radiative heat input Q_R and this uncertainty undoubtedly will not be resolved until suitable flight tests have been made. Radiative heat input will be confined for the most part to the forebody of the spacecraft (ref. 2). For the stagnation point, the total radiative input is 27,500 Btu/ft².

Certain characteristics of the heat pulse in figure 1 suggest desirable properties for the thermal shield. These characteristics are listed in the following table along with the resulting shield property requirements:

DECLASSIFIED

Characteristic of heating	Requirement
High heating rate	Ablator
High enthalpy	Large volatile fraction
Long time at lower heating rate	High surface temperature for reradiation
Large heat input	High surface temperature and large blocking effect
Long exposure time	Efficient insulator

The initial heating rates q are too high to be handled by reradiation alone and a material that ablates is indicated. The enthalpy is also high during the first pulse and therefore mass injection into the boundary layer is very efficient in reducing the convective heating to the body. This being the case, a substantial fraction of the ablator should be volatile.

About one-half of the total heat input is accumulated at heating rates less than $100 \text{ Btu/ft}^2\text{-sec}$. This characteristic, plus the fact that the total input is large, indicates that materials which operate with high surface temperatures should be used to obtain the beneficial effects of reradiation. Also, because of the large input, as much convective heating as possible should be blocked. The long exposure time requires that the material be an efficient insulator in order to minimize the amount of heat that soaks through to the spacecraft interior. In other words, an ablating radiator with a small value of thermal conductivity times density ($k\rho$) is appropriate.

It is not possible at present to simulate accurately the reentry environment in ground facilities. However, in view of the cost of flight tests, test facilities which are available must be used to determine the processes and the parameters which influence the performance of thermal-protection systems. These results may then be extrapolated to the actual environment by analytical means with the final verification accomplished by a limited number of flight tests.

Because of this philosophy, a series of tests was made in a Langley Research Center arc-heated air jet with the experimental arrangement shown in figure 2. The convective heating was provided by a 4-inch-diameter subsonic atmospheric pressure arc-heated air jet. A convective heating rate q_c of $100 \text{ Btu/ft}^2\text{-sec}$ was obtained with a stream enthalpy h_g of $3,500 \text{ Btu/lb}$. A cylindrical graphite grid radiator, mounted directly above the arc-jet nozzle, was used to

provide radiative heating rates q_R up to 200 Btu/ft²-sec. With this arrangement combined radiative and convective heating tests could be run in addition to the familiar convective tests.

The specimens, which were supported by a water-cooled sting, were 3-inch-diameter disks with thicknesses such that all specimens had a weight W of 3 lb/ft². A copper calorimeter was bonded to the back face of the specimen. The calorimeter had a heat capacity of approximately 1/2 Btu/ft²-°F which corresponds to about 2 lb/ft² of aluminum structure. The principal purpose of these tests was to evaluate the test materials in terms of their ability to limit the flow of heat to the back face. The temperature of the calorimeter and mass losses were measured.

Although these test conditions do not closely simulate the flight environment, it is expected that the relative behavior of materials in flight will be substantially the same as in the test environment. Those areas where the lack of exact simulation will most likely affect the results are indicated as the test data are discussed.

Figure 3 shows the temperature rise that the calorimeter experienced when the 3 lb/ft² specimens were exposed to convective heating alone at a cold wall rate of 100 Btu/ft²-sec. The tests were terminated when the calorimeter temperature reached 300° F which was selected as a representative structural temperature. The materials investigated can be divided into three classes and the calorimeter temperature histories are shown by bands for each of the classes: sublimers, ceramic composites, and charring composites. The sublimers tested were Teflon, nylon, and Fluorogreen which is basically Teflon with silica and other additives. These materials as a class showed the poorest ability to limit the calorimeter temperature rise, providing a maximum delay of less than 60 seconds. In addition, they experienced high mass-loss rates with the entire 3 lb/ft² being consumed during the tests.

The ceramic composites included foamed alumina, foamed zirconia, foamed silicon carbide, and these same foams impregnated with various resins. In all, 18 different combinations were tested. As a class, ceramic composites provided greater delay times than the sublimers. In general, the high-density unimpregnated foams provided the shortest delay times, and the low-density impregnated materials provided the longest delays. The ceramic composites experienced the smallest mass-loss rates of the three classes tested, being about 1/15 those of the sublimers. The ceramics experienced approximately a 20-percent mass loss.

The charring composites, in general, consist of phenolic, epoxy, or other resins filled with organic or inorganic materials in the form

03712301030

324

~~SECRET~~

of powder, fibers, or microballoons. Fifty-five different composites were evaluated including G.E. castable ablators, AVCO Avcoat series, Emerson Electric Thermo-Lag series, NARMCO series, and NASA series. The charring composites show the best ability to limit heat flow to the back surface, limiting the calorimeter temperature rise to 300° F for times up to 260 seconds. Again, the lower density materials generally provided protection for longer times than did the higher density materials. The right boundary of the charring composite band corresponds to materials typical of which is a 50-50 mixture of phenolic-nylon with 50 percent of the phenolic in the form of microballoons. The curve in the center of the band is for a 50-50 mixture of phenolic and powdered nylon without microballoons. This material, which was compounded at the Langley Research Center, was used as a reference material for experimental and analytical studies to be discussed subsequently. The charring composites experienced moderate mass-loss rates, these rates being in general about twice those experienced by the ceramic composites. About 85 percent of the material was consumed during the tests.

As previously mentioned, these tests were made with a stream enthalpy of 3,500 Btu/lb. If the enthalpy were increased to the higher levels encountered in the Apollo reentry environment, all three bands would shift to the right. However, it is expected that the charring composites would continue to show superior performance for the Apollo conditions.

The results presented in figure 3 indicate that charring ablators are the type of thermal-protection materials appropriate for the Apollo spacecraft. The advanced charring ablators which have additives to lessen the density, to increase the integrity of the char, and to lessen shape changes should be employed.

Reentry at escape velocity is expected to result in substantial radiative heat loads as previously indicated. The prospect of radiative heat loads has caused speculation as to the performance of ablative materials under combined radiative and convective heating. In view of this, a preliminary evaluation of the influence of radiative heat loads on ablation materials was made.

The initial results of this program are presented in figure 4. The efficiencies Q/W of three materials - Teflon, Fluorogreen, and phenolic-nylon - are given as a function of the total cold-wall heating rate. Efficiency is defined as the total cold-wall heat input to the specimen, before the calorimeter experienced a 300° F temperature rise, divided by the initial specimen weight, which was 3 lb/ft². Tests have also been made with initial specimen weights of 1½ and 6 lb/ft². These tests indicated that the initial weight has a small influence on efficiency with the larger weights leading to a slight increase in

~~SECRET~~

efficiency. Data are shown for radiative heating alone, convective heating alone, and combined radiative and convective heating.

For Teflon, the efficiency for convective heating only is about 1,900 Btu/lb. With radiative heating only the efficiency drops to essentially zero. This radical change in efficiency is caused by the transparency of Teflon to thermal radiation. When the convective heating is held approximately constant and the radiative component is increased, the efficiency again drops to a low level. The addition of only a small amount of radiative heating causes most of the decrease.

For Fluorogreen, which is essentially Teflon with additives that increase the opaqueness to thermal radiation, the efficiency for convective heating alone is the same as for Teflon. However, pure radiative heating does not decrease efficiency as much as it did in the case of Teflon. The series of tests with combined radiative and convective heating produced higher efficiency than in the case of Teflon.

For phenolic-nylon, a series of convective tests shows an increase in efficiency with increasing heating rate. At a comparable heating rate, phenolic-nylon has a much greater efficiency, 5,600 Btu/lb, than Teflon and Fluorogreen. The substantial increase in efficiency is caused by the char formation which reradiates heat.

A series of tests involving radiative heating alone shows the same level of efficiency and rate of increasing efficiency that was obtained in the convective tests. Tests of combined radiative and convective heating with the convective component approximately equal to 100 Btu/ft²-sec and with increasing amounts of radiative heating also produced about the same trend in efficiency. In all cases, as the total heating rate was increased, surface temperatures increased and caused increased reradiation and efficiency.

The point that can be made with these test results is that, for the test environment, phenolic-nylon has the same efficiency for convective or radiative heating. The presence of radiative heating does not cause a degradation in the performance of the material.

It has been established that the high surface temperatures, which are possible when chars are present, result in increased efficiency. There is, however, some question as to the amount of char required. Figure 5 shows the results of a preliminary study of char thickness. Chars were developed with a convective heating rate of 110 Btu/ft²-sec. Thick specimens, weighing 9 lb/ft², were used in this phase of the study to provide for long test times and thick char layers. The char thickness in inches and the mass-loss rate in lb/ft²-sec are plotted as

03712391030

326

functions of time. Experimental points have been fitted with a faired line to show the growth of the char thickness. The char thickness grew rapidly at first; however, the rate of the growth diminished with time and the char approached a thickness of about 0.25 to 0.3 inch under these test conditions with a slight decrease in thickness occurring after 240 seconds.

The mass-loss rate is shown by a curve which was derived from measurements of the mass losses. The mass-loss rate decreased rapidly with time when the char layer was thin and was rapidly building up. After the initial rapid decrease, the mass-loss rate changed very slowly and became constant. This shows that the mass-loss rate is strongly influenced by the initial char formation but not influenced as significantly by further development of thick chars.

It is interesting to note that the specimen surface temperature T_W , shown on the char-thickness curve, increased from 3,060° F at a 30-second exposure to 3,460° F at 120 seconds and remained essentially constant thereafter. The period of increasing temperature corresponds to the transient period in mass-loss rate.

The conclusion that can be drawn here is that char formation is important but the benefits diminish rapidly after a certain thickness is obtained. For phenolic-nylon this thickness appears to be about 0.2 of an inch, but it may differ for other materials. Although the test environment does not exactly simulate the flight environment, it is expected that the same conclusion applies to the flight environment - that is, in flight only a moderate thickness of char layer will be required to derive the major benefits.

The next item to be discussed is the thermal analysis which must be used to predict the required thermal-protection weight. Figure 6 shows one of the models which is currently being analyzed. The model incorporates a char layer and a layer of virgin material bonded to a honeycomb structural panel. A cooling system is utilized to maintain the interior wall at temperatures less than 100° F.

The mechanism of char removal is not at present well understood so provisions have been made in the computer program for either oxidation, which removes char at a calculated rate, or mechanical erosion, which produces a char layer of constant thickness. Test results obtained for charring ablators have indicated that combustion of the char or the gases of pyrolysis may be a significant factor in the performance of these materials. At the present time, this phenomenon is not understood well enough to be included in these calculations. The computer program has a provision for a variable temperature of pyrolysis but, in the results to be presented subsequently for phenolic-nylon, a constant pyrolysis temperature of 1,250° F was used.

The bond-line temperature was assumed not to exceed 600° F which is a representative maximum temperature for organic bonding materials. With the 600° F limitation on bond-line temperature, only small amounts of heat reached the interior wall because of the insulating qualities of the honeycomb panel (ref. 3).

The computer program permits both convective and radiative heating inputs. Both forms of heating contribute to the rate of pyrolysis. However, when the gases produced by pyrolysis are injected into the boundary layer, they block only the aerodynamic heating. The extent of the blocking has been determined from solutions of the boundary-layer equations (ref. 4) and has been programed into the routine.

The behavior of charring ablators is very complex and one might anticipate difficulties when attempting to analytically match experimental results. This was found to be the case, particularly during rapidly changing transient situations. A great deal of the difficulty arises because of the many unknown properties, such as the char conductivity, the specific heat of the gases resulting from pyrolysis, the heat of pyrolysis, and the temperature of pyrolysis.

When the test environment was programed into the calculating routine, analytical results were obtained which are in good agreement with the experimental data shown in figure 4 for phenolic-nylon. Agreement has been obtained for the three heating conditions: radiative heating only, convective heating only, and combined heating.

The analytical routine has also been used to determine that the decrease in char layer thickness, shown in figure 5, is caused by an increase in char removal rate. Experimentally determined char-loss rates were programed into the routine producing char-thickness curves similar to those shown in the figure.

For the most part, effort has been concentrated on determining the variation of char conductivity with temperature that would result in the measured char thickness and that would match experimentally determined internal temperatures. Figure 7 shows a comparison of calculated and experimental temperature histories obtained with phenolic-nylon heated at a rate of about 100 Btu/ft²-sec. Temperature is plotted as a function of time for several stations measured from the back surface. The solid curves are experimental temperature traces and the dashed curves are calculated results. The dashed curves shown in figure 7 are the best fit to the experimental results that has been obtained. It was found that the conductivity providing the best fit was a cubic function of temperatures with values as high as forty times the conductivity of the virgin material.

CONFIDENTIAL

The approach that has been taken in the present program is to determine what properties must be used to bring about good agreement between analytical and experimental results and to use these properties to analytically extrapolate to the flight conditions. With this estimate of the char properties of phenolic-nylon, predictions were made of the weight of thermal protection required to protect the stagnation area from the heat pulse shown in figure 1. The results are shown in figure 8 where the required weight per square foot for maintenance of a maximum bond-line temperature of 600°F is plotted as a function of maximum char layer thickness. In the computations, when the char thickness increased to a desired amount, it was thereafter assumed to remain constant. The required weight is shown by a band whose lower edge corresponds to the analytically determined conductivity and whose upper edge corresponds to twice that conductivity. Doubling the conductivity produces about a 30-percent increase in weight for the entire range of char thickness. In general, weight decreases as the char layer thickness increases. However, the most substantial decreases occur at the thinner char layers. At the right, the tick mark indicates the weight corresponding to the limiting case of a continuous buildup of char thickness.

There are no available experimental data relating char removal to the basic mechanisms which are currently postulated. In the high-dynamic-pressure flight environment associated with intercontinental ballistic missiles, char thickness of the order of 0.05 inch has been reported. At the present time, very little can be said about the thicknesses of char layers that will be obtained in the Apollo reentry environment.

However, char layers of about 0.1 inch appear to be a reasonable assumption for the Apollo environment. With this char thickness, the required weight of thermal protection given by the lower edge of the band is 13 lb/ft^2 . With the convective component of heating only, the weight is 10 lb/ft^2 . The radiative component of heating causes an increase of 3 lb/ft^2 or 30 percent. The 30-percent increase is almost equal to the increase in total heat input caused by the radiative component. This means that the weight increase results primarily because of an increase in total heat input and not because of the type of heating.

Thermal protection for the afterbody was considered and the results are shown in figure 9. The required weight per square foot is plotted as a function of the local heat input. Up to $100,000\text{ Btu/ft}^2$, the heating is assumed to be convective only. Beyond $100,000\text{ Btu/ft}^2$, the heat input is increased to the stagnation-point value of $127,000\text{ Btu/ft}^2$ by adding a radiative component. Efficiency, defined as the heat input divided by the required weight, is also shown. The significant point

to be made is that weight reduction is not proportional to the reduction in heat input. Because of the long exposure to lower heating rates more ablation material is required for self-insulation on areas aft of the stagnation point. More self-insulation weight leads to decreased efficiency, as can be seen in the figure. For total heat input greater than 100,000 Btu/ft², there is a small reduction in efficiency caused by the radiative component of heating. This is contrary to the previously presented experimental data and may result from the differences in the heating environments.

Although the presented experimental data and analytical predictions are at present limited in scope, they are believed to support the following conclusions regarding a thermal shield for Apollo:

1. An ablating radiator approach which achieves high efficiency by combining the desirable features of ablation and reradiation is appropriate.
2. In particular, advanced charring ablators which have low density and produce strong chars provide best efficiency.
3. A char layer is essential to the efficiency of charring ablators but only moderate thicknesses of char with good integrity appear to be required.
4. The presence of radiative heating in the Apollo reentry environment does not seriously affect the efficiency of charring ablators.
5. The efficiency of the thermal protection required for the afterbody is decreased because of exposure to lower heating rates which require more insulation weight.

03171020 1433

REFERENCES

1. Anon.: Apollo - Final Study Report. Vol. III - Supporting Design Analyses. Book 2 - Heat Control Systems. Rep. No. AE61-0363 (Contract NAS 5-304), Gen. Dynamics Corp. and AVCO Corp., May 15, 1961.
2. Seiff, Alvin, Goodwin, Glen, and Wick, Bradford H.: Effect of Vehicle Configuration on Combined Heating Loads With Special Reference to Radiative Heating. (Paper 21 of Present Compilation.)
3. Swann, Robert T., and Pittman, Claud M.: Analysis of Effective Thermal Conductivities of Honeycomb-Core and Corrugated-Core Sandwich Panels. NASA TN D-714, 1961.
4. Swann, Robert T.: Effect of Thermal Radiation From a Hot Gas Layer on Heat of Ablation. Jour. Aerospace Sci. (Readers' Forum), vol. 28, no. 7, July 1961, pp. 582-583.

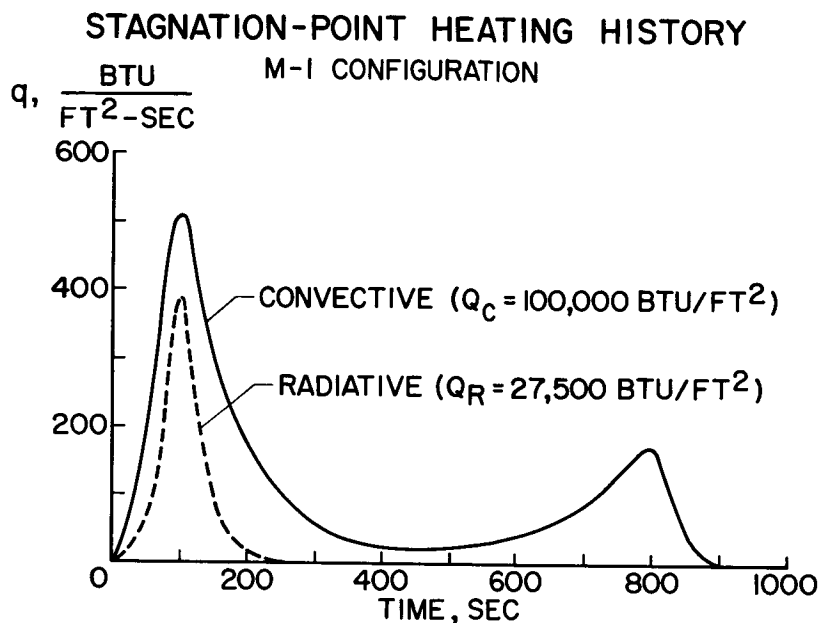


Figure 1

EXPERIMENTAL CONVECTIVE-RADIATIVE HEATING

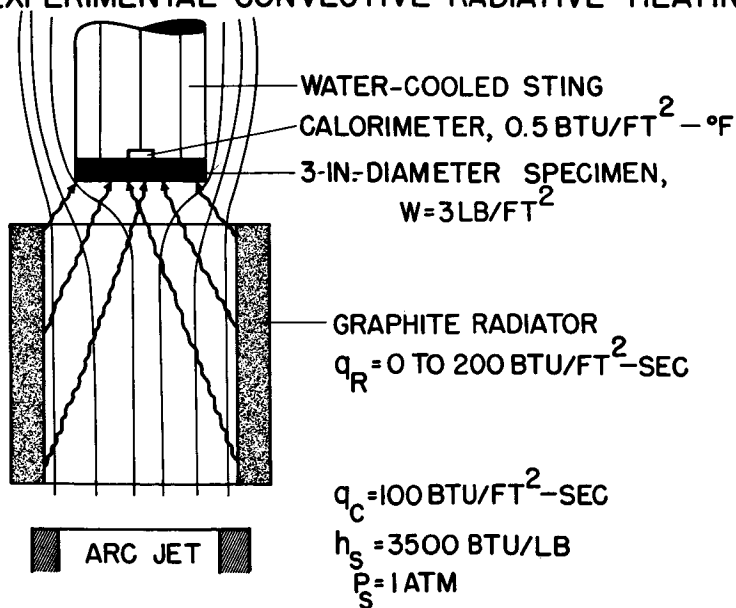


Figure 2

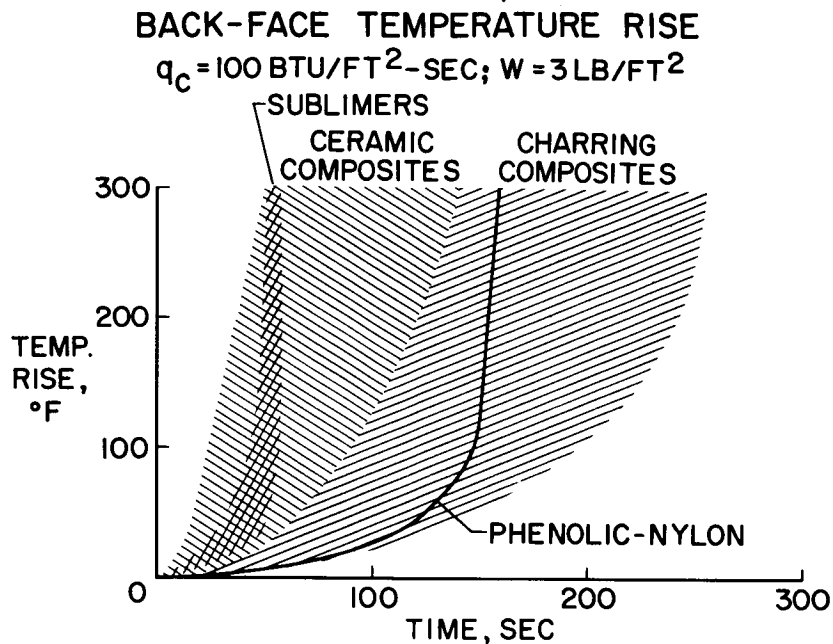


Figure 3

EFFECT OF RADIATIVE HEATING
 BACK-SURFACE TEMPERATURE RISE = 300°F ; $W = 3 \text{ LB/FT}^2$

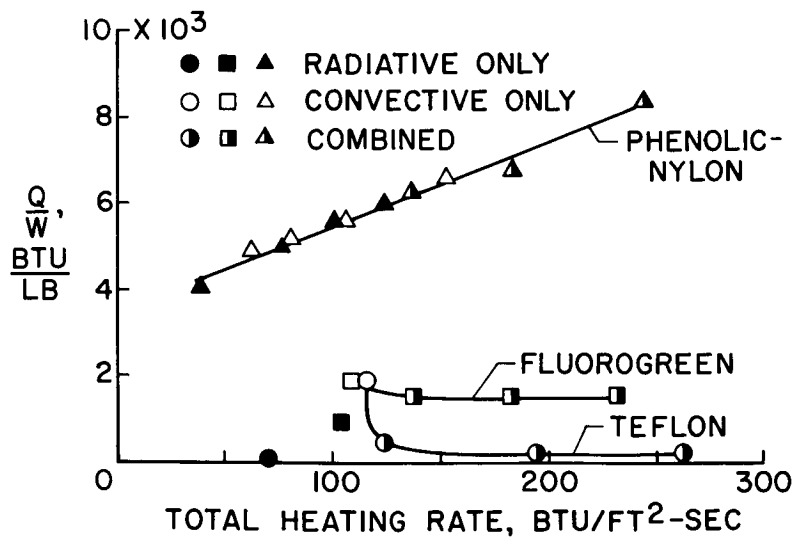


Figure 4

EFFECT OF CHAR ON MASS LOSS

PHENOLIC-NYLON; $q_c = 110 \text{ BTU/FT}^2\text{-SEC}$; $W = 9 \text{ LB/FT}^2$

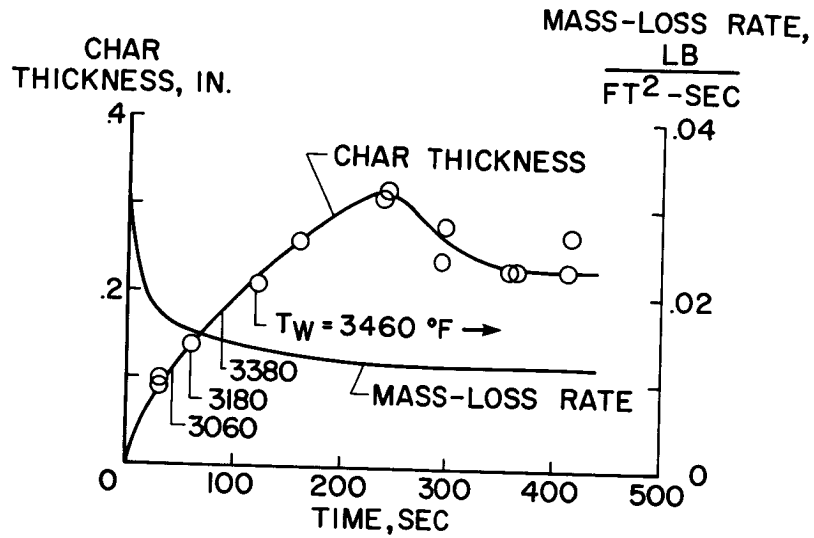


Figure 5

ANALYTICAL MODEL

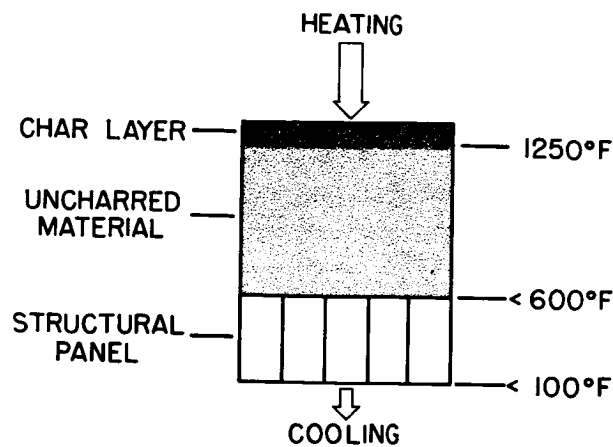


Figure 6

COMPARISON OF TEMPERATURE HISTORIES
PHENOLIC-NYLON, $q_c = 100 \text{ BTU/FT}^2 - \text{SEC}$

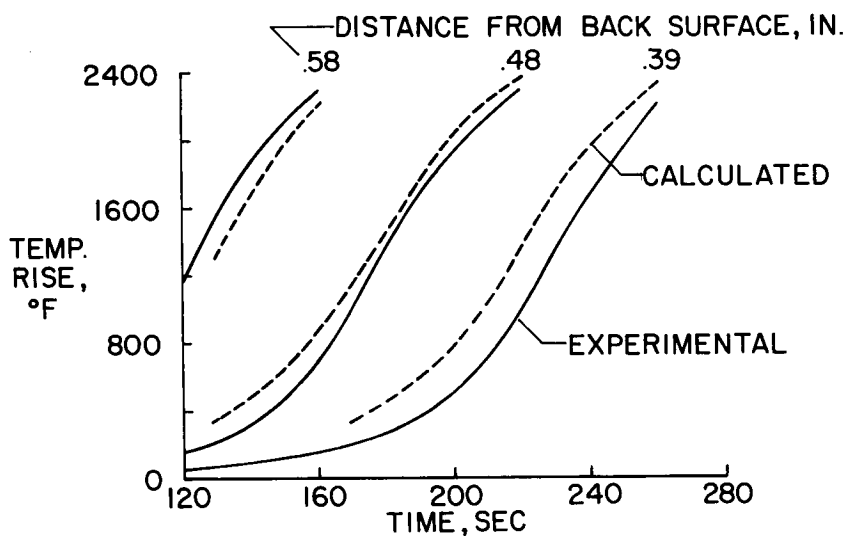


Figure 7

EFFECT OF CHAR ON STAGNATION-AREA WEIGHT
PHENOLIC-NYLON

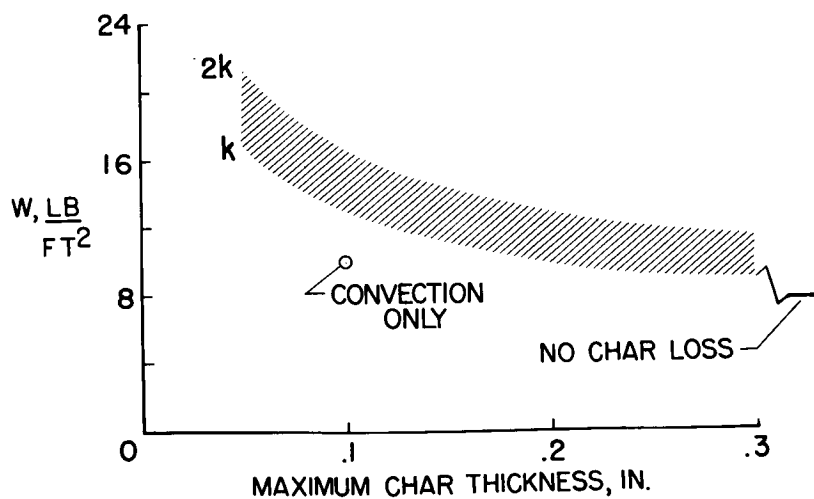


Figure 8

~~CONFIDENTIAL~~ 335

EFFECT OF TOTAL HEAT INPUT ON WEIGHT
PHENOLIC-NYLON

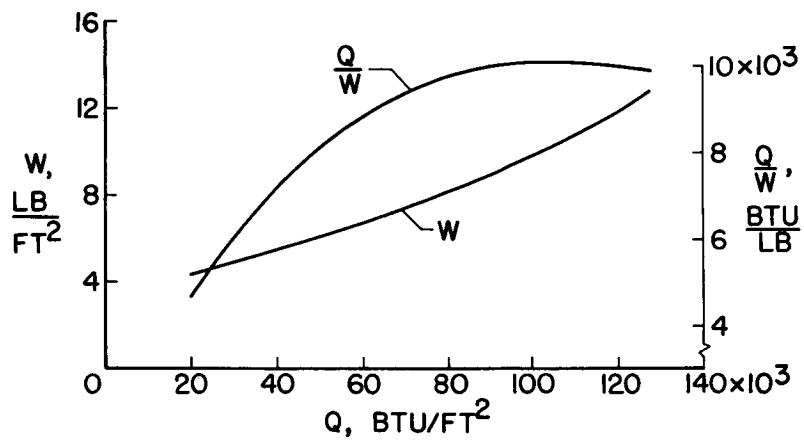


Figure 9

CHARACTERISTICS OF SMALL CONTROL ROCKETS

By James F. Connors and William T. Latta, Jr.

Lewis Research Center

INTRODUCTION

A large number of small rocket engines will be required on the Apollo vehicle to achieve and maintain precise attitude and trajectory control. Upon signal, these rockets must be capable of providing fast, reliable, accurate, and efficient impulse and must be structurally capable of long-duration usage with many restarts under space-environment conditions. Recent research at the Lewis Research Center pertinent to the development of such small motors varying from 25- to 500-pounds thrust and using storable liquid propellants are described herein in detail.

Because of its hypergolic characteristics, high bulk density, and high performance potential, hydrazine and nitrogen tetroxide were selected as the propellant combination in the experimental studies. High efficiency or specific impulse, of course, is the primary performance criterion and a determining factor insofar as overall system weight (as reflected in the amount of fuel) is concerned. Engine compactness or size is more important in relation to determining cooling requirements and, perhaps, ease of installation. In terms of reliability and durability, the method of cooling a small efficient rocket may become the critical factor in the selection of the type of reaction control system - dependent, of course, upon the particular mission requirements. Research experience on rocket chambers suitable for radiation, ablation, or regenerative cooling are now examined.

SYMBOLS

A_c	chamber cross-sectional area, sq in.
A_T	throat cross-sectional area, sq in.
c^*	characteristic exhaust velocity, fps
I	solenoid current

L^*	characteristic length
O/F	ratio of oxident weight flow to fuel weight flow rate
P_c	chamber pressure
ΔP_{inj}	injector pressure drop
\dot{Q}_a	ablation heat-flux rate, Btu/ft ² -sec
Q_u	uncooled heat-flux rate, Btu/ft ² -sec
T	thrust, lb
\bar{T}	average thrust, lb
T_{cs}	coolant side temperature
V	solenoid voltage
W_c	ablation coolant weight flow rate, lb/sec
W_t	total propellant weight flow rate, lb/sec

LOW-PRESSURE RADIATION-COOLED ROCKETS

Since the heat-flux rate is approximately proportional to chamber pressure to the 0.8 power, radiation cooling of chambers of conventional steel construction can be made practical through operation at very low chamber pressures. For the bipropellant combination of hydrazine and nitrogen tetroxide, the rocket must be operated at pressures of approximately 5 to 10 psia to maintain sufficiently low heat-flux rates. (See ref. 1.) For a specified thrust level, the size of a low-pressure rocket obviously becomes correspondingly large.

The injection techniques necessary to the attainment of stable and efficient operation under such extreme conditions have been investigated experimentally (ref. 2) on a nominal 50-pound-thrust rocket (fig. 1) at a chamber pressure of 10 psia. Highest performance was realized with this particular configuration by using a 6-element triplet injector and a characteristic chamber length L^* of 80 inches. At a chamber pressure of 10 psia, the injector was designed for a pressure drop of 25 psi. The performance for this low-pressure rocket is presented in

figure 2. Performance is shown as the ratio of actual to theoretical characteristic exhaust velocities assuming equilibrium composition. At a mixture ratio O/F of approximately 1.0, a characteristic velocity of 5,280 feet per second or 93 percent of the theoretical equilibrium value was attained with an L^* of 80 inches. Decreasing L^* to 40 inches resulted in a 4-percent decrease in characteristic velocity. Smooth, stable combustion was attained at $P_c = 10$ psia, and optimum ignition occurred when both propellants were introduced simultaneously into the chamber.

COMPACT LOW- L^* ROCKETS

As chamber pressures are increased, the physical size of the rocket for a given thrust can be reduced drastically; however, another method of cooling (e.g., regenerative or ablative) must be employed, or a high-temperature refractory metal might be used with radiation cooling. For representative space vehicles and with pressurized spherical propellant tanks having practical structural limits, minimum system weights are estimated to occur with chamber pressures of 200 to 300 psia.

An experimental investigation (ref. 3) was conducted on a nominal 100-pound thrust rocket (fig. 3) operating with hydrazine and nitrogen tetroxide at chamber pressures up to 300 psia. For comparison purposes, this chamber is shown with the 50-pound-thrust low-pressure rocket previously discussed. Both are drawn to the same scale to show that this rocket is significantly smaller. At 300 psia, the injector pressure drop was 60 psi. Coaxial injection principles which had previously been shown to have high efficiency with short chambers ($L^* = 10$ in.) using JP-4 fuel and liquid oxygen (ref. 4) were used in this study. A wide variety of chamber and injector geometries was investigated with hydrazine and nitrogen tetroxide. High performance was obtained with a 21-tube coaxial injector with a characteristic chamber length of 10.7 inches. A characteristic velocity equal to 95 percent of the theoretical equilibrium value was attained at a pressure of 300 psia and an O/F of approximately 1.0.

In figure 4, performance is shown for an L^* of 10.0 inches over a range of chamber pressures down to about 100 psia. In general, efficient operation (or characteristic velocities of 92 percent of theoretical) could be achieved over the range of chamber pressures by varying the geometry. This involved decreasing the chamber contraction ratio A_c/A_T by opening up the throat area as pressure was decreased. In this way, two factors were found to account for the improved performance at reduced chamber pressure: (1) opening up the throat area resulted in increased total propellant flow rate with attendant higher

037129.1077

injection pressure drop and better mixing; and (2), with constant L^* , opening the throat also resulted in increased chamber (or burning) length. In practice, of course, at a given chamber pressure it would be desirable to maintain high efficiency (or characteristic velocity) with minimum pressure drop (or correspondingly maximum contraction ratio) in order to keep the overall system weight down. For a given contraction ratio, performance falls off from the 92-percent level rather rapidly with decreased chamber pressure.

SMALL PULSE ROCKETS

For attitude control, the small pulse rocket offers considerable versatility and accuracy in thrust application. First of all, the primary objective of the pulse rocket (fig. 5) is to produce a very short time-width pulse of high specific impulse and high repeatability. Specific impulse, of course, is efficiency and reflects directly in system weight. With very short operating times (in the order of milliseconds) the starting and shutdown transients must be minimized for high average specific impulse (i.e., ideally to approach a square wave pulse shape). This requirement means low ignition delay times and propellant valving located at or very near the injector.

With the attainment of efficient, short-time, repeatable pulses, total impulse control may be accomplished with a high degree of accuracy simply by counting out the required number of pulses and applying them at maximum frequency. Thrust modulation could then be effected through frequency variation as illustrated in figure 5. Very small thrust pulse units are ideal for limit cycle operation (as described in ref. 5) in that the smaller and more accurate the pulse, the narrower the deadband limits of the controller.

Preliminary results of an experimental evaluation of a small pulse rocket (provided by the Marquardt Corporation) are indicated in figure 6. The pulse rocket is designed for approximately 25 pounds of thrust with a nozzle having a 40:1 area ratio. Injection of hydrazine and nitrogen tetroxide is accomplished through a single element of impinging jets at a chamber pressure of 100 psia. Electric solenoid propellant valves were located at the injector for minimum time response. In an effort to minimize ignition delay times, a short characteristic chamber length of approximately 3 inches was used to insure rapid chamber-pressure buildup time. Experimentally determined characteristics are shown for the pulse rocket with a nozzle of 4:1 area ratio operating at sea level and in an 85-cubic-foot vacuum tank with an initial pressure of approximately 10^{-6} millimeters of mercury absolute. The shapes of typical traces of solenoid voltage and current

037129.1077

and engine thrust and chamber pressure are indicated as a function of time. For the representative 10-millisecond pulses tabulated below, the difference in ignition delay times between sea level and vacuum conditions is less than 1 millisecond. The time from "signal-on" to the start of chamber-pressure rise was in the order of 8 milliseconds, of which about 7 were attributed to valve operating time. The thrust and pressure buildup times were approximately 1 millisecond. These results are very preliminary, but they do emphasize that ignition delay times can be kept to very small values through the use of low- L^* chambers and that more refined valves than the commercial solenoid units used for this study will be required to improve significantly minimum bandwidth times. Generally, the pulse shape appears to approach a square wave. With displacement-type flow meters, propellant flow rates are currently being determined to evaluate the specific impulse of these motors.

SMALL-ROCKET REGENERATIVE COOLING

In order to investigate the regenerative-cooling requirements of various rocket engines, an analysis (ref. 6) was made of a family of engines with various thrust levels and propellant combinations. The results are indicated in figure 7, where coolant utilization (or the ratio of heat rejected to the amount of heat the coolant is capable of absorbing) is presented as a function of nozzle throat area. The absolute numbers, obviously, are grossly dependent upon the assumptions made for the analytic model ($P_c = 300$ psia, 100-percent combustion efficiency, $T_{cs} = 1,000^\circ$ R, single-pass axial-flow coolant passage, etc.). However, for purposes of this discussion, only the relative trends are important. In general, the smaller the engine, the harder it is to cool regeneratively. The cryogenic propellant engines, because of the large heat-sink capacity of the hydrogen, are best suited for regenerative cooling. Hydrazine and nitrogen tetroxide with the basic engine design run out of capability in the small sizes. The effect of two design modifications aimed at improving this cooling capability is also indicated; these changes were (1) to reduce L^* by more than half (from 36 to 15 inches); and (2) to add a 0.020-inch insulating liner to the nickel chamber wall. Both changes resulted in significant reductions in the coolant heat loads, as shown in this figure. Another corollary that was drawn from this analysis is that the more efficient the engine (or the higher the characteristic velocity), the more critical are the cooling requirements.

Based on Lewis research experience, possible ingredients for a small regeneratively cooled rocket using nitrogen tetroxide and hydrazine are illustrated in figure 8. A 300-psia chamber with low L^* and

high efficiency (as discussed in figs. 3 and 4) is considered. A thin refractory metal liner (e.g., a tantalum-tungsten alloy) might be used to contain the insulating liner (e.g., zirconia oxide). Using hydrazine as the coolant and having shutoff valves in the injector to minimize starting and shutdown transients gives rise to the problem of dissipating the residual heat in the chamber materials after shutdown without causing violent decomposition of the hydrazine trapped in the coolant passages. One solution suggested might be the use of a spring-piston-type accumulator to allow sufficient through-flow to absorb the residual heat. The spring-actuated piston would be designed to open or close against a pressure differential equal to the injector pressure drop. Other seemingly more complicated schemes would be a flush system to remove the fuel (N_2H_4) from the jacket or an intercooler using the oxidant (N_2O_4) to lower the operating temperature of the hydrazine. A shutoff valve arrangement has been developed for the 21-tube coaxial injector of figure 3; however, a simpler injector design (i.e., fewer injection elements with splash-plate provisions as suggested in the sketch) is being explored.

SMALL-ROCKET ABLATION COOLING

Where regeneratively cooled systems are ideally capable of operation for indefinite time periods, many other mission control functions may be accomplished in relatively short times. In this latter case, ablation cooling becomes very attractive in terms of simplicity and reliability. An experimental study of various representative ablative materials (ref. 7) was conducted on a small 500-pound-thrust rocket using JP-4 fuel and liquid oxygen as propellants at a chamber pressure of 300 psia. The results are shown in figure 9. From oscillograph traces of thrust and chamber pressure and from weighings of the chamber and nozzle before and after runs of known time duration, the ablation rates of the various test materials were determined. Of the thermoplastics, nylon which ablates by liquefaction and subsequent vaporization appeared more effective, particularly in the high shear flow conditions in the throat. The reinforced thermosetting resins (of which phenolic silica was the best) performed well in the chamber where the mainstream shear forces were low, but mechanical erosion decreased the effectiveness of these materials at the throat.

For a control rocket, this time dependency of engine thrust caused by throat erosion with an ablation nozzle is intolerable. To avoid this situation, a refractory throat insert could be employed wherein advantage would be taken of the film cooling effectiveness of the ablative material. In this system the cooling film is produced by the ablation of a material of low melting temperature located upstream of

the throat. The heat flux at the nozzle wall is reduced by the presence of the insulating cooling film between the high-temperature combustion gases and the wall.

To investigate the feasibility of this approach, an experimental study (ref. 8) was made on a 500-pound-thrust rocket with JP-4 fuel and liquid oxygen at 300 psia. An instrumented copper heat-sink nozzle was cooled by the film produced by nylon inserts in the chamber wall. The results are shown in figure 10 where film effectiveness (percent reduction in heat flux to the nozzle wall due to the ablation film) is shown as a function of ablation coolant to propellant weight flow ratio. Nylon was selected for this study because of its low melting temperature and relatively large volume of vapor per unit weight of material ablated. The lengths of the inserts were varied to change the amount of coolant flow. With coolant weight flow equal to 2 percent of the total propellant weight flow, the film cooling effectiveness was 40, 23, and 5 percent in the convergent section, the throat, and the divergent section, respectively. Film effectiveness decreased with axial position in the nozzle. With a coolant flow of 2 percent, most of the cooling effectiveness in the throat section was achieved. Little was to be gained by going to higher coolant flows.

The effect of chamber pressure and mixture ratio on ablation film cooling effectiveness is indicated on figure 11. When the chamber pressure was reduced from 300 to 200 psia at 6.8-percent coolant flow, very large gains in effectiveness were realized, particularly in the throat and divergent section of the nozzle. In the throat, the effectiveness increased from approximately 30 to 85 percent. Increasing the mixture ratio from 2.4 to 3.4 at a chamber pressure of 300 psia decreased the film cooling effectiveness.

CONCLUDING REMARKS

In summary, this presentation is a survey of current research activity at the Lewis Research Center in the small control-rocket field. The results are rather general and cover a wide spectrum of application. Specific mission requirements will, of course, govern the actual selection of the control-rocket design. To aid in this selection, it is necessary to define the performance characteristics and operational limitations of the various motors. This has been the objective of the present survey. Some consideration is also currently being given to the use of the high-energy cryogenic propellants for control-rocket application. The problem for a control rocket using hydrogen and oxygen would be one of providing an igniter or using an additive (such as O_3F_2 , for example) to obtain hypergolicity.

REFERENCES

1. Hast, Drea R.: The Ultra-Low Pressure Liquid Propellant Space Propulsion System. TN 58-218, WADC, June 1958.
2. Wanhainen, John P., DeWitt, Richard L., and Ross, Phil S.: Performance of a Low Thrust, Storable-Bipropellant Rocket at Very Low Chamber Pressure. NASA TN D-678, 1961.
3. Wasserbauer, Joseph F., and Tabata, William K.: Performance of a Small (100-lb. Thrust) Rocket Using Coaxial Injection of N_2H_4 and N_2O_4 . (Prospective NASA paper.)
4. Stein, Samuel: A High-Performance 250-Pound-Thrust Rocket Engine Utilizing Coaxial-Flow Injection of JP-4 Fuel and Liquid Oxygen. NASA TN D-126, 1959.
5. Tripp, Charles N., and Boardman, Warren P.: Attitude Control Rocket Requirements for Space Vehicles. Presented at IAS-ARS Joint Meeting (Los Angeles, Calif.), June 1961.
6. Curren, Arthur N., Price, Harold G., Jr., and Douglass, Howard W.: Analysis of Effects of Rocket-Engine Design Parameters on Regenerative-Cooling Capabilities of Several Propellants. NASA TN D-66, 1959.
7. Cullom, Richard R.: Experimental Investigation of the Feasibility of Ablation-Cooling a Rocket Nozzle With Possible Application to Solid-Propellant Engines. NASA TM X-418, 1961.
8. Cullom, Richard R.: Experimental Investigation of the Effectiveness of an Ablation-Produced Film in Cooling a Rocket Nozzle. NASA TM X-476, 1961.

50-LB THRUST LOW-PRESSURE ROCKET

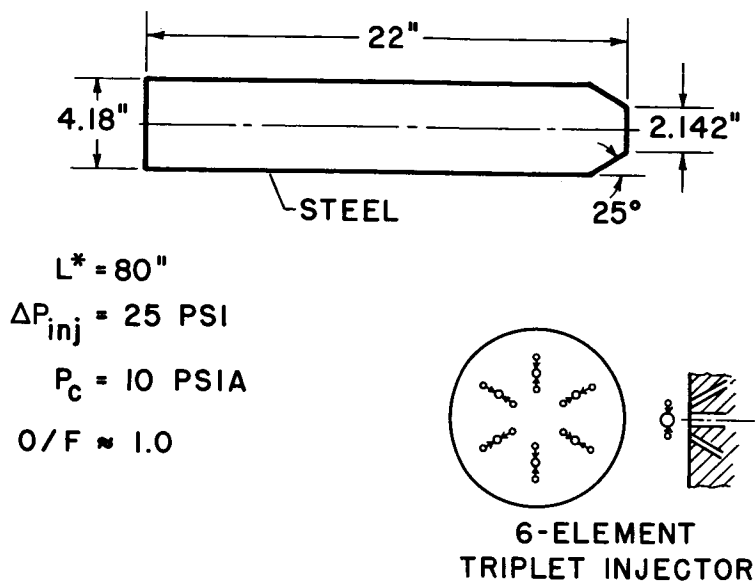


Figure 1

PERFORMANCE OF 50-LB THRUST ROCKET AT LOW CHAMBER PRESSURES

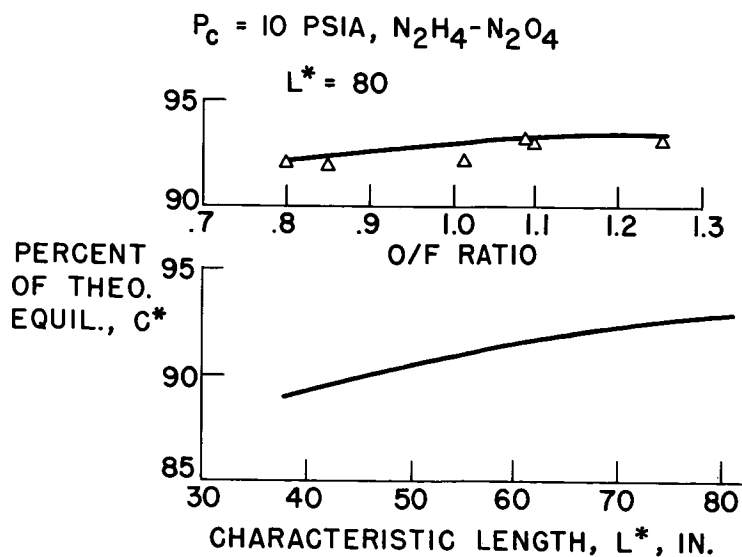


Figure 2

037120A [REDACTED]

100-LB THRUST LOW-L* ROCKET

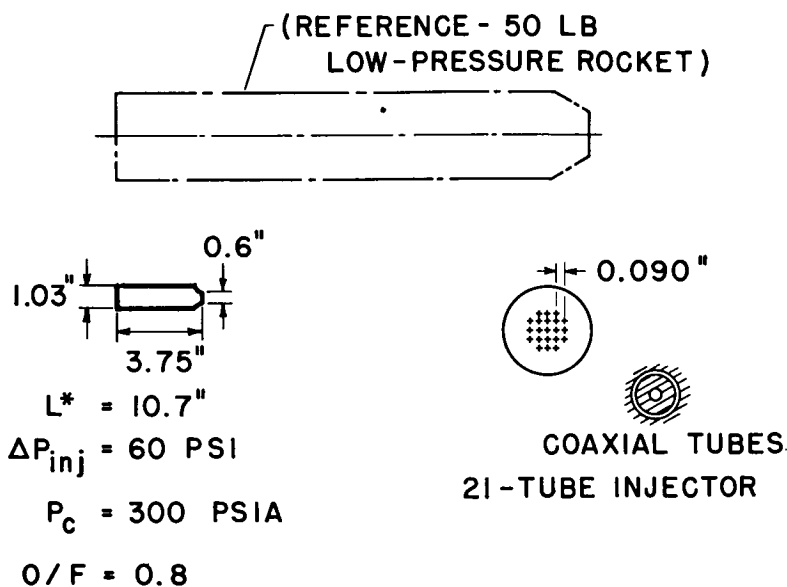


Figure 3

EFFECT OF CHAMBER PRESSURE
ON PERFORMANCE

THRUST ~ 100 LBS

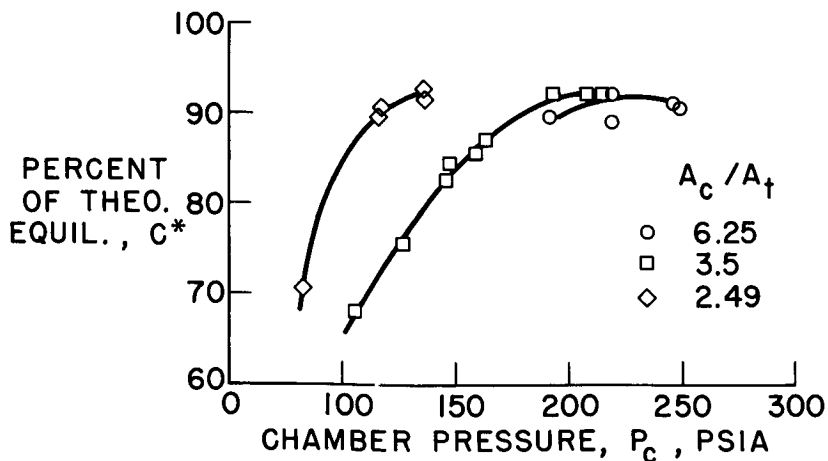
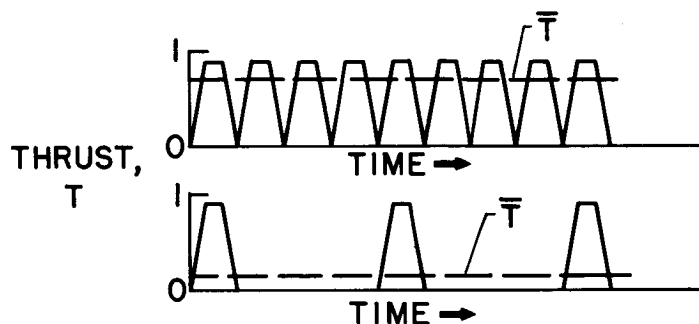
 $L^* = 10.0$ 

Figure 4

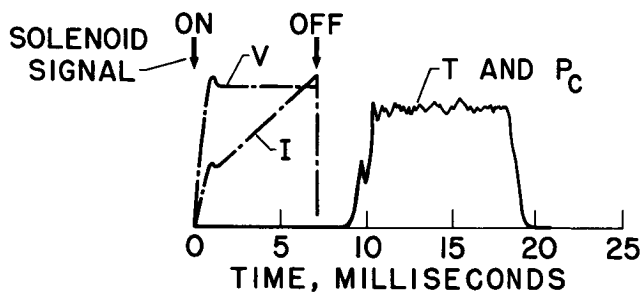
PULSE ROCKET FOR ATTITUDE CONTROL



1. TOTAL - IMPULSE CONTROL
2. THRUST MODULATION
3. LIMIT CYCLE OPERATION

Figure 5

PULSE ROCKET CHARACTERISTICS



	SEA LEVEL	VACUUM (10 ⁻⁶ MM Hg)
AVE. PRESSURE, \bar{P}_C , PSIA	67	78
PULSE WIDTH, MS	10.3	10
AVE. THRUST, \bar{T} , LB	15.8	16.2
TIME TO SIGNAL-OFF, MS	6.0	7.0
TIME TO P_C RISE, MS	7.2	8.8

Figure 6

SMALL ROCKETS ARE HARDER TO COOL REGENERATIVELY

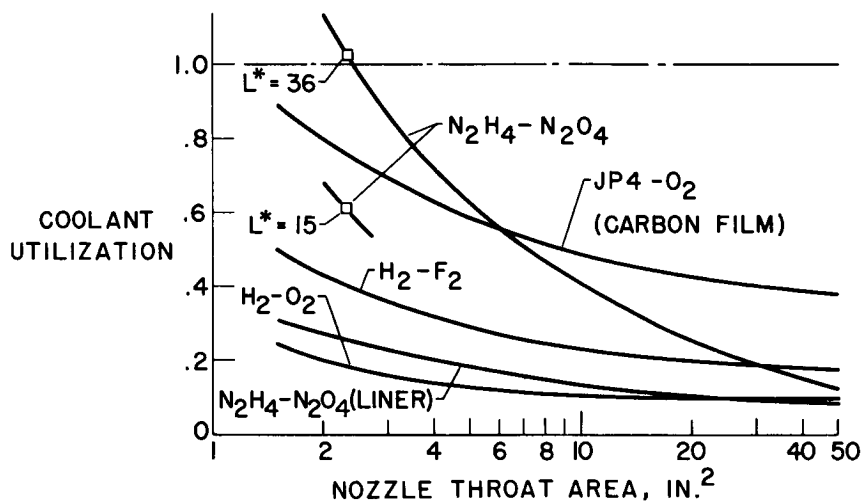


Figure 7

SMALL REGENERATIVELY COOLED ROCKET

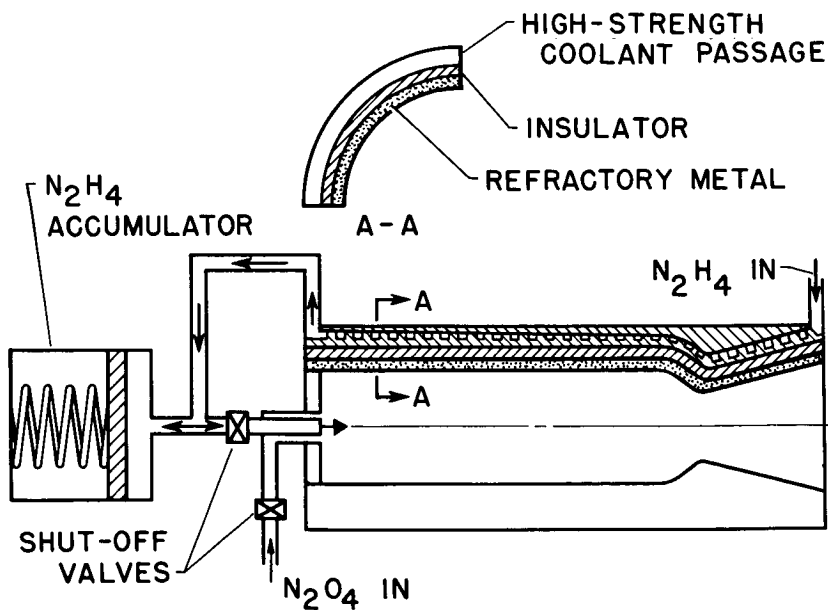


Figure 8

ABLATION RATES

$P_c = 300$ PSIA

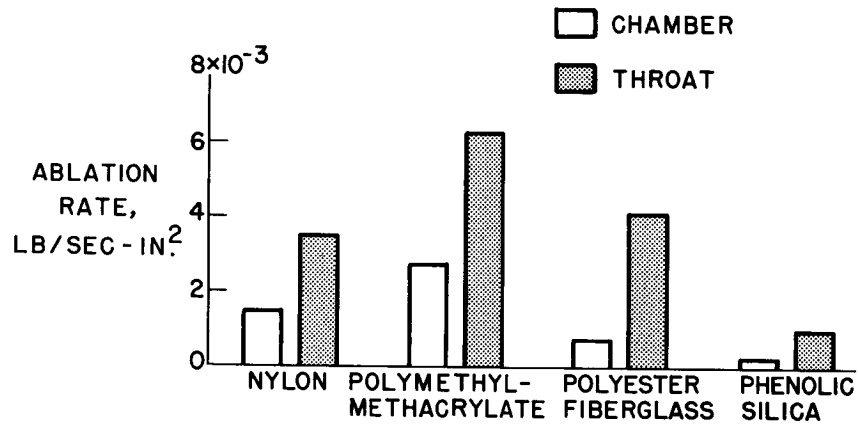


Figure 9

ABLATION FILM EFFECTIVENESS

$P_c = 300$ PSIA, O/F = 2.4

NYLON INSERTS

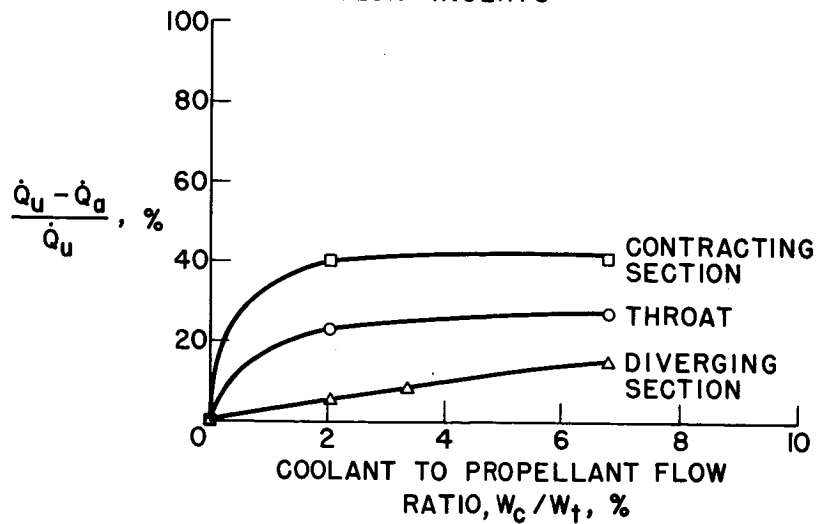


Figure 10

EFFECT OF PRESSURE AND MIXTURE RATIO ON FILM EFFECTIVENESS

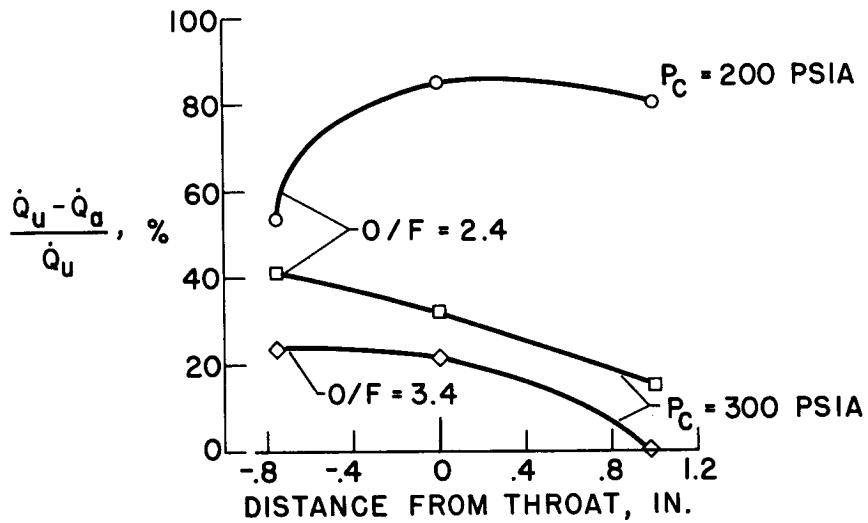


Figure 11

DECLASSIFIED

**VI.
ONBOARD
SYSTEMS**

ONBOARD PROPULSION SYSTEM FOR LUNAR MISSIONS

By Neil E. Munch and George R. Arthur

General Electric - MSVD

INTRODUCTION

The Apollo propulsion must fulfill the requirements for a variety of earth-orbital and lunar missions. An early capability in 1963 to 1964 will provide a power plant for earth-orbital and rendezvous missions with launch vehicles such as the Saturn C-1 and Titan II. In the following years, design improvements can be incorporated where indicated and experience and reliability built up for lunar missions as larger launch vehicles become available.

The Apollo propulsion study, to date, has been directed at lunar orbiting missions. Propulsion system growth to a lunar landing capability has been studied and will be discussed briefly, but the primary emphasis has been directed toward successful achievement of all missions through lunar orbit.

REQUIREMENTS AND FUNCTIONS

The functions to be performed by the propulsion system are summarized on table I. Since the large launch vehicles will not be manned, a safe, highly reliable abort system is essential. On the pad and during the atmospheric portion of powered flight, rapid-response abort engines are required to remove the manned spacecraft from potentially dangerous areas to an adequate altitude for escape. As flights progress beyond the atmosphere, the off-the-pad abort engines can be jettisoned and the abort function passes to the main onboard propulsion. Varying amounts of total abort impulse are required, with increasing amounts required as the flight progresses past orbital velocity to escape velocity. At this point, the most severe abort requirements exist, with a thrust-to-weight ratio of about 2 required to produce the rapid downward deflection of the vehicle velocity vector by about 5,600 ft/sec.

In addition to the superorbital abort, propulsion is required for midcourse corrections and for entry into and exit from lunar orbit. These functions can all be accomplished by the main onboard propulsion system, which will be discussed in some detail. The attitude control system is necessary for orientation of the spacecraft in space and will also be discussed briefly in this paper. Additional discussion of

attitude control components is included in the paper by James F. Connors and William T. Latto, Jr.

During this study, the General Electric Company has directed the efforts of a number of propulsion subcontractors. These companies are listed in table I, and many of the items discussed herein are the results of the studies performed by these companies.

There are specific requirements established for the study of the Apollo propulsion system. The required mission characteristic velocity totals 7,500 ft/sec for the lunar-orbit mission. This velocity is composed of about 250 ft/sec in about five starts each way for midcourse correction and about 7,000 ft/sec in four starts for orbiting and deorbiting the moon. Since these requirements exceed those for super-orbital abort, the propulsion is then amply capable of fulfilling either function.

Thrust requirements vary from the 24,000 pounds required to provide an average acceleration of 2g at superorbital abort to about 200 pounds required for small midcourse corrections. The major maneuvers - lunar orbit and lunar deorbit - can be accomplished at about 6,000 pounds of thrust.

For this study, it was assumed that the total spacecraft weight was limited to 15,000 pounds. However, additional studies were made for spacecraft weights which exceeded this 15,000 pounds.

Analysis of fuel energy management requirements indicated that 5 percent of the propellant should be carried as reserves. This is an important point, since this added propellant represents potential payload and necessitates substantial increases in vehicle and launch-vehicle weights.

Perhaps the most important, overriding design considerations for Apollo spacecraft are the safety and reliability. As with any manned aircraft rocket, safety is of prime importance to assure that rocket operation or malfunction will harm neither the spacecraft nor the crew. It is in the area of reliability that the uniqueness of the Apollo spacecraft propulsion is seen, for, once committed to orbit or landing on the moon, the propulsion system is essential for return of the craft to earth. Safe shutdown in the event of malfunction simply will not do. Thus, both safety and reliability must be pursued as basic tenets throughout the Apollo propulsion development program.

The conclusion was reached that the requirements for reliability and performance are best met in the use of the present state-of-the-art technology and existing components, where applicable, to build an engine which best matches the vehicle requirements. This conclusion

is in contrast to the possible fitting of the vehicle design to existing engines which must still be modified and adapted to final installation needs.

Specific considerations for the main onboard propulsion systems include three major factors which influence design selection:

- (a) Propellants
- (b) Propellant feed system
- (c) Thrust-chamber design

Each of these factors will be discussed to illustrate some of the trade-off effects and the recommended selection for Apollo spacecraft.

PROPELLANTS

Many propellant combinations were briefly considered for the main propulsion system, but the number was rapidly reduced to five general combinations. High-energy solid propellants with specific impulse (I_{sp}) in the 300-second category and with mass fractions of approximately 0.94 were studied. Current earth "storables," such as nitrogen tetroxide (N_2O_4) and mixed amines including hydrazine, monomethyl hydrazine (MMH), and unsymmetrical dimethyl hydrazine (UDMH), were considered at vacuum specific impulses of about 320 seconds. Future storables were considered typified by oxygen difluoride (OF_2) and MMH which might have an impulse over 390 seconds and a good bulk specific gravity. Also included were the high-energy cryogenic propellants, liquid O_2 /liquid H_2 with a specific impulse of about 430 seconds, and liquid F_2 /liquid H_2 with an impulse of 445 seconds.

The influence of propellant bulk specific gravity on Apollo payload is shown on figure 1. The solid lines represent various values of specific impulse and show the influence of density on payload carried by the spacecraft with a velocity increment (ΔV) capability of 7,500 ft/sec. The solid propellants are shown with a performance generally comparable to contemporary earth storables, N_2O_4 /amines, each carrying about 5,000 pounds of payload. Other proposed propellant combinations are included, such as oxygen/hydrogen (O_2/H_2) and fluorine/hydrogen (F_2/H_2) at payloads of 7,000 to 7,400 pounds, respectively. For this mission, propellant density is seen to have far less effect than specific impulse.

If vehicle weights are increased above the 15,000-pound limit, the resulting situation is shown in figure 2. Here, the comparative

[REDACTED]

nonpropulsion or payload weights are plotted against total spacecraft weight for the selected propellant combinations. The lowest curve is for the current storables and high-performance solids. Comparative performance of O_2/H_2 , the advanced storables, and F_2/H_2 is shown by the other curves.


The payload weight for one specific design is shown by the shaded area for comparison with actual vehicle weight variations. The payload weights vary slightly to include allowance of vehicle structure required to house the necessary propellant volume. Vehicle weights at escape can be seen to be approximately 16,400 pounds for F_2/H_2 , 17,300 pounds for OF_2/MMH , 18,000 pounds for O_2/H_2 , and 19,800 pounds for the presently available storables or solid propellants. These weights are all in excess of the 15,000-pound study limit for this payload. Payloads which can be achieved with the 15,000-pound limitation range from 5,400 to 7,000 pounds.

Since there are several propellant combinations which are adequate from a performance basis, these combinations can now be examined from other aspects for selection. Table II shows a brief summary of important features of the four primary propellant combinations. The presently available storables are eliminated because of limitations of performance, and the advanced storables, for now, because of lack of test performance data and handling experience. Solids have also been eliminated in view of the fact that their performance is no better than storables, and they have limited versatility and adaptability to various missions. This elimination leads to the recommendation of oxygen/hydrogen in preference to the highly reactive, toxic fluorine for manned spacecraft. Oxygen/hydrogen are safe, nonexplosive, non-toxic, noncorrosive, and readily available. Excellent experience is available from over a decade of testing, handling, and storage. The propellants are compatible logistically with the upper stages of proposed launch vehicles and are daily being handled safely on a tonnage basis.

Today's ignition methods for O_2/H_2 , particularly with redundant spark plugs, appear quite reliable, and perhaps by the time of the Apollo lunar mission the way to make hydrogen hypergolic with oxygen through addition of traces of O_3F_2 in liquid O_2 may be known. Solutions of 0.05 percent to 0.1 percent O_3F_2 in the liquid O_2 are now being studied by Temple Research Institute with excellent laboratory-scale results.

PROPELLANT FEED SYSTEM

Consider now the second factor influencing the selecting of a propulsion system - the propellant feed system. Pump-fed systems can



be compared with pressurized systems on the basis of weight. Figure 3 shows the results for a typical pump-fed system compared with a pressurized system using a currently available, efficient pressurization system. Propulsion-system weights for a velocity of 7,300 ft/sec¹ are shown for storables, O₂/H₂, and F₂/H₂ at combustion chamber pressures which were generally made optimum for each situation. For pressure-fed systems, chamber pressures were optimum at about 200 lb/sq in. abs for the storables and 60 lb/sq in. abs for the hydrogen combinations. Pump-fed systems appear best at high pressures of 600 lb/sq in. for storables and 300 lb/sq in. for the hydrogen systems.

As can be seen from figure 3, performance of the pressurized systems is equal to or better than the pump-fed system for this mission. It should be emphasized that different results might be reached for different missions, or for less efficient pressurization schemes.

The pressurized feed system is recommended for Apollo spacecraft in recognition of its inherent simplicity, reliability, and the capacity for multiple rapid starts. Pump-fed systems have advantages in many applications, but not for this mission. Pumped systems require too much care about the way propellants are supplied and waste too much propellant during start. Further, for this mission, the pressurized tanks can be sealed by using the newer "superinsulations" such as Linde SI-4. This sealing eliminates the necessity for venting the propellant tanks, a difficult and wasteful task, such as might be required with pumped systems.

It is therefore possible to take advantage of the "hard" vacuum of outer space in at least two ways. First, the chamber pressure can be lowered to 60 lb/sq in. abs and the gases will still expand through a nozzle area ratio of 40, by virtue of the low permissible nozzle exit pressure. Experience has shown that at these low chamber pressures excellent performance can be obtained if room is available for the larger chamber size. A specific impulse (I_{sp}) equivalent to over 430 seconds has been demonstrated by the Aerojet-General Corporation with hydrogen/oxygen at this pressure. This low chamber pressure allows operation with tank pressures in the vicinity of 100 lb/sq in. abs, a pressure which is found to be approximately that pressure which can be retained by tanks with minimum gauge walls consistent with rigidity and ruggedness standards.

A second use of the "hard" vacuum of space is in the evacuation of the multiple radiation barrier SI-4 type of tank insulation. This evacuation in turn facilitates storage of propellants, with minimum heat leak, for the desired mission.

¹For this particular analysis 7,300 ft/sec was used for the comparison although the final velocity requirement used in this paper was 7,500 ft/sec.

~~CONFIDENTIAL~~

There are many systems for pressurization, each with advantages and disadvantages of weight, complexity, performance, and so forth. The selection has been narrowed to two types of systems, each with outstanding features and efficiency with these propellants, H_2 and O_2 . (See fig. 4.) The system illustrated on the left in the figure uses heated H_2 and He to pressurize the propellant tanks. The helium is stored as a gas in the liquid O_2 tank and used to pressurize both the O_2 and a small reserve supply of liquid H_2 . The helium and the hydrogen are heated by a small settling rocket which, in turn, burns with available H_2 and O_2 from the propellant tanks. The small rocket also serves to settle the propellants to the bottom of the tanks, although the pressure-fed system can probably be started without such settling rockets, but with the main chamber providing settling during start.

The system shown on the right in figure 4 uses a small amount of heat - possibly waste heat from the spacecraft - to warm the propellants sufficiently to provide 100 lb/sq in. of vapor pressure. This pressure then provides self expulsion of the propellants with continued vaporization of the propellants to maintain a nearly constant pressure.


The use of both systems is proposed, since they are mutually compatible, for maximum reliability and safety. Our primary system, shown to the left, employs considerable use of redundant components for safety, reliability, plus a complete spare system. Should both the primary and the spare system fail, it is possible to use the system shown on the right by providing heat to the propellants.

The propellant flows can be controlled by system hydraulic pressure drops with overriding control for maximum propellant utilization. This appears to be one of the areas where crew assistance may be valuable for the override or monitoring of propellant flow. This assistance would be particularly valuable for both oxidizer-to-fuel (O/F) ratio control and best propellant utilization. However, it is noted that some of the proposed missions might be performed as unmanned missions - either for early test, experimentation, or freight-carrying vehicles. The propulsion system should therefore be capable of unmanned operation, if it should become necessary.

Of the three factors listed previously, propellants and pressurization systems have been discussed and the conclusion reached that this mission is best met by a pressure-feed hydrogen/oxygen system.

THRUST CHAMBERS

There are at least two types of thrust chambers which can be used with the Apollo mission - ablatively cooled and regeneratively cooled.



Ablatively cooled chambers have been developed and demonstrated for these propellants by Aerojet-General Corporation under the U.S. Air Force sponsored Hydra/Hylas Program. These chambers are simple and have proven reliable in repeated tests with H_2/O_2 at the low pressures for durations of at least 300 seconds. These ablative chambers appear to fit well with the Apollo mission and to eliminate potential difficulties associated with regeneratively cooled chambers, such as possible leakage and start and shutdown losses. Further, operation at partial thrust (low chamber pressure p_c) is enhanced with these chambers since there is no lower limit to cooling. At this pressure, the ablatively cooled chambers appear comparable in weight to regeneratively cooled chambers, and ablatively cooled chambers are therefore recommended.

The value of thrust chamber redundancy is illustrated in figure 5. The total thrust for superorbital abort is considered to be 24,000 pounds which can be achieved by one 24,000-pound, two 12,000-pound, or four 6,000-pound thrust chambers. It is further assumed that all midcourse and orbital maneuvers can be accomplished at a thrust of 6,000 pounds. The problem to be considered here is what the thrust chamber redundancy contributes to engine reliability.

If it is assumed that chambers can be throttled to $1/4$ thrust, the single-chamber reliability is the assumed value of 89 percent from 24,000 pounds to 6,000 pounds of thrust. The two-chamber cluster gives 79-percent reliability from 24,000 pounds to 15,000 pounds of thrust and 98.8 percent from 12,000 pounds to 3,000 pounds of thrust. The four-chamber cluster gives 66-percent reliability at 24,000 pounds, 95 percent at 18,000 pounds, 99.6 percent at 12,000 pounds, and 99.99 percent at 6,000 pounds of thrust. Thus, as would be expected, multiple chambers lower reliability at 24,000 pounds of thrust where there is no redundancy. But as soon as redundancy is introduced, that is, four chambers for 18,000 pounds of thrust, the reliability rises rapidly and reaches 99.99 percent at the design thrust of 6,000 pounds. Thus it is only necessary to demonstrate a chamber reliability of 89 percent (although a much higher reliability would be anticipated) to get a chamber-cluster reliability adequate for manned spacecraft. This facilitates an early, low-cost development program.

ATTITUDE CONTROL

A reaction jet system was selected for the vehicle attitude control and, as such, is considered a part of the Apollo propulsion system. The requirements for this attitude control system may be summarized for the spacecraft in the lunar-orbit mission. Many small impulses (at least 3,000) are required for the 14-day mission to produce a total impulse of about 60,000 pound-seconds. The maximum expected impulse is



The complete engine system, including attitude control, has an empty weight of 1,498 pounds and a total loaded weight of 10,027 pounds. The estimated probability of successful propulsion for the lunar-orbit mission, if the spacecraft is assumed to be successfully boosted to escape, is 0.954. The estimated probability of safe-return propulsion after escape, in the event of a mishap, is 0.978. It should be emphasized that these numbers are, at best, estimates and that actual numbers can only be determined during the Apollo development program.

A comparable propulsion-system weight for current earth storables, such as N_2O_4 and MMH, is 12,000 pounds. Thus, the loaded storable system is 2,000 pounds heavier than the loaded H_2/O_2 system.

The complete engine can be assembled, tested, and installed as a unit; thus the development of an integrated propulsion system is facilitated. With the pressure-fed system it appears most advantageous to integrate tanks and chambers since the individual pressurizing components and system operation are so interdependent as to preclude possible separation.

LUNAR LANDING VEHICLE

Consider now the lunar landing vehicle. The vehicle and propulsion system which has been described could be used for the return vehicle launched from the moon. This is illustrated in figure 7, with the return vehicle shown to the left and a new lunar landing stage interposed to the right between return stage and the launch vehicle. The lunar take-off propulsion would be somewhat larger, producing a typical velocity of about 9,000 ft/sec rather than the 7,500 ft/sec for the lunar-orbit mission. In addition, a new typical lunar landing stage would produce a velocity of about 9,250 ft/sec which includes gravity losses in landing. The landing stage would be left behind on the moon when the upper stage returned to earth.

Vehicle weight requirements for the lunar-landing mission are shown in figure 8 for various propellant combinations and payloads. The top value of each bar represents the weight that must be boosted to escape from the earth; the unfilled portion of each bar shows the weight launched on return from the moon. The three bars to the left show the launch weights for several propellants for payload weights considered realistic today - 10,780 pounds outbound to the moon and 8,740 pounds returned to the earth. The first bar, to the extreme left, shows the vehicle weights for contemporary storable propellants, such as mixed amines and nitrogen tetroxide in both stages. The bar second from left shows weights for the H_2/O_2 stage to the moon and storable propellants for return. The third bar from the left represents the

031712201030

necessary weights for H_2/O_2 both to and from the moon. Escape weight from earth varies from 120,000 pounds for all storables to 64,000 pounds for H_2/O_2 in both stages.

For larger payloads of 17,500 pounds to the moon and 15,000 pounds returned to the earth, these necessary weights increase proportionately as illustrated by the three bars at the right. Escape weights from earth are 205,000 pounds for all storables, 147,000 pounds for H_2/O_2 to the moon and storables for return, and 108,000 pounds for H_2/O_2 both to and from the moon.

Final selection of propellant combinations will, of course, depend on many factors, but if booster escape payloads are limited to the range of 50 to 70 tons and payloads approach 20,000 pounds, then H_2/O_2 both to and from the moon may be essential. If payloads can be held to about 10,000 pounds, storables and solid propellants can well be considered. However, for any vehicle weight carried to escape from the earth, H_2/O_2 will always provide a greater payload capacity which should inherently enhance the mission safety and reliability. For instance, with H_2/O_2 the propellant reserves can be increased and a greater margin of safety for both lunar landing maneuvers and take-off will be provided.

CONCLUSIONS

In summary, consider the general mission requirements and the way in which the Apollo propulsion system fulfills these requirements. Mission requirements include propulsion for earth orbit, circumlunar flight, lunar orbit, and lunar landing.

Figure 9 gives a summary of the range of propulsion configurations which meet the Apollo requirements. The basic propulsion required to provide a velocity of 7,500 ft/sec for an orbit 50 to 1,120 nautical miles from the moon has been discussed. This vehicle with a payload of nearly 8,000 pounds weighs 18,000 pounds at escape. By undertanking the propellants to reduce vehicle weight, the Apollo spacecraft can be launched for a variety of earlier missions with available launch vehicles. Undertanked to 15,000 pounds, the vehicle can accomplish circumlunar flights if a launch vehicle in the class of the Saturn C-2 is used, with sufficient propulsion onboard for superorbital abort, if abort should be necessary. Undertanked to 12,000 pounds, the vehicle can be launched with the Saturn C-1 or Titan II with sufficient onboard propulsion to assist in getting into low earth orbits for early tests and later rendezvous missions. These early missions could start in 1963 or 1964 as soon as launch vehicles become available.

A slightly enlarged vehicle can be used as the upper stage of a lunar landing vehicle, with safety and reliability built up in the

early part of 1960 in other space missions. This stage might weigh 22,300 pounds if H_2/O_2 were used as propellants, and 30,000 pounds for storable propellants. An additional lunar landing stage would be required which would be larger.

The various design considerations and a recommended approach for the lunar-orbit Apollo mission have been discussed. It can be seen that Apollo propulsion can be constructed from a basic platform of safety and reliability. By utilizing hydrogen/oxygen as the propellants, pressure fed from sealed redundant tanks, ample performance for lunar orbit may be achieved with redundant 6,000-pound thrust, low chamber pressure, and ablatively cooled thrust chambers. Instant-response, high thrust would be available for abort maneuvering. The recommended system can be available at an early date for successful achievement of a variety of Apollo lunar missions.

ACKNOWLEDGEMENT

The authors wish to acknowledge the work of Arnold D. Cohen and Louis Beers of the General Electric Company in the preparation of this paper.

TABLE I

APOLLO PROPULSION FUNCTIONS

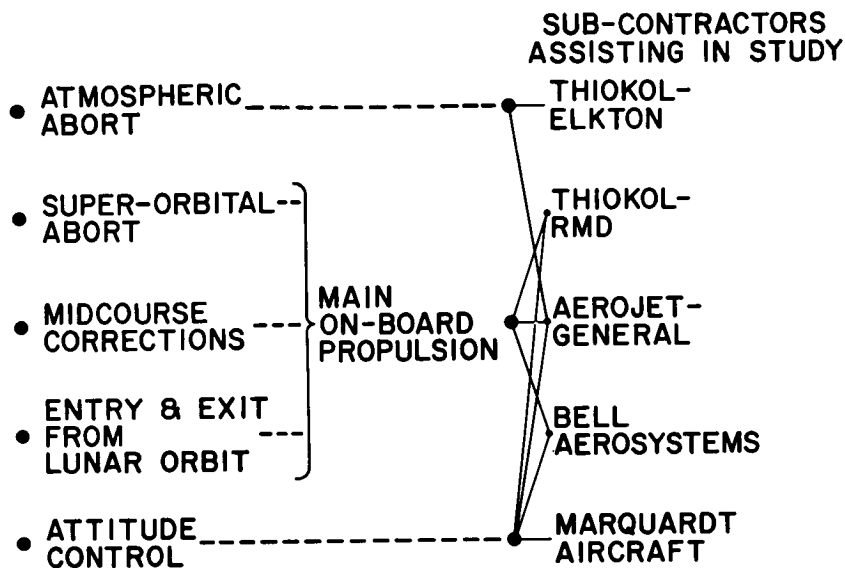


TABLE II

ON-BOARD PROPULSION PROPELLANTS COMPARISON

PROPELLANTS	H ₂ /O ₂	N ₂ O ₄ /MMH	OF ₂ /MMH	H ₂ /F ₂
STATUS	TESTED COMPONENTS SAFE PROPELLANTS	TESTED COMPONENTS STATE-OF-THE-ART	UNKNOWN OXIDIZER	SOME TESTED COMPONENTS HAZARDOUS OXID.
HYPERGOLICITY	POSSIBLE WITH O ₃ F ₂	YES	YES	YES
TOXICITY	NO	YES	?	YES
STORABILITY	YES, WITH SI-4 INSULATION	YES	YES, WITH INSULATION	YES, WITH SI-4 INSULATION
PAYLOAD FOR 15000 lb SPACECRAFT	6250 lb	5550 lb	6500 lb	7000 lb

TABLE III

ATTITUDE CONTROL SYSTEM SELECTION

- WEIGHT COMPARISON

STORED GAS	3340lb
MONOPROPELLANTS	330lb
N₂H₄ - MMH / N₂O₄	237lb
H ₂ /O ₂	219lb

- COUPLES SELECTED FOR PITCH, ROLL, YAW
GIVING INHERENT REDUNDANCY

- NITROGEN PRESSURIZATION WITH BLADDER
STORAGE FOR POSITIVE ACQUISITION

- ENGINE THRUSTS:

PITCH AND YAW	—	6lb
ROLL	—	8lb

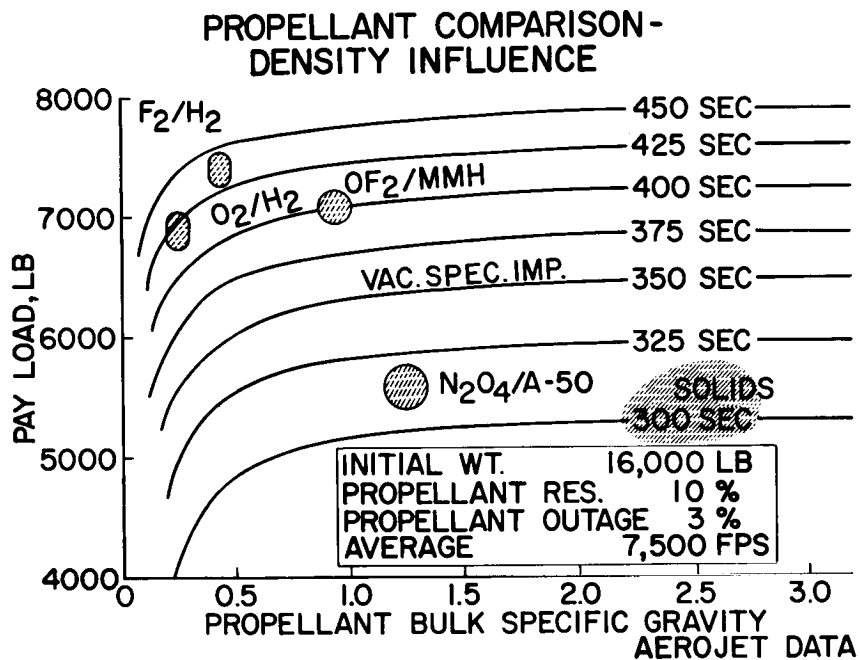


Figure 1

PROPELLANT COMPARISON - PAYLOAD VS TOTAL SPACE CRAFT WEIGHT

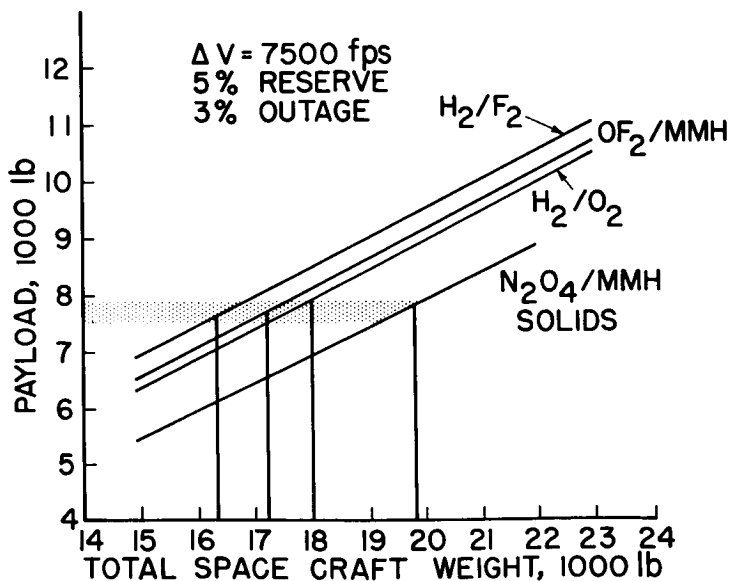


Figure 2

WEIGHT COMPARISON FOR PUMP VS. PRESSURE FED SYSTEMS

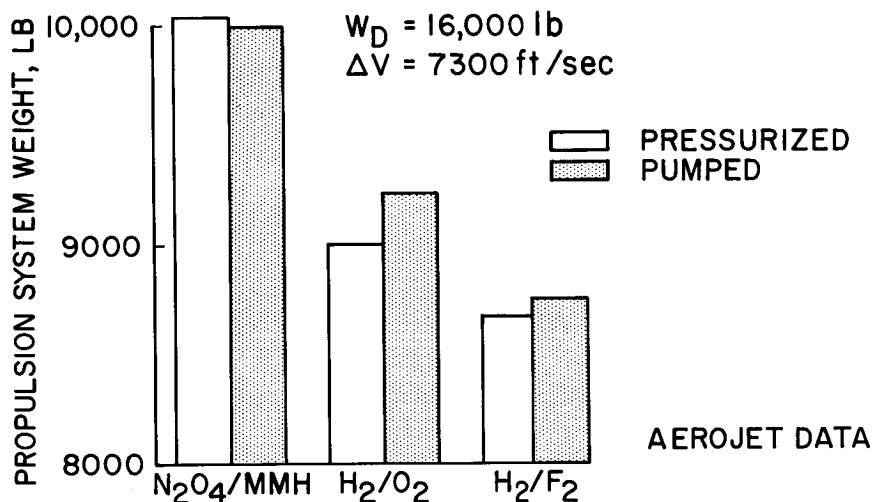


Figure 3

PRESSURIZED FEED SYSTEM DESCRIPTION

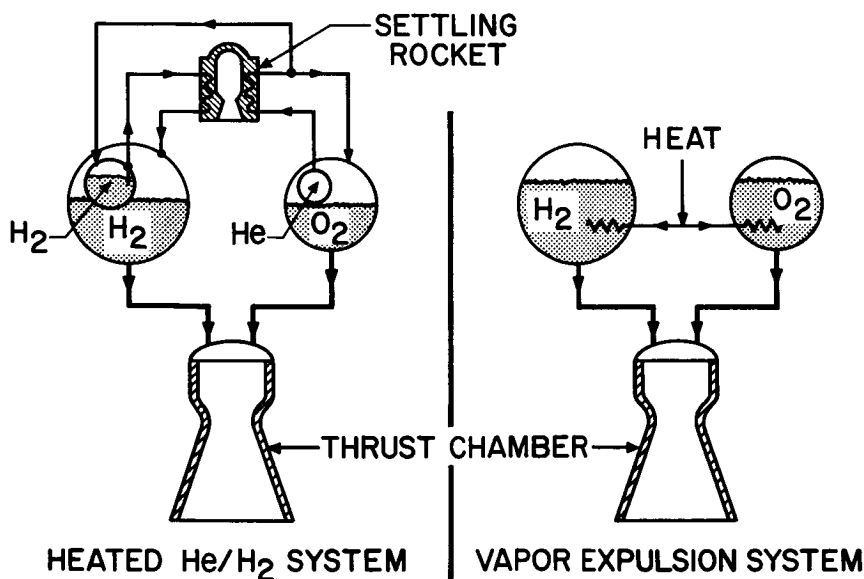


Figure 4

THRUST CHAMBER REDUNDANCY

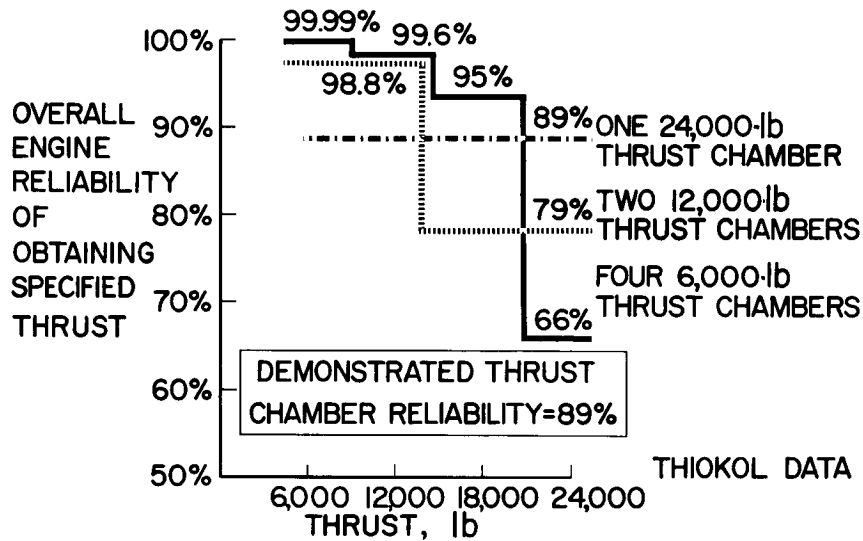


Figure 5

PROPOSED APOLLO MAIN PROPULSION SYSTEM

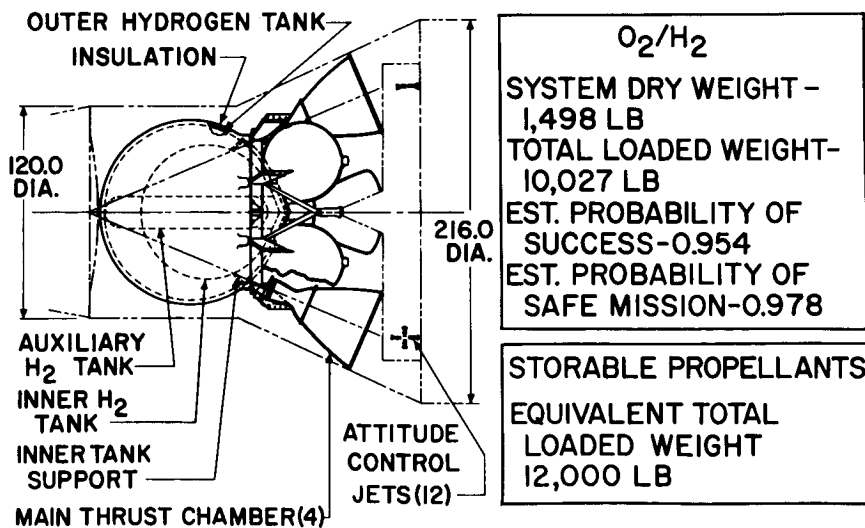


Figure 6

LUNAR LANDING VEHICLE

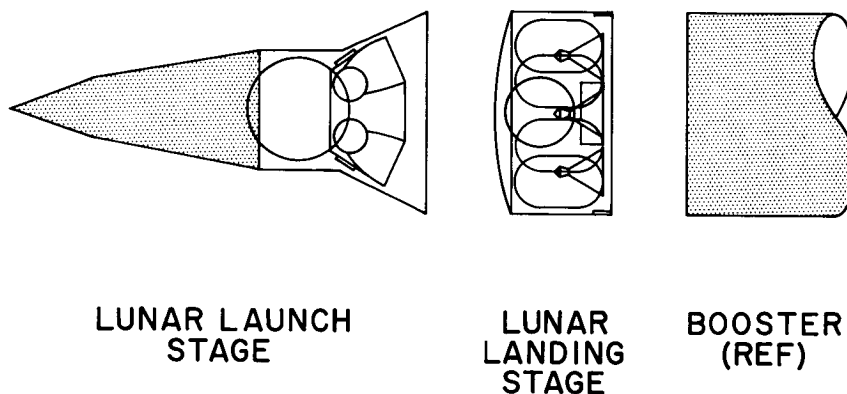


Figure 7

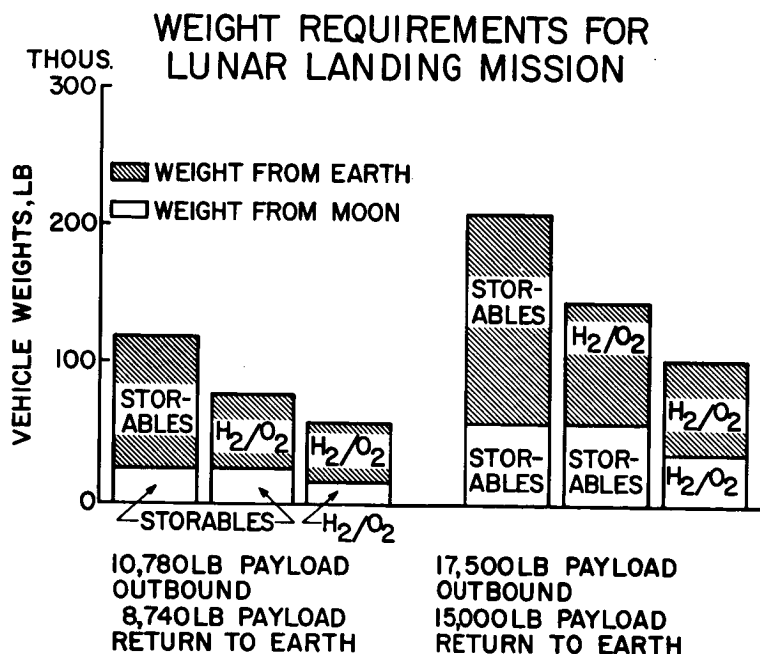


Figure 8

APOLLO MISSION CONFIGURATIONS

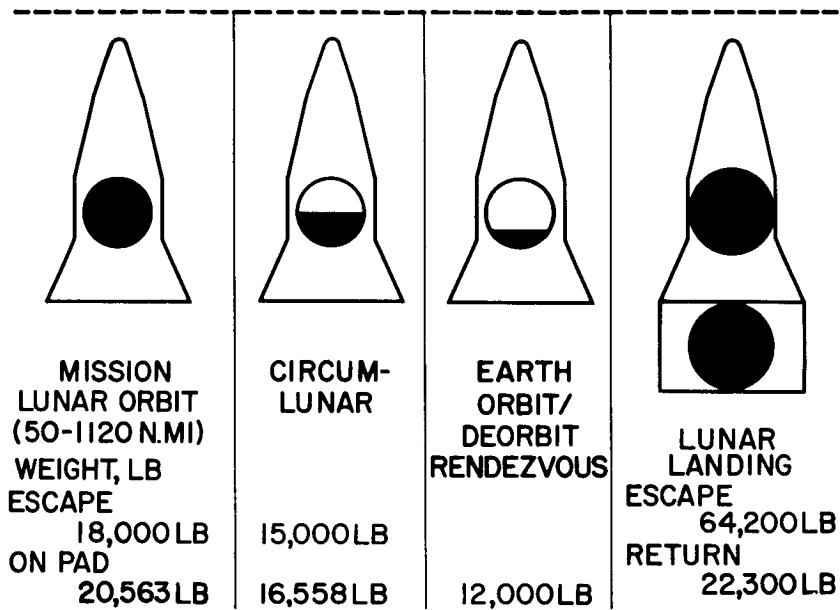


Figure 9

DECLASSIFIED

ENVIRONMENTAL-CONTROL SYSTEM FOR LUNAR MISSIONS

By Fred Parker

General Electric - MSVD

INTRODUCTION

An environmental-control system is required to provide a habitable atmosphere within the Apollo vehicle during the 2-week flight through the vacuum of space. In this paper, some of the parameters that the General Electric Company considered in determining the atmospheric pressure and composition that it would recommend for Apollo are presented, and the trade-offs made in selecting the system for maintaining the atmospheric composition and effective temperature within the limits selected are discussed.

ATMOSPHERE SELECTION

Because man normally spends his lifetime in a pressure environment of 1 atmosphere, it may intuitively be assumed that he should be provided with the same ambient conditions within the Apollo vehicle. From an engineering standpoint, however, consideration should be given to compromising man's natural environment without having to compromise his well-being. In order to resolve this bioengineering problem, consideration must be given to various pressures and gaseous compositions and their biological and mechanical effects.

Therefore, the "ground rules" used in selecting the internal atmosphere of the Apollo vehicle are as follows:

(1) The atmosphere must, in accordance with the "shirt-sleeve environment" philosophy, produce a minimum of physiological stress for the crew.

(2) If the vehicle is punctured, it should provide a livable atmosphere for as long as possible; and if the pressure vessel integrity of the vehicle is lost and it becomes necessary to maintain the crew at a reduced pressure by means of a secondary pressurization system, the total-pressure change should not cause aeroembolism.

(3) The atmosphere should not, insofar as possible, increase fire hazard by increasing the rate of combustion.

CONFIDENTIAL

(4) The atmosphere selected should be one which can be maintained with a minimum weight and volume system and require a minimum of electrical power.

Unfortunately, some of these objectives tend to place contradictory requirements upon various parameters and, therefore, it becomes necessary to trade-off one objective against another.

Man's physiological requirements will be considered first. Oxygen is the most important ingredient in the cabin atmosphere. Gross permissible limits of partial pressure can be selected based on physiological considerations. The lower limit is the one which just maintains the alveolar oxygen partial pressure, that is, the oxygen pressure within the lungs, above the hypoxic or oxygen starvation level, and the upper limit is the one which, if exceeded, will result in oxygen toxicity. For a 100-percent-oxygen atmosphere the minimum total pressure required to provide a normal alveolar oxygen pressure of 100 mm Hg is 187 mm Hg or 3.6 lb/sq in. abs. When an inert gas, such as nitrogen, is mixed with oxygen, the situation becomes somewhat more complicated than that for a 100-percent-oxygen system.

Figure 1 shows the effect of the diluent gas in the cabin atmosphere upon the minimum oxygen partial pressure required to maintain the alveolar oxygen partial pressure above 100 mm Hg. The maximum permissible oxygen partial pressure limit of 425 mm, shown at the right of the figure, was calculated by Mullinax and Beischer. (See ref. 1.)

A problem that must be eventually solved is that of atelectasis or lung collapse produced by breathing atmospheres devoid of or having greatly reduced concentrations of an inert gas. During the past 20 years, much speculation and scattered pieces of evidence concerning atelectasis in subjects breathing 100-percent oxygen at various pressures has appeared in the literature. From the literature it appears that nitrogen has an important function in "braking" lung collapse. Removal of the nitrogen brake apparently constitutes a stressing situation to which adaptation must occur. This situation indicates that a diluent gas should be included in the atmosphere selected, and the partial pressure of this gas should be relatively high.

Aeroembolism, or "the bends," occurs as the result of a decrease in atmospheric pressure, which, by decreasing the solubility of diluent gases in both body fat and blood, causes gas bubbles to form in various tissues. The severity of this sickness is a function of the pressure-change ratio and the original concentration of the diluent gas within the body. This consideration suggests that the diluent-gas partial pressure should be kept low.

DECLASSIFIED

371

The system considerations, other than physiological, are fan power, leakage, structures, gas storage, and the fire hazard.

The fact that the heat-exchanger fan power required to transport a given amount of heat is an inverse function of the square of the atmospheric density suggests that a high total atmospheric pressure should be selected. The fact that the danger from fire is directly proportional to the oxygen partial pressure and inversely proportional to the diluent partial pressure suggests that the oxygen partial pressure should be kept low and the diluent partial pressure should be kept high. On the other hand, the weight of the gas which must be stored aboard the vehicle to replace that lost through leakage, and possibly purging, and the effect of the atmospheric pressure upon the pressure vessel weight suggest that the total pressure should be kept low.

The atelectasis and fire-hazard considerations suggest that the oxygen partial pressure be kept close to the lower permissible level. The only consideration which contradicts the desirability of selecting a low partial pressure of oxygen is that the time available in the event of rapid leakage (due to meteoroid puncture or some structural or component failure) is enhanced by a high initial pO_2 . However, the presence of a readily available secondary pressure protection system, coupled with the low probability of either puncture or structural failure, has caused us to select the relatively low pO_2 of 180 mm Hg.

Figure 2 shows the effect upon the vehicle weight of increasing the cabin total pressure by adding nitrogen to the minimum permissible total pressure of 187 mm Hg. This figure shows the effect of all the variables discussed which are a function of atmospheric pressure. Nitrogen was selected as a diluent gas after a detailed comparison with helium. It is evident that the total system weight at first decreases and then increases with increasing pressure, the minimum weight occurring between 250 and 270 mm Hg.

It is important that the atmospheric pressure selected be related to the operating pressure selected for the secondary pressurization system because of the aeroembolism consideration mentioned earlier.

It is also desirable to have as low a pressure as possible in the secondary pressure protection system because the mobility of an astronaut, as well as the atmospheric leakage from the secondary pressurization and environmental control systems (as well as their weight and structural design complexity), is a direct function of the secondary pressure chosen. For these reasons a 187-mm (nitrogen-free) atmosphere is chosen for the secondary pressure protection system.

The approximate pressure-change ratio for which symptoms of aeroembolism begin to develop in some individuals is 2.25. Consequently, if

the pressure-change ratio is held below this value, no problems from aeroembolism should be experienced. It can be inferred that, if the pressure-change ratio exceeds 3.0, aeroembolism can be a serious problem.

Figure 3 superimposes upon the weight curve of figure 2 the effect upon the combustion rate of adding nitrogen to the basic pO_2 of 180 mm. It also shows the pressure range from which decompression to the selected secondary pressure level of 187 mm Hg can cause trouble.

The decision as to the total pressure to select is a difficult one. On the one hand, it is desirable to minimize system weight and completely avoid any problem from aeroembolism by selecting a low atmospheric pressure; on the other hand, the relatively intangible factors of increased danger from atelectasis and fire hazard tempt us to select a somewhat higher atmospheric pressure. A system total pressure of 360 mm Hg has been chosen. Although at this pressure the system weight is about 38 pounds more than that of the lightest system, it still presents no aeroembolism problem and provides somewhat more protection from atelectasis than would be achieved with the minimum weight system. In addition, it decreases the combustion rate below that of the minimum weight system by about 13 percent.

The General Electric Company therefore recommends a pO_2 between 170 mm and 190 mm and a total pressure between 350 mm and 370 mm. This atmosphere satisfies the basic "ground rules" stated at the beginning of this discussion. In addition, a maximum pCO_2 of 8 mm and a pH_2O of 5 mm to 15 mm are specified.

ATMOSPHERE CONTROL

Once the atmosphere for the Apollo vehicle is chosen, a system for maintaining it must be selected.

The total quantities of oxygen and nitrogen required for the Apollo mission, approximately 110 pounds of oxygen and 22 pounds of nitrogen, were determined as follows:

AL

Use	Oxygen required, lb	Nitrogen required, lb
Metabolic	80.6	----
Leakage	15.5	12.5
Purge	12.6	9.5
Total	108.7	22.0

The oxygen supply contains an overall safety factor of 32 percent over the expected maximum requirement for metabolism and leakage.

The methods of oxygen supply considered by the General Electric Company are: high pressure gas; supercritical and liquid storage; chemical sources such as potassium superoxide, hydrogen peroxide, and chlorate candles. Regenerative methods of oxygen supply, such as electrolysis of water, decomposition of carbon dioxide, and controlled growth of algae were not found to be desirable because of the high weight and volume penalties which are characteristic of these systems.

The stored oxygen supply systems were considered separately and as integrated with the onboard propulsion system of the spacecraft. The common storage of oxygen for the propulsion and life support systems is deemed inadvisable, since liquid oxygen can be stored in the cabin for approximately the same tankage weight that would be required if it were stored with the propulsion supply.

The spare propulsion oxygen, however, is of interest to the cabin system, especially the surplus oxygen that will be available unless the highest probable error launch trajectory is encountered. A line from the propulsion system is therefore recommended. This interconnection should preclude the possibility of the crew perishing from hypoxia while a surplus of oxygen is but a few feet away.

Figure 4 compares the oxygen storage weight and volume as a function of flight time for the various methods of storage. Both weight and volume considerations suggest that the liquid-oxygen storage system should be used.

The supply of nitrogen can be stored as a gas, as a cryogenic liquid, or at supercritical conditions for very nearly the same total system weight. (See fig. 5.) The high-pressure gaseous storage system has been selected as a result of this study because of its simplicity and the facility with which nitrogen can be added to the cabin in the event of a rapid decrease in cabin pressure. It should be noted that the liquid storage system would require about half of the cabin volume

that is taken by a 3,000-psi gas system; however, this difference in volume is only about 1 cubic foot.

It has been determined that the partial pressure of CO_2 in the cabin atmosphere should not exceed 8 mm Hg. The problem now is to select the best method of satisfying this requirement. An important question which must be resolved is whether it is advisable to recover the oxygen chemically bound in the carbon dioxide.

If complete recovery of the oxygen from the 75 pounds of CO_2 , which is produced during the mission, and a power weight penalty of 125 pounds per kilowatt is assumed, the total system weight required to recover the 54.5 pounds of oxygen contained in the CO_2 has been calculated to be 120 pounds. It is apparent therefore that it is not advisable to attempt recovery as it would only require a 98.0-pound Lox system to store the same amount of oxygen.

The following methods of controlling the carbon dioxide partial pressure are considered feasible:

- A freeze-out system using a regenerative heat exchanger
- A potassium superoxide system in which the CO_2 is absorbed and oxygen is liberated
- A lithium hydroxide absorption system
- A reactivateable molecular sieve system

An objective analytical study was made to compare these four methods. (See fig. 6.) It is evident from this analysis that the molecular sieve system is the lightest system.

Figure 7 shows a simplified functional schematic of the molecular sieve system considered. The atmosphere containing CO_2 is forced through silica gel canister 1 where it is dehumidified to prevent water poisoning of the molecular sieve, then through molecular sieve canister 1 where the carbon dioxide is adsorbed, back through silica gel canister 2 where the atmosphere is rehumidified, and then back to the cabin. Simultaneously, molecular sieve canister 2 is reactivated by exposure to space vacuum. Periodically, the core of each valve shown is rotated 90° and the operation of the system is reversed to start the next cycle.

After a number of methods of controlling the atmospheric humidity had been considered, it was evident that the simplest and lightest was

simply to collect the condensed water on the compartment heat exchanger. Figure 8 compares the weight of the air heat-exchanger condensation method with two other methods involving the water collected in the silica gel of the CO₂ removal system.

The potential hazard of toxic contaminants in the Apollo cabin atmosphere must be recognized and the problems resolved. Several methods are available for control of the concentrations of the toxic atmosphere contaminants in a spacecraft cabin. Periodic replacement of the cabin atmosphere, catalytic combustion, and adsorption may be used singly or in combination. The problem of contaminant control is one which should be explored during the early development phase of the program. As soon as the materials which will be contained in the vehicle are fairly well defined, a system test can be conducted to determine what objectionable gases are generated. Laboratory-type mass spectrometers and gas chromatographs can be used to determine precisely whether the concentration of any gas builds up to an annoying or toxic level. If so, and if possible, the source of the offending gas will be removed. If removal is not possible, a specific control mechanism can be added to the cabin environmental control system.

Considerable information has accumulated in recent years concerning the effect of ionized air on biological systems. These effects range from changes in emotional behavior to alterations of enzyme systems. Even though much of the data is open to question, sufficient evidence is at hand to indicate that definite biological effects do indeed exist. The simplest method of maintaining ion balance is by generating negative ions. A small radiation source, such as tritium, is a promising possibility for small ion generation because of its small size, high degree of ion-generation capability, and safety.

Another requirement which must be placed upon the environment control system is that it effectively control airborne particulate matter. A point worthy of note is that the settling rate of 0.1- to 0.5-micron particles - the size range which is most harmful - is so low that almost any air motion at all will keep the particulate matter airborne. Consequently, the loss of normal gravitational precipitation due to the zero gravity environment of the Apollo vehicle should not significantly increase the hazard from airborne particulate matter. Particulate filters are available which will do an adequate job of removing the airborne particulate matter which can be expected in the Apollo vehicle. Not only will the filters remove with a high efficiency the particles in the 0.1- to 0.5-micron range but they will, of course, remove the larger particles with a still higher efficiency.

After the systems required for maintaining the cabin atmosphere within prescribed limits are considered, a system for monitoring their

performance must be obtained. A mass spectrometer, infrared and magnetic susceptibility devices, polarographic sensors, or a gas chromatograph may be used singly or in combination to measure the concentration of one or more of the atmospheric constituents. The mass spectrometer is a multiple gas sensor with the capability of monitoring the mass spectrum of the complete atmospheric mixture as often as several thousand times per second. For this reason it has been selected to provide signals for cabin displays, provide signals for the regulation of the oxygen and nitrogen pressures in the cabin, and to provide a signal which will be telemetered to earth for command center analysis of the entire cabin atmosphere spectrum. Polarographic sensors have been selected, as a backup to the mass spectrometer, to sense the oxygen and carbon dioxide partial pressures.

THERMAL CONTROL

In addition to maintaining a healthful gas composition the temperature must be maintained within comfortable limits. Human thermal comfort is a function of three variables: the heat production rate of the body, the insulating effect of the clothing worn, and the effective ambient temperature. As the first two of these are fairly well defined for the Apollo mission, it is possible to define the third, that is, the effective ambient temperature.

Figure 9 shows, as a function of dry bulb temperature and humidity, the thermal comfort region, the physiological compensable region, and the intolerable region for relatively inactive and lightly clothed persons. Also shown is the region selected for the Apollo vehicle. The lower portion of the comfort region was selected to compensate for the relatively low convective heat-transfer coefficient between the astronauts and the cabin atmosphere due to the low atmospheric density and the lack of natural convection. As indicated in this figure, the expected range of coil surface temperatures is well within the range required to maintain the specific humidity between the limits selected (5 mm and 15 mm).

The thermal control system devised for the Apollo vehicle is shown schematically in figure 10. The compartment atmosphere is continuously circulated through the compartment heat exchanger at the rate of about 275 cubic feet per minute by one of the two blowers shown. Two blowers are provided for redundancy. The atmosphere is cooled while passing through the heat exchanger to about 45° F and dehumidified to a dewpoint of about 42° F. The heat is rejected within the heat exchanger to a liquid coolant which flows through the heat exchanger and then through the chassis of the electronic equipment, where it absorbs most of the

electrical heat. The coolant is then pumped through the radiator, where the heat absorbed in the cabin is rejected to space. The bypass valve short circuits just enough fluid past the radiator to maintain the coolant temperature leaving the bypass valve and entering the heat exchanger at 30° F to 35° F. The thermostat valve directs a part of the coolant flow either through or around the compartment heat exchanger, thereby the effective temperature of the cabin is maintained at the set level. There will always be a flow of coolant through a part of the compartment heat exchanger, as shown by a parallel circuit, to provide better thermal modulation and to insure humidity control. The cooling capacity of the parallel circuit is just adequate to remove the minimum net internal heat gain of the cabin.

Figure 11 shows an analog trace of the time-temperature history of the compartment inner wall and cabin atmosphere during recovery. With no internal cooling, the wall temperature reaches 105° F and the air temperature, 90° F at touchdown. However, because of the heat stored in the thermal protection system, it will be necessary to cool the internal compartment to prevent overheating after the command module lands. This cooling will be accomplished by circulating outside air through the reentry vehicle while on the ground. The dashed line shows what the atmosphere temperature trace would be if no outside air were drawn into the vehicle.

CONCLUDING REMARKS

The results show that, as defined by the NASA guidelines for the Apollo study, a "shirt sleeve" environment can be achieved and integrated into the Apollo vehicle. Tables I and II show in summary the atmosphere recommended for the Apollo vehicle and the weight and power required to maintain the gas composition and temperature within the recommended limits.

REFERENCE

1. Mullinax, T. F., Jr., and Beischer, D. E.: O₂ Toxicity in Aviation Medicine. Jour. Aviation Medicine, vol. 29, 1958, pp. 660-667.

TABLE I.- ATMOSPHERE COMPOSITION AND TEMPERATURE LIMITS FOR APOLLO

Pressure, mm Hg:

Total	350 to 370
pO ₂	170 to 190
pH ₂ O	5 to 15
pCO ₂	0 to 8
pN ₂	As required
Effective temperature, °F	Adjustable 70 to 80

TABLE II.- WEIGHT AND POWER OF THE ENVIRONMENTAL
AND THERMAL CONTROL SYSTEMS

Subsystem	Weight, lb	Power, watts
CO ₂ removal ¹	64	65
Thermal control ²	35	160
Particulate filters	5	---
Oxygen supply	196	---
Nitrogen supply	48	---
Sensing	25	30
Emergency systems	34	5
Total	407	260

¹Includes noxious and toxic gas control.

²Includes water collection device and proportional part of radiator weight.

PHYSIOLOGICAL LIMITS FOR pO_2

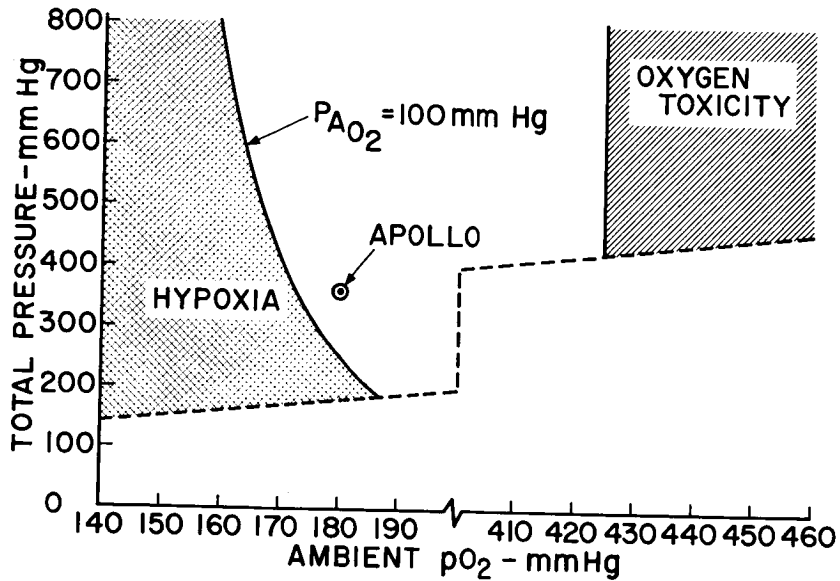


Figure 1

SYSTEM WEIGHT VERSUS ATMOSPHERIC PRESSURE

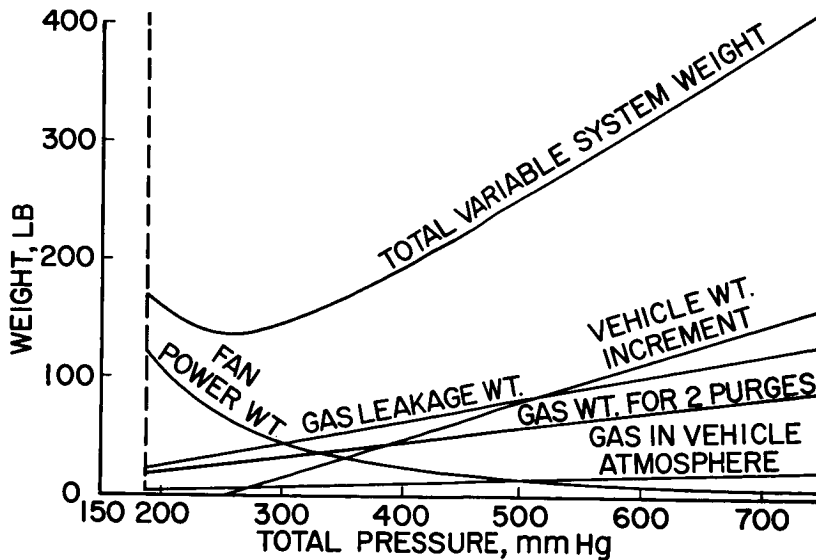


Figure 2

SYSTEM WEIGHT, AEROEMBOLISM AND FIRE HAZARD VERSUS ATMOSPHERIC PRESSURE

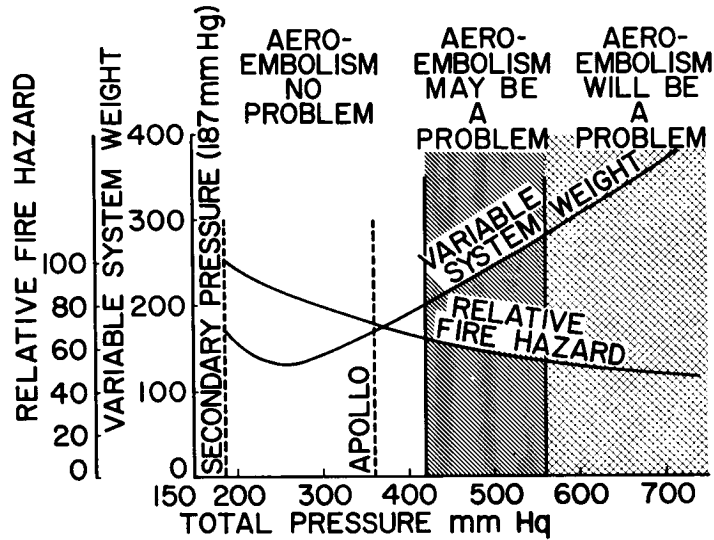


Figure 3

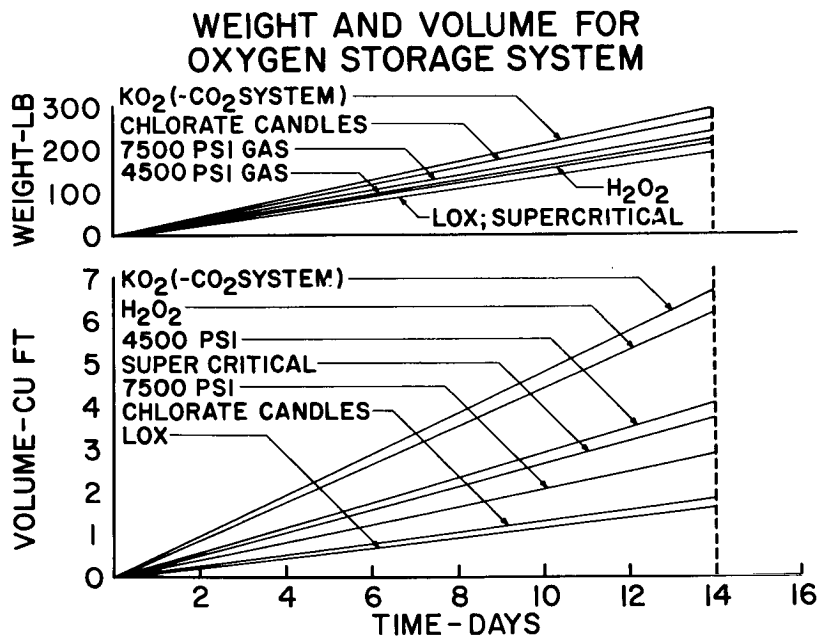


Figure 4

DECLASSIFIED

WEIGHT AND VOLUME OF NITROGEN STORAGE SYSTEMS

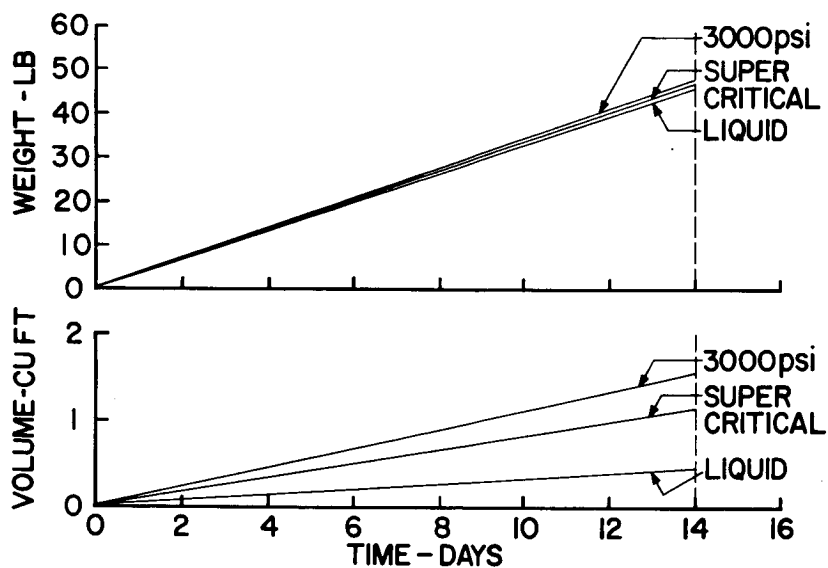


Figure 5

CO₂ REMOVAL SYSTEM COMPARISON

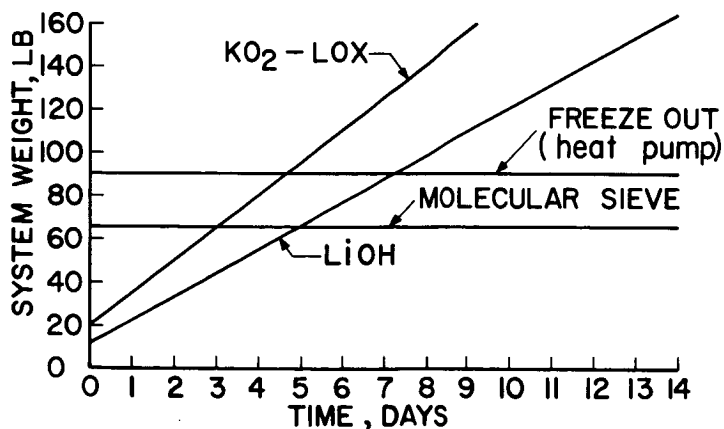


Figure 6

MOLECULAR SIEVE SYSTEM SCHEMATIC

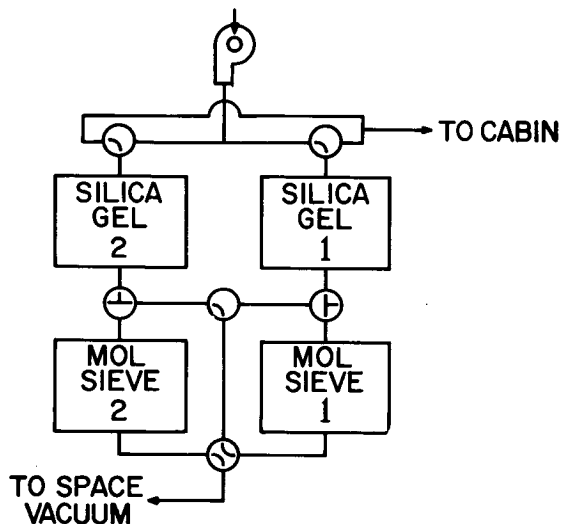


Figure 7

HUMIDITY CONTROL SYSTEM COMPARISON

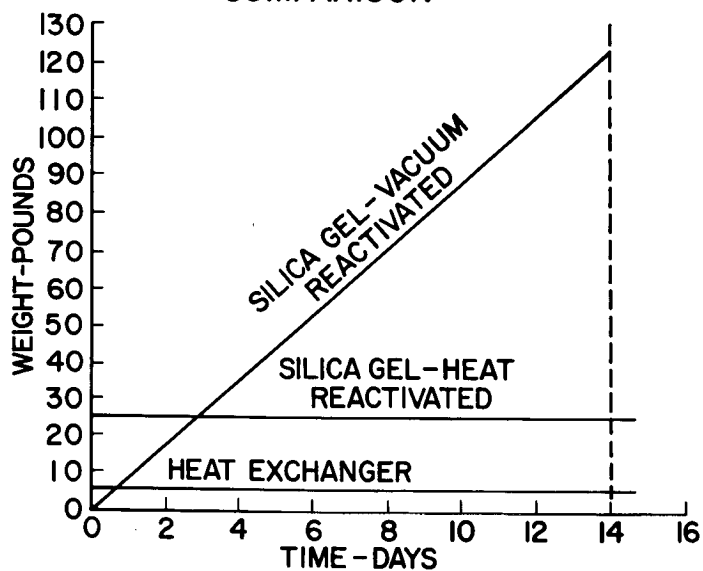


Figure 8

COMFORT ZONE AND HUMIDITY CONTROL

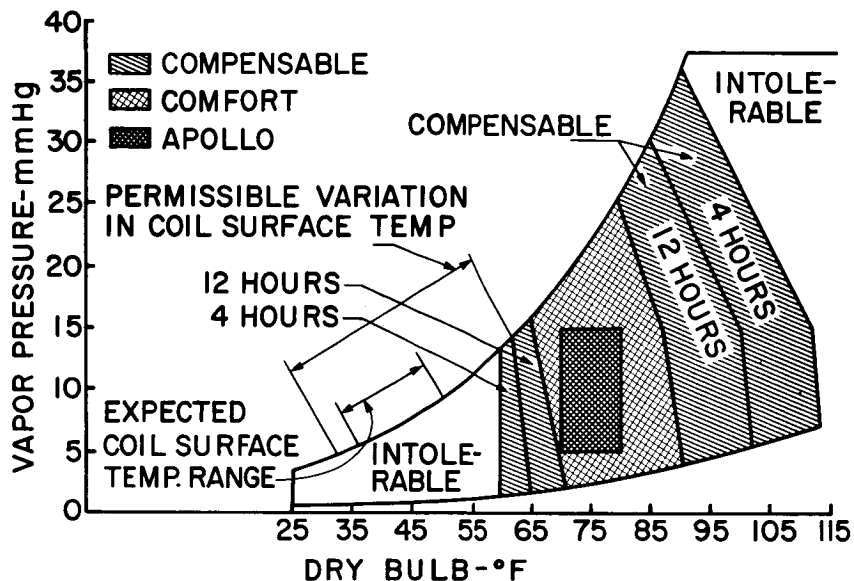


Figure 9

THERMAL CONTROL SYSTEM SCHEMATIC

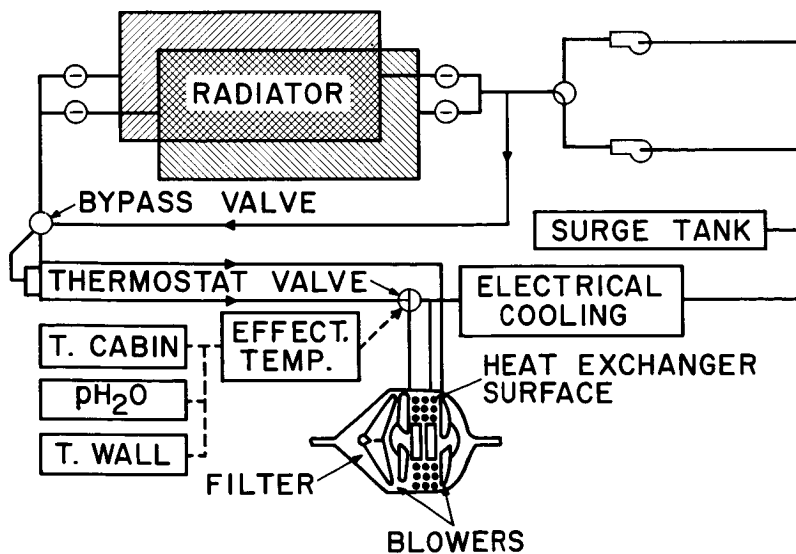


Figure 10

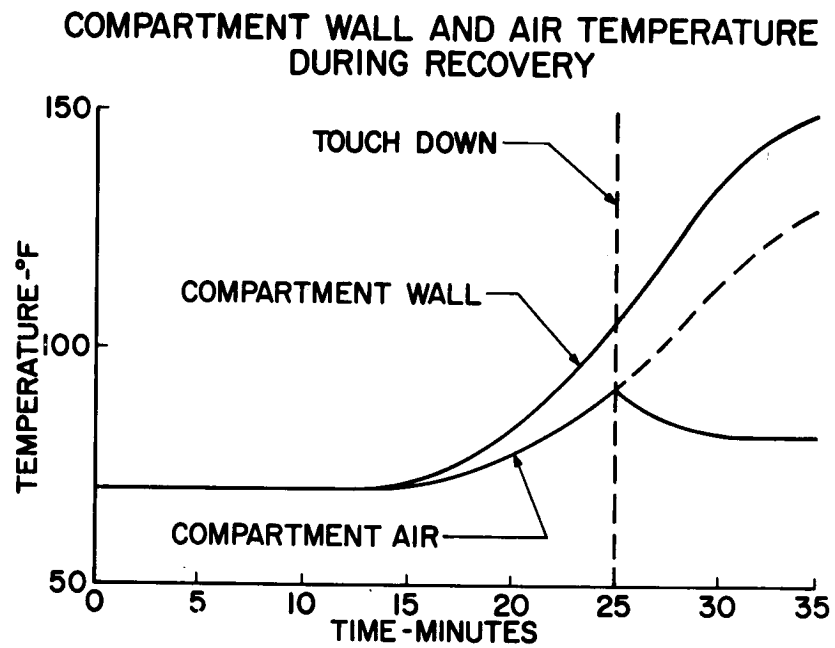


Figure 11

TRACKING AND COMMUNICATIONS SYSTEM FOR A LUNAR MISSION

By Ray E. Thompson

General Dynamics/Astronautics

The integrated tracking and communications system provides the only link between the crew of the Apollo spacecraft and the earth. Tracking and communications keep the ground crew informed of the status and performance of the mission by providing the tracking data, voice, telemetry, and ground updating capabilities. The design objectives are to provide communications and ground tracking throughout the lunar mission, except when the spacecraft is behind the moon. Primary command of the mission is the responsibility of the Apollo crew. This requirement does not preclude the use of information from earth-based tracking and computation facilities, but information provided must be in the form best suited for usage by the crew.

The tracking systems are concerned with gathering data which define the position and trajectory of the spacecraft, for the purpose of orbit determination. To the extent possible, continuous trajectory data for the lunar mission will be provided by ground tracking. The four basic types of tracking equipment to be used for the Apollo lunar mission are interferometer, FPS-16 radar, Deep Space Instrumentation Facilities (DSIF), and Tactical Air Communication and Navigation (TACAN).

Since the flight phase, extending from launch to injection into the lunar transfer trajectory, is inertially guided, the primary purposes of tracking are to satisfy range-safety requirements during powered flight, monitor injection points, and supply acquisition data to succeeding tracking stations. Launch constraints due to range safety and launch window limitations directly affect tracking coverage requirements.

During the launch phase, tracking may be accomplished by the system that satisfies the range-safety requirements of the Atlantic Missile Range. At the present time this system includes the interferometers of the Azusa Mark II or Mistrum class in conjunction with the FPS-16 radar. Tracking from lift-off until the spacecraft disappears below the horizon at Cape Canaveral is performed by Mistrum or Azusa facilities. The beacon equipment for the system is located on the Saturn vehicle.

The FPS-16 radar system is utilized to provide tracking after the Cape coverage is lost. This ground tracking equipment will determine

orbit acceptability and abort-landing predictions. Intervals on the parking orbit are tracked by FPS-16 radar. It is not considered practical to provide 100-percent coverage of most parking orbits, nor is it necessary after success of the orbit is established. Therefore, tracking stations are located principally to cover the injection points. This establishes initial conditions of the orbit trajectory and aids prediction computations. The spacecraft-borne portion of the tracking system will incorporate FPS-16 tracking beacons on the final stage of the Saturn and on the Apollo spacecraft. The launch-vehicle beacon provides tracking capability up to injection. The Apollo beacon will be used to provide coverage from shortly after injection until acquisition by the DSIF.

The DSIF has stations at Goldstone, California; Woomera, Australia; and Johannesburg, Union of South Africa. With the exception of the time the spacecraft spends behind the moon, these stations provide continuous coverage from just after lunar injection until a fraction of an hour prior to reentry. The DSIF system will provide the bulk of tracking data for the Apollo lunar mission. This system operates in conjunction with an ultra-high frequency (UHF) transponder located in the spacecraft.

Shortly before the spacecraft lands, the guidance system requires updating to assure that landing is within the target area. However, the uncertainties at reentry and landing that arise from the onboard navigation system are sufficiently small so that only simple radio-position measurements are required. Consequently, tracking through the radio blackout region is not required. The system that is used for this function is TACAN; this system is currently used as a general navigation aid for aircraft. The function performed is to determine at least one vehicle position measurement. Figure 1 shows three stations with fan beams, located at nominal distances of 50, 100, and 150 miles uprange from the landing area. The TACAN beacon in the landing area is used to provide bearing information after emerging from reentry blackout. As the spacecraft continues along its trajectory, it passes through antenna fan beams which provide distance measurements. Interrogation of the ground station also yields slant range. This information determines spacecraft position. For backup and reliability the process is repeated as the spacecraft passes through the remaining fan beams.

Special scanning or acquisition is not required with this system. All computations of position are done by onboard equipment. The moderate accuracy requirements at a range of 100 nautical miles to touchdown are approximately 1 nautical mile in position and 0.5 nautical mile in altitude.

DECLASSIFIED

387

During parachute phase, a localizer will provide the spacecraft with information on deviation from the nominal path; this information will be used for parachute maneuverability controls. Voice communications are also provided during this phase, completing the tracking requirements of the Apollo lunar mission.

The communications-system objectives are to provide spacecraft status and performance information throughout the various phases of flight. The functions of data transfer to be performed by the communications system and the selected design requirements for a maximum range of 240,000 miles are as follows:

Telemetry:

Maximum rate, bits/sec	12,500
Detected signal-to-noise ratio, db	18

Voice:

Bandwidth, cps	200 to 3,200
Detected signal-to-noise ratio, db	30

Range and Doppler:

Bandwidth, cps	20
--------------------------	----

Carrier for angle tracking:

Bandwidth, cps	10
Detected signal-to-noise ratio, db	20

The telemetry system that was selected is a Pulse Code Modulation System. It incorporates data transmission rates of 6,250 and 12,500 bits per second which include synchronization requirements. Four basic commutation modes cover the mission phases of launch and reentry, power maneuvers, coast, and a combination mode of coast and magnetic-tape-data playback. This last mode provides transmission to the ground of all recorded data without interrupting normal coast phase real-time data. Flexibility is obtained from the digital system, inasmuch as changes can be readily made in the logical switching and decoding matrix controls. An ample reserve capacity is also provided.

A standard 3-kilocycle bandwidth has been provided for a voice channel. The range, doppler, and carrier for angle tracking supply the data requirements for the ground tracking equipment.

The Apollo instrumentation that was used to establish the telemetry requirements is presented in table I. This table gives the general category breakdown, number of measurements, and percentage of the available data bandwidth. There are 255 measurements for the flight with a reserve of approximately 100, making a total measurement capacity of 355. This reserve capacity provides approximately 40-percent increased capability at the high-speed data rate.

The data-rate requirements by specific phase of the mission are presented in table II. This table gives the portions of flight that require the high or low data rates and the data channel capacity in bits per second.

The basic-communications-system block diagram for launch and mid-course is shown in figure 2. The FPS-16 tracking beacon shown on the left will use a slot antenna for hemispherical coverage during the launch phase.

Through the launch phase, communications will provide telemetry data and possible ground-activated abort commands. Sufficient power must be radiated to counteract scalloping effects of the airborne antenna pattern and fading due to rocket-exhaust attenuation. This system operates at the same frequency as the DSIF. A 25-watt transmitter and slot antenna in the Apollo spacecraft are sufficient to maintain communications. The antenna will provide adequate coverage if roll restrictions are placed on spacecraft orientation.

A near omnidirectional antenna provides the necessary coverage after the abort tower is jettisoned. This removes constraints on the spacecraft to perform any maneuver necessary for lunar injection or stellar platform alignment.

The omnidirectional antenna will provide the spacecraft with a ground-to-space communications link at lunar distances, using ground transmitters and antennas. This mode could be used in an emergency without restricting spacecraft orientation or requiring a tracking antenna on the spacecraft.

In order to stay within reasonable power limitations, it is necessary to add a high gain antenna system to the spacecraft for operation at lunar distance. The tradeoffs that must be evaluated to assess this antenna system are primarily spacecraft power source capabilities, precision antenna pointing systems, and antenna size. If the 25-watt transmitter is used, an antenna gain of 20 decibels is necessary for operation. This requires a 2-foot-diameter parabolic reflector with a 15° beamwidth. This antenna will be switched in at slightly greater than one-tenth the distance to the moon. At this point the antenna will provide complete earth coverage. Antenna orientation is not a major problem, inasmuch as a photoelectric detector can maintain proper direction within the nominal accuracy requirements of $\pm 1^\circ$.

Complete switching flexibility of equipment is also provided. Selection of receiver, transmitter, or antenna combination is readily available. This provides high reliability and ease of operation in any mission requirement. Voice, telemetry, television, and tracking data can be transmitted by the UHF transponder.

DECLASSIFIED

389

A communications link during the reentry blackout (high ionization) phase has not been provided. All data generated during this time will be recorded for playback later. This same operation occurs when the spacecraft is behind the moon. Ground station coverage requirements and spacecraft equipment are simplified by this approach.

The block diagram for landing approach and recovery is shown in figure 3. After reentry, the spacecraft must resume communications with terminal ground stations and transmit information required for recovery operations. Best coverage is provided with both VHF and HF equipment. The VHF link is for the air-search functions and provides line-of-sight communications. The HF provides over-horizon communications with system capabilities for frequency variations for best range. Two systems in each band will be used: a push-to-talk mode and a low-powered coded beacon. The beacons will transmit a coded signal on their respective international distress frequencies. The push-to-talk mode will provide voice communications on both bands.

The VHF link propagation distances are limited by radio horizon which depends upon the height of the terminal link above the earth's surface. For example, an aircraft at an altitude of 50,000 feet can cover a 500-mile-wide path across the earth's surface. If this is used as a criterion, the push-to-talk mode would operate at a maximum distance of 275 nautical miles after landing. However, this system was designed with a 550-mile range, as this provides added coverage during spacecraft descent. The system requires slightly in excess of 1 watt of transmitter power and uses a slot antenna after emerging from blackout; a 1-foot whip is provided as reserve to guard against any possible damage upon landing.

Standard HF equipment is presently available for both voice and beacon operations. The frequency of operation will depend on a variety of factors but can be predicted with fair reliability up to three months in advance of the operation. The transmitter power required for the HF system is not appreciably greater than that required for the VHF system. The HF voice frequencies will be determined prior to flight and equipment will be pretuned to these frequencies. Both the VHF and HF communications have sufficiently modest power requirements as to be completely solid state.

A 20-foot whip is deployed for HF communications just after main parachute deployment. An additional 20-foot whip is provided as a reserve.

As active communications satellites become available, they could be used to replace the current ground point-to-point communications systems. Active communications satellites offer high reliability of transmission path and the capability to provide single-hop

03:41:20.1030

390

communications-link distances up to 8,000 miles. The data requirements of the Apollo ground links would require only the lower portion of the channel bandwidth. The bandwidth capability of satellite systems is several orders of magnitude greater than required. The use of satellites on the Apollo project would have to be coordinated with other agencies, as the use of these systems depends upon economics and availability.

A summary of the weight and power of the communications equipment for the Apollo spacecraft is given in table III. The total weight of the electronics equipment is 295 pounds. The overall system has been analyzed from the reliability aspects to meet the requirements of a 14-day mission.

This completes the requirements for the tracking and communications system for the Apollo lunar mission.

TABLE I
MEASUREMENT ALLOCATION

	<u>TOTAL NO.</u>	<u>% CAPACITY</u>
AIRFRAME/STRUCTURAL	58	10.1
ENVIRONMENTAL CONTROL	30	3.4
ELECTRICAL	15	0.6
PROPULSION	31	8.5
GUIDANCE	58	12.4
BIO-MEDICAL	33	20.1
AUTOPILOT	30	5.6
RESERVE CAPACITY	100	39.3
TOTAL	355	100.0%

TABLE II
FLIGHT PHASE DATA REQUIREMENTS

	<u>BITS / SEC</u>	<u>AVAILABLE BITS / SEC</u>
LAUNCH	5,619	11,760
COAST	5,516	5,880
POWER MANEUVER	6,046	11,760
COAST PLUS LUNAR MAG. TAPE PLAYBACK	11,032	11,760
RE-ENTRY	5,684	11,760

03:17:29.1030

TABLE III

WEIGHT & POWER

COMMAND MODULE	130.5 LB
MISSION MODULE	164.5 LB
LAUNCH	222 WATTS
MIDCOURSE	162 WATTS
FAR SIDE OF MOON	72 WATTS
RE-ENTRY	136 WATTS
LANDING APPROACH	158 WATTS
RECOVERY MODE	61* WATTS

* TRANSMITTING MODE

RADIO NAVIGATION FOR RE-ENTRY

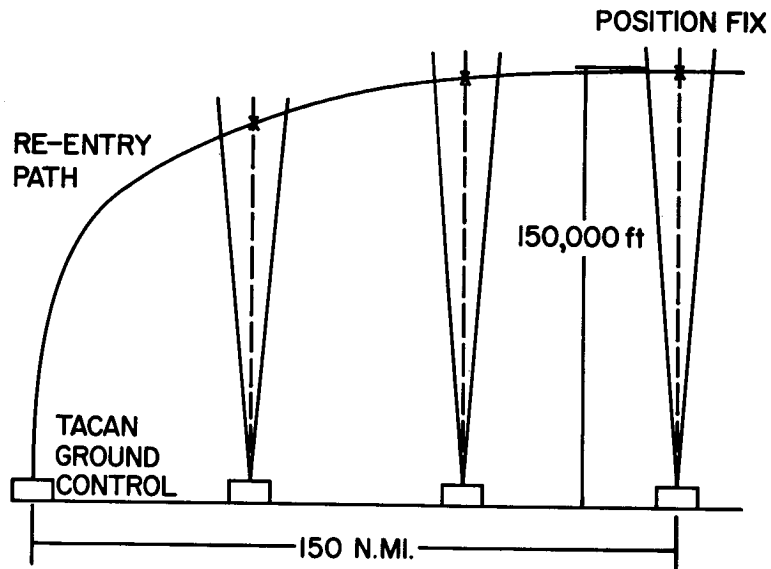


Figure 1

SYSTEM BLOCK DIAGRAM

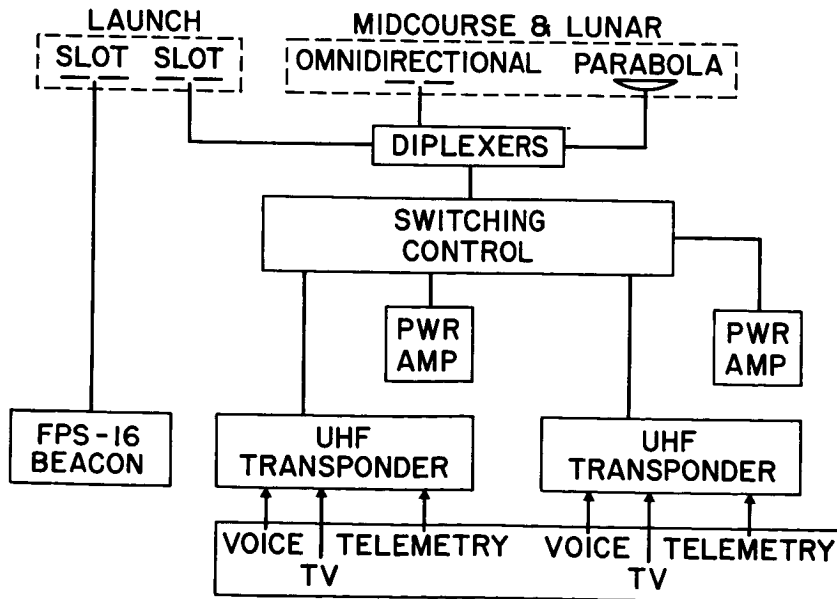
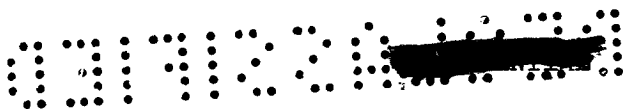


Figure 2



SYSTEM BLOCK DIAGRAM

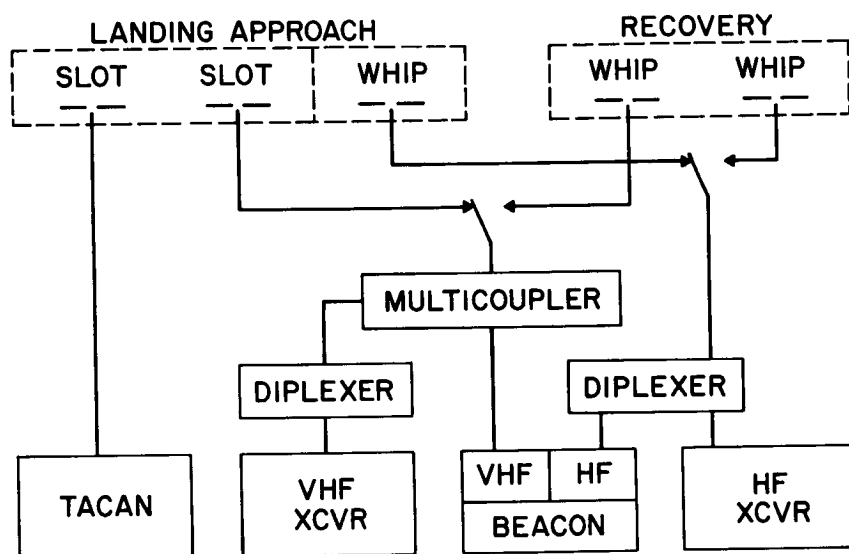


Figure 3



ELECTRIC POWER SUPPLY SYSTEM FOR APOLLO

By E. W. Colehower, G. O. Allen, and S. H. Scales

The Martin Company

INTRODUCTION

A number of systems for converting solar, nuclear, or chemical energy to electric power have been studied for use on Apollo. Preliminary system designs have been made and integrated with other subsystems. This paper compares the most promising electric power system designs for the Apollo spacecraft.

The requirements for the Apollo electric power system are shown as follows:


- (1) Two-kilowatt electric load for 2 weeks
- (2) One-hundred-watts postlanding electric power for 3 days
- (3) Assigned reliability of 0.99
- (4) Design mission of 7 days for translunar and transearth flight plus 7 days of lunar orbiting at an altitude of 1,000 miles

A number of load analyses have shown the electric load to be slightly less than 2 kilowatts except for reentry, where the load increases to slightly over 2 kilowatts.

It is a requirement of the NASA that the Apollo reentry vehicle have the capability of sustaining life for 72 hours after landing. Approximately 100 watts of electric power are required to operate the ventilation system and the location aids during this period.

The electric power system reliability requirement depends upon the reliability goal established for the entire Apollo system and the reliability allocation among the various onboard systems. For this study, the reliability requirement for the electric power system was established as 0.99.

There is an Apollo requirement that the spacecraft be capable of operating 2 weeks without resupply. A design mission was established for this study, consisting of 7 days for the round trip to the moon and 7 days of lunar orbit at an altitude of 1,000 miles.



There are two general types of electric power systems suitable for Apollo use. These are (1) solar power systems which collect solar energy and convert it to electric power and (2) nonsolar power systems which produce electric power from chemical or nuclear sources carried aboard the spacecraft.

A solar power system will have to be supplemented by a nonsolar power system during the periods of earth and moon shadow and during periods where navigational fixes are being made. For the design mission, this period amounts to 20 percent of the time.

A nonsolar power system, on the other hand, can be used either to supplement a solar power system or can be used, full time, to supply electric power for the entire 2-week mission.


SOLAR POWER SYSTEMS

Fourteen solar energy conversion systems were investigated. These systems produce electric power by four basic techniques. A comparison is made of the most applicable system of each of the four methods in table 1. The first system utilizes solar cells mounted on flat panels in direct sunlight. The second system uses parabolic reflectors to focus solar energy on the cathodes of vacuum diodes. The third system requires concentration of solar energy on the hot junction of thermocouples connected thermally in parallel and electrically in series. The fourth system is a solar thermal engine utilizing mercury as the working fluid. The second, third, and fourth systems require parabolic reflectors to concentrate solar energy.

For the entire Apollo electric power system to have a reliability of 0.99, and since a solar power system must be supplemented by a nonsolar system, the reliability requirement for the solar power system is slightly over 0.995. The redundancy required to achieve a 0.995 reliability is reflected in the installed capacity which varies from 15 percent for the solar cell system to 100 percent for the solar dynamic system.

The solar power systems require several hundred square feet of solar collector area. The system weights shown in table 1 are installed weights and include the structure required to protect the stowed systems during the launch phase.

In order to obtain 98 percent of rated power, the flat solar cell panels must be oriented to 11° with respect to the sun. Because the other solar power systems use parabolic reflectors, the orientation tolerances are tighter, varying from less than 0.5° to 2° . System



weights include the increased fuel required by the attitude control system to maintain the spacecraft orientation to the tighter tolerances or, for the thermionic system, the servos to orient the parabolic reflectors.

The solar cell system has the advantage that solar cells are in production status and have been successfully used in space for several years. The solar cell system is the lightest, has the maximum orientation tolerance, is easily expanded for load growth, and is unaffected by zero g. The solar cell system will therefore be further considered for Apollo usage.

NONSOLAR POWER SYSTEMS

As previously stated, a solar power system must be supplemented by a nonsolar power system for 20 percent of the design mission time. Approximately 50 on-off cycles are estimated for the nonsolar power system. Many nonsolar power sources are available to supplement a solar power system. Table 2 compares three auxiliary power units.

The hot-wheel auxiliary power unit is a hydrogen-oxygen four-stage turbine operated hydrogen rich to maintain combustion temperatures below $1,600^{\circ}$ R.


The cold-wheel auxiliary power unit is a combination three-stage reciprocator and three-stage multiple reentry turbine operated by the expansion of hydrogen.

The reciprocator is a two-stage three-cylinder internal combustion engine using hydrogen for the fuel.

The cycle inlet pressure of the hot-wheel turbine is compatible with supercritical pressures of hydrogen and oxygen; therefore, fuel pumping, which is a problem at zero g, is not required. The higher inlet pressures of the cold-wheel turbine and the reciprocator require fuel pumping for either liquid or supercritical stored fuel.

Since in the design mission the auxiliary power units will be operated for approximately 60 hours, fuel and tankage weights are significant. Therefore, the low fuel consumption rate of the reciprocator is attractive.

In order to achieve an overall electric power system reliability of 0.99, the auxiliary power units must have a reliability slightly over 0.995. Because of the high speeds and operating temperatures,



100-percent redundancy is necessary to meet this reliability requirement. This redundancy is reflected in the weights shown in table 2.

Two other nonsolar power sources are shown in table 3. The fuel cell system produces electric power by combining hydrogen and oxygen by an ionization process. The silver-cadmium secondary battery was chosen instead of a silver-zinc battery because of the large number of deep discharge cycles.

The low inlet pressure enables the fuel cells to utilize boiloff from cryogenically stored fuel. The fuel consumption rate for fuel cells is less than that for the auxiliary power units shown in table 2.

The fuel cell and secondary battery systems are static and the redundancy required to achieve a computed 0.995 reliability is 50 percent for the fuel cell system and 38 percent for the battery system. This redundancy is again reflected in the system weight.

The three auxiliary power units, the fuel cell system, and the battery system will all be considered for supplementing a solar cell system. In addition, because of the low fuel consumption rates, the reciprocator and the fuel cell systems will be considered for full-time usage as the Apollo electric power system.


A nuclear system similar to SNAP-2 could be used as a full-time electric power source. However, shielding requirements make the system extremely heavy. At a reactor distance of 20 feet from the crew compartment the system weight is 3,820 pounds.

INTEGRATED POWER SYSTEMS

As previously stated the solar cell system was selected for further study for use in the Apollo electric power system. Figures 1 and 2 show the weights of a solar cell system combined with three auxiliary power units, with fuel cells, and with batteries to form five complete Apollo electric power systems. Also shown is a reciprocator system and a fuel cell system used full time.

The blocks of the bar graphs labeled A indicate the weight of system components common to all seven systems. This includes reentry and recovery electric power, a distribution system, bus centers, and so forth. The blocks of the bar graphs labeled B show the weight of the hardware not common to all systems.

The areas on the graphs labeled C represent the weight of fuel and tankage plus the weight of fuel pumping systems where they are



required. All systems except the solar cell battery system utilize hydrogen and oxygen, and each has two sets of tanks so that a safe return is possible if a tank failure occurs.

If the main propulsion system utilizes hydrogen and oxygen stored in cryogenic form, the main propulsion tanks could be sized for use as one set of tanks for the electrical power system.

An optimum-weight tank for cryogenic storage of fuel is obtained when insulation weight equals boiloff weight. For the propulsion requirements of the Apollo mission, the minimum-weight tank for cryogenic storage of hydrogen permits boiloff sufficient for the needs of a 2-kilowatt fuel cell system. Oxygen boiloff is not sufficient; however, the weight of the additional oxygen is partially compensated by reducing the insulation thickness to get a greater boiloff rate. The use of boiloff from a hydrogen-oxygen propulsion system will reduce the weight of the fuel cell system to that shown by the dashed line on the fuel cell graphs.

Approximately 8 pounds of water per man per day (330 pounds total) is required for the Apollo mission. This weight can be reduced by adding a water reclamation system aboard the vehicle. The fuel cell system, however, produces about 500 pounds of potable water as a result of the combination of hydrogen and oxygen. Therefore, in the weight comparison, the weight of a water reclamation system (120 pounds including redundancy and power requirements) is added to all systems except the fuel cell system (blocks of graphs labeled D).

The areas labeled E represent approximately 50 pounds of supplementary cooling (water in this case) that must be provided for cabin conditioning during the lunar-orbiting portion of the design mission. This weight is added to all systems except the two fuel cell systems since they produce the necessary water during translunar flight.

The solar-cell-battery combination has the advantage of requiring the least development effort. However, the solar cell power system must have an installed capacity considerably larger than 2 kilowatts to recharge the batteries during solar-oriented periods. This requires a solar array area of about 350 square feet.

The five systems using solar arrays have a disadvantage in that the solar power system cannot be erected and checked out until after translunar injection. These arrays would also present a problem during orbital rendezvous maneuvers and lunar landing operations.

The full-time reciprocator and full-time fuel cell systems have the advantage that power system checkout can be performed on the launch

pad. These systems also show the greatest flexibility since their operation is independent of shade time and spacecraft orientation.

For the design mission, there is little difference in electric power system weights. If the main propulsion system is hydrogen-oxygen, the full-time fuel cell system is as light as the solar-cell-battery system. For a design mission consisting of 7 days of 50-mile-altitude lunar orbits, the fuel cell system would show a weight advantage since the excess water can be used for spacecraft cooling. The same is true for a 2-week earth orbit mission.

The fuel cell system is adaptable to a large variety of missions including lunar landing and rendezvous. It is independent of shade time and spacecraft orientation. It produces approximately 500 pounds of water which can be used by the crew and for supplementary cooling. It requires few moving parts and is not subjected to high thermal stresses. For these reasons, a fuel cell system is attractive for use on Apollo, especially if the main propulsion system uses hydrogen and oxygen.

TABLE 1

SOLAR POWER SYSTEMS

	Solar cell (flat panels, direct sunlight)	Solar thermionic (vacuum diode, modular)	Thermoelectric (modular)	Solar dynamic (Rankine cycle)
Total installed capacity, kw	2.3	3.0	3.0	4.0
Solar collector area, sq ft	288	329	361	616
^a Solar collector array misalignment tolerance, \pm deg	11	<0.5	2	<1
Development status	Production	Model	Models and materials	1 g model
Total installed weight, lb	335	743	777	504

^aFor 98-percent power.

SECRET

TABLE 2

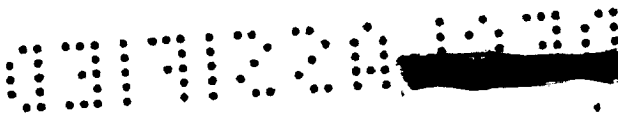
AUXILIARY POWER UNITS

	Hot-wheel turbine	Cold-wheel turbine	Reciprocator
Type of cycle	Hydrogen-oxygen external combustion	Hydrogen reheat	Hydrogen-oxygen internal combustion
Type of expansion	Multiple reentry turbine	Multiple reentry turbine plus reciprocator	Three-cylinder reciprocator
Fuel storage	Supercritical cryogenic	Low-pressure cryogenic; supercritical cryogenic	Low-pressure cryogenic; supercritical cryogenic
Fuel pumping	No	Yes	Yes
Fuel consumption for 2-kw load (O ₂ and H ₂), lb/hr	3.68	2.66	1.84
Hydrogen cooling capacity, Btu/hr	4,810	2,200	1,260
Redundancy, percent	100	100	100
Weight (less fuel and tankage), lb	158	160	126

TABLE 3

CHEMICAL ENERGY CONVERSION METHODS (STATIC)

	Fuel cells	Secondary battery (energy storage)
Type	Hydrogen-oxygen open cycle 15	Silver-cadmium
Fuel inlet pressure, psia		
Specific energy (complete battery), w-hr/lb		23 (2.6-hr discharge rate)
Specific fuel consumption (O_2 and H_2) for 2-kilowatt load, lb/hr	1.64	$\left\{ \begin{array}{l} 1 \text{ to } 100\% \\ 31 \text{ to } 37\% \\ 18 \text{ to } 50\% \\ 6,615 \text{ w-hr (4 batteries)} \\ 38 \end{array} \right.$
Discharge cycles (major)		
Capacity, total	3 kw (3 batteries)	
Redundancy, percent	50	
Weight (less fuel and tankage), lb	421	288



ELECTRIC POWER SYSTEM WEIGHT COMPARISON
7 DAYS OF LUNAR ORBITING AT 1000 N M (31 ORBITS)

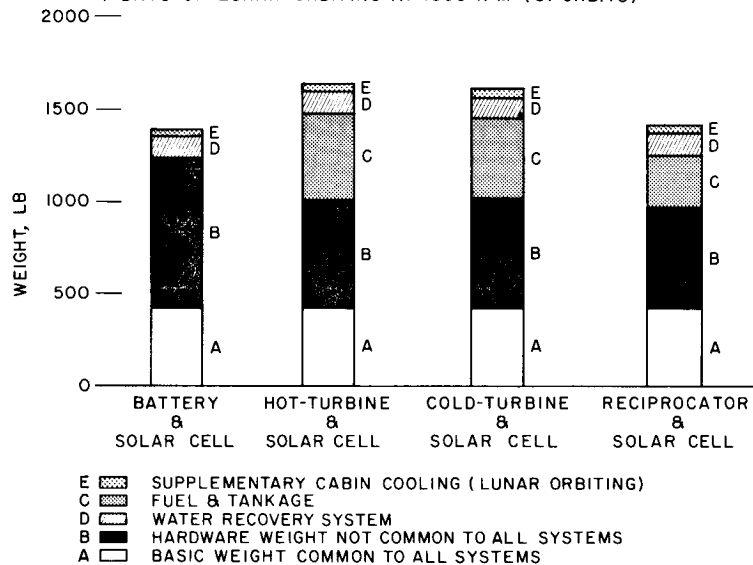


Figure 1

ELECTRIC POWER SYSTEM WEIGHT COMPARISON
7 DAYS OF LUNAR ORBITING AT 1000 N M (31 ORBITS)

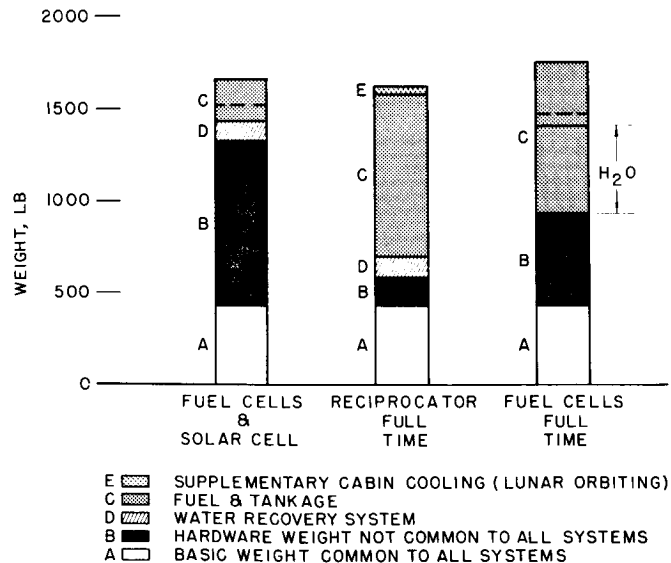


Figure 2



EARTH-LANDING-SYSTEM DESIGN ANALYSIS

By R. C. Chandler and R. L. Lohman

The Martin Company

SUMMARY

A landing-system survey has been conducted of vehicles with conventional landing capability, such as the Dyna-Soar, and of stowable landing devices. Detailed design analyses have been made of parachute and parawing systems with and without impact dissipation devices.

Stowable landing systems in combination with reentry vehicles with moderate lift-drag ratios (L/D) meet the Apollo landing requirements as defined in the study. Reentry vehicles with high lift-drag ratios (L/D) and intrinsic landing capability have higher weights and touchdown speeds.

A system comprising a steerable parachute and a retrosustainer rocket is probably the solution to Apollo landing requirements at the present time. Such a system can weigh as little as 7.6 percent of the reentry vehicle weight.

A parawing, because of its maneuverability and relatively low weight, definitely is attractive for Apollo. Use of the parawing, with or without a braking rocket, will be determined after deployment, stability, and control have been proven in flight.

INTRODUCTION

Safe return to earth from the various Apollo missions involves not only the spectacular reentry phase, but also the more commonplace but equally vital landing phase. The Apollo must land safely under as wide a variety of terrain, sea state, and weather conditions as possible because an aborted deep-space mission may require a return to earth almost anywhere. This paper examines a number of the possible design approaches to an Apollo landing system.

0374200 1:30

REQUIREMENTS

Before the different methods available for landing Apollo are considered, some ground rules and system constraints should be reviewed.

The basic function of a landing system as defined here is to reduce the spacecraft velocity from a free-flight value on the order of 300 to 500 fps to 0 at the landing surface in such a way that the crew is protected from injury and that the capsule itself remains inhabitable until rescue arrives. Specific requirements established by NASA in the request for study proposal are summarized as follows:

- (1) Normal landing "at one of several prepared ground surface locations"
- (2) "Safe crew recovery from aborted missions at any speed up to maximum velocity"
- (3) "Satisfactory landing on both land and water"
 - (a) Landing in a 30-knot wind
 - (b) Prevention of component started brush fires
 - (c) Landing in sea state 4 (10- to 12-foot waves)
 - (d) Provision of adequate flotation and water stability
- (4) Terminal-point control
 - (a) Avoidance of local obstacles
 - (b) Correction of residual navigation errors
- (5) Spacecraft designed for crew survival for at least 72 hours after landing

As shown in the preceding list, normal Apollo landings will be made on a prepared ground surface, but both land and water landings shall be safe in winds up to 30 knots. Terminal-point control must be provided to avoid local obstacles and to correct any residual navigational error following reentry. Safe recovery from aborts on the launch pad and throughout the launch and injection phases shall be possible. And the capsule itself must be in good enough condition after impact to provide a safe survival shelter for at least 72 hours.

Although not specified in the study request, there are many other desirable or essential requirements an integrated landing system should meet. Some are implied or derived from the specified requirements. Some of the additional possibilities, which may have very significant effects on the system design, are as follows:

- (1) Backup or emergency landing system to meet reliability goal
- (2) All-weather landing
- (3) Crew impact deceleration limit
- (4) Crew orientation at impact
- (5) Crew orientation after impact
- (6) Resistance to tumbling following impact
- (7) Minimum altitude to complete safe landing
- (8) Safe egress from any landing
- (9) Reusability of components or overall vehicle system
- (10) Potential growth of recoverable payload
- (11) Critical schedule

For example, in order to reduce crew risk to an acceptable level it is probable that many if not all of the landing system components should be redundant or an alternative system be provided. Also, it would obviously be desirable to have all-weather landing capability. Crew orientation at impact and the maximum deceleration as well as the rate of onset are all fundamental to safe landing. Limiting g's on the crew in the event of a partial system malfunction is also a worthwhile goal and a possible requirement. It must be possible to get out of the vehicle when it has come to rest in any probable position. It may be important that one type of system cannot accommodate weight growth. In addition to such design considerations, there are requirements which accompany the development of any new system. Perhaps the most important one for Apollo is the earliest date when a man-rated landing system must be available.

Finally, there are the overall Apollo system requirements. The spacecraft had to be compatible with the Saturn C-1 and C-2 launch vehicles for the study and now must be compatible with the C-3. Landing requirements can greatly influence the weight, size, and shape of the spacecraft. Moreover, Apollo will operate in space for periods up to

[REDACTED]

0371238 1030

14 days; and the landing system must operate reliably following this long exposure to hard vacuum and other environmental hazards of space.

SURVEY OF LANDING METHODS

In order to obtain a landing technique which would best satisfy the requirements just discussed, a wide range of possibilities was considered. Much of the basic data were provided by government agencies and industry consultation.

Landing systems fall into two major categories. The first category utilizes the aerodynamic characteristics of the reentry vehicle itself to perform a conventional dead-stick landing. By definition, then, this category is restricted to reentry vehicles with intrinsic landing capability. The second category of landing systems involves the use of devices stowed inside the reentry vehicle and deployed or positioned only during the terminal flight phase. The stowable landing systems provide the necessary deceleration, stabilization, and possibly, steering functions.

Configurations With Intrinsic Landing Capability

In order to decelerate a horizontal-landing vehicle to an acceptable touchdown speed while maintaining a very shallow flight path without power, a certain minimum aerodynamic performance must be available. Horizontal landings with aerodynamic characteristics which must be at or very close to a limit are demonstrated in reference 1. With a wing loading of 85 psf, successful landings were made with a maximum L/D of 2.8. If this value is considered to be the minimum for unpowered landings, only winged vehicles of the Dyna-Soar type or slender lifting bodies, such as the flat-topped cone M-2-2 or the lenticular L-7, can qualify. These vehicles are shown in figure 1.

It has been pointed out in a previous paper by Robert O. Piland, Caldwell C. Johnson, Jr., and Owen E. Maynard that safe return from the various Apollo missions requires a hypersonic L/D of no more than 0.3 to 0.8, whereas the vehicles with intrinsic landing capability all have maximum L/D values greater than 1.0. High L/D vehicles are, in general, appreciably heavier (at least 15 percent) than low or moderate L/D vehicles designed for the same mission. They have high landing speeds, greater than 120 knots, which in turn require long, prepared surface runways. These higher L/D vehicles tend to be more difficult

to mate with launch vehicles than lower L/D configurations because of the higher aerodynamic loads and control problems.

However, high L/D vehicles offer a number of significant advantages. They provide a subsonic glide range of about 60 miles, along with the ability to maneuver into a landing site with pilot control at all times. Depending on the type of reentry control used, large increases in reentry corridor width can be achieved with the high L/D vehicles compared with those achieved with moderate L/D configurations.

Conventional landing vehicles still fail to satisfy an important Apollo design constraint; that is, the ability to land safely in rough water. Furthermore, landing anywhere under poor weather conditions in a high-speed dead-stick vehicle will be extremely hazardous. These problems might be alleviated by the use of an auxiliary braking-rocket system at the price of even more weight. However, because of the early operational date and the exploratory nature of the missions, configurations with intrinsic landing capability are not considered appropriate for the Apollo program.

Stowable Landing Systems

The most significant benefit of using a stowable landing system is that the reentry vehicle shape and arrangement can be optimized around its primary function of safe hypersonic flight. Therefore, vehicles with moderate values of L/D can be used with an important weight advantage over vehicles with intrinsic landing capability.

There is a profusion of stowable-landing-system possibilities, ranging from purely conceptual designs to thoroughly proven systems such as that of Mercury. Several of the systems, discussed subsequently, are illustrated in figure 2.

Retrorockets.- Since lunar landing will require the development of a rocket landing system, it is appropriate to consider retrorockets for landing on earth. Lunar landing is simpler in several respects: the rocket system is more efficient on the moon because of the low gravity and high vacuum specific impulse; there is no atmospheric turbulence; and for some vehicular arrangements the lunar take-off stage provides an emergency system at no cost.

A retrorocket for landing on earth is relatively light even when completely redundant. However, the system is an active one and may not be as reliable as the semiactive and passive systems used by Mercury, for example. There are difficult arrangement and operation problems associated with the backup system and with control for both systems.

Balloons. - Two types of balloons were considered for landing adaptability. They were to be inflated after reentry to support the weight of the vehicle by either aerostatic or aerodynamic means.

The buoyant device presumably could be taken in tow and landed wherever desired. However, the necessity of carrying two containers, one for the gas when compressed and the other when it is to provide buoyant lift, presents a problem. The lift provided is barely enough to support the containers, to say nothing of the vehicle.


The use of an inflated ball around the vehicle is the ultimate in landing bag design since it serves both as a drag device and as an omnidirectional shock absorber. As with the buoyant balloon, however, system weight approaches payload weight so that its use is impractical.

Rotors. - A stowable rigid-rotor (autogyro) system has many attractive features including controllable rate of descent, maneuverable glide (L/D_{max} of about 1.7), and landing flare capability. Addition of tip rockets (using, for example, hydrogen peroxide through a catalyst) can ease the critical dead-stick touchdown problem and provide some helicopter cruise to a more desirable landing site. Reliability will tend to be lower than with other systems because no backup can be provided. Excessive weight and bulk make rigid rotor systems unattractive for Apollo application.

The Flexirotor was examined briefly. This system consists of a vortex-ring parachute as the hub of a rotor formed of unrolled, tip-weighted fabric panels. The limited information available indicated problems of deployment and steerability. Therefore the Flexirotor was not considered further.

Parachutes. - The parachute is perhaps the most highly developed aerodynamic decelerator. If deployment can be assured, the parachute is very reliable and predictable in its performance. Several thousand parachutes have been deployed consistently at dynamic pressures between 2 and 1,200 psf and at speeds up to a Mach number of 2.2. Many types of multiple-parachute recovery systems are in operational use on missiles and manned capsules. Mercury utilizes a ribbon drogue parachute and a Ringsail main-parachute system.

Parachutes, as units or in cluster, can provide sufficient drag for touchdown rates of descent as low as 18 to 20 fps. Below these speeds, parachute weight rapidly exceeds 10 percent of the vehicle weight. Practical applications including impact attenuation devices, redundancy, and minimum parachute-opening time dictate higher designed rates of descent and will be discussed later. A recent improvement, which will make parachutes appropriate for the Apollo, is a glide and steering



capability which hopefully can be developed to provide a modulated horizontal velocity up to the value of rate of descent. This improvement is achieved by incorporating a movable flap sector in the canopy. Test drops have demonstrated glide velocities up to 0.7 descent speed.

Parawing.- The glide range, maneuverability, and particularly the fly-in landing capabilities of the parawing make it most attractive. From NASA research data and The Martin Co. studies, it appears that, in comparison with parachute systems, the parawing system is as low in weight and is only slightly more difficult to stow.

The only serious unknown quantity of the parawing is its deployment under in-flight conditions. This complication arises from the fact that the required lengths of keel and leading-edge beams are several times the length of stowage area in the vehicle. Another difficulty is absorption of landing loads, particularly under rough water or terrain conditions, with touchdown speeds of 40 knots or more. At high wing loadings the suspended reentry body is a major contribution to system drag and significantly reduces overall $(L/D)_{max}$ from the wing-alone value of 7. This factor is considered subsequently in weight optimization studies. A description of parawing geometry and aerodynamic characteristics is given in the following paper by Donald E. Hewes, Robert T. Taylor, and Delwin R. Croom.

Impact Dissipation

All methods of landing described in the preceding section result in some residual horizontal and vertical velocity. This terminal energy must be dissipated in a way that will not injure the crew or destroy the integrity of the vehicle structure which must serve as a survival shelter. In a subsequent paper by Lloyd J. Fisher, Jr., a number of systems for landing impact dissipation are discussed. Only the criteria and the particular methods used in the present overall-landing-system comparison are mentioned in this paper.

A typical Apollo reentry vehicle structure can withstand an impact velocity of at least 10 fps without developing a leak. In the present landing system study, vertical velocities without a cushioning device have been limited to 8 fps. Tests by the Wright Air Development Division with human subjects in B-70 escape capsules show that 30g impacts resulted in no injuries. In the present study landing accelerations have been limited to a maximum value of 20g.

The two impact-dissipation methods used in this study are illustrated in figure 3. The corresponding plots of load F against stroke h are shown beside the pneumatic-bag system and the retrorocket system. The energy dissipated is determined by the area under the load-stroke curve.

Pneumatic-bag system.- The pneumatic bag is a proven system representative of the present state of the art. The particular system considered is inflated with stored gas rather than by the inhalation method used for Mercury. The selected system will stay intact in a lateral skid so that most of the vertical energy will be absorbed by the bag in the specified wind condition of 30 knots.

As shown in figure 3 the load-stroke curve for bags results in relatively high deceleration as a result of the limited stroke and low efficiency. A typical value is 16g. Loads transmitted to the vehicle structure may be high enough to require local strengthening. The additional structure could amount to 4 percent of the vehicle weight. However, this weight increment is a function of the particular vehicle design and is not included in the analyses to follow.

Pneumatic bags are much less efficient in landing on water than on a solid surface because energy is expended in moving the water laterally.


Retrorockets.- Retrorockets are more flexible than bags since higher residual velocities can be dissipated and deceleration levels can be held to much lower values. Retrorockets are equally effective on land or water. When used as an adjunct to a main landing system, the possible malfunction of an active system such as a retrorocket is not catastrophic. Other characteristics of rockets have been mentioned under the discussion of the main stowable landing systems. A rocket sustainer phase at a thrust level less than the weight of the vehicle as shown in figure 3 is useful for reducing the effect of errors in ignition timing.

Comparison of Landing Methods

Figure 4 shows the approximate regions where each of the landing systems surveyed would appear to be most applicable. The two parameters of most concern to the designer, system weight and touchdown velocity, are used as coordinates.

System weight is shown in percent of total vehicle weight. Touchdown velocity is measured either horizontally or vertically, depending upon the particular system under consideration. In the case of the fly-in reentry vehicles, all of the weight greater than 7,000 pounds is assigned to the landing system. Seven thousand pounds is the weight of a nominal reentry vehicle which meets all of the Appolo study requirements.

It can be seen in figure 4 that the parachute and parawing systems are lighter than the other systems. Composite systems coupling both parachutes and parawings with retro or braking rockets appear even more



attractive. Therefore, parachute and parawing configurations with and without impact dissipation devices were selected for further analysis and systems integration as discussed in the next section.

OPTIMIZATION OF PARACHUTE AND PARAWING SYSTEMS

Parametric analyses were made of both parachute and parawing systems to determine their weight and performance characteristics. For these analyses a vehicle weight of 7,000 pounds was assumed. System weights and volumes allow for steering controls, a location aid system, and a drogue system (8-ft diameter FIST ribbon parachute) assumed to be necessary for transonic stability and main parachute or wing deployment. System weights and volumes also allow for the redundancy or backup to meet a reliability goal for the fully developed landing system of 0.9995.

Parachutes

Figures 5 and 6 show the results of an analysis of a composite landing system employing a steerable main parachute with a pneumatic bag for impact absorption. Figure 6 shows individual component and total-system weights as a function of the sea-level rate of descent. Minimum system weight corresponds to 8.3 percent of the vehicle weight and occurs in a narrow velocity band centered on 38 fps. This study is based on the use of a Ringsail parachute with a movable flap sector for glide control (curve A). The bag is a neoprene-nylon toroidal section, inflated with helium and designed to limit impact to 16g. The bag weight, curve B in figure 6, increases so rapidly with rate of descent that this method of energy absorption is restricted to rather low rates of descent. Curve C is the sum of curves A and B plus a fixed allowance of 2.6 percent of the total vehicle weight for parachute deployment and steering and for location aids. Curve D adds another main and drogue parachute to the basic system for redundancy.

Figures 7 and 8 show the results of a similar analysis for a composite landing system employing a steerable main parachute with a retro-rocket to reduce impact loads. Part (a) of figure 8 shows the weight buildup for a retrorocket without the sustainer phase mentioned previously. The retrorocket is designed to decelerate the vehicle to 0 velocity at the landing surface. The system weight, even with redundancy, is very low. Unfortunately, this is not a practical system; variations in initial rate of descent, thrust and burning time, vehicle weight, and errors to rocket ignition timing result in probable impact rates of descent well above the 10-fps limit imposed by structural integrity of the capsule.

Figure 8(b) shows the same type of system with a sustainer thrust ($T/W = 0.92$) phase lasting 3.2 seconds added. This system will limit impact to 8 fps on a 3σ basis for a typical system design.


Parawing

A parametric evaluation of the parawing system weight for several sea-level touchdown speeds ($1.1 V_{stall}$) was performed for an inflatable beam wing. A rigid beam design with controlled unfolding and erection gives similar results. The computations include the aerodynamic effects of the 7,000-pound suspended vehicle payload.

The parawing landing sequence is shown in figure 9. Wing beams are inflated cylinders pressurized so as not to buckle at the ultimate design load; that is, skin tension due to internal pressure must be equal to the bending stress due to moment. Nonporous Mylar coated nylon parachute cloth forms the membrane and inflated surfaces of the wing. Pressurizing helium is stored in spherical titanium containers. A fixed weight of 1.5 percent of the total vehicle weight is included for a control winch system, deployment, and location aid gear. This increment is less than that for the parachute systems because of the smaller drogue and lighter cabling required for the parawing systems.

Results for the basic parawing system are shown in curve A of figure 10(a). In curve B an auxiliary system, which is 5 percent of the total vehicle weight, is added to the basic parawing system. This auxiliary system consists of a steerable parachute and a retrosustainer rocket to handle conditions requiring minimum horizontal speed and to provide redundancy necessary to reach the landing system reliability goal. Figure 10(a) shows that $(L/D)_{max}$ reduces rapidly with increasing W/S because of the greater influence of payload drag. The wing-alone $(L/D)_{max}$ of 7 was taken from reference 2. Slower touchdown speeds require sharply increased wing areas and, therefore, additional weight and stowage volume.

In order to reduce forward speed and cope with rough water or poor terrain situations, a 2g solid-propellant braking rocket was incorporated. This rocket would be fired at the pilot's discretion to provide sufficient counterenergy to stop all forward motion. Curves A, B, and C of figure 10(b) show the weight of a parawing, rocket, and combination system. A backup parachute system of 2.4 percent of the total vehicle weight is added to curve D to enhance reliability. This emergency system limits crew load factor to a tolerable 20g with seat shock absorbers.



Other problems arise at the high speeds for optimum system weight. At speeds of 100 to 125 fps, braking rocket deceleration takes 1 to 1.3 seconds and a distance of 40 to 63 feet. Since the craft is below flying speed, aerodynamic control is ineffective and omnidirectional impact could occur. Nevertheless, the light weight and high performance of the parawing landing system attracts further development of this technique.

Comparison of Suitable Systems

All of the parachute and parawing systems discussed are possible. Examples of each type have been selected for comparison by using practical systems integration reasoning. The characteristics of these systems are shown in table 1. Selection criteria were as follows:

System 1 - Steerable-parachute pneumatic bag:

The parachute size (81-foot diameter) was selected to give the maximum rate of descent (for highest glide speed to offset winds) consistent with crew impact tolerance. With a practical impact dissipation system built into the seats, the crew will experience no more than 20g for a rate of descent of 40 fps.

System 2 - Steerable parachute and retrosustainer rocket:

The parachute was sized identically to system 1.

System 3 - Parawing alone ($W/S = 6$ psf):

The wing keel length was the maximum which could be folded into a typical Apollo reentry vehicle in order to get the lowest touchdown speed and highest L/D possible.

System 4 - Parawing with braking rocket ($W/S = 6$ psf):

The wing keel length was sized identically to system 3.

System 5 - Parawing with braking rocket ($W/S = 20$ psf):

The wing loading was selected as high as believed to be practical to minimize system weight.

A comparison of systems 1 and 2 in table 1 shows that the parachute-retrorocket system is lighter, requires appreciably less stowage volume, has much lower impact velocities, and probably imparts lower deceleration on the crew than a parachute-bag system.

A comparison of the same size parawings (systems 3 and 4) shows a slight reduction in weight and volume and a major improvement in touchdown velocity for the system with a braking rocket.

A comparison of the two parawings with braking rockets (systems 4 and 5) shows the advantages in weight, size, and maneuvering velocity associated with the higher loading (system 5). It also shows the poorer maneuvering range.

A comparison of the minimum weight parachute and parawing systems (systems 2 and 5) indicates that a major improvement in maneuver range is available with the parawing system.

REFERENCES

1. Bray, Richard S., Drinkwater, Fred J., III, and White, Maurice D.: A Flight Study of a Power-Off Landing Technique Applicable to Re-Entry Vehicles. NASA TN D-323, 1960.
2. Rogallo, Francis M., Lowry, John G., Croom, Delwin R., and Taylor, Robert T.: Preliminary Investigation of a Paraglider. NASA TN D-443, 1960.

TABLE 1

CHARACTERISTICS OF SUITABLE LANDING SYSTEMS

System	Weight, percent total	Volume, cu ft	Touchdown speed, fps		Horizontal speed, knots	Range, nautical miles	Load factor on crew, g units
			Vertical	Horizontal			
Steerable parachute (redundant parachute system) Deployed at 15,000-ft altitude							
1. With pneumatic bags	8.5	30	40	-----	17	1.6	16 to 20
2. With retrosustainer rockets	7.6	18	0 to 8	-----	17	1.6	1 to 20
Parawing Deployed at 60,000-ft altitude With auxiliary parachute retrorocket system							
3. W/S = 6 psf With braking rocket and backup parachute system	11.2	22	-----	70	54	41	≈1
4. W/S = 6 psf	9.3	20	-----	0 to 10	54	41	≈1
5. W/S = 20 psf	6.4	11	-----	0 to 10	88	26	≈1

^aPlus weight of load-bearing structure.

0371021 [REDACTED]

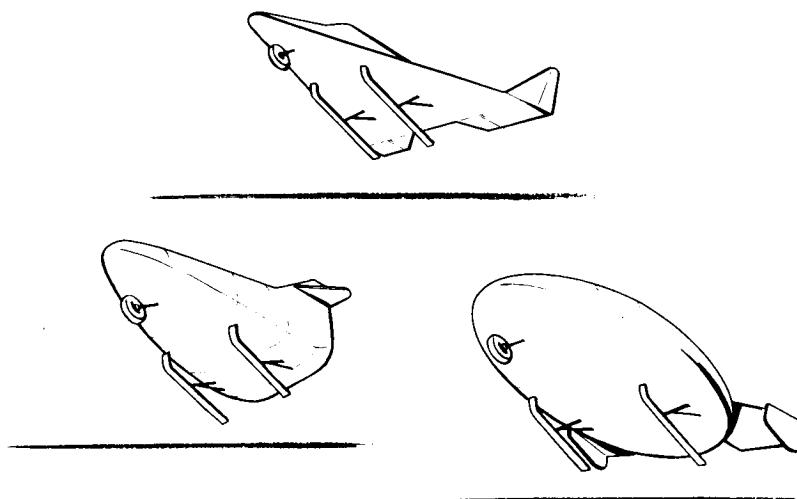
CONFIGURATIONS WITH INTRINSIC
LANDING CAPABILITIES

Figure 1

STOWABLE LANDING SYSTEMS

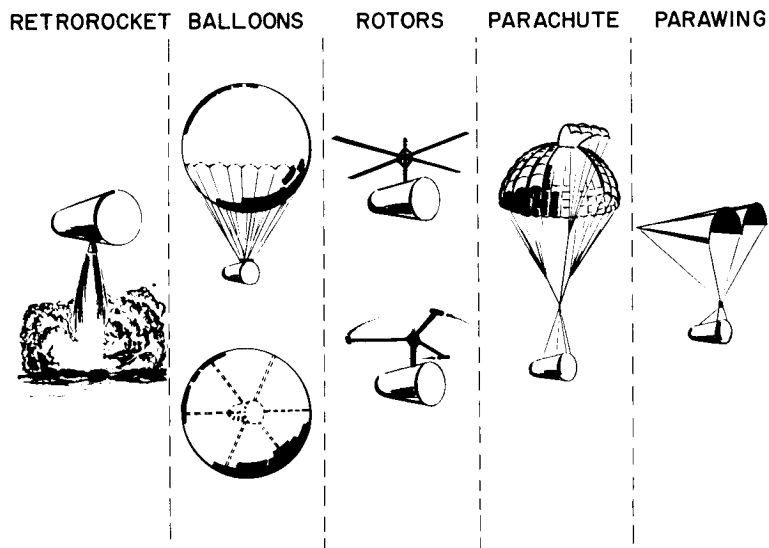


Figure 2

[REDACTED]

IMPACT ENERGY DISSIPATION

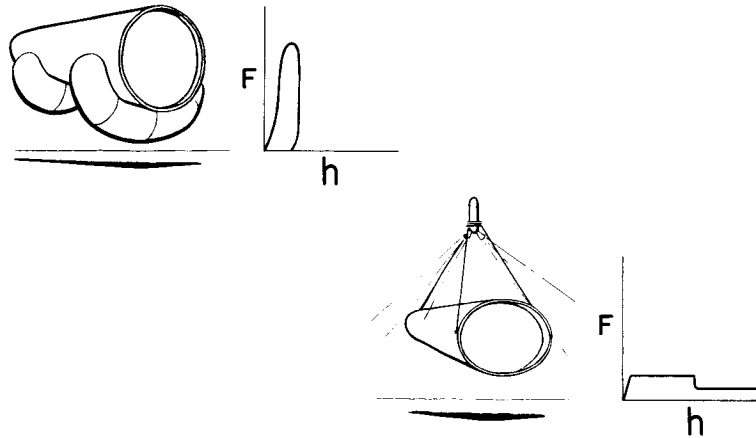


Figure 3

APOLLO EARTH LANDING SYSTEMS GENERAL WEIGHT AND SPEED REGIMES

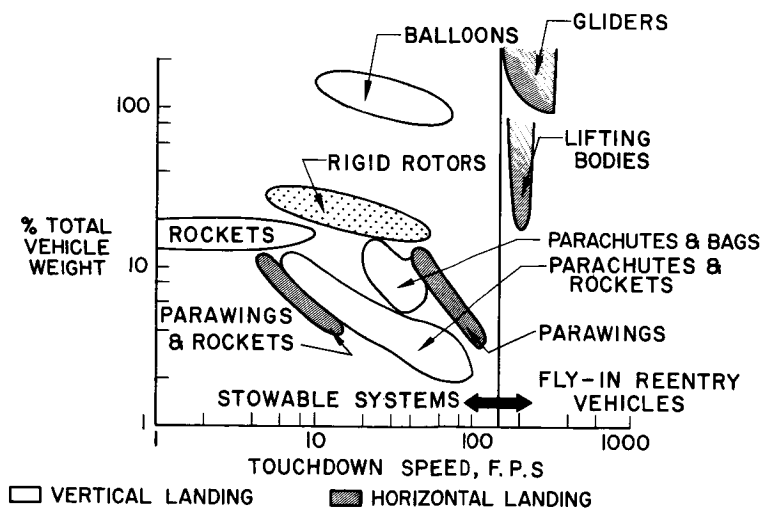


Figure 4

STEERABLE-PARACHUTE-BAG SEQUENCE

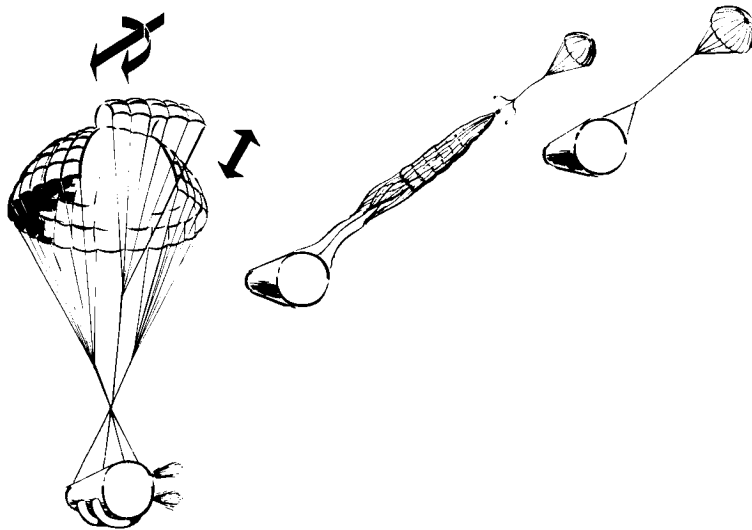


Figure 5

STEERABLE PARACHUTE PNEUMATIC BAG LANDING SYSTEM

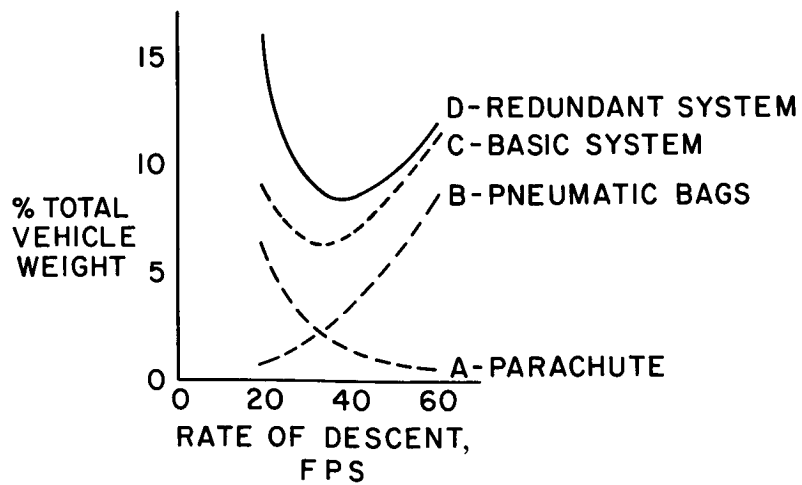


Figure 6

STEERABLE PARACHUTE-RETROROCKET SEQUENCE

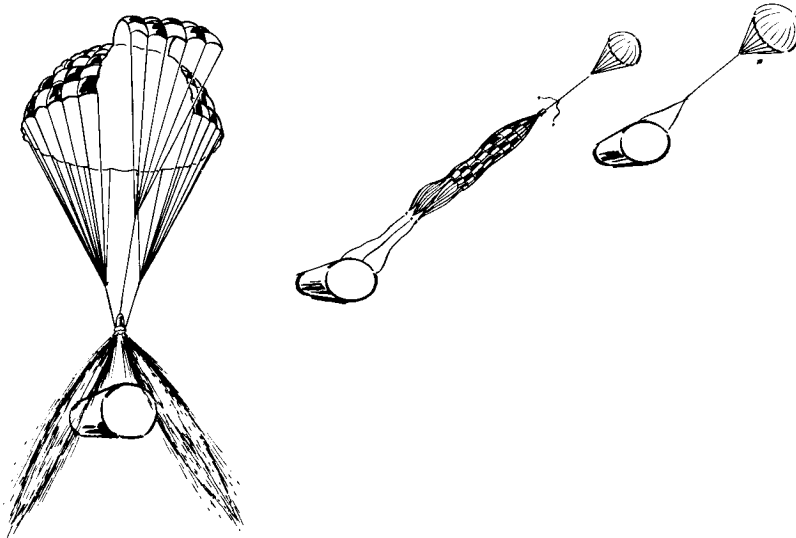


Figure 7

STEERABLE-PARACHUTE-RETROROCKET LANDING SYSTEM

a) LESS SUSTAINER
RETRO T/W = 4

b) WITH SUSTAINER
RETRO T/W = 4
SUSTAINER T/W = .92

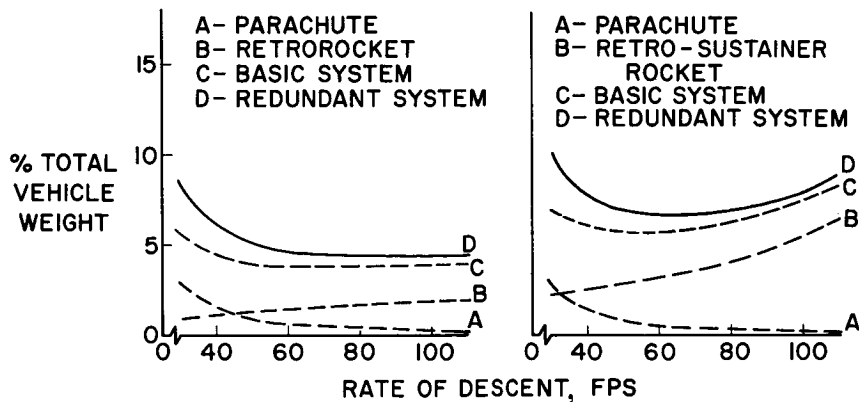


Figure 8

0371200 [REDACTED]

PARAWING SEQUENCE

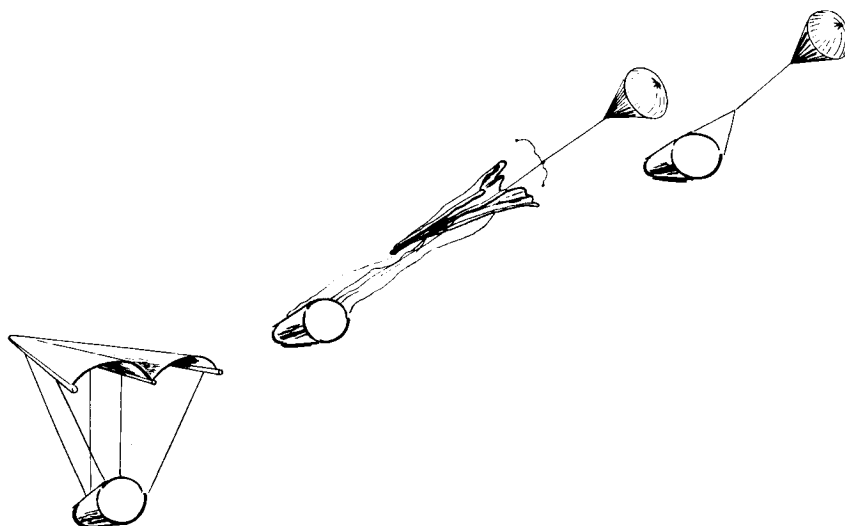


Figure 9

PARAWING LANDING SYSTEM (FOR VEHICLE WITH $C_D A = 60$ SQ FT)

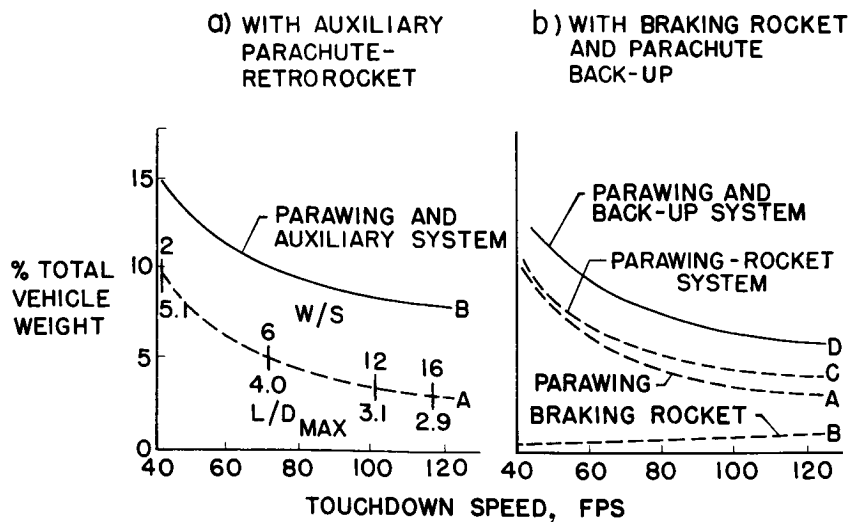


Figure 10

[REDACTED]

AERODYNAMIC CHARACTERISTICS OF PARAWINGS

By Donald E. Hewes, Robert T. Taylor,
and Delwin R. Croom

Langley Research Center

INTRODUCTION

A review of the basic requirements for recovery of the Apollo reentry vehicle and a discussion of several possible systems designed to meet these requirements has been given in the previous paper by R. C. Chandler and R. L. Lohman. The purpose of this paper is to present a brief summary of recent or current research studies pertaining to the devices incorporated in these or other possible systems. The devices which have been included in this summary fall in the following categories: drogues, rotors, wings, lifting surfaces, and rockets.

Because of the expressed need for providing gliding and maneuvering capability and for reducing the vertical velocity prior to touchdown, considerable interest has been shown in the use of the parawing which appears to be capable of fulfilling this need. The discussion, therefore, will be devoted primarily to the studies of the parawing. A summary of the research studies of the other devices is presented in the form of a chart given in table I. A list of pertinent reports and reference material has been compiled and appears at the end of this paper.

The present state of development of the parawing is such that extensive research and development testing must be carried out before it will be possible to define precisely the capabilities of this system and determine an optimum configuration for the Apollo application. Within the past few months, however, considerable research effort directed toward uses of the parawing has been initiated by both industry and government agencies.

The current NASA research studies of the basic wing and various configurations are summarized in table II. Studies of wing geometry, structure, rigging, and size have been initiated to evaluate the effects of these variables on the performance, stability, control, flare and landing capability, deployment, aeroelastic effects, aerodynamic loads, and structural design of the wing. Static wind-tunnel tests of wings with rigid and elastically scaled members have been made at low subsonic to high supersonic speeds. Wind-tunnel tests of a completely rigid wing equipped for pressure-distribution measurements have been made. Dynamic-

model tests are being conducted in various wind tunnels and at an outdoor test range where models up to 19 feet in length are being tested in free flight to evaluate deployment characteristics, stability, control, and flare capability. Analytical studies are also underway to evaluate various problems and to obtain correlation of experimental results.

SYMBOLS

A aspect ratio, $\frac{b^2}{S}$

b developed wing span, ft

C_D drag coefficient, $\frac{\text{Drag}}{qS}$

C_L lift coefficient, $\frac{\text{Lift}}{qS}$

$C_{L\alpha}$ lift-curve slope, $\frac{\partial C_L}{\partial \alpha}$ per deg

C_l rolling-moment coefficient, $\frac{\text{Rolling moment}}{qSb}$

$C_{l\beta} = \frac{\partial C_l}{\partial \beta}$

C_m pitching-moment coefficient, $\frac{\text{Pitching moment}}{qSc}$

C_n yawing-moment coefficient, $\frac{\text{Yawing moment}}{qSb}$

$C_{n\beta} = \frac{\partial C_n}{\partial \beta}$

C_Y side-force coefficient, $\frac{\text{Side force}}{qS}$

$C_{Y\beta} = \frac{\partial C_Y}{\partial \beta}$

c chord, ft

CONFIDENTIAL

c_n	section normal-force coefficient, $\frac{\text{Section normal force}}{qc}$
E	modulus of elasticity, lb/sq in.
I	moment of inertia, in. ⁴
L/D	lift-drag ratio
l	reference length, ft
M	Mach number
q	dynamic pressure, $\frac{1}{2}\rho v^2$, lb/sq ft
S	reference area, sq ft
V	free-stream velocity, ft/sec
W	weight, lb
x	distance along keel from apex, ft
y	distance from center line, ft
α	keel angle of attack, deg
β	sideslip angle, deg
Δ	canopy apex angle, deg
Λ	leading-edge sweep, deg
ρ	density, slugs/cu ft

Subscripts:

av	average value
max	maximum value
∞	free-stream conditions
o	point of normalization

037120 1034


DISCUSSION OF PARAWING

One possible parawing configuration is shown in figure 1 to illustrate the basic elements of this type of system. The size of the wing depends on several factors such as stowage volume, weight, deployment time, loads, glide range, and landing speed. During deployment, the wing initially will be trailing from the hatch in a streamwise direction and the suspension cables must be sufficiently long to permit the wing to clear the hatch completely. After the wing has unfolded and been properly inflated it will assume the attitude depicted in this diagram. Pitch control is achieved by changing the lengths of the fore and aft suspension cables which causes the vehicle to shift forward or rearward relative to the wing. Roll control, to produce turning flight, is achieved by changing the lengths of the lateral lines. With this system, a separate directional control appears to be unnecessary.

In order to predict the full-scale characteristics of the parawing system which is inherently an elastic or flexible system, model tests and analyses must take into account the effects of structural deformations on the static and dynamic characteristics. Some of the flexure modes which must be considered are flexing of the wing keel and leading-edge members, stretch and flutter of the fabric canopy, and relative motion of the wing and vehicle due to suspension cable elongation. Flexing of the wing members, and stretch of the canopy can produce very significant changes in the aerodynamic properties of the wing. The subsequent discussions will be limited generally to results of preliminary tests of models with rigid leading edge and keel but having cloth canopies. These results are helpful in obtaining a basic understanding of the parawing and in selecting an optimum aerodynamic configuration.

The variations with angle of attack of lift, drag, and pitching moment of a parawing model tested at low subsonic speeds are shown in figure 2. The coefficients of these and all subsequent data are based on the area of the flat planform of the fabric canopy and the length of the keel. These data illustrate that for the angle-of-attack range shown the parawing possesses aerodynamic characteristics quite similar to those for more conventional type wings. At low angles of attack where the airloads on the canopy are reduced the canopy loses its characteristic conical shape, and trailing-edge flutter and a luffing action of the canopy are encountered. This luffing is similar to that of a sail on a sailboat which is headed directly into the wind. Special study must be made of these phenomena because of their effects on the strength and aerodynamic properties of the wing.

The pitching-moment curves are shown for four center-of-gravity locations to illustrate the effect of shifting the weight of the vehicle



fore and aft relative to the wing to achieve pitch control. In order to provide, simultaneously, trim and longitudinal stability, the center of gravity of the configuration must be located below the wing. A distance of about 75 percent of the keel length is considered to be typical for the Apollo application. As a consequence of shifting the center of gravity rearward to trim at progressively higher lift coefficients, the stability is decreased as indicated by the slope of the curve. For these particular test data there is a region of instability at the higher angles of attack as indicated by the shape of the curve. For other test conditions this instability was not encountered.

Some effects of wing geometry variations have been determined from subsonic wind-tunnel tests. Wings with rigid leading-edge members and various amounts of sweep and with different canopies were tested.

The effects of changing the sweep angle of the leading edges of the parawing on the maximum lift $C_{L,max}$, lift-curve slope C_{L_α} , and maximum value of lift-drag ratio $(L/D)_{max}$ are shown in figures 3 and 4. The flat planform of the canopy used in these tests was cut to a 90° apex angle. As the angle of the wing structure was increased from 50° to 70° , the conical shape which the canopy assumed under load increased as indicated by the sketches in figure 3. The reductions of $C_{L,max}$, C_{L_α} , and $(L/D)_{max}$ with increasing sweep are attributed to changes in camber and aspect ratio.

The model was constructed with tubular leading edges with a diameter equal to 1.5 percent of the keel length. It is very likely that the actual $(L/D)_{max}$ values for full-scale parawings will vary appreciably from these measured values depending on the size and shape of the leading edges employed, the effects of structural flexibility, and the attention given to achieving aerodynamically clean surfaces and structural attachments. It is certain, however, that the full-scale values will not exceed those indicated by the dashed curve of figure 4 obtained from the calculations in which elliptical load distribution is assumed and the drag of the leading-edge members is neglected. The

equation $C_D = 0.013 + \frac{C_L^2}{\pi A}$ was used in the calculations and the value 0.013 corresponds to the estimated minimum skin-friction drag coefficient.

The effect of changing the canopy size by changing the flat-planform apex angle Δ from 70° to 110° on L/D for a wing with a fixed leading-edge sweep angle Λ of 60° is illustrated in figure 5 which shows the variation of L/D with C_L for each of three canopies tested. The shape of the wing with the different canopies is shown by the small

sketches. The highest value of L/D was achieved for the canopy with the least amount of fabric area. Reducing the fabric area decreased the drag due to skin friction; however, L/D is reduced more than would be expected just due to the change in wetted area. Typical measured values for $C_{Y\beta}$, $C_{n\beta}$, and $C_{l\beta}$ of a model wing with the same sweep

angle and canopy flat planform are shown in figure 6 along with the variations with sweep angle for two different values of lift coefficient. The data are given for a nominal center-of-gravity position of 75 percent of the keel length below the wing and 65 percent rearward of the keel leading edge. The increase in effective dihedral and directional stability with sweep angle is attributed, in part, to the increase in projected lateral or side-view area of the wing with increasing wing camber. At the present time there is no knowledge of what values of the lateral stability parameters will be required to provide sufficient stability for the complete configuration. Tests of the dynamic-scale free-flight models and the full-scale Ryan experimental vehicle both with wings having rigid leading edges with 50° sweep have indicated generally adequate lateral-directional stability over most of the angle-of-attack range.

The sketch in figure 7 shows the locations of the pressure orifices on a rigid-wing model which was tested in different wind tunnels over a Mach number range from 0.1 to 4.65 to study the pressure distribution on the canopy. A rigid canopy was used to facilitate the installation of the pressure orifices and tubes. The three-dimensional plot above the wing illustrates the typical distribution measurements which have been obtained. Integration of the measured pressures over the wing gave results which agreed very well with measured normal-force values for wings with flexible canopies. A typical spanwise-load-distribution diagram shown in this figure illustrates the unloading of the wing tip which is due, in part, to the effects of wing twist near the tips. It appears that approximately 70 percent of the total lift load is carried by the keel.

A simplified analysis has been made to obtain some information on the effects of suspension rigging on the magnitude and variations of the control forces. A few results are illustrated in figure 8 in which the calculated variations of the longitudinal stick forces with trimmed lift coefficients are given for three arrangements of the fore and aft suspension cables where the lengths and attachment parts were varied. The assumption was made that the cables passed through a common guide and were connected directly to the pilot's stick. Friction was neglected and a gross weight of 7,000 pounds was assumed. Zero control forces result when the weight vector bisects the angle between the two cables. Shifting of the weight vector due to change in trim produces a difference in the tension of the two cables. This difference must be balanced by a force on the control stick. The curves for the case of zero force are arbitrarily shown at a lift coefficient of 0.65. For all three

arrangements of the cables, the force variations are unstable; that is, when the stick is moved back to increase the lift coefficient or to decrease the speed a push force must be applied to maintain the stick at the desired position.

The length of the cables and the location of the attachment points are shown to affect the magnitude of the control forces. In all cases, however, the forces required to trim over the complete angle-of-attack range greatly exceed the normally specified limit for aircraft control systems. On the basis of this analysis, some form of control boost system must be used to control properly the parawing system utilizing the center-of-gravity shifting principle for control.

Some difficulty has been experienced with behavior of the wing canopy particularly at the trailing edge during various tests of the parawing. A series of tests is continuing in order to study the unsteady trailing-edge behavior. Preliminary results are shown in figure 9 for a particular model of the series. The trailing-edge flutter boundary has been established as a function of angle of attack and dynamic pressure over a range of Mach numbers. Various methods such as use of trailing-edge drawstrings and battens are being explored at the present time to minimize this behavior.

The results of some wind-tunnel tests of parawing models with flexible leading edges were used to obtain some indication of the effects of wing flexibility on the wing aerodynamic characteristics. Results of this analysis are given in figure 10 which shows the variations of $(L/D)_{\max}$, $C_{L,\max}$, and the estimated wing weight W/W_0 with the stiffness parameter $\frac{EI}{ql^4}$. The stiffness of the test models is calculated on

the basis of the deflection of the tip of the wing under a concentrated load. For the range of test conditions, increasing the wing stiffness parameter by a factor of about 3 had very little effect on $(L/D)_{\max}$, increased $C_{L,\max}$ somewhat, and increased the weight of the wing by a factor of 3. The curve for $C_{L,\max}$ was not well defined apparently due to the dependency of maximum lift on factors other than stiffness. It is necessary to evaluate the effects of wing stiffness on other characteristics, such as dynamic stability and control, before making conclusive remarks regarding leading-edge stiffness.

Figure 11 shows the variation of the stability parameter $\frac{\partial C_m}{\partial C_L}$ and the performance parameter $(L/D)_{\max}$ as a function of Mach number. The curves were obtained with an elastically scaled glider wing in combination with a rocket booster. The maximum lift-drag ratio changes


by a factor of 4 over the Mach number range of the test, while the stability parameter indicates about a 10-percent transonic shift.

Considerable work remains to be done in the area of deployment of the parawing under conditions to be encountered with the Apollo vehicle. Some preliminary deployment tests have been made utilizing a radio-controlled test model with a 6-foot parawing. These tests were intended to explore, in part, some of the dynamic problems associated with trailing the parawing behind the vehicle in a luffing condition as would occur following extraction from the vehicle and inflation of the member. The second part of the test was to study the dynamic behavior of the wing and body as the wing was forced to pitch up and carry the load of the vehicle and to evaluate methods for accomplishing this transition. Preliminary results have shown that the wing can be towed satisfactorily behind the vehicle and that a drogue parachute attached to the parawing used in combination with a line which controls the pitch rate of the wing relative to the body can be used to deploy the wing. It was estimated that the deployment loads were less than about 5g during a deployment from terminal-velocity conditions. The transition from the trailing condition of the wing to gliding flight was accomplished in about 7 seconds full-scale time.

The parawing has demonstrated the flare characteristic of other low-aspect-ratio wings, namely, that excess approach speed is required to overcome the high induced drag which rapidly dissipates the kinetic energy needed to complete the flare and touchdown. Flare characteristics of parawings have been demonstrated with free-flight models as well as the Ryan parawing experimental vehicle. Studies have shown that the flare should perform as rapidly as practical so as to conserve the available kinetic energy for making touchdown corrections.

CONCLUDING REMARKS

In summary, it is noted that a general review of the state of development of various devices which appear to be applicable to the Apollo vehicle indicates areas requiring additional technical information. At the present time considerable work is being done on the parawing to improve glide range and the ability to reduce the vertical velocity to zero at touchdown. The studies to date indicate that the parawing can be deployed, that stable and controllable configurations can be developed, and that control boost systems probably will be required to assist the pilot in controlling the vehicle.



BIBLIOGRAPHY

Drogue devices:

- Anon.: United States Air Force Parachute Handbook. WADC Tech. Rep. 55-265, ASTIA Doc. No. AD 118036, U.S. Air Force, Dec. 1956.
- Downing, J. Robert, Hawkins, Harold V., McClow, John H., Jr., and Pedersen, Paul E.: Recovery Systems for Missiles and Target Aircraft - Part III. High Subsonic and Transonic Track Borne Parachute Tests. A.F. Tech. Rep. 5853, Pt. III, Wright Air Dev. Center, U.S. Air Force, Dec. 1956.
- Dickens, Waldo L.: A Parachute Recovery Test of a Full-Scale Free-Flight Model of an Air-To-Surface Missile With Recovery Initiated at a Mach Number of 1.43. NASA TM X-451, 1961.
- Connors, James F., and Lovell, J. Calvin: Some Observations on Supersonic Stabilization and Deceleration Devices. Paper No. 60-19, Inst. Aero Sci., Jan. 1960.
- Maynard, Julian D.: Aerodynamics of Decelerators at Supersonic Speeds. Proc. of Recovery of Space Vehicles Symposium (Los Angeles, Calif.), Inst. Aero. Sci., Sept. 1960, pp. 48-54.
- Wiant, Harry W., and Fredette, Raymond O.: A Study of High Drag Configurations as First Stage Decelerators. WADC TN 56-320, U.S. Air Force, July 1956.
- Nebiker, F. R.: An Inflatable Balloon-Type Deceleration and Stabilization System for Recovery of Space Vehicles. [Preprint] 344C, Soc. Automotive Eng., 1961.
- Knight, R. E.: Recovery of an Earth Satellite. Rep. No. GER-8845, Goodyear Aircraft Corp., June 2, 1958.
- Engstrom, B. A., and Meyer, R. A.: Performance of Trailing Aerodynamic Decelerators at High Dynamic Pressures. Part III. Wind Tunnel Testing of Rigid and Flexible Parachute Models. WADC Tech. Rep. 58-284, U.S. Air Force, 1959.
- McShera, John T., and Keyes, J. Wayne: Wind-Tunnel Investigation of a Balloon as a Towed Decelerator at Mach Numbers From 1.47 to 2.50. NASA TN D-919, 1961.
- Maynard, Julian D.: Aerodynamic Characteristics of Parachutes at Mach Numbers 1.6 to 3. NASA TN D-752, 1961.

CONFIDENTIAL

Bowman, James S., Jr.: Dynamic Model Tests at Low Subsonic Speeds of Project Mercury Capsule Configurations With and Without Drogue Parachutes. NASA TM X-459, 1961.

Coats, Jack D.: Static and Dynamic Testing of Conical Trailing Decelerators for the Pershing Reentry Vehicle. AEDC-TN-60-188, Arnold Eng. Dev. Center, 1960.

Heinrick, Helmut G., and Riabokin, Toma: Analytical and Experimental Considerations of the Velocity Distribution in the Wake of a Body of Revolution. WADD TR-60-257, U.S. Air Force, 1959.

Barish, David T.: Technical Report Model Tests of Vortex Ring Parachute at the Princeton University 4 Ft. x 5 Ft. Wind Tunnel. Eng. Dept., Pioneer Parachute Co., Inc. (Manchester, Conn.), Feb. 19, 1959.

Barish, David T.: Technical Report on Vortex Ring Parachute Wind Tunnel Tests at United Aircraft Corporation on 13-15 April 1959. Project E-1574, Eng. Dept., Pioneer Parachute Co., Inc. (Manchester, Conn.), May 20, 1959.

Rotors:

Gessow, Alfred, and Myers, Garry C., Jr.: Aerodynamics of the Helicopter. The Macmillan Co., New York, c.1952.

Wernicke, R. K.: Preliminary Tests of Model Spacecraft Rotor Landing System. Rep. No. 8015-099-001, Bell Helicopter Corp., July 27, 1959.

Slaymaker, S. E., and Gray, Robin B.: Power-Off Flare-Up Tests of a Model Helicopter Rotor in Vertical Autorotation. NACA TN 2870, Jan., 1953.

Anon.: Technical Summary Rocopter Ballistic Carrier Studies. Rep. No. MD60-152, North American Aviation, Inc., April 19, 1960.

Anon.: Final Report of KRC-4. Rotochute Development. Rep. No. R-239 (Contract No. Nonr 901(00)), The Kaman Aircraft Corp., Aug. 1, 1958.

Anon.: Summary of Rotochute Development. Rep. No. R-117 (Contract No. Nonr 901(00)), The Kaman Aircraft Corp., Sept. 25, 1956.

Anon.: Preliminary Report on Rotochute Development. Rep. No. R-29 (Contract No. Nonr 901(00)), The Kaman Aircraft Corp., Oct. 15, 1953.



Scheiman, James: Preliminary Look at Rocket Stage Recovery With a Rotochute. WADC Tech. Rep. 59-481, U.S. Air Force, July 1959.

Anon.: Tests of Rotorchutes. WADC Tech. Rep. 52-125, U.S. Air Force, June 1952.

Anon.: Low Speed Wind Tunnel Test of 12 Ft. and 14 Ft. Diameter Rotochute. Rep. No. T-93 (Contract No. Nonr 901(00)), The Kaman Aircraft Corp., Jan. 22, 1957.

Herron, R. D., and Binion, T. W., Jr.: Tests of the Kaman KRC-6M Rotochute at Transonic Speeds. AEDC-TN-61-60 (Contract No. AF 40(600)-800 S/A 11(60-110)), Arnold Eng. Dev. Center, May 1961.

Haig, C. R., Jr.: Aerodynamic Analysis of a Rotor in the Fully Stalled Propeller Braking State. Rep. No. 8008-099-003, Bell Helicopter Corp., March 10, 1960.

Blottner, F. G.: Stability of an Aerodynamic Body With a Rotor. SC-4139 (TR), Sandia Corp. (Albuquerque, N. Mex.), Dec. 1957.

Liberatore, E. K.: Roto-Chute Handbook. Rep. No. 28-93-3, Prewitt Aircraft Co. (Clifton Heights, Pa.), Feb. 14, 1951.

Goldman, Robert L.: Some Observations on the Dynamic Behavior of Extremely Flexible Rotor Blades. Paper No. 60-44, Inst. Aero. Sci., Jan. 1960.

Wings and lifting surfaces:

Rogallo, F. M., and Lowry, J. G.: Flexible Reentry Gliders. Preprint No. 175C, Soc. of Automotive Eng., Apr. 1960.

Rogallo, Francis M., Lowry, John G., Croom, Delwin R., and Taylor, Robert T.: Preliminary Investigation of a Paraglider. NASA TN D-443, 1960.

Naeseth, Rodger L.: An Exploratory Study of a Parawing as a High-Lift Device for Aircraft. NASA TN D-629, 1960.

Ware, George M.: Static Stability and Control Characteristics at Low-Subsonic Speeds of a Lenticular Reentry Configuration. NASA TM X-431, 1960.

Hewes, Donald E.: Free-Flight Investigation of Radio-Controlled Models With Parawings. NASA TN D-927, 1961.

~~CONFIDENTIAL~~

- Dennis, David H., and Edwards, George G.: The Aerodynamic Characteristics of Some Lifting Bodies. NASA TM X-376, 1960.
- Kenyon, George C., and Edwards, George G.: A Preliminary Investigation of Modified Blunt 13° Half-Cone Re-Entry Configurations at Subsonic Speeds. NASA TM X-501, 1961.
- Paulson, John W., Shanks, Robert E., and Johnson, Joseph L.: Low-Speed Flight Characteristics of Reentry Vehicles of the Glide-Landing Type. NASA TM X-331, 1960.
- Smith, Willard G.: A Wind-Tunnel Investigation at Subsonic and Low Supersonic Speeds of a Reentry Vehicle With Retractable Wings. NASA TM X-398, 1961.
- Spencer, Bernard, Jr.: An Investigation at Subsonic Speeds of the Longitudinal Aerodynamic Characteristics at Angles of Attack From -4° to 100° of Delta-Wing Reentry Configurations Having Vertically Displaced and Cambered Wing-Tip Panels. NASA TM X-440, 1961.
- Ware, George M.: Low-Subsonic-Speed Static Longitudinal Stability and Control Characteristics of a Winged Reentry-Vehicle Configuration Having Wingtip Panels That Fold Up for High-Drag Reentry. NASA TM X-227, 1960.
- Shanks, Robert E.: Investigation of the Low-Subsonic Stability and Control Characteristics of a Hypersonic Boost-Glide Type Airplane With Wing, Fuselage, and Vertical-Tail Modifications. NASA TM X-450, 1961.
- Ware, George M., and Shanks, Robert E.: Investigation of the Low Subsonic Stability and Control Characteristics of a Model of a Hypersonic Boost-Glide Airplane Designed for High Lift-Drag Ratios at Low Speeds. NASA TM X-534, 1961.
- Kane, M. T.: A Guided Parachute System. Proc. of the Recovery of Space Vehicles Symposium (Los Angeles, Calif.), Inst. Aero. Sci., Sept. 1960, pp. 35-39.
- Anon.: Pararescue Personnel Parachute. WCLE - 55-72, Air Res. and Dev. Command, U.S. Air Force.
- Ewing, E. G.: Radioplane Dirigible Parachute Development. Rep. No. PTM-332, Radioplane (Van Nuys, Calif.), Feb. 1961.

~~SECRET~~ 435

Rockets:

Charczenko, Nickolai O., and Hennessy, Katherine W.: Investigation of a Retrorocket Exhausting From the Nose of a Blunt Body Into a Supersonic Free Stream. NASA TN D-751, 1961.

Ewing, E. G.: A Minimum Weight Landing System for Interplanetary Spacecraft. Proc. of the Recovery of Space Vehicles Symposium (Los Angeles, Calif.), Inst. Aero. Sci., Sept. 1960, pp. 40-47.

Weber, Richard J., and Pauson, Werner M.: Some Thrust and Trajectory Considerations for Lunar Landings. NASA TN D-134, 1961.

Fisher, Lloyd J., Jr.: Landing Energy Dissipation for Manned Reentry Vehicles. NASA TN D-453, 1960.

~~SECRET~~ L

TABLE I
RECOVERY SYSTEM DEVICES

Type	Specific device	Primary function	Sources of recent information	Remarks
Drogue	Conventional parachute	Deceleration Stabilization Vertical descent	General research effort by industry and government agencies on uses for speeds up to supersonic	Restricted to uses below about $M = 2.5$ Useful as backup system Cannot correct for drift due to winds
	Vortex-ring parachute	Deceleration Stabilization Vertical descent	Thomas Barish (Consulting Eng.) Pioneer Parachute Co., Inc. Air Force (WADD) NASA	Very stable and offers weight savings over conventional parachutes Limited data
	Rigid or inflatable cone, ring or balloon	Deceleration Stabilization	General research effort	Useful at supersonic speeds
Rotor	Rigid	Deceleration Maneuvering Touchdown flare and hovering	Kaman Aircraft Corp. Bell Helicopter Corp. NASA	Provides glide, hovering, and flared landing capability Requires extensive studies of stowage, deployment, stability and control
	Flexible	Deceleration Maneuvering Touchdown flare and hovering	Thomas Barish (Consulting Eng.) Vidya, Inc. Vertol Aircraft Corp. NASA	Provides glide, hovering, and flared landing capability Requires extensive studies of stowage, deployment, stability and control Very meager data Employs thin metal and cloth blades
Lifting surfaces	Rigid wing	Maneuvering Touchdown	General research effort on Dyna-Soar and other configurations	Provides glide and flared landing capability Must be compatible with reentry requirements
	Flexible and inflatable wing (Parawing)	Maneuvering Touchdown	Goodyear Aircraft Corp. North American Aviation, Inc. Ryan Aeronautical Co. Army (TRECOM) NASA	Provides glide and flared landing capability See table II
	Lifting body	Maneuvering Touchdown	General research effort on lenticular and other configurations Provides glide and flare landing capability	Generally requires use of auxiliary surfaces or devices to provide stability and control Must be compatible with reentry requirements
	Guided parachute	Descent Limited maneuvering	Sandia Corp. Radioplane Div. of Northrop Corp. Air Force (ARDC)	Appears to be capable of reducing drift to zero at touchdown Very meager data
Rocket (liquid or solid)	Thrust rocket	Glide range extension Assist landing	Reaction Motors Div., Thiokol Chemical Corp.	Use with rotor and wing devices Has been developed for use on helicopters
	Retrorocket	Deceleration at touchdown Lunar landings	General research effort	Use with maneuvering descent and devices to dissipate the final touchdown velocities Very meager data
	Control rocket	Roll, yaw, and pitch control	General research effort	Required for lunar landing Information available from use on X-15 and Mercury spacecraft

TABLE II
CURRENT PARAWING RESEARCH

Study area	Type of study	Variables	Measurements	Remarks
Performance	Wind tunnel ($M = 0.10$)	Planform Leading-edge sweep Leading-edge radius Trailing-edge camber	Static longitudinal and lateral aerodynamic forces and moments	Wing-alone tests Rigid leading edges and keel Determine optimum wing geometry
	Wind tunnel ($M = 0.10$)	Wing size ($W/S = 2, 6, 10$) Wing flexibility	Static longitudinal and lateral aerodynamic forces and moments Wing structure and canopy deformation	Elastically scaled model of complete configuration
Stability and control	Wind tunnel ($M = 0.10$)	Wing size ($W/S = 2, 6, 10$) Wing flexibility	Static longitudinal and lateral aerodynamic forces and moments Wing structure and canopy deformation	Elastically scaled model of complete configuration
	Free flight (low subsonic)	Rigging Center-of-gravity location and travel Wing size Wing flexibility	Motion-picture records of dynamic behavior	Approximately 1/5-scale radio-controlled model of a complete configuration, rigid wing structure Model with 19-foot inflatable wing
	Analytical	Parametric variation of aerodynamic and structural characteristics of complete configuration	Time histories of dynamic behavior Control forces	Flare capability Dynamic control response Control power requirements
Deployment	Wind tunnel (subsonic to supersonic)	Deployment methods Wing flexibility Wing loading	Time histories of deployment Deployment loads	Elastically scaled model
	Free flight (low subsonic)	Deployment methods Wing flexibility Wing size	Motion-picture records of dynamic behavior	Approximately 1/5-scale radio-controlled model with rigid wing structure Radio-controlled model with inflatable wing structure
Aerodynamic loads distribution	Wind tunnel ($M = 0.15$ to 4.65)	Leading-edge sweep	Upper and lower surface pressure distribution	Completely rigid wing
	Wind tunnel ($M = 0.10$)	Wing geometry	Vertical and horizontal bending moments in wing leading edges	Wing-alone tests Rigid leading edges and keel Determine optimum wing geometry
	Analytical	Wing flexibility Wing loading	Photographs of loaded elastically scaled wings	Calculation of wing bending moments from wing deflection
Aeroelastic	Wind tunnel (subsonic to transonic)	Wing flexibility Wing size	Flutter characteristics of wing structure and canopy	Rigid and elastically scaled wing structure

037120 [REDACTED]

PARAWING SYSTEM

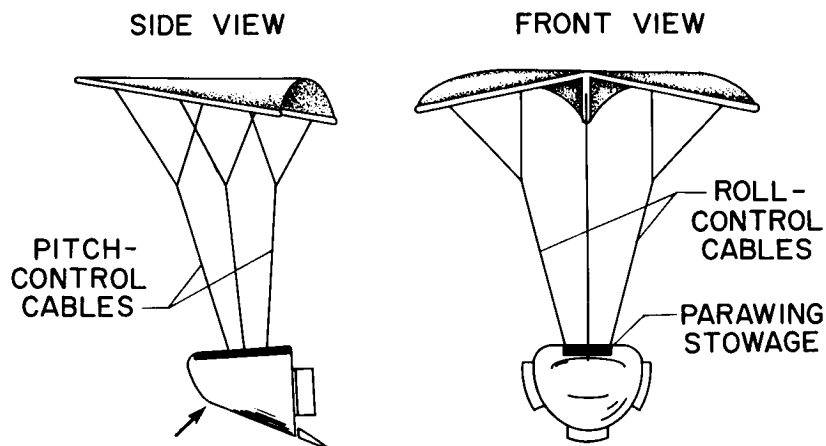


Figure 1

LONGITUDINAL AERODYNAMIC CHARACTERISTICS OF WING ALONE ($\Delta = 90^\circ$; $\Lambda = 55^\circ$)

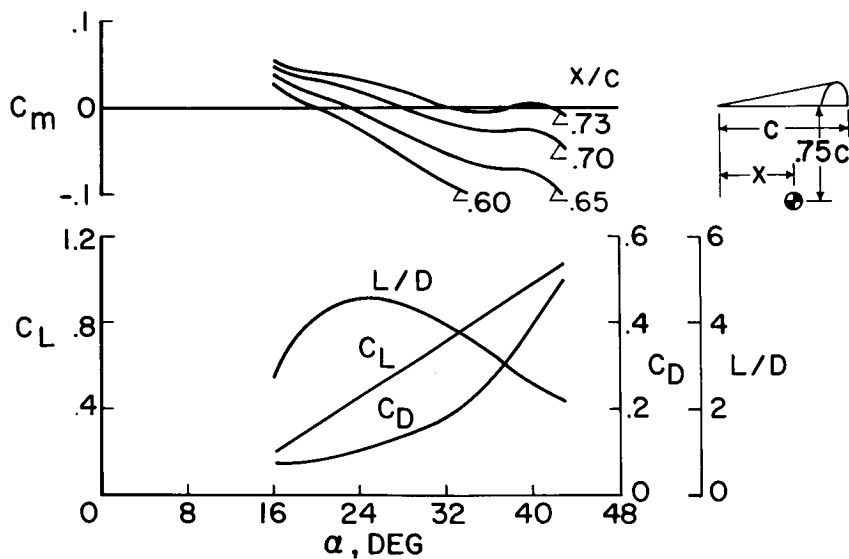


Figure 2

EFFECT OF PARAWING LEADING EDGE SWEEP ON
 $C_{L\alpha}$ AND $C_{L, MAX}$
 $\Delta = 90^\circ$

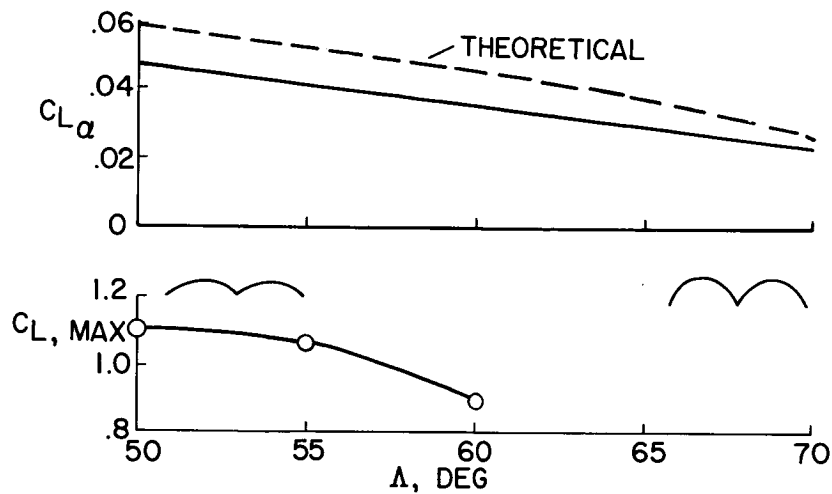


Figure 3

EFFECT OF PARAWING LEADING EDGE SWEEP
 ON $(L/D)_{MAX}$; ($\Delta = 90^\circ$)

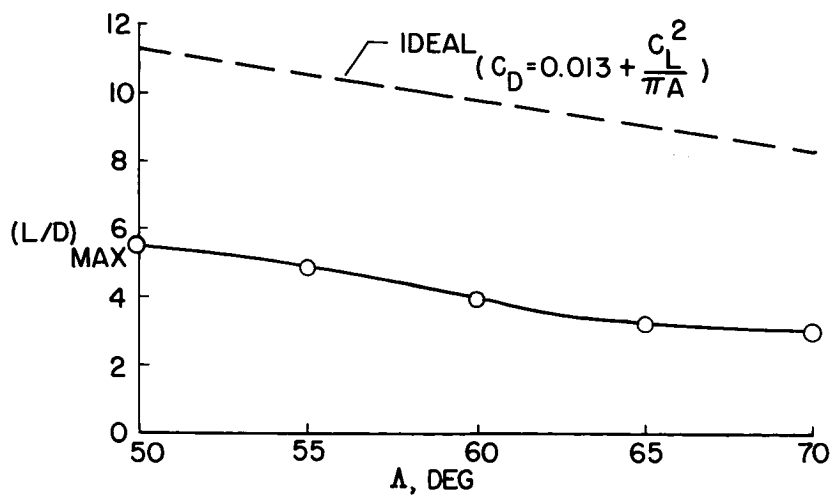


Figure 4

037120A [REDACTED]

EFFECT OF CANOPY SIZE IDENTICAL PROJECTED PLANFORM $\Delta = 60^\circ$

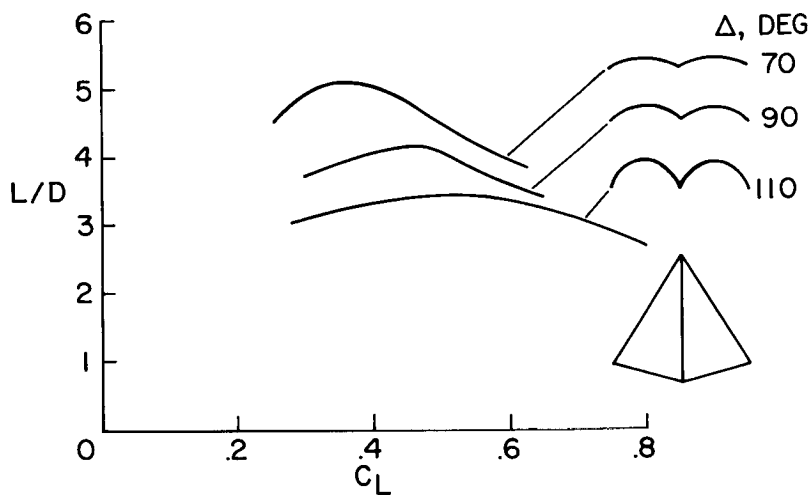


Figure 5

EFFECT OF SWEEP ON WING-ALONE LATERAL-STABILITY PARAMETERS $\Delta = 90^\circ$

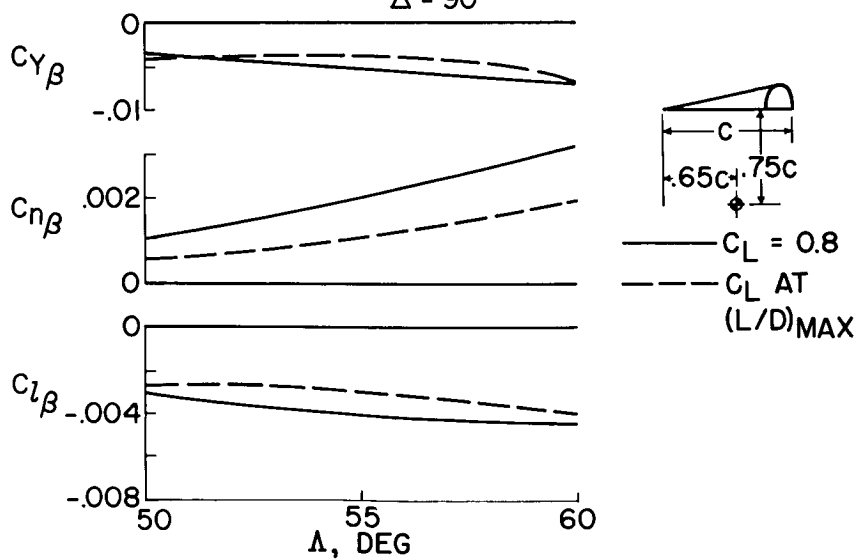


Figure 6

[REDACTED]

TYPICAL AIR-LOAD DISTRIBUTION AT $\alpha = 30^\circ$

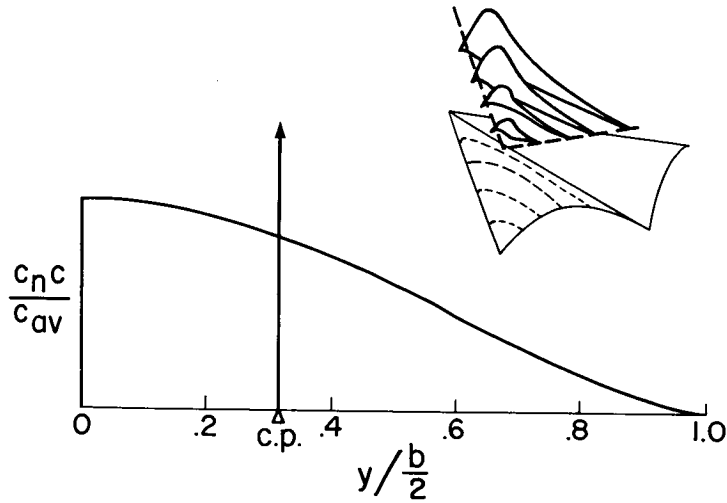


Figure 7

EFFECT OF CABLE RIGGING ON CONTROL FORCES $W = 7,000$ LB

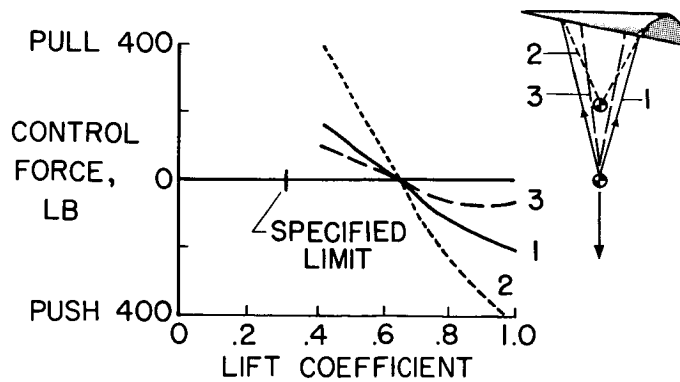


Figure 8

TRAILING-EDGE FLUTTER

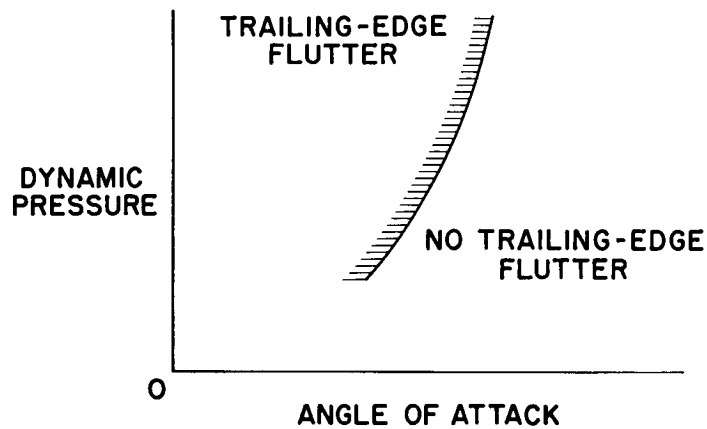
 $M_\infty = 0.10$ AND 1.05 

Figure 9

EFFECT OF PARAWING FRAME STIFFNESS

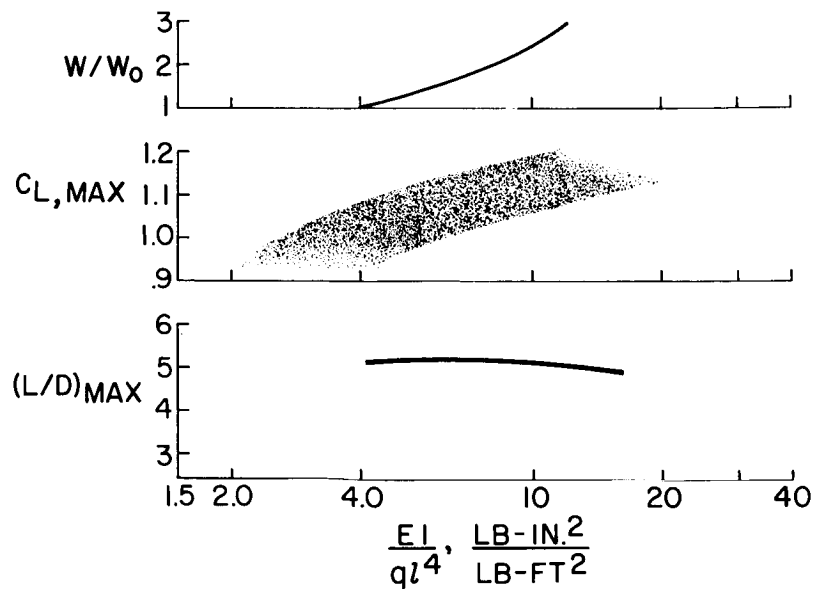


Figure 10

EFFECT OF MACH NUMBER ON STABILITY AND LIFT-DRAG RATIO

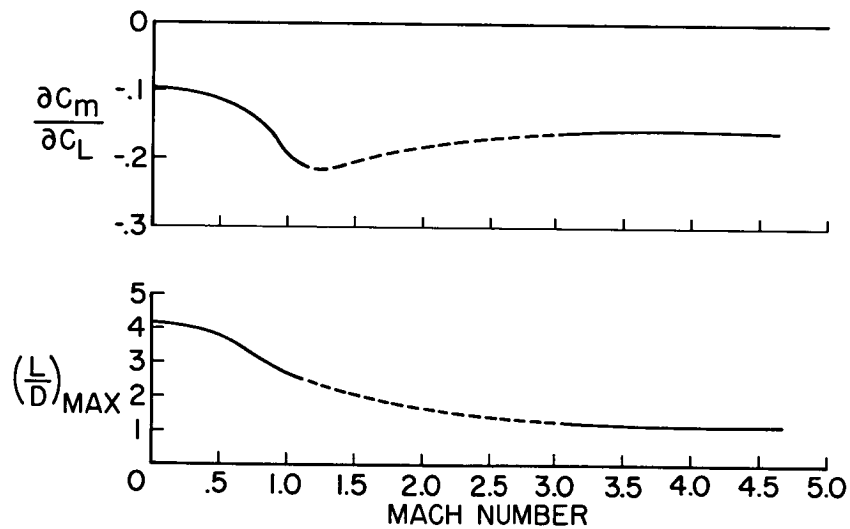


Figure 11

LANDING-IMPACT-DISSIPATION SYSTEMS

By Lloyd J. Fisher, Jr.

Langley Research Center

SUMMARY

Analytical and experimental investigations have been made to determine the landing-energy-dissipation characteristics for several types of earth-landing-impact systems having application to Project Apollo. The areas of study are divided into three velocity regions: (1) those having primarily vertical velocity, (2) those having both moderate horizontal and moderate vertical velocity, and (3) those having primarily horizontal velocity. The impact systems discussed are braking rockets, gas-filled bags, frangible metal tubing, aluminum honeycomb, balsa wood, strain straps, and both skid and skid-rocker landings on hard-surface runways and on water.

It appears feasible to evaluate landing-gear systems for an Apollo type of vehicle by computational methods and free-body landing techniques with dynamic models. There are several ways of dealing with the vertical energy dissipation for an earth landing of such a vehicle. Some systems are more efficient than others, some package better than others, and a variety of promising systems are under study. Horizontal energy dissipation is simpler to deal with than vertical energy dissipation since translational friction is all that is involved; however, runout behavior becomes a factor. Vertical velocity can also be a big factor when high flight-path angles are associated with even moderate horizontal velocities. High-speed landings are particularly a problem, especially high-speed water landings, and indications are that if large horizontal velocities are involved in hard-surface landings, a selected site will be required.

INTRODUCTION

The approach parameters for letdown systems having application to Project Apollo are found to divide the landing-energy-dissipation problem into three velocity regions. This paper is concerned with earth landings in these categories and, in particular, with soft landings survivable by man. The areas of study are illustrated in figure 1. The velocity regions are (1) those having primarily vertical velocity,

(2) those having both moderate horizontal and moderate vertical velocity, and (3) those having primarily horizontal velocity. The prime example of vertical velocity is the parachute letdown system. In its simplest application the parachute system would have vertical velocity only but in the more likely operational case the parachute letdown is complicated somewhat by the horizontal velocity that occurs with a landing in a wind or with a guided chute. Provisions must therefore be made for translation along the landing surface and for preventing dangerous turnover. The second area of study applies to the large and lightly loaded paraglider system which can have less vertical velocity than the parachute (approaching zero), but must have horizontal velocity and thus a slide-out capability. The third area encompasses high horizontal velocity as associated with conventional airplane landings and includes the high lift bodies, the winged space vehicles, and the small and highly loaded paragliders. Vertical velocity is still a design requirement but to much less a degree than in the first area. Runout performance is the most critical problem in this category.

DISCUSSION

A short motion-picture film supplement illustrating the effects discussed in this paper has been prepared and is available on loan.¹

Vertical Velocity Landings

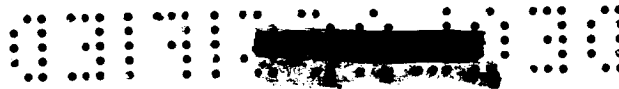
The landing-impact energy dissipation for the various configurations depends on the vertical velocity V_v of the vehicle at contact, the stroke geometry of the system, and the usable energy of the dissipation material. The case of parachute letdown with vertical velocity only which lends itself to an analysis based on materials involved will be considered first. For comparison, the forces are vertical; there are no side forces. Figure 2 shows results from a weight study of several such energy dissipation systems. The energy dissipators investigated consist of braking rockets, gas-filled bags, frangible metal tubing, aluminum honeycomb, and balsa wood. The weight was determined by adding the dissipator weight and assumed dissipator attachment weight, but the parachute weight was not included. All these systems are familiar ones except perhaps the frangible tube. This is a system for working metal to its ultimate strength and through a large percent of its length. An example of a frangible-tube installation could be a hard aluminum-alloy tube attached to a vehicle and a

¹This motion-picture film supplement (L-649) can be obtained from NASA Headquarters, Code ETV, Washington, D.C.

die attached to a landing skid or foot. (See fig. 3.) The tube presses over the die during impact and fails in fragments as shown. Because of structural considerations, the gas bags, frangible tube, honeycomb, and balsa wood systems (fig. 2) are short-stroke devices and for low g application (10g is used here) are most suitable at contact velocities of the order of 20 to 40 feet per second. There is a practical limit on usable stroke with these devices so the data were not extended to higher speeds because of suspected buckling failure at the correspondingly higher strokes required. The braking rocket, shown by the dashed line, has completely different characteristics from the dissipators described and is more suitable at longer strokes and higher speeds. The data for the braking rocket are based on duration, thrust, and weight of actual rockets and include the weight of both propellant and rocket case. There is a large difference weightwise between the several systems, with the frangible tube, honeycomb, and balsa wood being the lightest at the lower speeds but not suitable at the higher speeds because of structural difficulties. The braking rocket is more suitable at the higher speeds. The adaptability of the systems to attachment, packaging, and environment must be considered when choosing a landing gear. For example, the gas bag, even though somewhat heavy, is very adaptable to packaging, whereas some of the lighter weight systems are bulky.

A photograph of a model of the L-2C vehicle having a frangible tube system installed between the capsule and what could be the heat shield is shown in figure 4. There are four tubular legs made of 2024-T3 aluminum alloy. A snubber cord is seen at the center of the model. The tubes on an actual installation would be made retractable, probably by pivoting. Figure 5 is a sequence photograph of a vertical landing of this model in which velocity at contact simulates 30 feet per second. The strut length was chosen so that about three-fourths of the length of the tube would be used up in the experiment. The fragments of the tube can be seen as they scatter.

An acceleration time history of this landing is shown in figure 6. The peak at the beginning of the experimental curve (dashed line) is a typical starting load which could be regulated by precrushing the end of the frangible tube instead of using a squared-off tube as in this case. The peak at the end of the curve is due to a combination of a rate effect and the falling off of the stopping load below that required for continued fragmentation. The computed curve (solid line) is based on a force of 40 percent of the yield value of the material. This average load is an arbitrary value dependent on the curvature of the die used. The 40-percent value is considered a good workable compromise between a die curvature that is too hard and one that is too soft. The rectangular shape of the time-history curve indicates an efficient use of stopping distance for the frangible-tube system.



Water landings are another very useful way of dissipating the energy of a vertical letdown system. There are several NASA reports available on the subject and, since the recommended shapes are well known, they will not be discussed here. (See refs. 1 to 3.)

Moderate Horizontal and Vertical Velocity Landings

The problems of moderate horizontal velocity V_h due to a wind during parachute letdown or in a landing of a large area paraglider have been investigated with models of several reentry vehicles suitable for Apollo. Vertical force can be dissipated in much the same way as previously discussed. A landing skid or some such device is required for horizontal translation, and horizontal force must be dissipated by friction. Skid shapes investigated have been those of the heat shields for the vehicles shown in figure 7. Shown here are vehicles having a flat bottom or skid with a turned-up bow, a spheroidal-shaped skid, and a longitudinal curved skid. Dynamic model investigations have been made with these vehicles with several energy dissipation systems. Landings were made on a smooth hard surface, on sand, and on water. The sand was not meant to represent any particular full-scale terrain but was chosen to simulate a landing surface with penetration characteristics between those of the smooth hard surface and water.

The following sequence photographs (figs. 8 to 12) of dynamic models illustrate the characteristic landing behavior for several vehicles and systems at moderate horizontal speeds. The first sequence (figs. 8 to 11) shows landings on hard-surface runways. Full-scale speeds are given.

Figure 8 shows the model with frangible tubes for load alleviation. Alinement links are used to take shear loads. The landing speed is 18 feet per second horizontal and 13 feet per second vertical.

Figure 9 shows a landing with a flat-bottom skid and multiple-air-bag load alleviators. Landing speed is 60 feet per second horizontal and 30 feet per second vertical. The bags are installed between the capsule and the heat shield. Since air bags cannot take shear loads, alinement links are used and the bags are angled forward.

Figure 10 shows a sand landing of the vehicle with a longitudinally curved bottom. Landing speed is 30 feet per second horizontal and 15 feet per second vertical.

Figure 11 illustrates a landing of the vehicle having a spheroidal-shaped bottom used as a skid-rocker whereby vertical energy is converted into a rocking oscillation. Horizontal velocity is 80 feet per second.



DECLASSIFIED

449

Vertical velocity is low. The oscillation is dissipated by a combination of friction force and aerodynamic damping and the curvature of the bottom regulates acceleration. The relationships of the center-of-gravity height to skid-rocker length determine whether the vehicle will overturn.

Shapes and sizes such as are generally associated with the heat shields of manned reentry vehicles will begin to skip from the water surface at speeds of about 80 feet per second as shown in the next sequence (fig. 12). Figure 12 shows that skipping was slight for the vehicle with a spheroidal-shaped bottom. The vehicle with the longitudinally curved bottom and the flat-bottomed vehicle made somewhat longer skips.

There is nothing particularly wrong with skipping in itself but, if the landing speed is very high, the conditions of subsequent impacts are unpredictable.

Examples of the results obtained in investigations of the type just described are given as follows. All values are full scale. Turnover characteristics for skid-rocker landings of the L-2C type of vehicle at horizontal velocities of 30 feet per second and 80 feet per second and a vertical velocity of 10 feet per second are presented in figure 13. Experimental model landings were made on a hard-surface runway at friction coefficients of about 0.35 to 0.45. The open points indicate stable landings and the closed points indicate turnover. Computed limits of stability for friction coefficients C_F of 0.35 and 0.45 are shown by the solid lines. An attitude range of about -40° to 15° is satisfactory for ratio of center-of-gravity height to base diameter of 0.2, for example. At a higher center-of-gravity location the attitude range is reduced as indicated by the data points and limit lines. However, these are fairly reasonable attitude ranges. Acceleration in the landings (not counting turnover) was very low, about 3 or 4g. Landings made on a softer surface such as sand or on a hard surface at a higher friction coefficient would show narrower limits for stability and thus would indicate that the rocker bottom concept is critical to friction coefficient. The equations of motion show that turnover is independent of change in horizontal velocity and this is substantiated by the model test for the range of touchdown speeds investigated.

Figure 14 shows data for landings with multiple air bags on the flat-bottom L-1 vehicle at a vertical velocity of 30 feet per second. The shape of the acceleration-time-history curves indicates the characteristic triangular pattern for the gas bag with a fairly low rate of application of acceleration. The dashed lines show experimental data; one curve is for zero horizontal velocity, and one for a horizontal velocity of 30 feet per second. The difference in acceleration is due

03:11:30

to an interaction through the drag link and the angular setting of the bags. A computed curve (solid line) for zero horizontal velocity shows good agreement with experiment.

Horizontal Velocity Landings

The third category, encompassing high horizontal speed, is obtained with winged or lifting bodies and is primarily a condition of long runout; the runout behavior is then the most critical problem. In this category special methods of load alleviation which are adaptable to the heat requirement of space vehicles and which offer weight savings over conventional wheel landing gear have been investigated.

The following sequence photographs show some of the horizontal landing concepts which have been investigated. Figure 15 shows a landing of a model of a winged reentry vehicle having an all-skid landing gear incorporating strain-strap shock absorbers. Landing speed is 185 feet per second. Directional stability is very good with this gear.

Figure 16(a) shows a skid-rocker landing at 150 feet per second for a lenticular-shaped lifting body having deployable tail panels for control and for flaring into a conventional piloted type of horizontal landing. (See ref. 4.) Water landings with the lenticular vehicle, however, presented greater problems than the hard-surface landings. (See fig. 16(b).) The model frequently made a second or third contact in an uncontrolled condition. Ditching aids were not effective in improving the water landings of this vehicle; therefore, some consideration was given to reducing the landing speed. Devices such as drogue chutes or braking rockets might be suitable if adequate control could be obtained. Figure 16(c) shows a water landing of the model at a horizontal speed about one-half of the normal landing speed. Skipping was appreciably reduced.

The water landing behavior at high speeds of the manned reentry bodies is not greatly changed by using a different bottom shape. This fact is illustrated in figure 17 with the flat-bottom L-1 vehicle at 130 feet per second. The landing simulates approach conditions resulting with a small highly loaded paraglider. Behavior was much the same as that of the curved bottom vehicle; however, the flat-bottom vehicle is susceptible to higher peak accelerations.

Shown in figure 18 is a sketch of the all-skid gear investigated on the winged vehicle. The gear incorporates energy dissipators of the strain-strap type in combination with landing skids. The strain strap is a replaceable element which fails by plastic yielding and the skids

L

move aft and up. There is no bounce with such a gear. Questions have been raised concerning the landing runout stability of an all-skid gear but it has been found that a properly designed gear is directionally stable. In general, runout stability was satisfactory for landings at angles of roll and yaw up to 10° , the maximum investigated. The friction coefficient for the nose skid was 0.25 and for the main skid was 0.5 in these investigations. The difference in friction force between the front and rear skids is the major factor in the stability of the gear.

The peak normal and angular accelerations for the strain-strap energy dissipator on the winged vehicle are given in figure 19. The accelerations are relatively low, approximately 3g normal and 10 radians/sec² angular during landings at design sinking speeds of 4 to 12 feet per second. The data also show that the landing normal loads are constant with sinking speed as expected and computed for the strain-type energy dissipator as long as there is sufficient stroke.

Figure 20 shows acceleration time histories for a hard-surface landing of the lenticular vehicle. The sketches illustrate the rocking motion which converts the sinking speed energy into angular energy and stops the fall of the center of gravity as the vehicle rocks through 0° attitude. A small tail-skid shock absorber eases the vehicle onto the runway and very low acceleration occurs at initial contact. A maximum normal acceleration of about 5g occurs when the vehicle first rocks through 0° . Maximum angular acceleration of about 18 radians/sec² also occurs at this condition. The significant feature of this energy dissipation system is that, since the bottom of the vehicle serves as both a heat shield and as a skid rocker, only a small part of the weight of the vehicle is directly chargeable to the landing gear.

CONCLUDING REMARKS

It appears feasible to evaluate landing-gear systems for an Apollo type of vehicle by computational methods and free-body landing techniques with dynamic models. There are several ways of dealing with the vertical energy dissipation for an earth landing of such a vehicle. Some systems are more efficient than others, some package better than others, and a variety of promising systems are under study. Horizontal energy dissipation is simpler to deal with than vertical energy dissipation since translational friction is all that is involved; however, runout behavior becomes a factor. Vertical velocity can also be a big factor when high flight-path angles are associated with even moderate horizontal velocities. High-speed landings are particularly a problem, especially high-speed water landings and indications are that, if large

03:11:24:030
[REDACTED]

horizontal velocities are involved in hard-surface landings, a selected site will be required.

REFERENCES

1. McGehee, John R., Hathaway, Melvin E., and Vaughan, Victor L., Jr.: Water-Landing Characteristics of a Reentry Capsule. NASA MEMO 5-23-59L, 1959.
2. Vaughan, Victor L., Jr.: Water-Landing Impact Accelerations for Three Models of Reentry Capsules. NASA TN D-145, 1959.
3. Vaughan, Victor L., Jr.: Landing Characteristics and Flotation Properties of a Reentry Capsule. NASA TN D-653, 1961.
4. Blanchard, Ulysse J.: Landing Characteristics of a Lenticular-Shaped Reentry Vehicle. NASA TN D-940. (Prospective NASA paper.)

[REDACTED]

LANDING CONFIGURATIONS AND VELOCITY REGIONS

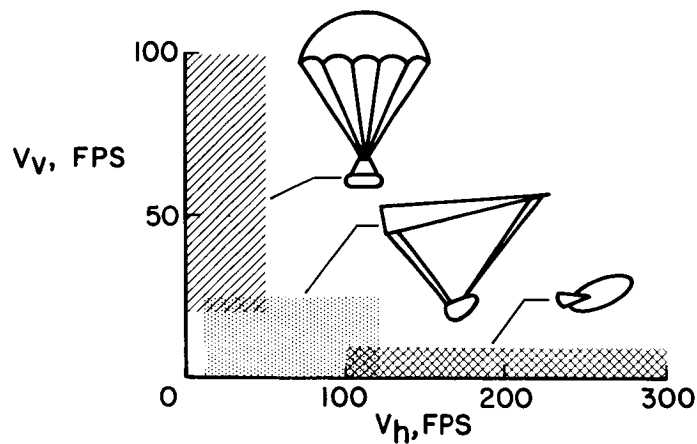


Figure 1

WEIGHTS OF LANDING SYSTEMS VERTICAL DESCENT; 7,000 LB ; 10 g AVERAGE

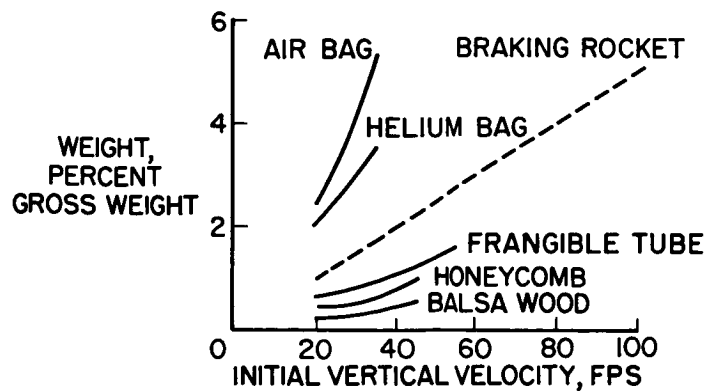


Figure 2

03171224 0300
[REDACTED]

FRANGIBLE-TUBE SYSTEM

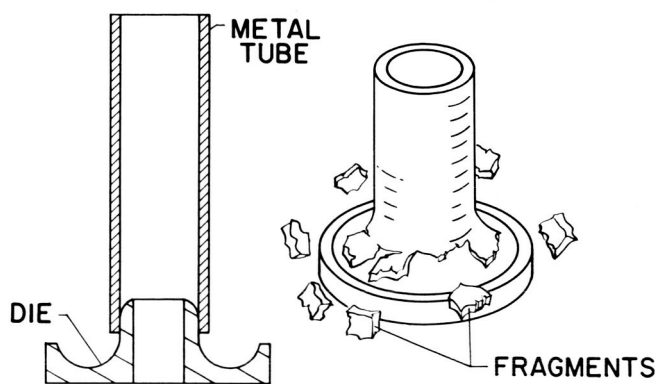


Figure 3

MODEL WITH FRANGIBLE-TUBE LOAD ALLEVIATORS

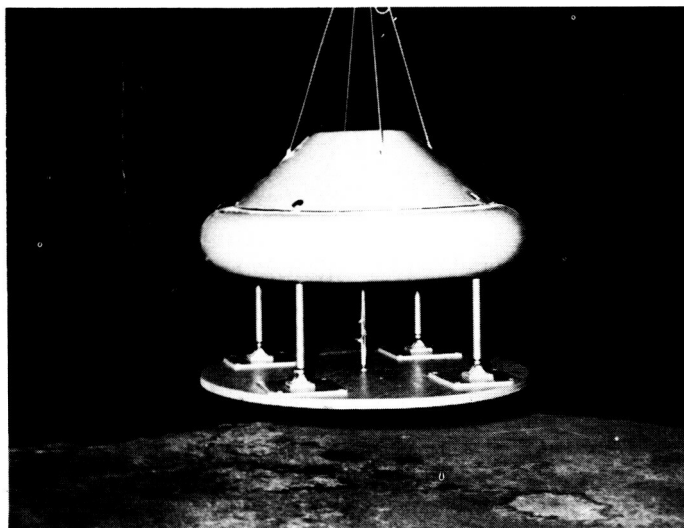


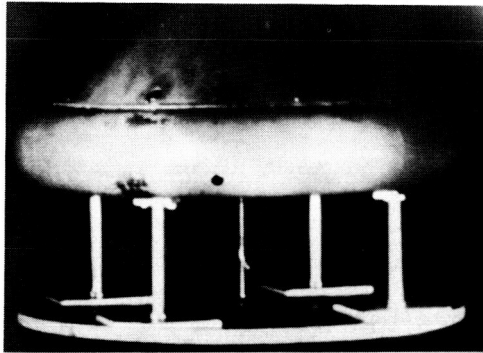
Figure 4

L-61-3475

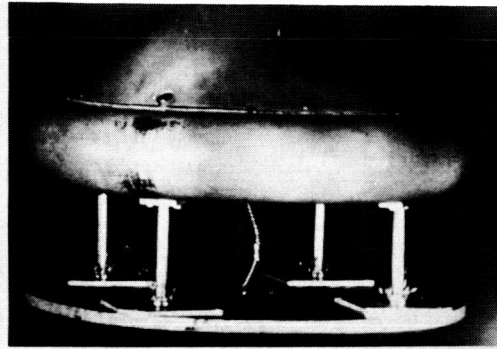
DECLASSIFIED

455

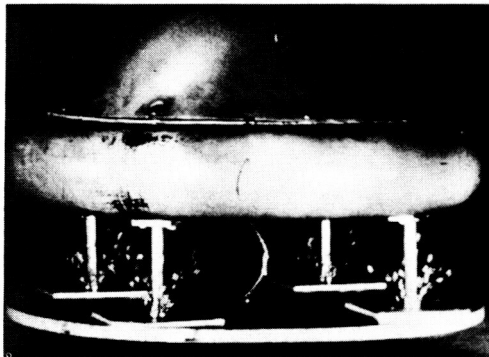
FRANGIBLE-TUBE MODEL LANDING ON CONCRETE
VERTICAL DESCENT; $V_V = 30$ FPS



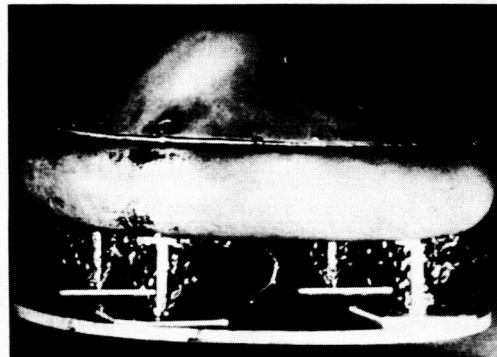
1



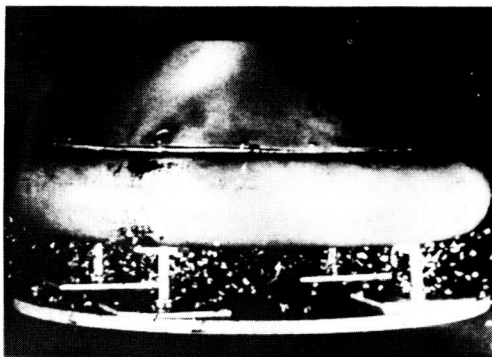
2



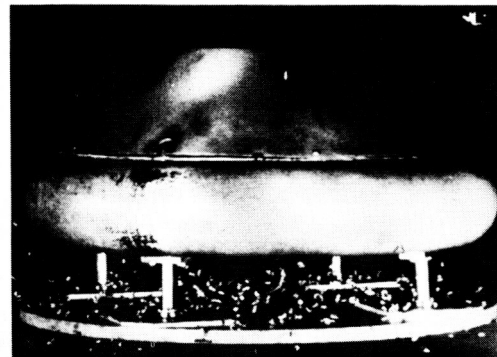
3



4



5



6

Figure 5

L-61-4808

DECLASSIFIED

031712001030

FRANGIBLE-TUBE LOAD ALLEVIATOR VERTICAL DESCENT; 30 FPS

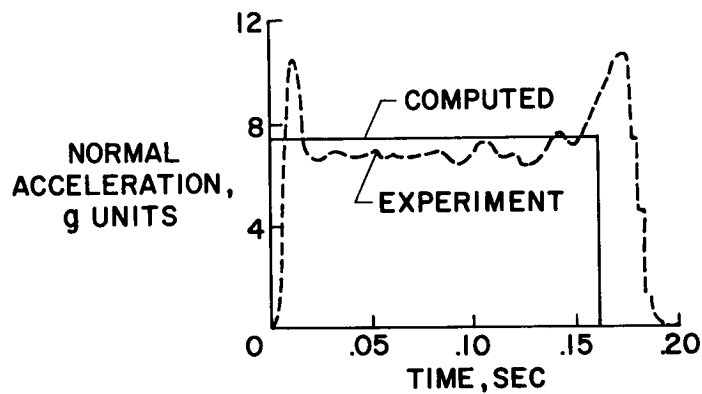


Figure 6

LANDING CONFIGURATIONS

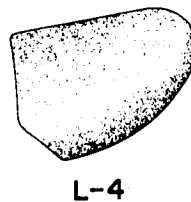
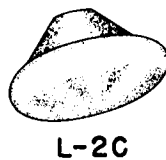
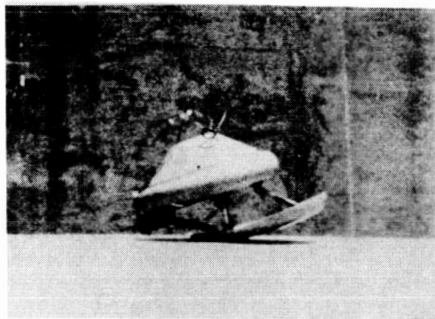


Figure 7

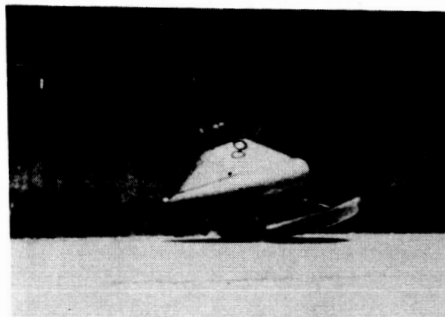
DECLASSIFIED

457

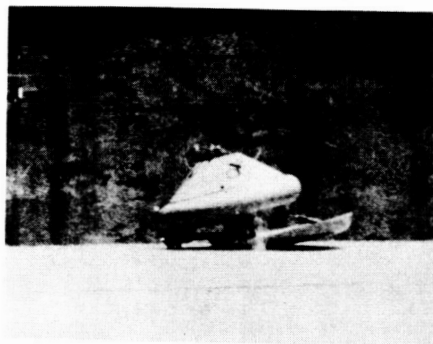
FRANGIBLE-TUBE MODEL LANDING ON CONCRETE
 $V_h = 18$ FPS; $V_v = 13$ FPS



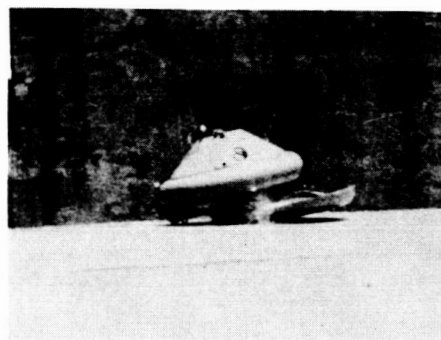
1



2



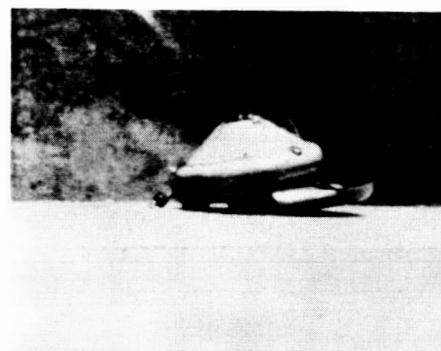
3



4



5



6

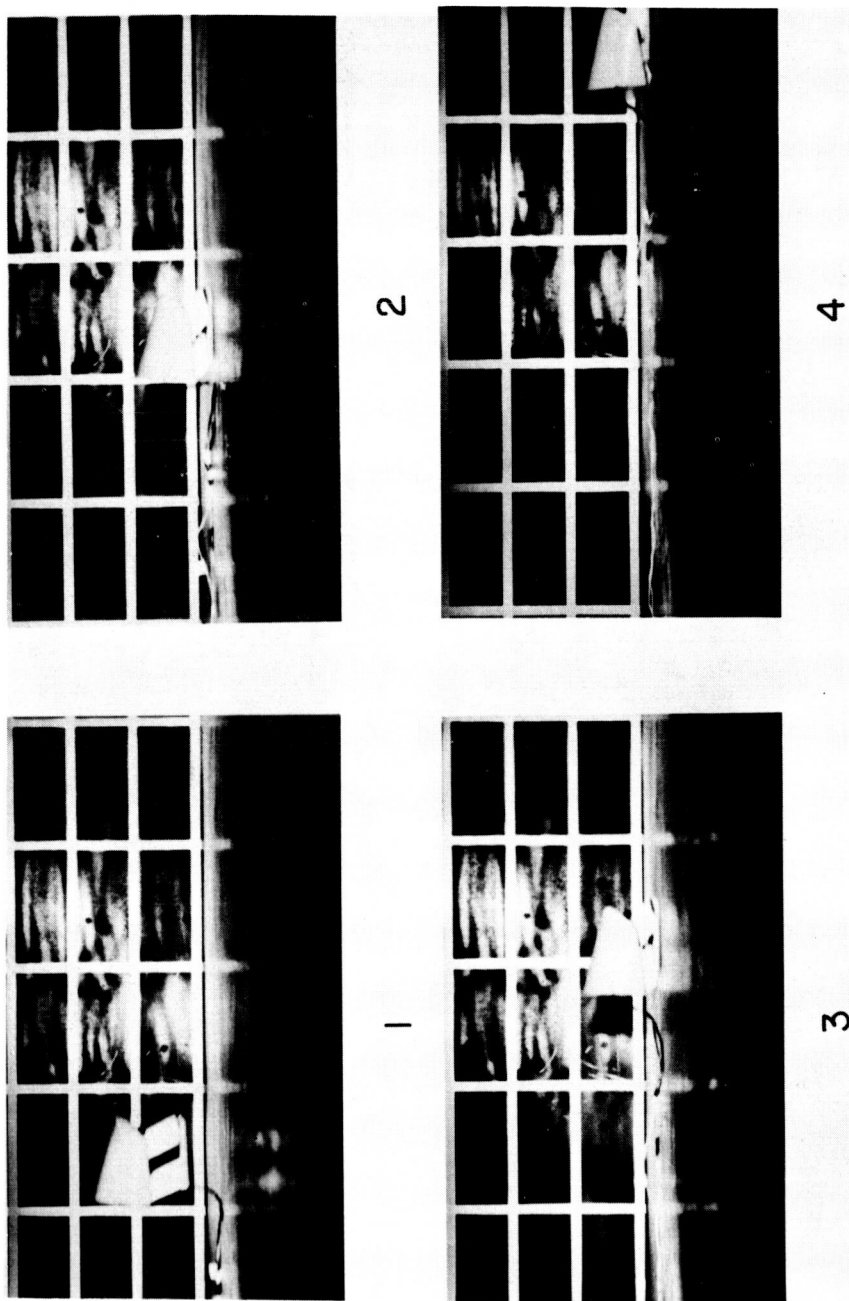
Figure 8

L-61-4813

DECLASSIFIED

037126036

MULTIPLE-AIR-BAG MODEL LANDING ON CONCRETE

 $V_h = 60 \text{ FPS}$; $V_v = 30 \text{ FPS}$ 

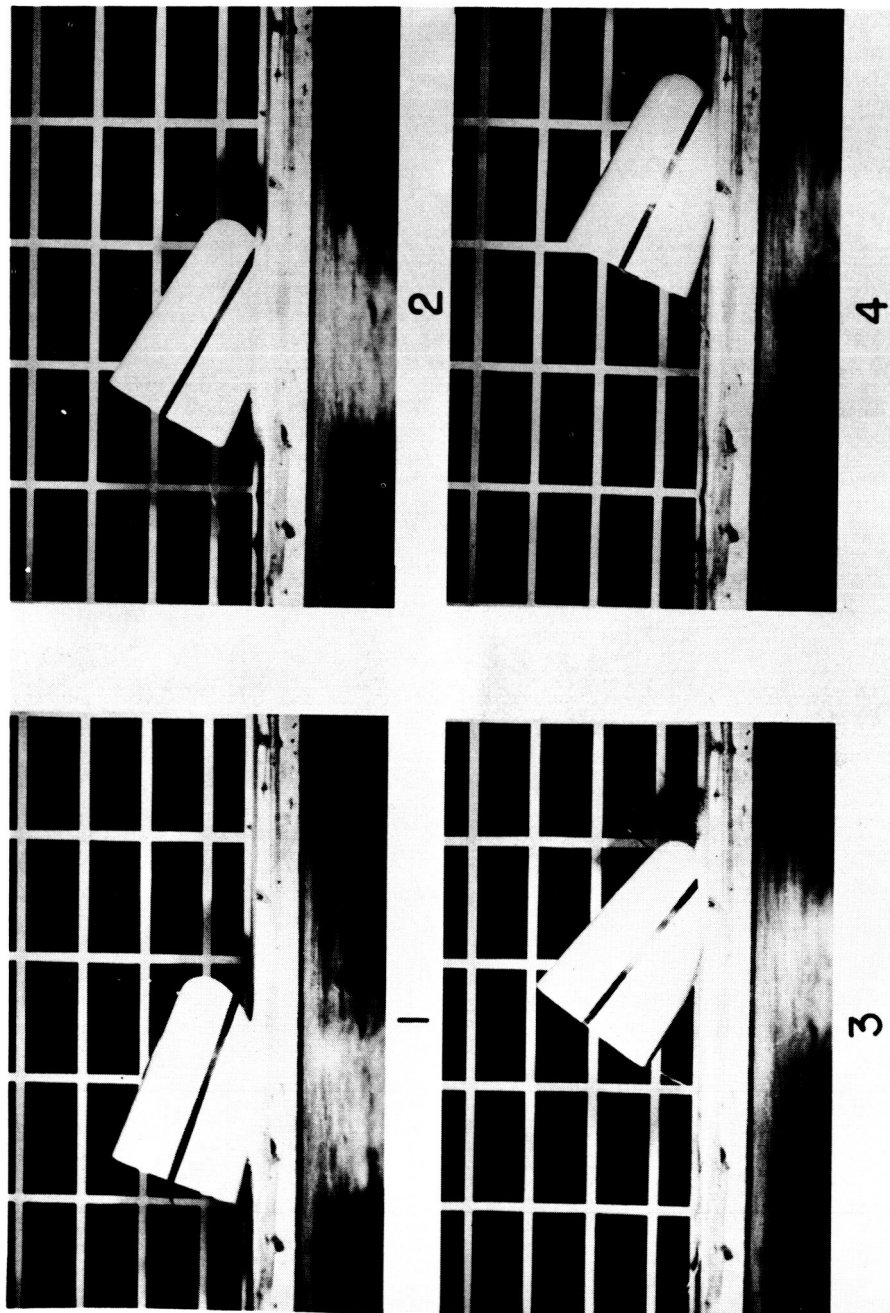
L-61-4812

Figure 9

DECLASSIFIED

459

L-4 MODEL LANDING ON SAND
 $V_h = 30 \text{ FPS}$; $V_v = 15 \text{ FPS}$



L-61-4814

Figure 10

03717-00000000

L-2C MODEL LANDING ON HARD-SURFACE RUNWAY

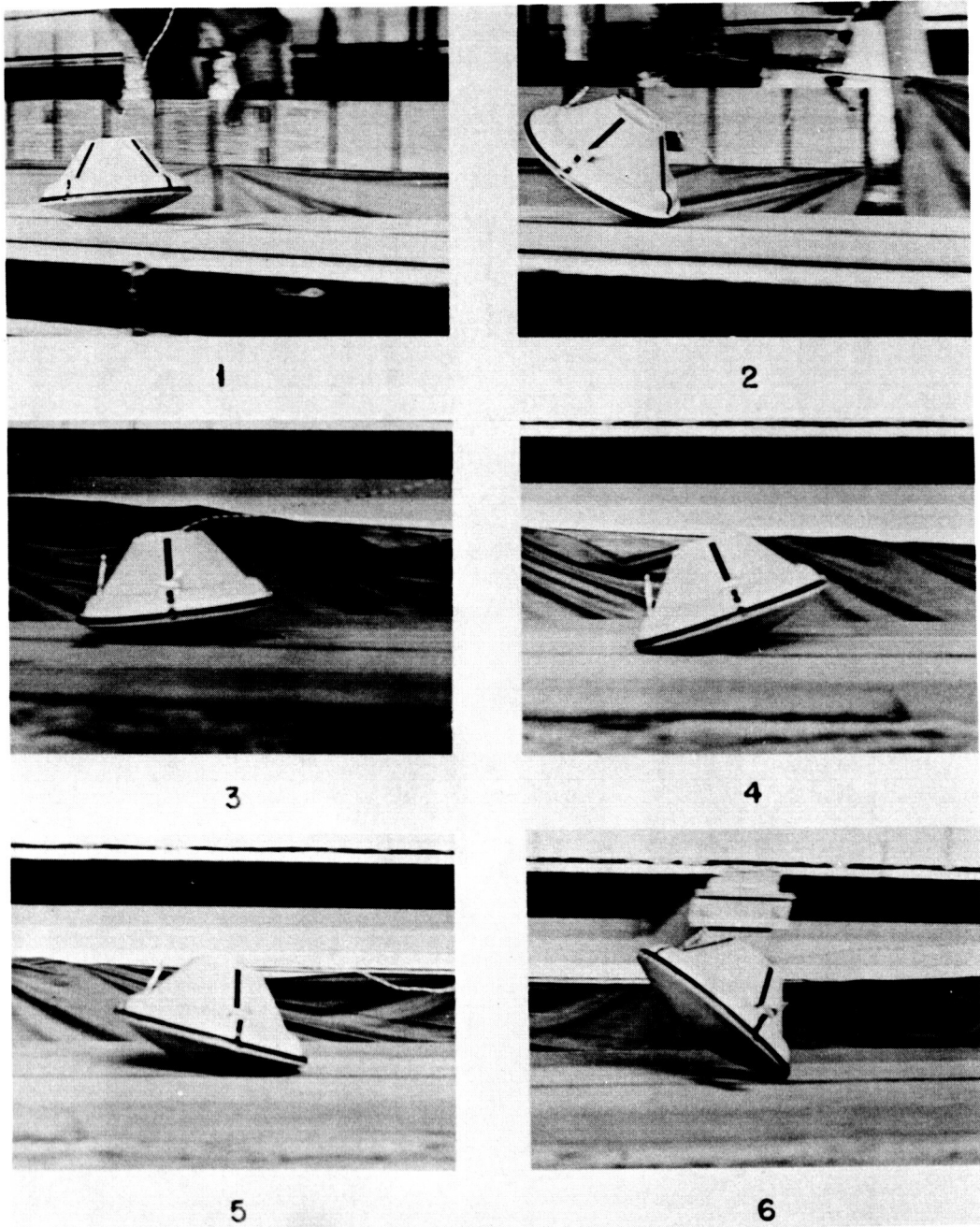
 $V_h = 80 \text{ FPS}; \frac{\text{CENTER OF GRAVITY}}{\text{BASE DIAM.}} = 0.2$ 

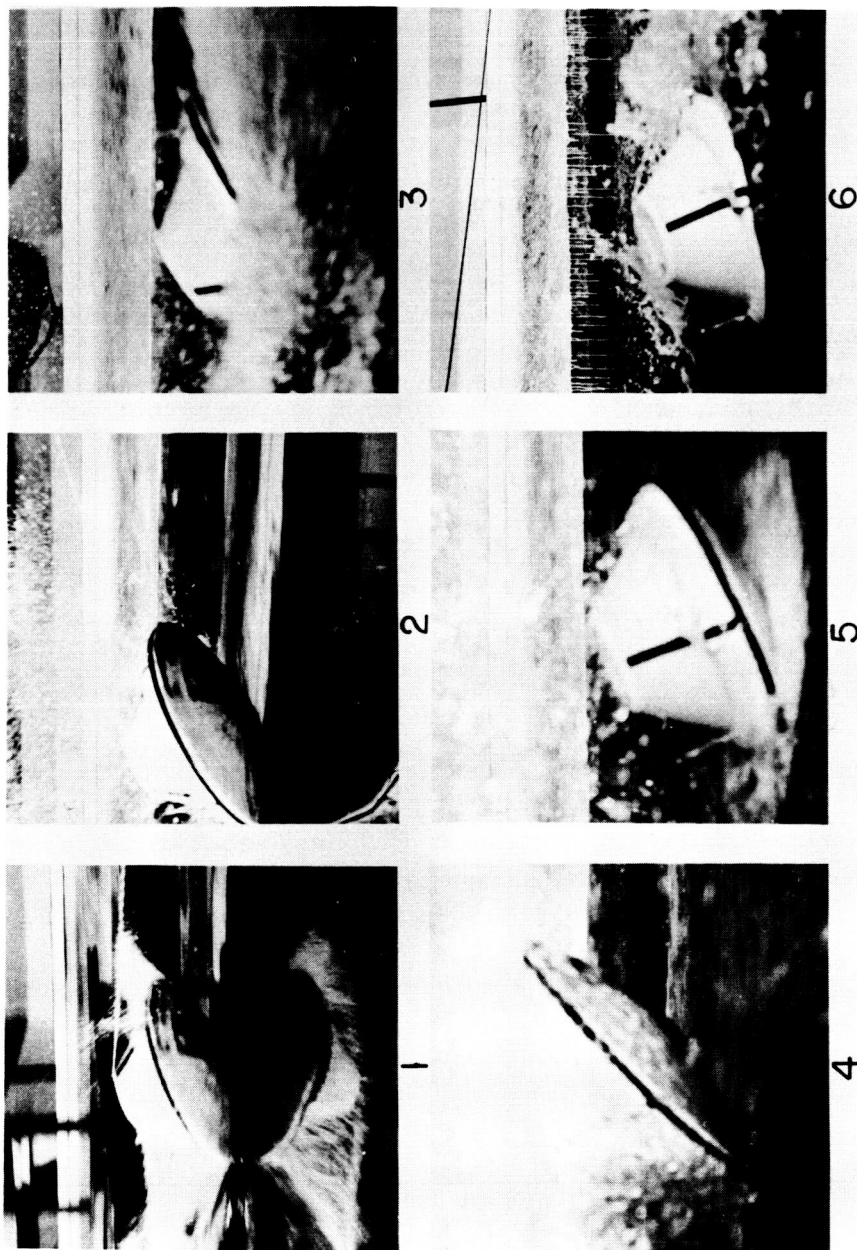
Figure 11

L-61-4811

DECLASSIFIED

461

L-2C MODEL LANDING ON WATER
 $V_h = 80 \text{ FPS}$; $V_v = 5 \text{ FPS}$



L-61-4810

Figure 12

0371 [REDACTED] 030

TURNOVER CHARACTERISTICS FOR L-2C CONFIGURATION

HARD-SURFACE RUNWAY; $V_V = 10$ FPS

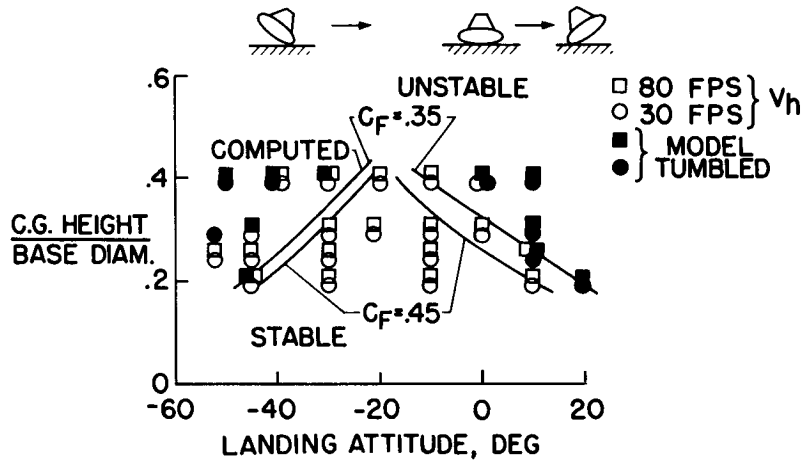


Figure 13

MULTIPLE-AIR-BAG LOAD ALLEVIATORS

$V_V = 30$ FPS

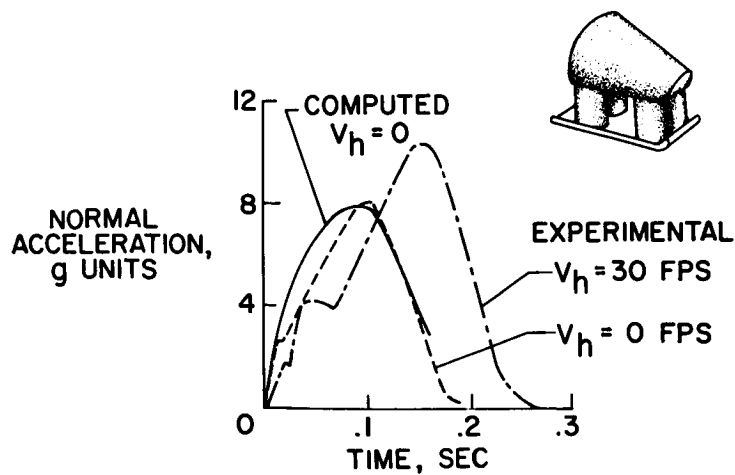
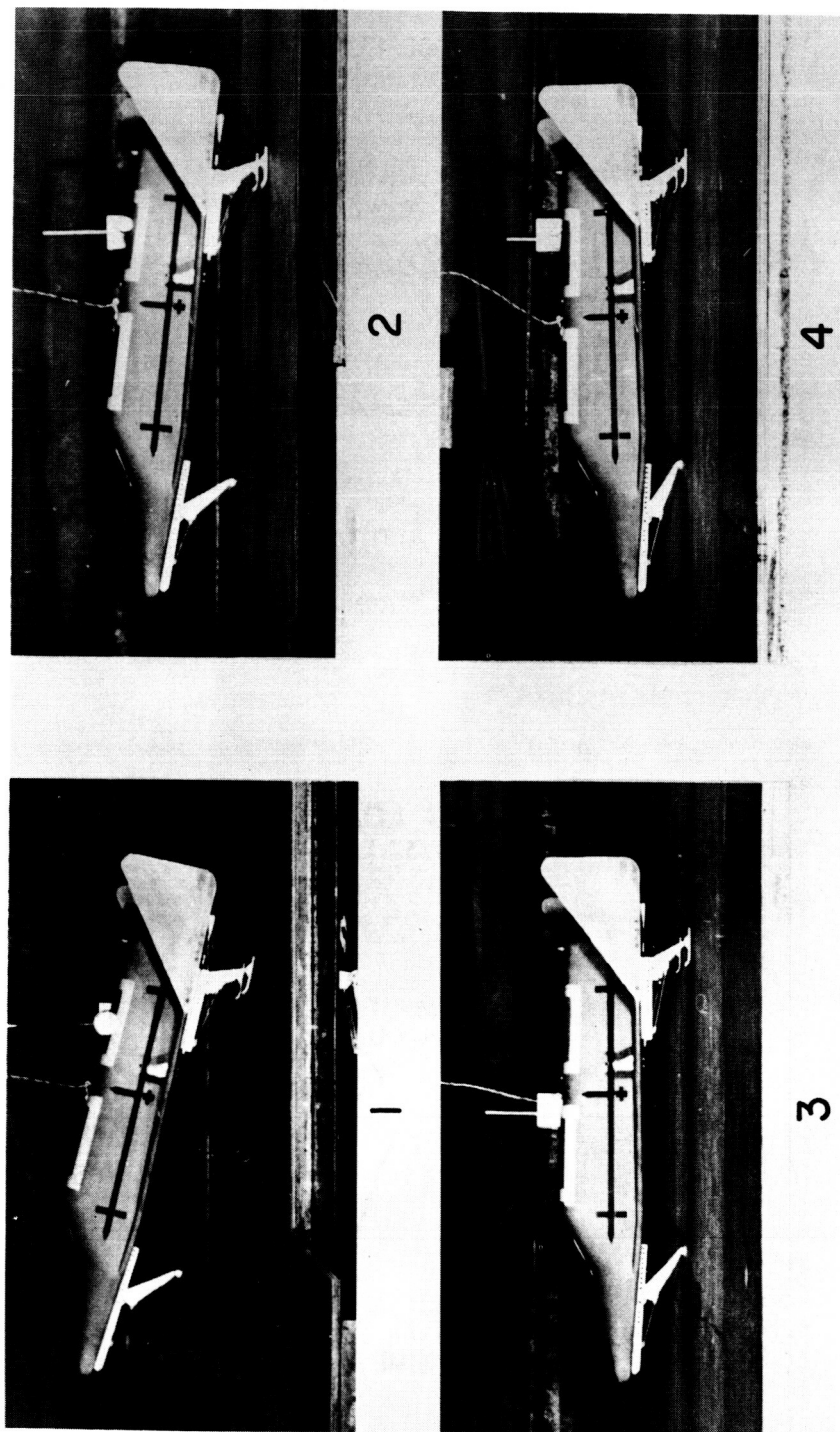


Figure 14

DECLASSIFIED

463

STRAIN-STRAP MODEL LANDING ON HARD-SURFACE RUNWAY
 $V_h = 185$ FPS



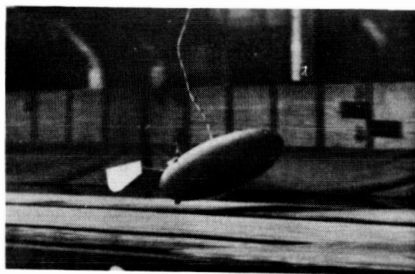
I-60-7693

Figure 15

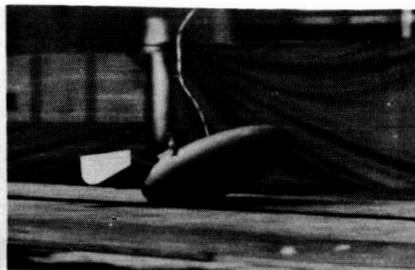
CONFIDENTIAL

031712000030

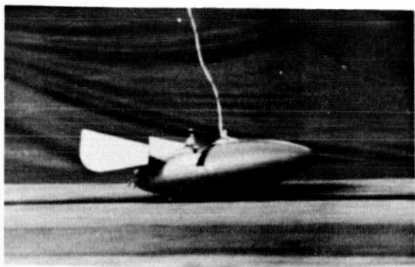
LENTICULAR MODEL LANDING ON HARD-SURFACE RUNWAY
 $V_h = 150 \text{ FPS}$



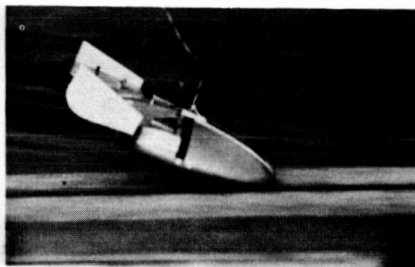
1



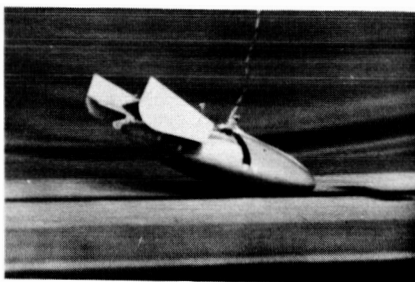
2



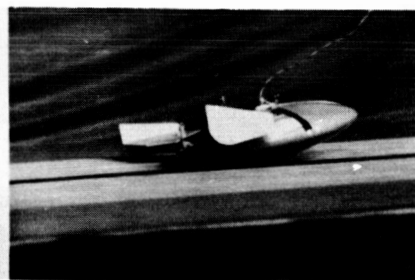
3



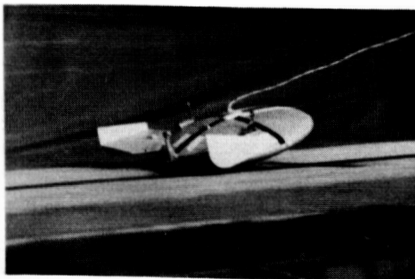
4



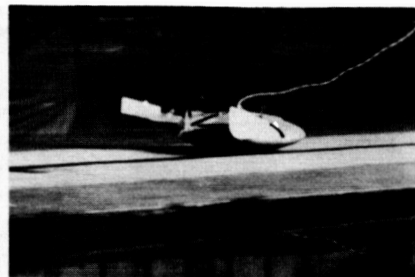
5



6



7



8

Figure 16(a)

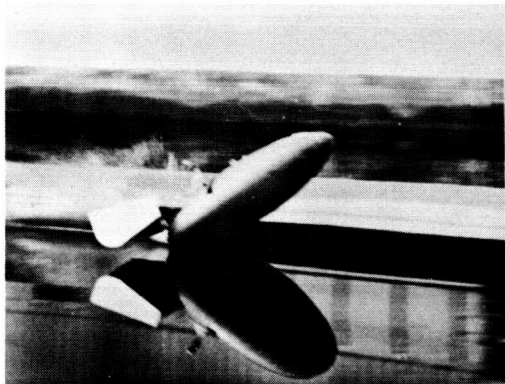
L-60-7694

DECLASSIFIED

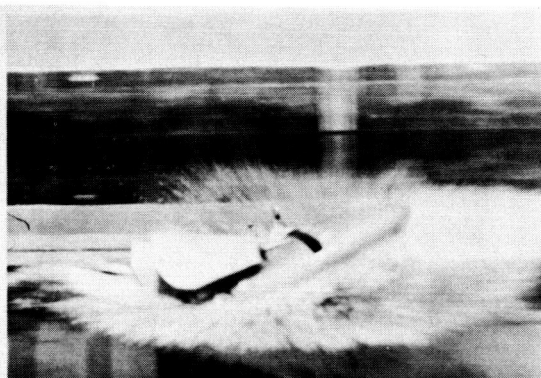
465

LENTICULAR MODEL LANDING ON WATER

$V_h = 135$ FPS



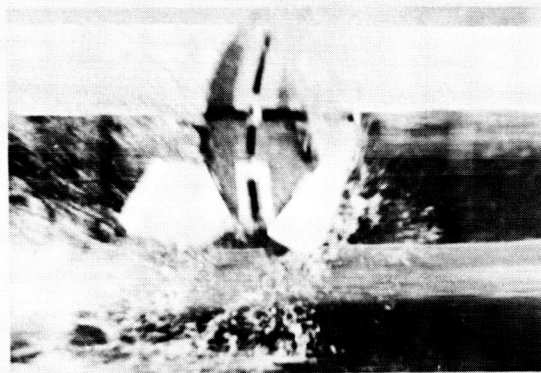
1



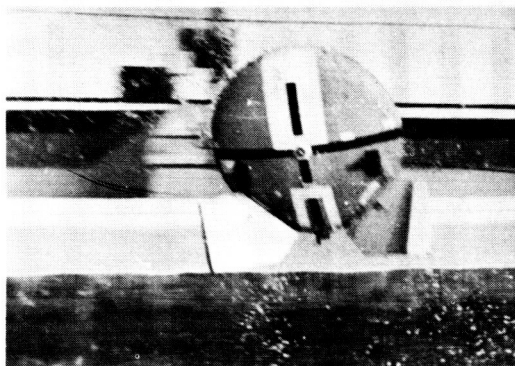
2



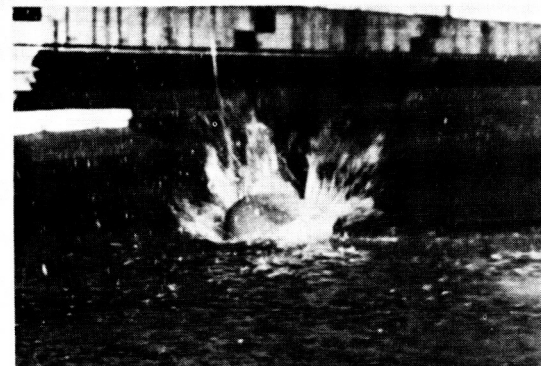
3



4



5



6

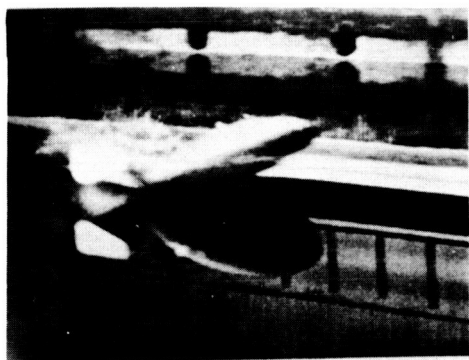
L-61-2102

Figure 16(b)

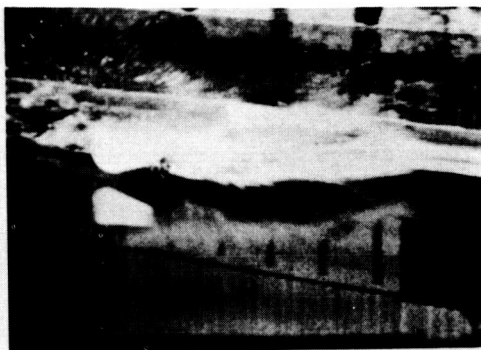
DECLASSIFIED

03 7 1 2 3 4 5 6 7 8 9 10 11 12 13 14 15 16 17 18 19 20 21 22 23 24 25 26 27 28 29 30 31 32 33 34 35 36 37 38 39 40 41 42 43 44 45 46 47 48 49 50 51 52 53 54 55 56 57 58 59 60 61 62 63 64 65 66 67 68 69 70 71 72 73 74 75 76 77 78 79 80 81 82 83 84 85 86 87 88 89 90 91 92 93 94 95 96 97 98 99 100

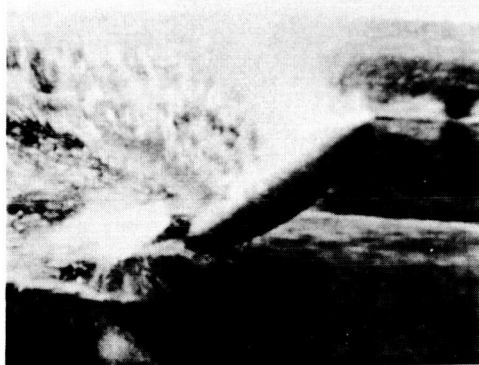
LENTICULAR MODEL LANDING ON WATER
 $V_h = 85 \text{ FPS}$



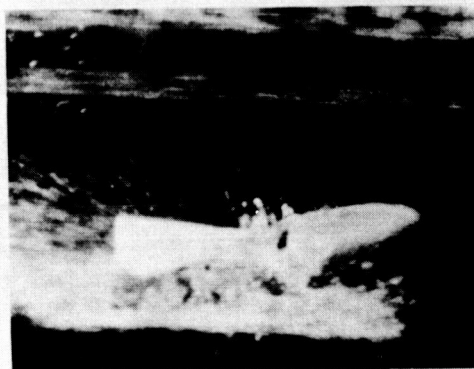
1



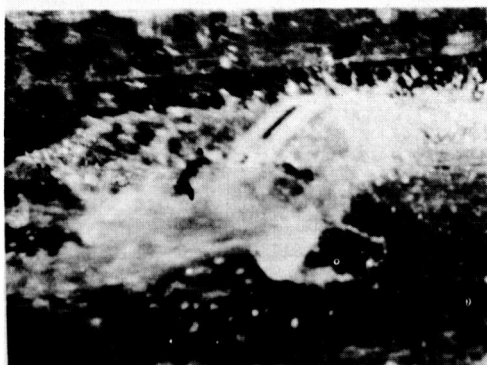
2



3



4



5



6

Figure 16(c)

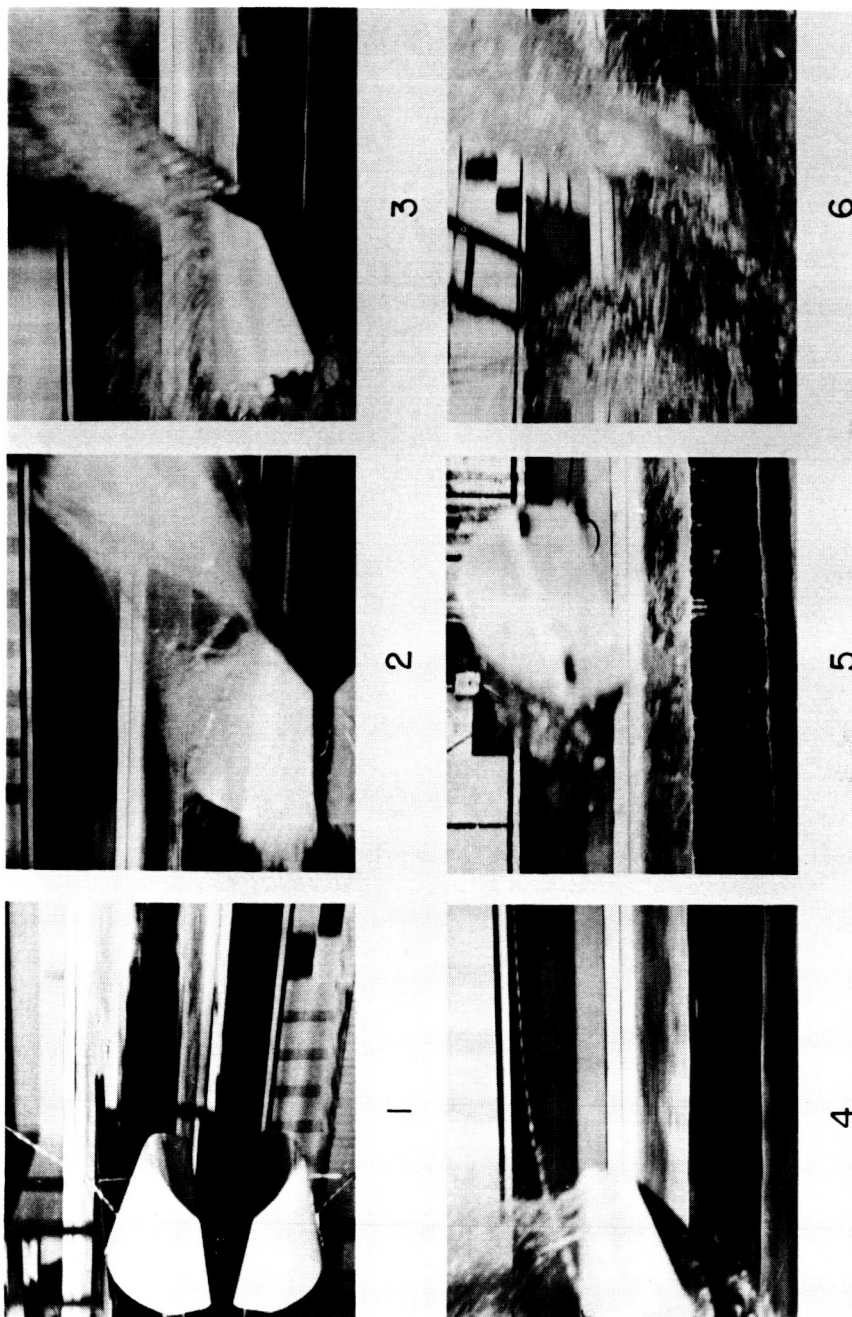
L-61-4807

ALL

CONFIDENTIAL

467

L-1 MODEL LANDING ON WATER
 $V_h = 130 \text{ FPS}$



L-61-4809

Figure 17

CONFIDENTIAL

03712001030

LANDING GEAR COMPONENTS

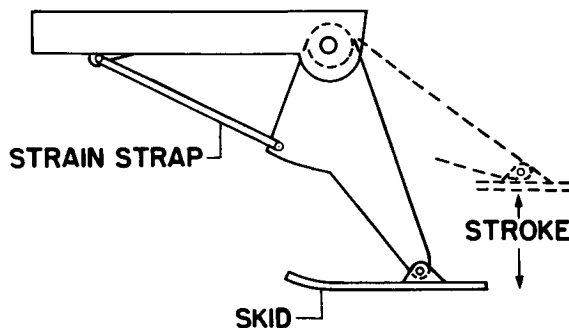


Figure 18

STRAIN-STRAP LOAD ALLEVIATOR

$V_h = 185 \text{ FPS}$; 8,000 LB; LANDING ATTITUDE, 15°

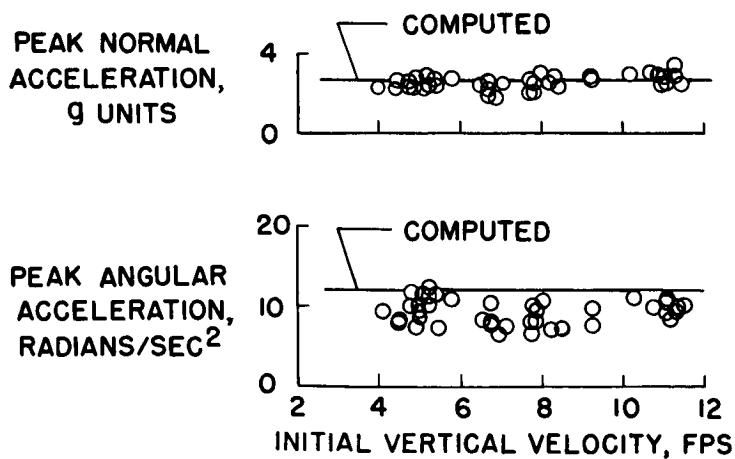


Figure 19

LENTICULAR-SHAPED REENTRY VEHICLE
 $V_h = 150$ FPS; WT., 5100 LB; LANDING ATTITUDE, 30° ; $V_v = 5$ FPS

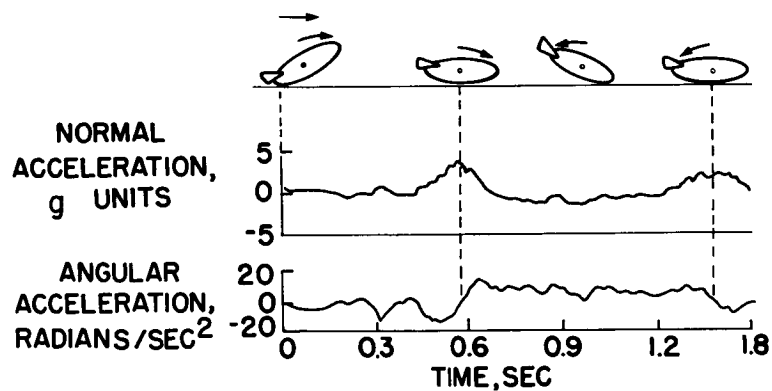


Figure 20

DECLASSIFIED

**VII.
CREW
PARTICIPATION**

DECLASSIFIED

471

CREW PARTICIPATION IN THE APOLLO MISSION

By Milton A. Grodsky, Gerard W. Levy,
Herbert B. Jacobson, and George J. Rosinger

The Martin Company

INTRODUCTION

The role of the crew in manned space systems has been debated at length for the last 4 years. During this period, man has been placed in space, and his operational proficiency has to some extent been demonstrated. However, the exact tasks a crew would perform and their contributions to the system when they perform those tasks have not as yet been clearly delineated. In conceptualizing the Apollo system it was evident that man's part in it influenced the operational concept, the various subsystem designs, and the training and selection of the crew. Two general design approaches were available:

1. Carry the crew as a passive element performing only primitive in-flight functions and onboard control. Here the crew would be relegated to the role of a biological testing organism or an experimenter collecting data on other biological organisms. This approach would then indicate that primary navigational and reentry control would not be onboard.
2. Carry the crew as a completely integrated portion of the Apollo system and assign them those tasks and functions which are within their capabilities.

The latter approach was chosen. The remainder of this paper considers in detail some of the important elements of this approach; the methods utilized to evaluate man's performance in the system, the function of the crew in relation to various subsystems in terms of operational and scientific tasks, the contributions to the system by crew task performance, and the crew information display requirements.

METHODS FOR EVALUATING CREW PERFORMANCE

Previous studies have developed methods for forecasting man's role in the space systems. The following steps are involved:

1. Determine the specific mission in terms of system performance tolerances.

2. Determine which of these system functions should be manned or unmanned by using analytical and empirical techniques to determine man's capabilities in terms of system performance. (The results provide an index of the contribution of man to system reliability, flexibility, etc.)

3. Determine the specific functions of the crew by means of man-machine analytic techniques.

4. From the outcome of the function analysis, determine the information requirements of the crew. Develop a display system concept based on the information requirements, the internal cabin configuration, and the operational concept.

5. Perform those studies necessary to insure efficient performance of the crew at all times. (For the Apollo system, this step included study of work-rest cycles, information processing, vigilance, and decision-making behavior.)

The feasibility of the system is estimated on the basis of these data and the physiological and psychological considerations necessary to keep the crew physically sound and capable of performing their assigned tasks.

CREW FUNCTIONS

Data were obtained from sequential activities analysis and a discontinuous control analysis predicated on the following two assumptions: First, man's capabilities will be used to the maximum degree without jeopardizing the feasibility of the system, and second, man will not be used in those conditions in which the environmental stress is high or in which his performance is limited by environmental stress. This latter assumption is based on the ability of the automatized systems to perform appropriate functions during these periods. The following results are based on these assumptions.

Sequential Activities Analysis

A sequential chart of events that occur within a typical lunar mission indicates five general functions of the Apollo crew:

1. Information processing
2. Decision making

3. Continuous psychomotor activity
4. Discrete psychomotor activity
5. Troubleshooting and maintenance.

The first four of these functions are actually capabilities of the operator while troubleshooting and maintenance is a specific system function. This specific function was, however, deemed important and unique enough to be considered with these other capabilities.

Information processing and decision making.- The functions of the crew with regard to information processing and decision making cannot be discussed independently. Adequate decision making requires the operator to detect and discriminate sensory inputs in a meaningful manner. Hence, adequate decision making involves information processing. From the proper or adequate processing of information, the operator would then choose a behavior from a set of alternative behaviors which would either maximize or minimize a certain index. In order to quantify this behavior, the performance of the system was divided into discrete mission periods as follows:

1. Launch
2. Coast
3. Injection into translunar orbit
4. Translunar orbit
5. Injection into lunar orbit
6. Lunar orbit
7. Injection into transearth orbit
8. Transearth orbit
9. Reentry

Considered as a separate item, although not temporally related to the discrete mission periods, were systems checks performed during coast and prior to, and subsequent to, injection into both lunar orbit and transearth orbit. Table I presents the number of information-processing and decision-making tasks performed during each mission phase. The best indication of crew information-processing functions is the number of information channels to be monitored, as shown in table I. Each information-processing task does not lead to an explicit decision

response; therefore, the number of decisions does not correspond to the number of information channels. As can be seen from the table, the major information-processing and decision-making activity takes place during the translunar orbit, lunar orbit, and transearth orbit phases. However, it should be noted that the time periods are longer during these periods than during launch and reentry. Other analyses have shown that the rates of decision making and information processing are similar during the launch and reentry periods and during the longer orbital periods.

The information channels monitored by the crew provide information concerning operational status of the system. As stated previously, at some point in time the information gained by the crew will be used in making a decision concerning the system. For example, given a situation where a subsystem malfunction has occurred during a lunar mission, the alternative decisions are:

1. Abort the mission and return to earth as quickly as possible.
2. Change the mission parameters; instead of attempting to complete a lunar orbit mission, shift emphasis to an earth orbit, a cislunar, or a circumlunar mission. (The choice of the particular shift in mission emphasis is dependent not only on the subsystem malfunction, but also on the time after launch that the malfunction takes place.)
3. Attempt to complete a lunar orbit mission without the subsystem or by performing maintenance to correct the malfunction.

For any one particular system malfunction, it is not difficult to make a decision with the help of an in-flight systems check. However, when there is a combination of reduced system performance indices or equipment malfunctions, the correct decision is clearly more difficult. An automated computer could present to the crew the probabilities involved. However, the choice of the estimated probabilities of successful mission completion which would be acceptable to the crew is still another matter. Using the crew in this decision capacity in the past has given greater flexibility to conventional systems. There does not seem to be any reason to believe that this flexibility would be lost in manned space flight.

In the operation of the navigation and propulsion systems, crew performance would be essentially as described previously. Consider now a specific example of the crew's functions with the propulsion system in a decision-making context. Assume that immediately after igniting the main engine for an injection into lunar orbit, the engine performance levels are much less than expected and that it is apparent that the main engine will expend excessive fuel before giving the vehicle the velocity increment to inject it into a lunar orbit. Since the crew will

DECLASSIFIED

475

have a continuous presentation of main-engine performance (fuel flow and thrust) and an indication of inertial velocity and inertial attitude, it is possible to shut the engine down, reverse the vehicle attitude, and fire the main engine again to counteract the original velocity impulse. This procedure would serve the purpose of putting the vehicle back into a circumlunar trajectory, and the safety of the crew would be insured.

Continuous psychomotor activity.- Continuous psychomotor activity is defined as behavior which involves the control of proprioceptive responses by the utilization of stored information over an extended period of time. During reentry and at various times during translunar, lunar, and transearth mission phases of a lunar orbit mission, reorientation of the vehicle attitude becomes necessary. This attitude reorientation function is an example of continuous psychomotor activity. Analysis has indicated that the pilot may have to change vehicle attitude perhaps 65 to 70 times in deep space during a lunar mission. Also, during reentry the crew will have continuous control of the vehicle flight path where vehicle attitude is controlled by the command module attitude control rockets and the control flaps.

Discrete psychomotor activity.- Discrete psychomotor activity involves control of proprioceptive responses by the utilization of stored information over a short interval of time. The following are examples of discrete psychomotor performance demanded of the crew:

1. Communication system:
 - a. Switch from VHF to deep space net after injection into translunar orbit.
 - b. Turn on deep space net at those times during lunar orbit phase when vehicle communications are not blocked by the moon.
2. Environmental control system:
 - a. Switch from LiOH filter system to molecular sieve filtering system after injection into translunar orbit.
 - b. Switch atmosphere (O_2 and N_2) supply from mission module to pressure suit prior to reentry.
3. Propulsion system:
 - a. Switch off main or vernier propulsion systems in deep space in case of abnormal firing.
 - b. Switch from nonoperational attitude rocket to backup attitude rocket in case of failure.
4. Electrical system:
 - a. Switch fuel cells in case of drop in output.
 - b. Switch from fuel cell bus to recovery bus just prior to dropping mission module.

5. Guidance system:

- a. Switch on automatic guidance routine when a fix is desired.
- b. Enter propulsion system parameters for midcourse guidance corrections and injections into correction control panel.

6. Miscellaneous activities:

- a. Serve as backup to boost stages during launch.
- b. Backup main parachute release during landing sequence.

Allowing the crew to perform these functions has certain advantages: It decreases the weight of additional sensors, switching mechanisms, computer circuitry and computer input-output devices; also, the flexibility of the system is increased, since the crew can adjust their outputs to variable situations more rapidly and with less complexity than can an automated system. The following table summarizes the number of discrete psychomotor tasks performed by the Apollo crew during a lunar orbit, the performance of which eliminates the need for equipment necessary to perform a total of 998 switching or adjusting functions:

Mission phase	Number of discrete psychomotor tasks
Launch	5
Coast	5*
Injection into translunar orbit	0
Translunar orbit	271*
Injection into lunar orbit	0
Lunar orbit	178*
Injection into transearth orbit	0
Transearth orbit	330*
Reentry	4

*Not including systems check.

Troubleshooting and maintenance.- Involved in the troubleshooting and maintenance functions are, first, the detection and localization of malfunctions and, second, the performance of an activity which reinstates the system or changes the mission parameters after a malfunction is localized.

Detection and localization of malfunctions is a type of behavior which primarily makes use of the crew's capability as information-processors and decision-makers. Various laboratory studies have been conducted by The Martin Company for Project Apollo which have indicated that the human operator approaches an ideal strategy in his ability as a malfunction diagnostician. In order to utilize this ability in the

Apollo system, an in-flight systems check was developed which gives the crew a more comprehensive evaluation of system operation than can be gained from monitoring system status alone. The systems check includes switching from operation to backup equipment and measuring performance, feeding artificial signals to various systems, measuring systems outputs, and examining present system levels and projecting them ahead in time to predict future conditions. The results of the systems check will give the crew an adequate basis for a decision to abort, to continue the lunar orbit mission, or to change mission parameters. The important aspect of this in-flight systems check is that it can be performed during coast phases, preinjection phases, and immediately after injection. This process allows the crew to ascertain the condition of the entire system prior to committing to another mission phase. The entire systems check is estimated to take approximately 30 to 35 minutes.

Following is an example of a system check to evaluate the electrical system:

1. Battery check:
 - a. Switch the fuel cells off the line.
 - b. Switch the battery on the line.
 - c. Check output voltage (28 volts).
 - d. Switch fuel cells back on line.
 - e. Check to see that the battery is being charged.
2. Fuel cell and voltage regulator check:
 - a. Turn off one fuel cell at a time.
 - b. Observe to see if the redundant system picks up the load evenly.
 - c. Observe temperature.
 - d. Observe bus voltage.

There are approximately 30 additional steps which the crew would perform to evaluate the status of the electrical system. The complete check would take approximately 10 to 12 minutes. All three crew members take part in the checks of all subsystems. Figure 1 presents the number of functions required by the crew during a systems check in terms of information-processing, decision-making, and discrete-psychomotor tasks. It can be seen from this figure that the predominance of tasks is in the monitoring and discrete psychomotor tasks and that these form the heart of the systems check.

Correction of a system malfunction in the Apollo system is considered to involve the switching in of a redundant component to replace a failed component, or the repair of a failed component. Spare modules and limited repair facilities are carried onboard. This in-flight

[REDACTED]

maintenance concept considers three types of system or component failures:

1. Random failures, usually expressed by hourly failure rates.
2. Failures caused by severe environment, such as vibration, high humidity, etc. (These failures were considered by multiplying the basic hourly failure rate by an appropriate environmental modifier.)
3. Failure caused by old age. (Given adequate test and storage this type of failure is not considered important.)

The type of maintenance performed would be the plugging in of spare modules which cannot be designed for automatic actuation in case of failure, and the switching on of spare modules by activating automatic circuitry. The manual maintenance allows the use to the best advantage of a limited number of modules in a large number of systems. This conclusion assumes, of course, that there are many modules which can be of similar design and are interchangeable within the various subsystems. An example of this type of maintenance is found in the primary guidance computer and its backup, which consist of a large number of similar modules. If the primary computer fails, the redundant computer is available. The primary computer may be repaired by replacing the failed module by a plug-in method or by switching in a module by activating automatic circuitry. Once the subsystem becomes operational, repair could take place on the failed module. This repair would consist of submodular replacement at the level of transistor modules. The repair would merely be plugging in these submodular elements. The repaired element would then be tested and returned to the spares area.

Work Load Analysis

From a task analysis of Apollo crew functions, estimates were made of the times involved in both monitoring tasks and discontinuous control tasks. Crew loadings were then developed in terms of time to accomplish each task. Thus, possible operator overload trouble points were eliminated and sequences modified when needed. The discontinuous control analysis, as stated previously, involves the time required by the operator to monitor information displays, check systems, switch, communicate, and perform all other discrete events. This analysis in Apollo was based not only on the task analysis but on the proposed display-control configuration.

The three crew members of the Apollo system were designated as Pilot-Commander (P-C), Navigator-Pilot (N-P), and Engineer-Scientist (E-S). The work loads were estimated on the basis of the duty stations these crew members occupied. As all the crew members cannot be on duty continuously for a 14-day mission, the work load analysis considered

[REDACTED]

the duty stations manned in a work-rest cycle of 10 hours on duty, 8 hours sleep, and 6 hours off duty. The 10-hour work period was interrupted by off-duty periods.

Tables II and III present the results of the work load analysis. As can be seen, there is no overload upon the crew. In fact, the operational tasks with a slight shift in emphasis, in terms of automation, could be conducted by only two crew members. The third crew member, however, increases the scientific capability of the system. It should be noted that these work load analyses do not consider lunar landing or lunar take-off. They are confined to the lunar orbit mission.

CONTRIBUTIONS AND INFORMATION REQUIREMENTS OF THE CREW

The contributions of man to the Apollo system in a quantitative sense are: (1) flexibility of the system and (2) maintenance and troubleshooting. These two elements have been discussed previously. A third element is reduction of reliability degradation.

One of man's major contributions is a high level of reliability over extended periods of time, which insures mission completion. The crew acts as a sensor, switcher, and decision computer. Figure 2(a) presents the results of analyses performed by The Martin Company concerning the variation of reliability with time of the Apollo guidance system with man, without man, and with redundant automatic systems. Figure 2(b) presents the variation of reliability with weight with man and without man for both the guidance system and the telemetry and communication subsystem. The results clearly indicate that man increases reliability for a 14-day period and decreases weight required for the systems analyzed as a function of reliability.

A display system concept was developed on the following assumptions:

1. Only the information required by the crew to perform their tasks will be displayed.
2. Information will be displayed to the crew in a form compatible with human sensory capabilities.
3. The various classes of displays associated with various categories of information will be integrated.
4. Sufficient redundant information will be provided to insure detection and reliability.

5. As an aid to display integration, the time-sharing of various displays will be utilized.

The basic categories of display to be provided to the crew will consist of vehicular information, environmental information, and scientific information. Figure 3 presents a possible display subsystem. The right and left sides of the main panel would each present launch and reentry sequence information. During critical mission phases, such as navigation corrections or reentry, it is desirable to have redundant displays and controls, since this redundancy allows the crew to check each other and provides increased reliability of the instruments. Reentry information can be displayed prominently before both the Pilot-Commander and the Navigator-Pilot. Between them and accessible to both are navigation displays and controls. Systems status warning lights, since they do not involve control actuation, are placed along the top of the main panel.

The panel for the Engineer-Scientist contains detailed information about systems such as environmental control, propulsion, and electrical power. Scientific displays are made available here and in the mission module. All displays can be observed from the Navigator-Pilot's seat with this display system concept. This concept allows one crew member to return the vehicle, with access to all displays and necessary controls.

CONCLUDING REMARKS

The method of analyses, crew functions, crew work loads, and the contributions and information requirements of the crew have been described. The results indicate that the crew can be well integrated into the Apollo system and can participate in most of the subsystems.

The results also indicate that the crew contributes to flexibility and reliability and insures the completion of the mission by being able to troubleshoot malfunctions and perform maintenance. The work load analyses indicates that the operational functions can be performed by two crew members as well as three. In case of emergency, the spacecraft can be operated by one man.

A display system concept is presented which transmits to the crew the information required to perform their functions.

TABLE I.- MONITORING AND DECISION FUNCTIONS

Mission phase	Number of channels monitored	Number of decision functions
Launch	39	10
Coast	8*	3*
Injection into translunar orbit	44	7
Translunar orbit	203*	48*
Injection into lunar orbit	38	7
Lunar orbit	109*	28*
Injection into transearth orbit	38	7
Transearth orbit	244*	51*
Reentry	24	6

*Not including systems check.

03 30 35 35

TABLE II.- OPERATOR WORK LOADS

Mission phase	Operator work load, percent of one man's total capability, for -		
	Pilot-Commander	Navigator-Pilot	Engineer-Scientist
Launch	57	53	22
Coast (systems check)	60	70	90
Navigation fix	78	30	--
Midcourse correction	61	2	--
Injection into lunar orbit	26	30	--
1 hour prior to reentry	38	36	20
5 minutes prior to reentry	16	5	35
Landing	65	60	15

TABLE III.- TOTAL WORK LOAD ESTIMATES

Mission phase	Command module, percent of one man's total capability for -			Total work load, percent of one man's total capability
	Pilot-Commander	Navigator-Pilot	Engineer-Scientist	
Launch	60	55	22	137
Coast	60	80	40	180
Injection	70	100	20	190
Separation	100	50	20	170
Translunar orbit:				
Beginning	60	70	25	155
Orbit	45	50	20	110
Navigation fix	100	95	15	210
Midcourse	61	10	30	191
correction				
Injection into	70	70	25	165
lunar orbit				
Lunar Orbit	75	100	25	200
Injection into	70	70	25	
transearth orbit				
Transearth orbit		(Same as translunar)		
Reentry:				
1 hour prior	85	65	35	185
5 minutes prior	60	45	50	155
Reentry	80	65	25	170
Landing	65	60	15	140

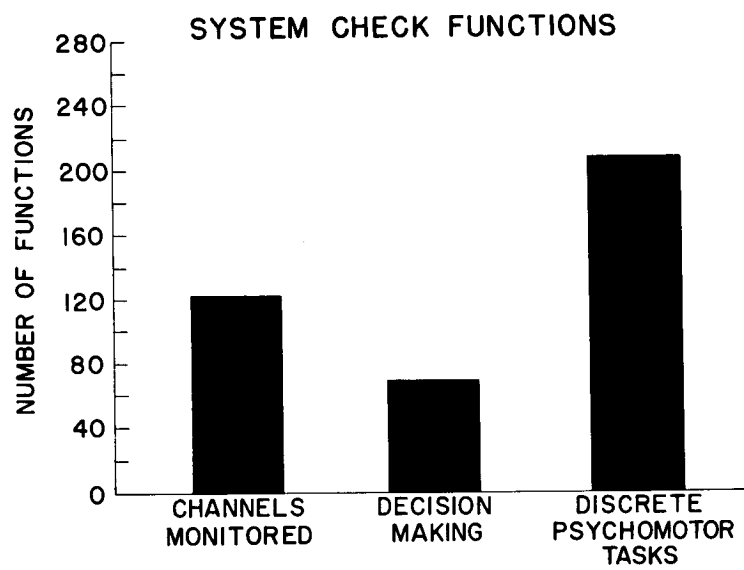


Figure 1

DECLASSIFIED

485

MAN'S CONTRIBUTION TO THE APOLLO SYSTEM

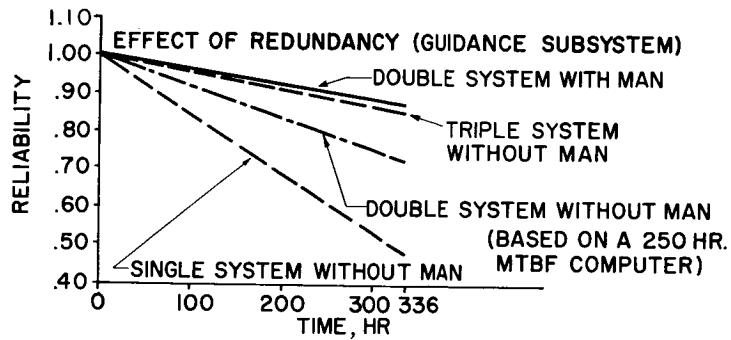


Figure 2(a)

MAN'S CONTRIBUTION TO THE APOLLO SYSTEM

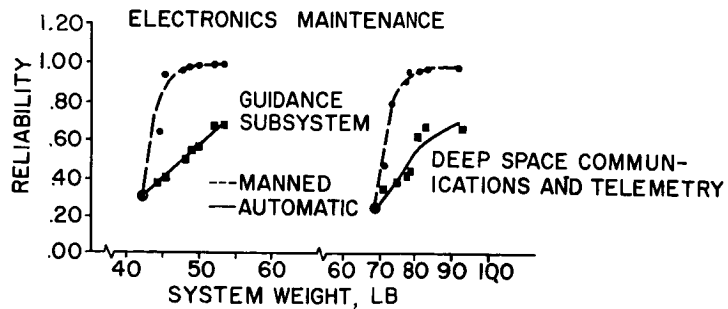


Figure 2(b)

DECLASSIFIED

03171229J030

486

DISPLAY SYSTEM CONCEPT

P-C PILOT-COMMANDER
N-P NAVIGATOR-PILOT
E-S ENGINEER-SCIENTIST

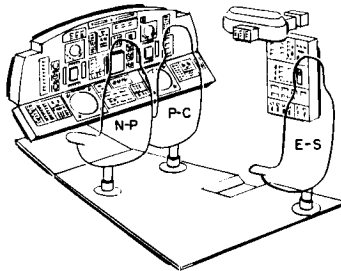


Figure 3